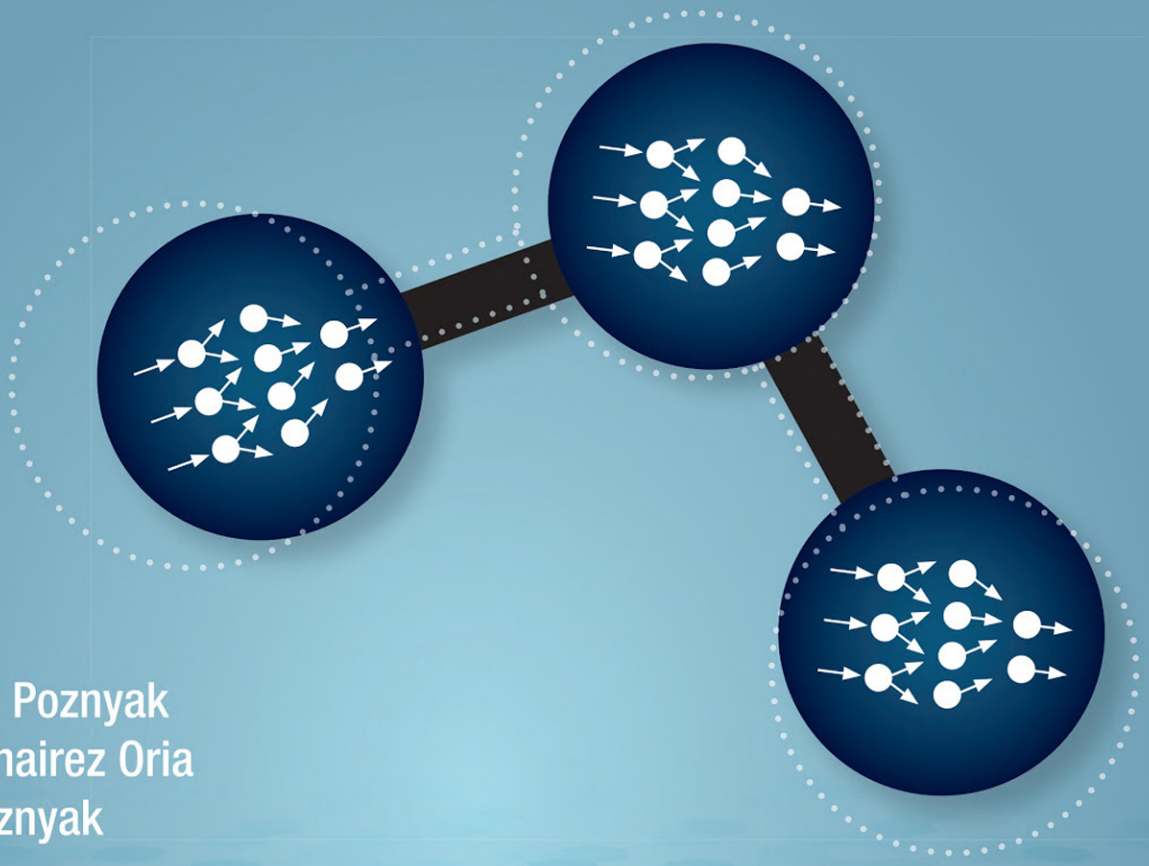

Tatyana Poznyak
Isaac Chairez Oria
Alex Poznyak

Ozonation and Biodegradation in Environmental Engineering

Dynamic Neural Network Approach

Ozonation and Biodegradation in Environmental Engineering

Dynamic Neural Network Approach

Ozonation and Biodegradation in Environmental Engineering

Dynamic Neural Network Approach

Tatyana I. Poznyak

Isaac Chairez Oria

Alexander S. Poznyak

Elsevier
Radarweg 29, PO Box 211, 1000 AE Amsterdam, Netherlands
The Boulevard, Langford Lane, Kidlington, Oxford OX5 1GB, United Kingdom
50 Hampshire Street, 5th Floor, Cambridge, MA 02139, United States

Notices

Knowledge and best practice in this field are constantly changing. As new research and experience broaden our understanding, changes in research methods, professional practices, or medical treatment may become necessary.

Practitioners and researchers must always rely on their own experience and knowledge in evaluating and using any information, methods, compounds, or experiments described herein. In using such information or methods they should be mindful of their own safety and the safety of others, including parties for whom they have a professional responsibility.

To the fullest extent of the law, neither the Publisher nor the authors, contributors, or editors, assume any liability for any injury and/or damage to persons or property as a matter of products liability, negligence or otherwise, or from any use or operation of any methods, products, instructions, or ideas contained in the material herein.

Library of Congress Cataloging-in-Publication Data
A catalog record for this book is available from the Library of Congress

British Library Cataloguing-in-Publication Data
A catalogue record for this book is available from the British Library

ISBN: 978-0-12-812847-3

Publisher: Jonathan Simpson
Acquisition Editor: Kostas Marinakis
Editorial Project Manager: Lindsay Lawrence
Production Project Manager: Omer Mukthar
Designer: Christian J. Bilbow

Typeset by VTeX

List of figures

List of tables

Preface

1) Environmental problems we face

All across the world, people are facing a wealth of new and challenging environmental problems every day. Some of them are local, but others are drastically changing a few wider ecosystems. Let us mention some major current environmental problems requiring urgent attention.

The high pollution degree of air, water and soil requires millions of years for their natural recuperation. Industry and motor vehicle exhaust of toxic compounds are the number-one pollutants, including heavy metals, aromatic compounds, nitrates etc. Water pollution may be caused by oil spill, industrial and domestic waste (as sanitary landfill leachate); air pollution may be provoked by volatile organic compounds (like BTEX), various toxic gases (like NOx, COy and others) produced in industries and by combustion of fossil fuels; the greater part of soil pollution is due to oil spill, industrial waste, and herbicides, contaminating the soil.

This book presents one of possible approaches to partially resolve ***water****,* ***air****, and* ***soil pollution*** problems with the ozone implementation technique.

2) Intended audience

First of all, this book is oriented toward researchers working in *Chemical Engineering* and, particularly, in *Environmental Engineering*, in particular those interested in the application of some modern results from *Computer Science* and *Automatic Control* areas. Besides, it may also be interesting for Computer Science and Automatic Control engineers who are looking for some real application examples to illustrate effectively new suggested methods and ideas.

The teaching experience and developing research activities of the authors convinced them of the need for such a type of book.

- It should be useful for the average student, yet also provide an in-depth and rigorous challenge for the exceptional student and acceptable to the advanced scholar.
- It should comprise a basic course of *Environment Engineering* that is adequate for all students of *Chemical Engineering specialties* regardless of their ultimate research area.
- It is hoped that this book will provide enough incentive and motivation to beginning researchers, both from the *Chemical Engineering* and *Computational Mathematics and Automatic Control* communities, and will help work in these areas.
- Generally speaking, this book is intended both for students (undergraduate, postdoctoral, research) and practicing engineers as well as designers in a variety of industries.

The book was written with two primary objectives in mind:

- to provide a list of references for researchers and engineers, helping them to find the information required for their current scientific work,
- and to serve as a text in an advanced undergraduate or graduate level course in Environmental Engineering and for Automatic Control Engineering, Computer Science and related areas.

3) Main idea of the applied approach

As mentioned above, the main approach, applied in this book for recuperation of contaminants concentration and their reaction constants with ozone, is related with *Dynamic* (in continuous-time *Differential*) *Neural Networks* (DNNs). Such a DNN is a type of advanced artificial neural network (ANN) that involves directed cycles in memory. One aspect of DNNs is the ability to build online artificial structures with a fixed size of input and output vectors, which provides a desired behavior to some variables characterizing a considered process. In fact, ANN and DNN in particular are computational models, based on the structure and functions of biological neural networks. Information that flows through the network affects the structure of the DNN, because a neural network changes or learns, based on the input and output.

One of the most impressive features of ANNs/DNNs is their ability to *learn*. Artificial neural networks are inspired by the biological nervous system (in particular, the human brain), and one of the most interesting characteristics of the human brain is its ability to learn. We should note that our understanding of how exactly the brain does this is still very primitive, although we do have a basic understanding of the process. It is believed that during the learning process the brain's neural structure is altered, increasing or decreasing the strength of its synaptic connections depending on their activity. This is why more relevant information is easier to recall than information that has not been recalled for a long time. More relevant information will have stronger synaptic connections and less relevant information will gradually have its synaptic connections weaken, making it harder to be recalled. ANNs/DNNs can model this learning process by adjusting the weighted connections found between neurons in the network. This effectively emulates the strengthening and weakening of the synaptic connections found in our brains. This strengthening and weakening of the connections is what enables the network to learn.

Learning algorithms are extremely useful, when it comes to certain problems that either cannot in practice be written by a programmer or can be done more efficiently by a learning algorithm. Facial recognition would be an example of a problem extremely hard for a human to accurately convert into code. A problem that could be solved better by a learning algorithm, would be a loan granting application, which could use past loan data to classify future loan applications. Although a human could write rules to do this, a learning algorithm can better pick up subtleties in the data, which may be hard to code for.

There are many different algorithms that can be used when training ANNs, each with their own separate advantages and disadvantages. The process of learning by ANNs is the result of altering the network's weights, with some kind of learning algorithm. The objective is to find a set of weight matrices, which when applied to the network should hopefully map any input to a correct output. There exist three major learning paradigms: supervised learning, unsupervised learning and reinforcement learning.

- *Supervised learning*: The learning algorithm would fall in this category if the desired output for the network is also provided with the input while training the network. By providing the neural network with both an input and output pair it is possible to calculate an error based

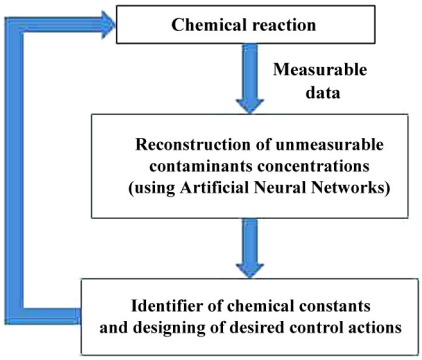

■ **FIGURE 1** Block-scheme illustrating the main idea of the approach applied in this book.

on its target output and actual output. It can then use that error to make corrections to the network by updating its weights.

- *Unsupervised learning*: In this paradigm the neural network is only given a set of inputs and it is the neural network's responsibility to find some kind of pattern within the inputs provided without any external aid. This type of learning paradigm is often used in data mining and is also used by many recommendation algorithms due to their ability to predict a user's preferences based on the preferences of other similar users it has grouped together.
- *Reinforcement learning*: This paradigm is similar to supervised learning in that some feedback is given; however, instead of providing a target output, a reward (or penalty) is given based on how well the system performed. The aim of reinforcement learning is to minimize the penalty of the system receives through trial-and-error. This paradigm relates strongly with how learning works in nature, for example an animal might remember the actions it has previously taken which helped it to find food (the reward).

This book follows the last paradigm, using reinforcement learning for the minimization of the *penalty function*, which reflects the proximity of the current outputs of the applied DNN to a desired trajectory realizing the so-called tracking process. Such penalty functions are usually referred to as *Lyapunov-like* (or "energetic") functions.

The main idea of this book may be expressed by the following step sequence (see Fig. 1).

- The first step consists in the application of the suggested Dynamic Neural Network Observer (DNNO) to reconstruct unmeasurable contaminant concentrations based only on available online data such as the input gas (ozone) flow rate, input and output gas (ozone) concentrations and some geometric characteristic of the reactor.
- Then, based on the obtained contaminant concentrations estimates, the chemical constants of the contaminant–ozone reactions are calculated and the adequate control actions (if necessary) are designed.
- Finally, these created control actions are applied to the real chemical reactor to optimize its functioning according to some preferences.

4) Structure of the book

The book contains 12 chapters and an appendix. The book is organized as follows.

Part 1: **Environmental engineering and dynamic neural networks**

Chapter 1 (Ozonation as main method for organic contaminants degradation in three different phases: liquid, solid, and gaseous) This chapter deals with the description of the experimental conditions of the ozonation procedure in three different phases: liquid, solid and gaseous. The applications of ozone in water, soil and air treatments are based on the very high oxidizing power of ozone. The ozonation destroys the initial pollutants with the formation of non-toxic and simpler substances. Ozonation of water and wastewater is carried out by dispersing ozone gas into the liquid phase. In the case of the soil ozonation, ozone also is dispersed in solid phase with its partial adsorption on the solid particles. Ozone may also be applied for the treatment of volatile organic compounds (VOCs) presented in air, such as derivatives of oil (BTEX), chlorine organics and others. In this chapter the ozonation procedures in three different phases, including the principal laboratory scheme and the design of reactors are presented. Additionally, the modeling and the automatic control of the ozone generator of the corona discharge type are discussed.

Chapter 2 (Modeling of ozonation) The simple mathematical model proposed here is one of possible approaches to a description of ozonation in water in a semi-batch reactor at constant pressure and temperature. This model permits one to characterize the ozone mass transfer in water by the use of the empirical saturation constant. This constant depends on several easily measured experimental variables (the gas flow, the volumes of gas and liquid phases, and the maximum ozone content in liquid phase). It can be easily calculated without any previous information as regards the diffusion coefficient, the specific interfacial area, the bubble size distribution and the bubble diameter. The proposed model includes differential equations describing the ozone dissolution in water and the occurring chemical reaction, including the ozonation mass balance relation. Based on the computer simulation, the optimal conditions to perform the complete or the maximum decomposition of organic pollutants in water are achieved. To evaluate the proposed simple mathematical model, the simulation of ozonation of the two unsaturated hydrocarbon pollutants (UHPs), like trichloroethylene (TCE) and tetrachloroethylene (perchloroethene PCE), was realized under different experimental conditions. A couple of additional mathematical models referring to the pH effect and the dynamics of byproducts formed during ozonation are also developed. Several numerical simulations demonstrate the validity of the suggested models.

Chapter 3 (Background on dynamic neural networks) This chapter presents an introduction to the problem field of ANNs, which are very effective performing tasks such as classification or segmentation. Two types of ANNs exist: feedforward NNs (or static NNs) and recurrent (in discrete time) or differential (in continuous time) NNs. The latter frequently are treated as dynamic NNs (DNNs). They turn out to be extremely useful when we deal with identification and/or control of dynamic processes with non-exactly given dynamic models: when noise perturbations or some unknown parameters are present in the expressions of a mathematical model. The envi-

ronmental problems considered in this book exactly deal with such an uncertain situation, and therefore DNNs will be used throughout this book. Mainly, the concept of DNNs will be applied for designing the so-called universal Dynamic Neuro Observer (DNO), which is used for designing both artificial software sensors (dynamic state observers) and robust controllers providing a good workability in the absence of complete and exact information on a mathematical model of the considered environment processes. The concept of the Attractive Ellipsoid Method (AEM) is discussed in detail: it is used to analyze numerically the quality of the corresponding state-estimation and control processes. Descriptions of the main ideas on how to design DNOs and controllers using standard MATLAB Toolboxes are given in the end of this chapter.

Chapter 4 (Neural observer application for conventional ozonation in water) A DNN is employed to estimate the state dynamics of diverse contaminants in ozone–water systems. A new technique based on the dynamic neural network observer (DNNO) is applied to an estimate of the decomposition of phenols and their mixture as well as to a calculation of their reaction constants without any mathematical model usage. The decomposition of phenols and their mixture by ozone in a semi-batch reactor is considered as a process with an uncertain model ("black box"). Only one variable is measured during ozonation, namely, the ozone concentration in gas phase in the reactor outlet. Its variation is used to obtain the characteristic curve for the phenol ozonation, the so-called ozonogram. Then, using the experimental behavior of the phenols and of their mixture decomposition, obtained by High Performance Liquid Chromatography (HPLC), the proposed DNNO is applied to an estimate of the ozonation constants of phenols in the separate ozonation and in the ozonation of their mixture at a pH of 12. Good correspondence between the experimental decomposition of phenols and the estimated ones by DNNO is obtained. The suggested technique makes online monitoring of the water treatment possible without implementation of any specific chemical (testing) sensors. The contribution of this chapter is the DNNO application to obtain both the numerical and the experimental reconstruction of the phenol decomposition, and the intermediate and accumulated byproducts obtained in ozonation. The DNNO developed here was successfully applied to obtain the state variation of the unmeasurable compound in ozonation at different pH values (2, 7 and 12). The ozone concentration variation in the reactor output is the output information used to tune the observer dynamics. As a result, the validity of the DNNO technique is demonstrated by good agreement of the predicted results with experimental data. The DNNO proposed in this chapter is the fundamental basis of the solutions presented in the following chapters.

Part 2: **Ozonation as a principal treatment method for organic contaminants elimination in liquid phase**

Chapter 5 (Catalytic ozonation) This chapter demonstrates the application of the different Activated Carbons (ACs) and the nickel oxide (NiO) as catalyst in ozonation. The catalytic ozonation with three diverse ACs was evaluated in the decomposition of three polyhydroxyalkanoates (PHAs) (anthacene, fluorene and phenanthrene). The kinetics of catalytic ozonation in the presence of ACs was studied. The catalytic ozonation in the presence of NiO was evaluated in the degradation of benzoic and phthalic acids, where the effect of the number of carboxalic groups on the degradation efficiency was proven. The feasibility of combining conventional and cat-

alytic ozonations was evaluated in the degradation of phenol (PH), 4-phenolsulfonic (4-PSA) and 2-naphtalenesulphonic acids (2-NSA) with NiO. The effect of ethanol as co-solvent in the ozonation of naphthalene and naproxen in the presence of NiO was investigated. Also, a novel mathematical model describing the effect of the catalyst in ozonation is discussed in detail. Two variants of the DNNO design are compared: the first one uses linear learning laws that ensure asymptotic zone-convergence of the estimation error, while the second implements normalized learning laws.

Chapter 6 (Photocatalytic ozonation) The aim of this chapter is to study the effect of vanadium oxide supported on zinc oxide as catalyst to enforce the terephthalic acid (TA) elimination using photocatalyst ozonation based on light emission diodes (UV-A LEDs). Characterization results indicated that vanadium oxide was not incorporated into the pores of zinc oxide, due to the formation of thinner flakes. The synthesized catalyst exhibited high stability because no significant changes between fresh and used catalyst were confirmed by the XPS results. All variants of ozonation (conventional, catalytic and photocatalytic) removed the terephthalic acid completely during 60 min; however, its reaction rate constant was higher in the catalytic and photocatalytic ozonation (22% and 25%, respectively). The ozone decomposition study indicated that terephthalic acid was degraded by the combined action of molecular ozone and hydroxyl radicals. This last oxidant species play an important role in promoting the elimination of byproducts generated during the ozonation of TA. The distribution of UV-A LEDs was evaluated in two configurations (the central and external irradiation) that resulted in significant differences. These differences were confirmed by the reaction rates of the accumulation of the byproducts and their decomposition. Even when the energy supplied in the two cases remained constant (4 W m^{-2}), the interaction between photons and active sites in the catalyst was twice higher when the UV-A LEDs were on the peripheral of the reactor. All these results show that V_{xy}/ZnO is a potential catalyst for photocatalytic ozonation using a portion of the visible electromagnetic spectrum.

Chapter 7 (Combination of physical-chemical methods and ozonation) The use of conventional ozonation and of advanced oxidation processes (AOPs), such as catalytic and photocatalytic ozonation, discussed above, show the good efficacy in the decomposition different organic contaminants and their mixture. However, in the treatment of the real wastewater the application of the combination of different physicochemical methods, as the pretreatment, with ozonation, is more effective. The selection of the methods depends on the chemical structure of the pollutants, their composition and the concentration. In this chapter the combination treatment of real wastewater samples is discussed.

Chapter 8 (Automatic control of ozonation systems in liquid phase) This chapter describes the application of two different automatic controllers for the ozonation process of residual waters. The first approach uses a new method to design a local optimal controller for an uncertain system governed by continuous flow transformations (CFT). The online solution of the adaptive gains adjusting a linear control form yields the calculus of the sub-optimal controller. A special performance index, oriented to solve the transient evolution of CFT systems, is proposed. The class of systems considered in this study is highly uncertain: some components of chemical reactions are not measurable online and then they cannot be used in the controller realization.

The recovering of this information was executed by a DNN structure. The ozonation process of a single contaminant (like for example CFT) is evaluated in detail using the control design proposed here. The second controller uses a trajectory tracking adaptive controller based on DNN to control the ozonation system. This approach uses a nonlinear transformation of the ozonation model to obtain a chain-of-integrators equivalent form. This controller was applied to the simple ozonation model with only one contaminant. The numerical and experimental validations of the tracking controller justify both designs.

Part 3: **Ozonation in solid and gaseous phases**

Chapter 9 (Ozonation modeling in solid phase) This chapter proposes the mathematical modeling of ozonation in solid phase; the example of the decomposition of the phenanthrene, adsorbed in the model (sand) and the real soil (agricultural soil), is chosen. The modeling scheme includes the ordinary differential equations with time-varying coefficients. This model deals with the adsorbed ozone and ozone, reacted with the contaminant, as well as the phenanthrene concentration in the soil. The main parameters, involved in the mathematical model, include a time varying ozone saturation function $k_{sat}(t)$ and reaction constants k_r. These parameters are calculated using the ozone concentration variation at the reactor output, and the phenanthrene decomposition by ozone. To validate the model we realized two series of experiments: soil, saturated with ozone in the absence of the contaminant, and soil with the phenanthrene. Also, this chapter discusses the possibility of the conventional ozonation in the solid phase in a two-phase system (soil–ozone) and a three-phase system (soil–water–ozone) to eliminate polyaromatic hydrocarbons (PAHs) from the contaminated model and real soil samples. Because ozone is a gas, it preserves the oxidative potential not only in the liquid phase (water), but also in the solid phase (soil). It is very important to notice that the ozonation kinetics practically is not different for both phases. The application of the DNN technique permits one not only to appraise the ozonation kinetics, but also to realize the reconstruction of the decomposition profiles of the intermediates of ozonation. Below, we describe the different examples of the decomposition of PAHs in solid phase.

Chapter 10 (Ozonation in the gaseous phase) In this chapter we discuss the ozonation in the gas phase in the tubular reactor to demonstrate the possibility of decomposing of the contaminants by ozone, in the same way as in the liquid and solid phases. As we see below, the ozonation is a direct mechanism, as it is realized in the liquid and solid under some specific conditions. The proposed mathematical model of ozonation is based on the material balance as in the previous cases. The emission of volatile organic compounds (VOCs), particularly BTEX or unsaturated organic compounds (UOCs) is one of the most important contributions to atmospheric pollution, which leads to the decreasing of the air quality. The individual identification of the unsaturated hydrocarbon pollutants (UHPs) was realized by the comparison of the flame ionization detector (FID) chromatogram and the ozonogram. A novel simple mathematical was developed allowing to calculate the ozonation constants for the different UHPs. A second mathematical model described the ozonation of the BTEX in the gaseous phase considering the spatial and temporal distribution of the contaminants and the ozone concentration. The model deals with the reaction between ozone and an organic volatile compound in the tubular reactor. This interaction is de-

scribed by two second order Partial Differential Equations (PDEs). The identification problem is solved using the exact expression for the weights dynamics, based on the DNN properties for PDEs. The numerical example is realized considering two practical scenarios: ozone and benzene are injected into the reactor directly and one assumes that benzene was added to the reactor by stripping from contaminated water.

Part 4: **Combination of ozonation and biodegradation**

Chapter 11 (Biodegradation) This chapter describes the general characteristics of biodegradation systems. The specific details of aerobic and anaerobic cultures are explained and the technical details of bioreactor operation are also discussed. The modeling describing the dynamics of microbial cultures are developed. The concept of the variable reconstruction based on state observers with discontinuous correction terms is analyzed. The observer is based on the application of the super-twisting algorithm structured in a step-by-step structure. A biodegradation system is considered to test the estimation capacities of the observer. The numerical results confirmed the observer workability to estimate the non-measurable states accurately enough.

Chapter 12 (Ozonation and biodegradation as complementary treatments) This chapter deals with the sequential combination of ozonation and biodegradation of toxic compounds in different synthetic and real effluents. In general, after the adequate ozonation time, a significant amount of initial toxic contaminants decreased, which then were transformed into non-toxic organic acids that were easily degraded by biodegradation. If ozonation is not considered as a pretreatment, the biodegradation system is not able to decompose the highly contaminant concentrations. Additionally, the acclimation of microorganisms plays a relevant role in the efficiency of the contaminant degradation. This fact was confirmed by the kinetics of the microorganism growth, which showed an increment of the specific growth velocity when the ozonation was used as pretreatment. The entire set of variables, describing the sequential process, was efficiently estimated by a variant of DNNO with discontinuous learning laws.

5) Acknowledgments

We express deep gratitude to our students and faculty colleagues, without whose evident year-long enjoyment and expressed appreciation the current work would not have been undertaken.

Finally, we wish to acknowledge the anonymous reviewers for their constructive critical remarks and useful suggestions and the Editors of Elsevier Limited for being so cooperative during the production process.

Tatyana I. Poznyak, Isaac Chairez, Alexander S. Poznyak

Mexico, 2018

To our teachers and our students

Notation and symbols

Mathematical notations and symbols

$:=$ means equal by definition;
$x_t \in \mathbb{R}^n$ is the n-dimensional state vector of the system at time $t \in \mathbb{R}^+ := \{t : t \geq 0\}$;
$\hat{x}_t \in \mathbb{R}^n$ is the n-dimensional state vector of a neural network at time $t \in \mathbb{R}^+$;
$x_t^* \in \mathbb{R}^n$ is the n-dimensional state vector of a reference model (the desired trajectory) at time $t \in \mathbb{R}^+$;
$u_t \in \mathbb{R}^k$ is the k-dimensional vector of the control action;
$y_t \in \mathbb{R}^m$ is the m-dimensional output vector at time $t \in \mathbb{R}^+$;
$f(x_t, u_t, t) : \mathbb{R}^{n+k+1} \to \mathbb{R}^n$ is a vector valued nonlinear function describing the system dynamics;
$\varphi(x_t^*, t) : \mathbb{R}^{n+1} \to \mathbb{R}^n$ is a nonlinear vector function describing a reference model;
$C \in \mathbb{R}^{m \times n}$ is an output matrix;
$\xi_x \in \mathbb{R}^n$ and $\xi_y \in \mathbb{R}^m$ are vector-functions representing external perturbations in dynamic equation and in the measured output;
$A \in \mathbb{R}^{n \times n}$ is a Hurwitz (stable) matrix;
$W_1^0 \in \mathbb{R}^{n \times W_1}$ and $W_2^0 \in \mathbb{R}^{n \times W_2}$ are weight matrices modulating the sigmoidal functions of a neural network;
$V_1^0 \in \mathbb{R}^{V_1 \times n}$ and $V_2^0 \in \mathbb{R}^{V_2 \times n}$ are internal weights that participate inside of sigmoidal functions;
$\sigma : \mathbb{R}^{V_1 \times n} \times \mathbb{R}^n \to \mathbb{R}^{W_1}$ and $\phi : \mathbb{R}^{V_2 \times n} \times \mathbb{R}^n \to \mathbb{R}^{W_2 \times p}$ are the activation sigmoidal functions of a neural network;
$e_t = y_t - C\hat{x}_t \in \mathbb{R}^m$ is the output estimation error at time $t \in \mathbb{R}^+$;
L_1, L_2, and L_3 are the Dynamic Neural Network Observer (DNNO) gain matrices;
c_0^g, c_t^g are the initial and current ozone concentrations in the gas phase (mol L^{-1});
W_g is the gas flow-rate (L s^{-1});
V_g is the volume of the gas phase (L);
Q_t is the current amount of ozone in liquid phase (mol);
$\limsup_{t \to \infty} z_t = \overline{\lim_{t \to \infty}} z_t = \lim_{t \to \infty} \sup_{\tau \geq t} z_\tau$ is an upper limit;
A^+ is the pseudoinverse matrix in the Moore–Penrose sense, satisfying $A^+AA^+ = A^+$, $AA^+A = A$;
$\|z\|_H := z^\top Hz$ is the weighted norm of the real-valued vector $z \in \mathbb{R}^n$ with weight matrix $H > 0$, $H = H^\top$; $H \in \mathbb{R}^{n \times n}$;
$M > N$ for two matrices $N \in \mathbb{R}^{n \times n}$ and $M \in \mathbb{R}^{n \times n}$ means that $(M - N)$ is a positive definite matrix;
$\mathrm{tr}\{H\} := \sum_{i=1}^{n} H_{ii}$ where H_{ii} is the diagonal element of the matrix H located at the row i and the column i;
$\mathrm{vec}(H)$ transforms a matrix H into a vector, by stacking all the columns of the matrix one underneath the other;
$\square$ means the end of the proof.
pH means the potential of hydrogen.
Ph means phenol compound.

Part 1

Environmental Engineering and Dynamic Neural Networks

Chapter 1

Ozonation as main method for organic contaminants degradation in three different phases: liquid, solid, and gaseous

CONTENTS

ABSTRACT

This chapter deals with the description of the experimental conditions of the ozonation procedure in three different phases: liquid, solid, and gaseous. The applications of ozone in water, soil and air treatments are based on the very high oxidizing power of ozone. The ozonation destroys the initial pollutants with the formation of no toxic and simpler substances. Ozonation of water and waste water is carried out by dispersing ozone gas into the liquid phase. In the case of the soil ozonation, ozone also is dispersed in the

Ozonation and Biodegradation in Environmental Engineering
https://doi.org/10.1016/B978-0-12-812847-3.00010-X

solid phase with partial adsorption on the solid particles. Ozone may also be applied for the treatment of volatile organic compounds (VOCs) presented in air, such as derivatives of oil (BTEX), chlorine organics, and others. In this chapter the ozonation procedures in three different phases, including the principal laboratory scheme and the design of reactors, are presented. Additionally, the modeling and the automatic control of the ozone generator of the corona-discharge type are discussed.

1.1 OZONATION OF ORGANIC CONTAMINANTS IN LIQUID PHASE

1.1.1 Basic reaction principles in liquid phase ozonation

Ozone is an allotrope form of oxygen molecule. If this molecule is dissolved in water, at room temperature, the solution exhibits a light blue color. Ozone dissolved in gaseous phase is an explosive gas that absorbs UV-radiation in the range of 220–290 nm. It is a bent molecule with a bond angle of 116.8 Å degree and an interatomic distance of 1.278 Å. The melting point is −193°C and boiling-point −112°C. The solubility of ozone in aqueous solutions is 14 mmol L^{-1} at 20°C, but it is more soluble in organic solution. Thus, it can be regarded as a hydrophobic molecule.

Ozone can oxidize practically all organic and inorganic substances, including silver (Ag), gold (Au) and platinum (Pt). Due to its reactivity and instability, ozone has to be generated *in situ* using the ozone generator aimed to produce ozone from air or oxygen.

The following important comments must be made:

- Ozone is intensively used in water and waste water treatment, disinfection, bleaching, and industrial oxidation processes. The practical applications are based on the very high oxidizing power of ozone.
- In the ozonation the initial pollutants with the formation of no toxic and simple substances are destroyed. These final products are more biodegradable, making the complementary biological treatment itself more efficient (Adams et al., 1997; Yordanov et al., 1999). In some cases, organic compounds can be oxidized completely by ozone to produce CO_2 and H_2O. However, the complete mineralization requires a long ozonation time and high ozone doses.
- Ozone can interact with organic compounds in water, depending on the experimental conditions, by two mechanisms:
  (a) direct, with molecular ozone and
  (b) indirect, with OH radicals.

In the presence of catalysts (catalytic ozonation) it is possible that these two mechanisms are combined simultaneously. In the case of the direct mechanism with molecular ozone, the kinetics of the contaminant decomposition depends on their chemical structure, whereas by the indirect mechanism, when the reaction is realized with non-selective OH radicals, this factor has no meaning at all (Camel and Bermond, 1998; Hoigné and Bader, 1983a,b; Razumovskii et al., 1984).

– Ozone is decomposed at high pH in water, as well in the presence of activated carbon and others catalysts. The ozone mass transfer in water was described by many kinetic models proposed by various authors (Grymonpre et al., 1999; Poznyak et al., 2003; Sánchez-Polo et al., 2005).

1.1.2 Ozonation procedure in liquid phase

In a pure aqueous solution ozone slowly decomposes in multiple steps involving radical formation. The depletion is a chain process and has been described by two different mechanisms: by the Hoigne–Staehelin–Bader (HSB) and the Gordon–Tomiyasu–Fukutomi (GTF) mechanisms.

HSB state that the initial step is an oxygen-atom transfer from ozone to a hydroxide ion, followed by a reverse one-electron transfer. In contrast, GTF only state an oxygen-atom transfer. However, the fundamental reaction in both mechanisms is the initial step, where ozone reacts with OH^-. Furthermore, removal of the superoxide anion radical, O_2^-, and the HO^- radical in the chain reaction reduces the speed of the ozone decomposition.

The test experiments were produced under the following conditions:

– the reactor was a semi-batch type (0.500 L);

– the initial ozone concentration varied from 23 mg L^{-1} up to 33 mg L^{-1} depending on the contaminant concentration;

– the ozone–oxygen mixture flow was 0.5 L min^{-1};

– all experiments were carried out at 20°C–22°C with agitation by bubbling of an ozone–oxygen mixture or by a magnetic agitation (operated at 120 rpm);

– aliquots of 3 mL reaction solution were withdrawn at desired time intervals from the reactor for sequent analyses by an UV-vis spectrometry, HPLC, GC-M, total organic carbon (TOC), chemical oxygen demand (COD), and biological oxygen demand (BOD_5).

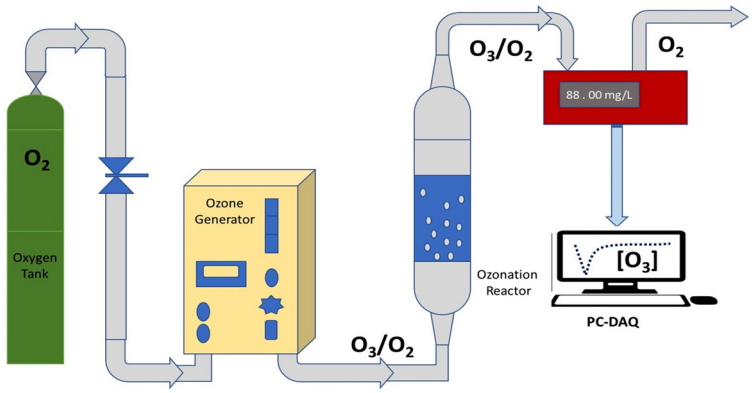

■ **FIGURE 1.1** Ozonation scheme.

The schematic diagram of the ozonation apparatus presents in Fig. 1.1, which includes an oxygen tank, an ozone generator, a reactor, an ozone analyzer, and PC.

The design of the reactor and the ozone distribution system in water may vary depending on the type of ozonation: we have conventional, catalytic, and photocatalytic types.

1.2 OZONATION OF ORGANIC CONTAMINANTS IN THE SOLID PHASE

1.2.1 Basic reaction principles in solid phase ozonation

In the solid phase, ozonation is usually applied for the elimination of the organic contaminants:

– Among others there are polycyclic aromatic hydrocarbons (PAHs), which are byproducts of the pyrolysis of petroleum at high temperatures as well as in acetylene synthesis from natural gas, refinery operations, etc. (Fouillet et al., 1991).

– In various studies the presence of PAHs in air, water, and soil has been detected.

– In some specific cases, the concentration of these contaminants were found larger than 10 g/kg (Lundstedt, 2003);

– Since PAHs are characterized by their hydrophobic nature they tend to be adsorbed on solid particles and this effect converts them into important pollutant of soil.

– Due to the low solubility in water, PAHs can be adsorbed in the surface of soil such that their biodegradation may provoke some difficulties in view of their highly hydrophobic property and a strong interaction with the soil (Cerniglia, 1993; Luthy et al., 1994; Mulder et al., 2001).

1.2.2 Ozonation procedure in solid phase

Basically, the principle of ozonation in solid phase is the same as in the liquid phase, which is the distribution method of the gas flow in a contaminated soil. The ozone–oxygen mixture passes through the solid phase with saturation and partial adsorption on the surface of the solid particles. The experimental conditions are the same: the gas flow, the ozone concentration, and the temperature. The changes concern only the reactor design and its volume (around 10 mL).

1.3 OZONATION OF VOLATILE ORGANIC CONTAMINANTS IN THE GASEOUS PHASE

The ozonation procedure is usually conducted in three sequential stages.

– *In the first stage*, oxygen is passed through the aqueous solution (250 mL), containing the dissolved volatile organic compounds (VOCs). This solution is enclosed in a reactor (500 mL), which has a diffuser plate at its bottom for the feeding of oxygen. This procedure provokes the stripping of benzene, toluene, ethylbenzene, and xylene (BTEX) from the liquid phase to the tubular reactor. The liberation of BTEX is performed using an initial concentration of 200 mg L^{-1} for benzene, toluene, and xylene, while ethylbenzene was 150 mg L^{-1}. The BTEX liberation from the water was performed with gas flows of 0.5 L min^{-1} and 0.2 L min^{-1}. The liberated BTEX are adsorbed in granular activated carbon (GAC) (1.0 g). The activated carbon is then settled in a bed. This bed was prepared with 1 g of GAC in a small tube with 1 cm diameter. To determine the stripping dynamics, the water samples are analyzed at different times (2, 5, 10, 15, 20, 30 until 60 min).

– *On the second stage*, the stripped BTEX pass through a tubular reactor, where the BTEX ozonation is carried out in gaseous phase. The ozonation in the tubular reactor (4) with fixed length (1.5 m length and diameter of 2.5 cm) is realized with the ozone concentration (30 and 15 mg L^{-1}) and the variation of gas flow (0.2 L min^{-1} and 0.5 L min^{-1}). Then the residual ozone, byproducts, and final products of ozonation are adsorbed in GAC (5) located at the reactor output.

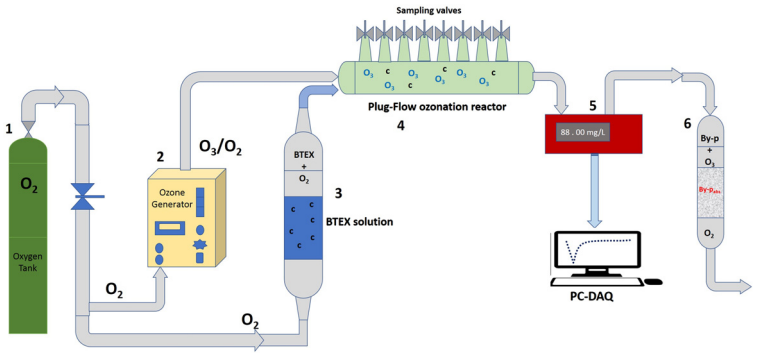

■ **FIGURE 1.2** Scheme of the reactor for ozonation in the gaseous phase (O_3 = ozone, O_2 = oxygen, c = contaminant, By-p = ozonation byproducts).

– *In the third stage*, all experiments are carried out at the ambient temperature. The measurements of ozone in gaseous phase at the reactor input was realized with an ozone sensor (6), connected to a PC (using an acquisition data board NI-6024(8)). Ozonation in the gaseous phase is carried out in the special tubular reactor, where ozone interacts with Volatile Organic Compounds (VOCs). Fig. 1.2 presents the schematic diagram of the laboratory scale for the ozonation in the gaseous phase. In this particular case, the synthetic solution of VOCs in water stripped from the reactor (3) by the oxygen flow to the tubular reactor (4) is mixed with the ozone–oxygen flow to react with ozone (Chairez et al., 2010).

The schematic diagrams at the laboratory level, presented above, and the experimental conditions of the ozonation process in three different phases, are described in general format. In each particular cases, for the resolution of the particular treatment problem may be amended using modifications described below.

1.4 TECHNOLOGICAL ASPECTS OF OZONATION

The ozonation efficiency depends completely on the consumption of ozone during the reaction. A complete consumption of ozone implies one of two possible options:

– the reaction occurs at a complete stoichiometric balance,

– or the quantity of ozone is not enough to decompose contaminants (initial, intermediates or accumulated).

The residual ozone must be destroyed by the activated carbon.

The solubility of ozone in water is pretty low, that is, approximately one tenth of the solubility of chlorine, which is a classical compound used in water treatment (Tizaoui et al., 2008). This can be considered as a major reason justifying the preference of chlorine over ozone in spite of the fact that the gas killing power over microorganisms is 400 times larger than chlorine. This physicochemical property of ozone enforces the application of a special chamber (bubble column, or contact tank, or contactor) to diffuse the ozone gas into water (Farines et al., 2003).

The ozone, dissolved in air, or oxygen, leaving the generator, enters the liquid phase by interfering into fine gas bubbles. These bubbles contain only a few percents of ozone within. By a low gas solubility the mass transfer of ozone and the reaction rates are also moderated with respect to other oxidant agents, in spite of the fact that ozone is an extremely powerful oxidant (only fluoride exhibits a higher oxidation potential (Tizaoui et al., 2008)). Based on the turbulent mass transfer occurring at the reactor's input, ozone enters in contact with bulks of contaminants.

Another limiting aspect of the ozone implementation is the reaction temperature. High temperatures (above 30°C) significantly decrease the ozone solubility and it remains stable, when the temperature approaches 0°C.

The water ozonation system presents a complex scheme due to the necessity of the ozone production in situ.

In general, ozonation systems use three principal elements:

– sensors,

– reactors,

– ozone generators.

Let us discuss each of these elements in detail.

1.4.1 Ozone sensors

Usually, ozone can be measured either in the liquid or in the gaseous phase. If the ozone concentration should be measured in liquid phase, there are two principal possibilities including chemical agents and electronic devices.

The ozone concentration injected into the reactor depends on the kind of microorganisms (for disinfection purposes) or organic pollutants that should be destroyed (for treatment purposes). The required reduction ratio, usually expressed in logarithmic scale, also strongly depends on the ozone concentration in liquid phase. If the percentage of the unused ozone in the reactor output is high, the design of the ozonation system, under this negative ef-

fect, may be considered as unsatisfactory. On the other hand, if ozone is not destroyed completely, due to its high toxicity, it can harm the health of the working personnel of the treatment plant. A long-term exposure of the personnel to 0.2 mg L^{-1} in weight may affect both lungs and respiratory tract. A person who is not used to work with ozone can smell it under a concentration around 40 μg O_3 m^{-3} air.[1] Many workspace rules, such as the *US Occupational Safety and Health Administration*, limit the maximum ozone concentration to 0.1 mg L^{-1}. Therefore, the residual dissolved ozone in treated water should be monitored continuously and maintained within the range of $5 \div 50$ ppbw. If this condition is not met, then it is necessary to decompose it using UV-radiation of 250 nm wavelengths (Farines et al., 2003; Yershov et al., 2009).

There are two main classes of methods for measuring ozone in water: specific or not specific to ozone.

The main specific methods for measuring the dissolved ozone are:

– *UV absorption*,

– *indigo*,

– *amperometric membrane method*,

– *stripping and gaseous phase detection*.

On the other hand, the dissolved ozone non-specific methods are:

– the potassium iodide,

– and the amperometric-bare one.

The first colorimetric oxidant recorder was developed in 1953. Almost 25 years later, in Switzerland, the *indigo method* was suggested firstly. Indigo *blue jeans* dye served as an indicator compound because of its rapid selective reaction with ozone. The reaction mechanism includes the ozone attack to the double bond of indigo, which turns out to be very informative because of its simplicity and lack of disturbance. The decolorization of indigo trisulfonate (ITS) in the presence of ozone provokes a linear drop in absorbance, when the ozone concentration increases. The indigo method is also preferred, when the UV absorption method is not suitable (because of the presence of other compounds absorbing at the same wavelength) or the ozone concentration is lower than 100 ppbw.

[1] In general, 0.1 mg L^{-1} in volume ozone concentration can be detected in the ambient air at usual conditions.

The so called *absolute method* (Tizaoui et al., 2008) of the ozone concentration monitoring in the liquid phase fixes the change of the gas volume, produced by the ozone decomposition according to the reaction

$$2O_3 \rightarrow 3O_2.$$

Another indirect method is named the *manometric* one. It is based on the measuring of changes in the oxygen pressure in a given volume. Unfortunately, all these methods are time-consuming. They are inaccurate because of the slow variation at the low ozone concentrations.

If we need to measure the ozone concentration in the gaseous phase, there are two main options:

– the UV absorption method,

– and the direct membrane oxidation.

The *UV absorption method* is specially intended to measure the ozone concentration in the gaseous phase. Clearly, by its chemical principles, this method is also applicable for the measuring of ozone dissolved in water if there are not any other compounds in the solvent that can absorb UV-radiation at 254 nm wavelength. This specific UV-radiation is produced by a low-pressure mercury lamp or high-technology UV Light Emission Diodes (UV-LEDs).

All the aforementioned drawbacks in ozone measuring methods can be eliminated by using an *ozone-specific membrane,* which is wetted with the flow of ozonated water. This method works as follows: the ozone diffuses through the membrane and it reacts with some active components that can produce either an electron current or a voltage difference. Some other membrane-type ozone sensors are either *amperometric* or *polarographic* electrochemical cells, which transform the measurement in water into measurement in air. Within this class of sensors, their head-space should be periodically recharged with clean air. Then the ozone-containing air after the measurement should be removed.

The *stripping* and *gas phase method* resemble membrane-type sensors, but ozone stripping from the liquid sample can be performed either by bubbling an inert gas (such as nitrogen) through the sampled water or by intensive shaking a vessel to expel the dissolved gas by a turbulent flow effect. Thin film semiconductor heated metal oxide sensors (HMOSs) use variations in resistivity on the grain boundaries enforced by the ozone adsorbed on the surface of the semiconductor device for monitoring the ozone concentration.

Both electrochemical and HMOS sensors can be calibrated with special experimental tests obtained from the indigo and the UV methods. The whole ozone concentration range is covered only by the UV method. All these sensors can be calibrated with respect to measurements obtained by UV spectrophotometers. Nevertheless, these instruments must be calibrated using the measurements of reference solutions or chemical methods like gas-phase titration or iodometry, which are cumbersome and require skillful personnel.

Nowadays, there is a tendency of expanding the measurement range toward lower limits of measurable ozone concentrations. This is motivated by new government regulations, which try to reduce the allowable concentrations in workplaces. Besides, there is also a tendency on reducing the values of residual ozone in the treated water.

1.4.2 Ozonation reactions

Ozone can react through the molecular mode and/or through the radical mode (the active oxidant is the hydroxyl radical created by the breakdown of ozone) depending on the composition of the medium into which it is transferred. This reaction can alter the transfer of ozone. Generally speaking, the reaction rate at which ozone interacts with mineral and organic compounds as well as microorganisms can be simply modeled by a second order equation with partial stoichiometric orders of 1 for each of the reactants, that is,

$$O_3 + \nu M \rightarrow \text{Products},$$

where

O_3 is the dissolved ozone concentration,

M is for the concentrations of initial reactants,

and ν is the stoichiometric coefficient.

Based on the reaction between ozone and the reactant, the reaction rate constants for ozone and the reactant can be calculated as follows:

$$r_{O_3} = k \cdot [O_3] \cdot [M], r_M = k \cdot \nu \cdot [O_3] \cdot [M].$$

Here

k is the reaction rate constant,

ν is the stoichiometric coefficient,

$[M]$ ($[O_3]$) is the concentration of compound M (dissolved ozone),

and r_M (r_{O_3}) is the rate at which compound M decomposes (the rate at which dissolved ozone is consumed).

Even when the reaction rate constant k does not depend on the reactants concentration, the decomposition velocity of r_M does. Therefore, a major challenge in designing an ozonation system consists of selecting, designing, and implementing a concrete reactor with some special characteristics that can favor the decomposition of organics by ozone.

There are various criteria to select the reactor configuration, dimensions, etc. One of them is the *Hatta parameter* (*Ha*), which is a number without physical dimensions, characterizing the oxidation reaction and subsequently providing a relevant guidance to select the gas–liquid reactor. Indeed, a low Hatta number means that the transfer capacity of the liquid film is high compared to the consumption rate of ozone: this is referred to as the *kinetic regime*. Conversely, when Ha is high, the ozone consumption rate can be greater than the flux of ozone transferred: this is named the *diffusion regime*. In particular, for an irreversible order 2 reaction, the Hatta number is

$$Ha = \frac{\sqrt{D_{O_3} \cdot k \cdot [M]}}{k_L a}, \tag{1.1}$$

where D_{O_3} is the ozone diffusivity ($m^2\ s^{-1}$), and $k_L a$ corresponds to the mass transfer in the liquid phase ($m\ s^{-1}$).

Table 1.1 demonstrates the relationship between operating regimen, the determining characteristic and the reactor type.

Let us consider Table 1.1.

a) The reaction is very slow and occurs in the liquid phase exclusively. Transfer easily takes place through the film.

b) The reaction is slow and exclusively occurs in the liquid phase. The reaction can be fast enough to produce a weak dissolved ozone concentration. This is slow and does not accelerate ozone transfer.

c) The reaction rate is moderate and occurs in the liquid phase and the film of the liquid.

d) The reaction occurs quickly and occurs in the liquid phase exclusively. There is a zero dissolved concentration in the liquid mass.

e) The reaction is very slow and occurs in the liquid phase exclusively. Transfer easily takes place through the film.

Table 1.1 Hatta number variation as a function of the operation regimen.

Operating regimen	Main setting	Reactor type
a) $Ha < 0.02$ $E = 1$	Liquid retention ϵ_L	Bubble column
b) $0.02 < Ha < 0.30$ $E = 1$	Liquid retention ϵ_L Interfacial area a	Bubble column Agitated reactor
c) $0.30 < Ha < 3.00$ $E = \sqrt{1 + Ha^2}$	Liquid retention ϵ_L Interfacial area a	Agitated reactor
d) $3.00 < Ha$ $E = Ha$	Interfacial area a	Packed bed column
e) $3.00 << Ha$ $E = Ha$	Transfer coefficient k_L Exchange surface area a	Static mixed ejector Packed bed column Perforated venturi column

The flux of ozone transferred according to Eq. (1.1) is

$$N = E \cdot k_L a \cdot \left(C_L^* - C_L\right) \cdot V_L,$$

where E represents the transfer acceleration factor. The value of this factor is defined by the volume of the liquid phase, which is close to the Hatta number.

1.4.3 Ozone generators

Ozone is an unstable molecule and, therefore, it cannot be stored in any way (Yershov et al., 2009). There are several reports claiming that the half-life time of ozone in distilled water is about 20 min (Cullen et al., 2009) and it decreases to half when raw potable water is the dissolution medium.

The low stability of the ozone molecule simplifies the problem of exceeding the ozone consumption. However, this fact enforces the installation of the ozone generator as a key section of the ozonation system (Guzel-Seydim et al., 2004; Kuraica et al., 2004).

The ozone generators may operate using as feeding gas either air (the output is 1–3% ozone) or pure extra dried oxygen (the output is about 6% ozone) if the corona-discharge technology is applied. Similar concentrations can be obtained if another high-voltage-based generator is used. A second option

to produce ozone considers the application of an UV or VUV generator, but the ozone concentration at the output are insufficient (0.5 % ozone or less).

1.5 CONTROL OF CORONA-DISCHARGE GENERATOR

This section deals with a switching robust feedback design for the corona-effect ozone generator. The generator is considered as a switched system in the presence of bounded model uncertainties as well as external perturbations, such as leakage currents, parasite voltages, and variations of the oxygen flow. The presented control design requires the whole state vector to describe the ozone generator dynamics. The switching model of the ozone generator, considered here, consists of three nonlinear dynamic equations assuming that sample-switching times are known. The control design is proposed as a mixed structure based on the application of a modified super-twisting algorithm (Levant, 1998) and a sequence of switching linear feedback controllers. The second method of Lyapunov is the main tool to prove the existence of a global asymptotic equilibrium point for the tracking error dynamics. The reference system used to define the tracking problem was developed considering previous experimental knowledge on the ozone generator performance. The set of numerical simulations discussed below was prepared to illustrate the performance of the controller, as well as the corresponding control action. The sequence of gains used in the switching structure are also depicted.

Generation of ozone is based on the silent discharge phenomena; electrolytic and opto-chemical reactions (Alonso et al., 2003). The dielectric-barrier-based silent discharge is the one most widely used in industrial pipeline applications, since it produces the highest gas concentrations. The ozone gas is generated from oxygen or air by the electron bombardment of molecules in a glass-barrier-based discharge. This bombardment breaks the oxygen molecules apart and their selective recombination with each other and with other stable oxygen molecules produces ozone. The class of ozone generators based on the dielectric-barrier-based silent discharge effect is known as Corona-Discharge Ozone Generators (CDOGs) (Murata et al., 2004).

A CDOG is a device fed with air or oxygen that produces ozone using high-voltage discharges. When the oxygen molecules pass through a reaction tube, where an electrical discharge occurs, they undergo partial dissociation as follows:

$$O_2 + e \rightarrow 2O^{\cdot} + e,$$
$$O^{\cdot} + O_2 \rightarrow O_3 + M \rightarrow O_3 + M,$$

$$O^{\cdot} + O_3 \rightarrow 2O_2,$$
$$2O^{\cdot} + M \rightarrow O_2 + M.$$

Here M is a third particle. The produced atomic energy reacts with molecular oxygen to form ozone. If ozone is presented in a fairly high concentration, it can react with the oxygen atoms and be converted into oxygen molecules. The competition between these two reactions sets a limit to the maximum ozone concentration in the gas mixture around 5–7% v/v (volume of ozone per volume of oxygen).

A CDOG consists of an oxygen generator/tank, silent discharged-type ozone generation tube, a high-frequency high-voltage transformer, series-compensated resonant inductor, two or three phase power-factor correction (PFC) converters and a water/air cooling system. The inverter output is connected to the load with the series-compensating resonant inductor via a high-voltage high-frequency transformer (Murata et al., 2004). A compensating inductor is necessary to provide tuned frequency conditions. The equivalent circuit of the voltage source inverter with high-frequency high-voltage transformer and the ozone-generation tube was developed in Alonso et al. (2003). The equivalent circuit of the newly developed voltage-source inverter with high-frequency high-voltage transformer and the ozone-generation tube is shown in Fig. 1.3 (where there is leakage inductance and magnetizing inductance).

Despite the fact that the ozone generator is driven by a high-frequency oscillator and that there exist a lot of existing controllers for this kind of systems, the number of automatic controllers for ozone generators is small enough (Murata et al., 2004). Today, commercial ozone generators are controlled in an open loop setting. The most advanced controllers for ozone generators are based on proportional-derivative-integral schemes (Michel et al., 2007). However, the presence of uncertainties and perturbations that may affect the ozone generator production can appear all the time. Therefore, robust controllers may be a relevant option to adjust the ozone concentration in real applications.

Among others, the sliding mode (SM) represents a trusty option. Classical features exhibited by sliding modes are robustness with respect to external "matched" uncertainties (acting in the same subspace as control actions) and finite-time convergence to a desired dynamics. The SM scheme is obtained by inducing a discontinuity in the control structure. Discontinuous injection must be designed such that the trajectories of the system are forced to remain on some sliding surface defined in the state space. The resulting motion on that surface is referred to as the sliding mode (Utkin, 1993). In continuous time systems the SM have been extensively studied, and the main theoretical

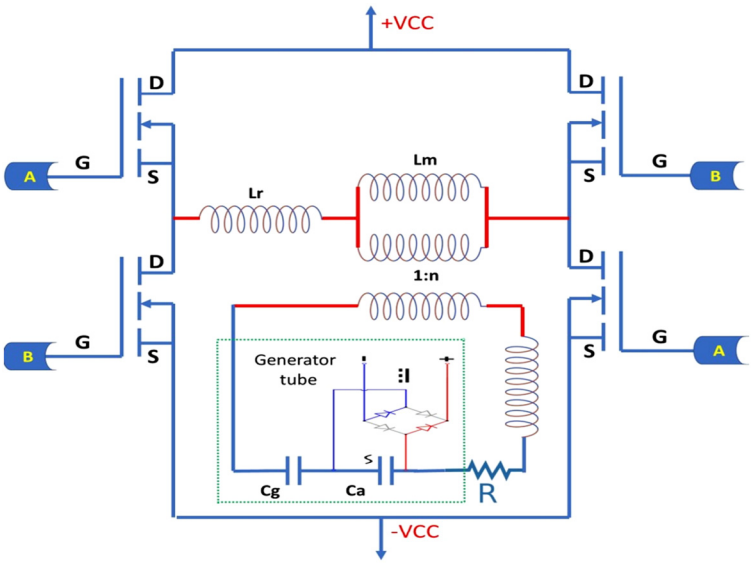

■ **FIGURE 1.3** Voltage-source inverter with high-frequency/high-voltage transformer and the ozone-generation tube (L_r = primary inductance, L_m = magnetizing inductance, R = Series resistance, C_a = capacitance of discharge gap, C_g = capacitance of dielectric layer, n = turns ratio ($N_1 = N_2$) of transformer).

results are presented in Utkin (1992), Utkin et al. (1999), and the references therein.

In particular, SM controllers have been applied to regulate voltage inverters (Yan et al., 2007b), (Abrishamifar et al., 2012), (Biel et al., 2001). These solutions are clearly applicable to regulating the ozone generator described above. However, many of these solutions do not consider the switching nature of these electronic circuits. The solution presented in this section takes into account both the switching nature of the ozone generator and the necessity of ensuring convergence within the period of switching.

The theoretical analysis given below can be successfully implemented to obtain robustness against uncertain systems with internal and external perturbations, finite-time convergence and order reduction. The basic approach of these controllers is by the so-called first order sliding modes (1-SMCs).

Unfortunately, 1-SMC also features the undesirable phenomenon known as chattering, which is a direct consequence of high-frequency signals in the input forced by the sliding controller (Levant, 2002). Several techniques have been proposed to improve the SMC performance. Most of them have as main objective the reduction of chattering (Rusu, 2002), (Sefriti et al., 2014). One way to avoid the chattering is to move the switching motion to

the high order derivatives of the control signal. These structures are known as high order sliding modes (Levant, 2007). The supertwisting algorithm is a second order sliding mode (SOSM) with a similar structure of a classic proportional-integral (PI) that has been applied for many practical and theoretical issues (Gonzalez et al., 2012).

This section describes the application of the SuperTwisting (ST) SM algorithm to control ozone generators.

1.5.1 State-space model

The state-space variables are

– the current of the high-frequency high-voltage transformer (i_r),

– the current (i_o),

– and voltage along the tubes (V_{CA} and V_{CB}).

Using these notations the nominal variable structure mathematical model for the ozone generation can be expressed as follows.

1. Positive semicycle:

$$\frac{d}{dt}x(t) = A_1 x(t) + B_1 u(t) + \zeta_1(x(t), t), \tag{1.2}$$

with the state vector

$$x = \left[i_r, i_o, V_{C_a}, V_{C_g}\right]^{\mathsf{T}}$$

and

$$A_1 = \begin{bmatrix} 0 & -\dfrac{nL_m R_s}{A} & 0 & -\dfrac{nL_m}{A} \\ 0 & -\dfrac{(L_m + L_r) R_s}{A} & \varepsilon & -\dfrac{(L_m + L_r)}{A} \\ 0 & \dfrac{1}{C_a} & 0 & 0 \\ 0 & \dfrac{1}{C_g} & 0 & 0 \end{bmatrix},$$

$$B_1 = \frac{1}{A}\begin{bmatrix} L_s + (n-1)\, nL_m \\ (n-1)\, L_m - L_r \\ 0 \\ 0 \end{bmatrix}, \; u(t) = E(t),$$

$$A = n^2 L_m L_r + L_s L_r + L_m L_s.$$

Table 1.2 Physical meaning of the parameters of the generator model.

Parameter	Units	Physical meaning
C_a	Faraday	Capacitance of discharge gap
C_g	Faraday	Capacitance of dielectric layer
L_s	Henry	Series-compensating inductance
L_r	Henry	Primary inductance
L_m	Henry	Magnetizing inductance
R_s	Ohm	Series resistance
n	NA	Turns ratio ($N_1 = N_2$) of transformer
ε	Ohm^{-1}	Self-conductance of capacitor C_a

The variable n represents the high-frequency high-voltage transformer ratio (N_1/N_2).

2. Negative semicycle:

$$\frac{d}{dt}x(t) = A_2 x(t) + B_2 u(t) + \zeta_2(x(t), t), \tag{1.3}$$

with $A_2 = A_1$ and $B_2 = -B_1$.

3. Non-discharge cycle:

$$\frac{d}{dt}x(t) = A_3 x(t) + B_3 u(t) + \zeta_3(x(t), t), \tag{1.4}$$

where the parameters of the model are changed as

$$A_3 = \begin{bmatrix} 0 & -\dfrac{nL_m R_s}{A} & -\dfrac{nL_m}{A} & -\dfrac{nL_m}{A} \\ 0 & -\dfrac{(L_m + L_r) R_s}{A} & -\dfrac{(L_m + L_r)}{A} + \varepsilon & -\dfrac{(L_m + L_r)}{A} \\ 0 & \dfrac{1}{C_a} & 0 & 0 \\ 0 & \dfrac{1}{C_g} & 0 & 0 \end{bmatrix},$$

$$B_3 = \frac{1}{A}\begin{bmatrix} L_s + n^2 L_m \\ nL_m \\ 0 \\ 0 \end{bmatrix}.$$

The terms $\zeta_i(x(t), t)$, $i = \{1, 2, 3\}$, represent the contributions of external perturbations and internal uncertainties over the state model.

In the model (1.2)–(1.4) the parameters have a physical meaning as indicated in Table 1.2.

Table 1.3 Values of the parameters for the ozone generator model.

Parameter	Value
C_a	$1.0 \cdot 10^{-4}$
C_g	$1.0 \cdot 10^{-3}$
L_s	$4.0 \cdot 10^{-6}$
L_m	$1.0 \cdot 10^{-6}$
L_r	$9.8 \cdot 10^{-5}$
R_s	120
n	$5.0 \cdot 10^{4}$

The controller design for the ozone generator should take into account its switched nature. A complete mathematical description of the hybrid controller intended to enforce the regulated production of ozone concentration is given in the appendix.

1.5.2 Numerical simulations

A set of numerical simulations has been performed to show how the designed controller works in practice. The parameters used in the numerical simulation are in Table 1.3.

The reference trajectories were created with the following reference function:

$$v_{\sigma(t)} = \begin{cases} 10 \cdot \chi(0.1, 5) & \text{if} \quad \sigma(t) = 1, \\ -10 \cdot \chi(0.1, 5) & \text{if} \quad \sigma(t) = 2, \\ 5 \cdot \chi(0.1, 5) & \text{if} \quad \sigma(t) = 3, \end{cases} \tag{1.5}$$

where $\chi(T_p, HD)$ is the square signal running with a period of T_p and a heavy duty given by HD. These parameters were obtained from the original study where the model presented in Alonso et al. (2003) was introduced. They correspond to the desired ozone concentrations that can be evaluated online. This reference function was selected because it proved to be adequate to produce a constant ozone concentration of 5.0 mg L^{-1}. This concentration is usual in various chemical applications. The ozone concentration value can be determined by a nominal nonlinear relationship between this ozone concentration and the values of i_r, i_o, V_{C_a} and V_{C_g}. For such a relationship Alonso et al. (2003) can be consulted.

The following set of gains for the controller of the ozone generator was applied in the numerical simulations presented in this part of the study:

$$H_{\sigma(t)=1} = -\begin{bmatrix} 0.5299 \\ 0.0376 \\ 0 \end{bmatrix}, \; H_{\sigma(t)=2} = \begin{bmatrix} 0.5299 \\ 0.0376 \\ 0 \end{bmatrix},$$

$$H_{\sigma(t)=3} = -\begin{bmatrix} 0.5299 \\ 0.0376 \\ 0 \end{bmatrix}.$$

These gains were obtained by a pole placement algorithm. The poles assignment were adjusted to -20, -30, and -40 for the system presented in (A.17). The procedure for obtaining each gain matrix was executed in Matlab. It should be mentioned that the poles were selected by trial and error without any guideline.

Once the controllers gains were obtained by the procedure described above, the numerical simulation of the ozone generator was executed. The reference trajectories obtained when the reference controller (1.5) was applied as well as the corresponding states for the ozone generator system appear in Fig. 1.4. In this figure, all the four different current and voltages are depicted. This figure shows the reference trajectories, as well as the corresponding currents and voltages. The lines depicted in dashed line (red color in the electronic version) represent the reference trajectories.[2] On the other hand, the solid line (blue color in the electronic version) lines correspond to the states of the ozone generator model (A.1). All the four trajectories demonstrate how the proposed controller forced each state to track the corresponding reference trajectory. Moreover, this solution is achieved in fixed time for the fourth state. However, in the remaining three states, the convergence appeared at least a couple of s later. In particular, one can notice the effect of the switching controller over the fourth state trajectory.

The sliding surface $s_{\sigma(t)}$ trajectory is showed in Fig. 1.5A. This signal clearly depicts what is maybe the most important drawback associated with the controller proposal of this study. High-frequency oscillations appear when the sliding surface value approaches zero. This is evident in the aforementioned figure. For visualization purposes, the sliding surface trajectory was filtered and it is depicted in Fig. 1.5B. Fig. 1.5C shows the control action applied to stimulate the circuit. This control action corresponds to the entire control action proposed in (A.7). Finally, the first component of the gain matrix $H_{\sigma(t)}$ was registered and appears in Fig. 1.5D. These four signals were

[2]Note: The color figures will appear in color in all electronic versions of this book.

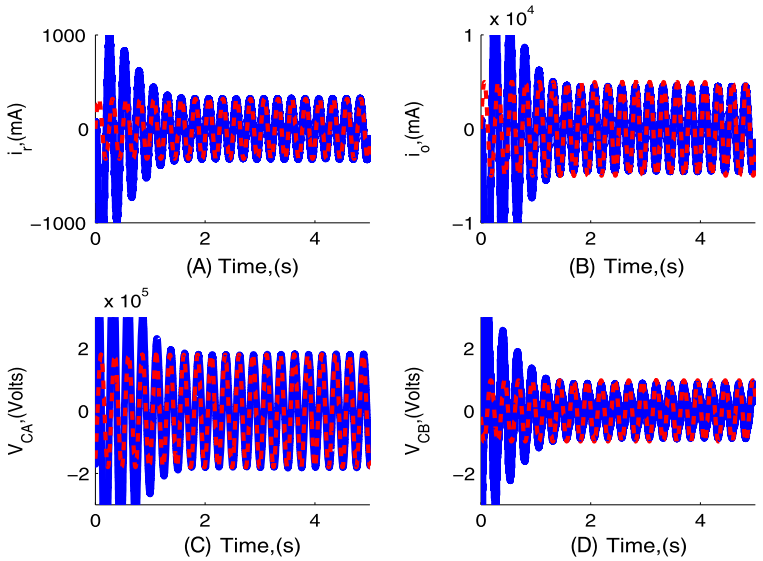

■ **FIGURE 1.4** Reference trajectories as well as their corresponding states obtained in the ozone generator.

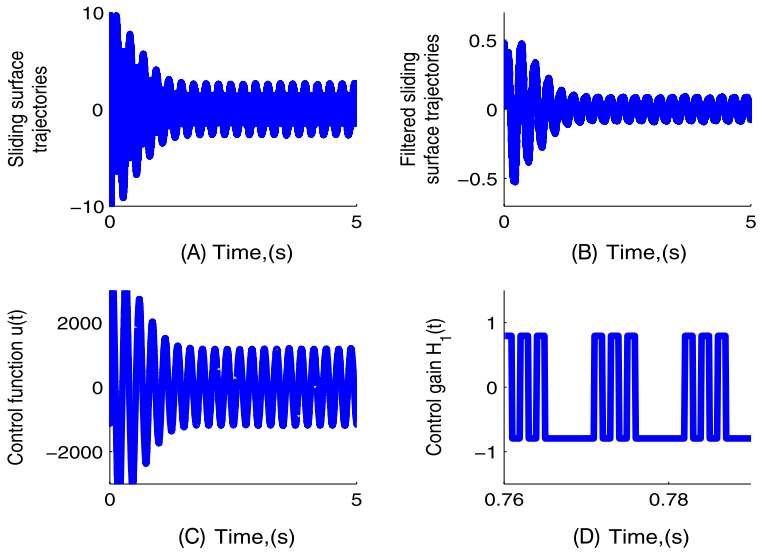

■ **FIGURE 1.5** Summary of several important results regarding the application of the mixed proposed controller.

useful to prove how the proposed controller was efficient to reproduce the reference trajectories using the mixed controller based on the application of the modified STA and the sequence of linear controller already presented here.

Fig. 1.4A shows the current i_r obtained as a consequence of the controller application on the ozone generator. Fig. 1.4B shows the time variation of current i_o. Fig. 1.4C shows the voltage V_{C_a} at the pseudo-capacitor formed by glass tube and the negative electrode formed by the metallic section in the reactor. Fig. 1.4D shows the voltage V_{C_g}.

Fig. 1.5A depicts the sliding surface s_σ trajectory. A filtered version of the same sliding mode trajectories is showed in Fig. 1.5A. The control function, obtained when both controllers the sliding mode and the switching linear, appear in Fig. 1.5C. Fig. 1.5D describes the time evolution of the first component of the switching gain associated with the linear controller.

1.6 CONCLUSIONS

In this chapter:

– Experimental conditions of ozonation procedure in three different phases, liquid, solid, and gaseous, were described.

– The ozone dispersion by various diffusers in the reactor was explained.

– The application of ozone for the treatment of VOCs in air was also detailed.

– The ozonation procedures in three different phases, including the description of the laboratory reaction systems, were described.

– The modeling and the automatic control of the CDOG were also developed.

Chapter 2

Modeling of ozonation

CONTENTS

ABSTRACT

The simple mathematical model proposed here is one of the possible approaches to a description of ozonation in water in a semi-batch reactor at

Ozonation and Biodegradation in Environmental Engineering
https://doi.org/10.1016/B978-0-12-812847-3.00011-1

constant pressure and temperature. This model permits one to characterize the ozone mass transfer in water using an empirical saturation constant. This constant depends on several easily measured experimental values (the gas flow, the volumes of gas and liquid phases, as well as the maximum ozone content in liquid phase). It can be calculated without any previous information as regards the diffusion coefficient, the specific interfacial area, the bubble size distribution, and the bubble diameter. The proposed model is given by the differential equations describing the ozone dissolution in water and the occurring chemical reaction, including the ozonation mass balance relation. Based on the computer simulation, the optimal conditions to perform the complete or the maximum decomposition of organic pollutants in water were achieved. To evaluate the proposed simple mathematical model, the simulation of ozonation of the two unsaturation hydrocarbon pollutants (UHPs), like trichloroethylene (TCE) and tetrachloroethylene (PCE), was realized under different experimental conditions. A couple of additional mathematical models referring to the pH effect and the dynamics of byproducts formed during ozonation were also developed. Several numerical simulations demonstrate the validity of the suggested models.

2.1 CHEMICAL BASIS OF OZONATION MODELING IN THE LIQUID PHASE

Several studies (Bader and Hoigné, 1981; Hoigné and Bader, 1983b; Razumovskii et al., 1984) addressing the oxidation kinetics of different organic compounds by ozone were realized. Some of them (Bin and Roustan, 2000; Oppenländer, 2003; Wright et al., 1998) investigate the ozonation of UHPs in semi-batch or continuous-flow reactors. Several system parameters having a great influence in the ozone mass transfer (gas flow rate, partial pressure of ozone, degree of mixing, bubble size, and reactor geometry) are inherently involved in the ozonation rate constant and the ozone dose. In some of the previous studies, the proposal was to analyze the ozone absorption in the liquid phase, and in other cases the aim has been the stripping of the soluble gas in the bulk of the liquid. Different theoretical models (Danckwerts and Lannus, 1970; El-Din and Smith, 2001; Fortescue and Pearson, 1967; King, 1966; Lamont and Scott, 1970; Theofanous et al., 1976) describe mass transfer between two phases (gas and liquid). Here, the mass transfer often is limited to the application of only one treatment. The experimental determination of the volumetric ozone mass-transfer coefficient ($k_L a$) in the liquid phase of a semi-batch system was applied by various researchers (Kuo, 1982; Wright et al., 1998). A continuous supply of a gaseous solute to the batch-added liquid contained in an agitated vessel or in a bubble column was done. In some cases, the values of the mass-

transfer coefficient (k_L) have been estimated from the determination of the volumetric mass-transfer coefficient and the specific interfacial area (a). However, the bubble size distribution determination in a disperse system is subjected to inaccuracies and experimental difficulties. In order to overcome this problem, some authors suggested to investigate the correlation that does not involve the representative bubble diameter (d_b) and bubble rise velocity (Akita and Yoshida, 1974; Beltrán et al., 2000; Deckwer and Schumpe, 1993; Hikita et al., 1981).

The correlation analysis requires knowledge of the column diameter, gas superficial velocity, and fluid parameters. In this case, the film and surface renewal theories are the most representative. Application of these theories allows for the establishment of the kinetic regime of gas absorption in a given liquid medium, as well as for the determination of fluid dynamic data, such as the specific interfacial area or the mass-transfer coefficient, which cannot easily be determined by most of the experimental data obtained.

The simple mathematical model proposed here is an alternative approach to the description of ozonation in water in a semi-batch reactor at constant pressure and temperature. This model permits one to characterize the ozone mass transfer in water by the use of an empirical saturation constant (k_{sat}). This constant depends on several easily measured experimental values (the gas flow, the volumes of gas and liquid phases, and the maximum ozone content in liquid phase). It can be easily calculated without any previous information as regards the diffusion coefficient, the specific interfacial area, the bubble size distribution and the bubble diameter. The proposed model includes differential equations describing the ozone dissolution in water and the occurring chemical reaction, including the ozonation mass balance relation. Based on the computer simulation, the optimal conditions to perform the complete or the maximum decomposition of organic pollutants in water are achieved.

2.2 MATHEMATICAL MODEL OF OZONATION IN LIQUID PHASE

We use the mathematical model proposed before (Poznyak and Vivero, 2005; Poznyak et al., 2003). In the previous investigation this model was used only for a determination of the ozonation constants for very quick reactions of ozone with amines and olefins based on the measurement of the ozone concentration in the gas phase in the reactor outlet without any computer simulations. It showed good agreement between the experimental and calculated values of the reaction constants (Poznyak et al., 2003).

Now, using the information on the reaction constants, obtained before, and the mathematical model as well, we design the model-based technique of an ozone mass transfer and the organics decomposition simulation. This provides complete and detailed information on the ozonation and may serve for the optimization of this process under different initial conditions. The model designed here includes the integral equation of material balance describing, in a very simple form, the ozone dissolution in water and the chemical reaction of organics and ozone (2.1):

$$\int_0^t W_g c_0^g d\tau = \int_0^t W_g c_\tau^g d\tau + V_g c_t^g + Q_t,\ c_{t=0}^g = c^g(0). \tag{2.1}$$

Here:

– c_0^g, c_t^g are the initial and current ozone concentrations in the gas phase (mol L^{-1}),

– W_g is the gas flow rate (L s^{-1}),

– V_g is the volume of the gas phase (L),

– Q_t is the current ozone amount in liquid phase (mol).

The auto-decomposition of ozone in water was not taken into account in the analysis and modeling of the ozonation. In this particular case, the part of the decomposed ozone was less than 1% of the initial concentration. This information was obtained by the comparison of the ozone concentration measured in the inlet and outlet of the reactor in an experiment without the presence of the contaminant (no chemical reaction in the reactor). By the differentiation of (2.1) we obtain the variation of the ozone concentration in the gas phase at the reactor's output:

$$\frac{d}{dt}c^g(t) = \frac{1}{V_g}\left[W_g(c_0^g - c^g(t)) - k_{sat}(Q_{\max} - Q(t))\right],\ \ c^g(0) = c_0^g, \tag{2.2}$$

where

– V_{liq} is the volume of the liquid phase (L),

– $Q_{\max}$ is the maximum amount of ozone in the saturation state of the liquid phase at a fixed temperature (mol),

– k_{sat} is the saturation constant of ozone in water (s^{-1}),

– Q_t is the ozone concentration in the liquid phase which satisfies the following expression:

$$Q(t) = Q_{\max}\left(1 - e^{-k_{sat}t}\right). \tag{2.3}$$

Eq. (2.3) is justified by the first order dynamics observed in several preliminary studies (Bin and Roustan, 2000). This first order dynamics is characterized by the generalized saturation parameter named k_{sat}. The time derivative of (2.3) yields

$$\frac{dQ(t)}{dt} = Q_{\max}k_{sat}e^{-k_{sat}t}, \quad Q(0) = 0. \tag{2.4}$$

Various authors (Hoigné and Bader, 1983b; Roth and Sullivan, 1981; Zhou et al., 1994) studied the ozone solubility in various solvents. The analysis of these data shows that the ozone's dissolution obeys the *Henry law (Bin and Roustan, 2000)*. Then, the maximum dissolved ozone in a given volume of liquid V_{liq} at constant temperature $Q_{\max}$ can be described by

$$Q_{\max} = Hc_0^g V_{liq}. \tag{2.5}$$

Here H is the *Henry constant* (mol L_{liq}^{-1}/mol L_g^{-1}).

2.2.1 Estimation of the saturation constant k_{sat}

The model proposed here includes the empirical constant k_{sat} (*the saturation constant*) as the characteristic parameter of the heterogeneous ozone–water system. This constant is calculated without any *a priori* information as regards the diffusion coefficient, the specific interfacial area, the bubble size distribution and a bubble diameter (Hoigné and Bader, 1983b; Roth and Sullivan, 1981; Zhou et al., 1994). The calculation can be realized using only the variation (2.2) of the current ozone concentration in the gas phase with a known initial ozone concentration, the gas flow W_g, and the volume of the gaseous phase V_g. Taking into account that $Q_0 = 0$ from (2.2) we obtain the following equation:

$$c^g(t) = c_0^g - \frac{Q_{\max}k_{sat}}{V_g k_{sat} - W_g}\left(e^{-\frac{W_g}{V_g}t} - e^{-k_{sat}t}\right). \tag{2.6}$$

Based on Eq. (2.6), we may calculate *the saturation constant* k_{sat} as

$$k_{sat} = \frac{W_g(c_0^g - c_t^g) - V_g\dfrac{d}{dt}c_t^g}{Q_{\max}}e^{k_{sat}t}. \tag{2.7}$$

Remark 2.1. *The solution of the transcendent equation (2.7) for a given time t exists if and only if (2.8) there exists a solution of the following equa-*

Table 2.1 Effect of solvents and gas flow on the saturation constant.

Solvent	W_g, [L s^{-1}]	k_{sat}, [s^{-1}]
Carbon tetrachloride	$1.94 \cdot 10^{-3}$	$1.05 \cdot 10^{-2}$
	$1.11 \cdot 10^{-3}$	$0.65 \cdot 10^{-2}$
	$0.42 \cdot 10^{-3}$	$0.20 \cdot 10^{-2}$
Heptane	$1.94 \cdot 10^{-3}$	$1.53 \cdot 10^{-2}$
	$1.11 \cdot 10^{-3}$	$0.90 \cdot 10^{-2}$
	$0.42 \cdot 10^{-3}$	$0.33 \cdot 10^{-2}$
Water	$1.94 \cdot 10^{-3}$	$16.7 \cdot 10^{-2}$
	$1.11 \cdot 10^{-3}$	$6.3 \cdot 10^{-2}$
	$0.42 \cdot 10^{-3}$	$2.1 \cdot 10^{-2}$

tion:

$$\ln(x) = x + \ln\left(\frac{W_g(c_0^g - c_t^g) - V_g \frac{d}{dt} c_t^g}{Q_{\max}} t\right),$$

which is possible if and only if

$$t\left[W_g(c_0^g - c_t^g) - V_g \frac{d}{dt} c_t^g\right] e \le Q_{\max}. \tag{2.8}$$

Remark 2.2. *When* $\frac{d}{dt} c_t^g = 0$ *(which means that we consider the measurement curve* c_t^g *at its minimum point) Eq. (2.7) simplifies to*

$$k_{sat} = \frac{W_g(c_0^g - c_t^g)}{Q_{\max}} e^{k_{sat} t}. \tag{2.9}$$

The numerical solution of (2.7) or (2.9) may be obtained by the standard regression iterative method.

Table 2.1 presents the values of the saturation constant k_{sat} for different solvents (CCl_4, H_2O, and heptane) under different gas flows with $W_g = 7, 4$ and 1.5 L h^{-1} in a reactor with V_{liq} of $3.2 \cdot 10^{-2}$ L.

The saturation constant k_{sat} varies its value depending on the solvent: it is the highest for water and low for organic solvents. It is very important to notice that this constant depends on the bubble diameter. The increase of this parameter by 5 times leads to the decrease of the constant value (see Table 2.2).

The simulation of ozone mass transfer at the different gas flows shows that the gas flow effect, both on the ozone saturation in water and on the ozone

Table 2.2 Dependence of the saturation constant on a bubble diameter for two gas flows. For CCl_4 at the temperature of 0°C for a reactor with V_{liq} of $0.6 \cdot 10^2$ L.

d_b, [mm]	W_g, [L s^{-1}]	k_{sat}, [s^{-1}]
1	$1.11 \cdot 10^{-3}$	$0.586 \cdot 10^{-2}$
5	$1.11 \cdot 10^{-3}$	$0.546 \cdot 10^{-2}$
1	$0.50 \cdot 10^{-3}$	$0.180 \cdot 10^{-2}$
5	$0.50 \cdot 10^{-3}$	$0.105 \cdot 10^{-2}$

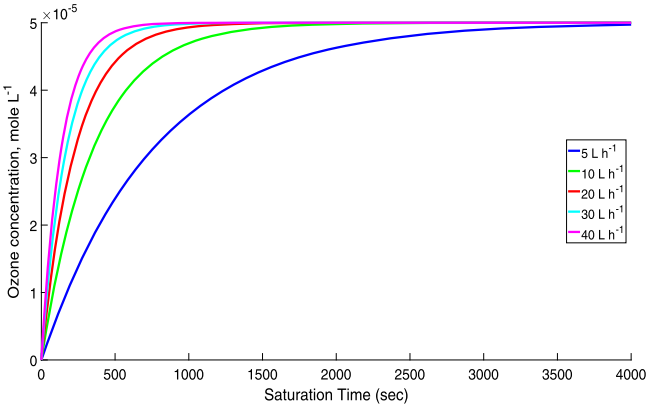

■ **FIGURE 2.1** The gas flow effect on the ozone saturation in water. From down to top, the gas flows are 5, 10, 20, 30, and 40 L h^{-1}.

concentration variation in the gas phase in the reactor outlet, is very significant (Fig. 2.1).

The increase of the gas flow from 5 L h^{-1} to 40 L h^{-1} decreases the saturation time from 3000 s to 400 s (Fig. 2.1). A similar effect is more noticeable when the flow is within the range of 5–20 L h^{-1}, since the increase of the gas flow from 20 L h^{-1} to 40 L h^{-1} has a destructive effect (from 700 s to 400 s). Another important factor in the ozone saturation is the reactor volume. It also affects the ozone concentration in the reactor outlet (Fig. 2.2). The reactor volume was varied from 2 to 4 L under the IOC $1 \cdot 10^{-1}$ mol L^{-1} keeping the gas flow equal to 40 L h^{-1}.

Notice also that the increase of the reactor volume increases the saturation time by a factor 2, approximately. In general, the relation between the saturation time and the reactor volume is linear (see Fig. 2.3).

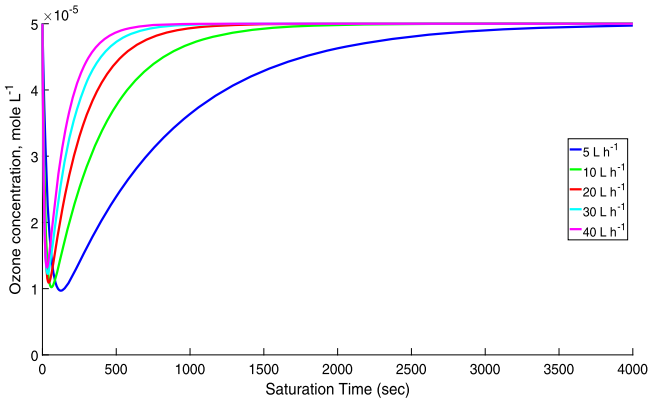

■ **FIGURE 2.2** The gas flow effect on the ozone concentration variation in the gas phase in the reactor outlet.

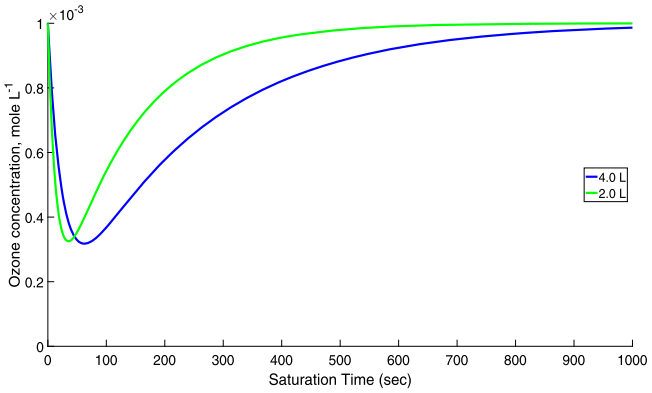

■ **FIGURE 2.3** Effect of the reactor volume on the variation of the ozone concentration in the gas phase: 4 L, 2 L.

2.2.2 Evaluation of the mathematical model by the simulation of ozonation of unsaturated hydrocarbon pollutants

The validation of the proposed simple mathematical model by the simulation of ozonation of two Unsaturated Hydrocarbon Pollutants (UHPs), as trichloroethylene (TCE) and tetrachloroethylene (PCE), was realized under the different experimental conditions. These conditions varied as follows: the gas flow varied from 5 to 40 L h^{-1}, the Initial Ozone Concentration (IOC) from $5.0 \cdot 10^{-5}$ to $1.0 \cdot 10^{-3}$ mol L^{-1}, and the reactor volume from 2 up to 4 L. The experiments were realized at a temperature of 20°C and the constant pH = 5, which guarantees the direct mechanism of ozonation with molecular ozone. The initial concentrations of TCE and PCE in water

were $c_{TCE} = 3.5 \cdot 10^{-6}$ mol L^{-1}, $c_{PCE} = 9 \cdot 10^{-7}$ mol L^{-1}. The reaction constants of ozone with the two UHPs were $k_{TCE} = 3.6$ L mol^{-1} s^{-1} and $k_{PCE} = 1.0$ L mol^{-1} s^{-1} (King, 1966), since these UHP have no high reactivity with ozone and are recalcitrant. The obtained simulation results demonstrate that the TCE decomposition is faster than the PCE decomposition related with their chemical reaction rate constants.

On the other hand, it is well known that the IOC is a parameter with very strong effects in ozonation, but its effect on the ozonation time of compounds is not linear and depends on the reactivity with ozone. In general, the increase of IOC by 20 times leads to the decrease of the ozonation time by a factor of 7 for TCE and of 25 for PCE. In the case of the low reactivity with ozone, the effect of IOC is more significant. To the contrary, the effect of the gas flows on the removal dynamics for the TCE and the PCE is not significant. A variation of the gas flow of 5, 10, 20, 30, and 40 L h s^{-1} practically does not affect the TCE and PCE degradation time.

The comparison of experimental data and simulation results for these UHP demonstrates that it necessary to take into account that, in this particular case, the radical route of the TCE and PCE degradation may be neglected. These substances are decomposed by direct reaction with molecular ozone. For this reason, the proposed mathematical model neither considers the auto-decomposition of ozone in water, nor the radical ozonation mechanism. The model also does not take into account the possible stripping of organic compounds, since, according to some preliminary studies (Farines et al., 2003; Wright et al., 1998), neither TCE nor PCE evaporation has been observed during water ozonation. The modeling errors were 5.23% for TCE and 8.43% for PC, which can be considered to be within an acceptable margin being good enough to validate the proposed simple mathematical model.

Based on the obtained results, we may conclude that online measurements of the ozone concentration in the gas phase can provide a good characterization of ozonation. The saturation constant k_{sat} can be calculated directly using the measurements of the current ozone concentration in the gaseous phase, and this parameter characterizes the mass transfer of ozone for some specific experimental conditions.

2.3 OZONATION MODEL OF SEVERAL CONTAMINANTS IN LIQUID PHASE

Ozone is capable to oxidize a variety of organic materials in aqueous solution. The process of oxidation by ozone involves the phenomenon of mass transfer with simultaneous chemical reaction. Therefore, the results obtained in Poznyak et al. (2004); Poznyak and Vivero (2005);

Poznyak (2003); Poznyak et al. (1977) considered a simple ozonation with i-component model mixture at pH = 7.

2.3.1 Model description

The following set of equations corresponds to the mathematical model of ozonation when the contaminants c_i are included. First, let us introduce the general model for the ozone concentration in the gaseous phase c_t^g in integral form:

$$\begin{gathered}\int_0^t W_g(\tau)\, c_{in}^g(\tau)\, d\tau = \int_0^t W_g(\tau)\, c^g(\tau)\, d\tau + V_g c^g(t) + Q_t, \\ c^g(0) = c_0^g,\end{gathered} \tag{2.10}$$

where c_{in}^g [mol L^{-1}] is the ozone concentration at the reactor input.

Taking the full-time derivative of (2.10), one gets

$$\frac{d}{dt}c^g(t) = V_g^{-1} W_g\left(c_{in}^g - c^g(t)\right) - V_g^{-1}\frac{d}{dt}Q(t). \tag{2.11}$$

The ozone mass balance in the liquid phase is given by

$$\frac{d}{dt}Q(t) = k_{sat}(Q_{\max} - Q(t)) - \frac{d}{dt}\left[V_{liq}\sum_{i=1}^{N}\left(c_{i,0} - c_i(t)\right)\right]. \tag{2.12}$$

The kinetic reaction between ozone and the contaminant is described by a bimolecular kinetic equation:

$$\frac{d}{dt}c_i(t) = -k_i\frac{Q(t)}{V_{liq}}c_i(t) \quad i = \overline{1, N}. \tag{2.13}$$

Notice that the only single variable that can be measured online is

$$y(t) = c^g(t). \tag{2.14}$$

Gathering all the previous equations yields

$$\left.\begin{array}{c} \dfrac{d}{dt}c^g(t) = V_g^{-1}W_g\left(c_{in}^g - c^g(t)\right) - \\ V_g^{-1}\left[k_{sat}(Q_{\max} - Q(t)) - Q(t)\sum\limits_{i=1}^{N} k_i c_i(t)\right], \\ \dfrac{d}{dt}Q(t) = k_{sat}(Q_{\max} - Q(t)) - Q(t)\sum\limits_{i=1}^{N} k_i c_i(t), \\ \dfrac{d}{dt}c_i(t) = -k_i\dfrac{Q(t)}{V_{liq}}c_i(t) \quad i = \overline{1,N}, \\ y(t) = c^g(t). \end{array}\right\} \tag{2.15}$$

Remark 2.3. *Notice that all components c_i and Q are not available for measuring online. Only one state of this process is measurable, which corresponds to $y = c_{gas}$; the initial contaminant concentrations c_0^g are available too.*

– The first equations correspond to the ozone mass balance in the gaseous phase of the reactor (2.1)–(2.2) and the ozone consumed by the reaction with contaminants.

– The second equation describes the kinetics of ozone dissolved in the liquid phase Q.

– The last N components in (2.15) describe the kinetics of the ozone reaction with the contaminant c_i.

2.3.2 Abstract format of the model

The model presented in Eq. (2.15) can be represented in a more abstract form. This structure uses the variable state theory. Thus, define the state vector x as

$$x = \begin{bmatrix} c^g \\ Q/V_{liq} \\ c_1 \\ \vdots \\ c_N \end{bmatrix}.$$

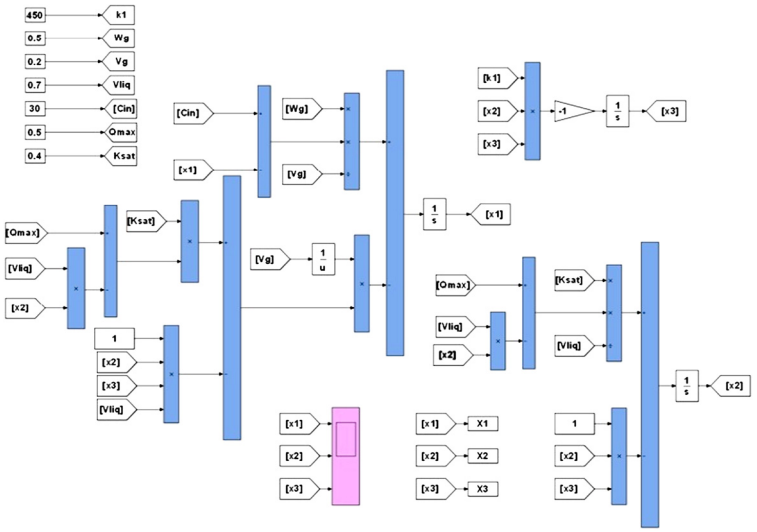

■ **FIGURE 2.4** Time evolution of the state variables (c_g, Q, c_1) of the ozonation model (2.16).

As a consequence, the dynamic equation for the vector state can be represented in abstract format by

$$\begin{aligned} \frac{d}{dt}x(t) &= f(x(t), t), \\ y(t) &= x_1(t), \end{aligned} \tag{2.16}$$

or, equivalently, in extended format:

$$\left.\begin{aligned} \dot{x}_1(t) &= V_g^{-1} W_g \left(c_{in}^g(t) - x_1(t)\right) - \\ V_g^{-1} &\left[k_{sat}(Q_{\max} - V_{liq}x_2(t)) - V_{liq}x_2(t)\sum_{i=1}^{N} k_i x_{2+i}(t)\right], \\ \dot{x}_2(t) &= \frac{k_{sat}}{V_{liq}}(Q_{\max} - V_{liq}x_2(t)) - x_2(t)\sum_{i=1}^{N} k_i x_{2+i}(t), \\ \dot{x}_{2+i}(t) &= -k_i x_2(t) x_{2+i}(t), \\ y(t) &= x_1(t). \end{aligned}\right\} \tag{2.17}$$

Remark 2.4. *As one can see the model (2.16) is* ***bilinear*** *with respect to the components x_i of the vector state x.*

2.3.3 Numerical illustration of the ozonation model

The numerical simulation of the model (2.16) is realized by the application of the Matlab/Simulink tool, according to the following block scheme

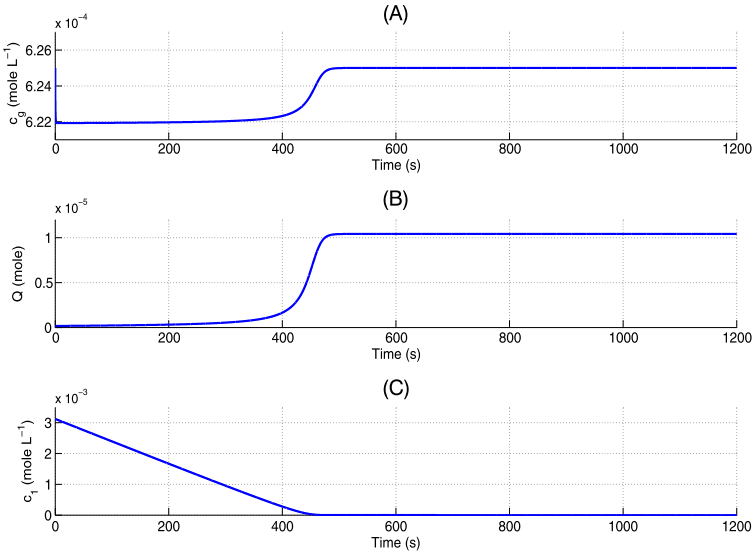

■ **FIGURE 2.5** Time evolution of the state variables (c_g, Q, c_1) of the ozonation model (2.16).

Table 2.3 Parameter values.

$V_g = 0.2$ L	$V_{liq} = 0.7$ L
$W_g = 0.5$ L min^{-1}	$Q_{\max} = 0.5$ mol
$k_{sat} = 0.4$ s^{-1}	$k_1 = 450$ L mol^{-1}
$c^g_{in} = 6.25 \cdot 10^{-4}$ mol L^{-1}	$c_1(0) = 6.25 \cdot 10^{-4}$ mol L^{-1}
$c^g(0) = 1.56 \cdot 10^{-3}$ mol L^{-1}	$Q(0) = 0.0$ mol

(Fig. 2.4). Fig. 2.5 demonstrates the behavior of the principal components of the model (2.16) under the values of the parameters ($N = 1$) given in Table 2.3.

2.4 APPLICATION OF A SIMPLE OZONATION MODEL TO ORGANIC CONTAMINANTS DEGRADATION IN WATER

Based on the proposed simple mathematical model (2.2), (2.6), and (2.4) to study the decomposition of the model mixtures in aqueous solution (Poznyak and Vivero, 2005), the corresponding kinetic constants of ozonation of three different phenols were calculated at $\text{pH}_1 = 3$ and $\text{pH}_2 = 7$. Under these experimental conditions, the direct mechanism with molecular ozone was guaranteed. The compounds were phenol (Ph), 4-chlorophenol (4-CPh) and 2, 4-dichlorophenol (2, 4-CPh).

It is well known that phenol and chlorinated phenols (CPhs) are commonly found as micropollutants in water. They can be formed indirectly during chlorination of municipal or industrial waste water, bleaching in paper industry, or during bioconversion of low molecular weight compounds. They are also widely used in pesticide production. Drinking water chlorination also produces chlorophenols due to oxidation of phenols. Phenolic compounds are common pollutants in waste water of oil refinery, petrochemical, coke, and grease, due, steel and textile industries (Beltrán et al., 1997; Grau, 1991). These contaminants are difficult to decompose in waste water (Boari et al., 1984; Hamdi, 1992). CPhs have the characters of toxicity, being refractory, and being difficult to oxidize by the traditional biological treatment. The efficiency of the conventional biological treatment is usually unsatisfactory due to its required long reaction time and limited initial pollutant concentration (Calvosa et al., 1991; Davis and Huang, 1990; Joglekar et al., 1991; Stowell et al., 1992).

2.4.1 Studied compounds

The studied organic pollutants were phenol (Ph), 4-chlorophenol (4-CPh), 2, 4-dichlorophenol (2, 4-DCPh) and their mixtures in the relation of 1:1:1. All chemicals purchased from Aldrich Co were of analytical grade.

2.4.2 Experimental conditions of ozonation

The ozonation of phenol, its chlorinated derivatives, and their mixtures was conducted with synthetic solutions in distilled water at the initial concentration of 200 mg L^{-1}. The reactor was the semi-batch type (0.5 L). The initial ozone concentration was 23 mg L^{-1}. The ozone–oxygen mixture flow was 0.5 L min^{-1}. All experiments were carried out at 20°C with agitation by bubbling of an ozone–oxygen mixture and by magnetic agitation (operated at 120 rpm). All ozonation experiments were conducted while varying the pH from 2 to 7. The pH variation was achieved with sulfuric acid and sodium hydroxide (0.1 N). For all experiments, aliquots of 3.0 mL reaction solution were withdrawn at desired time intervals from the reactor for sequential analyses.

Ozone was generated from dry oxygen by the ozone generator (corona discharge type) HTU500G (AZCO Industries Limited – Canada). An Ozone Analyzer BMT 963 (BMT Messtechnik, Berlin) provided the ozone detection in the gas phase in the reactor outlet for the ozone monitoring to control the ozonation degree, the ozone consumption, and the ozone decomposition.

Table 2.4 Retention times of compounds used for the identification of ozonation products by the HPLC.

Compound	Retention time, min
Hydroquinone	3.18
Catechol	3.70
Ph	4.87
4-CPh	6.87
Oxalic acid	2.68
Formic acid	3.40
Maleic acid /malonic acid	3.87
Fumaric acid	4.39
Hydroquinone	6.18
Muconic acid	8.06
Catechol	14.85

2.4.3 Analytical methods

The identification of intermediates and final products has been achieved by the high performance liquid chromatography (HPLC), by the liquid chromatograph (Perkin-Elmer) equipped with UV-Vis detector series 200 (190–460 nm). A reverse phase column was of C-18 (Nova Pack C-18, Waters), 300 mm in length and 3.9 mm in diameter. The used mobile phase was combined as water–acetonitrile–phosphoric acid, 50:50:0.1 for phenols and 89.9:10:0.1 for acids, with a flow rate of 0.8 mL min^{-1}. The identification of intermediates and final products was carried out by a comparison of the retention time and the UV spectra of the patterns at $\lambda = 210$ nm. The retention times of standards at $\lambda = 210\ nm$ used in the HPLC analysis are given in Table 2.4.

2.4.4 Effect of the pH on the ozone decomposition in a liquid phase

The ozone concentration in liquid and gas phases are in equilibrium, following the Henry law. The ozone decomposition degree in the liquid phase is proportional to its degrade in the gaseous phase (Razumovskii et al., 1984). The difference between the initial ozone concentration and its concentration after saturation is the degree of the ozone auto-decomposition. Fig. 2.6 presents the variation of the ozone decomposition degree at the pH of 0.0–12.0. In the majority of preliminary investigations, the complete decomposition of ozone (to 100%) under the pH > 7 was claimed. However, our experiments showed that the ozone decomposition under pH between 0

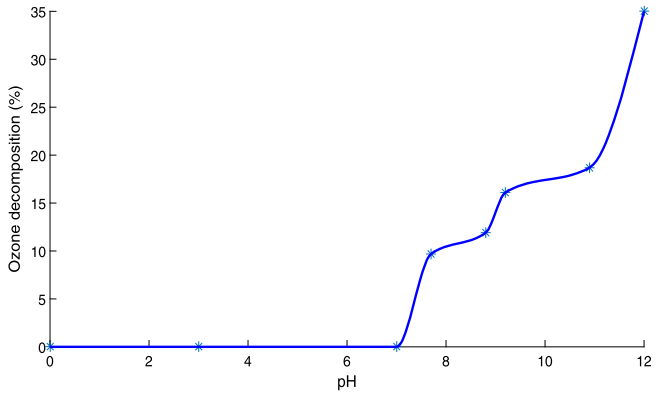

■ **FIGURE 2.6** Ozone decomposition degree in water as a function of the pH.

and 7 is not observed practically, and it increases up to 35% when the pH is 12.

2.4.5 Degradation by ozone of Ph, 4-CPh, and 2,4-DCPh, and their mixtures

According to Gould and Weber (1976); Hautaniemi et al. (1998a); Kuo and Huang (1995, 1998); Trapido et al. (1997), the ozonation intermediates are formed by several reaction mechanisms of ozone with phenols. Only a few studies have considered the possible reaction pathways and depicted the intermediates and final products of phenols with ozone (Hautaniemi et al., 1998a; Stowell et al., 1992). During the ozonation of monochlorophenols, the formation of chloride, hydroxylation products (4-chlorocatechol, chlorohydroquinone, catechol, and hydroquinone) and unsaturated acids (as products of the aromatic ring destruction by the electrophilic attack) were observed (Chen and Ni, 1999; Poznyak and Araiza G., 2005; Stowell et al., 1992; Tomiyasu et al., 1985). These studies also proved that diverse intermediates formed during ozonation, such as muconic, fumaric, and maleic acids which can react with ozone rapidly according to the Criege mechanism (Razumovskii et al., 1984).

In the final steps of ozonation, carboxylic acids and aldehydes of low molecular weight are accumulated. The nucleophilic reaction of ozone with a carboxyl group is extremely low (reaction constant of 50 L mol^{-1} s^{-1}). This fact justifies that these compounds with carboxyl group were accumulated during the ozonation. It was found also (Hautaniemi et al., 1998a; Kuo and Huang, 1995, 1998; Poznyak and Araiza G., 2005) that ozonation induces the denitration, dechloration or desulfuration of the substituted phenols in the initial stage of reaction. Table 2.5 shows the intermediates and

Table 2.5 Intermediates and final products obtained in ozonation of Ph, 4-CPh, 2,4-DCPh, and their mixture.

Comp.	pH 2	pH 7	pH12
Ph	Hydroquinone	Hydroquinone	Hydroquinone (trs)
	Catechol	Catechol (trs)	–
	Muconic acid	–	–
	Fumaric acid	Fumaric acid (trs)	Fumaric acid (trs)
	Maleic acid	Maleic acid	Maleic acid (trs)
	Oxalic acid	Oxalic acid	Oxalic acid
	Formic acid	Formic acid	–
4-CPh	Hydroquinone	Hydroquinone	Hydroquinone (trs)
	Catechol	Catechol	–
	Phenol (trs)	Phenol (trs)	Phenol (trs)
	Muconic acid (trs)	Muconic acid	–
	–	Fumaric acid	Fumaric acid (trs)
	Maleic acid	Maleic acid	Maleic acid (trs)
	Oxalic acid	Oxalic acid	Oxalic acid
	Formic acid	Formic acid	–
2,4-DCPh	Hydroquinone	Hydroquinone	Hydroquinone (trs)
	Catechol	Catechol	–
	4-Chlorophenol (trs)	4-Chlorophenol	4-Chlorophenol (trs)
	Phenol (trs)	Phenol	Phenol (trs)
	Muconic acid (trs)	Muconic acid (tr)	–
	Fumaric acid	Fumaric acid (tr)	Fumaric acid (trs)
	Maleic acid	Maleic acid	Maleic acid (trs)
	Oxalic acid	Oxalic acid	Oxalic acid
	Formic acid	Formic acid	–
Ph+ (4-CPh)+ (2,4-CPh)	Hydroquinone	Hydroquinone	Hydroquinone (trs)
	Catechol	Catechol	–
	Fumaric acid (trs)	Fumaric acid (trs)	Fumaric acid (trs)
	Maleic acid	Maleic acid	Maleic acid (trs)
	Oxalic acid	Oxalic acid	Oxalic acid

final products identified by HPLC during the ozonation of pH, 4-CPh and 2, 4-DCPh at the different pH values.

According to the compound distribution determined after ozonation, the intermediate and final products of the phenol decomposition are similar to those reported by other studies. In general, the compounds obtained after ozonations are: catechol, hydroquinone, muconic, fumaric, maleic, oxalic, and formic acids. Therefore, the presence of catechol (or derivatives of catechol) and hydroquinone at pH < 7 confirms the hydroxylation of the aromatic ring before its cleavage. It is important to notice that the presence of phenol is detected in the case of the 4-CPh and 2, 4-DCPh decomposi-

tion, as well as the presence of 4-chlorophenol, in the case of the 2, 4-DCPh decomposition at these pH values.

The formation of these compounds confirms *dechlorination* as the initial step of reaction of ozone with chlorinated phenols. The principal final products at these experimental conditions are oxalic and formic acids. While at pH = 12, catechol, hydroquinone, phenol, and 4-CPh have not been found, so that the final product is only oxalic acid. In general, the pH effect on the byproducts and the final products composition is very significant. Additionally, at the three different pH values of the ozonation reaction there were seven not identified intermediates when pH < 7. If ozonation occurs under basic pH conditions, the number of byproducts decreases to 2–5, depending on the initial contaminant.

On the other hand, the presence of unsaturated acids at different pH values confirms the cleavage of the aromatic ring; however, the mechanism of this reaction under acidic and basic pHs is different. Based on the results obtained in this study, we may conclude that ozonation at low pH (< 7) is carried out with molecular ozone, while at high pH (> 7) the radical mechanism takes place. The last statement coincides with the data of other authors (Chen and Ni, 1999; Hautaniemi et al., 1998a,b). However, based on the data of the ozone decomposition in water, obtained here by the measurement of the concentration of ozone dissolved in liquid phase, we may conclude that the ozone decomposition degree depends on the pH values, but it does not exceed 35% at a pH of 12. For this reason we may conclude that under the basic pH, a combination of two mechanisms takes place: *direct* with molecular ozone and *indirect* with the OH radicals.

Particularly, in the case of the phenols ozonation, the combination of two mechanisms increases the ozonation time from 1.3 up to 3.2 times at a pH of 7, and from 4 up to 13.3 at a pH = 12. In Table 2.6 the ozonation times are given required for the complete decomposition of phenols, depending on the pH. Besides, from a comparison of the ozonation time of phenols, it can be concluded that the presence of chlorine in the molecule increases the reactivity of the compound with ozone.

Applying the proposed simple mathematical model, the ozonation rate constants for individual phenols, in the case of the separate ozonation, as well as for the reaction of ozone with their mixture, were calculated at the pH values of 2 and 7, when the direct mechanism with molecular ozone takes place. The calculated constants are given in Table 2.7.

The comparison of the reaction rate constants obtained by other authors (Hautaniemi et al., 1998a,b; Razumovskii et al., 1984) demonstrates a good correspondence between these kinetic parameters ($1.6 \cdot 10^3$ for 2,4-DCPh

Table 2.6 Effect of the pH on the time of the complete degradation of phenols (s).

Compound	Ozonation time [s]		
pH of solution	pH = 2	pH = 7	pH = 12
Individual compounds			
Ph	4800	3600	1200
4-CPh	4800	2400	600
2,4-DCPh	4800	1500	360
Phenol mixture			
Ph	1500	1200	900
4-CPh	1800	1200	900
2,4-DCPh	1800	1200	1200

Table 2.7 Effect of the pH on the ozonation kinetics.

Compound	k [L mol^{-1} s^{-1}]	
pH of solution	pH = 2	pH = 7
Individual compounds		
Ph	$0.867 \cdot 10^3$	1.168×10^3
4-CPh	$1.040 \cdot 10^3$	3.090×10^3
2,4-DCPh	$0.871 \cdot 10^3$	6.171×10^3
Phenols mixture		
Ph	$3.193 \cdot 10^3$	$4.479 \cdot 10^3$
4-CPh	$2.544 \cdot 10^3$	$4.442 \cdot 10^3$
2,4-DCPh	$2.546 \cdot 10^3$	$6.104 \cdot 10^3$

at a pH of 2, $1.4 \cdot 10^3$, and $1.3 \cdot 10^3$ at the pH of 7, $1.9 \cdot 10^3$ for 4-CPh at the pH of 7, and $2.8 \cdot 10^3$ for 2,4-DCPh at a pH of 7). In view of the results obtained, we may conclude that the pH effect on the ozonation kinetics of phenols is very strong. So, the values of the constants increase significantly at a pH of 7. This phenomenon can be explained by the effect of the two factors: the partial ozone decomposition and the partial dissociation of phenols in water as the weak acid. On the other hand, it is very important to note the difference in the case of separate phenol decomposition and ozonation of their mixture. So, in separated phenol ozonation, the rate constants increase significantly with the pH increasing. This effect depends on the chemical structure of phenols. The rate constant increase is more essential for 2,4-DCPh in comparison with 4-CPh and Ph. But in the case of the mixture decomposition, the pH effect is significantly less. So, the rate constant increases 1.35–7 times in the separate ozonation, and 1.4–2.4 times in the mixture ozonation. The rate constant variation as a function of pH seems to

Table 2.8 Reaction mechanisms of ozone decomposition.

Hoigné, Staehelin, and Bader	Gordon, Tomiyasu, and Fukutomi
$O_3 + OH^- \xrightarrow{k_1} HO_2 + O_2^-$ $k_1 = 7.0 \times 10^1\ M^{-1}\ s^{-1}$	$O_3 + OH^- \xrightarrow{k_{10}} HO_2^- + O_2$ $k_{10} = 4.0 \times 10^1\ M^{-1}\ s^{-1}$
$HO_2 \overset{k_2}{\Longleftrightarrow} H^+ + O_2^-$ $k_2 = 1 \times 10^{-4.8}$	$HO_2^- + O_3 \xrightarrow{k_{11}} HO_2 + O_3^{\cdot -}$ $k_{11} = 2.2 \times 10^6\ M^{-1}\ s^{-1}$
$O_3 + O_2 \xrightarrow{k_3} O_3^{\cdot -} + O_2$ $k_3 = 1.6 \times 10^9\ M^{-1}\ s^{-1}$	$HO_2 + OH^- \overset{k_{12}}{\Longleftrightarrow} H_2O + O_2^-$ $k_{12} = 1.0 \times 10^{-4.8}$
$H^+ + O_3^- \underset{k_4^-}{\overset{k_4}{\Longleftrightarrow}} HO_3$ $k_4 = 5.2 \times 10^{10}\ M^{-1}\ s^{-1}$ $k_4^- = 2.3 \times 10^2\ s^{-1}$	$O_3 + O_2^- \overset{k_3}{\Longleftrightarrow} O_3^{\cdot -} + O_2$ $k_3 = 1.6 \times 10^9 M^{-1}\ s^{-1}$
$HO_3 \overset{k_5}{\Longleftrightarrow} HO^{\cdot} + O_2$ $k_5 = 1.1 \times 10^5\ s^{-1}$	$H_2O + O_3^{\cdot -} \xrightarrow{k_{13}} OH + O_2 + OH^-$ $k_{13} = 20\text{–}30\ M^{-1}\ s^{-1}$
$HO^{\cdot} + O_3 \xrightarrow{k_6} HO_4$ $k_6 = 2.0 \times 10^9\ M^{-1}\ s^{-1}$	$HO^{\cdot} + O_3^{\cdot -} \xrightarrow{k_{14}} O_2^- + HO_2$ $k_{14} = 6 \times 10^9\ M^{-1}\ s^{-1}$
$HO_4 \xrightarrow{k_7} HO_2 + O_2$ $k_7 = 2.8 \times 10^4\ M^{-1}\ s^{-1}$	$HO^{\cdot} + O_3^{\cdot -} \xrightarrow{k_{15}} O_3 + OH^-$ $k_{15} = 2.5 \times 10^9\ M^{-1}\ s^{-1}$
$2HO_4 \rightarrow H_2O_2 + 2O_3$ $HO_4 + HO_3 \rightarrow H_2O_2 + O_3 + O_2$	$HO^{\cdot} + O_3 \xrightarrow{k_{16}} HO_2 + O_2$ $k_{16} = 4.2 \times 10^8\ M^{-1}\ s^{-1}$

be logical and is consistent with a total ozonation time. At pH = 2, the rate constants for individual phenols and the total ozonation time did not differ significantly. But at pH = 7, the difference between the rate constants and the total ozonation time turns out to be notable. The rate constant at pH = 12 was not calculated: the ozonation mechanism, in this particular case, is more complicated, since the direct and indirect mechanisms in combination are realized simultaneously.

HSB and GFT reaction mechanisms can be described as in Table 2.8.

2.5 MATHEMATICAL MODEL TAKING INTO ACCOUNT THE pH EFFECT

Based on the HSB and GTF models, and since the reaction with OH^- is the initial decomposition step of ozone, the stability of the dissolved ozone is highly dependent on the pH and decreases as alkalinity rises. However, in acidic solutions, the reaction with OH^- cannot be the initial step only. Predicted reaction rates below pH = 4, including a mechanism based only

on reaction with OH^-, are much lower than those determined experimentally. According to (Sehested et al., 1991), the equilibrium ozone reaction becomes significant and the initiation reaction is surface catalyzed:

$$O_3 \underset{k_{17}^-}{\overset{k_{17}}{\Longleftrightarrow}} O + O_2, \quad k_{17} = 1 \cdot 10^{-7}\ s^{-1}, \quad k_{17}^- = 4 \cdot 10^9\ s^{-1}.$$

The atomic O continues to react with H_2O, or more likely forms an excited O_3^*, from recombination, which subsequently reacts with H_2O. The reaction rate for this step has been established at $k = 5\ M^{-1}\ s^{-1}$:

$$O + H_2O \Longleftrightarrow 2HO^{\cdot},$$
$$O_3^* + H_2O \Longleftrightarrow H_2O_2 + O_2.$$

The species formed can then react further forming other radicals such as O_2^-/HO_2. The propagating products, $HO^{\cdot}$ and HO_2, are diffused and react with O_3 in the bulk, continuing the chain reaction. Only low concentrations of the final species are present in the bulk, which is why the significant part of the termination reactions also takes place at the surfaces.

Contradictory to the behavior in weakly alkaline solution, the depletion rate of ozone is reduced in strongly alkaline solutions. The half-life of ozone at room temperature is about 2 min in 1 M NaOH solutions, to be compared with 40 min in 5 M and 83 h in 20 M solutions. One reason for the observed decrease in overall decomposition rate might be the formation of ozonide O_3^-, which reacts with H_2O_2 or OH^- radicals, which are produced in the ozone decomposition, re-forming ozone.

In 1977, Hoigné and Bader (Hoigné and Bader, 1983b) described the reaction of ozone in aqueous solution towards other compounds in two ways: by *direct reaction* or by *indirect reaction* with radical species formed in ozone decomposition. The direct reaction of ozone is often selective towards specific compounds and functional groups. The dipolar structure of ozone gives rise to cyclo-addition to the double bond, by the Criegee mechanism, forming ozonides. Ozone is also a strong electrophile and reacts quickly with both organic and inorganic compounds via an oxygen-atom transfer reaction. The reactivity is enhanced by electron-donating groups and decreased by electron-withdrawing ones. In the case of electron withdrawing groups, ozone acts as a nucleophile.

Regarding the radical-type reaction, chemicals or particles in the solution will affect the decomposition rate of ozone. They can act in four ways:

1) initiator, 2) promoter, 3) inhibitor, and 4) inhibitor with re-formation of ozone.

2.5.1 Modified mathematical model including the pH effect

The effect of the pH on the ozonation has to be taken into account in the mathematical model also. Therefore, a new variable c_{OH^-}, characterizing the variation of the OH^- ion concentration and their transformation into hydroxyl radicals (represented by $c_{OH^\cdot}$), must be included in the model. In view of this comment, the modified model can be represented as follows:

$$\left.\begin{aligned}
\frac{d}{dt}c^g(t) &= V_g^{-1}W_g\left(c_{in}^g - c^g(t)\right) - \\
V_g^{-1}&\left[k_{sat}(Q_{\max} - Q(t)) - Q(t)\sum_{i=1}^{N}k_i c_i(t)\right], \\
\frac{d}{dt}Q(t) &= k_{sat}(Q_{\max} - Q(t)) - Q(t)\sum_{i=1}^{N}k_i c_i(t) \\
&\quad -k_{OH,f}c_{OH^-}(t)Q(t), \\
\frac{d}{dt}c_i(t) &= -k_i\frac{Q(t)}{V_{liq}}c_i(t) - k_{OH,d}c_i(t)c_{OH^\cdot}(t) \quad i=\overline{1,N}, \\
\frac{d}{dt}c_{OH^\cdot}(t) &= k_{OH,f}c_{OH^-}(t)Q(t) - k_{OH,d}c_i(t)c_{OH^\cdot}(t), \\
\frac{d}{dt}c_{OH^-}(t) &= -\tilde{k}_{OH,f}c_{OH^-}(t)Q(t), \\
y(t) &= c^g(t),
\end{aligned}\right\} \tag{2.18}$$

where

- $k_{OH,f}$ [L mol^{-1} s^{-1}] is the reaction rate constant characterizing the formation of $OH^\cdot$ from OH^- reacting with Q;
- $k_{OH,d}$ [L mol^{-1} s^{-1}] is the reaction rate constant characterizing the decomposition of compound c_i by $OH^\cdot$.

The concentration of OH^- can be calculated using the value of pH:

$$OH^- = 10^{(pH-7)}. \tag{2.19}$$

2.5.2 Numerical illustration of the ozonation model with pH effect

The numerical simulation of the modified model (2.18) that included the pH effect is also solved with the Matlab/Simulink tool, according to the following block scheme (Fig. 2.7):

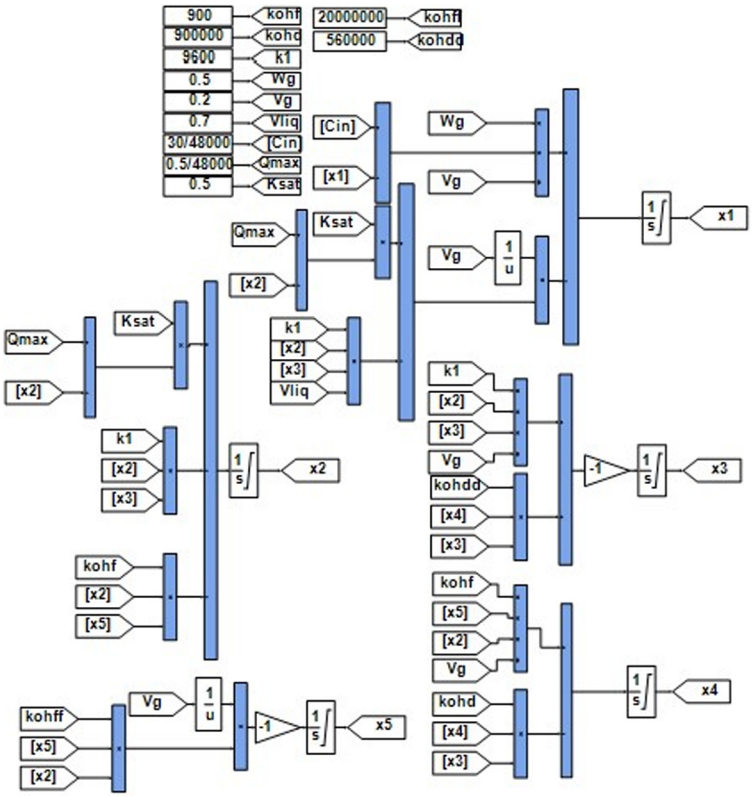

■ **FIGURE 2.7** Block scheme in Simulink to evaluate numerically the model (2.18) that considered the pH effect.

2.5.3 pH effect without the presence of contaminants

Fig. 2.8 demonstrates the behavior of the principal components of the model (2.18) for the following values of the parameters ($N = 1$):

$$V_g = 0.2 \text{ L} \qquad V_{liq} = 0.7 \text{ L}$$

$$W_g = 0.5 \text{ L min}^{-1} \qquad Q_{\max} = 0.5 \text{ mol}$$

$$k_{sat} = 0.4 \text{ s}^{-1} \qquad k_1 = 450 \text{ L mol}^{-1} \text{ s}^{-1}$$

$$k_{OH,f} = 128.25 \text{ L mol}^{-1} \text{ s}^{-1} \qquad k_{OH,d} = 58.3 \text{ L mol}^{-1} \text{ s}^{-1}$$

$$c_{in}^{g} = 6.25 \cdot 10^{-4} \text{ mol L}^{-1} \qquad c_1(0) = 6.25 \cdot 10^{-4} \text{ mol L}^{-1}$$

$$c^{g}(0) = 1.56 \cdot 10^{-3} \text{ mol L}^{-1} \qquad Q(0) = 0.0 \text{ mol}$$

The ozone concentration at the output of the reactor (ozonogram) changes, when the pH is modified from 8 (dashed line, blue line in the electronic

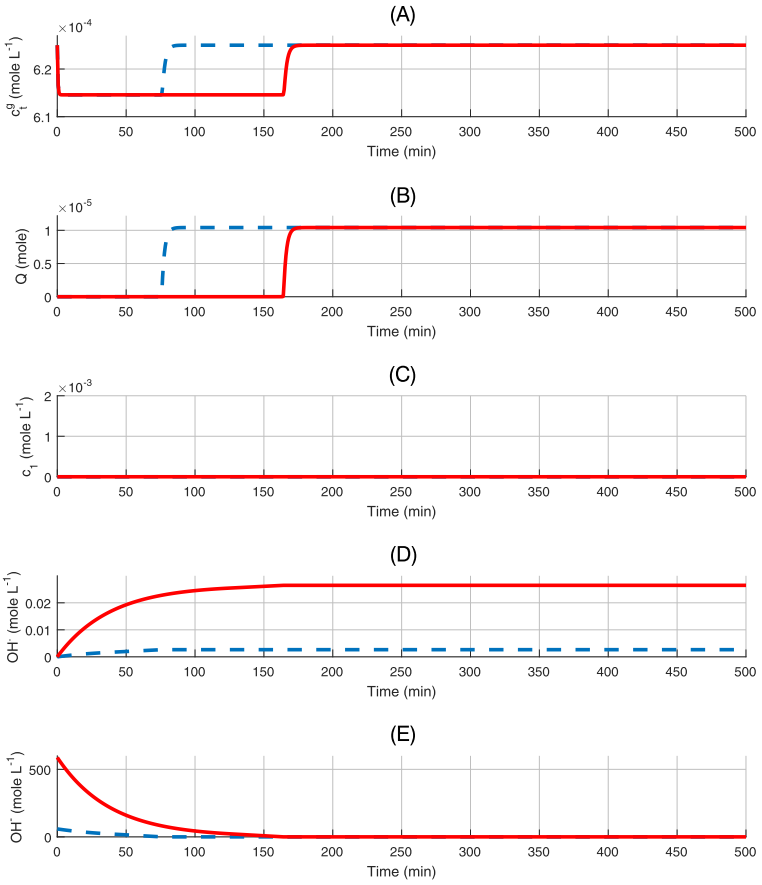

■ **FIGURE 2.8** Time evolution of the state variables (c_g, Q, c_1, $OH^{\cdot}$, OH^{-}) of the ozonation model (2.18), which considered the pH effect without the presence of contaminant.

version) to 9 (solid, red line in the electronic version) in Fig. 2.8.[1] When pH is 8, the ozone concentration returns to its initial value faster than in the case, when pH is 9 (Fig. 2.8A). This difference is a consequence of the ozone consumed by the reaction hydroxyl ions c_{OH^-} that are transformed to hydroxyl radicals. The same behavior is observed for the case of dissolved ozone Q_t, which has a similar tendency as regards c_t (Fig. 2.8B). In this numerical evaluation, no contaminant was considered as one can see in Fig. 2.8C. The hydroxyl radical concentration $c_{OH^{\cdot}}$ is larger (in the steady state), when pH = 9, because the number of available ions c_{OH^-} is also bigger than in the case of pH = 8 (Fig. 2.8D). The initial concentration of

[1] Note: The color figures will appear in color in all electronic versions of this book.

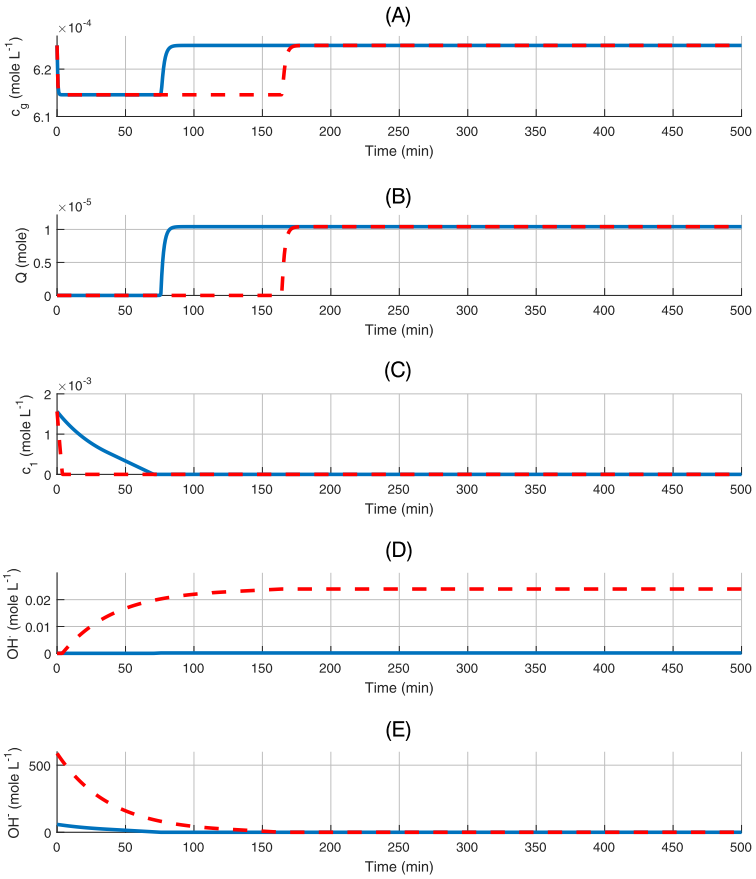

■ **FIGURE 2.9** Time evolution of the state variables (c_g, Q, c_1, $\mathrm{OH}^{\cdot}$, OH^{-}) of the ozonation model (2.18) which considered the pH effect when the initial contaminant is in the reactor.

c_{OH^-}, shown in Fig. 2.8E, is different because the pH changed (2.19), but the time needed to attain the complete conversion from ions to radicals is almost the same, 150 min.

2.5.4 Modeling of the pH effect in the presence of contaminants

If the contaminants participate in the ozonation, the pH effect provides the tendency of the ozone concentration at the output of the reactor (ozonogram) to follow the same behavior as observed, when no contaminant was in the reactor (Fig. 2.9A), that is, the ozone concentration returns faster to it initial value, when pH is smaller. The dissolved ozone Q_t achieves its maximum value ($Q_{\max}$) faster, when the pH is smaller (Fig. 2.9B). This effect is a

consequence of the smaller number of ozone molecules that should react with the contaminant and with the hydroxyl ions.

The contaminant degrades almost 15 times faster, when pH is bigger (9.0) because of the number of hydroxyl radicals that also react with the contaminant with a faster reaction rate (Fig. 2.9C). The concentrations of hydroxyl radical $c_{OH^{\cdot}}$ (Fig. 2.9D) and ions $c_{OH^{-}}$ (Fig. 2.9E) follow the same tendency as observed, when no contaminant is in the reactor.

The model (8.6) possesses several characteristics which may be considered in the observer design: a) they are bilinear with respect to the components of the state-vector, b) not all the parameters of this model are known, c) the contaminant concentrations can be measured using special and expensive laboratory equipment, such as UV-Vis spectrophotometer, high performance liquid chromatography, infrared spectroscopy, nuclear magnetic resonance, etc. and d) only some of components (frequently only one) of the state-vector can be measured during the process: in the case of ozonation, it is the current concentration c_l^g of ozone in the gas phase, that is, the output information, which can be measured online, and which is

$$y = c_l^g. \tag{2.20}$$

Remark 2.5. *Usually we deal with the start situation when*

*– **the liquid is free of ozone**, i.e.,*

$$Q(0) = 0,$$

*or **the liquid is saturated by ozone**, i.e.,*

$$Q(0) = Q_{\max}.$$

2.6 EFFECT OF INTERMEDIATE AND FINAL PRODUCTS ON THE OZONATION REACTION

A natural extension to the mathematical models presented in the previous sections must include the presence of intermediate and final products. These compounds formed along the ozonation by the serial–parallel reactions between ozone and the initial contaminants. The model considers a set of intermediates represented by R_j [mol L^{-1}], $j \in [1, N_I]$, where N_I is the number of intermediates. Additionally, the model also includes the concentrations of final products, B_k [mol L^{-1}], $j \in [1, N_F]$ (N_F is the number of final products) accumulated in ozonation.

Remark 2.6. – *The mathematical model (2.21) considers the generation of diverse intermediates formed as a consequence of the reaction between ozone and the initial contaminant mixture.*
– *These intermediates also react with ozone and therefore they are decomposed eventually.*
– *The consequence of this decomposition is the accumulation of several final products which usually correspond to low molecular weights organic compounds, such as organic acids, aldehydes, and carbon dioxide (CO_2). If the ozonation time is enlarged, then the only unique final product is CO_2, yielding the complete mineralization.*

The model has the following mathematical structure:

$$\left.\begin{aligned}
\frac{d}{dt}O_{3,gas}(t) &= -V_g^{-1}\left[c_t^g u_1(t) - u_2(t) + k_{sat}(Q_{\max} - Q(t)) \right.\\
&\qquad \left. - Q(t)\sum_{i=1}^{N} k_i c_i(t)\right],\\
\frac{d}{dt}\mathrm{O}_{3,liq}(t) &= k_{sat}(Q_{\max} - Q(t))\\
&\quad - Q(t)\sum_{i=1}^{N} k_i c_i(t) - k_{F,OH}\,Q(t),\\
\frac{d}{dt}c_i(t) &= -k_{i,O_3}c_i(t)\,O_{3,liq}(t) - \sum_{j=1}^{r} k_{i,j,R_i}R_j(t)\,c_i(t),\\
\frac{d}{dt}R_j(t) &= k_{cat,j}C_{cat}(t)\,O_{3,liq}(t) - \sum_{i=1}^{I} k_{ji,O_3}R_j(t)\,C_i(t),\\
\frac{d}{dt}B_k(t) &= \sum_{i=1}^{I} k_{k,i}C_i(t)\,O_{3,liq}(t) + \sum_{i=1}^{J} k_{k,j}C_i(t)\,R_j(t)\\
&\quad - k_k B_k(t)\,O_{3,liq}(t) - \sum_{j=1}^{r} k_{k,j}B_k(t)\,R_j(t).
\end{aligned}\right\} \tag{2.21}$$

The new variables and parameters included in the model which considers the intermediate and final products are:

– k_{j,R_j}, [L mol^{-1} s^{-1}] is the reaction rate constant corresponding to the decomposition of the intermediate R_j by the direct ozonation mechanism,

– k_{i,j,R_j}, [L mol^{-1} s^{-1}] is the reaction rate constant corresponding to the formation of the intermediate R_j by the ozone reaction with the contaminant c_i,

– k_{k,B_k}, [L mol^{-1} s^{-1}] is the reaction rate constant corresponding to the decomposition of the accumulated product B_k by the direct ozonation mechanism,

– $k_{k,j}$, [L mol^{-1} s^{-1}] is the reaction rate constant corresponding to the formation of the intermediate R_j by the ozone reaction with the contaminant c_i,

– $k_{k,j}$, [L mol^{-1} s^{-1}] is the reaction rate constant corresponding to the formation of the intermediates R_j by the ozone reaction with contaminant c_i.

2.7 ESTIMATION OF REACTION CONSTANTS

One of the most common manners to acquire good understanding of the reaction evolution is the developing of mathematical models, which may describe the mass balance and kinetics of ozonation.

Several simple mathematical models, describing the ozonation reaction, have been developed including experimental variables (initial ozone and contaminants concentrations, gas flow, pH, etc.) considering only one model compound or a mixture of model contaminants (Poznyak and Vivero, 2005). Besides, depending on the reaction conditions, the simultaneous combination of two reaction mechanisms can be realized: by molecular ozone and by indirect reactions (Poznyak et al., 2005). Thus, the mathematical modeling of ozonation, even when only one contaminant is in the reaction, is a hard task and frequently leads to contrasting results.

The application of adaptive DNN algorithms avoids the aforementioned modeling problems. This methodology uses just the output–input information to obtain numerical approximations of uncertain nonlinear mathematical systems.

2.7.1 Estimation of the reaction rate constants in the case of the direct mechanism

The kinetics of the ozonation reaction has been studied by several researchers (Trapido et al., 1995), (Taylor et al., 1999) and the values of the bimolecular reaction rate constants for phenols are reported from 10^3 to 10^4 L mol^{-1} s^{-1} (Poznyak et al., 2005). The kinetic equation describing the contaminant decomposition is

$$\frac{d}{dt}c_i(t) = -\frac{k_i c_i(t) Q(t)}{V_{liq}}, \quad i = 1, 2, ..., n, \tag{2.22}$$

where $c_i(t)$ is the contaminant concentration during the overall reaction (mol L^{-1}), while $\left(V_{liq}\right)^{-1} Q(t)$ is the liquid phase ozone concentration

(mol L^{-1}), $Q(t)$ is total ozone amount into the liquid phase, and V_{liq} is the liquid phase volume (L). Observe that $c_i(t)$, $Q(t)$ and $\frac{d}{dt}c_i(t)$ are available. It is possible to define the Least Square (LS) estimates of k_i (L mol/s) as the solution to the following optimization problem:

$$k_i^*(t) = \arg\min_{k_i} \int_{\tau=0}^{t} \left(\frac{d}{d\tau} c_i(\tau) + \frac{k_i c_i(\tau) Q(\tau)}{V_{liq}} \right)^2 d\tau. \tag{2.23}$$

The solution is as follows:

$$k_i^*(t) = \frac{V_{liq} \int_{\tau=0}^{t} c_i(\tau) Q(\tau) \frac{d}{d\tau} c_i(\tau) d\tau}{\int_{\tau=0}^{t} (c_i(\tau) Q(\tau))^2 d\tau}. \tag{2.24}$$

Eq. (2.24) represents the estimation of the ozonation constant, given in integral form and obtained based on the data available up to time t. The equivalent differential form for $k_i^*(t)$ can be estimated as follows:

$$\left.\begin{aligned} \dot{k}_i^*(t) &= \gamma^2(t) z(t) \left(\frac{d}{d\tau} c_i(t) - z(t) \gamma(t) g(t) \right), \\ \dot{\gamma}(t) &= -\gamma^2(t) z^2(t), \\ g(t) &= V_{liq} \int_{\tau=0}^{t} c_i(\tau) Q(\tau) \frac{d}{d\tau} c_i(\tau) d\tau, \\ \gamma(t) &= \left(\int_{\tau=0}^{t} (c_i(\tau) Q(\tau))^2 d\tau \right)^{-1}. \end{aligned}\right\} \tag{2.25}$$

The differential form of the estimated constant simplifies the numerical calculation and it can be done online.

2.7.2 Estimation of the reaction rate constants considering the pH effect

The reaction rate constants estimation technique, presented in (2.24), is also valid, when the pH effect is considered. Indeed, it is sufficient to extend the vector of parameters and the regressor structure as follows:

$$\left.\begin{aligned}
\begin{bmatrix} k_i^*(t) \\ k_{OH,d}^*(t) \end{bmatrix} &= \Gamma_1(t)\cdot G_1(t), \\
\Gamma_1^{-1}(t) &:= \int_{\tau=0}^{t} \begin{bmatrix} -\dfrac{Q(\tau)}{V_{liq}}\hat{c}_i(\tau) \\ -c_i(\tau)c_{OH^\cdot}(\tau) \end{bmatrix}\begin{bmatrix} -\dfrac{Q(\tau)}{V_{liq}}\hat{c}_i(\tau) \\ -c_i(\tau)c_{OH^\cdot}(\tau) \end{bmatrix}^\top d\tau, \\
G_1(t) &= -\int_{\tau=0}^{t}\left(\frac{d}{d\tau}c_i(\tau)\cdot\begin{bmatrix} \dfrac{Q(\tau)}{V_{liq}}c_i(\tau) \\ c_i(\tau)c_{OH^\cdot}(\tau) \end{bmatrix}d\tau\right),
\end{aligned}\right\} \tag{2.26}$$

$$\left.\begin{aligned}
\begin{bmatrix} k_{OH,f}^*(t) \\ k_{OH,d}^*(t) \end{bmatrix} &= \Gamma_t\cdot G_t, \\
\Gamma_t &:= \left\{\int_{\tau=0}^{t}\begin{bmatrix} c_{OH^-}(\tau)Q(\tau) \\ -c_i(\tau)c_{OH^\cdot}(\tau) \end{bmatrix}\begin{bmatrix} c_{OH^-}(\tau)Q(\tau) \\ -c_i(\tau)c_{OH^\cdot}(\tau) \end{bmatrix}^\top d\tau\right\}^{-1}, \\
G_t &= \int_{\tau=0}^{t}\left(\frac{d}{d\tau}c_{OH^\cdot}(\tau)\cdot\begin{bmatrix} c_{OH^-}(\tau)Q(\tau) \\ -c_i(\tau)c_{OH^\cdot}(\tau) \end{bmatrix}d\tau\right),
\end{aligned}\right\} \tag{2.27}$$

$$\left.\begin{aligned}
\tilde{k}_{OH,f}^*(t) &= \tilde{\Gamma}(t)\cdot\tilde{G}(t), \\
\tilde{\Gamma}^{-1}(t) &:= \int_{\tau=0}^{t}(c_{OH^-}(\tau)Q(\tau))^2\,d\tau, \\
\tilde{G}(t) &= \int_{\tau=0}^{t}\frac{d}{d\tau}c_{OH^-}(\tau)\,c_{OH^-}(\tau)Q(\tau)d\tau.
\end{aligned}\right\} \tag{2.28}$$

Eq. (2.26) is the generalization of the previous integral scalar expression to the matrix case. This is difficult to realize in practice and its equivalent realizable form is required. The next subsection gives such a representation in differential form.

2.7.3 Differential form for constants estimates

Direct differentiation of (2.23) and (2.24) leads to the following ordinary differential equation (ODE) for each $i = \overline{1, N}$:

$$\left.\begin{aligned}\frac{d}{dt}\begin{bmatrix} k_i^*(t) \\ k_{OH,d}^*(t) \end{bmatrix} &= \Gamma_1(t) z_1(t) \left(\frac{d}{dt} c_i(t) - z_1^\top(t) \Gamma_1(t) G_1(t) \right), \\ z_1(t) &:= \begin{bmatrix} -\dfrac{Q(\tau)}{V_{liq}} c_i(\tau) \\ -c_i(\tau)\, c_{OH^\cdot}(\tau) \end{bmatrix},\end{aligned}\right\} \tag{2.29}$$

where the time-varying functions $\gamma_i(t)$ and $g_i(t)$ are generated by

$$\left.\begin{aligned}\dot{\Gamma}_1(t) := -\Gamma_1(t) z_1(t) z_1^\top(t) \Gamma_1(t),\ \Gamma_1(0) = \varepsilon I_{N\times N},\ \ \varepsilon > 0, \\ \dot{G}_1(t) = \frac{d}{dt} c_i(t)\, z_1(t),\ G_1(0) = 0.\end{aligned}\right\} \tag{2.30}$$

In the case of the pH effect on the ozonation reaction, the estimations of the constants (2.27) and (2.28) in ODE format are given by

$$\begin{aligned}\frac{d}{dt}\begin{bmatrix} k_{OH,f}^*(t) \\ k_{OH,d}^*(t) \end{bmatrix} &= \Gamma_2(t) z_2(t) \left(\frac{d}{dt} c_{OH^\cdot}(t) - z_2^\top(t) \Gamma_2(t) G_2(t) \right), \\ z_2(t) &:= \begin{bmatrix} c_{OH^-}(t) Q(t) \\ -c_i(t)\, c_{OH^\cdot}(t) \end{bmatrix}, \\ \dot{\Gamma}_2(t) := -\Gamma_2(t) z_2(t) z_2^\top(t) \Gamma_2(t),\ \Gamma_2(0) &= \varepsilon I_{N\times N},\ \ \varepsilon > 0, \\ \dot{G}_2(t) = \frac{d}{dt} c_{OH^\cdot}(t)\, z_2(t),\ G_2(0) &= 0,\end{aligned} \tag{2.31}$$

and

$$\left.\begin{aligned}\frac{d}{dt}\tilde{k}_{OH,f}^*(t) = \gamma_{OH}(t)\, c_{OH^-}(t) Q(t) \times \\ \left[\frac{d}{d\tau} c_{OH^-}(t) - \gamma_{OH}(t)\, c_{OH^-}(t) Q(t) g_{OH}(t) \right]\end{aligned}\right\} \tag{2.32}$$

where the time-varying functions $\gamma_{OH}(t)$ and $g_{OH}(t)$ are generated by

$$\left.\begin{aligned}\dot{g}_{OH}(t) := c_{OH^-}(t) Q(t) \frac{d}{dt} c_{OH^-}(t),\ g_{OH}(0) = 0, \\ \dot{\gamma}_{OH}(t) = -\gamma_{OH}(t) \left(c_{OH^-}(t) Q(t) \right)^2 \gamma_{OH}(t), \\ \gamma_{OH}(0) = \varepsilon > 0.\end{aligned}\right\} \tag{2.33}$$

All the ODE forms (2.31)–(2.33), used to estimate the reaction rate constants, can be directly implemented in the Matlab-Simulink simulation platform.

2.8 CONCLUSIONS

In the case of the residual water treatment by ozone, any mathematical model cannot be directly applied because of the complex composition of organics and the possibility to realize in the same time two mechanisms of reaction by molecular ozone (direct reaction) and by OH-radicals (indirect ozonation). The latter situation we can have in the case of the basic pH, the presence of a catalyst (catalytic ozonation) or with a catalyst under UV-Vis irradiation (photocatalytic ozonation).

A lot of efforts have been made to analyze and explore a certain type of ozone reactions in liquid phase with different organic contaminants (Poznyak et al., 1977). Evidently, a complete mathematical model of ozonation belongs to the class of partial differential equations. Meanwhile, there exist some simplified mathematical models, one of which may be described using the system of Ordinary Differential Equations (ODEs) given above. The "degree of uncertainties" of this particular model is related to two uncertainty factors:

1. All organics concentrations (c_i) are not available for measuring online. Only one state of this process is really measurable: it is the ozone concentration variation in the gas phase in the reactor outlet (c^g).
2. The rate constants k_i of ozone reaction with the organic compounds are also a priori unknown.
3. When the pH effect is taken into account, the reaction rate constants $k_{OH,f}$, $k_{OH,d}$, and $\tilde{k}_{OH,f}$ are also unknown and must be estimated based on limited information (usually measurements of the concentrations of hydroxyl ions and radicals are not available online).

Based on the mathematical model of ozonation the problem of experimental estimation of reaction constants, involving in their mathematical description, may be abstracted to the problem of identification of a class of nonlinear systems with non-complete observable states.

One possible solution to this problem is the adaptive modeling based on differential neural networks. This possibility will be analyzed in detail in the next chapters.

Chapter 3

Background on dynamic neural networks

CONTENTS

ABSTRACT

This chapter presents an introduction to the problem field of Artificial Neural Networks (ANNs) which are very effective at their intended tasks such as classification or segmentation. Two types of ANNs exist: Feedforward NNs (or static NNs) and recurrent (in discrete time) or differential (in continuous time) neural networks. The latter ones frequently are treated as dynamic NNs (DNNs). They turn out to be extremely useful when we deal with the identification and/or control of dynamic processes with non-exactly given dynamic models: they occur when noise perturbations or some unknown parameters are present in the expressions of a mathematical model. The

Ozonation and Biodegradation in Environmental Engineering
https://doi.org/10.1016/B978-0-12-812847-3.00012-3

environment problems considered in this book exactly deal with such uncertain situation, and therefore DNNs will be used throughout this book. Mainly, the concept of DNNs will be applied for the construction of the so-called Universal Dynamic Neuro-Observer (DNO), which is used for designing both artificial software sensors (dynamic state observers) and robust controllers, providing a good workability in the absence of complete and exact information on a corresponding mathematical model of the environment processes considered. The concept of the Attractive Ellipsoid Method (AEM) is discussed in detail: it is used to analyze numerically the quality of the corresponding state-estimation and control processes. The description of the main ideas on how to design DNO's and controllers using standard MATLAB Toolboxes are given in the end of this chapter.

3.1 CLASSES OF ARTIFICIAL NEURAL NETWORKS

3.1.1 Artificial neural networks

Artificial neural networks (ANNs) are computational models inspired by biological neural networks, and they are used to approximate functions that are generally unknown. The concept of ANN is basically introduced as a subject of biology where the neural network plays an important and key role in the human body. In the human body functions are performed with the help of a neural network: it is just a web of interconnected neurons which are millions and millions in number. With the help of these interconnected neurons all the parallel processing is done in the human body; the human body is the best example of parallel processing.

Particularly, ANNs are inspired by the behavior of neurons and the electrical signals they convey between input (such as from the eyes or nerve endings in the hand), processing, and output from the brain (such as reacting to light, touch, or heat). The way neurons semantically communicate is an area of ongoing research (Abraham, 2005; Gershenson, 2003; Sharma et al., 2012).

Most artificial neural networks bear only a vague resemblance to their more complex biological counterparts, but they are very effective at their intended tasks (e.g. classification or segmentation). Some ANNs are adaptive systems and are used for example to model populations and environments, which constantly change. Neural networks can be hardware- (neurons are represented by physical components) or software-based (computer models), and they can use a variety of topologies and learning algorithms.

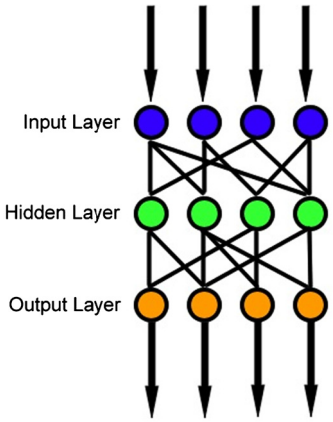

■ **FIGURE 3.1** Feedforward ANN.

There exist two types of ANNs:

- Feedforward NNs or FFNN,
- recurrent (in discrete time) or differential (in continuous time) neural networks.

3.1.2 Feedforward neural network

Feedforward NNs were the first and arguably most simple type of artificial neural network devised. In this network the information moves in only one direction—forward (see Fig. 3.1): from the input nodes data go through the hidden nodes (if any) to the output nodes. There are no cycles or loops in the network. Feedforward networks (also known as *associative*) can be constructed from different types of units, e.g. binary McCulloch–Pitts neurons (Anderson, 2006), the simplest example being the perceptron. Continuous neurons, frequently with sigmoid activation functions, are used in the context of backpropagation of errors.

3.1.3 Recurrent neural network

Recurrent neural network (RNN), also known as *Auto Associative* or *Feedback Network*, belongs to a class of artificial neural networks where connections between units form a directed cycle. This creates an internal state of the network which allows it to exhibit dynamic temporal behavior. Unlike FFNN, RNNs can use their internal memory to process arbitrary sequences of inputs. In RNN the signals travel both forward and backward by introducing loops in the network. The main simple structures of RNN are as follows.

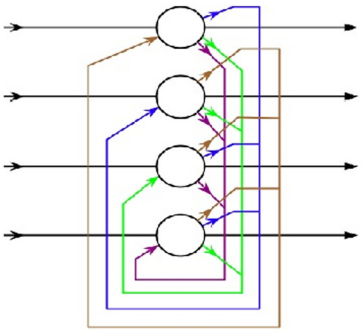

■ **FIGURE 3.2** Hopfield ANN.

- *Hopfield network*
  The Hopfield network is of historic interest although it is not a general RNN, as it is not designed to process sequences of patterns (see Fig. 3.2).
  Instead it requires stationary input if it is a RNN in which all connections are symmetric. Invented by Hopfield (1982), it guarantees that its dynamics will converge. If the connections are trained using Hebbian learning then the Hopfield network can perform as a robust content-addressable memory, resistant to connection alteration. A variation on the Hopfield network is the bidirectional associative memory (BAM). The BAM has two layers, either of which can be driven as an input, to recall an association, and produce an output on the other layer.
- *The Elman network*
  The following special case of the basic architecture above was employed by Elman. A three-layer network is used arranged horizontally as x, y, and z as in the illustration (see Fig. 3.3), with the addition of a set of "context units" m.
  There are connections from the middle (hidden) layer to these context units fixed with a weight of one (Elman, 1993) At each time step, the input is propagated in a standard feedforward fashion, and then a learning rule is applied. The fixed back connections result in the context units always maintaining a copy of the previous values of the hidden units (since they propagate over the connections before the learning rule is applied). Thus the network can maintain a sort of state, allowing it to perform such tasks as sequence-prediction, which are beyond the power of a standard multilayer perceptron.
- *The Jordan network*
  Jordan networks (Jordan, 1996) are similar to Elman networks. The context units are, however, fed from the output layer instead of the hidden layer. The context units in a Jordan network are also referred to as

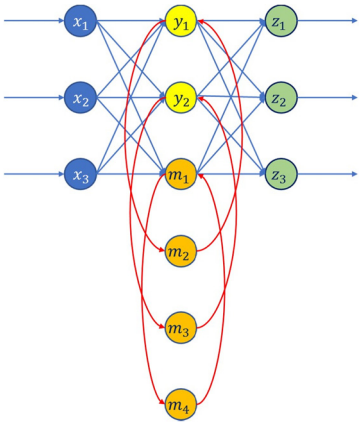

■ **FIGURE 3.3** Elman recursive ANN.

Table 3.1 Activation functions.

Threshold:	$\sigma_{\text{Th}}(x) = \dfrac{\sigma_{\max}}{2}(1 + \text{sign}(x - x_0))$
Piecewise linear	$\sigma_{\text{PL}}(x) = \begin{cases} \sigma_{\max} & \text{if} \quad x > x_r \\ \sigma_{\max}\dfrac{x - x_l}{x_r - x_l} & \text{if} \quad x \in [x_l, x_r] \\ 0 & \text{if} \quad x < x_l \end{cases}$
Sigmoid	$\sigma_{\text{Sig}}(x) = \dfrac{\sigma_{\max}}{1 + \exp\{-\alpha x\}}, \ \alpha > 0$
Gaussian	$\sigma_{\text{Gauss}}(x) = \dfrac{1}{\sqrt{2\pi}\sigma_0}\exp\left\{-\dfrac{x^2}{2\sigma_0^2}\right\}$

the state layer, and they have a recurrent connection to themselves with no other nodes on this connection.

The mathematical model of the Elman and Jordan networks (only some parameters are different) are governed by the following system of equations:

$$\left.\begin{aligned} h_t &= \sigma_h\left(W_h x_t + U_h y_{t-1} + b_h\right), \\ y_t &= \sigma_y\left(W_y h_t + b_y\right), \end{aligned}\right\} \tag{3.1}$$

where x_t is an input vector, h_t is a hidden layer vector, y_t is the output vector, W_h, U_h and b_h, b_y are weighting matrices and vectors, and σ_h and σ_y are *activating vector functions* with the widely used components. Activation functions are basically the transfer functions output from an artificial neuron and sending signals to the other artificial neuron. There are four forms of activation functions $\sigma = \sigma(x)$: threshold, piecewise linear, sigmoid, and Gaussian; all are different from each other (see Table 3.1).

3.1.4 Learning ability and reinforcement learning

In ANNs most of the learning rules are used to develop models of processes, while adopting the network to the changing environment and discovering useful knowledge. These *learning methods* are

- supervised,
- unsupervised,
- reinforcement learning.

Here and throughout the book we will consider *Reinforcement Learning* (RL) in *Differential Neural Network* (DNN) which realizes a special tuning of the weight matrix parameters providing the desired behavior of this DNN. In particular, in the DNN model given by

$$\frac{d}{dt}\hat{x}(t) = A\hat{x}(t) + W_\sigma(t)\,\sigma\left(\hat{x}(t)\right) + W_\varphi(t)\,\varphi\left(\hat{x}(t)\right)u\left(y(t)\right), \qquad (3.2)$$

$\hat{x}(t) \in \mathbb{R}^n$ is a vector of state estimates,

$\sigma\left(\hat{x}(t)\right) \in \mathbb{R}^{n\times k_\sigma}$, $\varphi\left(\hat{x}(t)\right) \in \mathbb{R}^{n\times k_\varphi}$ are vector and matrix of the activating functions,

$u\left(y(t), t\right) \in \mathbb{R}^{m\times k_\varphi}$ is an external signal (or control action) depending on a measurable system output $y(t)$.

The dynamic NN model (3.2) may be treated as an *DNN-software sensor* or a *state observer* of some dynamic process $x(t) \in \mathbb{R}^n$, which cannot be measured directly online by different natural reasonings. The RL process consists in the realization of an adequate adjustment of the weight matrix $W_\sigma(t)$ and $W_\varphi(t)$ process, namely,

$$\left.\begin{aligned}\dot{W}_\sigma(t) &= \Phi_\sigma\left(W_\sigma(t), \hat{x}(t), u\left(y(t)\right)\right),\\ \dot{W}_\varphi(t) &= \Phi_\varphi\left(W_\varphi(t), \hat{x}(t), u\left(y(t)\right)\right),\end{aligned}\right\} \qquad (3.3)$$

in such a way that the current state estimates $\hat{x}(t)$ would be as closed as possible to the current real state $x(t)$ of the modeled real-life system. The number of artificial neurons is defined by the numbers k_σ and k_φ of activating functions components. In fact, these numbers define the complexity of the used DNN. The RL rules (3.3) are specific for each considered problem.

3.1.5 Why DNNs are much more preferable compared to FFNNs when the modeling of some dynamic process is required

To illustrate the advantages of DNNs compared to FFNNs during the simulation of dynamic processes, let us consider the simplest first order dynamic model, given by

$$\dot{x}_t = -ax_t + f_t,\ a > 0. \tag{3.4}$$

Applying the Laplace transformation $\mathcal{L}\{\cdot\}$ to both parts of this equation we obtain

$$X = \frac{1}{s+a}F = \frac{1}{s}\left(\frac{1}{1+a/s}\right)F =$$
$$\frac{1}{s}\sum_{t=1}^{\infty}\left[\frac{(-1)^t}{t!}\left(\frac{a}{s}\right)^t\right] = \left[\sum_{t=0}^{\infty}\frac{c_t}{s^{t+1}}\right]F,$$

where

$$X = \mathcal{L}\{x_t\}, sX = \mathcal{L}\{\dot{x}_t\}, F = \mathcal{L}\{f_t\},$$

and

$$c_t = (-1)^t\frac{a^t}{t!}.$$

The operator $\frac{1}{s}$ represents the simple operation of integration, that is,

$$\mathcal{L}^{-1}\left\{\frac{1}{s}F\right\} = \int_{\tau=0}^{t} f_\tau d\tau,$$

which implies the following *feedforward realization* of the solution x_t of the differential model (3.4):

$$x_t = \sum_{t=0}^{\infty} c_t\left[\int_{\tau_{t+1}=0}^{t}\left(\cdots\int_{\tau_2=0}^{\tau_3}\left(\int_{\tau_1=0}^{\tau_2} f_{\tau_1}d\tau_1\right)d\tau_2\cdots\right)d\tau_{t+1}\right]. \tag{3.5}$$

The n final-terms approximation $\tilde{x}_{t,n}$ of (3.5) is

$$\tilde{x}_{t,n} = \sum_{t=0}^{n} c_t\left[\int_{\tau_{t+1}=0}^{t}\left(\cdots\int_{\tau_2=0}^{\tau_3}\left(\int_{\tau_1=0}^{\tau_2} f_{\tau_1}d\tau_1\right)d\tau_2\cdots\right)d\tau_{t+1}\right], \tag{3.6}$$

of which the block diagram is depicted in Fig. 3.4:

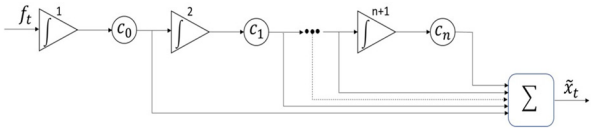

■ **FIGURE 3.4** Block diagram of static realization of solution x_t.

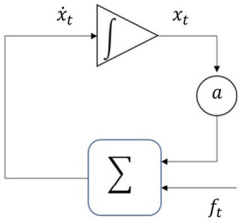

■ **FIGURE 3.5** Block diagram of feedback realization of solution x_t.

Corollary 3.1. *As one can see here (in Fig. 3.4), all signals move only* ***ahead*** *(feedforward): no feedback is involved! Notice also that for any finite number of integrators and amplifiers the signal $\tilde{x}_{t,n}$ is only an approximation of the process x_t. So, to have a "good" approximation there are required a large enough number of basic elements (usually $n \geq 10^4$) making the realizing electronic device sufficiently complex!*

On the other hand, the block diagram, realizing the exact (non-approximative) solution x_t of (3.4) with the use of only one feedback, is depicted at Fig. 3.5.

Corollary 3.2. *Obviously, the technical realization of the solution x_t of (3.4), using a feedback concept DNN, turns out to be* ***much more simple*** *than FFNN!*

3.1.6 Some limitations of ANNs

In this technological era every item has merits and some demerits: in other words, there is a limitation with every system, which makes the ANN technology weak in some points. Some limitations of ANN are as follows:

- ANN is not a daily life general purpose problem solver.
- There is no structured methodology available in ANN.
- There is no single standardized paradigm for ANN development.
- The output quality of an ANN may be unpredictable.
- Many ANN systems do not describe how they solve problems.
- They have a black box nature.

- There is a great computational burden.
- There is proneness to over fitting.
- The model development is of an empirical nature.

3.2 NEURAL OBSERVER AS A UNIVERSAL SOFTWARE SENSOR

3.2.1 Plant and the observer structures

Consider the following dynamic system:

$$\left.\begin{aligned} \dot{x}_t &= f(x_t, t) + g(x_t, t)\, u(x_t, t) + \xi_t, \\ x_0 &\text{ is given}, \\ y_t &= C x_t + \eta_t, \end{aligned}\right\} \tag{3.7}$$

where

$x \in \mathbb{R}^n$ is the state vector at time $t \geq 0$,
$u(x_t, t) \in \mathbb{R}^r$ is a control action applied to the system at time $t \geq 0$ or some measurable input,
$y \in \mathbb{R}^m$ is the output of the system at time $t \geq 0$,
$\xi \in \mathbb{R}^n$ is an external perturbation acting to the dynamics of the system,
$\eta \in \mathbb{R}^m$ is a noise in the output (usually associated with uncertainties of the sensors measurements),
$f : \mathbb{R}^n \times \mathbb{R}_+ \to \mathbb{R}^n$, $g : \mathbb{R}^n \times \mathbb{R}_+ \to \mathbb{R}^{n \times r}$ are given mappings,
$C \in \mathbb{R}^{m \times n}$ is a given output matrix.

3.2.2 Main assumptions

- y_t and $u(x_t, t)$ are available at any time $t \geq 0$;
- the matrix $C \in \mathbb{R}^{m \times n}$ is known;
- $f(x_t, t)$, $g(x_t, t)$ as well as $\xi \in \mathbb{R}^n$ and $\eta \in \mathbb{R}^m$ are unknown;
- the external perturbations ξ and η are assumed to be bounded with known upper bounds, i.e.,

$$\|\xi_t\| \leq \xi_+ < \infty, \ \|\eta_t\| \leq \eta_+ < \infty, \tag{3.8}$$

and they admit the existence of the solutions of ODE (3.7);

- $f(x_t, t)$ and $g(x_t, t)$ are globally *quasi-Lipschitz* on x_t and measurable on $t \geq 0$, that is, there exist matrices $A \in \mathbb{R}^{n \times n}$ and $B \in \mathbb{R}^{n \times r}$ such that for all $x \in \mathbb{R}^n$ and all admissible $u(x_t, t)$

$$\begin{aligned} \|f(x, t) - Ax\|^2 &\leq f_0 + f_1 \|x\|^2, \\ \|(g(x, t) - B)\|^2 &\leq g_0 + g_1 \|x\|^2 < \infty, \end{aligned} \tag{3.9}$$

- the control $u(x_t, t)$ is measurable and bounded, that is,

$$\|u(x(t), t)\| \leq k, \tag{3.10}$$

- for any control bounded as in (3.10) all trajectories of the systems remain uniformly bounded, i.e.,

$$\|x\|^2 \leq d_0 + d_1 k. \tag{3.11}$$

  We will refer to this property as the *BIBO-property* (Bounded Input–Bounded Output) or *"heterogeneity"*.

Below we will assume that the matrices $A \in \mathbb{R}^{n\times n}$, $B \in \mathbb{R}^{n\times r}$ as well as the non-negative constants f_0, f_1, g_0, g_1 are known.

3.2.3 Quasi-linear format of the model

Under these assumptions the plant (3.7) can be represented in *quasi-linear format* as

$$\left.\begin{aligned} \dot{x}_t &= Ax_t + Bu(x_t, t) + \tilde{\xi}(x_t, t), \\ y_t &= Cx_t + \eta_t, \end{aligned}\right\} \tag{3.12}$$

where

$$\tilde{\xi}(x_t, t) := \left[f(x_t, t) - Ax_t\right] + (g(x_t, t) - B)\, u(x_t, t) + \xi_t. \tag{3.13}$$

Remark 3.1. *Notice that for this new variable $\tilde{\xi}(x(t), t)$ the following property holds:*

$$\begin{aligned} \left\|\tilde{\xi}(x, t)\right\|^2 &\leq 4\|f(x(t), t) - Ax(t)\|^2 + \\ &4\left(k^2\|(g(x(t), t) - B)\|^2 + \|\xi(t)\|^2\right) \leq \\ 4\left(f_0 + f_1\|x\|^2 + k^2 g_0 + k^2 g_1\|x\|^2 + \xi_+^2\right) &= c_0 + c_1\|x\|^2 \end{aligned} \tag{3.14}$$

with

$$c_0 = 4\left(f_0 + k^2 g_0 + \xi_+^2\right),\ c_1 = 4\left(f_1 + k^2 g_1\right).$$

3.2.4 Universal neuro-observer structure

Below and throughout this book we will consider the dynamic neural network observer (*DNN-observer*) or DNN-software *sensor* having the follow-

ing structure:

$$\left.\begin{aligned}\frac{d}{dt}\hat{x}_t = A\hat{x}_t + Bu\left(x_t, t\right) + W_{0,t}\varphi\left(\hat{x}_t\right)\\ + W_{1,t}\psi\left(\hat{x}_t\right)u + L\left[y_t - C\hat{x}_t\right],\end{aligned}\right\} \tag{3.15}$$

where

$$\hat{x} \in \mathbb{R}^n,\ \varphi : \mathbb{R}^n \to \mathbb{R}^{k_\varphi},\ W_0 \in \mathbb{R}^{n\times k_\varphi},$$
$$\psi : \mathbb{R}^r \to \mathbb{R}^{k_\psi \times r},\ W_1 \in \mathbb{R}^{n\times k_\psi} \text{ and } L \in \mathbb{R}^{n\times m},$$

and the sigmoid vector $\varphi(x)$ and matrix functions $\psi(x)$ are supposed to be bounded fulfilling

$$\|\varphi(x)\| \le \varphi_+,\quad \|\psi(x)\| = \lambda_{\max}^{1/2}\left(\psi(x)^\intercal \psi(x)\right) \le \psi_+. \tag{3.16}$$

Remark 3.2. *The dynamic neuro-observer (3.15), in fact, is* ***universal****, since its structure does not depend on a concrete physical interpretation of a dynamic process (3.7) and depends only on the matrix parameters A, B, and C of the quasi-linear format (3.12), characterizing a wide class of real physical (chemical) processes.*

3.2.5 Learning law for weights adaptation

Define the *reinforcement learning law* as

$$\left.\begin{aligned}\dot{W}_0(t) = -k_0^{-1}\Lambda^{-1}\left(W_{0,t} - W_0^*\right)\varphi\left(\hat{x}_t\right)\varphi^\intercal\left(\hat{x}_t\right) - \frac{\alpha}{2}\left(W_{0,t} - W_0^*\right),\\ \dot{W}_1(t) = -k_1^{-1}\Lambda^{-1}\left(W_{1,t} - W_1^*\right)\psi\left(\hat{x}_t\right)u\left(\hat{x}_t, t\right)u^\intercal\left(\hat{x}_t, t\right)\psi^\intercal\left(\hat{x}_t\right)\\ -\frac{\alpha}{2}\left(W_{1,t} - W_1^*\right).\end{aligned}\right\} \tag{3.17}$$

Here W_0^* and W_1^* are matrices which will be defined below as a solution of the corresponding optimization problem with a matrix constraint.

There are two ways to define these matrices W_0^* and W_1^*:

1. By a training process based on a priori available data.
2. By a self-learning process, where W_0^* and W_1^* are estimated as the steady state solution of (3.17). The corresponding steady state solutions can be recovered after some time T_{SS}, which can be defined by the designer. After this steady state time, the following identities can be used:

$$W_0^* = W_0(T_{SS}),\quad W_1^* = W_1(T_{SS}).$$

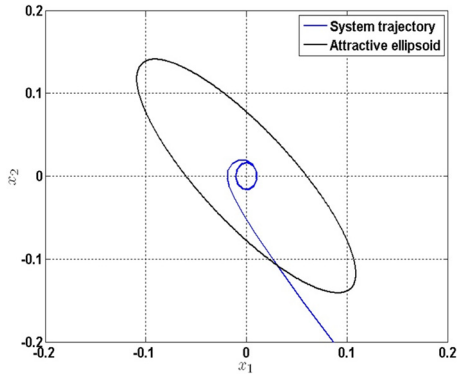

■ **FIGURE 3.6** Two dimensional attractive ellipsoid.

3.3 HOW TO ESTIMATE THE QUALITY OF APPLIED DNNS

3.3.1 Attractive ellipsoid method

Hereafter throughout this book we will apply the concept of *attractive ellipsoid* (Poznyak et al., 2014) which turns out to be a very useful instrument for the stability analysis of a wide class of nonlinear systems and physical processes.

Obviously, the quality of any observation process may be defined by the state-estimation error,

$$e := \hat{x} - x, \tag{3.18}$$

where the state estimate $\hat{x}$ and the real state x are governed by (3.12) and (3.15), respectively.

If the process $\{e_t\}_{t\geq 0}$ is bounded, then it can be placed within some ellipsoid which is usually referred to as an *attractive ellipsoid* $\mathcal{E}$ (see the two dimensional case in Fig. 3.6) and the three dimensional case in Fig. 3.7.

Remark 3.3. *If the error $e(t)$ of the state-estimation process is "smaller" (in fact, the attractive ellipsoid $\mathcal{E}$ is smaller), then the quality of the corresponding DNN is higher.*

3.3.2 How can we characterize an attractive ellipsoid?

Recall the following definitions.

Definition 3.1. • *The set $\mathcal{E}(\bar{x}, P)$ of points x from $\mathbb{R}^n$ is referred to as the **ellipsoid** with the center in the point $\bar{x}$ and with the corresponding*

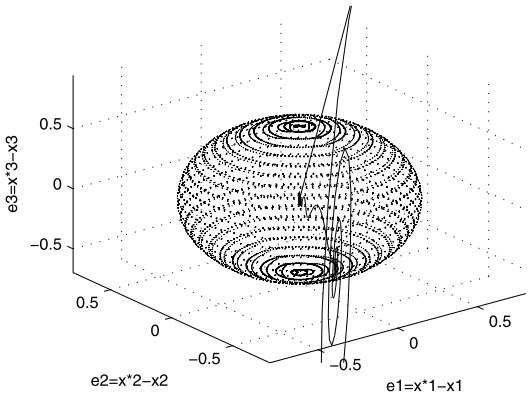

■ **FIGURE 3.7** Three dimensional attractive ellipsoid.

ellipsoidal matrix $P = P^{\mathsf{T}} \geq 0$ *if for any* $x \in \mathcal{E}(\bar{x}, P)$ *the following inequality holds:*

$$(x - \bar{x})^{\mathsf{T}} P (x - \bar{x}) \leq 1. \tag{3.19}$$

- *If* $\bar{x} = 0$ *then the ellipsoid is called the* ***central ellipsoid*** *if any point of it satisfies*

$$x^{\mathsf{T}} P x \leq 1,$$

and it is denoted by $\mathcal{E}(P)$.
- *The* ***semi-axes*** $r_i(P)$ *of the ellipsoid* $\mathcal{E}(\bar{x}, P)$ *(or* $\mathcal{E}(P)$*) are equal to*

$$r_i(P) = \frac{1}{\sqrt{\lambda_i(P)}} \, (i = 1, ..., n) \, . \tag{3.20}$$

- *If all* $r_i(P) < \infty$*, or equivalently, all* $\lambda_i(P) > 0$ $(i = 1, ..., n)$*, then such ellipsoid is named a* ***bodily ellipsoid****.*

Obviously an ellipsoid $\mathcal{E}(\bar{x}, P_1)$ is upload inside of an ellipsoid $\mathcal{E}(\bar{x}, P_2)$, that is,

$$\mathcal{E}(\bar{x}, P_1) \subset \mathcal{E}(\bar{x}, P_2), \tag{3.21}$$

if its semi-axes $r_i(P_1)$ are less than the corresponding semi-axes $r_i(P_2)$ of another ellipsoid,

$$r_i(P_1) < r_i(P_2) \;\; (i = 1, ..., n) \, ,$$

which equivalently can be expressed as

$$\lambda_i(P_1) > \lambda_i(P_2) \;\; (i = 1, ..., n) \, ,$$

or as

$$\begin{aligned} P_1 > P_2 \qquad & (P_1 - P_2 > 0), \\ P_1^{-1} < P_2^{-1} \qquad & \left(P_1^{-1} - P_2^{-1} < 0\right). \end{aligned} \tag{3.22}$$

Definition 3.2. *The ellipsoid $\mathcal{E}(\bar{x}, P_{att})$ is called the **Attractive Ellipsoid** (AE) for the trajectory $\{x(t)\}_{t\geq 0}$ if it tends asymptotically to being inside of this ellipsoid. Mathematically this property is expressed as*

$$\limsup_{t\to\infty} (x(t) - \bar{x})^{\mathsf{T}} P_{att} (x(t) - \bar{x}) \leq 1. \tag{3.23}$$

Of course, below we will be interested in the statement of the following attractive property of a central ellipsoid $\mathcal{E}(P)$:

$$e_t \underset{t\to\infty}{\to} \mathcal{E}(P), \tag{3.24}$$

which mathematically can be expressed as

$$\limsup_{t\to\infty} e_t^{\mathsf{T}} P_{att} e_t \leq 1 \tag{3.25}$$

for the state-estimation error e_t.

3.3.3 Numerical quality estimation of state observation process using DNN

Proposition 3.1. *The neuro-observer (3.15), supplied by the learning law (3.17) with the gain parameter L, satisfying the matrix inequality*

$$\mathsf{W} = \mathsf{W}\left(P, L, W_0^*, W_1^*, \Lambda \mid \alpha, \varepsilon\right) =$$

$$\begin{bmatrix} P(A_\alpha - LC) + \\ (A_\alpha - LC)^{\mathsf{T}} P \\ +2P\Lambda P \end{bmatrix} \quad \begin{matrix} PL \\ \end{matrix} \quad \begin{matrix} -P \\ \end{matrix} \quad \begin{matrix} PW_0^* \\ \end{matrix} \quad \begin{matrix} PW_1^* \\ \end{matrix}$$

$$\begin{bmatrix} L^{\mathsf{T}} P \\ -P \\ \left(PW_0^*\right)^{\mathsf{T}} \\ \left(PW_1^*\right)^{\mathsf{T}} \end{bmatrix} \quad \begin{matrix} -\varepsilon I_{m\times m} \\ 0 \\ 0 \\ 0 \end{matrix} \quad \begin{matrix} 0 \\ -\varepsilon I_{n\times n} \\ 0 \\ 0 \end{matrix} \quad \begin{matrix} 0 \\ 0 \\ -\varepsilon I_{k_\varphi \times k_\varphi} \\ 0 \end{matrix} \quad \begin{matrix} 0 \\ 0 \\ 0 \\ -\varepsilon I_{k_\psi \times k} \end{matrix} \Bigg] < 0$$

$$A_\alpha := A + \frac{\alpha}{2} I_{n\times n}, \tag{3.26}$$

*for some positive definite matrix $P = P^{\mathsf{T}} > 0$, some matrices W_0^*, W_1^*, Λ, and positive constants $\alpha > 0$, $\varepsilon > 0$ shows the **attractivity property** (3.25)*

with the ellipsoidal matrix P_{att} equal to

$$P_{att} = \frac{\alpha}{\varepsilon\beta} P, \tag{3.27}$$

where

$$\begin{gathered} \beta := C_0 + k^2 C_1, \\ C_0 := \eta_+^2 + c_0 + c_1 d_0 + \varphi_+^2, \ C_1 := \psi_+^2 + c_1 d_1. \end{gathered} \tag{3.28}$$

The proof of this proposition is in the appendix of this chapter.

Corollary 3.3. *The **best parameters of the neuro-observer** (3.15), providing the smallest attracting ellipsoid, correspond to the solution of the following constrained optimization problem:*

$$\begin{gathered} \left(P^*, L^*, W_0^{**}, W_1^{**}, \Lambda^*, \alpha^*, \varepsilon^*\right) = \underset{P>0, L, W_0^*, W_1^*, \Lambda>0, \alpha>0, \varepsilon>0}{\arg\sup} \operatorname{tr}\left\{\frac{\alpha}{\varepsilon} P\right\} \\ \textit{subject to the matrix constraint} \\ \mathsf{W} = \mathsf{W}\left(P, L, W_0^*, W_1^*, \Lambda \mid \alpha, \varepsilon\right) < 0. \end{gathered}$$

Proof. It directly follows from the simple relation (3.20). □

3.3.4 The best parameters finding using MATLAB toolboxes

Notice that the matrix constraint (A.38) is a bilinear one: it includes the matrix products PL, PW_0^*, and PW_1^*. It also includes the quadratic term $P\tilde{\Lambda}P$ on P. Estimating this term from above as

$$P\tilde{\Lambda}P \le Q, \tag{3.29}$$

we have

$$\begin{gathered} \mathsf{W} \le \mathsf{W}_Q := \\ \begin{bmatrix} \mathsf{W}_{Q,11} & PL & -P & PW_0^* & PW_1^* \\ L^\mathsf{T}P & -\varepsilon I_{m\times m} & 0 & 0 & 0 \\ -P & 0 & -\varepsilon I_{n\times n} & 0 & 0 \\ \left(PW_0^*\right)^\mathsf{T} & 0 & 0 & -\varepsilon I_{k_\varphi \times k_\varphi} & 0 \\ \left(PW_1^*\right)^\mathsf{T} & 0 & 0 & 0 & -\varepsilon I_{k_\psi \times k} \end{bmatrix} < 0, \\ \mathsf{W}_{Q,11} = P\left(A_\alpha - LC\right) + \left(A_\alpha - LC\right)^\mathsf{T} P + Q. \end{gathered} \tag{3.30}$$

Notice that by the Schur complement (Poznyak, 2008a) the matrix inequality (3.29) can be equivalently represented as

$$0 \leq \begin{bmatrix} Q & P \\ P & \tilde{\Lambda}^{-1} \end{bmatrix}. \tag{3.31}$$

But the standard MATLAB procedures SEDUMI and YALMIP are oriented only for solving the optimization problems with Linear Matrix Inequalities (LMIs). The variable transformation

$$X = P,\ Y = PL,\ Z_0 = PW_0^*,\ Z_1 = PW_1^*,\ Z_2 = \frac{1}{2}\Lambda^{-1},$$

permits one to represent (3.30) as the following LMIs:

$$\left.\begin{array}{c} \tilde{\mathrm{W}}_Q = \tilde{\mathrm{W}}_Q\left(X, Y, Z_0, Z_1, Z_2, Q \mid \alpha, \varepsilon\right) = \\ \begin{bmatrix} \tilde{\mathrm{W}}_{Q,11} & Y & -X & Z_0 & Z_1 \\ Y^{\intercal} & -\varepsilon I_{m\times m} & 0 & 0 & 0 \\ -X & 0 & -\varepsilon I_{n\times n} & 0 & 0 \\ Z_0^{\intercal} & 0 & 0 & -\varepsilon I_{k_\varphi \times k_\varphi} & 0 \\ Z_1^{\intercal} & 0 & 0 & 0 & -\varepsilon I_{k_\psi \times k} \end{bmatrix} < 0, \\ \tilde{\mathrm{W}}_{Q,11} := XA_\alpha + A_\alpha^{\intercal} X + Q - YC - C^{\intercal} Y^{\intercal}, \\ 0 \leq \begin{bmatrix} Q & P \\ P & Z_2 \end{bmatrix}. \end{array}\right\} \tag{3.32}$$

Finding the numerical solution $\left(X^*, Y^*, Z_0^*, Z_1^*, Z_2^*, Q^*, \alpha^*, \varepsilon^*\right)$ of the problem

$$\mathrm{tr}\left\{\frac{\alpha}{\varepsilon}P\right\} \to \underset{X>0, Y, Z_0, Z_1, Z_2>0, Q>0, \alpha>0, \varepsilon>0}{\arg\sup}$$

subject to the matrix constraints

$$\tilde{\mathrm{W}}_Q = \tilde{\mathrm{W}}_Q\left(X, Y, Z_0, Z_1, Z_2, Q \mid \alpha, \varepsilon\right)$$

$$0 \leq \begin{bmatrix} Q & P \\ P & Z_2 \end{bmatrix}$$

the optimal parameters of the neuro-observer can be found as follows:

$$L^* = Y\left(X^*\right)^{-1},$$

$$W_0^{**} = Z_0^*\left(X^*\right)^{-1},\ W_1^{**} = Z_1^*\left(X^*\right)^{-1},\ \left(\Lambda^*\right)^{-1} = 2Z_2^*,$$

and the best attractive ellipsoid for tracking error will be defined by the matrix P_{attact}, which is

$$P_{att} = \frac{\alpha^*}{\varepsilon^* \beta} X^*. \tag{3.33}$$

3.4 ADAPTIVE CONTROLLERS BASED ON DNN ESTIMATES

To realize the control of uncertain plants (when we do not know exactly the model of the process or cannot measure online all coordinates of the process to be controlled) let us apply the so-called *separation principle*, which is based on the following inequality:

$$\left\| x_t - x_t^* \right\| = \left\| \left(x_t - \hat{x}_t \right) + \left(\hat{x}_t - x_t^* \right) \right\| \leq \left\| \hat{x}_t - x_t \right\| + \left\| \hat{x}_t - x_t^* \right\|, \tag{3.34}$$

where x_t is the state vector of the controlled plant, $\hat{x}_t$ is its estimate, and x_t^* is a desired trajectory which we intend to track.[1]

Proposition 3.2 (Separation principle)**.** *If*

a) *we are able to realize a good enough state estimations, namely, fulfilling for all* $t \geq T_1$

$$\left\| \hat{x}_t - x_t \right\| \leq \varepsilon_1,$$

b) *and we can realize a good tracking of our model (generating* $\hat{x}_t$*) to the desired trajectory* x_t^**, fulfilling for all* $t \geq T_2$

$$\left\| \hat{x}_t - x_t^* \right\| \leq \varepsilon_2,$$

then we can guarantee a good enough control of our uncertain plant, that is,

$$\left\| x_t - x_t^* \right\| \leq \varepsilon_1 + \varepsilon_2,$$

for all $t \geq T := \max\{T_1, T_2\}$.

Below, we will extensively apply this *separation principle*, designing the state estimations $\hat{x}_t$ (3.15) of ozonization processes x_t (2.16) using DNN-observers as software sensors.

[1] When we have the exact equality (=) in (3.34) we will call this property the exact separation principle, which takes place only in stochastic systems.

3.5 CONCLUSIONS

Here we present a short review of the concept of ANNs, which turns out to be an efficient method to approximate uncertain relationships between inputs and outputs. A clear explanation describing the superiority of DNNs versus feedforward NNs is given. The advantages of introducing feedback in the ANN structure are emphasized and their application within the identification and/or control of dynamic processes is explained. Based on the feedback idea, the universal DNNO tool has been developed yielding the design of both artificial software sensors (dynamic state observers) and robust controllers. AEM used as a tool of optimization for the convergence region of the estimation error is also explained as a primary element to enhance the quality of the estimation and tracking provided by the DNN application. The next chapters describe the application of different versions of DNNOs and adaptive controllers for a wide diversity of ozonation and biodegradation systems.

Chapter 4

Neural observer application for conventional ozonation in water

CONTENTS

ABSTRACT

A dynamic neural network (DNN) is employed to estimate the state dynamics of diverse contaminants in ozone–water systems. A new technique based on the dynamic neural network observer (DNNO) is applied to an estimate of the decomposition of phenols and their mixture and to a calculation of their reaction constants without using any mathematical model. The decomposition of phenols and their mixture by ozone in a semi-batch reactor is considered as a process with an uncertain model ("black box"). Only one variable is measured during ozonation, namely, the ozone concentration in the gas phase in the reactor outlet. Its variation is used to obtain the characteristic curve for the phenol ozonation, the so-called *ozonogram*. Then, using the experimental behavior of the phenols and of the decomposition

Ozonation and Biodegradation in Environmental Engineering
https://doi.org/10.1016/B978-0-12-812847-3.00013-5

of their mixture, obtained by High Performance Liquid Chromatography (HPLC), the proposed DNNO is applied to an estimate of the ozonation constants of phenols in the separate ozonation and in the ozonation of their mixture at a pH of 12. A good correspondence between the experimental decomposition of phenols and the estimated ones by DNNO is obtained. The suggested technique makes possible an online monitoring of the water treatment without implementation of any specific chemical (testing) sensors.

4.1 STATE ESTIMATION METHODS

The assumption that all states of a dynamic process are completely accessible seems to be unrealistic. This is the main reason for taking the state observation as an important solution for the analysis of chemical processes and the corresponding effective control design. Several approaches dealing with state estimation problem are widely used in practical applications. Among them, one may mention some key results such as:

– the Lie-algebraic method (Knobloch et al., 1993),

– Lyapunov-like observers (Slotine, 1984),

– high gain observation (Ciccarella et al., 1993), (Nicosia and Tornambe, 1989),

– optimization-based observer (Krener and Isidori, 1980),

– the reduced-order nonlinear observers (Garcia and D'Atellis, 1995),

– DNNO (Levin and Narendra, 1995), (El-Din and Smith, 2002), (Poznyak et al., 2001).

4.1.1 State estimation: a brief survey

The *state estimation (observation) problem* arises during *identification* or *feedback control* when the current system states cannot be directly measured and the only available information at each time instant is the output of the system which is a function of the current state, usually corrupted by "output noise". Modern *identification theory* (Eykhoff and Parks, 1990), (Ljung, 1979) basically deals with the problem of the efficient extraction of signal and a system's dynamic properties based on available data measurements. Nonlinear system identification is traditionally concerned with two issues:

a) estimation of parameters based on direct and complete state space measurements, and

b) state space estimation (filtering) of completely known nonlinear dynamics.

Here we will deal with issue *b*). The contribution on the observer construction problem for nonlinear systems in the presence of *complete information* about the nonlinear dynamics, was performed by Williamson (1977), Krener and Isidori (1983), Krener and Respondek (1985), and Xia and Gao (1989). Most of these results deal with the situation where it is possible to obtain a set of rather restrictive conditions when the dynamics of the observation errors is linear and there is no observation noise. By Walcott and Zak (1988) a class of observers for nonlinear systems subjected to bounded nonlinearities or uncertainties was suggested. A canonical form and a necessary and sufficient observability condition for a class of nonlinear systems, which are linear with respect to the inputs, was established by Gauthier and Bornard (1981). The extended Luenberger observer for a class of SISO nonlinear systems was designed by Zeitz (1987). These results were extended in Birk and Zeitz (1988) for a class of MIMO nonlinear systems. An exponentially convergent observer was derived in Gauthier et al. (1992) for nonlinear systems that are observable for any input signal. More advanced results were obtained in Ciccarella et al. (1993), where (based on simple assumptions of regularity) the global asymptotic convergence of the estimated states to the true states was shown. A further line of investigation relates to the observation problem subjected to bounded nonlinearities or *uncertainties* (Walcott and Zak, 1987), (Walcott et al., 1987). In the situation when the plant model is incomplete or uncertain, the implementation of high-gain observers seems to be convenient (Tornambè, 1989), (Dabroom and Khalil, 1997), (Nicosia and Tornambe, 1989), (Boizot et al., 2010). In Yaz and Azemi (1994) a robust/adaptive observer is presented for state reconstruction of nonlinear systems with uncertainty having unknown bounds. A robust adaptive observer for a class of nonlinear systems is proposed in Zhu et al. (1997) and based on generalized dynamic recurrent neural networks. A robust nonlinear observer is considered in Yu and Shields (1996) for a class of singular nonlinear descriptor systems subject to unknown inputs. This class is partly characterized by globally Lipschitz nonlinearities. A suboptimal robust filtering of states for finite dimensional linear systems with time-varying parameters under nonrandom disturbances was considered in Poznyak and Cordero (1994). Sliding-mode observers were studied in Utkin (1992). The approach described in the book of Edwards and Spurgeon (1998) is conceptually similar to that proposed by Slotine (1984). References Walcott and Zak (1987, 1988) seek global error convergence for a class of uncertain systems using some algebraic manipulations to effectively solve an associated constrained Lyapunov problem for systems of reasonable order. This approach is discussed in detail in Walcott (1990). One thus also describes a hyperstability approach to observer design by Balestrino and Innocenti (1990), based on

the concept of positive realness. A comprehensive survey of these problems can be found in Poznyak (2004b).

In this chapter, we follow the approach presented in Poznyak et al. (2006b) using the DNNO concept.

4.2 SOFTWARE SENSORS BASED ON DNNO

The majority of chemical processes and, in particular, ozonation can be described in the general format given by the system (2.16) of ordinary equations which have several joint specific properties:

- they are bilinear with respect to the components of the state vector,
- not all parameters of this model are known or can be estimated before a laboratory experiment: the special expensive physical devices (such as the UV-Vis spectrophotometer, high performance liquid chromatography, gas chromatography, infrared spectroscopy, nuclear magnetic resonance, etc.) are required,
- only some of components (frequently only one) of the state vector can be measured during the process: in the case of ozonation it is the current concentration $c^g(t)$ of ozone in the gas phase.

To realize successfully the further analysis of the ozonation reaction and a control process the complete current knowledge of all components of the process is required. That is why their good estimation during the process seems to be necessary. Because of the absence of physical devises, which can realize the corresponding identification, the usage of *artificial software sensors* with only the application of computer programs can be suggested. In this book we will apply the DNNO as the universal software sensor device for obtaining current information (identification or state estimation) using only the available online measurements of a considered process. Then, based on these obtained data we show how to estimate the parameters of chemical reactions participating in the dynamic model description (2.16).

4.3 DNNO WITH DISCONTINUOUS AND TIME DERIVATIVE TERMS

Let us represent the dynamic model given by (4.1) as

$$\left.\begin{aligned} \dot{x}(t) &= f\left(x(t), u(t), t\right) + \xi_1(t), \\ y(t) &= C^\top x(t) + \xi_2(t), \end{aligned}\right\} \tag{4.1}$$

where $x \in \mathbb{R}^n$ is the state vector of the system, $y \in \mathbb{R}^p$ is the output signal, $u \in \mathbb{R}^m$ is a control action that belongs to the following admissible set:

$$U_{adm} = \left\{ u \mid \|u\| \leq u^+ \right\}.$$

The function $f : \mathbb{R}^n \times \mathbb{R}^m \times \mathbb{R}_+ \to \mathbb{R}^n$ is a mathematical model for the plant given by (4.1), $\xi_1 \in \mathbb{R}^n$ and $\xi_2 \in \mathbb{R}^p$ are the state and output *bounded* unknown perturbations, respectively:

$$\|\xi_i\|^2_{\Lambda_{\xi_i}} \leq \Upsilon_i < \infty, \quad 0 < \Lambda_{\xi_i} = \Lambda^{\mathsf{T}}_{\xi_i}, \ i = 1, 2. \tag{4.2}$$

Below, we will consider the special situation when

$$C^\top = \begin{bmatrix} 1 & 0 & \cdots & 0 \end{bmatrix},$$

that is, only the first component is measured:

$$y(t) = x_1(t) \ \ (p = 1).$$

If the nonlinear vector-function $f(x, u, t)$ is known, then, according to standard techniques (Ciccarella et al., 1993), the following Luenberger-like structure for the corresponding observer is usually considered:

$$\left.\begin{aligned} \frac{d}{dt}\hat{x}(t) = f\left(\hat{x}(t), u(t), t\right) + L_1 e(t), \\ e(t) = y(t) - C^\top \hat{x}(t). \end{aligned}\right\} \tag{4.3}$$

Here $\hat{x} \in \mathbb{R}^n$ is the state vector of the observer or (in other words) the state estimation, $e \in \mathbb{R}^p$ is the output estimation error, $L_1 \in \mathbb{R}^{n \times p}$ is a gain matrix to be designed. The device realizing the process (4.3) will be referred to as the *software sensor* for the considered process.

Remark 4.1. *Applying the observer (4.3), one can find that the measurable component is estimated sufficiently quickly and with good accuracy. But, as a consequence, the output error turns out to be very small, and this practically does not permit one to adjust effectively the other states estimations. One of the possible outputs from such a situation is to add new corrections terms which are not so sensible to small values of* $e(t)$.

This may be done as suggested in Poznyak et al. (2001), Poznyak (2004a). Let us add:

- the sign term (discontinuous or *sliding-mode type*): $L_2 \text{sign}\,(e(t))$, $L_2 \in \mathbb{R}^{n \times p}$,

- the output error time derivative approximation: $L_3\left(e(t)-e(t-h)\right)$, $L_3 \in \mathbb{R}^{n\times p}$,

which transforms (4.3) into

$$\begin{aligned}\frac{d}{dt}\hat{x}(t) = f\left(\hat{x}(t), u(t), t\right) + L_1 e(t) + \\ L_2 \text{sign}\left(e(t)\right) + L_3\left(e(t)-e(t-h)\right).\end{aligned} \tag{4.4}$$

Here two additional gain matrices L_1, L_2, and L_3 appear to be designed. It is clear that when the output error is small enough, the sliding-mode term still keeps a significant value to correct the estimation dynamics. The same is true for the derivative estimation term.

In real situations when we have no complete information on the nonlinear function $f(x,u,t)$ which may contain unknown parameters, instead of f we may use its estimate $\hat{f}(x,u,t \mid W,V)$ depending on some unknown *adjusted parameters* or *weights*. Let us represent now the plant dynamics (4.1) by

$$\frac{d}{dt}x(t) = f_0\left(x(t), u(t), t \mid W_0, V^0\right) + \tilde{f}\left(x(t), u(t), t \mid W_0\right) + \xi_1(t), \tag{4.5}$$

where

$$f_0\left(x,u,t \mid W^0, V^0\right) = Ax + W_1^0 \sigma(V_1^0, x) + W_2^0 \phi(V_2^0, x)u$$

and

$$\tilde{f}\left(x,u,t \mid W^0, V^0\right) = f(x,u,t) - f_0\left(x,u,t \mid W^0, V^0\right). \tag{4.6}$$

By assumption,

$$\left\| \tilde{f}\left(x,u,t \mid W_0, V^0\right)\right\|^2 \le \eta_0 + \eta_1 \|x\|^2. \tag{4.7}$$

Here:

– the matrix $A \in \mathbb{R}^{n\times n}$ has all its eigenvalues on the left-hand side of the complex plane (in other words it is stable),

– $W_1^0 \in \mathbb{R}^{n\times W_1}$ and $W_2^0 \in \mathbb{R}^{n\times W_2}$ correspond to the external weights,

– $V_1^0 \in \mathbb{R}^{V_1\times n}$ and $V_2^0 \in \mathbb{R}^{V_2\times n}$ are some internal weights that participate as modulators of the state as argument of the so-called activation functions,

$$\sigma : \mathbb{R}^{V_1\times n} \times \mathbb{R}^n \to \mathbb{R}^{W_1},\ \phi : \mathbb{R}^{V_2\times n} \times \mathbb{R}^n \to \mathbb{R}^{W_2\times p},$$

for the neural network approximation (4.5). These functions satisfy

$$\begin{gathered}\|\sigma(V_a, x_a) - \sigma(V_a, x_b)\| \le L_\sigma \|x_a - x_b\|, \quad x_a \in \mathbb{R}^n, x_b \in \mathbb{R}^n, \\ \|[\phi(V_b, x_a) - \phi(V_b, x_b)]u\| \le L_\phi \|x_a - x_b\| \cdot \|u\|, \\ V_a \in \mathbb{R}^{V_1 \times n}, \ V_b \in \mathbb{R}^{V_2 \times n}.\end{gathered}$$

Moreover, the activation functions are absolutely bounded, that is, there exist two positive constants, $L_\sigma^+ \in \mathbb{R}_+$, $L_\phi^+ \in \mathbb{R}_+$, such that

$$\|\sigma(V_a, x_a)\| \le L_\sigma^+, \qquad \|\phi(V_b, x_b)u\| \le L_\phi^+ \|u\|, \ u \in U_{adm}.$$

Adjusting online these weight *parameters* we may obtain the best (or appropriate) approximation of the unknown dynamic operator. According to this approach we may suggest the following dynamic neural observer:

$$\begin{gathered}\frac{d}{dt}\hat{x}(t) = f_0\left(\hat{x}(t), u(t), t \mid W(t), V(t)\right) + L_1 e(t) + \\ L_2 \operatorname{sign}(e(t)) + L_3(e(t) - e_{t-h}),\end{gathered} \tag{4.8}$$

supplied with a special updating law:

$$\left.\begin{aligned}\frac{d}{dt}W(t) &= \Phi\left(W(t), V(t), \hat{x}(t), y(t), u(t), t\right), \\ \frac{d}{dt}V(t) &= \Psi\left(V(t), W(t), \hat{x}(t), y(t), u(t), t\right).\end{aligned}\right\} \tag{4.9}$$

Such a *robust adaptive observer* seems to be a more advanced device, which provides a good estimation under an incomplete state measurement. Below we will select the approximation function using the NN structure with one internal hidden layer (Poznyak et al., 2001). Despite the estimation technique based on neural networks and the sliding-mode technique, it is necessary to make the following assumptions:

– the original system is stable,

– the original system control functions are bounded.

The DNN observer (4.8)–(4.9) is described by the following ordinary differential equation:

$$\begin{gathered}\frac{d}{dt}\hat{x}(t) = A\hat{x}(t) + W_{1t}\sigma(V_{1t}\hat{x}(t)) + W_{2t}\phi(V_{2t}\hat{x}(t))u(t) \\ + L_1 e(t) + L_2 \operatorname{sign}(e(t)) + L_3(e(t) - e(t-h)).\end{gathered} \tag{4.10}$$

Here $\hat{x} \in \mathbb{R}^n$ is the state vector of DNNO representing the current estimates of the real process states, A, $L_1 \in \mathbb{R}^n$, $L_2 \in \mathbb{R}^n$, $L_3 \in \mathbb{R}^n$ are constant ma-

trices adjusted during DNN training,

$$\sigma : \mathbb{R}^{V_1 \times n} \times \mathbb{R}^n \to \mathbb{R}^{W_1}, \quad \phi : \mathbb{R}^{V_2 \times n} \times \mathbb{R}^n \to \mathbb{R}^{W_2 \times p}$$

are standard sigmoid functions, h is a data delay constant, and V_i $(i = 1, 2)$ are the hidden-layer weights tuning by an online *learning* procedure (Poznyak, 2004a) given by the following differential equations:

$$\left.\begin{aligned} \dot{W}_j(t) = &-k_j P N_\delta C^\intercal e(t) \psi_j\left(\hat{x}(t)\right) + \frac{k_j}{2} P N_\delta C^\intercal e(t) \hat{x}(t)^\intercal V_{jt} D_{jt} \\ &-\frac{k_j}{2} P N_\delta \Pi_{1,j} N_\delta P \tilde{W}_{1t} \psi_j\left(\hat{x}(t)\right) \psi_j^\intercal\left(\hat{x}(t)\right), \\ \dot{V}_j(t) = &\frac{k_{j+2}}{2} D_{jt}^\intercal W_{j0}^\intercal P N_\delta \Pi_{2,j} N_\delta P W_j D_{jt} \tilde{V}_{jt} \hat{x}(t) \hat{x}(t)^\intercal \\ &-\frac{k_{j+2}}{2} D_{jt}^\intercal W_{j0}^\intercal P N_\delta C^\intercal e(t) \hat{x}(t)^\intercal + l_j \Lambda_j \tilde{V}_{jt} \hat{x}(t) \hat{x}(t)^\intercal. \end{aligned}\right\} \tag{4.11}$$

Here

$$\begin{gathered} \psi_1\left(\hat{x}(t)\right) := \sigma(V_{1t} \hat{x}(t)), \quad \psi_2\left(\hat{x}(t)\right) := \phi(V_{2t} \hat{x}(t)) u(t) \\ D_{jt} = \nabla_{\hat{x}} \psi_j\left(\hat{x}\right)\big|_{\hat{x}=\hat{x}(t)}, \quad \tilde{V}_{jt} = V_{jt} - V_{j0}, \\ \Pi_{1,j} = \Lambda_{1,j} + \delta C^\intercal \Lambda_j C, \quad \Pi_{2,j} = \Lambda_{2,j} + \delta C^\intercal \Lambda_j C. \end{gathered}$$

The gain matrix L_1 in (4.10) corresponds to a linear (*Luenberger type*) correction term, L_2 is *a sliding-mode* correction term matrix, and L_3 is a gain matrix of a *derivative estimation* correction term and they are described by

$$L_1 = P^{-1} C^\intercal, \; L_2 = k P^{-1} C^\intercal, \; L_3 = h^{-1} P^{-1} C^\intercal, \tag{4.12}$$

where the matrix P corresponds to the attractive ellipsoid described in the appendix.

4.3.1 Training of DNNO

To guarantee a small enough (near zero) state estimation error, the adequate DNNO parameters at (4.10) should be selected. The *offline* adjustable parameters A, K_1, and K_2 may be tuned during the "training" process, where the weights $W_{i,t}, i \in 1, 2$, are quickly adjusted online by the matrix differential learning law (4.11). The training procedure has two ways of the DNNO training:

1. Using any simplified mathematical model of phenols ozonation, including the byproducts dynamics, to generate the corresponding trainer input–output

data sequences, which may serve for the DNNO parameters adjustment and for adequate selection of the initial conditions in the applied ($W_{j,0}$) learning procedure as described (Poznyak et al., 2005).

2. Using the experimental data of the phenol ozonation, training data for the DNNO adjustment procedure may be obtained too. The data set, composed of the gaseous phase ozone concentration variation and the phenol and byproduct decomposition dynamics, must have representative information about the phenol decomposition with ozone (an observability requirement) to apply successfully any adaptive nonlinear observer and DNN, particularly.

In this chapter, the second method was used to train the DNNO observer. The phenols at different pH values (2.0, 7.0, and 12.0) were decomposed. With the difference between the ozonation mechanisms at acid and basic pH, the DNNO training was carried out under the following conditions:

- The adjustable parameters on DNNO structure were selected based on the data set generated at the pH values of 2.0 and 9.0.
- The state estimation, using DNN approach, was tested with the data generated at the pH values of 7.0 and 12.0.
- The trained DNNO at the pH value of 2.0 was used to reconstruct the ozonation dynamics at the pH 7.0 since the reaction is direct between the molecular ozone and the organics.
- The ozonation at the pH value of 12.0 was tested with the trained DNNO using the data set supplied at a pH of 9.0. At these two pH values the reaction mechanism is similar, where the combination of free radicals and the direct reaction with molecular ozone takes place.

4.4 APPLICATION OF DNNO TO RECONSTRUCT THE CONTAMINANT DYNAMICS IN OZONATION

The estimation process (reconstruction of immeasurable variables) was carried out by special software designed to connect the acquisition board with a virtual instrument (computer-assisted sensor). This "artificial sensor" measures the ozone concentration in the gas phase in the reactor output. The generated information is applied to the DNNO software that reconstructs (using the algorithm described by (4.10)–(4.12)) the unknown variables involved in the ozonation (phenol decomposition, byproduct formation and decomposition, final product formation). In fact, the suggested algorithm is running during the ozonation, so the reaction is realized simultaneously with the online estimation providing a current concentration value for each phenol and its byproducts.

Below we would like to present the DNN algorithm (4.10)–(4.12), realizing the contaminant dynamic reconstruction, in the original variables $Q(t)$ and $c_i(t)$ $(i = 1, ..., N)$ with direct calculation of the kinetic constants k_i. These constants may be calculated (offline or online) based on the obtained current estimates $\hat{Q}(t)$ and $\hat{c}_i(t)$ of the original model variables.

Recall that there exists a direct relation, Eq. (4.13), between the abstract variables $x(t)$ and the original variables $Q(t)$ and $c_i(t)$:

$$x = \begin{bmatrix} c^g & \frac{Q}{V_{ilq}} & c_1 & \vdots & c_N \end{bmatrix}^\top. \tag{4.13}$$

Define the vector of current estimates

$$\hat{x} = \begin{bmatrix} \hat{c}^g & \frac{\hat{Q}}{V_{ilq}} & \hat{c}_1 & \vdots & \hat{c}_N \end{bmatrix}^\top.$$

In view of this relation, the DNNO algorithm (4.10)–(4.12) of the **contaminants' dynamic reconstruction** looks as follows:

$$C = (1, 0, 0..., 0), \quad e(t) = y(t) - C\hat{x}(t) = y(t) - \hat{c}^g(t),$$

- *$\hat{c}^g(t)$-reconstruction of the ozone concentration $c^g(t)$ in the gas phase*

$$\left.\begin{aligned} \frac{d}{dt}\hat{c}^g(t) = a_{1,1}\hat{c}^g(t) + a_{1,2}\hat{Q}(t)/V_{liq} + \sum_{i=1}^{N} a_{1,2+i}\hat{c}_i(t) \\ + \sum_{s=1}^{W_1} W_{1:1,s}(t)\,\sigma_s(V_{1,l}(t)\,\hat{x}(t)) + \\ \sum_{s=1}^{W_2} W_{2:1,s}(t) \sum_{k=1}^{r} \phi_{s,k}(V_{2t}\hat{x}(t))u_k(t) + \\ L_{1,1}e(t) + L_{2,1}\mathrm{sign}(e(t)) + L_{3,1}[e(t) - e(t-h)], \end{aligned}\right\} \tag{4.14}$$

- *$\hat{Q}(t)$-reconstruction of the ozone $Q(t)$ dissolved in the liquid phase*

$$\left.\begin{aligned} \frac{1}{V_{liq}}\frac{d}{dt}\hat{Q}(t) = a_{2,1}\hat{c}^g(t) + a_{2,2}\hat{Q}(t)/V_{liq} + \\ \sum_{i=1}^{N} a_{2,2+i}\hat{c}_i(t) + \sum_{s=1}^{W_1} W_{1:2,s}(t)\,\sigma_s(V_{1,l}(t)\,\hat{x}(t)) + \\ \sum_{s=1}^{W_2} W_{2:2,s}(t) \sum_{k=1}^{r} \phi_{s,k}(V_{2t}\hat{x}(t))u_k(t) + \\ L_{1,2}e(t) + L_{2,2}\mathrm{sign}(e(t)) + L_{3,2}[e(t) - e(t-h)], \end{aligned}\right\} \tag{4.15}$$

- $\hat{c}_i(t)$*-reconstruction of the contaminant concentrations* $c_i(t)$ $(i = 1, ..., N)$ *in the liquid phase*

$$\left.\begin{array}{c} \dfrac{d}{dt}\hat{c}_i(t) = a_{2+i,1}\hat{c}^g(t) + a_{2+i,2}\hat{Q}(t)/V_{liq} + \\ \sum\limits_{s=1}^{N} a_{2+i,2+s}\hat{c}_s(t) + \sum\limits_{s=1}^{W_1} W_{1:2+i,s}(t)\sigma_s(V_{1,l}(t)\hat{x}(t)) + \\ \sum\limits_{s=1}^{W_2} W_{2:2+i,s}(t)\sum\limits_{k=1}^{r}\phi_{s,k}(V_{2t}\hat{x}(t))u_k(t) + \\ L_{1,2+i}e(t) + L_{2,2+i}\operatorname{sign}(e(t)) + \\ L_{3,2+i}[e(t) - e(t-h)]. \end{array}\right\} \tag{4.16}$$

Here the vector parameters

$$\left.\begin{array}{l} L_1 = \left(L_{1,1}, L_{1,2}, L_{1,3}, ..., L_{1,N+2}\right)^{\mathsf{T}}, \\ L_2 = \left(L_{2,1}, L_{2,2}, L_{2,3}, ..., L_{2,N+2}\right)^{\mathsf{T}}, \\ L_3 = \left(L_{3,1}, L_{3,2}, L_{3,3}, ..., L_{3,N+2}\right)^{\mathsf{T}}, \end{array}\right\} \tag{4.17}$$

are defined by (4.12), and the learning dynamics of the weights

$$\left.\begin{array}{l} W_1(t) = \left\| W_{1:l,s}(t) \right\|_{l=1,...,N+2;s=1,...,W_1}, \\ W_2(t) = \left\| W_{1:l,k}(t) \right\|_{l=1,...,N+2;k=1,...,W_2}, \end{array}\right\} \tag{4.18}$$

is given by (4.11). We have also used the definition

$$A = \left\| a_{s,k} \right\|_{s=1,...,N+2;k=1,...,N+2}.$$

Notice that the variable $c^g(t)$ is measurable (available) online. Its estimate $\hat{c}^g(t)$ is required only for completion of the estimation algorithms of other components. It also may effectively serve when *the ozone concentration* $c^g(t)$ *in the gas phase is measured with some noise, significantly reducing (suppressing) this noise-effect.*

4.5 ESTIMATION OF THE SIMULATED OZONATION VARIABLES USING DNNO

To guarantee a small enough state estimation error, the adequate parameters of DNNO (7) should be selected. The stationary parameters A, L_1, L_2, L_3 may be tuned during the so-called "*training*" process. The weights W_i, V_i $(i = 1, 2)$ are quickly adjusted online by the differential learning law (4.11).

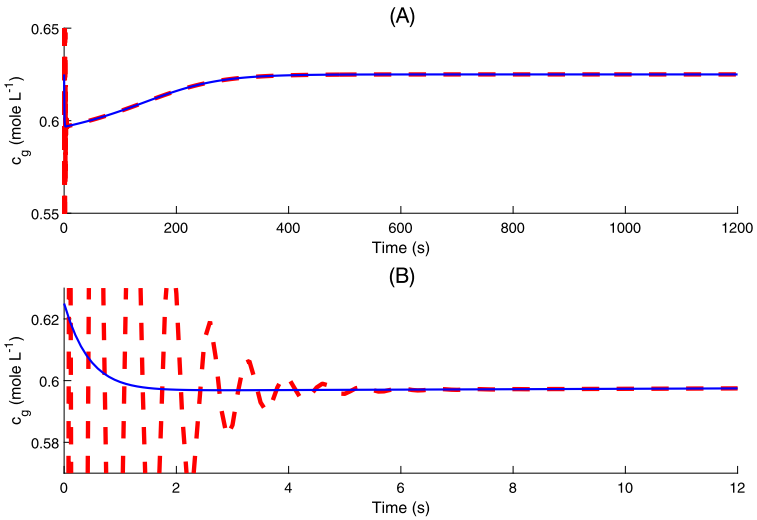

■ **FIGURE 4.1** Comparison between DNNO approach and proposed model for the ozone concentration variation in the gas phase for the phenol decomposition. The solid (blue line in the electronic version) corresponds to the ozonation model and dashed (red line in the electronic version) corresponds to the DNNO states.

In this section we consider details of the training procedure. It may be conducted using some simple mathematical model of ozonation (the complete model is never practically available) to generate the corresponding input–output data sequences, which may serve for the correction of the parameters of DNNO as well as for adequate selection of the initial conditions in the applied learning procedure.

Based on the available results Poznyak et al. (1977) and Poznyak (2003) where the simple ozonation with i component model mixture at pH $= 7$ has been treated, we can describe this process using the system of ODEs (2.16). The numerical simulation of this ODEs system appears in Fig. 4.1.

Using the ozonation mathematical model (4.14)–(4.15) and applying the suggested DNNO (4.10) with one output layer, one hidden layer and ($k_i = n_i = n = 5$), we can simulate the separate phenol decomposition and their mixtures by ozonation using their rate constants (Hoigné and Bader, 1983a):

$$k_{Ph} = 1.3 \cdot 10^3 \text{ L mol}^{-1} \text{ s}^{-1},$$
$$k_{4-CPh} = 1.9 \cdot 10^3 \text{ L mol}^{-1} \text{ s}^{-1},$$
$$k_{2,4-DCPh} = 2.8 \cdot 10^3 \text{ L mol}^{-1} \text{ s}^{-1},$$

based only on the monitoring data. If just one organic compound (phenol) or the phenol mixture is reacted with ozone, we have fast convergence between

Table 4.1 DNNO parameters obtained in training procedure for each phenol and its model mixtures.

Two compounds	DNNO parameters			
Mixtures	A	K_1	K_2	K_3
Ph+ 4-CPh	$\begin{bmatrix} -0.5 & 0 & 0 \\ 0.8 & -2.3 & 0 \\ 0.3 & 0 & -3.5 \end{bmatrix}$	$\begin{bmatrix} 0.5 \\ 3.9 \\ 6.7 \end{bmatrix}$	$\begin{bmatrix} 0.8 \\ 3.1 \\ 4.5 \end{bmatrix}$	$\begin{bmatrix} 0.3 \\ 0.2 \\ 0.7 \end{bmatrix}$
Ph+ 2,4-DCPh	$\begin{bmatrix} -0.5 & 0 & 0 \\ 0.8 & -2.3 & 0 \\ 0.3 & 0 & -3.5 \end{bmatrix}$	$\begin{bmatrix} 0.5 \\ 3.9 \\ 6.7 \end{bmatrix}$	$\begin{bmatrix} 0.8 \\ 3.1 \\ 4.5 \end{bmatrix}$	$\begin{bmatrix} 0.3 \\ 0.2 \\ 0.7 \end{bmatrix}$
4-CPh+ 2,4-DCPh	$\begin{bmatrix} -0.5 & 0 & 0 \\ 0.8 & -2.3 & 0 \\ 0.3 & 0 & -3.5 \end{bmatrix}$	$\begin{bmatrix} 0.5 \\ 3.9 \\ 6.7 \end{bmatrix}$	$\begin{bmatrix} 0.8 \\ 3.1 \\ 4.5 \end{bmatrix}$	$\begin{bmatrix} 0.3 \\ 0.2 \\ 0.7 \end{bmatrix}$

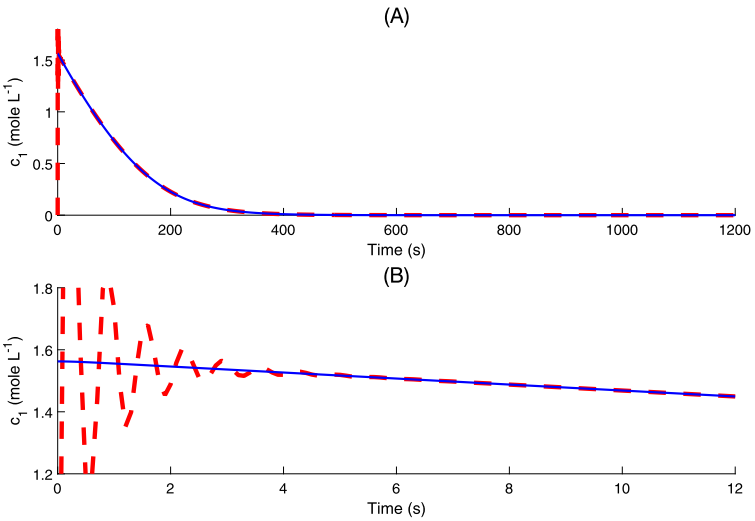

■ **FIGURE 4.2** Comparison between DNNO approach and proposed model for the contaminant concentration variation. The solid (blue line in the electronic version) corresponds to the ozonation model and dashed (red line in the electronic version) corresponds to the DNNO states.

the dynamic evolution generated by the given model (4.8) and DNNO (4.10) with the estimated parameters presented in Table 4.1. The numerical results appear in Fig. 4.2.

These parameters correspond to the *best* estimation dynamics and have been obtained by a simple *try-to-test* technique. Using the experimental data of

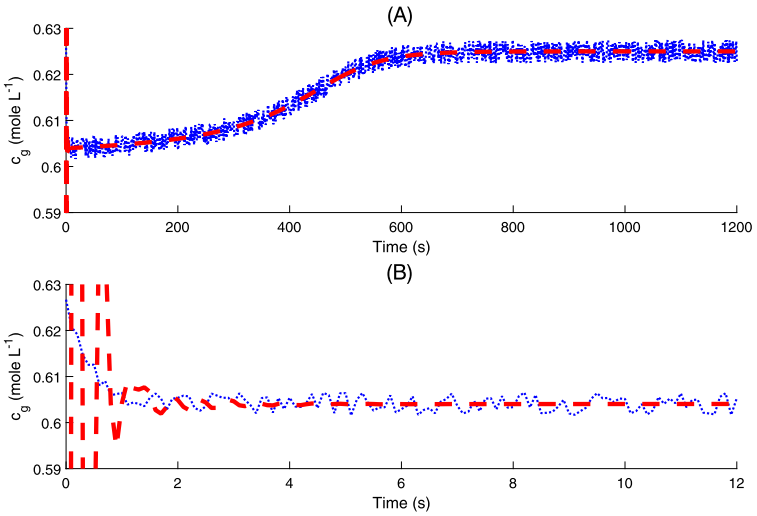

■ **FIGURE 4.3** Comparison between DNNO approach and proposed model for the ozone concentration variation in the gas phase for the phenol decomposition.

ozonation dynamics of the model mixtures of

$$\text{Ph} + \text{4-CPh},\ \text{Ph} + 2,\ \text{4-DCPh},\ \text{4-CPh} + 2,$$
$$\text{4-DCPh},\ \text{Ph} + \text{4-CPh} + 2,\ \text{4-DCPh},$$

at different pH $(2, 7, 12)$, obtained by HPLC, a good correspondence between the real decomposition dynamics (Poznyak et al., 2001) and the estimated ones by DNNO was obtained (Figs. 4.3 and 4.4).

In Figs. 4.3–4.4, the dashed line (red line in the electronic version) corresponds to the simulation of the ozonation model affected with artificial noise (produced by the signal generator of bounded noise in Simulink-Matlab), while the solid line (blue line in the electronic version) represents the estimation obtained by the DNNO.[1]

4.5.1 Estimation of the reaction rate constants of phenols

From the previous sections, it follows that DNNO can be successfully used to estimate the ozonation kinetic parameters. The rate constant is an important parameter for the reaction mechanism interpretation in the case of liquid phase complexity composition. Observe that $\hat{c}_i$, $\hat{Q}$, and $\dfrac{d\hat{c}_i(t)}{d\tau}$ are available.

[1] Note: The color figures will appear in color in all electronic versions of this book.

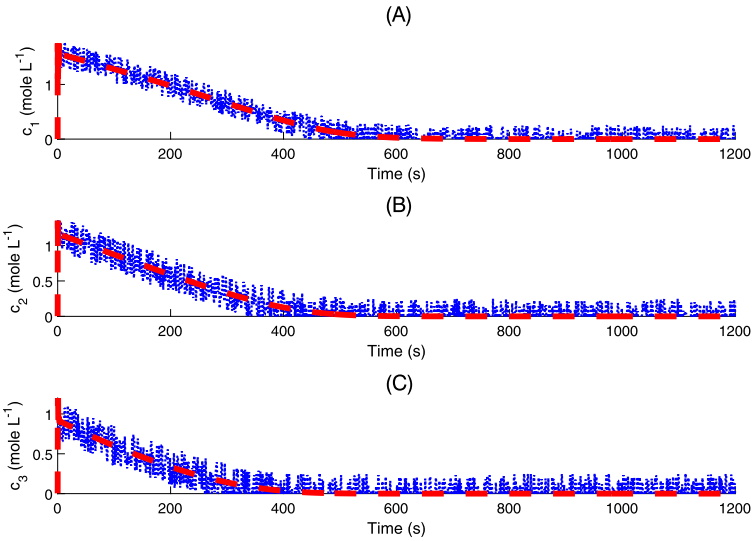

■ **FIGURE 4.4** Comparison between DNNO approach and proposed model for the concentration variation of three contaminants (Ph, 4-CPh, and 2,4-DiCPh). The solid (blue line in the electronic version) corresponds to the ozonation experimental variables and dashed (red line in the electronic version) corresponds to the DNNO states.

In view of this, it is possible to define the LS (Least Square) estimates k_i as the solution to the following optimization problem:

$$\hat{k}_i^*(t) = \arg\min_{k_{i,t}} \int_0^t \left(\frac{d\hat{c}_i(\tau)}{d\tau} + k_i \left(v_{liq}\right)^{-1} \hat{c}_i(\tau)\, \hat{Q}(\tau) \right)^2 d\tau. \tag{4.19}$$

The solution is as follows:

$$\hat{k}_i^*(t) = v_{liq} \frac{\int_0^t \hat{c}_i(\tau)\, \hat{Q}(\tau) \frac{d\hat{c}_i(\tau)}{d\tau} d\tau}{\int_0^t \left(\hat{c}_i(\tau)\, \hat{Q}(\tau) \right)^2 d\tau + \vartheta}, \ \vartheta > 0. \tag{4.20}$$

Here $\vartheta > 0$ is a small regularizing parameter (0.01).

The performance index given by this observer was compared with one generated by the *"classical"* observer with only one proportional term, and we obtained a faster (around 250 s) convergence between the ozonation model dynamics and DNNO (Fig. 4.5).

The estimation of the rates constants for three different compounds (phenol, 4-chlorophenol and 2,4-dichlorophenol) in their mixture under $v_{liq} = 0.8(L)$ show an excellent correspondence with the experimental dynamics

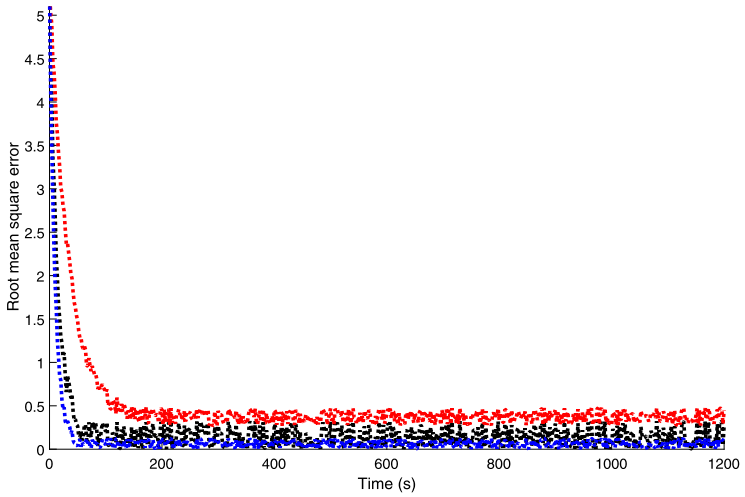

■ **FIGURE 4.5** Comparison of the root mean square for the estimation error with different gain terms: the blue line corresponds to the case when the three corrections terms are in the DNNO, the black line corresponds to the case when discontinuous and linear terms are considered and the red line refers to the case with the linear term only.

(Fig. 4.3 and Table 4.2). Here the quicker decomposition dynamics exactly corresponds to the high value of the reaction rate constant. The numerical results concerning the ozonation rate constants are given in Table 4.2.

As one can observe, the reactivity of the phenols with ozone have the following order:

$$\text{Ph} < \text{4-CPh} < \text{2, 4-DCPh}$$

which is not changed at the different pHs in the ozonation of individual phenols. With the increase of the pH, the value of the reaction constant for each phenol increases significantly also. In the case of the phenol mixture ozonation, their reactivity with ozone is not the same as that for the individual phenols. At a pH of 2, when the direct reaction with molecular ozone takes place, the reaction constants increase for the phenols mixture almost by a factor 2–3, depending on the mixture composition. In the case of the combined mechanism at pH > 7, the reaction constants decrease, in comparison with individual phenols. However, the difference of the values between phenols is not significant. This phenomenon can be explained by the presence of the OH-radicals, which are not selective and do not depend on the chemical structures of the compound. More important seems to be the fact that the reactivity with ozone of the individual compounds and their mixtures is not the same.

Table 4.2 Reaction rate constants (10^3) for the phenols and their mixtures at different pH values.

Compound	k_i, [L mol^{-1} s^{-1}]		
	pH = 2	pH = 7	pH = 12
Individual phenols			
Ph	0.867	1.168	3.274
4-CPh	0.940	3.091	8.474
2,4-DCPh	1.073	6.173	17.032
Mixtures of two phenols			
Ph+4-CPh	1.678	2.456	4.767
	1.765	2.578	4.487
Ph+2,4-DCPh	1.756	2.859	3.490
	1.927	2.920	3.576
4-CPh+2,4-DCPh	1.644	2.703	4.303
	1.745	2.818	4.406
Mixture of three phenols			
Ph+4-CPh+2,4-DCPh	2.546	4.443	5.515
	2.545	4.673	5.433
	3.793	6.272	6.091

To study the pH effect on the ozonation kinetics of the phenols mixtures with the different phenols composition, the pH variation from 2 to 12 has been performed. In Table 4.4 the intermediates and final products obtained in ozonation of the phenol mixture number 1 at different values of pH are presented.

The intermediates and the final products of the phenol destruction by ozone are similar to the ones cited before. They are as follows: catechol, hydroquinone, muconic acid, fumaric acid, maleic acid, oxalic acid, and formic acid. According to the time of the appearance of the byproducts and their distribution in ozonation, it can be affirmed that muconic acid is the initial product; catechol, hydroquinone, fumaric acid, maleic acid are intermediate products, and oxalic and formic acids, accumulating in ozonation, are final products.

The ozonation of the phenol mixtures were conducted with synthetic solutions in distilled water with the variation of the initial organics concentration (see Table 4.3).

From Table 4.4, the pH effect on the composition of intermediates and final products of ozonation also is very significant. Therefore, the presence of catechol (or derivatives of catechol) and hydroquinone in an aqueous solution at pH = 2 and 7 confirms the hydroxylation before the cleavage of

Table 4.3 Initial composition of phenols in the model mixtures.

Number of mixture	Ph mg L^{-1}	4-CPh mg L^{-1}	2,4-DCPh mg L^{-1}	Total conc. mg L^{-1}
1	100	100	100	300
2	125	125	50	300
3	83.33	33.33	83.33	200
4	33.33	83.33	83.33	200

Table 4.4 Intermediates and final products of the ozonation of the phenols mixtures.

Compound mg L^{-1}	pH = 2	pH = 7	pH = 12
Catechol	8.3	14.5	ND
Hydroquinone	33.3	48.0	Traces
Muconic acid	Traces	Traces	ND
Fumaric acid	Traces	9.7	Traces
Maleic acid	25.0	42.1	Traces
Oxalic acid	139.6	174.0	436.7
Formic acid	235.2	270.9	ND

the aromatic ring. The principal final products at pH values of 2 and 7 are oxalic and formic acids. On the other hand, at a pH of 12, catechol, hydroquinone, phenol, and 4-CPh have not been found in the water solution. The final product is only oxalic acid. These data confirm the well-known fact that the mechanisms of the phenol ozonation under basic and acidic conditions are different. Indeed, ozonation at low pH (2 or 7) proceeds mainly through the reaction with molecular ozone. In ozonation at high pH (> 7) the radical mechanism takes place together with the direct reaction of molecular ozone. It is important to notice that the increasing of the phenol concentration in the first stage of 4-chlorophenol ozonation and the increasing of the 4-chlorophenol concentration in the first stage of the 2,4-dichlorophenol ozonation are detected at all pH (2, 7, 9, and 12). The formation of these compounds in ozonation of the phenol mixtures confirms the dechlorination of 4-CPh and 2,4-DCPh at the initial reaction stage. The principal final products at pH values of 2 and 7 are oxalic and formic acids. On the other hand, at pH = 12, catechol, hydroquinone, phenol, and 4-CPh have not been found. At this pH the final product is only oxalic acid.

To study the phenomenon of the change of the ozonation kinetics of the individual compounds and the same organics in their mixture, the ozonation of the phenols mixture at the different pH and with the different initial

Table 4.5 Ozonation constants k (L/mol s) $\cdot 10^3$ of phenols at the pH values of 9 and 12 in the different mixtures.

	Mixture							
	1		2		3		4	
pH	9	12	9	12	9	12	9	12
Ph	5.38	5.52	2.57	2.77	2.29	3.28	1.61	1.90
4-CPh	5.20	5.43	2.71	2.82	3.13	3.74	1.73	2.45
2,4-DCPh	6.46	6.09	6.82	5.23	7.24	7.40	3.19	4.17

concentration of the phenols in the mixture were carried out. By the same technique of the dynamic neural network observer (DNNO), the kinetic parameters of the phenols mixture ozonation were estimated. The calculated reaction constants are presented in Table 4.5.

As can be seen from these data, the ozonation constants of phenols for all mixtures have the tendency to increase (2.6–30.5%) with the increase of the pH from 9 to 12. The effect of the pH depends on the composition of the mixture, namely on the phenol ratio. For the other three mixtures (2, 3, and 4), when the ratio of the concentration of phenols is varied; the pH effect is more significant in the comparison with the mixture 1, when this ratio is 1:1:1. As can be seen, the reaction constant decreases to 48% for mixture 2 (excluding 2,4-DCPh at the pH of 9, which increases to 5.2%). In the case of mixture 3, we observe another tendency: for Ph and 4-CPh the reaction constants decrease to 40%, to be compared with mixture 1; however, for 2,4-DCPh the constants increase to 12%. In the case of mixture 4, the values of the constants decrease to 50–70%. Based on the ozonation kinetics of phenols in their mixtures, we may conclude that the reaction constants of the phenols strongly depend on their initial concentration. In this particular case, it is difficult to explain the observed tendency; however, at a pH of 9 and 12 the effect of the initial composition of phenols is very significant. This phenomenon must be taken into account in the ozonation of complex mixtures of different organic contaminants, bearing in mind that the kinetics of ozonation for the individual compounds and for their mixtures are different.

The convergence of the LS estimate constants ($k_i^*(t)$) for phenols to the real values ($k_i^*(T)$), obtained by the standard methods (Poznyak et al., 2004), is shown in Fig. 4.6. It is important to emphasize that the reaction constant determination for individual compounds can be realized by other simple methods, but for an organics mixture there do not exist other approaches to the estimate of these parameters.

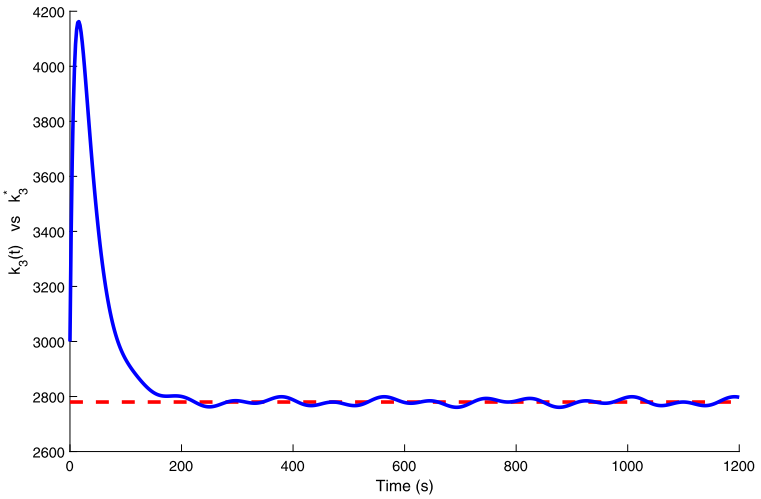

■ **FIGURE 4.6** Convergence of the estimated reaction rate constant k_3 to its actual value when the estimated states are used in the identification algorithm.

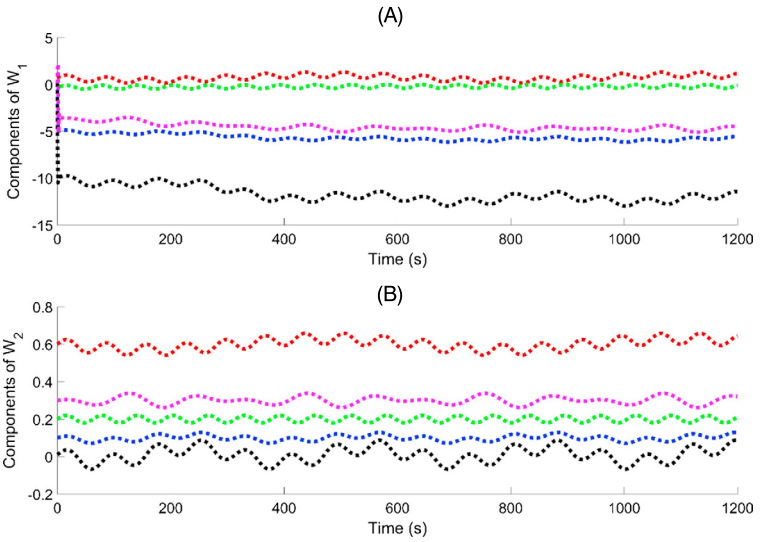

■ **FIGURE 4.7** Time variation of some components of weights W_1 and W_2 included in the DNNO and used to estimate the components of the ozonation of the mixture of phenols.

Fig. 4.7 depicts the variation of some components of W_1 and W_2. These weights evolve according to the learning laws proposed in Eq. (4.11). Notice that these components do not converge to a fixed value. This is a consequence of the ozonation dynamics and its impact on the weights dynamics.

Based on the results given above, we may conclude that the DNNO approach has been shown to guarantee a good state estimation in the phenol decomposition without any mathematical model usage. The decomposition behavior predicted by DNNO shows a good enough correspondence to the real experimental data. In particular, the estimates of the ozonation rate constants, obtained by this method, exactly correspond to the experimental decomposition of phenols. The unique monitoring, demanded for the realization of this method, is the ozone concentration variation measurements in the gas phase in the reactor output.*The suggested dynamic neural observer (DNNO) can be incorporated into a real-time control system to optimize the decomposition dynamics without the online contaminant concentration measurements*.

4.6 RECONSTRUCTION OF PHENOLS BEHAVIOR AS WELL AS THEIR INTERMEDIATES AND FINAL PRODUCTS USING DNNO

Most of the AOPs studies usually investigate only the decomposition of the initial compound, but they do not consider the byproduct decomposition. The importance of control of the byproducts is due to their toxicity, which can be higher than of the original contaminants (Adams et al., 1997; Beltrán et al., 1999a,b,c, 2002c; Buffle and von Gunten, 2006; Faungnawakij et al., 2006; Griffini et al., 1999; Gurol and Nekouinaini, 1984; Kitis et al., 2000; Santos et al., 2004; Trapido et al., 1997; Yordanov et al., 1999).

4.6.1 Ozonation procedure

The ozonation of the phenols' solution (with the initial concentration 100 mg L^{-1}) was carried out at pH values of 2, 7, 9, and 12. The initial pH was controlled using H_2SO_4 and NaOH 0.05N solutions, and this parameter was measured by a Conductronic pH-meter, model PC 18 with a P100C-BNC electrode.

The corresponding organic compound concentration was measured in different reaction times being compared with the decomposition dynamic generated by DNNO.

4.6.2 Fundamentals of the phenols behavior reconstruction

The first stage in the DNNO numerical realization is the corresponding training. To train the DNNO the experimental "trainer" data are used. Then, applying the suggested DNNO, the phenol decomposition dynamics and the

Table 4.6 DNNO parameters obtained in the training procedure.

Initial comp.	A	K_1	K_2	K_3
Ph	$\begin{bmatrix} -0.5 & 0 & 0 \\ 0.8 & -2.3 & 0 \\ 0.3 & 0 & -3.5 \end{bmatrix}$	$\begin{bmatrix} 0.5 \\ 3.9 \\ 6.7 \end{bmatrix}$	$\begin{bmatrix} 0.8 \\ 3.1 \\ 4.5 \end{bmatrix}$	$\begin{bmatrix} 0.3 \\ 0.2 \\ 0.7 \end{bmatrix}$
4-CPh	$\begin{bmatrix} -0.5 & 0 & 0 \\ 0.8 & -2.3 & 0 \\ 0.3 & 0 & -3.5 \end{bmatrix}$	$\begin{bmatrix} 0.5 \\ 3.9 \\ 6.7 \end{bmatrix}$	$\begin{bmatrix} 0.8 \\ 3.1 \\ 4.5 \end{bmatrix}$	$\begin{bmatrix} 0.3 \\ 0.2 \\ 0.7 \end{bmatrix}$
2,4-DCPh	$\begin{bmatrix} -0.5 & 0 & 0 \\ 0.8 & -2.3 & 0 \\ 0.3 & 0 & -3.5 \end{bmatrix}$	$\begin{bmatrix} 0.5 \\ 3.9 \\ 6.7 \end{bmatrix}$	$\begin{bmatrix} 0.8 \\ 3.1 \\ 4.5 \end{bmatrix}$	$\begin{bmatrix} 0.3 \\ 0.2 \\ 0.7 \end{bmatrix}$
Ph 4-CPh 2,4-DCPh	$0.1 \begin{bmatrix} 1 & 1 & 1 & 1 & 1 \\ 1 & 1 & 1 & 1 & 1 \\ 2 & 2 & 2 & 2 & 2 \\ 3 & 3 & 3 & 3 & 3 \\ 4 & 4 & 4 & 4 & 4 \end{bmatrix}$	$\begin{bmatrix} 0.1 \\ 0.1 \\ 0.2 \\ 0.3 \\ 0.4 \end{bmatrix}$	$\begin{bmatrix} 0.1 \\ 0.1 \\ 0.2 \\ 0.3 \\ 0.4 \end{bmatrix}$	$\begin{bmatrix} 0.1 \\ 0.1 \\ 0.2 \\ 0.3 \\ 0.4 \end{bmatrix}$

byproducts and final products trajectories were reconstructed. This method was used with the experimental data supplied by the ozonation of phenols at pH values of 2.0 and 9.0.

The adjustable parameters were selected by the *try-to-test* technique. Obviously, the DNNO parameters involved in each reaction change a little, because the computer algorithm, realizing the DNNO numerical algorithm, is strongly dependent on the ozonation variables. As an example, the parameters (A, K_1, and K_2), derived by the training method in the 4-CPh ozonation at the pH 2, are presented in Table 4.6. The training represents the most important part in the DNNO design, since this guarantees a better possible correspondence between the experimental data and the reconstructed variables given by the state estimator.

Fig. 4.8A–F presents the experimental ozonograms for three phenols and their numerical reconstructed decomposition in ozonation at a pH of 7 and 12.

In Table 4.7 the physical meaning of each component $\hat{x}_{s,t}$, $s \in [1, l]$ of the estimated state vector is presented. Similar tables can be proposed for the reactions of ozone with other phenols. An abridged version of this table, describing the corresponding byproducts and the accumulated acid, is presented below.

The main objective in the DNNO designing is to reproduce the trajectories given by a partially unknown nonlinear system, without the complete and exact model usage. As mentioned, the quality of the training process guar-

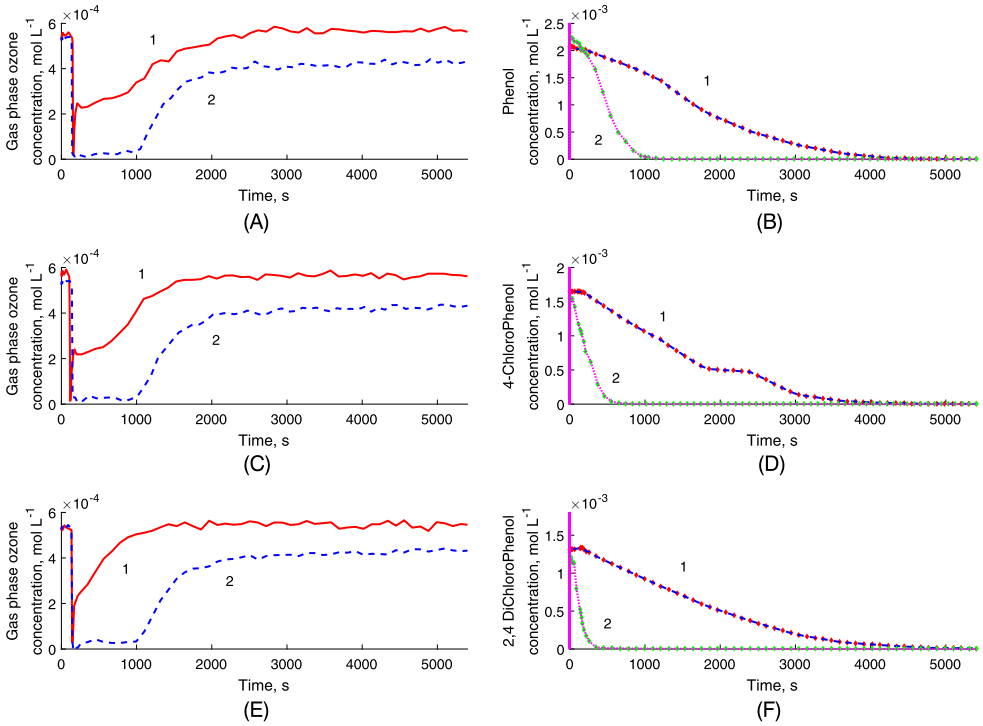

■ **FIGURE 4.8** Comparison between DNNO approach and experimental data for the ozone concentration variation in the gas phase at the pH 7 (1) and 12 (2) in ozonation of phenol (A), 4-chlorophenol (B) and 2,4-dichlorophenol (C); the decomposition of phenol (D), 4-chlorophenol (E), and 4-dichlorophenol (F).

antees the quality of the estimation technique. The section above introduces the "best possible" (at least in a computational sense) DNN parameters in order to make the estimation error as small as possible. The observing (estimation) process is proved at the pH values (7.0 and 12.0) considering that three phenols (Ph, 4-CPh, and 2,4-DCPh) were studied at four different pH values, but the data at pH values of 2.0 and 9.0 were used to train the DNNO.

4.6.2.1 Reconstruction of phenol and its byproducts profiles in ozonation

The basic byproducts in the phenols ozonation are catechol and hydroquinone, muconic, fumaric, and maleic acids, while oxalic and formic acids are the final products. The DNNO application in the phenol ozonation allows for the reconstruction of all byproducts and accumulated acids using the corresponding online data (gas-phase ozone concentration) at the pH values of 7 and 12, and a suitable training generating the adequate static parameters described above.

The estimation capability for the introduced DNNO approach is not only for the specific reaction conditions. This fact can be demonstrated by phe-

Table 4.7 Differential neural network observer state structure.

Variable	Treatment
$\hat{x}_1$	Ozone concentration variation in the gas phase
$\hat{x}_2$	Ozone concentration variation in the liquid phase
$\hat{x}_3$	Decomposition dynamics for the Ph concentration variation
$\hat{x}_4$	Accumulation and decomposition dynamics for catechol concentration variation
$\hat{x}_5$	Accumulation and decomposition dynamics for hydroquinone concentration variation denitrifying conditions
$\hat{x}_6$	Accumulation dynamics for formic acid concentration variation
$\hat{x}_7$	Accumulation dynamics for oxalic acid concentration variation
$\hat{x}_8$	Accumulation and decomposition dynamics for maleic acid concentration variation denitrifying conditions
$\hat{x}_9$	Accumulation and decomposition dynamics for muconic acid concentration variation denitrifying conditions
$\hat{x}_{10}$	Accumulation and decomposition dynamics for fumaric acid concentration variation denitrifying conditions

nol ozonation carried out at pH = 12.0, where the combination of the two mechanisms of ozonation is presented. In this case, the complete phenol decomposition is reached at 1000 s, to be compared with the previous examples at pH = 2.0, finishing at 3000 s (Fig. 4.9B). Furthermore, the important differences between these two cases are:

1. The reduction of the hydroquinone concentration is 10 times less than at pH 2.0 (Fig. 4.10A).

2. Catechol is formed during the first 2000 s, but it is also completely decomposed within the next 2000 s (Fig. 4.10B).

3. Formic acid is accumulated during the entire reaction time until a final concentration of $5.5 \cdot 10^{-3}$ mol L^{-1} (Fig. 4.10C).

4. Maleic acid concentration follows a similar behavior to the observed values for catechol while oxalic acid dynamics appear similar to the formic acid with a smaller final concentration of $0.25 \cdot 10^{-3}$ mol L^{-1} (Fig. 4.10D).

5. Muconic and fumaric acids are completely decomposed after 5400 s.

In all of these cases, the DNNO was able to reconstruct the dynamics of all the byproducts formed during the ozonation of phenol when the pH of the reaction was initially fixed at 2.0.

The ozone concentration in the output of the reactor and the phenol concentration, obtained when the pH was fixed to 7.0, were also reconstructed by the DNNO (Fig. 4.11). The DNNO estimation of the two variables c_g and c_1 was completed within the first 100 s.

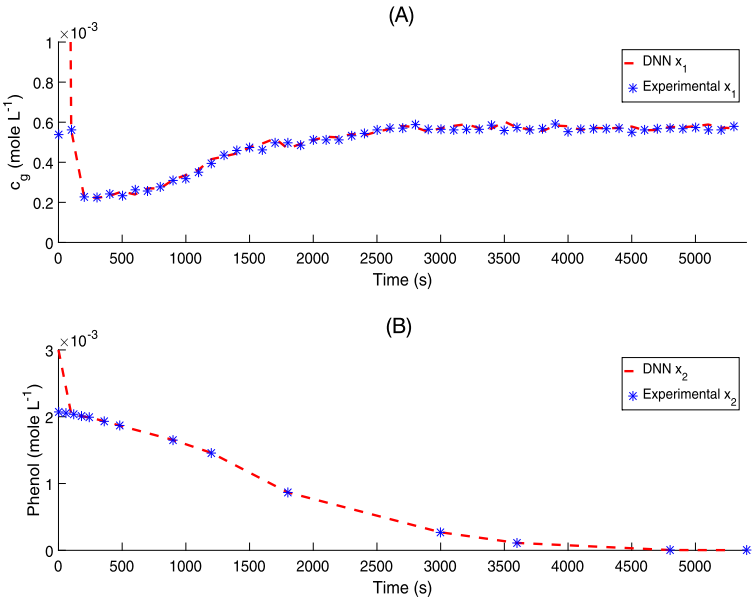

■ **FIGURE 4.9** Estimation of ozone concentration c_g in the gaseous phase (A) and phenol concentration c_1 (B) at pH $= 7.0$.

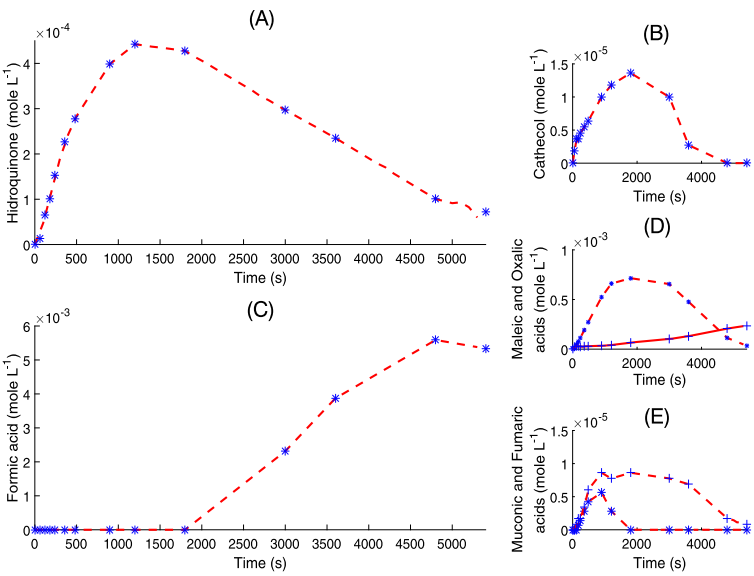

■ **FIGURE 4.10** Experimental concentrations and dynamic reconstruction of byproducts formed during ozonation of phenol at pH $= 7.0$.

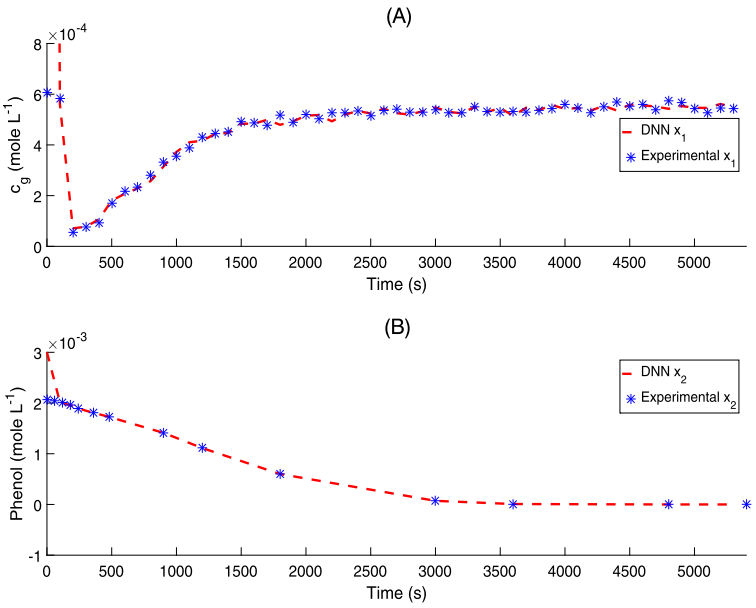

■ **FIGURE 4.11** Estimation of ozone concentration c_g in the gaseous phase (A) and phenol concentration c_1 (B) when pH $= 2.0$.

Regarding the ozonation byproducts when pH was fixed at 7.0, the following conclusions may be drawn:

1. Hydroquinone and catechol were simultaneously formed during the first stage of the reaction (1000 s). Both compounds were completely decomposed in a period of time of 1000–3500 s (Fig. 4.12A).

2. The accumulation of formic acid started when both catechol and hydroquinone were decomposed (3500 s). This compound attained a final concentration of $3.0 \cdot 10^{-3}$ mol L^{-1} (Fig. 4.12B).

3. The dynamics of fumaric acid is similar to the ones exhibited by hydroquinone and catechol; this compound was completely removed after the 5400 s of ozonation (Fig. 4.12C).

4. Maleic acid was accumulated in a similar manner to fumaric acid, yielding an accumulation of oxalic acid during the entire period of time needed to complete the ozonation of phenol when pH was 2.0 (Fig. 4.12D).

When pH was initially fixed at 12.0, the ozone concentration in the output of the reactor and the phenol concentration were significantly different from the ones observed in the case of neutral (7.0) and acidic (2.0) pH. The ozone concentration kept close to zero during the first 1000 s because of the

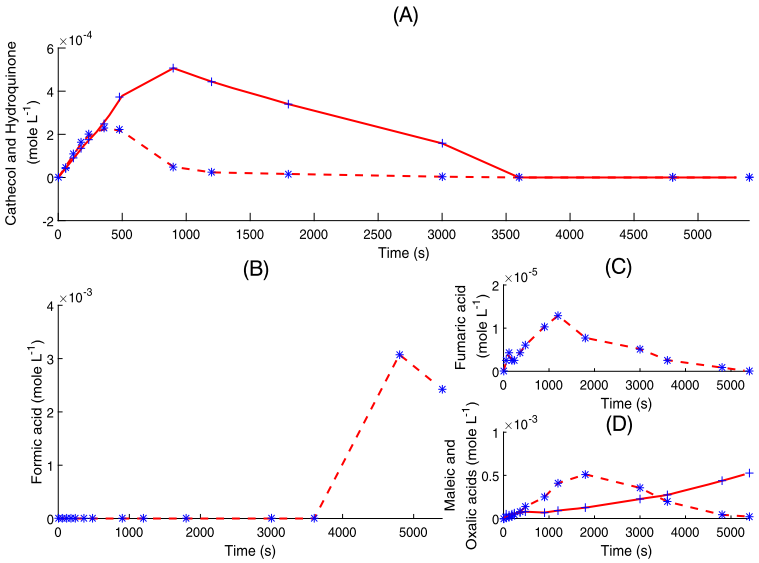

■ **FIGURE 4.12** Experimental concentrations and dynamic reconstruction of byproducts formed during ozonation of phenol at pH $= 7.0$.

increased ozone consumed by its reaction with OH ions. The phenol concentration c_1 was reconstructed by the DNNO (Fig. 4.13), despite the fact that the ozone concentration variation was not large enough.

When the ozonation of phenol was executed fixing pH $= 12.0$, the byproducts dynamics could be summarized as follows:

1. Hydroquinone was formed faster (500 s) than the neutral and acidic pH cases (1000 s). This effect is a consequence of the $OH^{\cdot}$ radicals formed by the ozone reaction with the OH^{-} ions. These radicals reacted with phenol faster and therefore, its byproducts are formed faster. This compound decomposed after 3000 s (Fig. 4.14A). Catechol was not detected in this reaction.

2. Fumaric acid was accumulated during the first 1000 s of ozonation. Its maximum concentration was smaller when the initial pH in the reaction was basic: $7.0 \cdot 10^{-6}$ mol L^{-1} vs. $1.2 \cdot 10^{-5}$ mol L^{-1} when pH was neutral (Fig. 4.14B).

3. The accumulation of formic acid started when both catechol and hydroquinone were decomposed (3500 s). This compound attained a final concentration of $3.0 \cdot 10^{-3}$ mol L^{-1}.

4. The dynamics of maleic acid was similar to the one obtained for the case of formic acid (Fig. 4.14C). This acid was formed and completely decom-

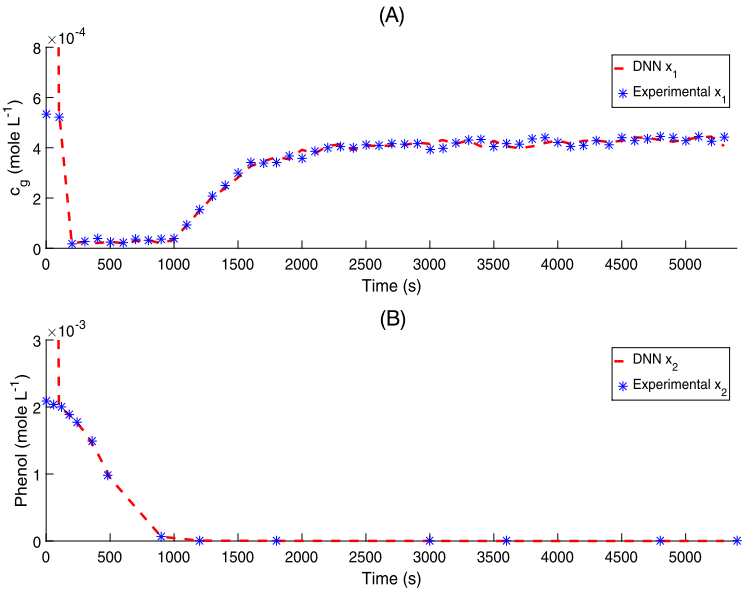

■ **FIGURE 4.13** Estimation of ozone concentration c_g in the gaseous phase (A) and phenol concentration c_1 (B) when pH $= 12.0$.

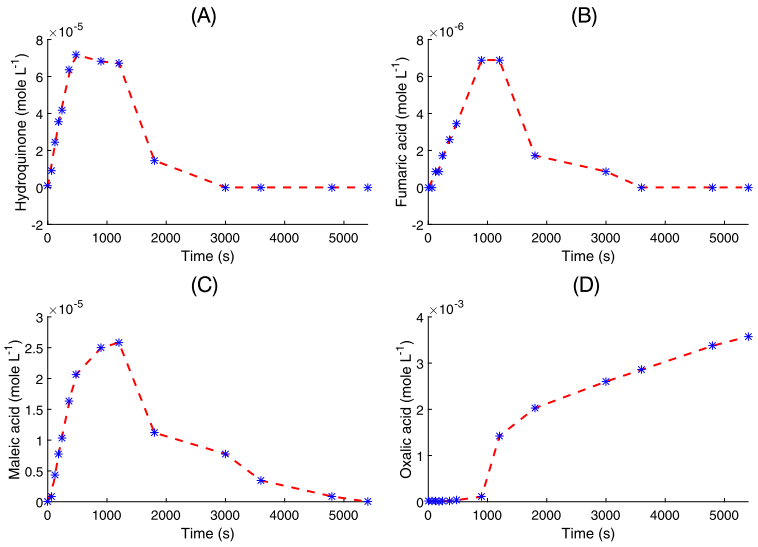

■ **FIGURE 4.14** Experimental concentrations and dynamic reconstruction of byproducts formed during ozonation of phenol at pH $= 12.0$.

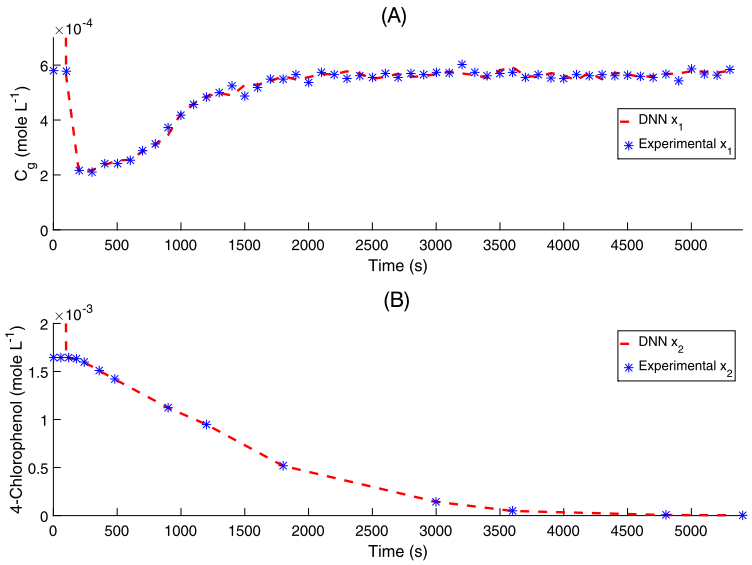

■ **FIGURE 4.15** Estimation of ozone concentration c_g in the gaseous phase (A) and 4-chlorophenol concentration c_1 (B) at pH $= 2.0$.

posed during the ozonation reaction time of 5400 s. This result is similar to the ones obtained in the previous cases (pH neutral and acidic), but in this case the maximum concentration was smaller ($2.4 \cdot 10^{-5}$ mol L^{-1}).

5. Oxalic acid was continuously accumulated along the whole ozonation until attaining a final concentration of $4.0 \cdot 10^{-3}$ mol L^{-1} (Fig. 4.14D).

4.6.2.2 Reconstruction of 4-chlorophenol and its byproducts

The most important element of the DNN behavior is the capability to reconstruct a wide class of nonlinear system without previous exact knowledge of the system's structure. Thus, it is possible to apply the same observer for the ozonation of other phenols, but after a new training process based on different experimental data sets.

For example, the 4-CPh decomposition was reconstructed using the corresponding ozonogram (Fig. 4.15A). In this case, the DNNO trained in the phenol ozonation was used for the 4-CPh reconstructed decomposition (Fig. 4.15B). It is possible to apply the same technique for the reconstruction of the intermediate and final products in the 4-CPh ozonation at pH $= 2.0$ (Fig. 4.16). In this case, the phenol formation during the 4-CPh dechlorination with other intermediates like catechol, hydroquinone, muconic, and malonic acids was observed.

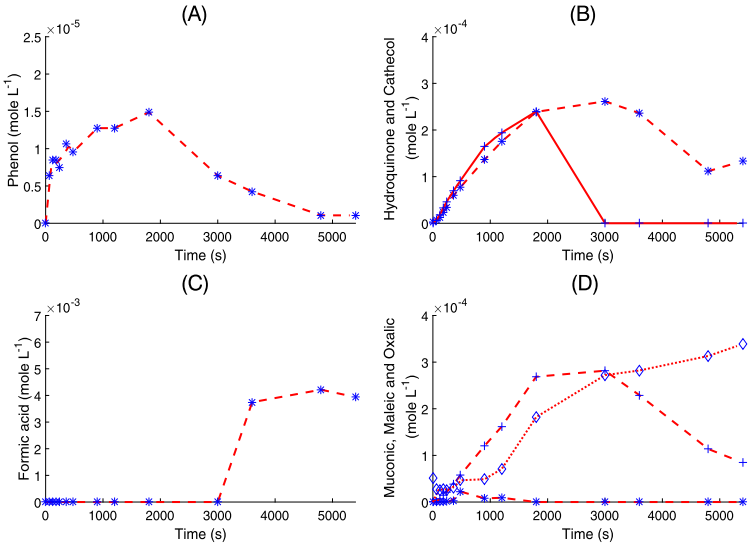

■ **FIGURE 4.16** Experimental concentrations and dynamic reconstruction of byproducts formed during ozonation of 4-chlorophenol at pH $= 2.0$.

The ozone concentration at the output of the reactor c_t (Fig. 4.15A), as well as the dynamics of 4-CPh concentration (Fig. 4.15B) during ozonation, is reproduced by the states of the observer in 100 s.

All byproducts formed by the decomposition of 4-CPh were also reconstructed by the observer. These byproducts obey the following guidelines:

1. Phenol is produced as a consequence of the dechlorination of 4-CPh. This compound is the first byproduct formed during the ozonation but it is decomposed according to the dynamics observed above (Fig. 4.16A).

2. Hydroquinone and catechol are formed as consequence of the phenol decomposition. However, their maximum concentrations appeared after 2000 s. The increment of the time when the maximum values appear is a consequence of the phenol formation, which preceded the accumulation of hydroquinone and catechol. Notice that catechol was decomposed during 5400 s of ozonation, while hydroquinone was not completely decomposed after this reaction time (Fig. 4.16B).

3. Formic acid started to be accumulated after 3000 s. As in the case of phenol, this compound, accumulated after catechol, was completely decomposed (Fig. 4.16C).

4. Muconic and fumaric acids followed a similar tendency to those observed in the case of phenol ozonation under acidic conditions (Fig. 4.16B).

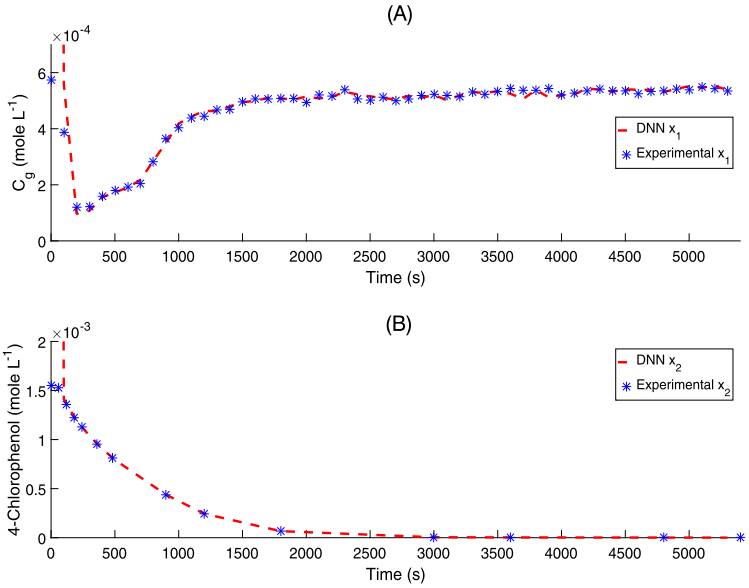

■ **FIGURE 4.17** Estimation of ozone concentration c_g in the gaseous phase (A) and 4-chlorophenol concentration c_1 (B) when pH $= 7.0$.

Once more, oxalic acid accumulated to reach a final concentration of $3.4 \cdot 10^{-4}$ mol L^{-1} (Fig. 4.16D), which is ten times smaller than the phenol case (under the same pH conditions). This decrement may be explained by the reaction time needed to form phenol from the 4-CPh decomposition.

In the neutral case (pH $= 7.0$), the ozone concentration in the output of the reactor and the 4-CPh concentration were reconstructed by the DNNO (Fig. 4.17). As in the case of acidic pH, the two variables c_g and c_1 are estimated after 100 s of reaction.

The following outcomes are obtained with respect to the byproducts obtained in the ozonation of 4-CPh:

1. The increment of pH produced a faster accumulation and decomposition of phenol, which is the first byproduct formed by the decomposition of 4-CPh (Fig. 4.18A).

2. Both intermediates (hydroquinone and catechol) were accumulated during the first 1000 s of reaction. After this reaction time, they were partially decomposed until the end of the reaction (Fig. 4.18B).

3. This experiment shows that formic acid is accumulated from the beginning of the reaction. This is not true for the oxalic acid, which was

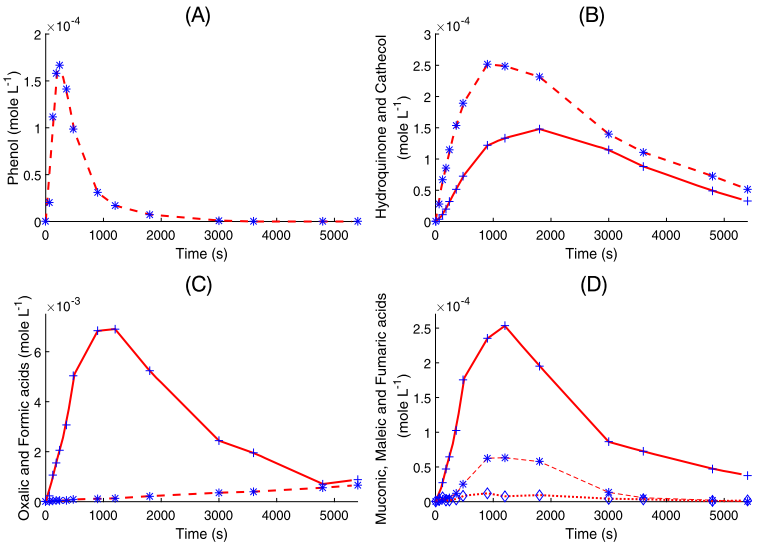

■ **FIGURE 4.18** Experimental concentrations and dynamic reconstruction of byproducts formed during ozonation of 4-chlorophenol at pH $= 7.0$.

accumulated during the first 1000 s, but after that time, it was decomposed during the ozonation (Fig. 4.18C).

4. Muconic, maleic, and fumaric acids have the same accumulation–decomposition dynamics during ozonation. Only fumaric acid was not completely decomposed after 5400 s (Fig. 4.18D).

In the case of ozonation of 4-CPh at pH $= 12.0$, the ozonogram shows the ozone concentration to be close to zero during the reaction interval 200–500 s (Fig. 4.19A). This effect corresponds to the ozone consumption by its reaction with the hydroxyl ions, because the pH was 12. The 4-CPh is decomposed during the first 500 s, which corresponds to the time when the ozone concentration c_g increases its value (Fig. 4.19B).

The byproduct concentrations observed in this case have different behaviors from those observed in previous sections.

1. Phenol accumulation was not detected; however, its decomposition was completed after 400 s only (Fig. 4.20A).

2. Hydroquinone was formed and decomposed within the first 100 s. This result is a consequence of the fast decomposition of ozone by the combined effect of molecular ozone and hydroxyl radicals (Fig. 4.20B).

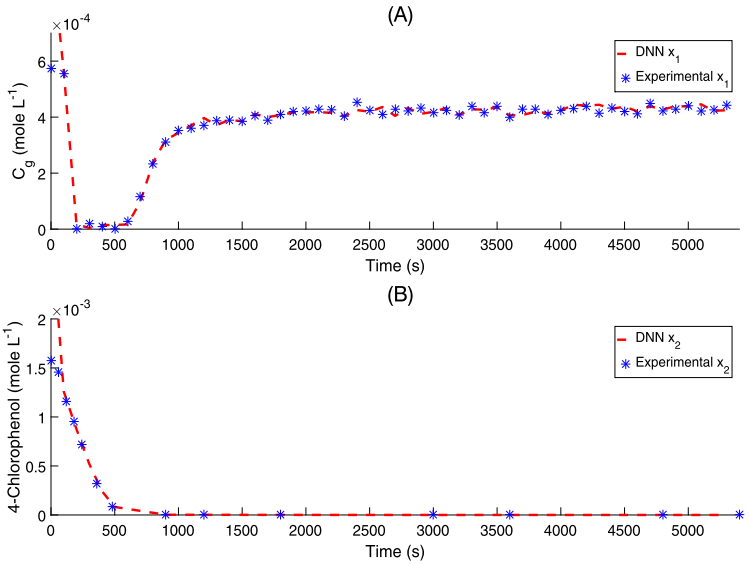

■ **FIGURE 4.19** Estimation of ozone concentration c_g in the gaseous phase (A) and 4-chlorophenol concentration c_1 (B) when pH $= 12.0$.

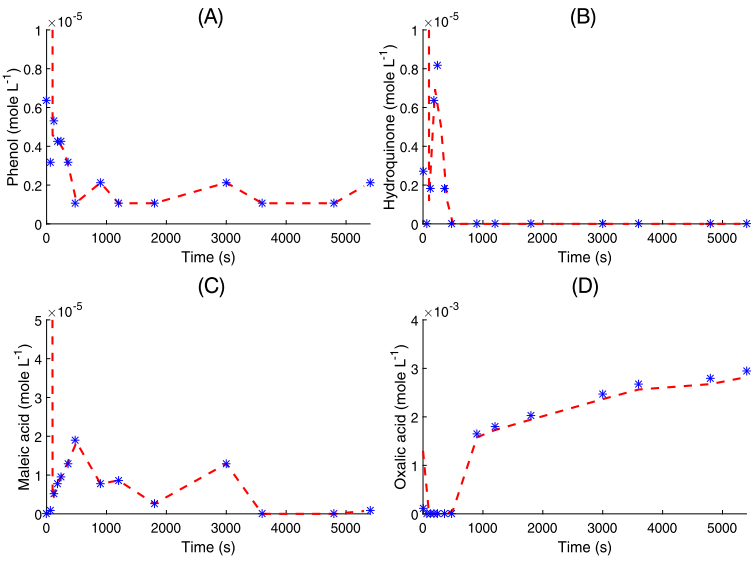

■ **FIGURE 4.20** Experimental concentrations and dynamic reconstruction of byproducts formed during ozonation of 4-chlorophenol at pH $= 12.0$.

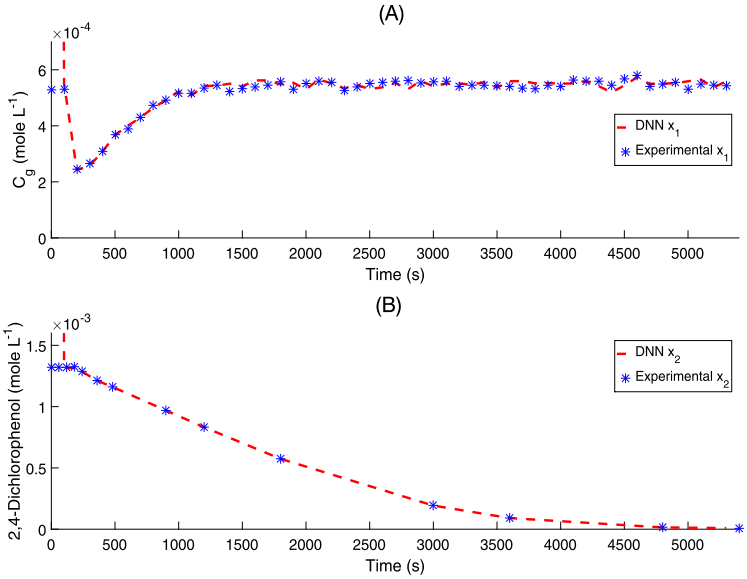

■ **FIGURE 4.21** Estimation of ozone concentration c_g in the gaseous phase (A) and 2,4-dichlorophenol concentration c_1 (B) when pH = 2.0.

3. Maleic acid was the only intermediate acid detected in this ozonation (Fig. 4.20C).

4. Oxalic acid started to be accumulated just after 700 s, which corresponds to the time when the maleic acid was being decomposed.

4.6.2.3 Reconstruction of 2,4-dichlorophenol and byproducts

The ozonation of 2,4-DCPh was treated also at four different pH values: 2, 7, 9, and 12 (Figs. 4.21–4.26). As above, at pH = 2.0 and 7 the DNNO was trained based on the ozonogram and the 2,4-DCPh decomposition (Figs. 4.21A, 4.23A, and 4.25A). In these cases, the 4-CPh and phenol formation as products of the 2,4-DCPh dechlorination is observed too (Figs. 4.22A, 4.24A, and 4.26A). Furthermore, similar intermediates and oxalic acid as final product are formed (Figs. 4.22D, 4.24D, and 4.26D). The pH increase has a significant effect on the 2,4-DCPh decomposition:

1. The decomposition time reduced from 4700 s at pH = 2.0 up to 500 s at pH = 12.0 (Figs. 4.21A, 4.23A, and 4.25A).

2. The concentration of all byproducts was reduced. Thus, the hydroquinone content decreases from 10^{-4} up to 10^{-6} mol L^{-1} (Figs. 4.22B, 4.24B and 4.26B).

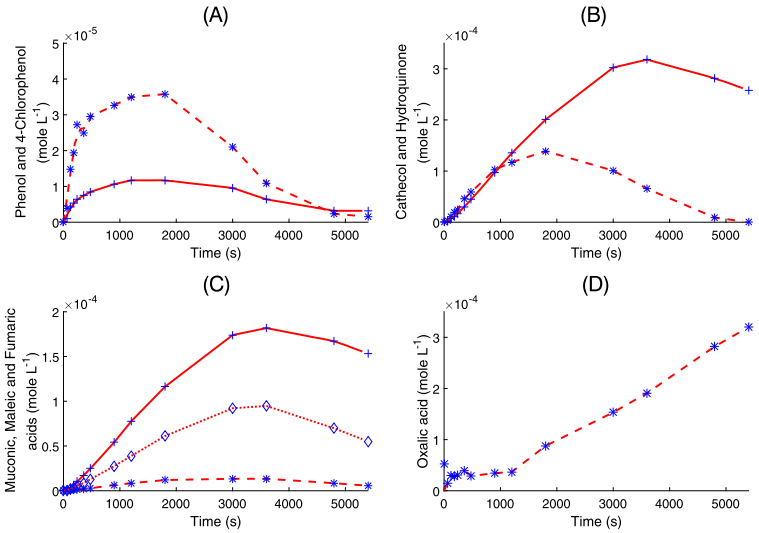

■ **FIGURE 4.22** Experimental concentrations and dynamic reconstruction of byproducts formed during ozonation of 2,4-dichlorophenol at pH $= 2.0$.

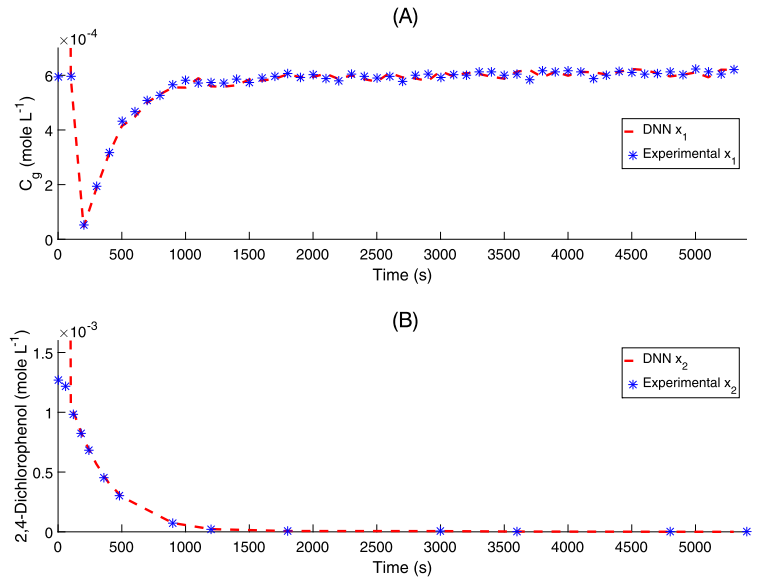

■ **FIGURE 4.23** Estimation of ozone concentration c_g in the gaseous phase (A) and 2,4-dichlorophenol concentration c_1 (B) when pH $= 7.0$.

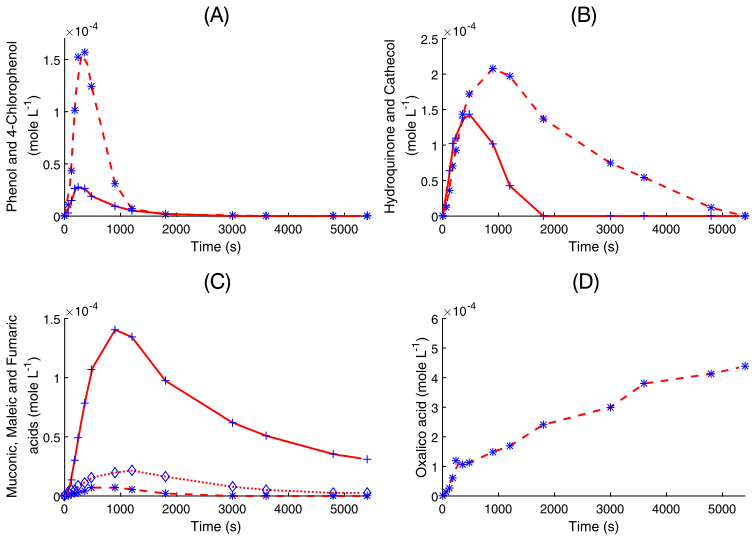

■ **FIGURE 4.24** Experimental concentrations and dynamic reconstruction of byproducts formed during ozonation of 2,4-dichlorophenol at pH $= 7.0$.

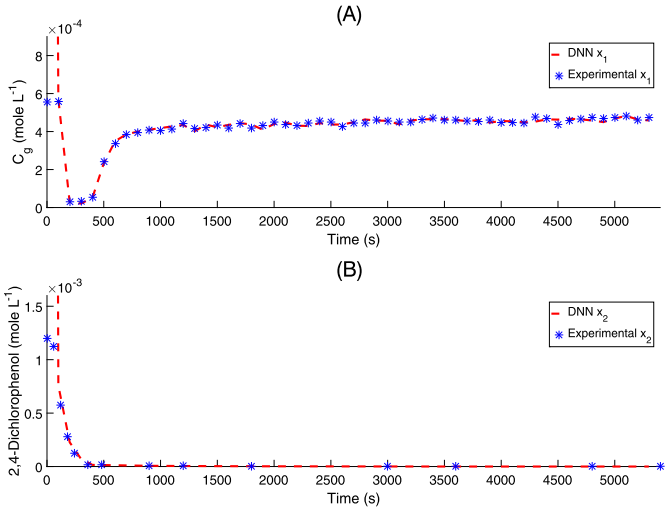

■ **FIGURE 4.25** Estimation of ozone concentration c_g in the gaseous phase (A) and 2,4-dichlorophenol concentration c_1 (B) when pH $= 12.0$.

3. The oxalic acid increased the concentration in 5 times compared with ozonation at pH $= 7.0$ (Figs. 4.22D, 4.24D, and 4.26D).

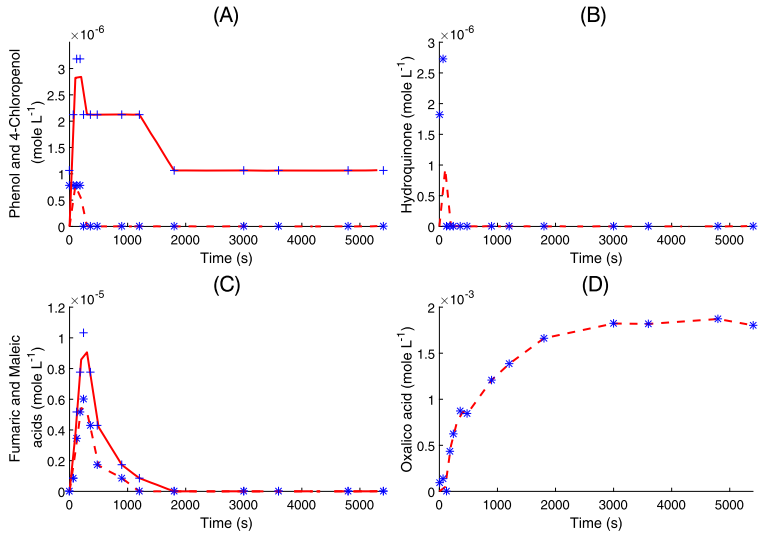

■ **FIGURE 4.26** Experimental concentrations and dynamic reconstruction of byproducts formed during ozonation of 2,4-dichlorophenol at pH $= 12.0$.

All these results show that the proposed DNNO technique is extremely promising for the reconstruction of the phenols ozonation, as well as for the formation and decomposition of byproducts and the final product accumulation.

4.7 LIMITS OF THE PROPOSED RECONSTRUCTION METHOD

It should be emphasized that the estimation method cannot reproduce any dynamics that has not been considered during the training process, because the DNN state has its own constant order, i.e., the number of states involved in the observer description remains constant during the ozonation reaction.

Based on the results described above, we may conclude that:

1. The DNNO approach shows good phenol decomposition dynamics estimation (the reconstruction), byproduct accumulation, and decomposition, as well as the final compound accumulation with the DNNO training based on the experimental data.

2. The phenol ozonation at different pH values has been applied to a demonstration of the robust behavior (robust with respect to different experimental conditions) of the suggested DNNO provided by the new learning laws, which includes the correction (discontinuous) terms.

3. The behavior of byproducts and final compounds, predicted by DNNO, shows a good enough correspondence with experimental data.

4. The effect of the pH increase from 2 to 12 on the decomposition of Ph, 4-CPh, 2,4-DCPh is very significant and reduces the total decomposition time by a factor 10 (from 5000 s to 500 s).

5. The presence of chlorine in the molecule of chlorophenol also reduces the degradation time by ozonation.

4.8 CONCLUSIONS

The contribution of this chapter is the DNNO application to obtain both the numerical and the experimental reconstruction of phenols decomposition, and their intermediates, as well as accumulated products. The DNNO developed here was successfully applied to obtain the state variation of the unmeasurable compound in ozonation at different pH values (2, 7, and 12). The ozone concentration variation in the reactor output is the output information used to tune the observer dynamics. As a result, the validity of the DNNO technique is demonstrated by the good agreement of the predicted results with the experimental data. The DNNO proposed in this chapter is the fundamental basis of the solutions presented in the following chapters.

Part 2

Ozonation as a Principal Treatment Method for Organic Contaminants Elimination in Liquid Phase

Chapter 5

Catalytic ozonation

CONTENTS

Ozonation and Biodegradation in Environmental Engineering
https://doi.org/10.1016/B978-0-12-812847-3.00015-9

ABSTRACT
This chapter demonstrates the application of the different Activated Carbons (ACs) and the nickel oxide (NiO) as catalyst in ozonation. Catalytic ozonation with three diverse ACs was evaluated in the decomposition of three PHAs (anthacene, fluorene, and phenanthrene). The kinetics of catalytic ozonation in the presence of AC was studied. The catalytic ozonation in the presence of NiO was evaluated in the degradation of benzoic and phthalic acids, where the effect of the number of carboxalic groups on the degradation efficiency was proven. The feasibility of combining conventional and catalytic ozonations was evaluated in the degradation of phenol (PH), 4-phenolsulfonic (4-PSA) and 2-naphtalenesulphonic acids (2-NSA) with NiO. The effect of ethanol as cosolvent in the ozonation of naphthalene and naproxen in the presence of NiO was investigated. Also, a novel mathematical model describing the effect of the catalyst in ozonation is discussed in detail. Two variants of the DNNO design are compared: the first one uses linear learning laws that ensure asymptotic zone-convergence of the estimation error, while the second implements normalized learning laws.

5.1 CATALYTIC OZONATION IN THE WATER TREATMENT AIMED AT REMOVING RECALCITRANT CONTAMINANTS

As is well known, the direct ozonation by the molecular ozone is selective, since the rate of its reaction depends on the chemical structure of the organic compound. The advanced oxidation processes (AOPs) are applied to produce the hydroxyl radicals ($^{\cdot}OH$), which are not selective and have a reaction rate with organic compounds higher than molecular ozone. To augment the efficiency of the conventional ozonation in the decomposition of organic contaminants with a low reactivity with the molecular ozone (so-called recalcitrant compounds), ozonation in the presence of a catalyst (catalytic ozonation) is applied. Catalytic ozonation may be realized in homogeneous and heterogeneous systems. We will discuss only the heterogeneous systems with an activated carbon and metal oxides.

Ozonation in the presence of the activated carbon (AC) causes a great deal of interest as a novel process, which has been successfully used for the elimination of organic compounds in water (de Oliveira et al., 2011), (Kurniawan

Table 5.1 Basic characteristics of ACs: MCP = Micropol, AS = Aqueous solution.

AC	pH of AS	Surface area [$m^2\ g^{-1}$]	Pore volume [$cm^3\ g^{-1}$]	pH_{zcp}
MCP9LS	3.5–5.0	900	0.80	3
MCP9LSN	6.0–8.0	900	0.80	8
MCP9	8.8–10.0	900	0.80	9

et al., 2006). The O_3/AC (named carbozone) combination was firstly studied by Jans and Hoigné (1998), who introduced the term *carbozone process* to define the coupling of ozone and the AC as a new type of the AOPs. This process includes different steps: direct or indirect ozonation on a liquid phase, the adsorption on the AC surface, and direct or indirect oxidation of compounds on the catalyst surface. Moreover, the interactions between O_3 and the functional groups on the AC surface can lead to the generation of the hydroxyl radical ($^{\cdot}OH$). These radicals are highly reactive, in comparison with molecular ozone, they are not selective and can decompose into a wide range of organic pollutants in water.

5.2 OZONE DECOMPOSITION IN WATER IN THE PRESENCE OF AC

To study the ozone decomposition in water in the presence of the AC, three types of AC were selected, such as *Micropol9LS*, *Micropol9LSN*, and *Micropol9*, which have the same specific surface area, 900 $m^2\ g^{-1}$, but a different zero charge point (pH_{zcp}). Table 5.1 contains the basic characteristics of the ACs studied.

One of the factors having an effect on the O_3–AC process is the pH of the solution, which is directly linked with the ozone decomposition efficiency. Some researchers proposed two mechanisms to explain the ozone decomposition in the presence of the AC: homogeneous and heterogeneous surface reactions (Beltrán et al., 2002c). In both cases, the ozone decomposition efficiency was found to be a function of the pH.

On the generation of $^{\cdot}OH$, the influencing AC characteristics are the superficial area, the diameter of the pores, microporosity, structure, functional groups in its surface, the isoelectric point, and besides the pH of the solution, the ozone concentration, the gas flow, and the AC concentration (de Oliveira et al., 2011), (Liu et al., 2009). Fig. 5.1 presents the behavior of the ozone decomposition degree depending on the activated carbon concentration.

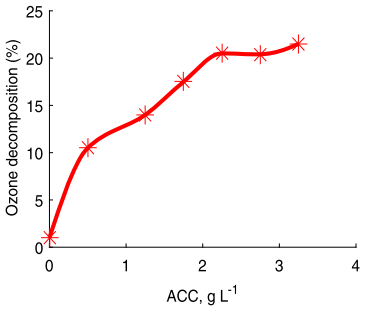

■ **FIGURE 5.1** Ozone decomposition degree depending on the activated carbon concentration.

As one may notice, if the concentration of Micropol9LSN and Micropol9 increases, the degree of the ozone decomposition also increases (reaching a maximum of 15% and 16%, respectively). This is due to the basic pH_{zcp} of these ACs, which implies the presence of the surface groups, such as chromene and pyrona. The latter favors the decomposition of ozone. On the other hand, at a concentration of Micropol9LS greater than 2 g L^{-1} the ozone decomposition decreases (reaching 12%), most probably due to the excess of the oxygen groups that subtract the electrons from the aromatic rings, causing a smaller adsorption of ozone on its surface.

Fig. 5.2 shows the effect of the initial ozone concentration on the ozone decomposition.

The degree of ozone decomposition at the ozone concentration of 39.9 mg L^{-1} is almost the same that at 78.4 mg L^{-1} (25 vs. 29%). However, the amount of the dissolved ozone is different. With an ozone concentration of 39.9 mg L^{-1} in the gaseous phase, 0.9 mg of ozone in the aqueous phase decomposed, whereas in the case of 78.4 mg L^{-1} there is a decomposition of 1.76 mg of dissolved ozone. Therefore, we may conclude that the increment of the initial ozone concentration in the gas phase has a positive effect on the production of OH radicals. Fig. 5.3 shows the influence of the gas flow on the ozone decomposition degree.

The observed effect can be explained by the augment by a factor of five of the contact time of ozone and the AC at the *flow* of 0.1 L min^{-1}. The ozone decomposition increases to 25–27% in the presence of three ACs. On the other hand, under a flow of 0.5 L min^{-1}, the ozone decomposition degree decreases to 10–13%, and there is observed a tendency that it decreases with the increase of the pH_{zcp} of the AC. This phenomenon is a consequence of the relation of the pH of the solution and the pH_{zcp} of the AC, which leads to a positive or negative surface electric charge. Table 5.2 presents the values of the initial pH of a solution and the pH_{zcp} of three ACs.

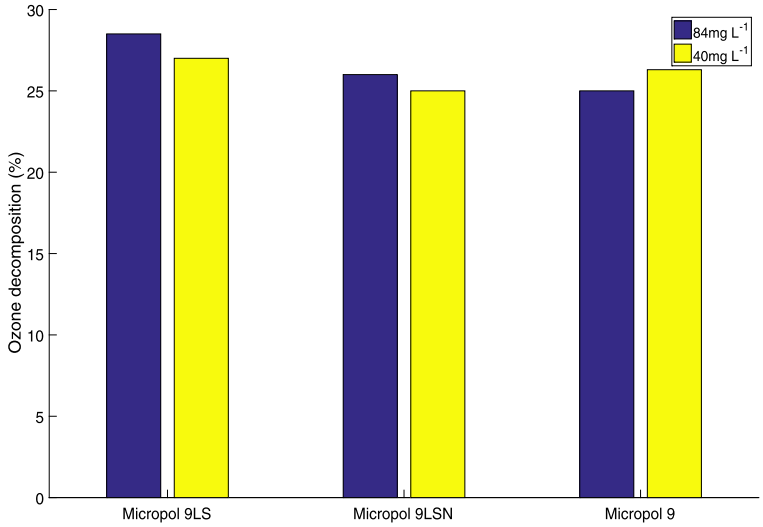

■ **FIGURE 5.2** Effect of the initial ozone concentration on the ozone decomposition degree in water in the presence of the AC ($1\ g\ L^{-1}$).

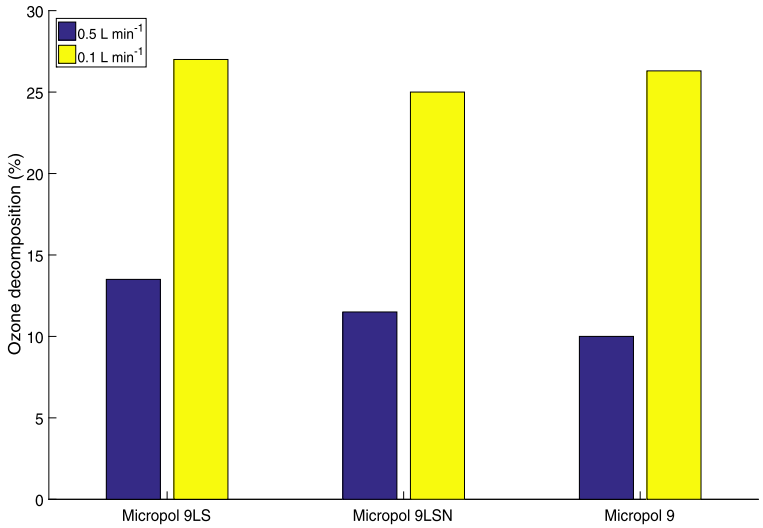

■ **FIGURE 5.3** Effect of the gas flow on the ozone decomposition in the presence of the AC ($1\ g\ L^{-1}$).

As can be seen from the data presented in Table 5.2, the Micropol9LS has also acidic surface properties, but due to the initial pH it acquires a negative surface charge. This fact provokes a slightly higher degree of ozone decomposition than the other two coals, which may be due to the distri-

Table 5.2 Initial pH of a solution and pH_{zcp} of three ACs.

AC	Initial pH	pH_{zcp}	Surface charge	Final pH
Micropol9LS	5.45	3	Negative	3.5–5.0
Micropol9LSN	5.45	8	Positive	6.0–8.0
Micropol9	5.45	9	Positive	8.8–10

Table 5.3 Surface charges of three ACs acquired under different pH values of the solution.

AC	Initial pH	pH_{zcp}	Surface charge
Micropol9LS	2.17	3	Positive
Micropol9LSN	2.17	8	Positive
Micropol9	2.17	9	Positive
Micropol9LS	6.58	3	Negative
Micropol9LSN	6.58	8	Positive
Micropol9	6.58	9	Positive
Micropol9LS	9.41	3	Negative
Micropol9LSN	9.41	8	Negative
Micropol9	9.41	9	Negative

bution of the functional groups on its surface. The last coincides with the published hypotheses regarding the total contribution of acidic and basic groups on the AC surface (Chairez, 2013). It would be expected that the Micropol9LSN and the Micropol9 showed better performance due to their basic surface properties and to the positive surface charge. It is possible that the competition between the two effects produces an opportunity to augment the ozone decomposition. Therefore, it would be interesting to study the effect of the pH of the solution on the surface properties of the AC (Table 5.3) and the ozone decomposition (Fig. 5.4). In the same figure, notice that at acidic pH, the ozone decomposition degree is found to be between 8 and 13%. The Micropol9LS ($pH_{zcp} = 3$) and the Micropol9 ($pH_{zcp} = 9$) increase the degree of the ozone decomposition as the pH increases, whereas the Micropol9LSN ($pH_{zcp} = 8$) decreases its decomposition. As a summary, in the presence of the AC the pH of the solution has a very important effect on the ozone decomposition, because, depending on this parameter, the carbon surface is negatively or positively charged. Table 5.3 presents the surface charges of three ACs acquired under various pH values of the solution.

This phenomenon is well known, and it must be taken into account to correctly select the AC for the catalytic ozonation (Li et al., 2000; Lin and Lee, 1991; Wang and Mendel, 1992).

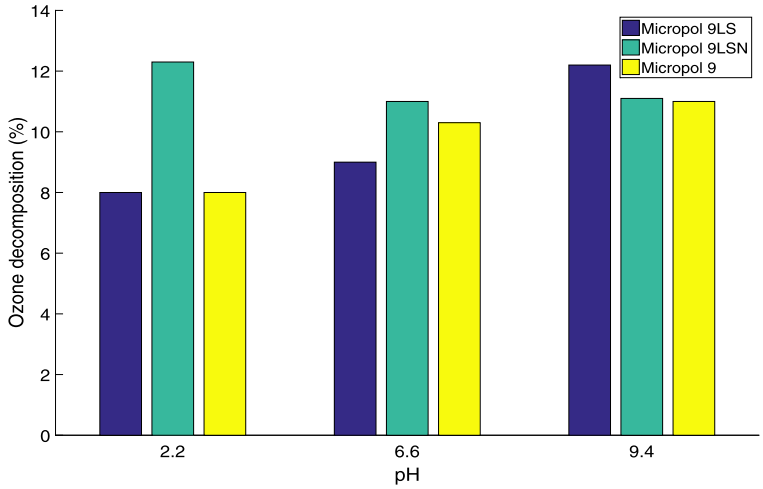

■ **FIGURE 5.4** Effect of the pH on the decomposition degree of ozone under the AC concentration of 1.5 g L^{-1}.

5.3 CATALYTIC OZONATION WITH ACTIVATED CARBON FOR THE PAHS DECOMPOSITION IN WATER IN THE PRESENCE OF METHANOL

Polynuclear aromatic hydrocarbons (PAHs) are the group of compounds composed of two or more fused aromatic rings, which are lipophilic organic compounds of high chemical stability. The major source of PAHs is the incomplete combustion of carbon-containing fuels, such as coal, oil, wood, and tobacco. Other sources of PAHs are the pyrolysis of petroleum products, acetylene synthesis from natural gas, refinery operations, and the transportation of oil products (Sanches et al., 2011). Several studies confirm that PAHs represent a real threat to human health, because they are toxic and many of them are carcinogenic (Cachada et al., 2012), (Farmer et al., 2003). Their assimilation and possible transformation increase once they enter the human body. The PAHs are well-known hazardous and environmental persistent pollutants, which can be found in air, natural water systems, marine sediments and foods (de Bruyn et al., 2012), (Shemer and Linden, 2007), (Mottier et al., 2000). Therefore, they are listed as priority contaminants by the European Union and the US Environmental Protection Agency (U. D. of Health, H. Services, et al., 1995). Environment regulations in different countries have established diverse limits for the maximum allowed concentration of these compounds in water. The limit PAHs concentration in water, recommended by the WHO (World Health Organization), is fixed at 0.2 μg L^{-1} (Sayre, 1988). A more restrictive condition, introduced by the WHO for drinking water, is 0.025 μg L^{-1} as the permissible amount

of PAHs, because their carcinogenic activity has been observed already at this concentration (Andelman and Suess, 1970). A number of investigations have reported that the PAH concentration in the surface waters varies from 1.0 ng L^{-1} to 72.4 μg L^{-1} (W. H. Organization, 2004), (Zhang et al., 2004). This large variation in the PAHs concentration requires an effective treatment to reduce their toxicity. However, solubility of the PAHs in water at 20–25°C is really small. For example, it is 0.0434 mg L^{-1} for anthracene, 1.29 mg L^{-1} for phenanthrene, and 1.98 mg L^{-1} for fluorene (Andelman and Suess, 1970). In an aquatic environment, they are commonly found adsorbed on the suspended and particulate materials, as well as in sediments. On the other hand, a lot of publications concerning the decomposition of PAHs have appeared: photolysis (Sanches et al., 2011), ozonation (Trapido et al., 1995), (Beltran et al., 1995), sono-chemical (Taylor et al., 1999), Fenton oxidation (Beltrán et al., 1998), photocatalysis (Minero et al., 2000), and biological degradation. The last process depends on various experimental conditions, such as the chemical structure of the compounds, pH, temperature, oxygen concentration, the number and type of the microorganisms (microbial consortium), acclimation, accessibility of nutrients, cellular transport properties, and the toxicity of PAHs (Haritash and Kaushik, 2009). Therefore, it is difficult to apply biological processes to the removal of PAHs in water.

The chemical oxidation seems to be especially advisable for the treatment of water contaminated with PAHs. In particular, ozonation was extensively used to eliminate complex and very toxic organics by the decomposition of the recalcitrant compounds into non-toxic substances, which can be more effectively removed by conventional methods (Kornmüller and Wiesmann, 1999), (Rivera-Utrilla et al., 2006). Some researchers demonstrated that ozonation is a feasible alternative to degrade the PAHs in water (Trapido et al., 1995). Nowadays, new methods (basically a combination of oxidation processes) have been proposed to increase the efficiency of their degradation (Andreozzi et al., 1999).

The O_3–AC combination includes different steps: direct or indirect ozonation in water, adsorption on the AC and direct or indirect oxidation of compounds on the AC surface. Moreover, interaction between O_3 and AC surface groups can lead to $^{\cdot}OH$ generation. This combination of ozonation with AC shows good results due to the reduction of the reaction time and the ozone consumption, as well as to the increment of the decomposition efficiency (Faria et al., 2008a,b), (Beltrán et al., 2009). Nevertheless, these effects are strongly dependent on the selected operating conditions.

In particular, in this book, the catalytic ozonation of three PAHs (fluorene, anthracene, and phenanthrene) was carried out with the AC (Darco-

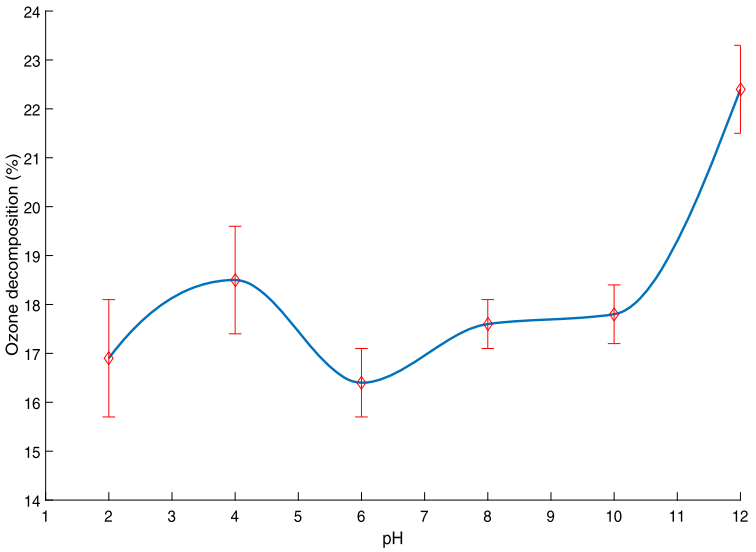

■ **FIGURE 5.5** Effect of the pH on the ozone decomposition degree in the presence of the AC (1.57 g L^{-1}).

G60, particle size of 149 μm, BET-area of 707 m^2 g^{-1}, pore volume of 0.95 cm^3 g^{-1}, $pH_{zcp} = 8.5$) to study the effect of the pH on the PAH decomposition in the presence of methanol. A mixture of water and methanol is proposed to realize by the modeling of possible natural situations, when more than one organic contaminant is in the water. The alcohol concentration in water was constant, 16% v/v. At this concentration, methanol may serve also as a cosolvent, which leads to an increment of the PAH solubility in water up to 35 mg L^{-1} for anthracene and fluorene and 50 mg L^{-1} for phenanthrene. This factor is very important for the evaluation of the real concentration of the PAHs in the water, and therefore must be taken into account for choosing experimental conditions of ozonation. The experimental conditions were as follows: the initial ozone concentration was 30 mg L^{-1} with the ozone–oxygen mixture flow of 0.5 L min^{-1}. The initial pH was reached by sulfuric acid and sodium hydroxide (0.1N). The initial concentration of all PAHs was 20 mg L^{-1}. The ozonation of anthracene, phenanthrene, and fluorene was carried out in synthetic solutions of distilled water and methanol (84:16). The AC was dried at the temperature 100–120°C during 24 h to completely remove the moisture.

To minimize the PAH adsorption on the AC, a minimum concentration of activated carbon of 1.57 g L^{-1} was selected. This AC concentration provides the maximum self-decomposition of ozone (22%). Fig. 5.5 shows the effect of the pH on the ozone decomposition in the presence of the AC (1.57 g L^{-1}).

Table 5.4 Content of the PAHs in water and on the AC surface after ozonation.

PAHs	In water	On the AC surface
Anthracene, mg (%)	0.35(99.94)	$0.21 \cdot 10^3$(0.06)
Fluorene, mg (%)	0.57(99.30)	$4.0 \cdot 10^3$(0.7)
Phenanthrene, mg (%)	1.33(99.81)	$2.4 \cdot 10^3$(0.19)

In Fig. 5.5, two phenomena can be noticed:

- First, the ozone decomposes at acidic pH (2–6), which confirms the catalytic effect of the AC, since without the AC the ozone decomposition realized only under a basic pH of the solution (> 7).
- Second, the pH of the solution has a significant effect on the decomposition of ozone in the presence of the AC, because the AC has an amphoteric nature. Its surface could be positively or negatively charged depending on the pH of the solution (Faria et al., 2006), and thereby may increase or decrease the attraction of the hydroxyl ions on the AC surface.

According to Beltrán et al. (2002b); Guiza et al. (2004), the decomposition mechanism of ozone in the presence of AC is governed by the pH of a solution, since it depends on the type of attack involved in the AC. Despite the very low constant of the reaction rate between ozone and methanol ($k = 0.02\ M^{-1}\ s^{-1}$), but considering that the concentration of methanol is high, the consumption of molecular ozone is significant in this reaction. This leads to an alcohol decomposition of 23% at the pH = 10, which slightly increases up to 26% in the presence of activated carbon (AC), which confirms its catalytic effect too.

5.3.1 Effect of the pH and AC on the decomposition of the PAHs in the presence of methanol

The adsorption capacity of AC plays an important role in the interaction of ozone with organics, because some organic compounds can remain on the AC surface during the ozonation. However, this is not the case with methanol, because the adsorption isotherms confirm that methanol was not adsorbed on the AC during 60 min (results not shown). This excludes the influence of alcohol on the catalytic capacity of the AC in ozonation.

To distinguish the catalytic effect of the AC and the adsorption on its surface in ozonation, the extraction of PAHs and the decomposition products were got from water and from the AC surface after 1 h of ozonation. The content of the PAH in the water and on the AC surface is presented in Table 5.4.

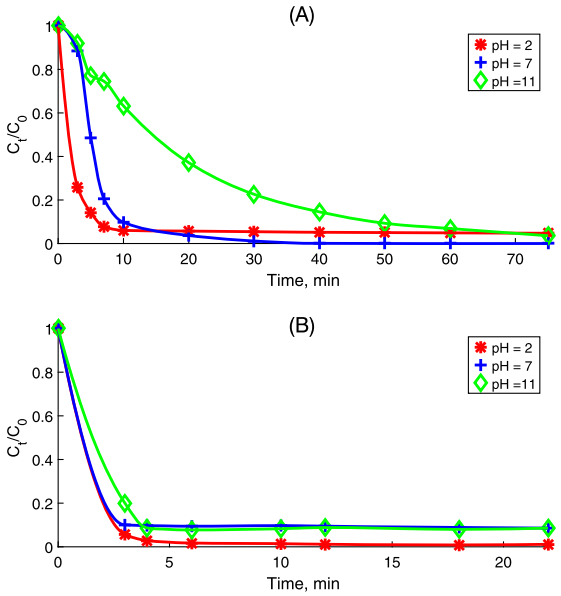

■ **FIGURE 5.6** Anthracene decomposition at various pH values in the absence (A) and in the presence of the AC (B).

Based on the data obtained, we may claim that the adsorption effect of the AC under these experimental conditions is insignificant ($< 1.0\%$), and, in this case, the ozonation of PAHs is mainly realized in liquid phase.

5.3.1.1 Anthracene decomposition

Fig. 5.6 presents the effect of the pH and the AC on the anthracene decomposition. The fast decomposition of anthracene to 99% is achieved after 20 min at the initial pH values of 2 and 6.8 without the significant difference between the reaction rate in the acidic and neutral media in the absence of the activated carbon (Fig. 5.6A). In this particular case, the direct mechanism of the reaction with the molecular ozone is predominant. At a pH of 11.91 the anthracene decomposition is achieved after 75 min. This particular effect is observed because of the interaction of ozone with hydroxide ions and methanol. In this case, there is competition between the two reactions, which reduces the rate of the anthracene decomposition.

Fig. 5.6B depicts the decomposition of anthracene in the presence of the AC. The reaction rate increases independently of the pH. Indeed, the anthracene decomposition is achieved after 6 min at the acidic and neutral pH values, to be compared to pH = 11.1, when the decomposition finishes after 10 min. So, the decomposition time decreases from 20 min to 6 min at the acidic and

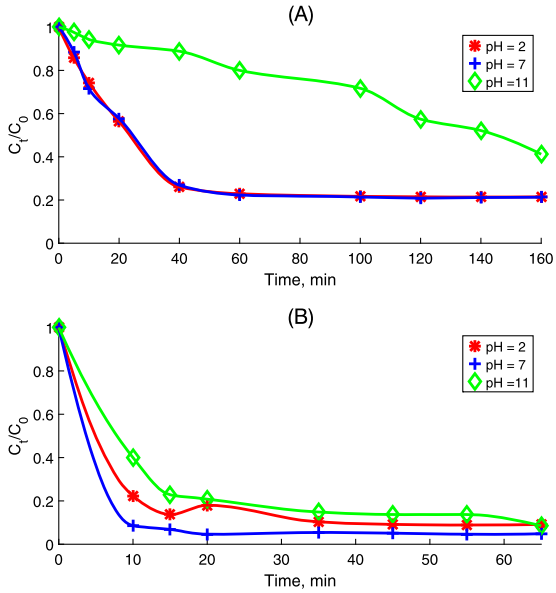

■ **FIGURE 5.7** Fluorene decomposition at various pH values in the absence (A) and in the presence of the AC (B).

neutral pH values, and from 75 min to 10 min at the basic pH. In summary, we may confirm the AC catalytic effect in the ozonation of anthracene at various pH values. The reaction rate is faster at pH = 2.0 and 6.8 (with and without AC) to be compared to the value obtained at pH = 11.1. However, the maximal effect of activated carbon on the anthracene decomposition is observed at the basic pH.

5.3.1.2 Fluorene decomposition

In the case of the fluorene ozonation, a similar tendency is observed, namely, the decomposition is the same, 80%, at the pH values of 2.57 and 6.97 during 110 min; however, at the basic pH the decomposition efficiency is only 45% during 160 min (Fig. 5.7A, B).

Similar to the previous case, the direct reaction with the molecular ozone is predominant. This effect is different from the anthracene case: at pH = 11.25 the fluorene does not decompose totally within the observed time by the combination of the direct and the indirect mechanisms of ozonation. The difference between fluorene and anthracene is due to their chemical structures; the reaction rate constant of ozone with fluorene is less than with anthracene ($0.8 \cdot 10^2$, contrasting with $2.4 \cdot 10^3$ M^{-1} s^{-1}).

In the presence of the AC a significant positive effect is observed at three pH values. Indeed, the decomposition time decreases up to 20 min on av-

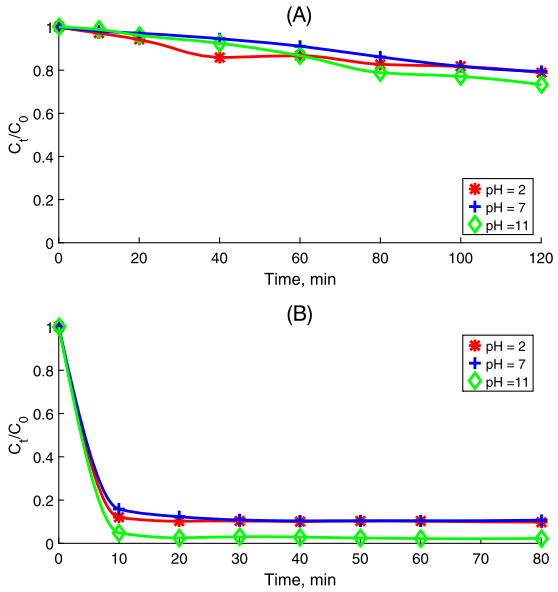

■ **FIGURE 5.8** Phenanthrene decomposition at various pH values without the AC (A) and in its presence (B).

erage with the very good efficacy of the organic degradation up to 85–90% (Fig. 5.7B), which confirms the catalytic effect of the AC.

5.3.1.3 Phenanthrene decomposition

The ozonation of phenanthrene is different from the cases represented above. In the absence of the AC, the pH has not at all had effect on the decomposition dynamics of this compound (Fig. 5.8A, B).

Notice that no more than 20% of the phenanthrene decomposition is obtained after 120 min of ozonation at three pH values (2.52, 7.64, and 11.65). This compound is more resistant to ozone and OH radicals, which is the reason of the non-efficacy of its elimination. It seems feasible that in this case, the steric effect of the phenanthrene molecule is observed, which is different from the anthracene molecule by its spatial configuration. In the presence of the AC, the decomposition time is reduced significantly (Fig. 5.8B). At the pH values of 3 and 7, 85% of phenanthrene is decomposed after 5 min of ozonation, and at a pH of 11 for 10 min reaches 98% of the decomposition. In this case, the AC catalytic effect is very significant.

Several byproducts (about 11) are formed in the ozonation of the three studied compounds with and without the AC at the various pH values. However, in all experiments only three organics were identified, which are the

final products of ozonation, such as phthalic acid (PA) and (9,10-A) or 9, 10-phenanthroquinone (9,10-P), depending on the initial PAH. The rest of all intermediates, disappearing during the ozonation, or considering their final concentration, was not significant with respect to the pair of main final products. In general, the AC reduced the intermediate concentration to traces (less than 1 mg L^{-1}).

5.3.2 Estimation of the reaction rate constants

The kinetics of the ozonation of the PAHs was studied by several researchers (Alvarez et al., 2006; Beltrán et al., 2002c; de Oliveira et al., 2011; Dehouli et al., 2010), where the values of the bimolecular reaction rate constants were reported to range from 10^3 to 10^4 L mol^{-1} s^{-1}. In this chapter the reaction rate constants are estimated by differential neural networks (DNNs) using the variation of the ozone concentration in the gas phase and the PAH decomposition obtained by the HPLC. From the previous investigations (Poznyak et al., 2004; Poznyak and Chairez, 2011; Poznyak et al., 2005) it follows that the DNN can be used to estimate the rate constants of the PAH ozonation described by Eq. (2.15). The numerical values of the ozonation rate constants of three PAHs (anthracene, fluorene, and phenanthrene) at various pH values are presented in Table 5.5. As we may observe, with the increase of the pH, the reaction rate constants decrease. In Table 5.5, also the values are included of the ozonation rate constants obtained by some other authors (Beltran et al., 1995; Trapido et al., 1994, 1995), and their comparison demonstrates a good correspondence between constants obtained at similar pH values. Besides, the calculated values of the rate constants correspond to the experimental ozonation dynamics in the absence of the AC (Fig. 5.6A–5.8A). The equation used to define the pseudo-first order reaction is

$$\frac{d}{dt}c_i\,(t) = -k_{ps,i}c_i\,(t)\,,$$

where c_i, is the current concentration of the i-th contaminant [mol L^{-1}] and $k_{ps,i}$, is the pseudo-first order reaction constant for the i-th contaminant [s^{-1}]. The constants $k_{ps,i}$ can be estimated as presented in Chapter 2 (2.25).

Table 5.6 presents the value of the ozonation constants of the pseudo-first order of three PAHs (c_i, $i = 1, 2, 3$) in the presence of the activated carbon.

Based on the results obtained for the system O_3/AC for the PAH decomposition, we may conclude that:

1. The presence of the high concentration of methanol in water (16% v/v) leads to ozone consumption in the whole pH range (2–12).

Table 5.5 Ozonation rate constants of anthracene, phenanthrene, and fluorene at different pH values.

Compound	k_i [L mol^{-1} s^{-1}]		
	pH		
	2.0	7.0	12.0
Anthracene	$3.9 \cdot 10^4$ ($2.55 \cdot 10^4$)[a]	$7.2 \cdot 10^3$ ($2.7 \cdot 10^4$)[a]	$2.4 \cdot 10^3$
Phenanthrene	$2.9 \cdot 10^3$ ($5.85 \cdot 10^3$)[a]	$8.3 \cdot 10^2$ ($1.0 \cdot 10^4$)[a] ($2.4 \cdot 10^3$)[b] ($1.57 \cdot 10^4$)[c]	$1.3 \cdot 10^3$
Fluorene	$8.2 \cdot 10^3$ ($2.5 \cdot 10^3$)[a] ($4.50 \cdot 10^4$)[c]	$6.7 \cdot 10^3$ ($4.2 \cdot 10^3$)[a]	$0.8 \cdot 10^2$

[a] *Beltran et al. (1995)*
[b] *Trapido et al. (1994)*
[c] *Trapido et al. (1995)*

Table 5.6 Pseudo-first order reaction constants of PAHs in the presence of the AC.

Compound	$k_{ps,i}$, s^{-1}		
	pH		
	2.0	7.0	12.0
Anthracene	9856.0	9812.2	9925.2
Phenanthrene	12,259.58	12,045.25	12,452.25
Fluorene	504.25	498.56	512.63

2. In conventional ozonation, the chemical structure of the PAHs significantly influences the decomposition kinetics at a pH of 2.0 and 7.0; however, at the pH values of 11.0–12.0 its effect is not so obvious. The order of the PAH decomposition in water at the acidic and neutral pH values is as follows: anthracene > fluorene > phenanthrene.
3. In the absence of activated carbon, the decomposition of the PAHs at the pH of 2 and 7 is faster than at the pH of 12. This indicated that the predominant mechanism of decomposition of the PAHs is with the molecular ozone (direct reaction).
4. The presence of the AC influences positively the decomposition rate of three studied compounds with the significant reduction on the ozonation time of 5–10 min, contrary to 180 min, compared with conventional ozonation. The order of the decomposition of the PAHs in water in the presence of the AC is as follows: anthracene > fluorene = phenanthrene.

5. In the O_3/AC system, the role of AC not only promotes the ozone decomposition, but also the catalytic effect of the decomposition of the PAHs.

5.4 CATALYTIC OZONATION WITH THE METAL OXIDES

Commonly, activated carbons and metal oxides mostly were studied as catalysts used in the heterogeneous catalytic ozonation, for example, the titanium oxide (TiO_2), the supported metals, such as Ni on TiO_2, and unsupported or supported NiO, and other metal oxides. However, a general conclusion, concerning the reactivity of the catalysts or the mechanism of the reaction, is not clear yet. For example, it is well known that noble metals are efficient in the generation of surface carboxylate complexes in ozonation, but a low pH condition is always necessary to achieve a higher degree of contaminant degradation; however, the catalyst effect is observed in the case of the supported metal thanks to the influence of the oxide or oxides of this metal, which formed almost instantly in the oxidation by ozone.

In recent investigations, two reaction mechanisms of the catalytic ozonation were proposed (Rodríguez et al., 2013a). In the first mechanism, organics are adsorbed on the catalyst surface and then they are attacked by ozone or hydroxyl radicals. In the second mechanism, both ozone and organics are adsorbed on the surface of the catalyst and by the redox process forming the organic radicals, which are oxidized by ozone and hydroxyl radicals. However, until now, the mechanism of catalytic ozonation seems not to be clear and it shows a lot of contradictions (Ikhlaq et al., 2015), because the possible mechanisms of reaction are more varied and depend on different factors, such as the solution pH, chemical structure of organic compounds, etc. The literature concerning catalytic ozonation proposed several analytic techniques in order to establish and/or explain its reaction mechanism (Tong et al., 2013). Recently, the Mexican research group has proposed X-ray photoelectron spectroscopy (XPS) as a basic tool to elucidate the reaction mechanism in the catalytic ozonation (Rodríguez et al., 2013b). XPS provides information as regards the presence and the nature of the functional groups on the catalyst surface, as well as regarding the surface properties of the spent catalyst after ozonation of the organic compound. Our previous studies showed that it was possible to degrade the 2,4-dichlorophenoxyacetic acid (2,4-D) by the catalytic ozonation in the presence of the nickel oxide due the formation of the complex of organic compounds with the active sites on the catalyst surface (Rodríguez et al., 2013b). The XPS spectra revealed the presence of two important signals: a nickel-oxalate complex and nickel chlorine (NiCl). This information was used to include these compounds in the reaction pathway. The nickel oxide (NiO) significantly increased the

mineralization degree of 2,4-D during the catalytic ozonation at pH = 3.1, and it also showed a high stability in the presence of ozone (Rodríguez et al., 2013b). In most of the reported studies, the effect of the different reaction parameters on the degradation degree of the different pollutants has been studied (Avramescu et al., 2008; Beltrán et al., 2002a; Xing et al., 2007); however, there is a lack of the investigations concerning the influence of the chemical structure of the organic compounds on the kinetics and the reaction mechanism.

5.4.1 Catalytic ozonation (NiO) of the benzoic and phthalic acids

In general, the catalytic ozonation is considered as a non-selective process; however, the chemical structure of the initial compound is a primordial factor that defines the interactions with the catalyst during ozonation. To study this effect the benzoic and phthalic acids were chosen as the model compounds owing to their chemical structure, which is closely similar (the only difference being the number of carboxyl groups in each molecule). Both compounds are toxic and exhibit low biodegradability (Abdel-Daiem et al., 2012; Velegraki et al., 2011). Benzoic acid (BA) is found in waste water of the pharmaceutical industry (Gandhi et al., 2011; Pariente et al., 2008), and phthalic acid (PA) is used in the painting industries and for the acylation–esterification in dyes. As a consequence, they are detected in different aqueous matrices, for instance: landfill leachates, surface water, sediments, and even in atmospheric aerosols (Magallanes et al., 2015; Wang et al., 2013). With respect to the degradation of benzoic and phthalic acids by catalytic ozonation, studies are scarce.

Some researchers reported the details of the selectivity of the catalytic ozonation of the compounds with a similar chemical structure. Zhang et al. (2012) studied the selectivity of six carboxylic acids (acetic, citric, malonic, oxalic, pyruvic, and succinic acids) that have relatively low reactivity with molecular ozone. Their results clearly showed that these carboxylic acids were not decomposed by the catalytic ozonation in the presence of CuO/CeO. Acetic, malonic, and succinic acids were decomposed less than 20% in comparison with the other acids. The authors employed IR spectroscopy (FTIR) to characterize the surface interaction of six carboxylates, which were found as a part of a metal-carboxylate complex. In this case, the catalytic ozonation of toxic organic acids (BA and PA) in the presence of the NiO catalyst was studied using the FTIR and XPS techniques to analyze the C1s and O1s regions after ozonation that permit one to obtain information as regards the interactions on the NiO surface.

The model solutions of both acids (BA or PA) were prepared with 80 mg L^{-1} of the organic compound (Sigma Aldrich, 99%) and dissolved in distillate water. The initial pH was 3.2 and it was not controlled during the ozonation. All chemicals were of analytical grade. NiO (Sigma-Aldrich, 99%) was used as a catalyst.

The concentration of BA and PA was determined by the HPLC technique, using a Perkin-Elmer Flexar instrument equipped with a DAD detector and a "Prevail Organic Acid" 5 m Grace column. In the case of PA, the mobile phase was acetonitrile and 25 mM KH_2PO_4 buffer, previously adjusted at a pH of 2.6 with H_3PO_4 (60:40 v/v) solution. The flow rate was set to 1 mL min^{-1}. For the BA, the mobile phase was acetonitrile: water (70:30 v/v), and the C18 (Grace) column was used. The external standard method and a KH_2PO_4 buffer mobile phase, at a 210 nm wavelength, were used to identify the products and the byproducts of the BA and the PA degradation. The mineralization degree of the organic acids was monitored using a Torch instrument (Teledyne, Tekmar).

All presented results correspond to the average of the triplicate determinations of each sample. pH_{zcp} was determined by a Malvern Zetasizer at 25°C, and the HCl titration was used to adjust the NaOH values for each sample. The FTIR spectra were obtained by the spectrophotometer LabRna HR800 with a lens with Attenuated Total Reflection (ATR), operating in the infrared middle range, with a diamond crystal tip and a magnification of 36 in a reflection configuration.

The XPS analyses were performed using a ThermoFisher Scientific K-Alpha X-ray photoelectron spectrometer with a monochromatized AlKa X-ray source (1487 eV). The base pressure of the system is 10.9 mbar. Prior to the XPS analysis, all samples were dried at 100°C for 24 h. Then each powder was dispersed and embedded in a 5.5 mm foil, after they had been fixed with Cu double side tape to the sample holder. The position of the C1s peak at 284.5 eV was monitored for each sample to ensure that no binding energy shift had occurred due to charging. Narrow scans were collected at a 60 eV analyzer pass energy and a 400 mm spot size.

5.4.1.1 Simple kinetic model

The proposed kinetic model of the organic acid (OA) decomposition agrees with the pseudo-monomolecular order reaction. This approach does not take into account some aspects of the reaction, however, the complexity of the combination of the parallel and series reactions and the presence of the catalyst limits the application of a more complicated and realistic model, where the accumulation and the degradation of the product are considered. The

modeling strategy considers two different types of reactions: the first one is the decomposition of the initial OA, while the second one describes the accumulation of the main byproduct as oxalic acid (OXA), generated as a consequence of the decomposition of the OA. The first type of reaction is modeled using a decaying exponential function defined as

$$\mathrm{OA}(t) = \mathrm{OA}(0)e^{-kt},$$

where

- $\mathrm{OA}(t)$ is the concentration of OA measured during the reaction (mg L^{-1}),
- $\mathrm{OA}(0)$ is the initial concentration of the same organic acid (mg L^{-1}) and k is the pseudo-monomolecular reaction rate constant (min^{-1}).

For the second reaction, the selected model characterizes the accumulation of the product OXA

$$\mathrm{OXA}(t) = \mathrm{OXA}(t^*)\left(1 - e^{-k_f t}\right),$$

where $\mathrm{OXA}(t)$ is the current concentration of the oxalic acid (mg L^{-1}). The term referred to as $\mathrm{OXA}(t^*)$ is the concentration of the same product at the time t^*, which coincides with the time of the maximum concentration of this organic. The parameter k_f is the accumulation rate constant. Finally, the third type of reaction is modeled using the same decaying exponential function defined as

$$\mathrm{OXA}(t) = \mathrm{OXA}(t^*)e^{-k_d(t^* - t)}.$$

Here $\mathrm{OXA}(t)$ is the concentration of the product to be decomposed, and $\mathrm{OXA}(t^*)$ is the maximum concentration of the oxalic acid. The parameter k_d is the decomposition constant of this product.

5.4.1.2 Degradation and mineralization of the benzoic acid and the phthalic acid by the conventional and catalytic ozonation

Fig. 5.9 shows the degradation profiles of both aromatic organic acids (BA and PA) by the direct reaction with molecular ozone, as well as in the presence of the catalyst. In the first case (Fig. 5.9A), it is clearly noticed that the degradation rate of benzoic acid is higher than obtained for the phthalic acid, since 50% of the BA degradation is reached after 3.5 min, while the PA degradation requires twice that time. These results indicate that the benzoic acid is easily degraded by ozone, which agrees with the value of the reaction rate constant of $k = 1.2\ \mathrm{M}^{-1}\ \mathrm{s}^{-1}$, reported by Neta et al. (1988).

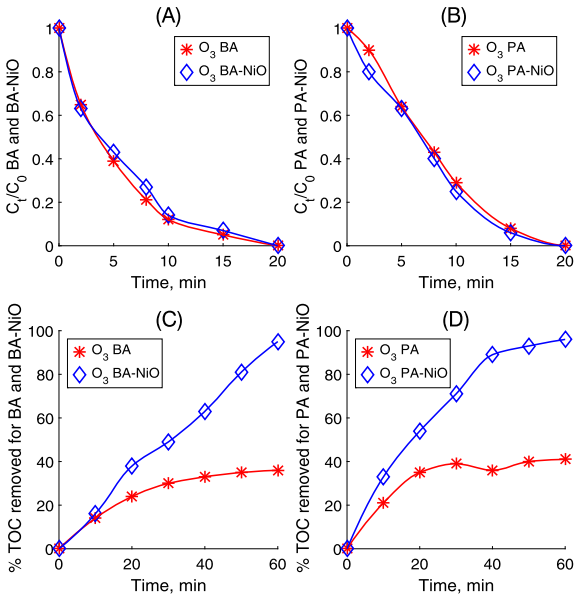

■ **FIGURE 5.9** Removal of the BA (A) and the PA (B) in ozonation and the TOC behavior in conventional (C) and catalytic ozonation (D) in the presence of the NiO.

In the case of the phthalic acid, by Wen et al. (2011) the value of 0.092 ± 0.042 M^{-1} s^{-1} was determined. Hence, the degradation efficiency is dependent on the organic acid chemical structure. It is worth noting that direct reaction with molecular ozone is very effective to decompose the BA and the PA, achieving in 20 min 95% of the removal of both compounds.

As can be seen, the degradation of the BA and the PA in the catalytic ozonation with the NiO did not present the significant difference compared to the conventional ozonation. This result also confirms the predominant reaction of the acids with the molecular ozone in the presence of the catalyst too. A similar result has been observed by Wang et al. (2010) in the degradation of acetylsalicylic acid using unsupported Fe_3O_4 and supported on SiO_2, as catalysts.

On the other hand, the behavior of the total organic carbon (TOC) shows that the mineralization degree significantly increases in the catalytic ozonation compared to the conventional process (Fig. 5.9B).

In conventional ozonation, only 35% and 42% of the mineralization degree is reached during 60 min for the BA and the PA, respectively. Despite the fact that ozone is a strong oxidant, it cannot remove the recalcitrant intermediates in a reasonable time due to their reactivity with ozone (Lee and von

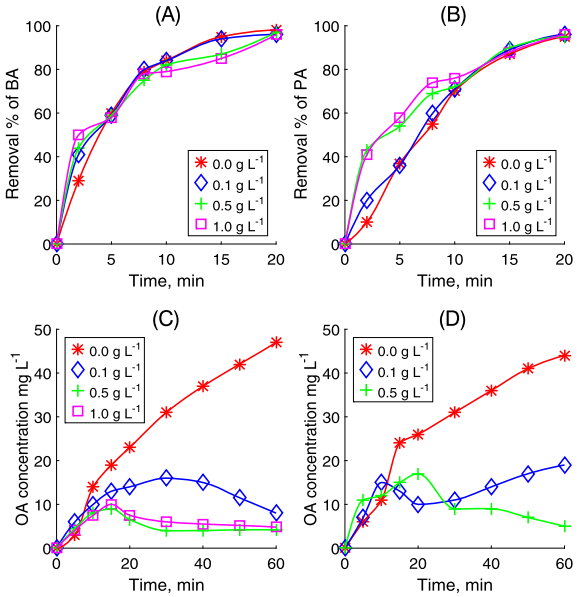

■ **FIGURE 5.10** Effect of the catalyst concentration on the removal (%) of the BA (A) and the PA (B) and on the oxalic acid concentration formed in the degradation of the BA (C) and the PA (D).

Gunten, 2010). In contrast, in catalytic ozonation a significant removal of the TOC (around 95%) is attained at 60 min. The mineralization rate of PA is faster than of BA, probably due to an increase of the generated oxidant species.

5.4.1.3 Effect of the catalyst concentration

The heterogeneous catalytic ozonation is a complex process, which involves gas, liquid, and solid phases, where the catalyst concentration plays a relevant role. Therefore, some experiments were carried out to study the effect of the catalyst concentration on the degradation of the acids, and to determine the optimal catalyst concentration. Fig. 5.10 shows the degradation of the BA as a function of catalyst concentration (0.1, 0.5, and 1.0 g L^{-1}). As can be observed, there is not a significant effect of the catalyst concentration on the degradation of the acid.

In the case of the PA (Fig. 5.10B), the effect of the catalyst concentration is more noticeable, namely: the increase of the degradation up 30% during the first 2 min at the 1.0 g L^{1} of the catalyst. However, these results are not in the agreement with the results obtained by other researchers, which reported that upon increasing of the catalyst concentration a better degradation rate of organic pollutants is obtained (Muruganandham and Wu, 2008; Na et al.,

Table 5.7 Reaction rate constants for the BA and PA decomposition and for the OXA formation–decomposition, calculated on the basis of the proposed kinetic model: BA = benzoic acid, OA = oxalic acid, PA = phtalic acid.

NiO $g\ L^{-1}$	BA $k_1 \cdot 10^{-1}$ min^{-1}	OA $k_f \cdot 10^{-2}$ min^{-1}	OA $k_d \cdot 10^{-2}$ min^{-1}	PA $k_2 \cdot 10^{-1}$ min^{-1}	OA $k_d \cdot 10^{-2}$ min^{-1}
0	2.07	3.85	NA	1.26	NA
0.1	1.91	17.21	0.92	1.33	0.62
0.5	1.85	21.46	3.18	1.42	2.86
1.0	1.76	3.18	1.18	1.61	–

2005). Most likely, the influence of the catalyst concentration depends on the chemical structure of organic compounds.

After the identification of all byproducts generated in ozonation, it is found that oxalic acid (OXA) is the main recalcitrant product of the decompositions of two acids. The efficiency of the decomposition of this acid depends on the mineralization degree of the ozonation. For this reason the influence of the catalyst concentration on the oxalic acid behavior was studied. Figs. 5.10C and 5.10D display the effect of the catalyst concentration on the behavior of the oxalic acid generated in the BA and PA degradation. In the direct reaction with molecular ozone, the OXA was accumulated during the observed time up to 45 mg L^{-1}. In the presence of the NiO the behavior of the OXA significantly changed. In the cases of both acids, the OXA was accumulated in the first 15–20 min up to 15 mg L^{-1} and then it is decomposed to 4–5 mg L^{-1} at 60 min, which confirms its mineralization. The best mineralization degree was obtained at the NiO concentration of 0.5 g L^{-1}. The kinetic study of the BA and PA decomposition permits one to characterize more exactly the effect of the catalyst and its concentration on the acids degradation. Table 5.7 lists the reaction rate constants for the BA and PA decomposition and for the OXA formation–decomposition, calculated based on the proposed kinetic model.

According to the results presented in Table 5.7, the presence of the catalyst, as well as the increase of the catalyst concentration, slightly decreases the decomposition rate of the BA. In the case of the PA ozonation, the catalyst increases the degradation rate constants of the acid, and their values are augmented with the increase of the catalyst concentration.

The different tendencies observed for the two acids may indicate the difference in the ozonation mechanism for BA and PA. It is feasible to claim that the chemical structure of the acid affects the predominant ozonation mechanism, which for the BA is the direct mechanism and indirect for the PA.

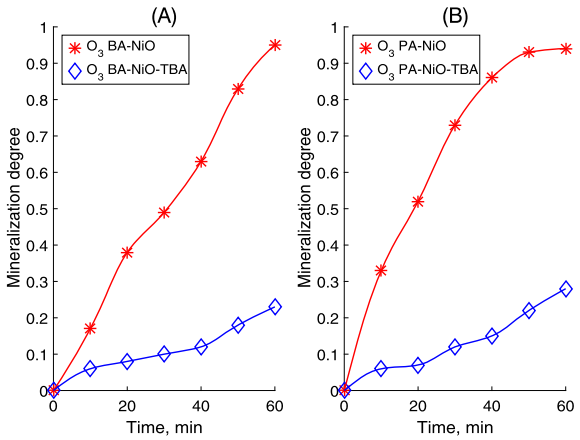

■ **FIGURE 5.11** Mineralization degree of the BA (A) and the PA (B) in the absence and in the presence of the TBA. The TBA concentration is 200 mg L^{-1}, the NiO concentration is 0.5 g L^{-1}.

On the other hand, in contrast, for the oxalic acid a similar tendency was observed for the two cases, namely, the increase of the formation rate and the decomposition rate of the OXA in the presence of the catalyst. In this case, the optimal catalyst concentration is 0.5 g L^{-1}.

5.4.1.4 Effect of the hydroxyl radical scavenger

It is well known that tert-butyl alcohol (TBA) acts as a scavenger of the hydroxyl radical. TBA is commonly used to distinguish the oxidation by the molecular ozone from the oxidation by the hydroxyl radical in ozonation (Andreozzi et al., 1999; Zhang et al., 2012). Fig. 5.11 presents the mineralization degree of the BA and the PA in catalytic ozonation in the absence and the presence of the TBA (200 mg L^{-1}).

As can be seen, the presence of the TBA significantly depressed the mineralization degree of the two acids from 95 to 22% for BA and from 92 to 30% for PA. This result confirms the predominance of the indirect mechanism of ozonation in the presence of the NiO. On the other hand, it is feasible that the inhibition of the catalyst activity could be ascribed to the adsorption of the TBA on the catalyst surface. This fact was confirmed by a study of the surface chemical composition of the catalyst using the XPS technique after ozonation in the presence of TBA.

5.4.1.5 XPS of the fresh and ozonated NiO

According to the literature (Rodríguez et al., 2013b; Yang et al., 2010; Zhang et al., 2012), ozone interacts with the hydroxyl groups, generated

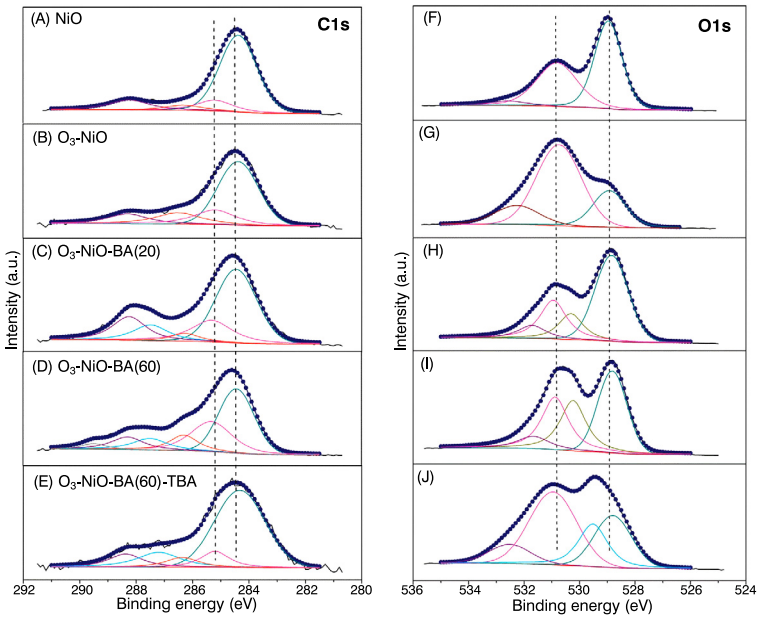

■ **FIGURE 5.12** XPS high resolution spectra of the C1s (A)–(E) and O1s (F)–(J) regions for the NiO catalyst: (A, F) fresh, (B, G) ozonated, (C, H) at 20 min, (D, I) at 60 min and (E, J) at 60 min in the presence of TBA, after ozonation of the BA.

by the water adsorption on the Lewis acid sites of the catalyst, and then initiates the formation of the oxidant species that favors the degradation of the acids. The analysis of the NiO by the XPS technique permits one to obtain the information as regards functional groups, when the oxidation state and the chemical environment of the elements, that are present on the catalyst surface. Although the Ni species are considered as the only active sites, the diverse XPS spectra of Ni2p did not show differences in all analyzed samples. For this reason, C1s and O1s XPS core lever spectra are analyzed for fresh and ozonated NiO, as well as for the BA decomposition. The raw data were fitted with a combination of the Gaussian–Lorentzian mix function and Shirley background subtraction (Fig. 5.12).

From the C1s XPS core level spectra fitting, it was established that, for all cases, the main peak at 284.5 eV corresponds to adventitious carbon, which presents an almost constant concentration in all samples. The C1s region for the NiO and the O_3–NiO samples has been fitted employing three basic contributions, situated at 285.3, 286.5, and 288.3 eV, which correspond to –C–C–, CQO, and –COOH, respectively.

The fresh NiO contents the lowest amount of C–OH species, whereas the O_3–NiO exhibited the decay tendency for C–C and CQO. Regarding the

samples, used in the BA decomposition, besides the –C–C–, CQO, and –COOH, the noticeable presence of the additional chemical species at high binding energies can be seen in Fig. 5.12. The latter is foreseeable due to the adsorption of some intermediaries onto the catalyst surface during the BA ozonation.

The analysis in the O1s region is in agreement with the above mentioned facts. In Fig. 5.12F to 5.12J, the passage from a two-component system of the fresh nickel oxide to a four-component system after ozonation and the BA decomposition can be elucidated. The O1s XPS spectrum of the fresh nickel oxide decomposed into two peaks located at 528.80.1 eV, assigned to lattice oxygen in Ni–O and 530.8 0.1 eV related to Ni–OH bonds, specifically $Ni(OH)_2$ (Fig. 5.12F).

Applying the same model to the ozonated sample, a new contributed signal is needed to recover the experimental spectrum (Fig. 5.12G). An additional contribution can be assigned to the $(O_2)_2$-peroxy species, 532.3 0.1 eV, but this species is less stable, so the signal likely corresponds to H_2O. For the samples of O_3–NiO–BA(20) and O_3–NiO–BA(60), the presence on the NiO of the adsorbed organic groups is confirmed by two additional peaks, assigned to C–O, 530 0.1 eV and at 531.7 0.1 eV for CQO.

The relative amount of those signals increases as a function of the ozonation time including the peak of $Ni(OH)_2$ (Figs. 5.12H and 5.12I). On the other hand, the samples O_3–NiO and O_3–NiO–BA(60)–TBA showed a decrease in intensity for the Ni–O bond contribution, while for the rest samples no significant change is perceived (Figs. 5.12G and 5.12J).

Furthermore, the two samples presented a bigger intensity of the peak attributed to $Ni(OH)_2$, which acts as Lewis acid sites contributing to the generation of the active oxidizing species. In view of these results, we establish that the interaction of ozone with the NiO favors the production of $Ni(OH)_2$ (Fig. 5.13). Nonetheless, in the presence of organic matter, $Ni(OH)_2$ reacts with the intermediates generated in the BA ozonation. In the presence of the TBA, the active centers Ni–O on the catalyst surface is blocking, therefore the XPS spectra are similar to O–NiO for the peak of Ni–O and Ni(OH).

Fig. 5.13 summarizes the types of the surface-bound functional groups, identified by the XPS, on the NiO under the different reaction conditions. In the case of the region of C1s, Fig. 5.13A shows the intensity of –C–C–, –C–OH, –CQO and –COOH for each analyzed catalyst (NiO, O_3–NiO, O–3–NiO–BA(20), O_3–NiO–BA(60) and O_3–NiO–BA(20)–TBA), excluding the adventitious carbon, which remained constant on all studied catalysts.

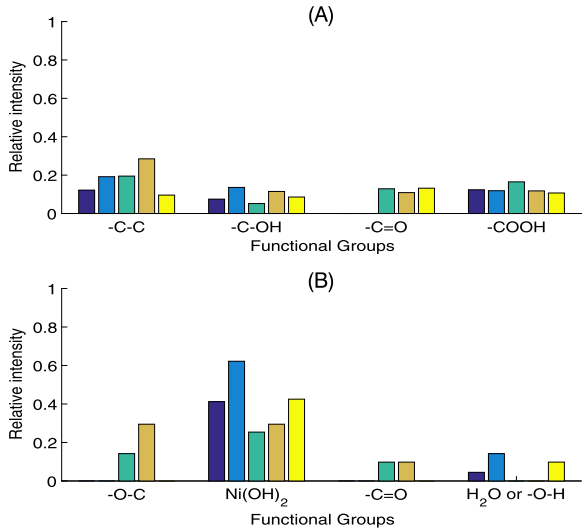

■ **FIGURE 5.13** Relative intensity of the functional groups estimated from C1s (A) and O1s (B) for the NiO under the different ozonation conditions.

As it can be observed, all functional groups are detected, in greater or lesser intensity in all catalysts, except for the –CQO– group, which was not negligibly detected in NiO or O_3–NiO. Let us note that the higher amount of –C–C– species is found after 60 min of ozonation of the BA (i.e. O_3–NiO–BA(60)); however, around 12% of the intensity for –C–OH, –CQO and –COOH groups is identified for the same catalyst.

In the case of the catalyst without BA (NiO and O_3–NiO), the functional groups –C–C, –COH and COOH are also identified, which are attributed to the interaction of adventitious carbon with ozone. As expected, the TBA addition decreased the intensity of the majority of functional groups, except for –CQO, which was attributed by the decrease of the mount of OH radicals, responsible for the BA oxidation. As a preliminary conclusion, these results indicate that the NiO surface is involved in the BA degradation due to the presence of organic matter (intermediates) (Fig. 5.13A).

Furthermore, the analysis of the O1s region (Fig. 5.13B) shows the presence of –O–C, $Ni(OH)_2$, –CQO and H_2O (O–H) signals in all studied catalysts with the predominance of the Ni hydroxylated species. As one can see, the ozonation of the NiO produces the highest $Ni(OH)_2$ (65%) and O–H (12%) intensity signals, which can be considered as the creation of the surface active sites. Contrary, in the presence of the BA (O_3–NiO–BA(60)) the $Ni(OH)_2$ and O–H intensity signals are decreased at around 50% and 100%, respectively after 60 min of ozonation in comparison with O_3–NiO. In ad-

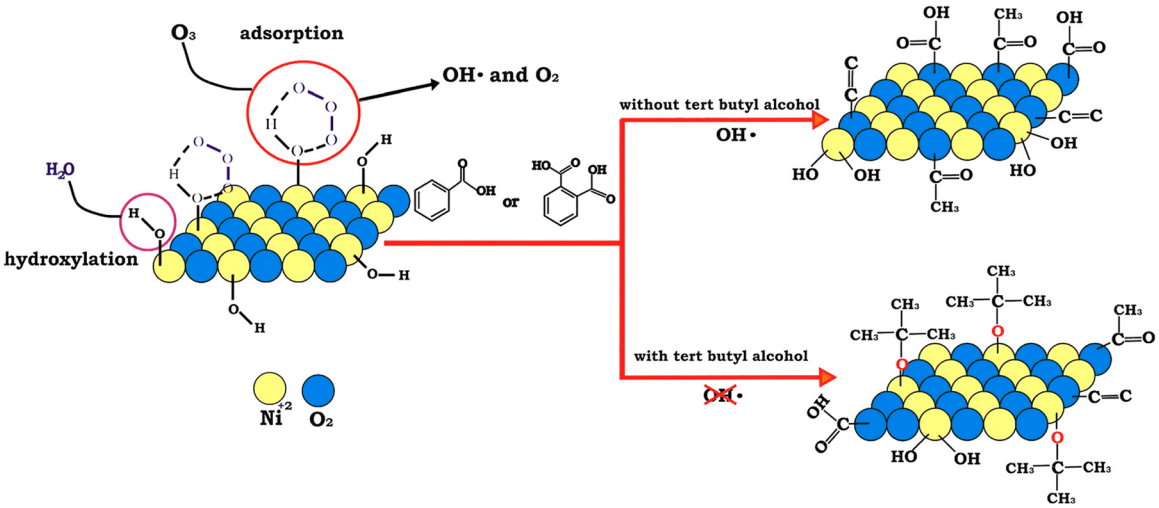

■ **FIGURE 5.14** Proposed reaction mechanism for the BA decomposition in the presence of the NiO with and without the TBA.

dition, the presence of –O–C, and –CQO signals confirms the presence of the intermediates, generated in the BA decomposition and adsorbed on the NiO surface. It is worthwhile mentioning that the consumption of the active site in the studied systems is different. For example, the intensity of $Ni(OH)_2$ and O–H signals is reduced only by 15% and 5%, respectively, in O_3–NiO–BA(60)–TBA, in the comparison with O_3–NiO. The –O–C and –CQO signals not detected. The XPS spectra and analysis of functional groups in C1s and O1s regions in the PA ozonation have a similar behavior and by this reason are not shown here.

Fig. 5.14 illustrates the proposed mechanism for the catalytic ozonation of the BA in the absence and the presence of TBA.

The NiO promotes the ozone decomposition and the byproduct adsorption. The TBA blocks part of the active sites, and reduces the BA decomposition degree (as previously demonstrated in Fig. 5.11). Fig. 5.15 shows the elemental composition on the catalyst surface, obtained from the XPS spectra of the NiO, as the atomic percentages, before and after ozonation at different ozonation times for the benzoic and phthalic acids.

As it can be observed, the atomic percentages is not changed significantly after 20 min of ozonation for two acids. Nevertheless, at 60 min the PA and the BA increase the atomic percentage of a carbon that indicates to the adsorption of the organic matter on the catalyst surface in ozonation. Hence, we can conclude that the number of the carboxyl groups in the acid practically has no influence to the mechanism of the catalytic ozonation.

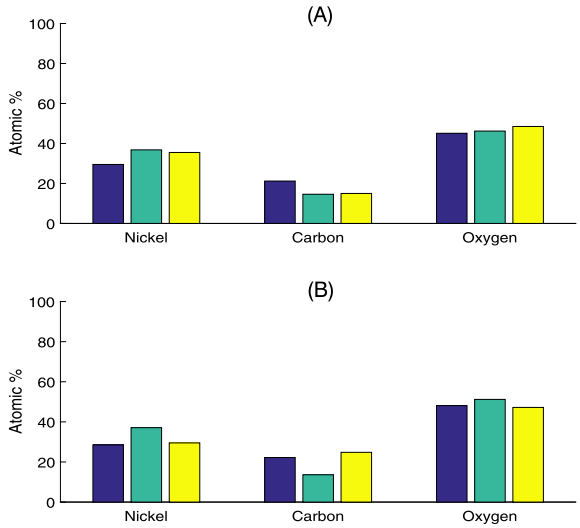

■ **FIGURE 5.15** Elemental composition on the catalyst surface obtained from the XPS spectra for the BA (A) and the PA (B).

Notice that during the decomposition of both acids the direct reaction with molecular ozone is predominant and very effective, achieving in 20 min 95% for both compounds, to be compared with the catalytic ozonation in the presence of the NiO as a catalyst.

In the last case, the effect of the catalyst is insignificant: about 5%. However, the influence of the NiO increases significantly for the decomposition of the intermediates and final products, which are less reactive with ozone. This fact is confirmed by the increases of the mineralization degree of both acids in the presence of the catalyst from 40% up to 95% during 1 h of ozonation, which was attributed to the combination of two consecutive reactions as direct reaction with molecular ozone and the indirect decomposition by the OH radicals.

The identified final product is oxalic acid, which was accumulated in the conventional ozonation up to 45 mg L^{-1} and decomposed in the presence of the NiO after 60 min of ozonation. Furthermore, the presence of the diverse groups in the region O1s, detected by the XPS, confirms that ozone is adsorbed on the catalyst surface forming hydroxyl radicals, which decompose the oxalic acid.

5.4.2 Combination of conventional and catalytic ozonation

Based on the data presented above, we may conclude that the catalyst has no any impact to the decomposition of the initial compound; however, the

presence of the catalyst (NiO) has a significant influence on the decomposition of intermediates and final products (for example, the oxalic acid), the major part of which are recalcitrant.

In view of this fact, it seems to be interesting to study the combination of the conventional and catalytic ozonation. Namely, in the case when the direct ozonation mechanism predominates, the catalyst should be added after the beginning of the reaction, when the initial compound is almost degraded. For this purpose, for the following studies the phenol (Ph), 4-phenolsulfonic (4-PSA) and 2-naphtalenesulphonic acids (2-NSA) were selected. These compounds are toxic contaminants, besides that the molecules of both acids have the sulphonic group ($^{-}SO_3H$). The total degradation of the 2-NSA is achieved during 25 min, for the Ph during 35 min, while for 4-PSA we have approximately 42% after 60 min. This difference is justified by the chemical structure of the organics and by the selectivity of the molecular ozone.

Based on the formation–decomposition dynamics of the intermediates and the accumulation of the oxalic acid, catalyst addition times of 20 and 40 min were selected. These times were chosen according to the following criteria:

1. Some intermediates have the maximal concentration or at least one of them shows an essential accumulation during the first 20 min of ozonation.
2. After 40 min of ozonation, the decomposition of some of the byproducts is observed.

Besides, the behavior of the oxalic acid can be considered as an additional criterion to select the time of the catalyst addition into the system, which is highly recalcitrant and is difficult to decompose by conventional ozonation ($k = 0.04\ M^{-1}\ s^{-1}$).

Notice that the addition of the catalysts like the NiO, as well as CuO, did not affect the decomposition of the initial compounds (4-PSA and 2-NSA), which was an expected result; however, for the intermediates and the oxalic acid, in both cases, excluding the phenol, the positive effect of the catalysts was also not observed, since the sulfate ions, which were formed in the first stage of the 4-PSA and the 2-NSA ozonation by the desulfonation and being accumulated in the medium, are able to inhibit the active centers of the catalyst. To the contrary, in the phenol case, a significant effect of the catalysts on the behavior of the intermediates and the oxalic acid was observed. Fig. 5.16 represents the behavior of the oxalic acid accumulation in ozonation of phenol for the five experimental systems.

The decomposition degree of the oxalic acid, achieved with the O_3–O_3/NiO (20 min) system, is 15% and 53% with O_3–O_3/NiO (40 min) during 80 min

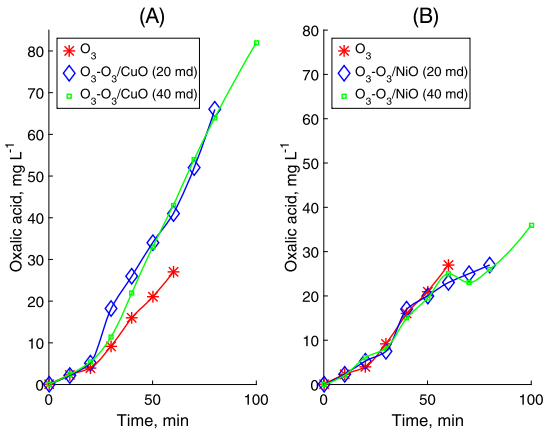

■ **FIGURE 5.16** Behavior of the oxalic acid in ozonation of phenol in five systems with CuO (A) and NiO (B).

of ozonation. On the other hand, in the O_3–O_3/CuO (40 min) system the catalytic effect is not so significant, the oxalic acid degradation began after 80 min of ozonation, decomposing only 6% of the acid. These results were obtained by the comparison of the experimental concentration of the oxalic acid and the theoretical one. It is possible to conclude that the catalytic activity of the NiO is more significant than CuO. The partial mineralization of the Ph is confirmed also by the formation of the formic acid in ozonation.

5.4.2.1 XPS study of the NiO surphase after ozonation of phenol, 4-phenolsulfonic and 2-naphthalenesulfonic acids

To confirm the possible inhibition of the active centers of the catalyst by the sulfate ions, the XPS study of the NiO surface after ozonation of phenol, 4-PSA and 2-NSA was realized. Fig. 5.17 shows the XPS spectra of the Ni2p3/2, AQF O1s and C1s regions of the NiO before and after ozonation.

As may be observed above, we work in the Ni2p3/2 region for the four NiO, represented by the two bands (853.7 eV) and $Ni(OH)_2$ (856 eV), with their respective satellites located at higher bond energies (860.9 eV). In general, there are no significant differences among these four catalysts in the $Ni_2p_{3/2}$ region; however, in the catalysts after ozonation of the 4-PSA and the 2-NSA a small contribution in 857 eV, corresponding to $NiSO_4$, is presented. This indicates an interaction between the sulfate ions, presented in the aqueous solution, and the catalyst, forming a salt on the NiO surface. In the O1s region, the rest of the catalysts (II, III, and IV) show a similar spectrum. The difference lies in the presence of the sulfate group (532.2 eV) for catalysts III and IV. The $NiSO_4$ signal is consistent with the values re-

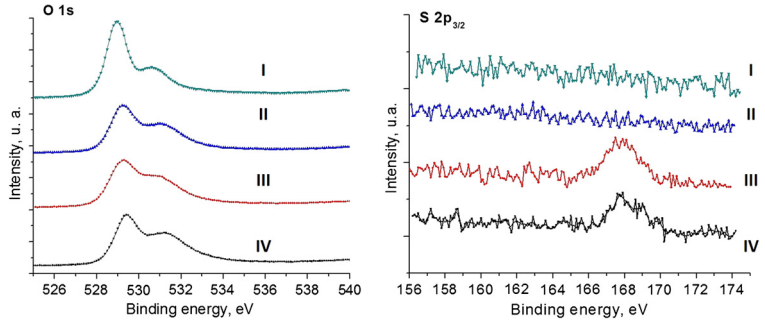

■ **FIGURE 5.17** XPS spectra of the NiO before ozonation (I), and the catalyst after ozonation of the phenol (II), the 4-PSA (III), and 2-NSA (IV).

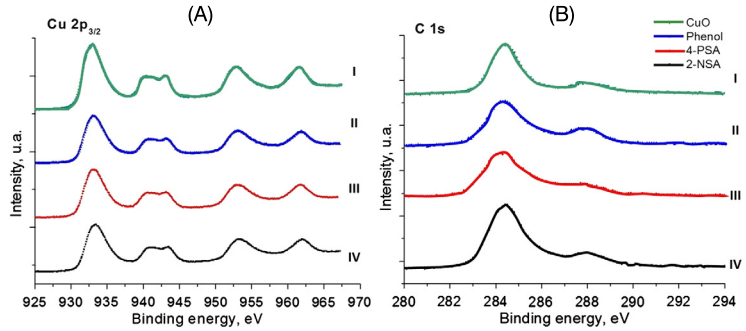

■ **FIGURE 5.18** XPS spectra of the regions $Cu2p_{3/2}$, O1s (A), C1s y $S2p_{3/2}$ (B) of the CuO before ozonation (I) and after ozonation of the phenol (II), the 4-PSA (III), and the 2-NSA (IV).

ported in the literature (Zhao et al., 2009b). In the $S_2p_{3/2}$ region one detects two bands, located at 167.7 eV and 168.9 eV, assigned to SO_2 and $NiSO_4$, respectively. These bands, present only on NiO, were used in the ozonation of 2-PSA and 4-NSA. Equally to the case of the presence of NiO, the XPS spectra of the $Cu_2p_{3/2}$, O1s and C1s regions for each of the CuO catalysts were also obtained (Fig. 5.18).

In the XPS spectra of the commercial CuO in the region of Cu2p3/2 four signals were observed: the species Cu^{2+} (932.8 eV) and $Cu(OH)_2$ (934.42 eV) with their satellites, which are located at 940.7 and 943.26 eV. In general, four catalysts also do not exhibit significant differences; however, in the case of the catalysts used in the ozonation of the 4-PSA and the 2-NSA, a small signal is observed corresponding to $CuSO_4$ (936.7 eV), indicating the formation of a salt on the CuO surface, which coincides with reports in the literature. In the region of O1s, for the CuO before ozonation (I), there are two bands located at 529.1 eV and 530.7 eV, which are attributed to

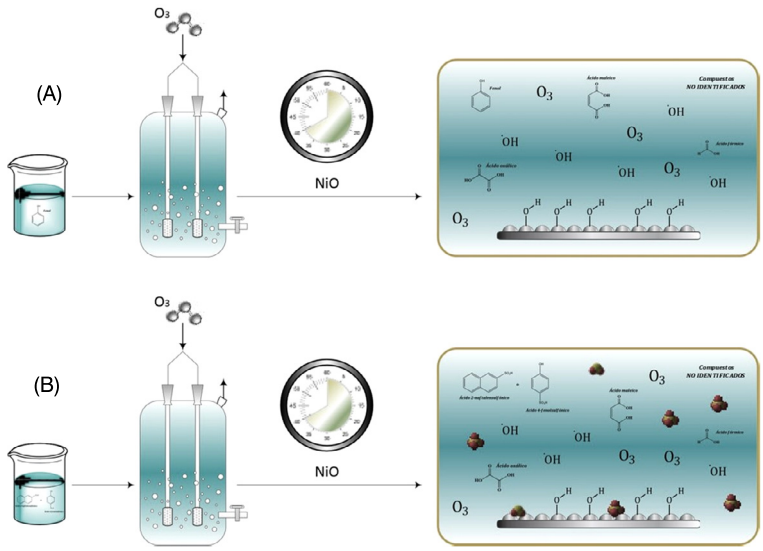

■ **FIGURE 5.19** Proposed scheme of the interactions in the ozonation of phenol (A), PSA, and NSA (B) in the presence of NiO.

the Cu–O and Cu–OH bonds, respectively. In the case of the catalysts II, III, and IV, another signal, located at 532.2 eV, may correspond to the salt $CuSO_4$. The signals in the $S_2p_{3/2}$ region detected only for the catalyst after ozonation of 4-PSA and the 2-NSA, consisting of two bands, located at 167.6 eV and 168.7 eV, and corresponding to SO_2 and $CuSO_4$, respectively. The results obtained by XPS confirm the presence of the sulfate ions on the surface of the catalyst, but their content is not significant, since the signal S2p3/2 is not intense; however, it confirms the evidence of the interaction of the sulfate ion with the catalyst. In this particular case, the presence of the sulfate ions significantly affected the behavior of the oxalic acid. It should be noted that sulfate ions are not only on the surface of the catalyst, but also within the solution. The last statement was confirmed by the augment of the electrical conductivity in ozonation. Therefore, the absence of the catalytic effect in the sulfonated aromatic compounds ozonation is due to the presence of sulfate ions in both phases on the catalyst surface and in the liquid phase, that is, the presence of the sulfate ions causes the inhibition of the hydroxyl radicals. In this case, a negative effect of the ions can be expected only, if they have affinity to the catalyst surface. Fig. 5.19 presents a possible scheme of the interactions in the case of ozonation of phenol, PSA, and NSA in the presence of NiO.

5.5 CATALYTIC OZONATION OF THE NAPROXEN WITH NIO IN THE PRESENCE OF ETHANOL

The typical consumption of pharmaceutical products has created a new environmental problem due to the inappropriate disposal of unused medicines, fecal extraction or urinary by humans or animals and from pharmaceutical manufacturing discharges. Pharmaceutical products and/or their metabolites have been found in waste waters because they are discharged widely without any restriction in the environment. The presence of this kind of compounds has shown the potential danger in water bodies. Furthermore, pharmaceuticals may be able to change the reproduction cycles in aquatic species. Therefore, treatment methods and remediation technologies have been applied for the pharmaceutical compounds elimination due to the potential threats that these contaminants cause to both the ecological system and the health of human beings. Conventional biological waste water treatments have limited the degradation efficacy. Therefore, advanced oxidation processes are considered to be a suitable option due to their high capacity of oxidizing and partially mineralizing many organic contaminants.

Among diverse pharmaceutical compounds, anti-inflammatory drugs are frequently found in effluents of waste water treatment plants (Kosjek et al., 2005). In this study, we have chosen to address naproxene (NAP), which is a non-steroidal anti-inflammatory drug. This medicament is usually prescribed in the treatment of rheumatoid arthritis and inflammation of diverse articulations and muscles. Moreover, this anti-inflammatory drug can be purchased without prescription. This is a major feature, leading to its common presence in municipal waste waters. This compound has shown a low degradation rate under the effects of different treatments (Arany et al., 2013; Quintana et al., 2005) only 70% of naproxen in a period of 28 days having been removed using a reactor membrane bioreactor.

Taking into consideration the available reports on photolysis of naproxen, some limited studies on TiO_2 photocatalysis are available. There is research, which studies this process of the naproxen degradation in ultrapure water, but considering a radiation source coming from a solar simulator equipped with a xenon lamp. Various reaction conditions were explored including various factors affecting the degradation, including TiO_2 concentration, temperature, volumetric flow, and the dissolved oxygen concentration (Méndez-Arriaga et al., 2008a). Higher naproxen removal was obtained when direct photolysis was executed compared to TiO_2-based photocatalysis. The extent of mineralization after 180 min of treatment, as determined by the dissolved organic carbon content, was not relevant under direct photolysis with only a 5% reduction. Nevertheless, 20% removal was obtained, when 0.1 g L^{-1}

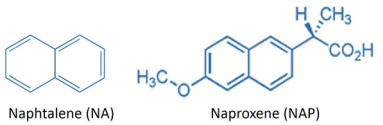

■ **FIGURE 5.20** Chemical structures of NA and NAP.

TiO_2 was used. A subsequent study showed that the temperature of the reactor had a significant effect on the degradation of naproxen (Méndez-Arriaga et al., 2008b).

In the previous sections, we noted the efficacy of catalytic ozonation in the presence of nickel oxide, which leads to the augment of the mineralization degree by the decomposition of recalcitrant intermediates and final products. In the case of real contaminated water, the toxic compound composition may be very complex, and for each of the organics mixture must be selected the optimal conditions of ozonation. With the aim of modeling the real treatment conditions, the catalytic ozonation of the recalcitrant toxic compound, such as NAP, in the presence of a high concentration of ethanol (as cosolvent) was carried out. The selection of this compound is justified due to its toxicity and prevalence in the environment. Fig. 5.20 depicts the chemical structures of NAP as well as its reference compound naphtalene (NA).

Naphthalene (NA) is one of the 16 PAHs classified by US EPA as priority pollutants. The NA is the major aromatic component in crude oil, petrol, and creosotes (Sigman et al., 1998) and it can be found in air, water, and soil. This compound is very toxic and its acute exposition causes in humans liver and kidney damage, cataract formation, changes in hemoglobin oxidation, and neurological and DNA damage, among other affections (Bagchi et al., 1998; Epa, 2004; Stohs et al., 2002). Moreover, this compound represents the chemical basis of several other compounds, such as naproxen (Fig. 5.20).

In the catalytic ozonation of different pollutants several catalysts, such as TiO_2, SiO_2, Al_2O_3, etc. were evaluated. The efficacy of the catalytic processes depends on the chemical structure of organics and the experimental conditions. Particularly, in the case of the herbicide 2,4-D ozonation, the NiO led to a great mineralization compared with the TiO (Rodríguez et al., 2012). Besides, in waste water phosphates, organic matter, carbonates, sulfates, surfactants, and cosolvents may be present, which negatively affect the efficacy of the conventional (O_3) and the catalytic ozonation (O_3-*cat*) (Fatta-Kassinos et al., 2011), (Chong et al., 2010). Indeed, there are some investigations focused on the inhibition of $^{\cdot}OH$, associated with a small concentration of the certain compounds in the water (for instance, tert-butanol and methanol) (Beltran, 2003).

To evaluate the influence of a high concentration of ethanol, the NAP degradation was carried out by the catalytic ozonation with NiO in the presence of ethanol in the proportions of 30 and 50% v/v. To the contrary of the PAHs degraded by the catalytic ozonation with the AC in the presence of methanol (16% v/v), the content of the ethanol augments, and the ozone concentration decreased to 5–6 mg L^{-1}. The NiO concentration is 0.1 g L^{-1}. At such high content of the ethanol about 75% of the initial ozone concentration was consumed in the reaction with it.

5.5.1 Experimental

5.5.1.1 Materials

All reagents used in the experiments were analytic grade. Commercial nickel (II) oxide nanoparticles with diameters smaller than 50 nm (Sigma-Aldrich, 99%) were used in the experiments as catalysts. A model solution was prepared with 20 mg L^{-1} of naproxen (Sigma-Aldrich, 99.8%) in mixtures of 30:70 and 50:50 ethanol/distillate water. Absolute ethyl alcohol was used as cosolvent (Chemical Meyer, 99.5%). This compound was used without further purification. The solution was vigorously stirred and protected from light during 5 h. This process was executed at room temperature (22.0 ± 2.0 centigrade degrees). The initial pH was 5.5 ± 0.5 and it was not controlled during the ozonation. The reagents used in the analysis of the naproxen degradation were HPLC grade.

5.5.2 Adsorption studies

The absorption experiments were conducted under mechanic agitation during 60 min with 40 mg L^{-1} NiO (the catalyst was previously dried at 100°C during 1 h) in 400 mL of 20 mg L^{-1} of naproxen solution of the two mixtures of 30:70 and 50:50 ethanol : water. The pH and temperature were kept constant during the experiment. The naproxen concentration was followed by HPLC by taking 4 mL samples at different times. The amount of naproxen absorbed was measured in terms of concentration detected by the HPLC analysis accordingly to the following mathematical expression:

$$\mathrm{NAP}_{adsorbed} = \frac{c_0 - c_t}{c_0} \cdot 100\ (\%) \tag{5.1}$$

where c_0 and c_t are initial and time dependent NAP concentrations (mg L^{-1}), respectively.

5.5.3 Analytical methods

The naproxen degradation was monitored by UV-Vis spectroscopy in a Perkin-Elmer Lambda 25 equipment in the range of 200 to 400 nm. The naproxen degradation, intermediates and final byproducts of ozonation were analyzed by HPLC using a Perkin-Elmer Flexar apparatus coupled with a DAD detector. The column used for naproxen detection was a platinum C18 (250 mm × 4.6 mm, 5 μm), with a mobile phase acetonitrile:water 50:50, adjusted to pH = 2.5 using orthophosphoric acid in isocratic flow of 0.3 mL min^{-1}. All experiments were run at room temperature and a wavelength of 240 nm was used to obtain the concentration measurements.

The analysis conditions of byproducts (organic acids) were obtained in a Prevail organic acid column (150 mm × 4.6 mm, 5 μm) with mobile phase of KH_2PO_4 buffer at 25 mM, adjusted to pH 2.3 with H_3PO_4 at 210 nm using a liquid flow of 1 mL min^{-1}. All the samples were filtered with 0.2 μm acrodisc syringe filter. All results are presented as the mean of triplicate determinations obtained for each sample. To complete the compound quantification, an external standard procedure was used for both calibration and model sample analysis.

5.5.4 Mathematical model of naproxen ozonation

The model characterizing the reaction kinetics throughout the ozonation of naproxen has the mathematical structure given by

$$\frac{d}{dt}c_{NAP}(t) = -k_{NAP}c_{NAP}(t), \tag{5.2}$$

where k_{NAP} is the reaction rate constant associated with the concentration changes; $c_{NAP}(t)$ is the variation of the naproxen concentration during ozonation. Even when this relation may appear to be heuristic, it can be used to characterize the effect of ozone on the naproxen decomposition. In the case of byproduct concentration, this simplified model has the form

$$\frac{d}{dt}c_j(t) = k_{j,a}c_{NAP}(t) - k_{j,d}c_j(t), \quad c_j(0) = 0, \tag{5.3}$$

where $k_{j,a}$ is the reaction rate constant associated with the accumulation of the intermediate j, $c_j(t)$ is the variation of the corresponding product, and $k_{j,d}$ is the reaction rate constant associated with the decomposition of this byproduct j. In the case of the final product, the constant $k_{j,d}$ can be set to zero. A better option was to propose an alternative reaction, where the connection between intermediates and accumulated materials can be high-

lighted. This model satisfies

$$\frac{d}{dt}c_k(t) = k_{jk,a}c_j(t) - k_{jk,d}c_k(t), \quad c_k(0) = 0. \tag{5.4}$$

Here $k_{jk,a}$ is the reaction rate constant, which characterizes the accumulation of the final product k, c_k is the variation of the main accumulated final product at the end of the reaction, and $k_{jk,d}$ is the reaction rate constant associated with its decomposition. The models, described by Eqs. (5.1), (5.2), and (5.3), are linear with respect to their corresponding parameters. The solution of this parametric identification problem, that is, to get all the parameters k_{NAP}, $k_{j,a}$, $k_{j,d}$, $k_{jk,a}$, and $k_{jk,d}$, can be obtained by the application of a robust exact differentiator (Cruz-Zavala et al., 2011c). This differentiator can be implemented by the supertwisting algorithm.

As an example, the model presented in (5.3) can be described as follows:

$$y(t) = k_{j,a}c_{NAP}(t) - k_{j,d}c_j(t) + \varepsilon(t), \tag{5.5}$$

where the variable y is the approximation of the time derivative (by the super-twisting) of the variable that should be differentiated. The term $\varepsilon(t)$ describes the approximation error produced by the implementation of the differentiator.

The model proposed in (5.5) can be represented as

$$y(t_k) = \theta^\top \phi\left(c_{NAP}(t_k), c_j(t_k)\right) + \varepsilon(t_k),$$

where $y(t_k)$, $c_{NAP}(t_k)$, and $c_j(t_k)$ are the output y, naproxen concentration, and product concentrations measured at the time instant t_k, respectively.

Here the vector θ represents the unknown parameters in the model and the function $\phi\left(c_{NAP}(t), c_j(t)\right)$ collects the experimental data in the model. The available samplings are t_k, $1 \le k \le K$. The solution to the parametric modeling strategy is

$$\theta^* = \left(\sum_{k=1}^{K} \phi^\top\left(c_{NAP}(t_k), c_j(t_k)\right)\phi\left(c_{NAP}(t_k), c_j(t_k)\right)\right)^{-1} \cdot \cdot \sum_{k=1}^{K} \phi^\top\left(c_{NAP}(t_k), c_j(t_k)\right) y(t_k).$$

5.5.5 Results and discussion

5.5.5.1 Naproxen adsorption

The naproxen adsorption on NiO in the treatments with 30:70 and 50:50 ethanol : water (Fig. 5.21) shows that the naproxen concentration in the

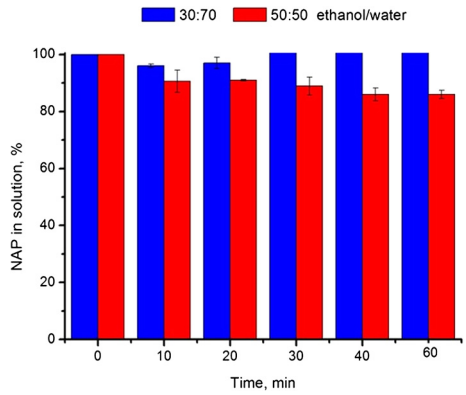

■ **FIGURE 5.21** Time variation of the NAP adsorption on NiO.

30:70 ethanol : water remains unchanged, while the cosolvent reduced less than 10%. Based on the latter adsorption results, the removal of naproxen shows scarce contribution to the treatments of O_3–NiO and O_3-conv.

5.5.5.2 UV-Vis analysis

Fig. 5.22 shows the UV-Visible absorption spectra of the degradation of NAP in the solutions of 30:70 and 50:50 ethanol : water by O_3-conv and O_3-cat. The absorption spectra of the initial samples present peaks of the maximum absorption at the wavelengths of 230 nm (near 3.5 mUA) and 330 nm, and three more peaks in the region between 255 and 290 nm. Such characteristic peaks of the model pollutant vary during conventional and catalytic ozonation. There is a hyperchromic effect in the absorption spectrum at the wavelengths of 240 and 230 nm showing higher absorbance values at the first minutes of the treatment. After 60 min of treatment, the maximum absorption peaks between 255 and 290 nm disappeared, leaving absorbance values close to the initial ones. The structural modifications of the molecule and formation of byproducts, of which the absorption spectra are in these wavelengths, might be responsible for the latter absorbance values. In the treatments with 50:50 ethanol : water (Fig. 5.22B and D), the increase of the absorbance happens at the initial times of the treatment (peak formed at the 2 min time at 230 nm).

The variation of UV-Vis absorbance was used to demonstrate that the presence of the catalyst affected the formation of byproducts. The catalytic ozonation presented an increment of absorption at 230 nm after 2 and 5 min of treatment as observed in Fig. 5.22 (B and D) and that effect was absent in conventional ozonation (Fig. 5.22A and C). In the work of Jallouli et al. (2016), the increment of the absorbance associ-

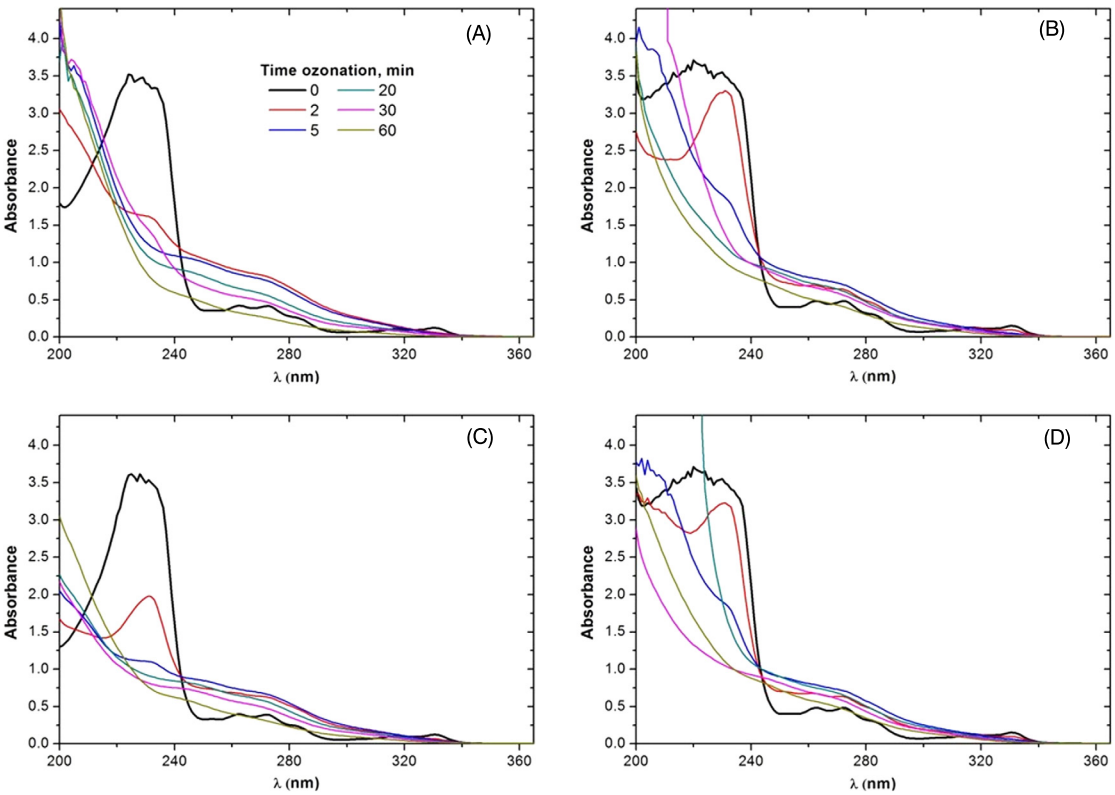

■ **FIGURE 5.22** UV-Vis spectra variation of the NAP in conventional (A, B) and catalytic ozonation (C, D) in the ethanol : water systems: 30:70 (A, C) and 50:50 (B, D).

ated with the presence of byproducts was demonstrated while working with naproxen treated by photolysis and photocatalysis (UV-TiO_2) after 210 min of treatment. The presence of these byproducts with two aromatic rings (1-(6-methoxynaphtalen-2-yl) ethylhydroperoxide, 2-ethyl-6-methoxynaphtalene, 1-(6-methoxynaphtalen-2-yl) ethanol, 1-(6-methoxynaphtalen-2-yl) ethanone) was demonstrated by UHPLC-MASS. In our experiments, the increments in the region of 255 and 290 nm for all treatments might be associated with the presence of byproducts as well.

5.5.5.3 Naproxen decomposition

The degradation profile of naproxen, obtained by HPLC for both concentrations of cosolvent in O_3-conv and O_3–NiO, reached 98% of the pollutant degradation after 10 min (Fig. 5.23). There was a difference of 24.5% in the degradation between O_3 conv 30:70 and O_3 conv 50:50 after 3 min of treatment, as well as in O_3–NiO (24.7%). Therefore, the presence of high concentrations of ethanol decreased the degradation rate of the naproxen.

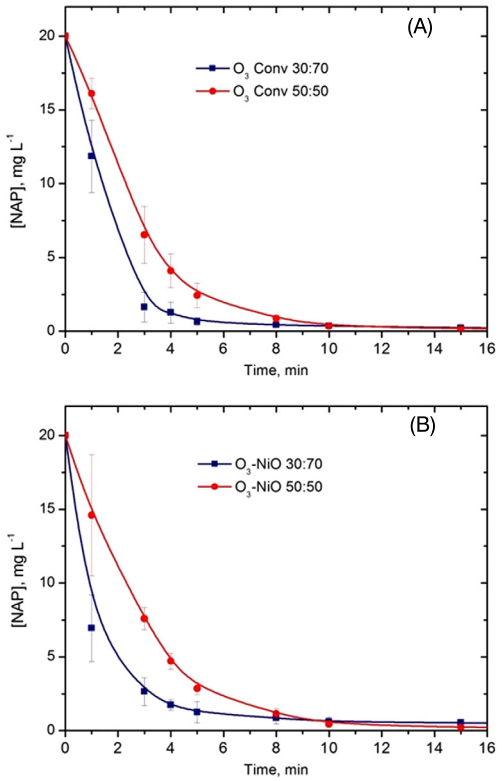

■ **FIGURE 5.23** Degradation of the NAP in the ethanol : water systems of 30:70 (A) and 50:50 (B).

Such an effect is more evident during the first minutes of the treatment, when the degradation is close to 95%. The analysis of the reaction rates after 2 min of treatment demonstrates the effect of the catalyst, when the naproxen degradation is higher in the catalytic treatment.

In Rosal et al. (2008), the degradation of the naproxen by catalytic ozonation with TiO_2 was evaluated. The elimination of naproxen occurred during the first minutes of the treatment. The TOC analysis proved that the presence of the catalyst affected the formation of byproducts having lower TOC values rather than the conventional ozonation. The degradation of naproxen with different concentrations of TiO_2 (2 g L^{-1}–0.1 g L^{-1}) and the influence of anions and the aqueous matrix was studied in Kanakaraju et al. (2015). The concentration of 1 g L^{-1} of TiO_2 obtained the best degradation rates of naproxen during the first 15 min of treatment. Despite the elimination of the naproxen signal, the mass spectrometric analysis detected byproducts with the intact aromatic structure of naproxen (two fused aromatic rings). The

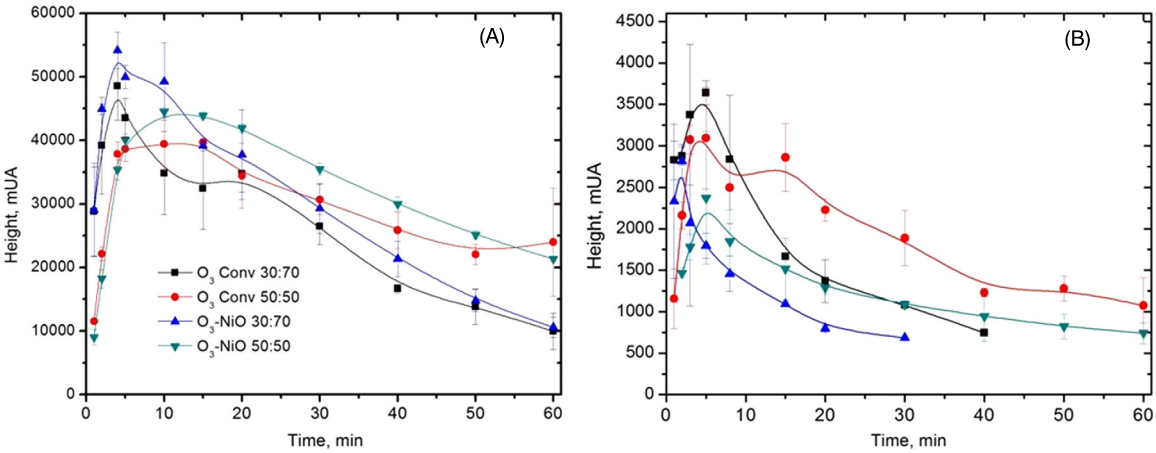

■ **FIGURE 5.24** Behavior of the intermediates of the NAP ozonation: (A) RT of 12.29 min. (B) RT of 14.9 min.

presence of high concentrations of cosolvent affected the degradation rate (reduction of 45%) (Aguilar et al., 2016) in the degradation of naphthalene with concentrations of 50% of ethanol. The degradation of naphthalene after 60 min of treatment was 55% in 50:50 ethanol : water, while in 30:70 ethanol : water it reached nearly 99%.

In Ghauch et al. (2015), the authors studied the interference of ethanol as electron scavenger in the degradation of naproxen (50 μM) treated by thermally active persulfate in proportions of 40000:100:1 ethanol/persulfate/naproxen, respectively. The presence of ethanol affected the elimination of naproxen reaching 32% of degradation after 60 min of treatment, whereas in the absence of ethanol the elimination was 82%. Here, despite the identification of the interference of ethanol in O_3-cat and O_3-conv, the signal corresponding to naproxen was undetected after 15 min of treatment, regardless of the ethanol concentration.

5.5.5.4 Intermediates obtained in ozonation of the naproxen

UV-Vis spectroscopic analysis demonstrated the possible formation of byproducts. The HPLC analysis of the naproxen ozonation yields two signals at the retention times (RTs) of 12.29 min and 14.9 min. The compounds corresponding to these signals have not been completely identified yet (Fig. 5.24). The byproduct obtained at the 12.29 min RT (Fig. 5.24A) highlights the effect of the ethanol concentration in both O_3-conv and O_3–NiO reaction systems. The higher concentration of this byproduct was detected in the samples with 30:70 ethanol : water during the first 5 min. In comparison, the maximum concentrations of these compounds for the samples

with 50:50 ethanol : water were obtained at 10 and 15 min, respectively. The smaller ethanol content implies the lower byproduct concentrations. At the end of the treatment, these byproducts were not decomposed completely in both O_3-conv and O_3-cat. Unlike the byproduct of the 12.29 min RT, the presence of the catalyst affected the formation of the byproduct, detected at RT of 14.9 min (Fig. 5.24B). The samples, treated by O_3–NiO with 30:70 and 50:50 ethanol : water, presented a smaller formation and a higher degradation rate for this byproduct than conventional ozonation.

The organic acids were the main degradation byproducts of ozonation treatments. The analysis of oxalic and formic acids, as well as the unidentified signal at 3.15 min RT, obtained in both ethanol concentrations and for both ozonation reaction (O_3-conv and O_3–NiO), is shown in Fig. 5.25. The analysis of oxalic acid (Fig. 5.25A) describes an accumulation profile in all the treatments. The higher concentration of cosolvent yields a duplication of the final oxalic acid concentration.

Catalytic ozonation produced faster increments in the concentration of oxalic acid after the first minutes of treatment. Nevertheless, the same final concentrations of oxalic acid after 60 min of reaction were obtained. The change in the molecules of naproxen during the ozonation can justify such an increment. The study presented in Jallouli et al. (2016) suggests the deletion of a three-carbon fragment from the substituent where the carboxylic link follows a transformation to malic acid (four-atom carbon acid). The degradation of malic acid could lead to the formation of oxalic acid. In the case of formic acid (Fig. 5.25B), the signal was determined at 30.15 min RT (Fig. 5.25C). The accumulation of this product was driven by the presence of the catalyst. The high concentration of ethanol forced the faster accumulation of this organic acids, like in the case of oxalic acid. The degradation of ethanol contributes to the increase of the concentration of organic acids in ozonation (Aguilar et al., 2016).

The identification of the compounds formed in the ozonation of the naproxen is carried out with the use of the electro-spray masses (ESI-masses), which allows for the injection of the substance mixture without prior separation and by means of a gentle ionization. Regardless of the system, the composition of the intermediates is the same, only their concentrations were changed. The fragmentation patterns of the ions are: 237.41, 221.05, 205.08, 177.09, and 149.06 m/z, as well as the proposed structure for the naproxen ozonation in the O_3-*conv* and the O_3–NiO systems after 60 min. The possible chemical structures of the intermediates obtained are presented in Table 5.8.

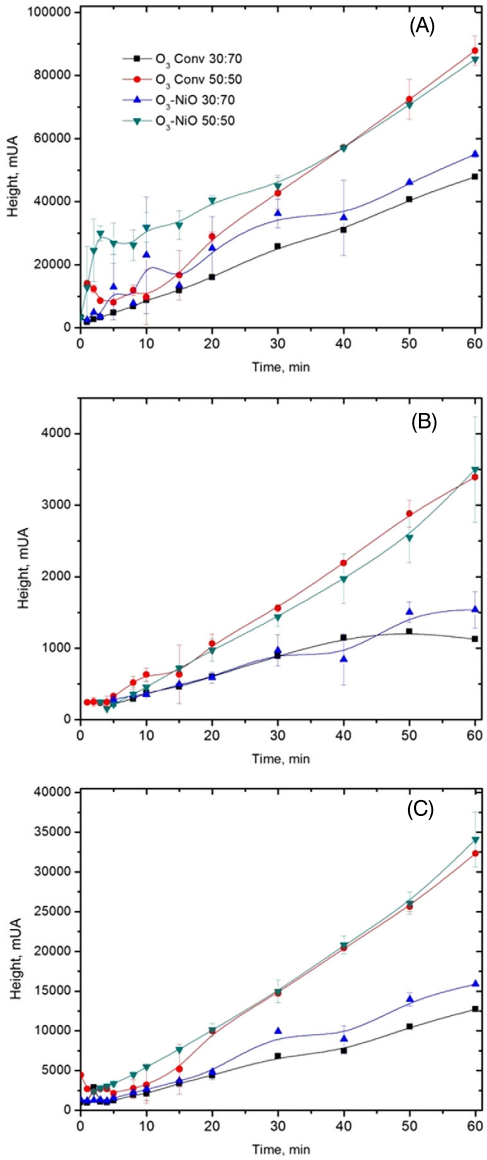

■ **FIGURE 5.25** Product accumulation during the NAP ozonation: (A) oxalic acid, (B) formic acid, and (C) signal at 3.15 min of retention time.

Based on the intermediates identified by the ESI-ms-ms technique, a possible simplified reaction scheme of the naproxen degradation was proposed in Aguilar Melo (2018). Fig. 5.26 presents this pathway of the naproxen ozonation. Thus, it is possible that the degradation pathway of the naproxen

Table 5.8 Possible intermediates of the NAP decomposition in conventional and catalytic ozonation with NiO.

Ion	w/z (negative mode)	Structures
Ion m/z detected by ESI-ms-ms		
$(C_{14}H_{13}O_3)^-$ (Naproxen)	229.09	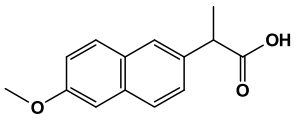
$(C_{13}H_{17}O_4)^-$	237.11	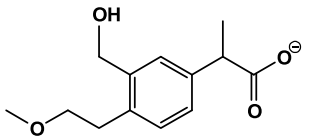
$(C_{12}H_{13}O_3)^-$	205.09	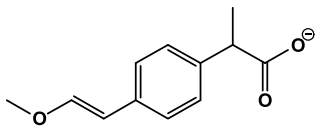
$(C_{10}H_9O_3)^-$	177.06	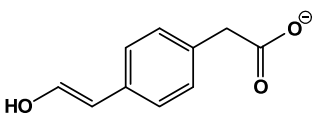
$(C_9H_9O_2)^-$	149.06	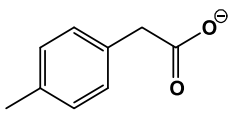
Ion m/z detected by ESI-ms		
$(C_{14}H_{17}O_5)^-$	265.11	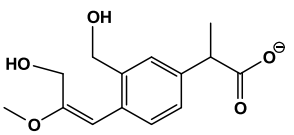
$(C_{14}H_{17}O_4)^-$	249.11	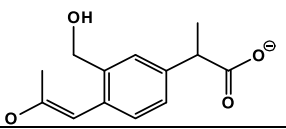

is similar regardless of the interaction with the different concentrations of ethanol and the presence of the catalyst. This proposed pathway used our own information and the results reported in other studies (Fig. 5.26). As can be seen, during 60 min of ozonation in the absence, as well as in the

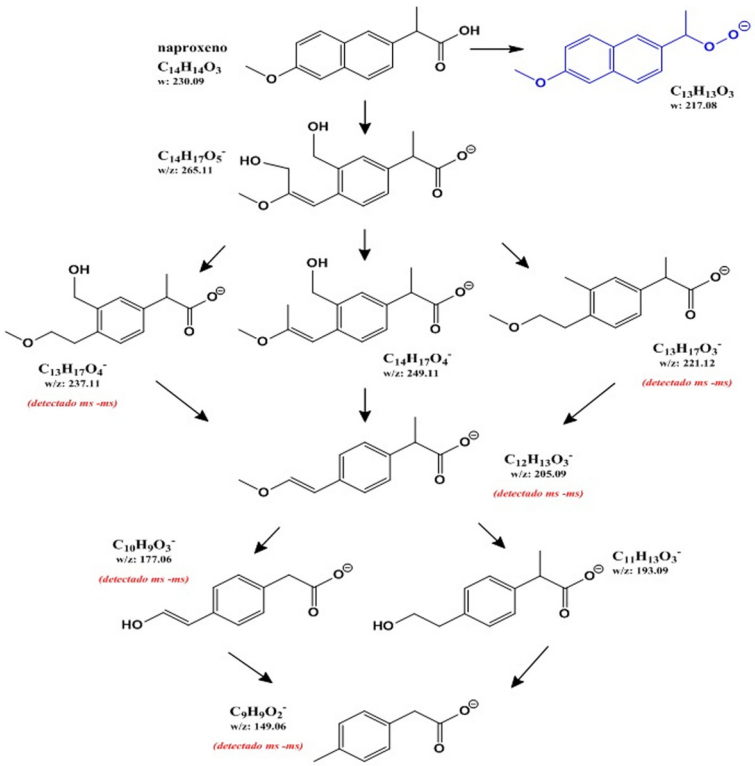

■ **FIGURE 5.26** Reaction pathway of the naproxen degradation in catalytic ozonation with NiO.

presence, of the catalyst only one aromatic ring broke. The complete mineralization can be achieved in a longer time consequently.

5.5.5.5 XPS spectrum of the catalyst

To determine the interaction of the naproxen, catalyst and ethanol in ozonation, the XPS spectra of the ozonated NiO with the two different ethanol proportions 30:70 and 50:50 (Fig. 5.27) were analyzed. Fig. 5.27 shows the Ni2p, O1s, and C1s spectra of the ozonated NiO samples. The Ni2p3/2 has a main peak at 853.3 eV, which corresponds to Ni^{2+} in NiO. The O1s region is represented by two peaks associated with NiO—528.7 and 530.6 eV. The first one is assigned to O within the oxide crystal (O^{2-}) and the second one to oxygen contiguous to Ni vacancies (O_{def}). Also, some oxygen species, associated with carbon, have been detected. These species may also be seen in the C1s region: –COH (286.3 eV), –C=O (287.7 eV), and –OC=O (288.6 eV). The –C–C/–CH peak at 284.6 eV is dominant. Only a shoulder for NiO (Ni^{2+}) is seen in the raw data. This spectra also shows

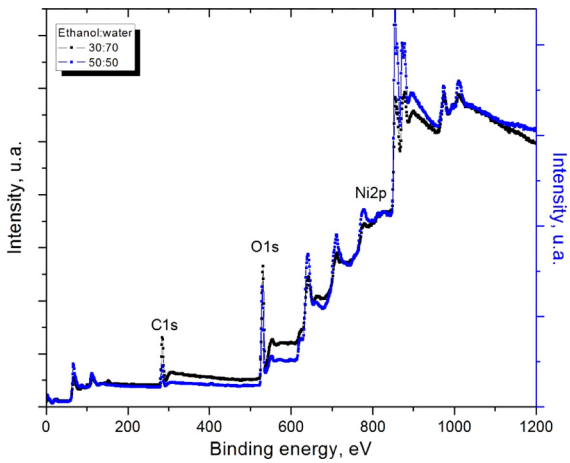

■ **FIGURE 5.27** XPS spectra of the NiO ozonation in presence of two ethanol concentrations (30:70) and (50:50).

the peak at 856.4 eV, labeled as NiOH, comes up. This means that the NiO was chemically transformed during ozonation in the presence of ethanol. The deconvolution of the Ni–OH peak is not easy, as there are several possible chemical species lying at this energy. Due to the ozone effect and the solvent (ethanol–water) applied to the NiO powder, the most likely products should be mixtures of nickel hydroxides; most favorable are $Ni(OH)_2$, NiO–OH, and possibly nickel-carbonate hydroxide $Ni_2CO_3(OH)_2$, indicated as Ni-carbonaceous. The spectrum of the O1s region is comprised of several components: a peak for O^{2-}, along with that for O_{def}, is concurrent with the shoulder seen for NiO (Ni^{2+}). Another peak at 531.1 eV entails –OH-type species associates to nickel (Payne et al., 2009). This peak may be interpreted as $Ni(OH)_2$ and/or NiO–OH, which is consistent with the Ni–OH peak binding energy for this type of compound. Also, a peak at 531.4 eV assigned to $–CO_3$ species can be recognized, which is evident in the C1s region. In addition, peaks for the organic species –COH, –C=O, and –OC=O are found, as well as a peak at high binding energy that seems far in energy from the organic species. It can be assigned to the adsorbed water $(H_2O)_{ads}$. This hypothesis can be acceptable, if we take into account the hydrophilic character of the ethanol–water mixture, which could easily be transferred to the nickel surface after the contact with ozone. The C1s region reveals a somewhat large organic carbon species, which are the intermediates of the ethanol ozonation. In addition, a peak at 290.1 eV for the $–CO_3$ species is clearly detected. Typically, the carbonates form a complex with a metal. In our case, it might be linked to the formation of the nickel-carbonate hydroxide.

5.6 THE NOMINAL MODEL OF CATALYTIC OZONATION

The majority of chemical processes, in particular ozonation, can be described by the system of ordinary differential equations, considering both the ozone mass-transfer and its reactions with the initial contaminants, the formed–decomposed byproducts, as well as the hydroxyl radicals formed in the presence of the catalyst. A catalytic ozonation model may include two sections: a) the first one formed by a basic nominal model represented by f_0 that contains the mass-transfer of ozone and its reaction with contaminants and b) an uncertain section that includes all the non-modeled reactions taking place. Let us introduce the variables considered in the model for catalytic ozonation. The ozone dissolved in the aqueous phase (Q, mol) is transferred from the gaseous phase (with a given ozone concentration c^g) conforming with double layer theory. This Q is consumed by the reaction with the contaminants and the corresponding byproducts and it is also used to produce hydroxyl radicals. The initial contaminants (c_i, mol L^{-1}, $i \in [1, N]$) are decomposed by the reaction with the dissolved ozone as well as with the hydroxyl radicals (mol L^{-1}). These radicals are produced from the self-decomposition of dissolved ozone and by the action of the catalyst. Then the state of the model can be represented by $x \in \mathbb{R}^n$, $n = N + 3$; $x := [c^g, Q, c_1, ..., c_N, \mathrm{OH}]^\top$ and it is governed by the following ordinary differential equations:

$$\frac{d}{dt}x(t) = f_N(x(t), u(t)) + \xi(t), \; x_{t=0} = x_0, \quad \|x_0\| < \infty, \tag{5.6}$$

where $f_N : \mathbb{R}^n \times \mathbb{R}^m$ ($m = 1$) represents the nominal model of the catalytic ozonation. The vector $u_t \in \mathbb{R}$ describes the variables used to represent the control elements that adjust the ozonation dynamics, that is, u is the initial ozone concentration. A more realistic model must consider the presence of external perturbations that may affect the catalytic ozonation and that cannot be included as part of the reactions occurring in the reactor. These perturbations or uncertainties are represented by $\xi_t \in \mathbb{R}^n$ and satisfy the boundedness condition given by

$$\|\xi(t)\|^2 \leq \xi^+ \; \forall t \geq 0, \quad \xi^+ \in \mathbb{R}^+. \tag{5.7}$$

The nominal model f_N can be represented as follows:

$$f_N = \begin{bmatrix} -V_g^{-1}\left[c_t^g W_g - u_t + k_{sat}(Q_{\max} - Q_t) + Q_t \sum_{i=1}^{N} k_i c_{i,t}\right] \\ k_{sat}(Q_{\max} - Q_t) - Q_t \sum_{i=1}^{N} k_i c_{i,t} - k_{F,OH} Q_t \\ -\left(k_1 \frac{Q_t}{V_{liq}} + k_{1,OH} OH_t\right) c_{1,t} \\ \vdots \\ -\left(k_N \frac{Q_t}{V_{liq}} + k_{N,OH} OH_t\right) c_{N,t} \\ k_{F,OH} \frac{Q_t}{V_{liq}} - OH_t \sum_{i=1}^{N} k_{i,OH} c_{i,t} \end{bmatrix} \tag{5.8}$$

where

– V_g is the volume of the gaseous phase (L),

– W_g is the gas flow (L s^{-1}),

– k_{sat} is the saturation constant of ozone in water (s^{-1}),

– $Q_{\max}$ represents the maximum amount of ozone in the saturation state of the liquid phase at a fixed temperature (mol),

– k_i is the reaction rate constant of the corresponding initial contaminant $c_{i,t}$ with the ozone dissolved in the aqueous phase (L mol^{-1} s^{-1}),

– $k_{F,\mathrm{OH}}$ represents the reaction rate that characterizes the conversion of dissolved ozone into hydroxyl radicals (s^{-1}),

– V_{liq} is the volume of the aqueous phase (L),

– $k_{i,\mathrm{OH}}$ is the reaction rate constant of the corresponding initial contaminant $c_{i,t}$ with the hydroxyl radicals (L mol^{-1} s^{-1}).

The model (5.8) possesses several characteristics that may be considered in the observer design: a) they are bilinear with respect to the components of the state-vector, b) not all the parameters of this model are known, c) the contaminant concentrations can be measured using UV-Vis spectrophotometer, HPLC, Fourier Transformation InfraRed spectroscopy (FTIR), nuclear magnetic resonance methods, etc., d) only some components (frequently only one) of the state-vector can be measured during the ozonation: the current ozone concentration in the gaseous phase $c_{g,t}$, that is, the output

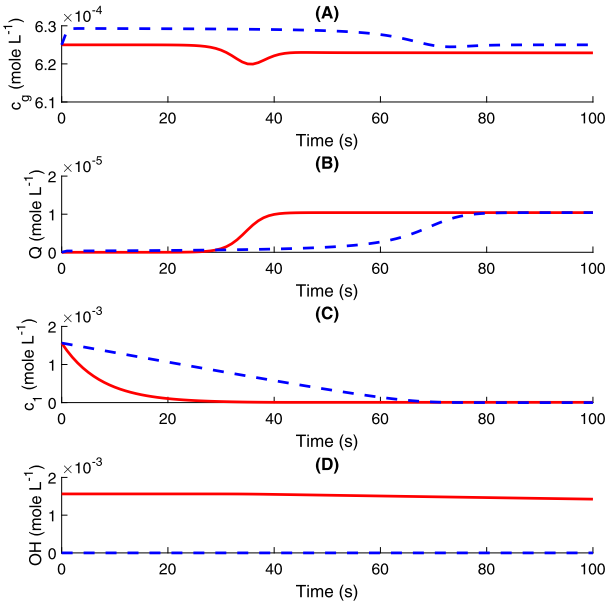

■ **FIGURE 5.28** Comparison of the ozonation variables with and without the catalyst: (A) c_g, (B) Q, (C) c_1, and (D) $^{\cdot}\mathrm{OH}$.

information that can be measured online is

$$y = c^g. \tag{5.9}$$

Fig. 5.28 depicts the comparison of the ozonation variables in the presence (solid line and red color in the electronic version) and in the absence (dashed line and blue color in the electronic version) of the catalyst.[1] Observe that the contaminant *decomposes faster* in the presence of the catalyst.

5.6.1 Estimation of reaction rate constants based on the nominal mathematical model

The estimation of the reaction rate constants for the catalytic ozonation introduced in (5.8) can be solved by the application of the least-square method in the same way as in (2.26). It is sufficient to consider the new extended

[1] Note: The color figures will appear in color in all electronic versions of this book.

vector of parameters and the regressor structure as follows:

$$\left.\begin{array}{c}\left[\begin{array}{c}k_i^*(t)\\ k_{i,OH}^*(t)\end{array}\right]=\Gamma_i(t)\cdot G_i(t),\quad i=1,..,N,\\ \Gamma_i^{-1}(t):=\int\limits_{\tau=0}^{t}\left[\begin{array}{c}-\dfrac{Q(\tau)}{V_{liq}}c_i(\tau)\\ -c_i(\tau)OH(\tau)\end{array}\right]\left[\begin{array}{c}-\dfrac{Q(\tau)}{V_{liq}}c_i(\tau)\\ -c_i(\tau)OH(\tau)\end{array}\right]^{\top}d\tau,\\ G_i(t)=\int\limits_{\tau=0}^{t}\left(\dfrac{d}{d\tau}c_i(\tau)\cdot\left[\begin{array}{c}-\dfrac{Q(\tau)}{V_{liq}}c_i(\tau)\\ -c_i(\tau)OH(\tau)\end{array}\right]d\tau\right).\end{array}\right\}\tag{5.10}$$

The differential version of (5.10) is

$$\left.\begin{array}{c}\dfrac{d}{dt}\left[\begin{array}{c}k_i^*(t)\\ k_{i,OH}^*(t)\end{array}\right]=\Gamma_i(t)z_i(t)\left(\dfrac{d}{dt}c_i(t)-z_i^{\top}(t)\Gamma_i(t)G_i(t)\right)\\ z_1(t):=\left[\begin{array}{c}-\dfrac{Q(t)}{V_{liq}}c_i(t)\\ -c_i(t)OH(t)\end{array}\right]\end{array}\right\}\tag{5.11}$$

where the time-varying functions $\Gamma_i(t)$ and $G_i(t)$ are generated by

$$\left.\begin{array}{c}\dot{\Gamma}_i(t):=-\Gamma_i(t)z_i(t)z_i^{\top}(t)\Gamma_i(t),\quad \Gamma_i(0)=\varepsilon I_{N\times N},\quad \varepsilon>0,\\ \dot{G}_i(t)=\dfrac{d}{dt}c_i(t)\,z_i(t),\quad G_i(0)=0.\end{array}\right\}\tag{5.12}$$

5.6.1.1 Kinetics of the naproxen decomposition and the intermediates formation–decomposition

Table 5.9 presents the ozonation rate constants $k_{j,a}$, $k_{j,d}$, and $k_{jk,a}$ (pseudo-first order) having been calculated by the method described above, as well as their confidence intervals.

The narrow confident intervals obtained for the values of all the reaction rate constant and, additionally, the high correlation coefficients confirmed the validity of the calculation method. All values were over 0.90.

As can be seen, in the presence of ethanol, the decomposition of the naproxen decreased in 91.2%, while the presence of the catalyst does not have a significant impact on the ozonation rate.

Table 5.9 Ozonation rate constants and statistical analysis at the different concentrations of ethanol.

Compound	k (s^{-1})	Ozonation system	k, s^{-1} 10^{-2}	Confident interval	Correl. factor
Naproxen		Conv. 30–70	8.45	0.0844–0.0846	1.0000
	k_{Nap}	Conv. 50–50	0.51	0.0050–0.0053	1.0000
		Cat. 30–70	8.51	0.0849–0.0853	1.0000
		Cat. 50–50	1.01	0.1009–0.1011	1.0000
Intermediates		Conv. 30–70	76.95	0.7687–0.7702	0.9883
	$k_{j,a}$	Conv. 50–50	48.67	0.4861–0.4873	0.9735
		Cat. 30–70	81.28	0.8120–0.8136	0.9828
		Cat. 50–50	30.48	0.3043–0.3054	0.9532
Intermediates		Conv. 30–70	2.51	0.0249–0.0254	0.9981
	$k_{j,d}$	Conv. 50–50	1.46	0.0144–0.0147	0.9987
		Cat. 30–70	2.23	0.0221–0.0223	0.9985
		Cat. 50–50	1.40	0.0138–0.0141	0.9991
Oxalic acid		Conv. 30–70	441.36	4.3856–4.4325	0.9965
	$k_{jk,a}$	Conv. 50–50	769.58	7.6896–7.7125	0.9693
		Cat. 30–70	490.86	4.8896–4.9356	0.9351
		Cat. 50–50	616.59	6.0256–6.2152	0.9310

When the ethanol concentration is 30%, there is no significant difference observed between the catalytic and the conventional ozonation. However, if the ethanol concentration increased to 50%, the presence of the catalyst doubled the ozonation rate, but this value was 8 times smaller than the ethanol concentration of 30%.

At an ethanol concentration of 30% the accumulation of the aromatic intermediates showed similar behaviors in conventional and catalytic ozonation

($k_{j,a} = 76.95 \cdot 10^{-2}$ vs. $81.20 \cdot 10^{-2}$, s^{-1}). Nevertheless, this tendency was not preserved, when the ethanol concentration increased to 50%. In the conventional ozonation the accumulation rate is higher ($k_{j,a} = 48.67 \cdot 10^{-2}$ vs. $30.48 \cdot 10^{-2}$, s^{-1}).

Notice that the accumulation rate of an aromatic intermediate is higher than the decomposition rate of the naproxen ($76.95 \cdot 10^{-2}$ vs. $8.45 \cdot 10^{-2}$ s^{-1}). This might be a consequence of the faster transformation of the naproxen into this aromatic compound. In consequence, the rate of the oxalic acid formation is higher than the decomposition of the naproxen and the aromatic intermediates.

The increase of the ethanol concentration leads to the augment of the formation rate of the oxalic acid. The last fact may be related with the partial decomposition of the ethanol, and oxalic acid is the product of this process. The effect of the catalyst, in this case, is insignificant.

No relevant difference between the reaction rates of the intermediates decomposition was obtained, when the catalytic and the conventional ozonation were compared.

An increment of only 11% in the reaction rate was characterized by the catalytic ozonation and the lower concentration of ethanol. This condition was similar to the case, when the ethanol concentration was higher (50.0%). Then the selected intermediates were eliminated equally efficiently, despite the presence of catalyst. Therefore, the cosolvent defined the reaction mechanism, when intermediates should be transformed to final products.

The higher concentration of ethanol in the ozonation showed the slower reaction rates to decompose both the naproxen and the aromatic intermediates. Under this reaction condition, the bigger oxalic acid concentration was determined at the end of the reaction. In the conventional ozonation, the reaction rate constant increased up to 74.3%, if the ethanol concentration was 50.0%. Also, the biggest oxalic acid concentration was obtained in the catalytic ozonation, but the reaction rate increased up to 25.6% only.

Taking into consideration the results obtained for the initial contaminant, as well as the intermediates and the oxalic acid, we may conclude that the ethanol strongly affected the ozonation efficiency. This condition is more evident, if the higher accumulation of recalcitrant low molecular organic acid is taken into account. As expected, the removal of oxalic acid was not detected in all the ozonation reaction systems.

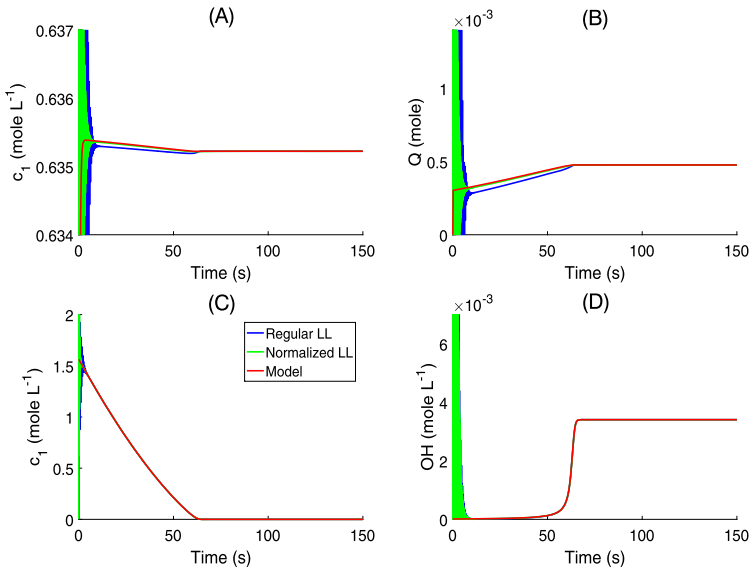

■ **FIGURE 5.29** States comparison of the catalytic model as well as the estimates by the DNN observers with regular and normalized learning laws.

5.7 NUMERICAL EVALUATION OF THE DNN OBSERVER

Fig. 5.29 shows the time variation of the states included in the catalytic ozonation (5.8). The first 15 s of numerical simulation appear in Fig. 5.30 to highlight the transient period, when the DNN approaches the trajectories of the ozonation system.

This figure also depicts the variation of estimated states obtained by the DNN observer using both regular learning (presented in Chapter 4) and the modified (normalized) laws developed in this chapter that satisfied

$$\frac{d}{dt}W_1(t) = -\frac{k_1^{-1}P^a\Delta(t)\sigma^\top(\hat{x}(t))}{1+\Delta^\top(t)P^a\Delta(t)}, k_1 \in \mathbb{R}_+,$$
$$\frac{d}{dt}W_2(t) = -\frac{k_2^{-1}P^a\Delta(t)u^\top(t)\phi^\top(\hat{x}(t))}{1+\Delta^\top(t)P^a\Delta(t)}, k_2 \in \mathbb{R}_+.$$

5.8 CONCLUSIONS

In this chapter, the positive effect of ACs and NiO in ozonation of some PAHs was demonstrated. The effect of catalyst concentration, the pH, and the cosolvent content on the degradation efficiency was proven. The pseudo-monomolecular kinetics study was done in the case of ozonation with both

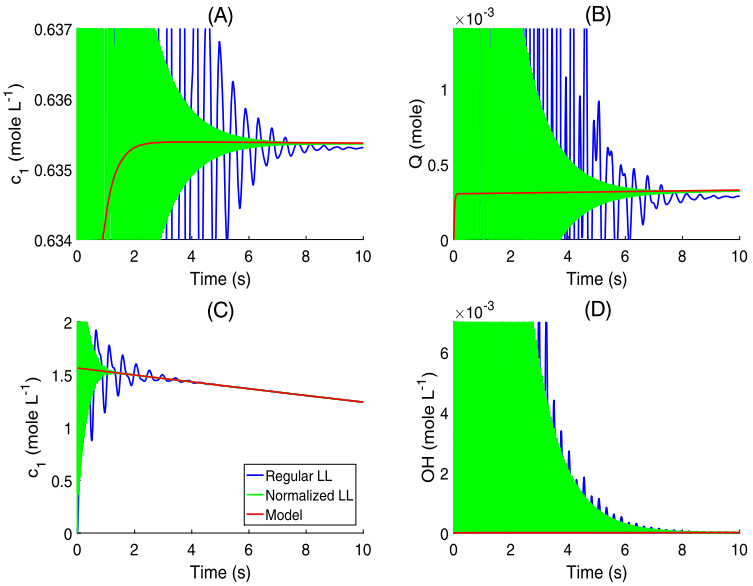

■ **FIGURE 5.30** States comparison during the first 15 s of the catalytic ozonation, as well as the estimates by the DNN observers with regular and normalized learning laws.

catalysts. A novel mathematical model based on ordinary differential equations was proposed to estimate the bimolecular rate constants of the ozonation of the PAHs in the presence of catalyst and at high pH (> 7.0). Also, the reconstruction of the intermediates concentration profiles in catalytic ozonation (based on DNNO) was obtained.

Chapter 6

Photocatalytic ozonation

CONTENTS

ABSTRACT

Vanadium oxide, supported on zinc oxide (ZnO), was prepared and used as a catalyst to enforce terephthalic acid (TA) elimination, using photocatalytic ozonation based on light emission diodes (UV-ALEDs). The catalyst characterization indicated that vanadium oxide was not incorporated into the pores of zinc oxide, due to the formation of thinner flakes. The synthesized catalyst exhibited high stability, because no significant changes between fresh and used catalyst were confirmed by the XPS results. All variants of ozonation (conventional, catalytic, and photocatalytic) removed

Ozonation and Biodegradation in Environmental Engineering
https://doi.org/10.1016/B978-0-12-812847-3.00016-0

the terephthalic acid completely during 60 min; however, its reaction rate constant was higher in the catalytic and photocatalytic ozonation (22% and 25%, respectively). The ozone decomposition study indicated that terephthalic acid was degraded by the combined action of molecular ozone and hydroxyl radicals. The latter oxidant species play an important role in promoting the byproduct elimination generated during the ozonation of TA. The distribution of UV-ALEDs was evaluated in two configurations (central and external irradiation), which resulted in significant differences. These differences were confirmed by the reaction rates of the byproducts accumulation and their decomposition. Even when the energy supplied in both cases remained constant (4 W m^{-2}), the interaction between photons and active sites in the catalyst was twice higher, when the UV-ALEDs were on the peripheral of the reactor. All these results show that V_xO_y/ZnO is a potential catalyst for photocatalytic ozonation using a portion of the visible electromagnetic spectrum.

6.1 EFFECT OF UV-ALEDS ON TEREPHTHALIC ACID DECOMPOSITION BY PHOTOCATALYTIC OZONATION WITH V_xO_y/ZNO AND V_xO_y/TIO_2

Recent environmental concerns have led to the development of new treatment methods such as Advanced Oxidation Processes (AOPs) (Malato et al., 2010). AOPs are physico-chemical methods of changing the chemical structure of the pollutant resulting from species generation with a high oxidizing power (Andreozzi et al., 1999). Among AOPs, the photocatalytic ozonation process takes the advantages of both processes: ozonation and photocatalysis. On the one hand, the photocatalytic process allows for degradation of a variety of compounds, but with the disadvantage of applying the method at lower concentrated solutions (Elmolla and Chaudhuri, 2010). On the other hand, the ozonation treatment presents the drawback of accumulating recalcitrant products, so that a low mineralization degree could be obtained; however, this method can eliminate high concentrations of pollutants (Imai et al., 2009; Valsania et al., 2012; Xiao et al., 2015). Therefore, the combination of both processes seeks to increase the elimination rate of contaminated effluent and also reduces the treatment time. Moreover, one of the advantages of the photocatalytic ozonation with respect to the oxidation is reflected in the production of $OH^{\cdot}$. Previous studies show that in photocatalytic ozonation, a photogenerated electron yields the production of an $OH^{\cdot}$, to the contrary three electrons are needed in the photocatalytic oxidation with oxygen to produce only one $OH^{\cdot}$ (Zou and Zhu, 2008). Therefore, photocatalytic ozonation is a viable process to eliminate toxic and hazardous compounds.

Recently, the photocatalytic ozonation has been used for removing pharmaceutical compounds, organic acids, phenols, alcohols, dyes and pesticides (Xiao et al., 2015). It is worth to mention that in some cases the reaction rate of the compound degradation is higher in photocatalytic ozonation in comparison with the ozonation, photocatalysis, and photocatalytic oxidation due to the synergy of both processes (Wang et al., 2002a). Furthermore, an important factor in photocatalytic ozonation is the presence of a semiconductor, which must convert the absorbed photons into chemical energy (Mills and Le Hunte, 1997) to eliminate the contaminants subsequently. Theoretically, any semiconductor could be used in photocatalytic ozonation. However, in organic compound elimination, it is necessary that the valence band of the photocatalyst be sufficiently positive to permit the degradation of the compound and/or the generation of $OH^{\cdot}$; meanwhile the conduction band should be negative enough to carry out oxygen reduction and subsequent production of $OH^{\cdot}$ (Mehrjouei et al., 2011). In this sense, titanium oxide TiO_2 is the preferred semiconductor due to the optical and electronic properties, low cost, availability, high stability, and non-toxicity in both processes (photocatalytic oxidation and photocatalytic ozonation). Nonetheless, it is not the only semiconductor that could submit the previous characteristics. Indeed, there is an alternative catalyst, because of the valence position and the conduction bands, able of generating OH radicals as well (Vinu and Madras, 2012). ZnO may contribute to the degradation of organic pollutants and/or formation of $OH^{\cdot}$, which makes it a viable candidate for usage in photocatalytic ozonation.

The major limitation of both semiconductors (TiO_2 and ZnO) is their band gaps located at 3.2 eV (Karunakaran and Dhanalakshmi, 2008), which is only active in the UV region of the electromagnetic spectrum. For this reason, different techniques have been developed to reduce the band gap of various semiconductors and increase the energy absorption in the visible spectra (Qiu et al., 2008; Seabra et al., 2011; Vinodgopal and Kamat, 1995). Some of the methods, used for this purpose, are surface modification via organic materials and semiconductor coupling, band-gap modification by creation of oxygen vacancies, oxygen sub-stoichiometry (Karunakaran and Dhanalakshmi, 2008), nonmetal doping, co-doping of nonmetals, and modification by transition metal doping (Rehman et al., 2009). To the best of the author's knowledge, only TiO_2 and some of its modifications have been considered in the photocatalytic ozonation, but neither ZnO nor any of its modifications has been reported.

The photocatalytic treatment involves the irradiation of suitable semiconductor particles with light energy that exceeds the band gap, producing charge carriers (electrons and holes) that can be recombined and migrate

to the particle surface. Generally, a variety of publications reported the usage of mercury lamps, xenon lamps, and fluorescent lamps (Ahmed et al., 2011; Park et al., 2013). However, the photocatalytic process requires the presence of a source with a narrow irradiation spectrum of emission, so that the use of light emitting diodes, or LEDs, may be beneficial for the treatment of contaminated water. LEDs present a relevant advantage, since the LEDs have a lifetime between 30,000 to 50,000 h in comparison with fluorescent lamp (6000 h) or halogen lamp (2500 h) (Sayigh, 2013). Besides, almost the entire amount of energy, fed to a LED, is turned into light (Bahnemann and Robertson, 2015). Moreover, LEDs are an alternative to mercury lamps, since they have longer lives, lower energy consumption, and higher efficiency.

The aim of this chapter is to synthesize the catalysts based on V_xO_y supported on ZnO *and* TiO_2, as well as to evaluate their effect in the terephthalic acid (TA) degradation via photocatalytic ozonation. The TA was chosen as a model compound due to the wide application in manufacture industry of several products and also for its potential risk for human beings and environment impact due to its high COD (up to 20 kg m^{-3} per ton of compound produced) (Cheng et al., 2006; Kleerebezem et al., 1999). The effect of irradiation, generated by UV-ALEDs, which is located at the center and over the external perimeter of the reactor, is also studied.

6.1.1 Catalyst preparation

All used chemicals (TA, ammonium metavanadate, muconic acid, oxalic acid) as well as ZnO and TiO_2 were purchased from Sigma-Aldrich and applied without further treatment. The V_xO_y/TiO_2 and V_xO_y/ZnO catalysts synthesized by the impregnation method, which consisted of the adsorption of the ammonium metavanadate (NH_4VO_3), as precursor, from an aqueous solution on the supports (TiO_2 and ZnO) with the oxalic acid (•) or without it (×) during 12 h. After the impregnation, all samples were dried at 80°C (24 h) and finally calcined during 4 h at 400, 450 and 500°C (Fuentes et al., 2014). Table 6.1 presents the conditions of the synthesis of the catalysts.

6.1.2 Photolysis and photocatalysis

All the experiments were carried out in a double-vessel Pyrex semibatch cylindrical photoreactor with 2.0 L capacity at 25°C. The photoreactor lid has four ports for the inlet of the ozone–oxygen mixture that was distributed in the reactor by four ceramic porous filters in the form of tubes. In the central part of the reactor, the irradiation source (LEDs and UV lamp) was placed with 4 W m^{-2}. The LEDs, operating at 380–430 nm (model

Table 6.1 Influence of the synthesis conditions on the bandwidth energy of the metal oxides.

Catalysts of TiO_2			***E* (eV)**	**λ (nm)**
	Oxalic acid	**Temperature of calcination (°C)**		
TiO_2	×	×	3.42	361
V_xO_y/TiO_2(1)	•	400	3.39	365
V_xO_y/TiO_2(2)	•	500	3.37	367
V_xO_y/TiO_2(3)	×	450	3.29	376
Catalysts of ZnO			***E* (eV)**	**λ (nm)**
	Oxalic acid	**Temperature of calcination (°C)**		
ZnO	×	×	3.28	377
V_xO_y/ZnO(1)	•	400	3.25	381
V_xO_y/ZnO(2)	•	500	3.23	383
V_xO_y/ZnO(3)	×	450	3.21	385

FSL-5050SP150-N/B), used a 12.0 V DC power source, while the UV lamp (model HEL-20 W/BLB) has shown a wider emission (365–465 nm). The agitation in the system was provided by a magnetic bar, which was located at the bottom of the reactor. The TA (30 mg L^{-1}) adsorbed from an aqueous solution on the TiO_2 (0.1 g L^{-1}) in the dark during 30 min, then it irradiated in the reactor (1.5 L). An aliquot of 3 mL irradiated solution was withdrawn from the reactor at time intervals during 60 min.

6.1.3 Conventional, catalytic, and photocatalytic ozonations

The same experimental conditions of the photocatalysis maintained in the ozonation. An initial pH solution of 4.0 was considered in all experiments. This parameter was not adjusted during the ozonation to avoid the ion interference with the catalyst. The UV-ALED irradiation was performed in two ways: one used a glass body located at the center of the reactor to provide central emission ($LEDs_c$), and the other one placed the UV-ALEDs in the outer walls of the reactor ($LEDs_p$). The initial ozone concentration in gas phase was 10 mg L^{-1} and V_xO_y/TiO_2 and the V_xO_y/ZnO concentration was 0.1 g L^{-1}. The dissolved ozone in water was determined by a Dissolved Ozone Analyzer (DOA, LEPSE, Russia). For further information as regards the ozonation schematic diagram, see the previous publication Fuentes et al. (2014).

6.1.4 Analytic methods

The samples obtained during the ozonation were analyzed by Liquid Chromatography (HPLC) with a Flexar coupled with PDA detector (Perkin-Elmer) following the conditions reported in Fuentes et al. (2014).

6.1.5 Catalyst characterization

The UV-Vis diffuse reflectance spectra were recorded on an UV-Vis Perkin-Elmer Lambda 9 with an integration sphere. Specific surface area was determined from the nitrogen adsorption isotherms at −196°C measured in a Micromeritics. Photoelectron core-level spectra of samples were obtained with an X-ray photoelectron spectroscopy (XPS) system, SPECS brand, equipped with a Phoibos 15 0 mm wide angle hemispherical energy electron analyzer, using a 2D-delay line detector: Micro-Focus 500 model monochromatic Al $K\alpha$ X-ray source (1487 eV). The base pressure of the system was $6 \cdot 10^{-10}$ mTorr. The powder samples were mounted on a double-sided carbon tape. High resolution scans were collected on a 400 μm spot size at 50 eV analyzer pass energy. C1s at 284.6 eV was the internal reference for charge correction (spectra not shown for the sake of clarity). In general, no substantial differences were observed for the carbon signal for the different samples, which were of a similar shape. All the spectra are fitted with a main peak for –C–C, –CH species and minor peaks for oxidized carbon species. Raw data were fitted with Gaussian–Lorentzian (70–30%) curves and a Shirley-type background. The CasaXPS 2.3.16 software package was employed to process the data. The samples were also characterized by TEM, using a JEOL JEM 2010 operated at 200 kV. The specimens were prepared by dispersing the sample in isopropyl alcohol with an ultrasonic bath. A drop of dispersion was left on a carbon-coated Cu grid.

6.2 RESULTS AND DISCUSSION

6.2.1 V_xO_y/TiO_2 and V_xO_y/ZnO characterization

6.2.1.1 Diffuse reflectance UV-Vis spectroscopy

The diffuse reflectance technique provides the information regarding the bandwidth of both commercial metal oxides and the synthesized catalysts modified by vanadium. Some synthesis by impregnation uses oxalic acid for its possible contribution to increase the solubility of the ammonium metavanadate precursor. Table 6.1 presents the conditions of the catalyst synthesis and their influence on the bandwidth energy of the metal oxides.

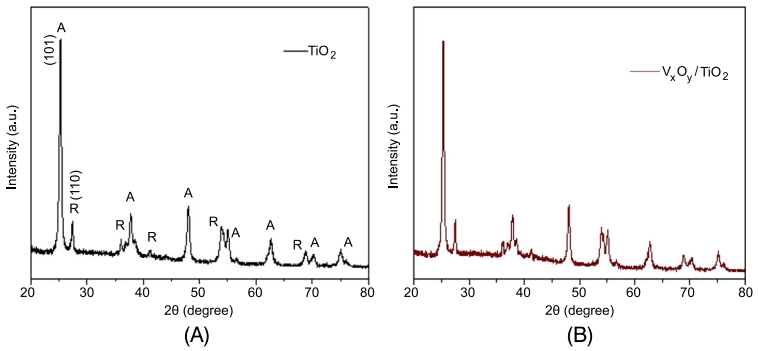

■ **FIGURE 6.1** Diffraction pattern of the zinc oxide and TiO_2.

The commercial ZnO banned band is 3.28 eV, being modified with vanadium in the presence of oxalic acid, and at a calcination temperature of 500°C, its band banned decreased to 3.23 eV. By the removal of the oxalic acid and the calcination at 450°C, the prohibited band changes to 3.21 eV, corresponding to a wavelength of 385 nm. Similar results were obtained by the modification with other ions. In the case of TiO_2, a similar effect was obtained in the absence of oxalic acid and a calcination temperature of 450°C. The prohibited band changed to 3.29 eV, corresponding to a wavelength of 376 nm. These results indicate that the impregnation method with vanadium permits the modification of the prohibited band (the best result did not use the acid). Based on the data in Table 6.1, we selected only the materials synthesized by the route (3), i.e. without oxalic acid and with a calcination temperature of 450°C.

6.2.2 **X-ray diffraction**

In addition to the optical properties of the metal oxides before and after being surface modified, it is also necessary to determine the crystal structure of both semiconductors prior to and after their impregnation with vanadium. This characterization was carried out by the X-ray diffraction technique (XRD). As shown in Fig. 6.1, the TiO_2 has two most stable crystalline phases, anatase and rutile, and they were kept invariant after the impregnation with vanadium.

Fig. 6.2 shows the diffraction patterns of the fresh ZnO and it is an impregnated variant with vanadium. The same signals were detected in the commercial oxides. This similarity indicates that the original structures in the oxide are preserved. However, the intensity and the width of vanadium peaks decreased in the case of unmodified oxides. The decrease of the intensity indicates that the crystallinity of the supports is affected. The peak

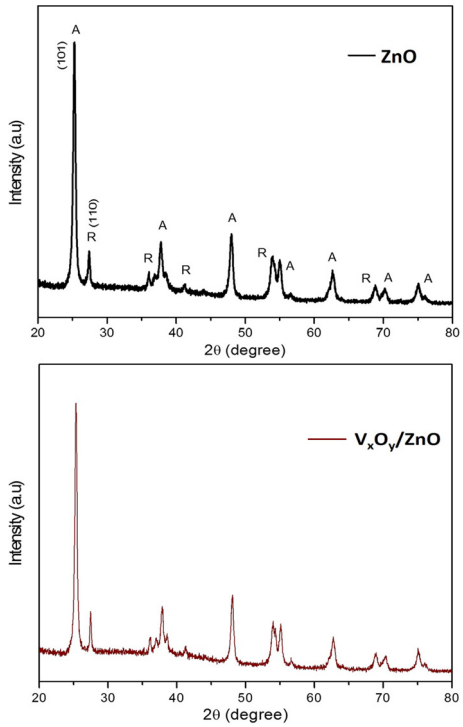

■ **FIGURE 6.2** Diffraction pattern of the TiO_2 impregnated with vanadium.

width change corresponds to an increase in the crystal size. No additional vanadium signal was detected. This result may be a consequence of its low concentration (1% by weight), which was below the detection limit.

A similar analysis was proposed for the ZnO. Based on the diffraction patterns, we calculated the crystal size using the Scherrer equation and the percentage of anatase present in the TiO_2. The ZnO sample has a crystal size of 39 nm with no anatase content. If the vanadium oxide is impregnated in the ZnO, then the crystal size increases up to 41 nm, but anatase is still not detected. On the other hand, the crystal size of TiO_2 is smaller (22 nm) but the content of anatase is 81%. The presence of vanadium modified the crystal size to 24 nm but the anatase content did not change. The increase of the crystal size was observed for both catalysts due to the presence of vanadium.

6.2.3 **Surface area**

Table 6.2 summarizes the textural properties of the semiconductors with and without vanadium impregnation.

Table 6.2 Microstructural properties of the semiconductors with and without vanadium impregnation.

Catalyst	Surface area $m^2\ g^{-1}$	Pore volume $cm^3\ g^{-1}$	Pore diameter A°
ZnO	5.80	0.022	153.03
V_xO_y/ZnO	8.60	0.0192	115.45
TiO_2	48.35	0.164	168.07
V_xO_y/TiO_2	14.57	0.072	231.75

The presence of the vanadium on the ZnO caused a 50% increase in the specific area, practically without affecting the pore volume. This result is consistent with some preliminary studies, where it was reported that there is an increment of the specific area caused by the presence of the vanadium (Li et al., 2005). The presence of the vanadium does not affect significantly the semiconductor band gap, considering that the amount of the vanadium is $\sim 1\%w$. The opposite effect was in the case of the TiO_2, where the vanadium caused a drastic decrease in the specific area by 70%. Also, the pore volume decreased by 50%. This indicates that possibly the most of the vanadium mass penetrated in the pores of the support and remained deposited in them. Notice that the specific area of TiO_2 is 10 times higher than the ZnO area, and the pore size also is higher, by 83%. Even after the impregnation the specific area of V_xO_y/TiO_2 is almost twice more than the area of V_xO_y/ZnO. So, we expect a higher activity of the V_xO_y/TiO_2 in photocatalysis and in photocatalytic ozonation.

6.2.4 Surface electron microscopy

Surface electron microscopy (SEM) is a technique characterizing the morphology of catalysts and it can be used to establish the presence of vanadium (Fig. 6.3A–C).

Fig. 6.3A shows the morphology of the TiO_2 as almost cylindrical particles with large particle sizes (on the order of 50–100 nm). This figure also shows the presence of thinner flakes with a lighter contrast and dotted by whiter spots, mixed in between the TiO_2 crystals, which could correspond to vanadium oxide. Fig. 6.3B shows the EDS analysis showing the weak signal corresponding to V_xO_y. Nonetheless, the thinner flakes appear to be unsupported on TiO_2, which may be a limiting factor in the transfer of photogenerated electrons. These results agree with the result of TEM because unsupported flakes increase the surface area of V_xO_y/TiO_2 catalyst. Fig. 6.3C demonstrates the SEM study for the case of ZnO. A less structured flake is shown here, which corresponds to the ZnO structure, and some small sections that may correspond to the presence of vanadium oxide. In the case

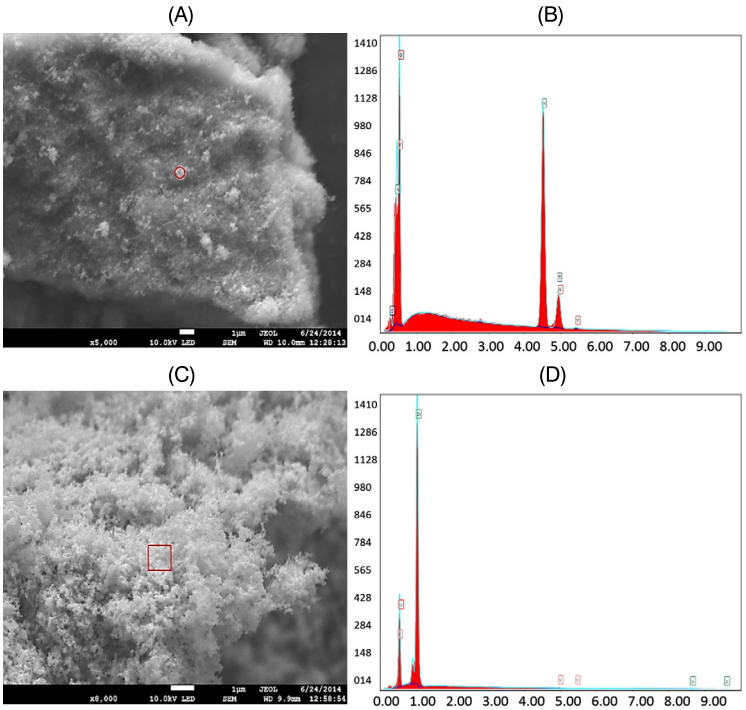

■ **FIGURE 6.3** SEM analysis for powders, (A) V_xO_y impregnated on the TiO_2 and (B) V_xO_y impregnated on the ZnO including the EDS analysis.

of ZnO with vanadium, the particles have a regular semispheric form, their size coincided with the value calculated by the XRD technique (20–50 nm). The EDS study confirms that the vanadium metal was poorly observed, as a consequence of its intromission in the pores of the support or its introduction in the crystalline section to the ZnO (Fig. 6.3D).

6.2.5 X-ray photoelectron spectroscopy (XPS)

Fig. 6.4 displays the XPS spectra for the ZnO and TiO_2. This study and the corresponding deconvolution confirmed that the region with Zn2p reveals the presence of Zn^{4+} with a $2p_{3/2}$ peak at 1021.2 eV only; the fittings are very close to the raw data. In the O1s region, besides the expected $–O^{2-}$ species, peaks of relatively large intensity are disclosed for –OH, $–CO_x$ and H_2O. The region for $V2p_{3/2}$ forms a *curved* background. Once the vanadium is incorporated onto the ZnO surface, V_xO_y/ZnO new spectra are recorded. While no major changes are observed for Zn2p, the O1s contributions for –OH, $–CO_x$ and H_2O are now strongly diminished. The peak for $V2p_{3/2}$ has a maximum at 516.6 eV, which lies in between the reported

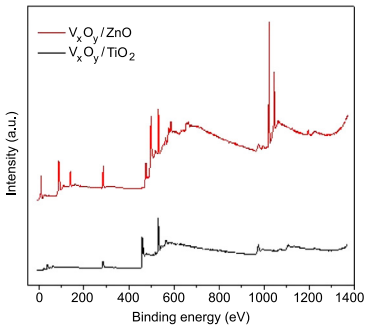

■ **FIGURE 6.4** High resolution general XPS spectra of V_xO_y/ZnO (upper line) and V_xO_y/TiO_2 (lower line).

Table 6.3 Atomic percentages obtained by the XPS of the catalysts prior to photocatalytic ozonation.

Catalyst	**%V [V/Zn]**	**%Zn [Zn/Zn]**	**%O [O/Zn]**	**%C [C/Zn]**	**V^{3+} V^{4+}**
V_xO_y/ZnO	3.4[0.09]	35.8[1]	40.5[1.13]	20.3[0.57]	0.38
Catalyst	**V[V/Ti] %**	**Ti[Ti/Ti] %**	**O[O/Ti] %**	**C[C/Ti] %**	**V^{5+} V^{4+}**
V_xO_y/TiO_2	1.7[0.1]	20.1[1]	52.1[2.6]	26.1[1.3]	0.56

energies for VO_2 and V_2O_5. The application of a precise fitting procedure is not possible due to the background features brought up by ZnO.

In the case of V_xO_y/TiO_2, the vanadium species of V^{4+} (516.2 eV) and V^{5+} (517.2 eV) are also present (Fig. 6.5A). In the region of Ti2p, there are two signals, one at 458.4 eV and the other at 464.2 eV, both corresponding to Ti^{4+} (Fig. 6.5B). However, the signal at 460.4 eV was not identified, probably due to the modification of Ti. Additionally, the signals corresponding to the oxygen are presented in the metal oxide (529.7 eV) and as a result of the hydration of the material (531.4 eV) (Fig. 6.5C). The carbon signals (C1s) from the environment or after the synthesis are presented in Fig. 6.5D.

Table 6.3 contains the concentration of the surface species of the photocatalysts prior to their contact with ozone. The content of the vanadium is higher in V_xO_y/ZnO (3.4%) than V_xO_y/TiO_2 (1.7%) due to the vanadium deposited inside the pores of the TiO_2. Notice that each material has a different vanadium species. In V_xO_y/ZnO the ratio of V^{3+}/V^{4+} (0.38) is lower than the ratio of V^{5+}/V^{4+} (0.56) in V_xO_y/TiO_2. The instensity of V^{4+} is higher in V_xO_y/ZnO.

In the catalytic and photocatalytic ozonation, it is very important to know what the stability of the catalyst is after its contact with ozone and how

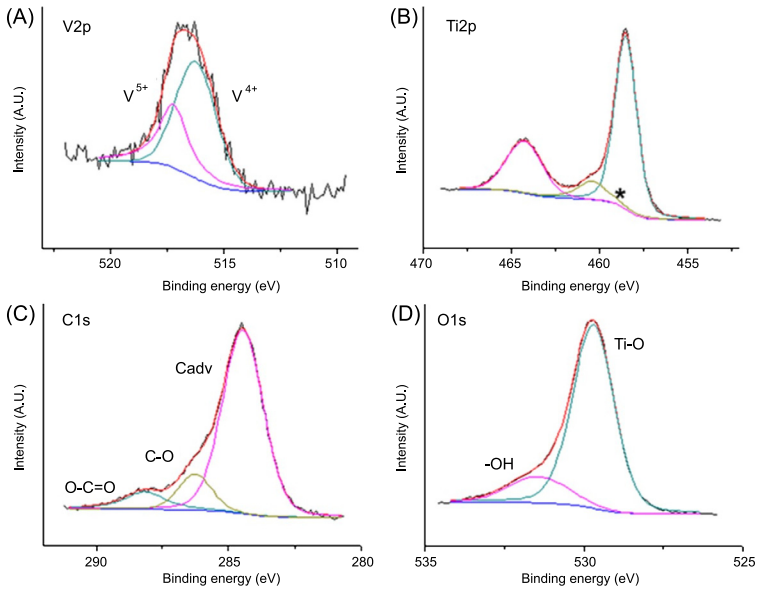

■ **FIGURE 6.5** XPS spectrum of the V_xO_y/TiO_2 before the photocatalytic ozonation: V2p (A), Ti2p (B), C1s (C) and O1s (D).

Table 6.4 Atomic percentages of the V_xO_y/ZnO and V_xO_y/TiO_2 after the contact with ozone obtained by the XPS technique.

Catalyst	V[V/Zn] %	Zn[Zn/Zn] %	O[O/Zn] %	C[C/Zn] %
O_3–V_xO_y/ZnO–LEDs	3.1[0.09]	35.3[1]	41.7[1.18]	19.8[0.56]
Catalyst	**V[V/Ti] %**	**Ti[Ti/Ti] %**	**O[O/Ti] %**	**C[C/Ti] %**
O_3–V_xO_y/TiO_2–LEDs	0.7[0.03]	21.2[1]	50.2[2.4]	27.9[1.3]

this changes the composition of the active species on the catalyst surface. Table 6.4 contains the concentration of the surface species of the photocatalysts after their contact with ozone.

It is observed that after contact with ozone and irradiation in the V_xO_y/ZnO surface no V^{3+} was detected. In the V_xO_y/TiO_2 also V^{5+} was not detected. The percentage of the vanadium in the V_xO_y/ZnO was reduced by 0.3% only, while in the case of V_xO_y/TiO_2, the vanadium content decreased by 1%. This indicates that V_xO_y/ZnO has greater stability in the photocatalytic ozonation than V_xO_y/TiO_2.

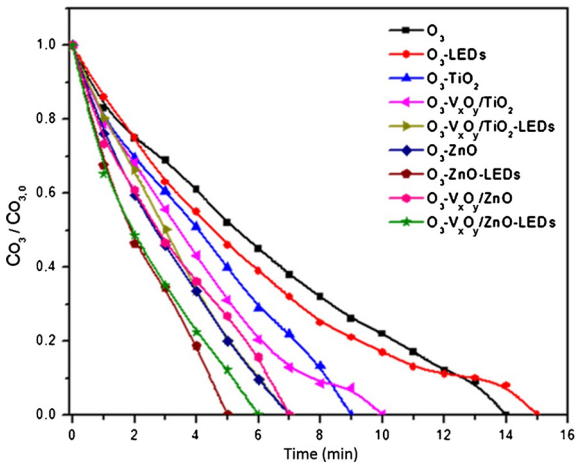

■ **FIGURE 6.6** Ozone decomposition in all studied systems.

6.2.5.1 Ozone decomposition

The dissolved ozone measurements provide an indirect way to determine the ozone decomposition and the possible formation of oxidant species. Conventional and catalytic ozonation may produce hydroxyl radicals as a result of ozone decomposition and this production may be faster in the catalytic process. Photocatalytic ozonation besides the presence of hydroxyl radicals has a contribution of other species like ions, radicals, electrons, and holes generated by the irradiation of the photocatalyst. All of these species can participate in further pollutant degradation. It may be reasonable to suppose that systems with higher ozone decomposition may eliminate a greater proportion of the initial compound and its intermediates. Fig. 6.6 shows the ozone decomposition profiles for the nine systems.

The decomposition of the dissolved ozone shows a linear trend in time; however, the decomposition rate strongly depends on the system. It is worth noting that a faster ozone decomposition (5–7 min) occurred in the systems with ZnO, such as O_3–ZnO, O_3–V_xO_y/ZnO, O_3–ZnO–LEDs, and O_3–V_xO_y/ZnO–LEDs, and the presence of ZnO and V_xO_y/ZnO contributed to an increment of the ozone decomposition. In the other two systems with TiO_2, such as O_3–TiO_2, O_3–V_xO_y/TiO_2, the time of the ozone decomposition is increased to 9–10 min; however, the O_3–V_xO_y/TiO_2–LEDs system demonstrated the total degradation of ozone during only 7 min, which confirms the higher ability of this system in the photocatalytic ozonation of the phthalic acid. The life time of ozone is larger ($\sim$ 15 min) without the catalyst and only under the irradiation. Probably the systems that decompose

the ozone faster achieve a greater degree of mineralization than the rest of the systems.

6.2.5.2 Photolysis and photocatalysis

Considering that the adsorption of the model compound on the surface of the solid material did not exceed 6–8% for two catalysts during 60 min, going to equilibrium as regards the adsorption and the desorption of the terephthalic acid, the irradiation of the reactor started after 30 min. The photolysis with LEDs and the black light lamp is ineffective and eliminates only 5% and 3% of the terephthalic acid, respectively, while the photocatalysis shows better results. The photocatalysis with the ZnO eliminates only 20% of TA, the surface modification of zinc oxide with vanadium causes a decrease up to 12%. Similar results were obtained for TiO_2 (18%), and the surface modification with vanadium decreased its catalytic effect up to 2%. So, the modification of the catalyst surface with the vanadium leads to a decrease of the efficacy of the TA decomposition. The observed negative effect of the catalyst modification may be explained by the fact that the vanadium lamellae, observed in TEM, are not supported in the semiconductor. In the case of V_xO_y/TiO_2, it could be due to the decrease in surface area. In this case, photocatalysis is an inefficient process due to the use of oxygen as an oxidizing agent, since it requires three electrons for each generated hydroxyl radical. For this reason, it is better to use ozone as a photogenerated electron capture agent, due to a lower electron consumption for the formation of OH radicals in conventional, catalytic, and photocatalytic ozonation.

6.2.5.3 Decomposition of the terephthalic acid by the conventional, catalytic and photocatalytic ozonation

6.2.5.3.1 Conventional ozonation

Fig. 6.7 shows the decomposition of the TA in three systems (conventional, and photocatalytic ozonation with both catalysts TiO_2 and ZnO). One may notice that there is an insignificant difference of the TA decomposition in the three systems.

Therefore, the combination of conventional ozonation with the LEDs (photolytic ozonation) accelerated the formation of some intermediates, but their decomposition slowed down and they not completely eliminated for one hour. In general, the significant difference with the conventional ozonation was not observed.

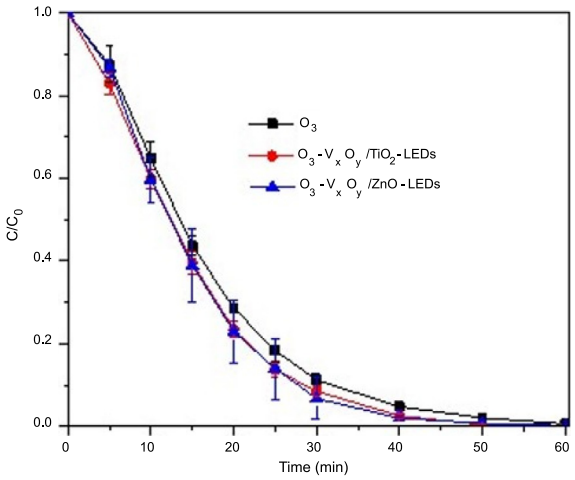

■ **FIGURE 6.7** Decomposition of the TA in the conventional and photocatalytic ozonation in the presence of both catalysts ZnO and TiO_2.

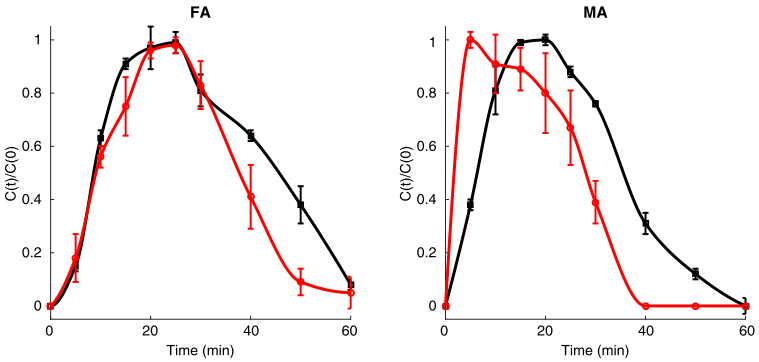

■ **FIGURE 6.8** Comparison of the profiles of fumaric (left) and muconic (right) acids in the presence of the two catalysts ZnO and TiO_2.

6.2.5.3.2 Catalytic ozonation

The profiles of the intermediates were presented in Fig. 6.8 (left and right sub-figures) in the presence of the two catalysts ZnO and TiO_2.

There is a difference in the profiles of the byproducts (fumaric and muconic acids). The presence of the ZnO accelerated the formation (during 5 min) and the decomposition (40 min) of the muconic acid in comparison with TiO_2 (up to 60 min). In the case of the fumaric acid, both catalysts produced the same formation profiles. However, its decomposition is faster with ZnO (50 min).

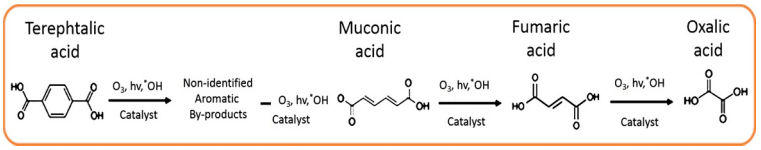

■ **FIGURE 6.9** Reaction scheme of the TA decomposition in the photocatalytic ozonation.

In the presence of the ZnO, the formation of muconic acid was faster (5 min) than with the TiO_2 (20 min). The decomposition profile was also faster (40 min).

6.2.5.3.3 Photocatalytic ozonation

Previous studies (Fuentes et al., 2014; Sayigh, 2013) demonstrated that the TA decomposition by conventional, catalytic and photocatalytic ozonation was very similar in the studied systems. The photocatalytic ozonation of the TA in the presence of the ZnO, the TiO_2 and the metal oxides, modified by the vanadium did not show the significant difference compared with the catalytic ozonation. The profiles of some intermediates have demonstrated several differences. Therefore, one may claim that the reaction scheme of the TA decomposition did not show significant differences in comparison to the catalytic or photocatalytic ozonation (Fig. 6.9).

6.2.5.3.4 Oxalic acid characterization

Depending on the value of the OA concentration, as well as its decomposition are two criterions to define the efficacy of the treatment system. In this particular case, it did not show the decomposition during the observed time (60 min). As a summary, Fig. 6.10 shows the similar accumulation of oxalic acid in each studied system, (catalytic and photocatalytic ozonation).

Also, we may observe that the lowest concentration of the oxalic acid (10 mg L^{-1}) is formed in the systems of O_3, O_3–TiO_2, O_3–LEDs and O_3–TiO_2/LEDs. On the other hand, the modification of the TiO_2 by the vanadium leads to the maximum concentration of the oxalic acid (21 mg L^{-1}) in the catalytic, as well as in the photocatalytic ozonation. On the contrary, the systems with the ZnO are more active in the catalytic and the photocatalytic ozonation, because the oxalic acid concentration increases up to 13–15 mg L^{-1}. However, the effect of the modification of the ZnO with the vanadium is equal to zero. This result coincides with the catalyst activity in the decomposition of the ozone dissolved in water.

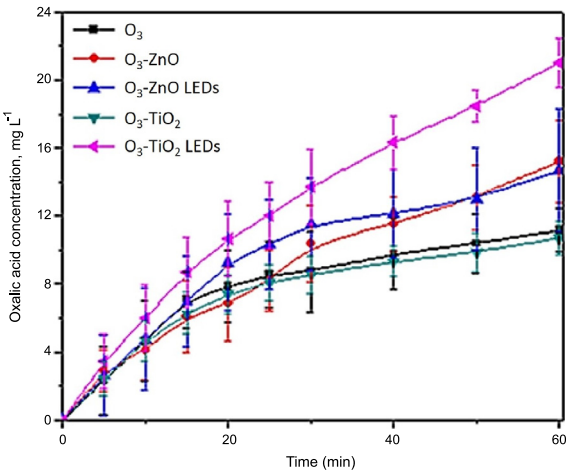

■ **FIGURE 6.10** Oxalic acid behaviors in the catalytic and the photocatalytic ozonation with the ZnO and the TiO_2.

6.2.6 **Simple kinetics**

The model characterizing the reaction kinetics throughout the ozonation of the TA has the mathematical structure given by

$$\frac{d}{dt}c_{TA}(t) = -k_{TA}c_{TA}(t), \quad c_{TA}(0) = c_{TA,0}. \tag{6.1}$$

Here k_{TA} is the reaction rate constant associated to the TA variation, $c_{TA}(t)$ is the time variation of the main contaminant during ozonation. This simple model is proposed to represent a pseudo-first order reaction that describes the decomposition of the TA. In the case of intermediates concentration, this simplified model has the form:

$$\frac{d}{dt}c_j(t) = k_{j,a}c_{TA}(t) - k_{j,d}c_j(t), \quad c_j(0) = c_{j,0}, \tag{6.2}$$

where $k_{j,a}$ is the reaction rate constant associated to the accumulation of the byproduct j, $c_j(t)$ is the variation of the corresponding byproduct and $k_{j,d}$ is the reaction rate constant, associated to the decomposition of the byproduct j. In the case of the OA, the constant $k_{j,d}$ can be set to zero. Nevertheless, this condition assumes that accumulated byproducts should be produced directly from the decomposition of the TA. A better option is to propose an alternative model, where the connection between intermediate and final products accumulated can be highlighted. This model is given by

$$\frac{d}{dt}c_k(t) = k_{jk,a}c_j(t) - k_{jk,d}c_k(t), \quad c_k(0) = c_{k,0}. \tag{6.3}$$

The parameter $k_{jk,a}$ is the reaction rate constant that characterizes the accumulation of the final product k, $c_k(t)$ is the variation of the main byproduct accumulated at the end of the reaction and $k_{jk,d}$ is the reaction rate constant associated to the decomposition of the byproduct k. The models described by Eqs. (6.1), (6.2) and (6.3) are linear with respect to their corresponding parameters. However, they have, as independent variables, the time derivatives of the variables under modeling analysis (the TA and its corresponding intermediate and final byproducts). This situation complicates the parametric characterization of the reaction proposed to model the effect of ozone on these two variables. The solution of the parametric identification problem, that is, to get either k_{TA}, $k_{j,a}$, $k_{j,d}$, $k_{jk,a}$ and $k_{jk,d}$ can be obtained by the application of a robust exact differentiator such as the one presented by Cruz-Zavala et al. (2011a). The robust differentiator produces an approximation for the derivative of the concentration for each compound (6.5). The output of the differentiator is represented as $y(t)$. As an example, under the condition proposed to the gains, the model presented in (6.2) can be represented as follows:

$$y(t) = k_{j,a}c_{TA}(t) - k_{j,d}c_j(t) + \varepsilon(t). \tag{6.4}$$

The variable $y(t)$ is the approximation of the time derivative of the variable under analysis. The term $\varepsilon(t)$ describes the approximation error produced by the implementation of the differentiator applied in the following manner:

If the signal that must be differentiated is represented as $\nu(t)$, let introduce the variables $\nu = \nu_1$ and $\frac{d}{dt}\nu = \nu_2$. Therefore, ν can be represented in a state variable form such as:

$$\begin{aligned} \frac{d}{dt}\nu_1(t) &= \nu_2(t), \\ \frac{d}{dt}\nu_2(t) &= \frac{d}{dt}\nu_2(t). \end{aligned}$$

If the second derivative of $\nu(t)$ is bounded, that is,

$$\left|\frac{d}{dt}\nu_2(t)\right| \leq \nu^+, \quad \nu^+ \in \mathbb{R}_+,$$

the corresponding differentiator obeys

$$\begin{aligned} \frac{d}{dt}z_1(t) &= z_2(t) + k_1|e_1(t)|^{1/2}\text{sign}(e_1(t)), \\ \frac{d}{dt}z_2(t) &= k_2\text{sign}(e_1(t)) + \frac{d}{dt}\nu_2(t), \\ e_1 &= z_1 - \nu_1. \end{aligned} \tag{6.5}$$

Then if the gains are positive with $k_1 > k_2 > \nu^+$, then

$$\hat{d}(t) = z_2(t) + k_1|e_1(t)|^{1/2}S(e_1(t))$$

where $\hat{d}(t)$ is the approximation of the derivative for $\nu(t)$.

The parametric identification problem presented in Eq. (6.4) can be solved by the well-known least mean squares method. This method cannot be applied directly because the signals of $x\,(t)$ and $O_3\,(t)$ are measured with different sampling times. Therefore, an interpolation algorithm was applied to homogenize the number of samples that can be used in the parametric identification method, applying an equally time span with similar sampling time. The interpolation algorithm used an approximation based on third order polynomials (cubic) of ozonogram. The model proposed in (6.4) can be represented as

$$y(t_k) = \theta^{\intercal}\varphi(c_{TA}(t_k), c_j(t_k)) + \varepsilon(t_k). \tag{6.6}$$

The vector θ represents the unknown parameters in the model and the function $\varphi\left(C_{AT}\,(t)\,, C_j\,(t)\right)$ collects the experimental data in the model. The time t_k represents the sampling time ($1 \leq k \leq K$). The term ϵ represents the modeling error obtained as a solution of the least mean square model. The solution of the parametric modeling strategy is

$$\theta^* = \left[\sum_{k=1}^{K} \varphi(c_{TA}(t_k), c_j(t_k)) \cdot \varphi^{\intercal}(c_{TA}(t_k), c_j(t_k))\right]^{-1} \cdot \left[\sum_{k=1}^{K} \varphi(c_{TA}(t_k), c_j(t_k)) \cdot y(t_k)\right] \tag{6.7}$$

Table 6.5 contains the summary of the reaction rate constants, as well as their confident intervals. The kinetic study was supported by the narrow confident intervals obtained for the reaction rate constants calculated by the method proposed in this study. The additional parameters, which confirmed the validity of this analysis, were the correlation coefficients. All these values were over 0.80.

As the first result of the kinetic analysis, the decomposition rate of the TA increased (28.5%) by the presence of the catalyst, while the presence of UV-ALEDs showed not relevant effect over the catalytic reaction. A no significant variation, less than 4.0% for the reaction rate was obtained, when UV-ALEDs were used in the reaction compared with the catalytic reaction.

Conventional ozonation showed a slower (20% of the larger velocity showed by catalytic ozonation) accumulation of muconic acid. The photocatalytic ozonation increases this accumulation velocity 152.0% (central)

Table 6.5 Reaction rate constants for the conventional, catalytic and photocatalytic ozonation. TA = Terephtalic acid, MA = Muconic acid and OA = Oxalic acid.

Acid	Rate s^{-1}	Ozonation process	Value	Conf. interv.	Corr. coef.
TA		O_3	0.0512	0.0510–0.0515	0.9984
		O_3/ZnO	0.0523	0.0511–0.0596	0.9968
	k_{AT}	O_3–V_xO_y/ZnO	0.0656	0.0654–0.0659	0.9986
		O_3–V_xO_y/ZnO–LEDSc	0.0644	0.0641–0.0647	0.9983
		O_3–V_xO_y/ZnO–LEDSp	0.0628	0.0623–0.0629	0.9979
MA		O_3	0.0457	0.0454–0.0460	0.9202
		O_3/ZnO	0.5680	0.5512–0.5785	0.9356
	$k_{1,a}$	O_3–V_xO_y/ZnO	0.2164	0.2155–0.2173	0.8691
		O_3–V_xO_y/ZnO–LEDSc	0.1152	0.1145–0.1160	0.8025
		O_3–V_xO_y/ZnO–LEDSp	0.1827	0.1821–0.1834	0.8255
		O_3	0.0679	0.0677–0.0682	0.9202
		O_3/ZnO	0.0789	0.0706–0.0956	0.8895
	$k_{1,d}$	O_3–V_xO_y/ZnO	0.1478	0.1471–0.1484	0.8691
		O_3–V_xO_y/ZnO–LEDSc	0.0654	0.0649–0.0660	0.8025
		O_3–V_xO_y/ZnO–LEDSp	0.1214	0.1209–0.1219	0.8255
OA		O_3	0.0500	0.0498–0.0503	0.8912
		O_3/ZnO	0.0365	0.0342–0.0398	0.9212
	$k_{11,a}$	O_3–V_xO_y/ZnO	0.0359	0.0356–0.0362	0.9325
		O_3–V_xO_y/ZnO–LEDSc	0.0424	0.0421–0.0427	0.8365
		O_3–V_xO_y/ZnO–LEDSp	0.0296	0.0293–0.0300	0.0821

and 300.0% (peripheral) with respect to the conventional process. They were slower than the one obtained, when only the catalytic reaction was evaluated. This condition can be either a consequence of a faster transformation of muconic acid into their corresponding byproducts or a slower transformation from the TA into this aromatic byproduct. However, the similarities of the decomposition reaction rate has been obtained for the TA, and therefore the first possibility seems to be more appropriate. A relevant difference of the muconic acid decomposition was observed, when the catalytic reaction was compared to the conventional ozonation. An increment of 117% in the reaction rate was characterized by the catalytic process studied in the Chapter 5. This property was similar to the case, when the photocatalytic process with peripheral UV-ALEDs was evaluated (the increment was 78%), but it was equally incorrect, when the UV-ALEDs were placed in the interior of the reactor. Then the MA was eliminated more efficiently if UV-ALEDs were placed on the peripheral, because photons can travel along the whole trajectory of the reactor. This condition cannot be attained, when UV-ALEDs are placed in the interior, because photons travels only a distance corresponding to the radius of the reactor.

The initial rate of the OA accumulation, in the case of the conventional ozonation, coincides with the decomposition rate of the TA ($5.12 \cdot 10^{-2}$ s^{-1} and $5.00 \cdot 10^{-2}$ s^{-1}). The presence of the catalyst and the irradiation decreases it to $2.96 \cdot 10^{-2}$ s^{-1}. This fact can be explained by the more effective decomposition of all intermediates, including the partial degradation of the OA, although, during the observed time (60 min) the degradation of OA was not detected.

In this case, the constant $k_{j,d}$ can be set to zero, because the OA is not decomposed. Taking into consideration the results obtained for the TA, as well as for the muconic acid, the photocatalytic ozonation with *UV-ALEDs*, placed at the peripheral of the reactor, can provide the most appropriate condition to remove the TA and its ozonation byproducts.

6.3 MATHEMATICAL MODEL OF THE PHOTOCATALYTIC OZONATION

An extension to the mathematical model, presented in Chapter 2, taking into account the presence of intermediate and final byproducts, must consider the effect of catalyst with irradiation. The proposed model has the following

mathematical structure:

$$\left.\begin{aligned}\frac{d}{dt}O_{3,gas}(t) = -V_g^{-1}\left[c_t^g u_1(t) - u_2(t) + \right.\\ \left. k_{sat}(Q_{\max} - Q(t)) - Q(t)\sum_{i=1}^{N} k_i c_i(t)\right],\end{aligned}\right\} \tag{6.8}$$

$$\left.\begin{aligned}\frac{d}{dt}O_{3,liq}(t) = k_{sat}(Q_{\max} - Q(t)) - \\ Q(t)\sum_{i=1}^{N} k_i c_i(t) - k_{F,OH}(t)\,Q(t),\end{aligned}\right\} \tag{6.9}$$

$$\left.\begin{aligned}\frac{d}{dt}c_i(t) = -k_{i,O_3}c_i(t)\,O_{3,liq}(t) - \\ \sum_{j=1}^{r} k_{i,j,R_i}R_j(t)\,c_i(t) - k_{OH,i}c_i(t)\,c_{OH^\cdot}(t),\end{aligned}\right\} \tag{6.10}$$

$$\left.\begin{aligned}\frac{d}{dt}R_j(t) = k_{cat,j}c_{cat}(t)\,O_{3,liq}(t) - \\ \sum_{i=1}^{I} k_{ji,O_3}R_j(t)\,c_i(t) - k_{OH,R_j}R_j(t)\,c_{OH^\cdot}(t),\end{aligned}\right\} \tag{6.11}$$

$$\left.\begin{aligned}\frac{d}{dt}B_k(t) = \sum_{i=1}^{I} k_{k,i}c_i(t)\,O_{3,liq}(t) + \\ \sum_{i=1}^{J} k_{k,j}c_i(t)\,R_j(t) - k_k B_k(t)\,O_{3,liq}(t) - \\ \sum_{j=1}^{r} k_{k,j}B_k(t)\,R_j(t) - k_{OH,B_k}R_j(t)\,c_{OH^\cdot}(t),\end{aligned}\right\} \tag{6.12}$$

$$\left.\begin{aligned}\frac{d}{dt}c_{OH^\cdot}(t) = k_{OH,F}(t)\,c_{OH^-}(t)Q(t) - \sum_{i=1}^{N} k_{i,O_3}c_i(t)\,c_{OH^\cdot}(t) \\ - \sum_{j=1}^{N} k_{OH,R_j}R_j(t)\,c_{OH^\cdot}(t) - \sum_{j=1}^{N} k_{OH,B_k}B_k(t)\,c_{OH^\cdot}(t).\end{aligned}\right\} \tag{6.13}$$

The new variables and parameters included in the model that consider the intermediate and final products are

- k_{i,j,R_j}, is the reaction rate constant of the formation of the intermediate R_j [L mol^{-1} s^{-1}],
- $\tilde{k}_{i,j,R_j}$, is the reaction rate constant of the decomposition of the intermediate R_j [L mol^{-1} s^{-1}],
- $k_{k,i}$, is the reaction rate constant of the formation of the final product B_k [L mol^{-1} s^{-1}],
- k_{k,B_k}, is the reaction rate constant of the decomposition of the final product B_k [L mol^{-1} s^{-1}].

Notice that the photocatalytic effect can be characterized by the new time-varying reaction rate parameter of the $^{\cdot}$OH formation $\left(k_{F,OH}(t)\right)$ as follows:

$$k_{F,OH}(t) = \tilde{k}_{F,OH} \frac{e^{-a(\lambda(t)-\lambda_0)^2}}{1 + be^{-c(I(t)-I_0)}},$$

or, in differential form,

$$\left.\begin{aligned} \dot{k}_{F,OH}(t) = -a^2(\lambda(t)-\lambda_0)\, k_{F,OH}(t)\, \dot{\lambda}(t) + \\ \frac{c k_{F,OH}(t)}{b^{-1}e^{c(I(t)-I_0)} + 1} \dot{I}(t), \\ k_{F,OH}(0) = k^0_{F,OH}, \end{aligned}\right\} \tag{6.14}$$

where

– $\tilde{k}_{F,OH}$ is the reaction rate constant of the $^{\cdot}$OH formation at $\lambda(t) = \lambda_0$ and $I(t) \to \infty$,

– λ, is the current wavelength of the light used to stimulate the catalyst (nm),

– λ_0 is the characteristic wavelength of the catalyst (nm),

– a is a constant characterizing the variation of the gain with respect to the wavelength (m^{-2}),

– I is the current irradiance of the light applied over the catalyst (E m^{-2} s^{-1}),

– I_0 is the irradiance corresponding to the light saturation of the catalyst (E m^{-2} s^{-1}),

– b is a characteristic parameter that defines the saturation property of the catalyst with respect to the light intensity (E^{-1} m^2 s^1).

Considering the functions $k_{F,OH}(t)$ as the new variable of the dynamic photocatalytic model (6.8)–(6.13), we can apply the DNN observer, described above in Chapter 4, to obtain the estimates $\hat{k}_{F,OH}(t)$ and $\frac{d}{dt}\hat{k}_{F,OH}(t)$ for any measurable variables $\lambda(t)$, $I(t)$ and any parameters a, b, c. Fig. 6.11

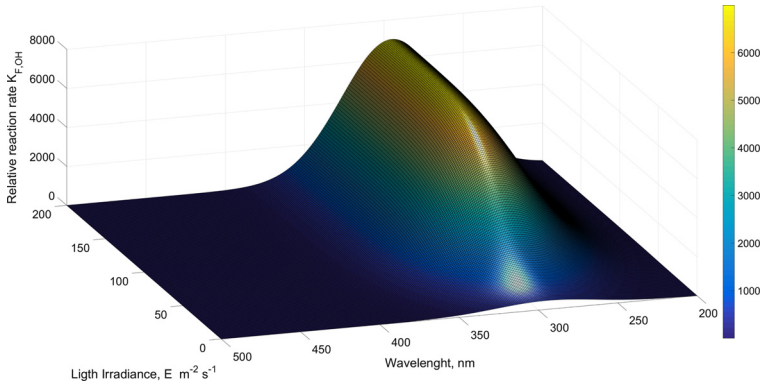

■ **FIGURE 6.11** Reaction rate parameter $k_{F,OH}$ as a function of the wavelength and light irradiance.

depicts the variation of the gain $k_{F,OH}(t)$ as a function of the wavelength λ and the relative intensity I with $I_0 = 50$ E m^{-2} s^{-1} and $\lambda_0 = 295$.

6.3.1 Parameter estimation

Using the DNN version of the original dynamic photocatalytic model, it may be approximated by

$$\left.\begin{aligned} \frac{d}{dt}\hat{k}_{F,OH}(t) = -a^2(\lambda(t)-\lambda_0)\hat{k}_{F,OH}(t)\dot{\lambda}(t) + \\ \frac{c\hat{k}_{F,OH}(t)}{b^{-1}e^{c(I(t)-I_0)}+1}\dot{I}(t). \end{aligned}\right\} \tag{6.15}$$

The simplified form of this equation is

$$a^2 r_1(t) + \frac{c}{b^{-1}e^{cr_3(t)}+1} r_2(t) = r_4(t), \tag{6.16}$$

where the available online functions $r_i(t)$, $i = 1, 2, 3, 4$ are defined by

$$\begin{aligned} r_1(t) &= -(\lambda(t)-\lambda_0)\hat{k}_{F,OH}(t)\dot{\lambda}(t), \\ r_2(t) &= \hat{k}_{F,OH}(t)\dot{I}(t), \\ r_3(t) &= I(t) - I_0, \\ r_4(t) &= \frac{d}{dt}\hat{k}_{F,OH}(t). \end{aligned}$$

As one can see Eq. (6.16) is highly nonlinear. This fact does not permit to identify all the parameters a, b, c for any possible input sequences $I(t)$. But, realizing the special offline first experiment when

$$I(t) = I_0$$

and implying $r_3(t) = 0$, we can simplify (6.16) to the form

$$a^2 r_1(t) + c r_2(t) = r_4(t),$$

which can be represented in the regression form

$$r_4(t) = \theta^\top \varphi(t),$$
$$\theta = \begin{bmatrix} a^2 \\ c \end{bmatrix}, \ \varphi(t) = \begin{bmatrix} r_1(t) \\ r_2(t) \end{bmatrix}.$$

Application of the classical *Least Square Method*, discussed in Chapter 4, yields the following estimate:

$$\frac{d}{dt}\hat{\theta} = \Gamma(t)\varphi(t)\left(r_4(t) - \varphi^\top(t)\,\Gamma(t)G(t)\right)\Big\} \tag{6.17}$$

where time-varying functions $\gamma_i(t)$ and $g_i(t)$ are generated by

$$\begin{aligned} \dot{\Gamma}(t) := -\Gamma(t)\varphi(t)\varphi^\top(t)\Gamma(t), \ \Gamma(0) = \varepsilon I_{N\times N}, \ \ \varepsilon > 0, \\ \dot{G}(t) = \varphi(t) r_4(t), \quad G(0) = 0. \end{aligned} \tag{6.18}$$

Let's consider the second experiment, when $I(t) \neq I_0$ is any suitable irradiance applied at the photocatalytic ozonation. Then the parameter b can be estimated:

$$\hat{b}(t) = \frac{\left(r_4(t) - \hat{a}^2 r_1(t)\right) e^{\hat{c}(t) r_3(t)}}{\left[\hat{c}(t)\, r_2(t) - r_4(t) + \hat{a}^2 r_1(t)\right]}.$$

6.4 NUMERICAL EVALUATION OF THE DNNO WITH DISCONTINUOUS LEARNING LAW

In this chapter, we considered the DNNO observer with discontinuous learning law

$$\begin{aligned} \frac{d}{dt}W_j(t) &= -K_{2,j} P N_\delta \Phi_{2,j}(e(t))\Gamma_j^\top(\hat{x}(t), u(t)) \\ &\quad + \frac{K_{2,j}}{2} P N_\delta C^\intercal e(t)\hat{x}(t)^\intercal V_j(t) D_j(t) \\ -\frac{K_{2,j}}{2} P N_\delta \Pi_{1,j} N_\delta P \tilde{W}_1(t)\, &\Gamma_j(\hat{x}(t), u(t))\psi_j^\intercal\left(\hat{x}(t)\right), \\ \Gamma_1(\hat{x}, u) = \sigma(V_1(t)\,\hat{x}), \ \ \Gamma_2(\hat{x}, u) &= \phi(V_2(t)\,\hat{x}). \end{aligned} \tag{6.19}$$

The functions Φ_1 and Φ_2 are defined as follows:

$$\left.\begin{aligned}\Phi_1(e) &= \Lambda_1 \text{diag}\left(|e|^{1/2}\right)\text{Sign}(e) + \Lambda_1 e,\\ \Phi_2(e) &= \Lambda_1^2\text{Sign}(e) + \Lambda_2^2 e + 1.5\Lambda_1\Lambda_2\text{diag}\left(|e|^{1/2}\right)\text{Sign}(e),\end{aligned}\right\} \quad (6.20)$$

where the square positive definite matrices $\Lambda_1 \in \mathbb{R}^{n\times n}$ and $\Lambda_2 \in \mathbb{R}^{n\times n}$ are the free parameters that must be adjusted to enforce the convergence of Δ to the origin. The functions $|e|^{1/2}$ and $S(e)$ satisfy

$$|e|^{1/2} = \left[|e_j|^{1/2}\right]_{j\in\{1,2,\ldots,n\}}, \quad \text{Sign}(e) = \left[\text{sign}\left(e_j\right)\right]_{j\in\{1,2,\ldots,n\}}.$$

The Matlab/Simulink model used to implement the DNNO with discontinuous learning law is presented in Fig. 6.12.

Fig. 6.13 shows the time variation of the states included in the photocatalytic ozonation (6.8)–(6.13). This figure also depicts the variation of estimated states obtained by the DNN observer using both, the regular learning (presented in Chapter 4) as well as the discontinuous learning laws given by (6.19).

Notice that the no measurable states of the photocatalytic ozonation systems are recovered during the first 5 min of simulation if the discontinuous learning laws are used. However, if the regular (linear) learning laws are applied, the reconstruction is obtained after 15 min. Fig. 6.14 demonstrates a close-up to the first 5 min of simulation, where the improvements of the state estimations are highlighted.

6.5 CONCLUSIONS

From the results presented above, some key conclusions can be outlined:

– The method of impregnation with vanadium at a calcination temperature of 450°C and in the absence of the OA modified the forbidden band of the TiO_2 (3.42 eV) up to a value of 3.29 eV and for the ZnO (3.28 eV) up to a value of 3.21 eV.

– The effect of the modification with the vanadium showed the presence of the vanadium lamellae for the V_xO_y/ZnO, which correlates with an increment of 50% in a specific area. In the case of V_xO_y/TiO_2, TEM did not show the presence of the vanadium, but the drastic reduction of the area (70%) points out that the vanadium deposited in the pores of the material. Regarding the XPS data, in the V_xO_y/ZnO presented V^{3+} and V^{4+}, compared to the V_xO_y/TiO_2, in which are present V^{5+}, V^{4+} and an unidentified

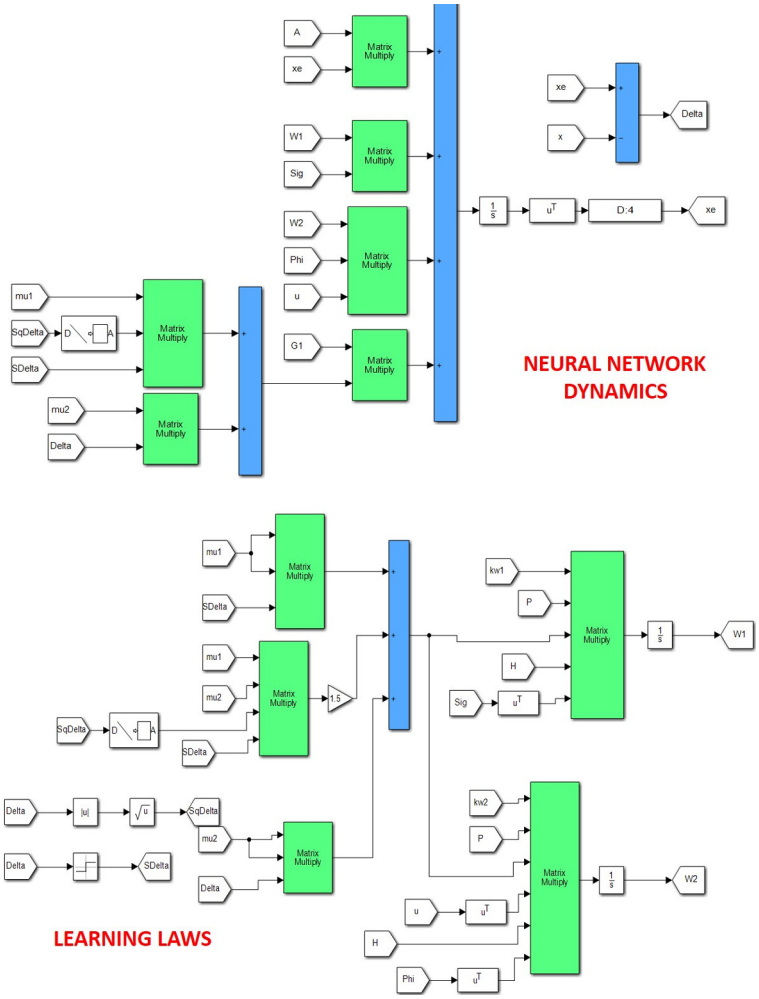

■ **FIGURE 6.12** Matlab/Simulink block diagram used to simulate the DNNO with discontinuous learning laws.

species of a Ti*. The last probably can leaded to the change of the pH_{pzc} from 5.6 up to 3.16.

– Photolysis and photocatalysis with the commercial semiconductors and coupled with the vanadium in the presence of the black light lamp and the LEDs showed the low efficiency of the terephthalic acid removal, which is less than 3% in photolysis and has maximum 20% with LEDs.

– By the conventional ozonation, the TA is almost completely eliminated (> 98%) during the 60 min. Similar results obtained in the systems

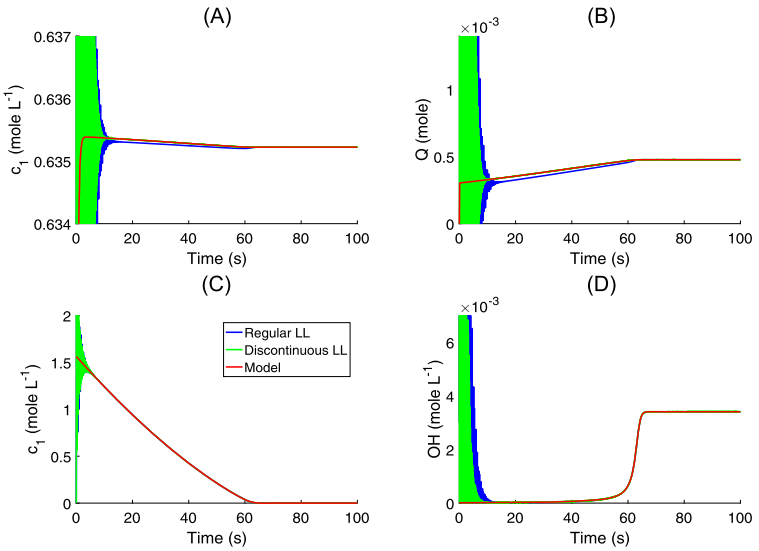

■ **FIGURE 6.13** States comparison of the catalytic model as well as the estimates by the DNN observers with regular and discontinuous learning laws.

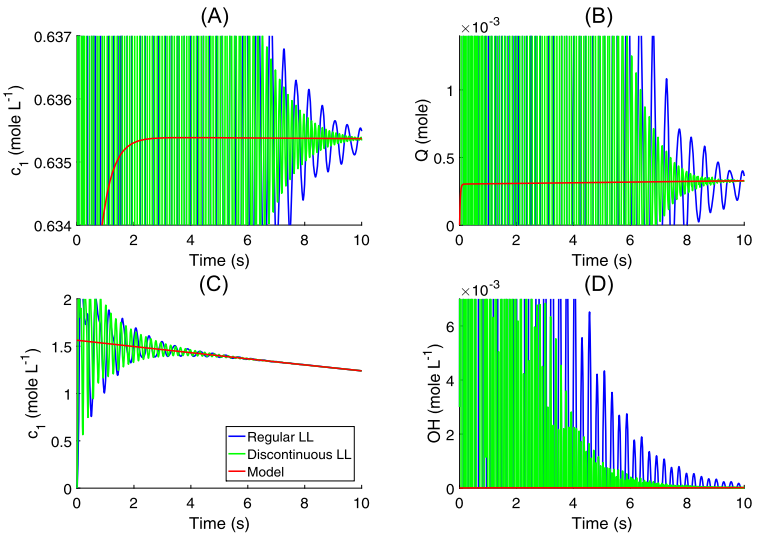

■ **FIGURE 6.14** States comparison during the first 10 min of the photocatalytic model as well as the estimates by the DNN observers with regular and discontinuous learning laws.

O_3–ALEDs, O_3–ZnO, O_3–V_xO_y/ZnO, O_3–V_xO_y/ZnO–ALEDs, when the light source has the central position in the reactor. For its part, the catalytic ozonation showed that the ZnO and the V_xO_y/ZnO accelerate the formation–decomposition of muconic acid and other intermediates. Similar results observed in the photocatalytic ozonation with the same catalysts and with the ALEDs also in the central position.

– In all studied systems, are identified muconic, fumaric, and oxalic acid with the similar profiles of the formation and the decomposition, but the final oxalic acid concentration is different. In the systems O_3, O_3–ALEDs, O_3–TiO_2, O_3–TiO_2–ALEDs the concentration of the acid is 9 mg L^{-1}, and, in addition, the time of the decomposition of ozone in water is longer (9–15 min). In the systems with the modified TiO_2 (O_3–V_xO_y/TiO_2 and O_3–V_xO_y/TiO_2–ALEDs) the concentration of the oxalic acid is maximum (21 mg L^{-1}), probably due to the presence of V^{5+} and V^{4+}. While in all systems with the ZnO (O_3–ZnO, O_3–ZnO–ALEDs, O_3–V_xO_y/ZnO, O_3–V_xO_y/ZnO–ALEDs) the concentration of the oxalic acid 13–15 mg L^{-1} reached, probably as the consequence of the short time of the decomposition of ozone in water (5–7 min) and the presence of the vanadium V^{3+} and V^{4+}.

– In the photocatalytic ozonation with the modified catalysts (V_xO_y/ZnO and V_xO_y/TiO_2) with the *ALEDs* observed the highest decomposition of the fumaric acid (80% for the V_xO_y/ZnO and 95% for the V_xO_y/TiO_2). In the case of the V_xO_y/ZnO catalyst, one observed that an external irradiation accelerated the formation–decomposition of the muconic acid and also contributed to a greater percentage of the fumaric acid elimination, although the profile of the oxalic acid nearly did not change. These results demonstrate the advantages of the use of *ALEDs* over lamps commonly used in photocatalytic processes.

– The photocatalytic ozonation affects the stability of the modified catalysts. In the case of V_xO_y/ZnO, the V^{3+} signal was not detected, and the calculation of the content of V (%) indicated that its loss is only 0.3%, so all the remaining vanadium in the catalyst is in the oxidation state of V^{4+}. Also a signal is presented related to the organic compounds (OC=O). Regarding the V_xO_y/TiO_2, the signals of Ti^* and V^{5+} disappeared, and the loss of V is 1%. This indicates that V_xO_y/ZnO has greater stability against ozone and *ALEDs* than V_xO_y/TiO_2.

– The development of the DNNO with discontinuous learning laws was proposed. The observer is aimed to estimate the states of the photocatalytic ozonation system. This model includes a time-varying reaction rate parameter, which is a function of the wavelength and light irradiance. The observer

served to obtain the numerical reconstruction of states and their intermediate and accumulated final products of ozonation. Once more, the ozone concentration variation in the reactor output is the output information used to tune the observer dynamics.

Chapter 7

Combination of physical-chemical methods and ozonation

CONTENTS

Ozonation and Biodegradation in Environmental Engineering
https://doi.org/10.1016/B978-0-12-812847-3.00017-2

ABSTRACT
The use of the conventional ozonation, as well as of AOPs, such as the catalytic and photocatalytic ozonation, discussed above, has shown the good efficacy in the decomposition of different organic contaminants and their mixtures. However, the treatment of the real waste water is more effective the application of the combination of different physicochemical methods, like the pretreatment, with ozonation. The selection of the methods depends on the chemical structure of the pollutants, their composition, and concentration. In this chapter the combination treatment of real waste water samples is discussed.

7.1 COMBINATION OF CHEMICAL SEDIMENTATION AND OZONATION FOR THE LIGNIN ELIMINATION

The degradation of lignin and its derivatives in the waste water of a paper industry by simple ozonation was investigated in De los Santos Ramos et al. (2009). The remediation of lignin was realized using a combination of the pretreatment with the chemical sedimentation by the concentrated sulfuric acid (97.1%) at a pH of 1 and 3, and of the simple ozonation of the filtered residual water at a pH of 1, 3, 8, and 12. Because of the high contaminants content (COD of 70,000 mg L^{-1}), in the experiments we used diluted

samples (1:10). The previous precipitation showed a significant effect on the reduction of the COD (77%) and the color (96.1%). In the precipitation of the sludge formed sulfolignin, which was obtained by the reaction with sulfuric acid. In ozonation of the filtered residual water at a pH of 1, 3, 8 and 12 during 25 min the following byproducts formed: fumaric, maleic, malonic, and formic acids. The biodegradability of water, treated by ozonation, increases from 0.067 up to 0.24–0.29 and up to 0.23–0.38 during 25 and 60 min, respectively. Also the effect of the conditions of precipitation and ozonation on the kinetics of the water decolorization and the contaminants decomposition was evaluated.

7.1.1 Main contaminants formed in pulp and paper industry

The pulp and paper industry has been considered as one of the biggest consumers of the natural resources (wood, water) and energy (fossil fuels and electricity), and as a huge source of toxic pollutants (Amat et al., 2005a; Nataraj et al., 2007; Savant et al., 2006; Wang et al., 2007). These pollutants are characterized by the high values of biochemical oxygen demand (BOD), chemical oxygen demand (COD), suspended solids (SSs), toxicity, and color. Pulp and paper mills generate different pollutants depending on the type of the pulping process (Pokhrel and Viraraghavan, 2004), (Savant et al., 2006).

The current environmental limitations cause the decrease of the natural resources consumption for this industry, for example, the recycling of fibrous raw materials and/or the alternative (Helble et al., 1999; Yeber et al., 1999). The high water consumption (20,000–60,000 gallons t^{-1} of product (Nemerow and Dasgupta, 1991)) leads to generation of large quantities of waste water, which is dependent on the technology and the product obtained (Griesbeck et al., 2012):

- carton: 3–8 m^3 t^{-1} of product,
- newspaper: 10–15 m^3 t^{-1} of product,
- papel tisu: 15–20 m^3 t^{-1} of product,
- writing paper: 10–20 m^3 t^{-1} of product.

The sources of the contamination of the water circuits in the production of the paper and cardboard are as follows: the fibrous raw materials, the additives and the feeding water, which provide a lot of pollutants such as resinous acids, wax, as well as lignin and their derivates, such as organic chlorides, dioxins, benzophenils, etc. (Amat et al., 2005a; Li et al., 2007; Nataraj et al., 2007; Savant et al., 2006; Wang et al., 2007). These effluents are characterized by high coloration and high suspended solid content, un-

stable pH, high values of the COD and the DBO_5, and chlorides, sulfates, etc. (Calvo et al., 2007; Çeçen, 1999; Kemeny and Banerjee, 1997; Li et al., 2007; Rajeshwari et al., 2000).

On the other hand, these pollutants can be carcinogenic, due to the presence of chlorine lignin and chlorophenols, which formed in this process (Freire et al., 2001; Rajeshwari et al., 2000). The chemical structure of lignin, as the principal toxic contaminant, is not defined. It is a natural irregular biopolymer, which consists of phenyl propane units with various substitutes (–OCH3, –OH, –COOH) combined with the bonds of the different types (Korhonen and Tuhkanen, 2000; Ledakowicz et al., 2006). This is an important group of compounds with the complex chemical structure, which are responsible for the toxicity of the waste water and adversely affect the microbial systems of the bioreactors, so these compounds are resistant to the biodegradation (Kemeny and Banerjee, 1997; Laari et al., 1999; Rajeshwari et al., 2000; Ralph et al., 2004; Werker and Hall, 1999), (Helble et al., 1999; Korhonen and Tuhkanen, 2000; Roy-Arcand and Archibald, 1996).

Makris and Banerjee (2002) studied the behavior of the resinic acids in a secondary treatment system, which are toxic components with the permissible limit concentration of 0.4–1.1 mg L^{-1} (Werker and Hall, 1999). Many authors reported the presence of the toxic species in fish or the toxic effects on fish, such as respiratory stress, mixing of the function of the oxygenase activity, liver damage, or genotoxic and lethal effects on fish exposed to these waste waters (Ericson and Larsson, 2000; Johnsen et al., 1998; Schnell et al., 2000). Based on these facts, novel technologies or the combination of different alternative methods are required for the treatment of this type of waste water (Korhonen and Tuhkanen, 2000; Ledakowicz et al., 2006; Roy-Arcand and Archibald, 1996; Werker and Hall, 1999). There are alternative methods to treat the waste water of the paper industry, like a catalytic process, biocatalysis, membranes, and water treatment with high temperatures and pressures. However, these processes are not efficient and their operations are very costly. Ozonation (Fontanier et al., 2006; Johnsen et al., 1998; Kemeny and Banerjee, 1997) and advanced oxidation processes (AOPs), including photocatalytic oxidation and the catalytic ozonation (Balcıoğlu et al., 2007; Catalkaya and Kargi, 2007; Fontanier et al., 2006; Freire et al., 2001; Yeber et al., 1999), are the alternatives to degrade lignin and their derivatives in water; however, the efficiency of the methods of the treatment depends on the operation conditions and the quality of the waste water. The most interesting perspective is the combination of two or more alternative methods. Thus, a combination of the coagulation and wet oxidation (Laari et al., 2001; Verenich and Kallas, 2001), ozonation and a biofilm reactor (Helble et al., 1999) and biodegradation (Freire et al., 2001), etc., have

Table 7.1 Some characteristics of native waste water.

Parameter	Value
pH	9.0
Color (Pt–Co)	109,284
COD, mg L^{-1}	70,000
BOD5, mg L^{-1}	503
Suspended solids, g L^{-1}	91.5

shown to lead to high removals of the COD and the total organic carbon (TOC) and a reduction of the acute toxicity.

7.1.2 Materials and methods

7.1.2.1 Chemical precipitation of lignin by sulfuric acid

In all experiments the samples of original waste water from the paper plant Kimberly Clark of Orizaba City, Veracruz, Mexico, are used. Table 7.1 depicts some characteristics of this waste water that coincides with the information reported in Koyuncu et al. (1999); Wu et al. (2005). The lignin precipitation in the diluted samples (1:10) was carried out using the concentrated sulfuric acid (97.1%, FERMONT) with the agitation. The acid concentration varies from 1.025 to 2.25% vol at the initial values of pH 3 and 1, respectively. For the maximal formation of sulfolignin, the treatment of the samples was carried out during 24 h. The effects of the acid dose on the efficacy of the precipitation and the color elimination are determined by UV-Vis spectrophotometry.

7.1.2.2 Ozonation procedure

All ozonation experiments were carried out at room temperature (23°C) in a semi-continuous glass reactor (230 mL) with an initial ozone concentration of 30 mg L^{-1} during 60 min. The ozonation of the diluted and filtered samples after precipitation was executed with an initial pH of 1, 3, 8 and 12.

7.1.2.3 Samples analysis

To control the dose of sulfuric acid, the filtered solution was analyzed by the spectrophotometer UV-Vis (Perkin-Elmer Lambda 2B). The control of the lignin decomposition in ozonation, as well as its decolorization was carried out using the wavelengths of 254 and 465 nm, respectively. The samples of the sludge, after their filtration and drying, was analyzed by a Fourier-transform infrared spectroscopy (FTIR) by the spectrophotometer

Table 7.2 Effect of the sulfuric acid concentration to the precipitation efficiency for diluted samples (1:10): CD = Color decrease, SP = Sludge precipitation.

Acid conc. $(\%)_{vol}$	pH	Color Pt-Co	COD $\frac{mg}{L}$	BOD_5 $\frac{mg}{L}$	CD (%)	SP (%)
2.25	1.0	430	1599	175	96.1	89.9
1.01	3.0	800	1819	123	92.67	81.80

(Perkin-Elmer 1600 Series FTIR) with a KBr cell. The intermediates and final products obtained in the lignin ozonation are identified by the high performance liquid chromatography (HPLC) using the liquid chromatograph Perkin-Elmer series 200 coupled with an automatic UV detector, accompanied by the chromatographic column Nova Pack C-18 (250 mm · 4.6 mm) with the mobile phase of water : acetonitrile : phosphoric acid (79.9:20:0.1), with a flow of 0.5 mL min^{-1}. The injected sample volume is 30 μL and the wavelength used was 210 nm. The BOD_5 and the COD of the samples were determined by standard methods (Laari et al., 1999).

7.1.3 Results and discussion

7.1.3.1 Effect of sulfuric acid dose on the lignin precipitation efficiency

In the preliminary study (De los Santos Ramos et al., 2009) a ferric sulfate was used as the coagulant, which demonstrated the good results in the color removal and in the ozonation time reduction; however, the sludge formed in the coagulation is toxic and provokes a negative impact on the environment. During the lignin precipitation, the sulfuric acid was used, which led to the formation of the sulfolignin. This compound is not toxic and has an application as additives in cement production.

Based on the obtained results presented in Table 7.2, we can conclude that the use of sulfuric acid is a good alternative method for the precipitation of the pollutants with high molecular weight. So, only the first stage of the treatment, like precipitation with the sulfuric acid, allows for the decrease of the initial color by 96%. On the other hand, the precipitated lignin, in the form of the sulfolignin, is 89.90% of the initial volume of water. However, the effect of the acid dose on the mass of the sludge, as well as on the decreases of the color, the COD and the BOD_5 is significantly less. The variation of sulfuric acid content from 1.01 to 2.25% leads to slight changes of these parameters.

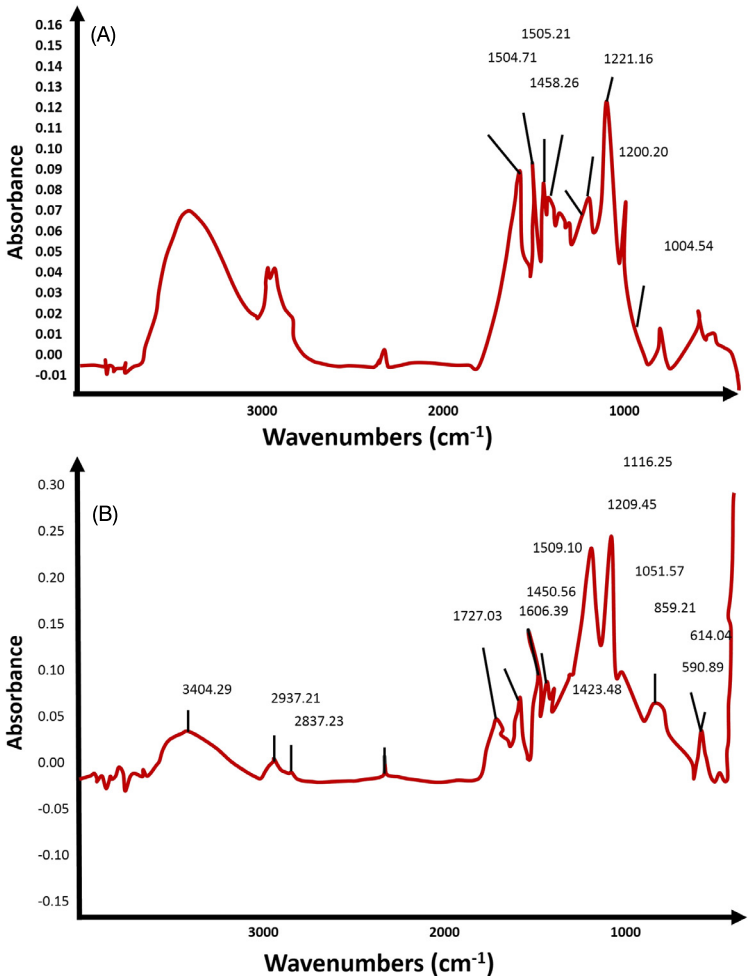

■ **FIGURE 7.1** IR spectra of the native lignin (A) and the precipitated sludge (B).

7.1.3.2 Comparison of the sludge structure

The structure of the native and precipitated sludge was analyzed by the IR technique. In Fig. 7.1 the corresponding IR spectra are presented. As we can see, the spectra are very similar: they have the characteristic peaks of the lignin at 1131, 1594, and 3415 cm^{-1}. However, in the spectrum of sulfolignin are presented the intense characteristic picks 1116 and 1209 cm^{-1}, which correspond to the sulfogroups. From the comparison of the IR spectra, it is possible to conclude that during the precipitation by sulfuric acid the sulfolignin was obtained.

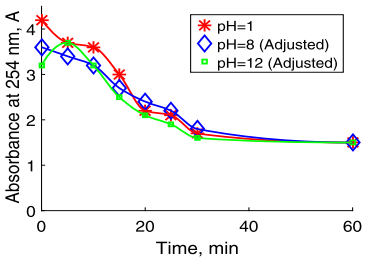

■ **FIGURE 7.2** Lignin decomposition in ozonation (254 nm) at the different pH: pH 1 (red, ∗), pH 8 (blue, ◇) and pH 12 (green, □). The precipitation pH is 1.0.

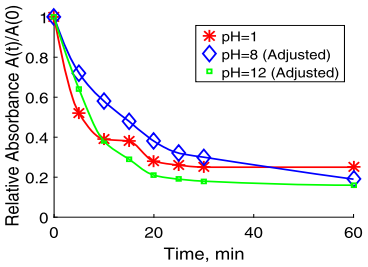

■ **FIGURE 7.3** Lignin decoloration in ozonation (465 nm) at the different pH: pH 1 (red, ∗), pH 8 (blue, ◇) and pH 12 (green, □). The precipitation pH is 1.0.

7.1.3.3 Ozonation of residual water at different pH values after the precipitation stage

To compare the pH effect on the discoloration and the decomposition, the water after the precipitation and filtration is ozonated at various initial pH values: 1, 3, 8, and 12. It should be taken into account that the color reduction or its elimination does not necessarily mean the total decomposition of pollutants. In some cases, the discoloration leads to the formation of the highly toxic intermediates. The precipitated samples at pH = 1 were ozonated at a pH of 1, 8 and 12, and the precipitated samples at pH = 3 were ozonated at the pH values of 3, 8 and 12. The pH was not controlled during the ozonation. In Figs. 7.2 and 7.3, the dynamics of the decomposition (254 nm wavelength) and decolorization (465 nm wavelength) of the previously treated water at pH = 1 appear.

As can be seen, the decolorization dynamics is faster than the contaminant decomposition (removal of 85% during 30 min, and of 70% during 60 min, respectively). However, the final results of ozonation are the same (Figs. 7.4 and 7.5) without a significant effect of the pH.

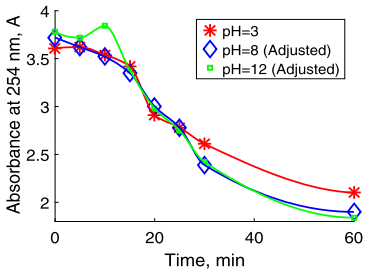

■ **FIGURE 7.4** Lignin decomposition in ozonation (254 nm) at the various pH values: pH 3 (red, ∗), pH 8 (blue, ◇) and pH 12 (green, ■). The precipitation pH is 3.0.

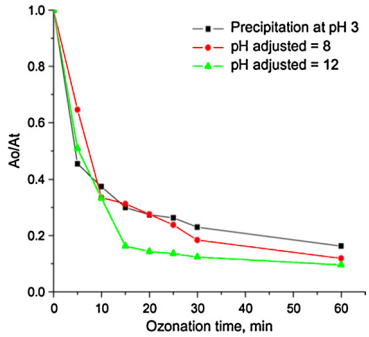

■ **FIGURE 7.5** Lignin decoloration in ozonation (465 nm) at the different pH: pH=3 (black, ■), pH=8 (red, ●) and pH=12 (green, △). The precipitation pH is 3.0.

The BOD_5/COD ratio is commonly used as a biodegradability measure (Chamarro et al., 2001; De los Santos Ramos et al., 2009; Poznyak and Araiza G., 2005). The effect of ozonation on the biodegradability of the dissolved contaminants is investigated by a comparison of this parameter before and after the ozonation. In Table 7.3, the variation is presented of the COD, the BOD_5 and the biodegradability in ozonation during 25 min, and Table 7.4 presents the same parameters after 60 min, where the initial $COD_i = 1599$ mg L^{-1} and the initial $BOD_5 = 175$ mg L^{-1} after the precipitation at pH $= 1$, $COD_i = 1819$ mg L^{-1}, and the initial $BOD_5 = 123$ mg L^{-1} after the precipitation at a pH of 3.

The precipitation conditions have influence on the initial biodegradability of water. So, the change of the precipitation pH from 3 to 1 provokes the increase of the initial biodegradability from 0.067 to 0.11. These values are in agreement with the one reported by Balcıoğlu et al. (2007). Nevertheless, the final biodegradability value after the ozonation during 25 min has, practically, the same values (0.25–0.29 or 0.24–0.31), which independent on the precipitation conditions.

Table 7.3 The variation of the COD, the BOD5 and the biodegradability (BOD_5/COD) in ozonation during 25 min.

pH	$\frac{BOD_5}{COD}\Big\vert_i$	COD_{25} mg L^{-1}	$BOD_{5,25}$ mg L^{-1}	$\frac{BOD_5}{COD}\Big\vert_{25}$
	Precipitation at pH 1			
1	0.11	1400	336	0.24
8	0.11	1240	295	0.24
12	0.11	1150	358	0.31
	Precipitation at pH 3			
3	0.067	1226	350	0.29
8	0.067	1153	293	0.25
12	0.067	1139	298	0.26

Table 7.4 The variation of the COD, the BOD5 and the biodegradability (BOD_5/COD) in ozonation during 60 min.

pH	COD_{60} mg L^{-1}	$BOD_{5,60}$ mg L^{-1}	$\frac{BOD_5}{COD}\Big\vert_{60}$
	Precipitation at pH 1		
1	1290	298	0.23
8	810	306	0.38
12	1115	343	0.31
	Precipitation at pH 3		
3	1019	328	0.31
8	1186	306	0.21
12	1166	306	0.26

In the prolonged time of ozonation (60 min) this parameter also has not changed significantly. Based on the results presented above, we can conclude that the precipitation conditions have no influence on the final biodegradability of water after the treatment with ozone. The lignin and their derivates were destroyed in ozonation during 25 min, with total decolorization.

7.1.4 Identification of the products formed in ozonation

Table 7.5 presents the identified compounds formed in ozonation. As it may be seen, the main compounds are: catechol and fumaric, maleic, malonic and formic acids. The content of the catechol in some cases is very small (0.61–5.90 mg L^{-1}) and it does not affect the toxicity of the treated water. So, the produced mixture of the simple acids is biodegradable and not toxic. On the other hand, the pH of the lignin precipitation and of the ozonation

Table 7.5 Products formed in ozonation of lignin and its derivatives.

pH	O_3 time	Concentration (mg L^{-1})				
		Catechol	Fumaric acid	Maleic acid	Malonic acid	Formic acid
		Precipitation at pH 1				
1	25	5.90	26.30	29.42	17.80	407.00
	60	1.80	21.00	32.17	ND	375.70
8	25	0.61	12.50	39.02	ND	ND
	60	ND	6.10	46.42	ND	ND
12	25	ND	5.40	50.41	ND	ND
	60	ND	4.00	50.44	ND	ND
		Precipitation at pH 3				
3	25	ND	38.80	13.20	ND	326.60
	60	ND	23.80	14.89	ND	239.40
8	25	ND	12.00	20.67	37.20	ND
	60	ND	6.40	19.80	41.20	ND
12	25	ND	4.10	4.44	8.80	ND
	60	ND	3.90	20.91	47.80	ND

is a very significant parameter, which determines the concentration of the ozonation products. The concentration of the formic acid, as a final product, varies from 0 to 407.00 mg L^{-1}. This maximum concentration of acid was formed at the pH = 1 during 25 min, which corresponds the minimum maleic acid concentration (29.42 mg L^{-1}). It is complicated to select the optimal operating conditions of this combined treatment. To select the optimal conditions for the lignin precipitation and its ozonation, a kinetic study of these processes may help.

7.1.5 Estimation of lignin decoloration constants

The kinetics of ozonation of the model compounds as guayacol, maleic acid, phenol derivatives has been studied by several researchers (Am. Water Works Res. et al., 1991; Amat et al., 2005b; Larisch and Duff, 1997). The decoloration rate constants were estimated by the numerical calculations based on a simplified mathematical model (Poznyak and Araiza G., 2005; Poznyak et al., 2005, 2008). These constants were calculated using the variation of the gas phase ozone concentration in the reactor outlet and the lignin decoloration dynamics. The differential neural network (DNN) method is used to estimate the ozonation kinetics:

$$\frac{d}{dt}\hat{c}_i(t) = -\frac{k_i \hat{c}_i(t)\hat{Q}(t)}{V_{liq}}. \tag{7.1}$$

Table 7.6 Effect of pH on the lignin decoloration.

pH of precipitation	pH of ozonation	k ($M^{-1}\,s^{-1}$)
1	1	$2.98 \cdot 10^2$
	8	$2.14 \cdot 10^2$
	12	$4.32 \cdot 10^2$
3	3	$6.75 \cdot 10^2$
	8	$10.46 \cdot 10^2$
	12	$5.45 \cdot 10^2$

Here $\hat{c}_i(t)$ is a numerical estimate (as a result of DNN application) of the contaminant concentration during the overall reaction (mol L^{-1}), while $\hat{Q}/V_{liq}$ is the estimate of the DNN-liquid phase ozone concentration (mol L^{-1}), $\hat{Q}$ is the estimate of the total ozone amount into the liquid phase and (V_{liq}) is the total liquid phase volume (L). The technique, based on DNN, is usually used to obtain the physical "model-free" representation of some dynamics as was mentioned before (Oller et al., 2011). Observe that $\hat{c}_i(t)$ and $\hat{Q}$ as well as $\frac{d}{dt}\hat{c}_i$ are available. It is possible to define the LS (least square) estimates of k_i as the solution of the following optimization problem:

$$k_i^*(t) = \underset{k_i}{\operatorname{argmin}} \int_{t=0}^{t} \left(\frac{d}{dt}\hat{c}_i(\tau) + \frac{k_i \hat{c}_i(\tau)\hat{Q}(\tau)}{V_{liq}} \right)^2 d\tau \tag{7.2}$$

The solution of this optimization problem is

$$k_i^*(t) = \frac{V_{liq} \int_{t=0}^{t} \left(\frac{d}{d\tau}\hat{c}_i(\tau) \right) \hat{c}_i(\tau)\hat{Q}(\tau) d\tau}{\int_{t=0}^{t} \left(\hat{c}_i(\tau)\hat{c}_i(\tau)\hat{Q}(\tau) \right)^2 d\tau + \varepsilon} \quad \varepsilon > 0, \tag{7.3}$$

or in differential form as in Eq. (2.25).

Using the experimental data of the lignin decoloration, the corresponding ozonograms and the equation set (7.3) for the i-th contaminants, the decoloration rate constants were calculated for the diluted sample of the pretreated effluent. Table 7.6 presents the calculated constants.

We observe a significant effect of the lignin precipitation pH, as well as the pH of ozonation on the decoloration kinetics. Thus, with the precipitation pH increases from 1 to 3, and the decoloration constants increase in all cases. On the other hand, the ozonation pH also affects the decoloration kinetics. So, for the first case, a more rapid decoloration ($4.32 \cdot 10^2$

L mol^{-1} s^{-1}) is carried out at an ozonation pH of 12, and for the second case, at a pH of 8.0 ($10.46 \cdot 10^2$ L mol^{-1} s^{-1}). The lignin decoloration rates have the following orders:

- pH = 12 > pH = 1 > pH = 8 for the precipitation at pH = 1,
- pH = 8 > pH = 3 > pH = 12 for the precipitation at pH = 3.

The results of the kinetic study were unexpected. One would expect that at the basic pH the decoloration must be faster, and slower at the acidic pH. However, this trend was not implemented, because the effect of the precipitation pH is very strong. A possible explanation of such a strong influence of the precipitation conditions on the decoloration kinetics is the significant variation of the composition of the contaminants dissolved in water after the precipitation with sulfuric acid. This hypothesis is confirmed by the data of Table 7.6: the composition of the contaminants in water at the pH of 3 was more complicated, which makes their decomposition difficult. This fact was confirmed by the higher values of the COD, the BOD_5 and the BOD_5/COD.

7.2 COAGULATION AND OZONATION OF LANDFILL LEACHATE

This case is an example of a combination of the coagulation and ozonation for the treatment of the sanitary waste (including domestic and industrial) of the landfill leachate of Bordo Poniente of Mexico City by the coagulation with $Fe_2(SO_4)_3$ (2.5 g L^1 at a pH of 4–5). The content of the humic substances after the coagulation decreased by 70%. Then the leachate obtained from a solid with an initial COD of 1511 mg L^{-1} and the pH = 8.5 was treated by ozone. The aqueous samples were analyzed by a UV–Vis and a HPLC technique. The partial identification of the initial composition of the organic matter, as well as of intermediates and final products, was carried out after the extraction of the initial and ozonated leachate with benzene, chloroform : methanol (2:1) and hexane. Then the extracts were analyzed by a gas chromatography with the mass detector and FID. In ozonation, the malonic and the oxalic acids with the initial concentrations of 19 mg L^{-1} and 214 mg L^{-1} were identified. The last acid was accumulated in ozonation. The color disappears (visually) by 100% during 5 min of ozonation. The organic substances, extracted with chloroform : methanol were destructed during 15 min of ozonation; the organic matter, extracted with benzene, was destructed completely during 5 min. However, the organic compounds extracted with hexane were considered as recalcitrant, because of their low ozonation rates. The toxic compounds in leachate were decomposed completely during 15 min of ozonation. The ozonation rate constants for each

group of organics (as observed constants) were calculated applying a simplified mathematical model and the recurrent least square method.

7.2.1 Landfill leachate contamination

Economic considerations continue to maintain landfills as the most attractive option for the municipal solid waste disposal. The alternative methods to landfilling (incineration and composting) are actually considered as the volume reduction process, since they produce waste fractions (ashes and slag), which ultimately must be landfilled (Bingemer and Crutzen, 1987; Emberton and Parker, 1987; Nozhevnikova et al., 1992). Despite the evolution of landfill technology, from open uncontrolled dumps to highly engineered facilities designed to eliminate or minimize the potential adverse impact of the waste on the surrounding environment, the generation of the contaminated leachate remains an inevitable consequence of the practice of waste disposal in landfills. Leachate is formed, when the moisture content exceeds its field capacity, which is defined as the maximum moisture that can be retained in a porous medium without downward percolation (Blakey, 1992).

There are many factors related to the quality and quantity of the water formed at landfills: seasonal weather variations, the landfilling technique, phase sequencing, the piling and compaction method, etc. The organic and inorganic contaminants of landfill leachates are released from waste due to the successive biological, chemical, and physical processes (Amokrane et al., 1997; Rodrıguez et al., 2004; Trebouet et al., 2001). On the other hand, the amount and composition of leachates at a landfill site depend on the refuse nature and the composition, the pretreatment, the biological stage, the age, and the structure of the landfill (Baig et al., 1999; Harmsen, 1983; Schultz and Kjeldsen, 1986). According to the numerous investigations, three types of leachates by landfill age can be classified: young, intermediate, and stabilized (Table 7.7). As we can see, the young leachate is highly contaminated with the organic compounds: ammonia, halogenated hydrocarbons, and heavy metals. The Humic Substances (HSs) constitute an important group of the leachate organic matter (Harmsen, 1983; Kang et al., 2002; Öman and Hynning, 1993).

Nevertheless, the principal components of organic compounds in landfill leachates do not vary significantly: only the composition of organics can vary depending on the landfill age (Table 7.8) (Christensen et al., 1998; Gourdon et al., 1989; Manning and Bewsher, 1997; Mejbri et al., 1995).

As long as the age of the landfill increases, the produced leachates are characterized by the presence of substantial quantities of recalcitrant, difficult-

Table 7.7 Leachate classification (Kang et al., 2002; Öman and Hynning, 1993).

Leachate type	Young	Intermediate	Stabilized
Landfill age (years)	< 5	5–10	> 10
pH	< 6.5	6.5–7.5	> 7.5
COD (mg L^{-1})	$> 20{,}000$	3000–5000	< 5000
BOD_5/COD	> 0.3	0.1–0.3	< 0.1
Organic matter VFA (%TOC)*	70–90	20–30	5
HMW (%TOC)	–	–	> 60
Kjeldhal nitrogen (mg·L^{-1})	100–2000	–	–
Metals (g L^{-1})	2	< 2	< 2

* *VFA: volatile fatty acids; HMW: high molecular weight humic and fulvic-like material.*

Table 7.8 Composition of the organic compounds of non-stable leachates (references summary).

Compound	Concentration (mg L^{-1})	% of TOC
Aliphatic carboxylic acids	30,000	> 95 volatile fatty acids
Aromatic carboxylic acids	1000	–
Methylphenols	100	–
Ethylphenols	50	–
Alkylbenzenes	1.21	–
Aliphatic compounds (hydrocarbons, alcohols and ketones)	300	0.04 (0.7 of alcohols)
Amines	300	0.8
Humic and fulvic acids	100–420	1.3

to-treat, "hard" COD compounds. The degradation method of the organic matter necessarily depends on the chemical composition of the organic matter and the ambient conditions, which can significantly modify this chemical process (Gourdon et al., 1989; Öman and Hynning, 1993). The degradation method uses various treatments, such as electrochemical oxidation (Moraes and Bertazzoli, 2005), coagulation–flocculation (Amokrane et al., 1997; O'melia et al., 1999; Tatsi et al., 2003; Wang et al., 2002b), chemical precipitation and an adsorption on the activated carbon (Kurniawan et al., 2006), membranes (Li et al., 2009; Marttinen et al., 2002), com-

bination of coagulation, flocculation and chemical oxidation (Rivas et al., 2004), advanced oxidation (De Morais and Zamora, 2005), ozonation (Bila et al., 2005; Monje-Ramirez and De Velasquez, 2004; Poznyak and Chairez, 2011), the combination of ozonation, Fenton, biodegradation and adsorption onto activated carbon (Welander and Henrysson, 1998), wet air oxidation at high temperature (Rivas et al., 2005), and the electro-Fenton method (Zhang et al., 2006). Ozone has been suggested as an alternative for the treatment of landfill leachates (Beaman et al., 1998). It may be used in the beginning (preozonation), as well as in intermediate phase and at the end of the treatment (Camel and Bermond, 1998). In preozonation, the main objective is the decomposition of large organic molecules (Kerc et al., 2003) to increase the effectiveness of the following treatment steps, such as the biodegradation or the adsorption on activated carbon (Fettig et al., 1996). To remove color, odors, and the COD of leachates, ozone also is used with the coagulation (Orta de Velásquez et al., 1998) that avoids the production of associated sludges. In the previous research it has been found that ozone is most effective in leachates, which do not contain *hard* COD (Haapea et al., 2002).

7.2.2 Materials and methods

7.2.2.1 Description of the site and the characterization of the waste

The leachate treated in this study comes from Mexico City waste sanitary landfill of Bordo Poniente, which included domestic and industrial waste. The total area of the site is about 1999 ha. Four controlling wells are situated on three old parts with the arias of 74 ha, 80 ha, and 104 ha, which are closed. The new waste bank started to work in 1996, and receives a solid waste of about 7000–8000 ton·day^{-1}. To obtain a representative distribution of the leachates organic matter composition, the sampling site was selected in the treatment plant (a deposal tank), where inflows from all sites were received. Thus, the selected leachates represented the averaged characteristics of the landfill. The samples (300 L) were collected in the summer and in the winter during 2 years (1998 and 1999). To avoid the composition change of the samples, they were mixed and stored at 4°C (Monje, 2004). The initial COD is 4580 mg L^{-1} at a pH of 8.6. The content of heavy metal is reported in Table 7.9. These values coincide with previous investigations (Manning and Bewsher, 1997).

7.2.2.2 Coagulation

The coagulation of the leachate was carried out by the $Fe_2(SO_4)_3$ at the optimal conditions proposed by Monje (2004) (in the pH range of 4–7, the co-

Table 7.9 Content of heavy metals in leachate.

Metal	Concentration (mg L^{-1})
Fe	4.3
Ni	1.2
Cr	0.9
Pb	0.8
Zn	0.5

agulant dose was 2400 mg L^{-1}, the treatment time is 30 min), which was investigated in detail in Monje-Ramirez and De Velasquez (2004); Orta de Velasquez et al. (2008). In ozonation experiments landfill leachates, obtained from the solid waste after the coagulation with a COD of 1511 mg L^{-1} and a pH of 8.5, were used (after preliminary neutralization). In these samples heavy metals were not found.

7.2.2.3 Analytical methods

The partial identification of the initial organics composition of leachate, intermediates and final products of ozonation was carried out by the extraction of the initial and ozonated leachate with benzene, chloroform : methanol (2:1) and hexane for the organics separation based on their chemical structure in three conditional groups: aromatic, polar, and aliphatic compounds, as proposed by Harmsen (1983).

The samples in the extraction were concentrated with the ratio 100:1. These extracts were analyzed with a gas chromatography with a mass detector (GC/MS) and a FID. The analysis conditions were a FID by the chromatograph Varian CP 3380 with the capillary column Quadrex 007 (methyl 50%-phenyl silicon) of 250 · 0.25 mm, with temperature programming from 30°C to 200°C during 2 min with 6°C/min, and at 200°C during 8 min; with gas flow (nitrogen) 1.4 mL min^{-1}; T_{det} of 250°C and T_{inj} of 220°C; and a sample volume of 1 µL (Harmsen, 1983; Nanny and Ratasuk, 2002; Schultz and Kjeldsen, 1986).

The chromatographic analysis conditions with a mass detector were chosen using the chromatograph AutoSystem XL, Turbo Mass, Perkin-Elmer, with a capillary column SPB-225 (30 m · 0.25 mm), a sample volume of 1 µL, temperature programming from 30°C up to 220°C during 5 min with 6°C·min^{-1}, and at 220°C during 8 min; with gas flow (nitrogen) of 1.4 mL min^{-1}; T_{det} of 250°C and T_{inj} of 220°C.

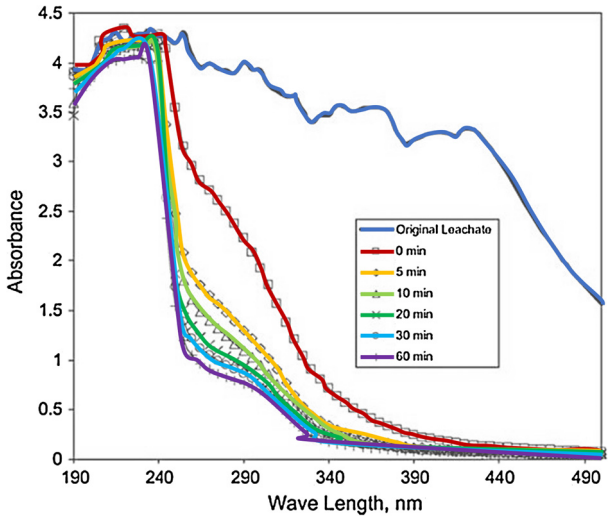

■ **FIGURE 7.6** UV-Vis spectra of the original landfill leachate and after coagulation in ozonation at a pH of 8.5.

The aqueous samples were analyzed by the UV-Vis spectrophotometry and HPLC technique. The summary information of the organic pollutants decomposition in water was obtained by a spectrophotometer (Perkin-Elmer Lambda 2B) in the absorbency range from 190 nm to 485 nm. Fig. 7.6 presents the UV-Vis spectrum variation of the original landfill leachate and treated leachate during 60 min of ozonation at the pH 8.5. The characteristic absorbance peak is at $\lambda = 254–280$ nm (Kerc et al., 2003).

The HPLC analysis used a Perkin-Elmer liquid chromatograph with UV detector, Series 200; the mobile phase was water : acetonitrile : phosphoric acid (89.9:10:0.1), with a flow rate of 0.8 mL min^{-1}, with the Spheri-5 ODS, Silica 5μ, 250 mm · 4.6 mm column, at λ of 210 nm.

To identify heavy metals in pretreated samples of leachate, an atomic absorption spectrophotometry (AA) (Perkin-Elmer) was applied, using the solutions of Fe, Ni, Cr, Pb, and Zn with the concentrations 0.1 ppm, 0.5 ppm, 1.0 ppm and 1.5 ppm according to the standard methods (APHA, AWWA, and WPCF).

7.2.2.4 Ozonation kinetics

In the case of such a complicated composition of organic matter, we suggest to apply the simplified mathematical model discussed above. In view of the used pH values (7.0 and 8.5) for ozonation, the preferable mechanism is the direct reaction with molecular ozone. Based on the results of the partial identification in the fractions of the landfill leachate (Table 7.10), the prin-

Table 7.10 Compounds identified in the different extracts.

After coagulation	After ozonation
Extract with hexane	
2,2-Dimethylbutane	2,2-Dimethylbutane
2-Methylpentane	2-Methylpentane
Chloroform	Chloroform
Aliphatic hydrocarbons (C_{26}–C_{27})	Aliphatic hydrocarbons (C_{26}–C_{27})
	Methylcyclopentane
	Cyclohexane
Extract with benzene	
6-Methylpyrene	ND
Methylcyclohexane	Methylcyclohexane
Norborane	ND
Toluene	ND
Extract with chloroform–methanol	
Hydroxypropionic acid	ND
Di-p-oxyrane	Di-p-oxyrane
Diphenyloxyrane	ND

cipal organics, according their reactivity with ozone, were organized in four groups:

1. Fulvic acids (FAs) and light fraction of humic acids (LFHA).

2. Simple acids (SAs) and the humic substances ozonation byproducts (HSOPs).

3. Aromatic hydrocarbons (ArHs).

4. Aliphatic hydrocarbons (AHs).

Then the ozonation rate constants (as observed constants) for each group (or "factor group") were calculated by the program MATLAB, based on the simplified mathematical model, used before for the kinetic constants calculation of phenols and their mixtures (Poznyak and Vivero, 2005; Poznyak et al., 2005). There, the simple ozonation with the i component mixture at a pH of 7–8 has been treated. To obtain these constants the so-called *switching structure filtering method*, suggested in Correa et al. (2001) was applied to construct a numerical estimation of the ozone concentration in water (Q_t, mol) and the rate constants $k_{i,t}$, L mol^{-1} s^{-1}), based on the online measurements of two sets of data:

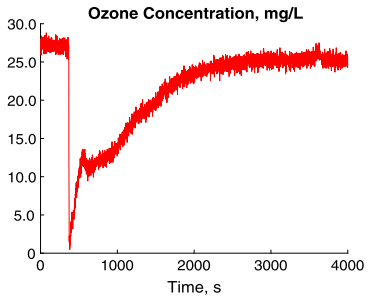

■ **FIGURE 7.7** Ozone concentration at the reactor's output (ozonogram).

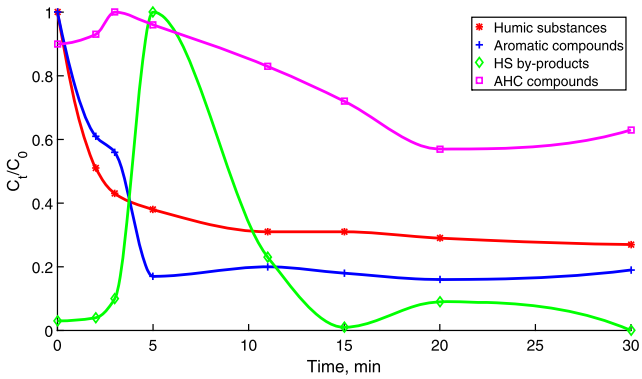

■ **FIGURE 7.8** Behavior of humic substances decolorization (red, ∗), HS byproducts (green, ◇), decomposition dynamics of the organics extracted with benzene (blue, +) and chloroform : methanol (magenta, □).

- The ozone concentration in the gas phase in the outlet of the reactor (c_t^{gas}, mol L^{-1}) (Fig. 7.7).
- The contaminants decomposition (c_t^i) as the summary effect (or factor-group concentration) of the organics in each of three fractions of the landfill leachate (Fig. 7.8).
- The *LS*-method (the continuous-time version) applied to an estimate of k_i.

7.2.3 Results and discussion

7.2.3.1 HPLC analysis

The results, obtained by the HPLC technique, showed the presence of two compounds, with an absorbency at 210 nm, which were identified as oxalic and malonic acids. Both were found in the pretreated sample (oxalic acid of 214 mg L^{-1} and malonic acid of 19 mg L^{-1}). Fig. 7.9 shows that the oxalic

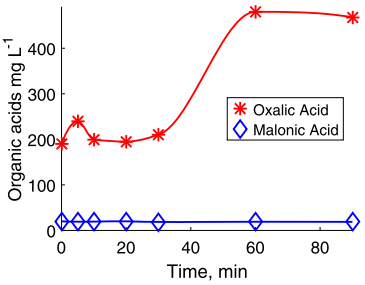

■ **FIGURE 7.9** Behavior of the oxalic and the malonic acids.

acid was accumulated up to 486 mg L^{-1}, and the malonic acid concentration did not vary.

7.2.3.2 Partial identification of same organics with GC/FID and GC/MS

Table 7.10 presents the principal compounds identified in three extracts by the GC/MS technique. As can be seen, after ozonation methyl-cyclopentane and cyclohexane were formed and detected in the fraction extracted with hexane. These compounds are the products of ozonation of fulvic and humic acids. The presence of chloroform traces after coagulation and ozonation may be explained as the effect of extraction with chloroform : methanol.

In the fraction extracted with benzene, very toxic compounds, such as the derivatives of pyrene and borane, were identified (USEPA), but these compounds were decomposed completely by ozone.

In the polar fraction, the hydroxypropionic acid and diphenyl-oxirane were identified, which also were decomposed by ozone.

Fig. 7.8 presents the decomposition of organics in two extracts (with benzene and chloroform : methanol) in ozonation (results obtained by the GC/FID technique). These data were obtained due to the summary effect of the principal compounds variation in each fraction. Furthermore, the decolorization of the HS (results obtained by UV-Vis spectrophotometry) is also presented. As may be observed, the initial HS and the aromatic compounds were decomposed after 5 min of ozonation; the latter was degraded, practically completely. Then the ozonation byproducts were accumulated in the polar fraction at 5 min of the reaction, and, finally, all polar organics were decomposed during 10 min. It is important to emphasize that the organic compounds concentrations in the three extracts are different (Table 7.11).

So, the maximal organics concentration is in the polar fraction (71.8%), and the minimal compounds concentration is in the aromatic fraction

Table 7.11 Organic matter distribution in three fractions.

Fraction	Initial composition (%)
Aromatic	0.4
Polar	71.8
Aliphatic	27.8

(0.4%), which coincides with the results of other authors (Nanny and Ratasuk, 2002; Senior, 1995). Therefore, after the coagulation of the landfill leachate, the presence of different compounds, such as aliphatic carboxylic acids, methyl-phenols, ethyl-phenols, alkyl-benzenes, aliphatic compounds, amines (Christensen et al., 1998; Gourdon et al., 1989; Harmsen, 1983; Manning and Bewsher, 1997; Mejbri et al., 1995; Nanny and Ratasuk, 2002; Schultz and Kjeldsen, 1986), and light fractions of HS with molecular weight 165–287 (Wang et al., 2004) may be found in residual water. Furthermore, the water may contain fragments of proteins, lignin, cellulose, and polysaccharides (Nanny and Ratasuk, 2002; Senior, 1995) too. These compounds may react with ozone by a different rate and mechanism, and they are decomposed until the formation occurs of the mixture of organic acids.

7.2.4 Decomposition of different groups of organics after the coagulation

The main components of the landfill leachate are humic substances (HSs) with molecular weights in the range of 170–7000 Da (Wang et al., 2004). These substances are refractory anionic macromolecules with a molecular weight of 1000 Da for fulvic acid (FA) and of 7000 Da for humic acid (HA). Humic substances consist of alkyl-aromatic units cross-linked mainly by oxygen and nitrogen groups; carboxylic acid, phenolic and alcoholic hydroxyls, and ketone and quinone groups. Fulvic acids are richer in carboxylic acid, phenolic, and ketonic groups. The fulvic acids structure is more aliphatic and less aromatic than that of humic acids. The carboxylic functional groups account was 60–90% for all groups (Hong and Elimelech, 1997).

The best result of the coagulation treatment is the decreasing of the organic matter content of about 70% detected by the comparison of the initial and final value of the COD (4580 mg L^{-1} contrary 1511 mg L^{-1}) (Monje, 2004). After the coagulation of the landfill leachate, the organic substances are separated by the extraction with different solvents to facilitate the partial compound identification. The polar fraction of the pretreated

Table 7.12 Estimation of the observed reaction rate constants for the extracted compounds from leachates.

Group of compounds	Observed constant k_i (L mol^{-1} s^{-1})
FA and LFHA	$3.3 \cdot 10^5$
SA and HSOP	$4.6 \cdot 10^3$
ArH	$3.8 \cdot 10^2$
AH	3.4

landfill leachate, extracted with chloroform : methanol, contains Simple Acids (SAs) and a mixture of Fulvic Acids (FAs) and a Light Fraction of Humic Acids (LFHA). These last organics were destructed completely by ozone in 5 min (decolorization), and byproducts of ozonation, also accumulated in the polar fraction, destroyed in 10 min. The organics, extracted with benzene (ArH), were degraded significantly by ozone in 5 min with the intermediates species accumulation also in polar fraction. The substances extracted with hexane (AH) had a lower ozonation rate and their concentration did not vary during ozonation.

7.2.5 Estimation of the reaction rate constants

Due to the complex leachate composition, it is difficult to elucidate the mechanisms of ozonation and the reaction rate constant determination. Using only the measurements *online* of the ozone concentration in the gas phase in the outlet of the reactor (ozonogram) and the summary distribution of the organics of four groups of the landfill leachate (Fig. 7.8), the observed ozonation constants were calculated for the i component mixture (where i is 4) by the MATLAB program (Poznyak and Vivero, 2005). The values of the observed constants are presented in Table 7.12.

Based on the obtained results, we may conclude that the FA and LFHA are decomposed at a high rate. This agrees with the leachate decolorization. The next group of organics, which also are reactive with ozone, is the group of byproducts of the FA and LFHA decomposition, present also in the polar fraction. These compounds are also decomposed completely by ozone after 10 min. The aromatic compounds also are degraded enough after 5 min due the very small their concentration in water (0.4%). Aliphatic compounds have a low ozonation rate constant, therefore their concentration is not changed significantly in ozonation. In our opinion, four organics groups, characterized by their reactivity with ozone, may be grouped according to another principle. This depends on the solvents, used for their separation, as well as on an order of the organics extraction. Notice that the

proposed method permits one to use the same approach to the study of the ozonation kinetics of different landfill leachates.

7.3 FLOCCULATION–COAGULATION WITH BIOPOLYMER AND OZONATION

7.3.1 Contamination of municipal waste waters

We now address the example of the combination of the flocculation–coagulation (Fl/Co) with the biopolymer (BP) and ozonation for the treatment of the municipal waste water (MWW) from Mexico City. The Fl/Co pretreatment is developed with a galactomannan-type polymer (HPTAC-GUAR), which is used at the same time for the flocculation and coagulation to reduce the non-dissolved organic matter, as well as the microbiological factors: total coliforms (TC), fecal coliforms (FC), and helminth eggs (HE). By the subsequent ozonation of the pretreated effluent the dissolved organic matter is decomposed. The efficacy of Fl/Co was evaluated by measuring the formation of the sludge as well as the Z-potential variation. The variation of the COD is used as the main indicator of the ozonation efficiency. The UV-Vis absorbance variation is considered as a nonspecific indicator of the organic matter decomposition and byproducts of ozonation.

Treatment of real waste waters (municipal, agricultural, and industrial) represents a major challenge due to the complex composition and high number of physicochemical and microbiological indicators (Blatchley et al., 2012), (Xu et al., 2002).

In the case that waste waters (with or without the previous treatment) are reused for agricultural purposes, there is a wide spectrum of illnesses (from intense diarrheas to cancer) that can be caused by this practice. The presence of many bacteriological elements (viruses, bacteria, protozoa, and helminthes eggs) and chemical toxic compounds is the main source of such sicknesses (Paraskeva and Graham, 2002). Due to the diverse nature of contaminants and pathogens, present in water, the application of a single treatment method is not effective (Gehr et al., 2003), (Mezzanotte et al., 2007). A combination of the different physical and chemical treatments can be considered as an alternative aimed at reducing costs and technological constraints. The main idea of this combination is to potentiate the advantages of each individual method and to minimize their corresponding disadvantages (Espejo et al., 2014), (Hermosilla et al., 2015). The different combinations of the treatment methods is regularly designed using physical, chemical and biological methods. Several published results showed that there is the usually scheme that includes the application of flocculation/co-

agulation (Fl/Co) followed by either chemical oxidation or biodegradation (Yan et al., 2007a), (Beltran et al., 2000).

The Fl/Co used as an initial treatment in the sequential schemes has evaluated different flocculants/coagulants. For example, Selcuk (2005) shows that ferrous and aluminum sulfates are equally effective in decreasing the COD, color, and toxicity of the real textile waste water. A comprehensive review on the combination of Fl/Co with some other chemical treatments can be consulted in Verma et al. (2012). In particular, the sequential application of Fl/Co and ozonation is not a new trend, and it has shown remarkable results. The combination of Fl/Co and ozonation was evaluated in two ways: Fl/Co followed by ozonation and vice versa. The first scheme showed to be the more effective (De los Santos Ramos et al., 2009). Besides, some studies proved the effectiveness of the preliminary ozonation for improving the Fl/Co results using biopolymers (Chiang et al., 2009; Yan et al., 2005). This modification enhanced the effect of the Fl/Co due to the polar compounds produced in ozonation. The stabilization of pretreated leachates was studied in Ntampou et al. (2006), where ozonation was used after the Fl/Co with ferrous salts yielding the initial COD by 72%.

In Monje-Ramirez and De Velasquez (2004) the efficacy of the treatment of real landfill leachates was evaluated using the same treatment scheme. This combination seems to be effective not only for removing the COD, but also for transforming the recalcitrant organic matter in the simpler organics with lower molecular weight. The COD was removed by 99% and the biodegradability increased more than 200%. A deeper study of the decomposition kinetics of the different groups of the toxic contaminants was performed in Poznyak et al. (2008), where some toxic substances were also partially identified, as well as some byproducts extracted with different solvents, by the HPLC and the gas chromatography methods.

In all cases discussed above, the application of inorganic chemical coagulants and flocculants was considered. Even when the reported results demonstrated improvements in the removal of contaminants, the types of byproducts generated by the oxidation are harmful and toxic. In De los Santos Ramos et al. (2009), there is a detailed description of all possible byproducts, generated by the application of Fl/Co and ozonation, most of which are toxic contaminants. Such byproducts formed by an incomplete oxidation of the initial contaminants or the interaction between ozone and the molecules of flocculants/coagulants. This is a very important issue, which should be considered in the case of the application of Fl/Co and ozonation, as part of MWW treatment plants (Zamudio-Pérez et al., 2014).

An alternative to inorganic salts, as flocculant–coagulant, is natural gums, which are biopolymers, such as starches, pectins, galactomannans, and exudates widely used in food, pharmaceutical, textile, cosmetics, and wine industry (Torres et al., 2012). They are also good for use in the Fl/Co process. The extra benefit of the biopolymer is the formation of the more biodegradable sludge, since for COD removal a further adjustment of the pH was not required.

The study presented by Carpinteyro-Urban et al. (2012), reported the use of guar gum, locust bean gum, mezquite and Opuntia mucilage flocculants/coagulants agents in the treatment of the MWW, where the adequate dose of the coagulant improved significantly the removals of COD, FC, and TC, and it reduced the treatment costs. The use of the biopolymer HPTAC-guar yields an efficient removal of the COD, the turbidity, the decrement of biological indicators (more than 99% removal of TC and FC), even greater than the one obtained with the application of $FeCl_3$. The sludge volume is ten times less than with the salt (Zamudio-Pérez et al., 2014). An extra benefit of the natural gums is that they are also decomposed by ozone (Evelyn et al., 2013).

7.3.2 Materials and methods

7.3.2.1 Characterization of the MWW

The waste water samples were collected from a treatment plant located in the State of Mexico (San Juan Ixhuatepec), twice sampled (120 L) in the step before the standard treatment and stored at 4°C. The general characterization of MWW performed by the measuring of physicochemical and microbiological parameters (pH, COD, turbidity, TC, FC, and HE) was established in terms of the Mexican Official Standard NOM-003-SEMARNAT-1997 and NOM-001-ECOL-1996. The last document confirms that FC and HE are pathogenic contaminants and it obeys the international regulation (World Health Organization, 2004 Integrated Guide to Sanitary Parasitology).

7.3.2.2 Experimental methodology of the MWW samples treatment

The experimental scheme is divided in three stages. The first one focused on the single Fl/Co treatment of MWW. The Fl/Co process used square jars with the capacity of 2 L, running in speed of 100 rpm for 3 min (coagulation) and then at 20 rpm for 15 min (flocculation). All experiments were carried out with two different concentrations of HPTAC-guar (25 and 30 mg L^{-1}) to choose the best dose. These concentrations were selected based on the results obtained in a previous study (Evelyn et al., 2013). The initial pH of

the MWW was adjusted using different concentrations of NaOH 4% v/v. The pH was measured using a potentiometer (Portable pH/CON 10 and Waterproof pH/CON 10 m, OAKTON). After the pH modification, the Fl/Co process was done by duplicate. To select the best flocculant–coagulant (HPTAC-guar) concentration, the parameters (COD, turbidity, pH, conductivity, sludge volume, TC, FC, and HE) were evaluated.

The second stage dealt with the single ozonation of the same MWW samples used in the first stage. In this stage, two different ozone concentrations were used (15.0 and 30.0 mg L^{-1}) (Evelyn et al., 2013). The third stage considered the sequential treatment of the MWW using the Fl/Co and ozonation.

7.3.2.3 Determination of sludge volume and Z-potential

The sludge volume was measured using Imhoff cones (1 L), where it was settling for 1 h. The Z-potential was determined at the original pH of the sample by a commercial Z-meter (Malvern, USA).

7.3.2.4 Coliforms quantification method

The coliforms quantification method is based on the direct filtration of the sample or the aliquot of the sample through a cellulose membrane, which retains the organisms, either by placing the membrane in a selective culture medium: *m-Endo agar LES* (for the TC growth) or m-*FC agar* (for the FC growth). The membranes were incubated for 24 h, either at 35–37°C for the detection of coliform organisms, or alternatively at 44.0 ± 1°C because of the presence of the thermotolerant coliform organisms. A direct count of the colonies was carried out on the membrane prepared with a selective culture medium.

7.3.2.5 HE quantification

The HE quantification method is based on the principles of the biphasic flotation method (Carpinteyro-Urban et al., 2012). 5 L of the initial waste water was allowed to stand for 8 h, then its supernatant was aspirated by vacuum and discarded. The sediment was filtered in a sieve with 160 μm, and washed with 5 L of water. The washed water along with the sediment filter was recovered. The samples were allowed to stand overnight and the recovered washed water was aspirated again. The sediment was deposited in centrifuge containers rinsing 3 times the little volume of distilled water and it was placed in containers for centrifugation. The tubes were centrifuged at 400 rpm for 5 min.

The supernatant was decanted by vacuum ensuring that the bottom of the tablet container was empty. The pellet was suspended in 150 mL of solution

of zinc sulfate ($ZnSO_4$). All pellets were centrifuged at 400 rpm for 5 min, and the supernatant was recovered by pouring it into a plastic container of 2000 mL. The samples were diluted in 1000 mL of the distilled water and were allowed to settle overnight. The upper phase was aspirated by a vacuum pump and the pellets were re-suspended with 1 mL of distilled water.

The suspension was centrifuged at 480 rpm for 3 min. The supernatant was decanted and the pellet was re-suspended with the distilled water by centrifuging at 480 rpm for 3 min. The supernatant was decanted and the pellet was re-suspended in 15 mL of the acid–alcohol solution using a shaker. 10 mL of ethyl acetate was added to the tubes and gently stirring occasionally uncovered to strip the gas. The sample was centrifuged at 660 rpm for 3 min and the supernatant was aspirated as much as possible. In the tube, there was left less than 1 mL. The loss of the wafer was prevented. The pellet was homogenized and the HE quantification was proceeded by the microscopic visual identification.

7.3.2.6 UV-spectrophotometry

During the ozonation, 3 mL of the samples was taken from the reactor at different times (0, 5, 10, 15, 20, 30, 45, and 60 min). These samples were filtered and analyzed by an UV-Vis Spectrophotometer (Lambda 2B, Perkin-Elmer) at a wavelength range of 200–300 nm.

7.3.3 Results and discussions

7.3.3.1 Characterization of the MWW

The characterization of the physicochemical and microbiological parameters of the MWW were obtained by the certificated laboratory of the Universidad Autónoma Metropolitana, Campus Azcapotzalco. In Table 7.13, the averaged values of the three samples collected from the waste water plant are presented.

The MWW samples were slightly acid (pH = 6.8), the COD was 960.0 mg L^{-1}, which was twice larger than the COD value reported for other waste waters, generated in Mexico City (Nacheva et al., 1996). The BOD_5 was 403.76 mg L^{-1}; furthermore, FC, TC, and HE were ten times bigger than reported in some other studies (Rojas-Valencia, 2011). In this sense, the waste water samples may be characterized as highly contaminated.

The TC concentration was about $2.8 \cdot 10^7$ $MPN/100$ mL and the FC concentration was $8.48 \cdot 10^6$ $MPN/100$ mL, which were higher than the reported in previous studies. The number of the HE (470 HE/L) corresponded

Table 7.13 Physicochemical and microbiological parameters of the MWW samples.

Parameter	Value	Normal value
pH	6.76	5.0–10.0
Turbidity (FAU)	141	NA
Total solids (mg L^{-1})	890.90	20.0–30.0
Conductivity (μs)	1335.00	NA
Color (Pt/Co)	1450.00	NA
BOD_5 (mg L^{-1})	403.76	20.0–30.0
Hardness (mg L^{-1})	258.21	NA
Total alkalinity (as $CaCO_3$) (mg L^{-1})	NR	
COD (mg L^{-1})	970.00	100.00–160.00
MBAS (mg L^{-1})	11.61	5.00–8.00
Cr (mg L^{-1})	< 0.01	0.75
Fe (mg L^{-1})	0.247	NA
Pb (mg L^{-1})	0.078	0.10
Z-Potential (mV)	15.73*	NA
Total Coliforms (MPN mL^{-1})	$2.8 \cdot 10^7$	NA
Fecal Coliforms (MPN mL^{-1})	$8.48 \cdot 10^6$	240.00–1000.00
Helminth eggs (HE L^{-1})	470.00**	1.00–5.00**

* *At the original pH = 6.76.*
** *Values are dependent on the pH. Label NA means: not applicable, because the current norm does not consider these parameters.*

to the values reported in Mexican rural or peri-urban areas (Jimenez-Cisneros and Maya-Rendon, 2007) and were higher than found in some other similar studies (Quinzaños et al., 2008).

The HE species were *Diphyllobothrium latum, Ascaris lumbricoides, Hymenolepis nana and Toxocara canis*. The *Diphyllobothrium latum* had 67 to 71 μm in length and 40 to 51 μm width. In humans, these organisms can lead to the nonspecific abdominal symptoms, and a small percentage of cases can provoke macrocytic hypochromic anemia. The *Ascaris lumbricoides* size was from 45 to 75 μm long and 35–50 μm width. The most common symptom in infected patients is vague abdominal pain, the larvae causes sensitization of the host and reactions such as pulmonary infiltrates, asthma attacks, and edema of the lips. *Hymenolepis nana* size is in the range between 30 and 44 μm. This parasite has a cycle of internal autoinfection. Mild cases are usually asymptomatic, the larval forms destroy and injure villi, adults irritate the intestinal wall, causing a mild enteritis: cases with moderate or massive parasitization abdominal pain, nausea, vomiting, weight loss, diarrhea, nervousness, headache, etc. *Toxocara canis* measures are 90 μm

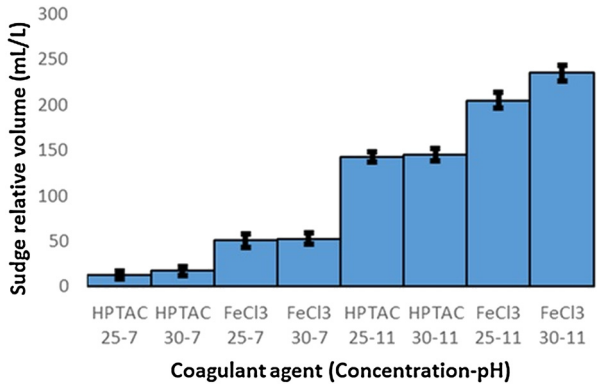

■ **FIGURE 7.10** Effects of the coagulant concentration and the pH on the sludge volume.

long and 75 μm width. Toxocariasis is a clinical syndrome that is caused by the invasion of human viscera by larvae. These parasites are roundworms of dogs and cats. In humans, the larvae are released from ingested embryonated eggs, and they may penetrate the intestinal mucous membrane and travel to the liver, lungs, and other organs. More details of these HE can be found in Zamudio-Pérez et al. (2014) and the references therein.

7.3.3.2 Sludge volume and COD, turbidity, TC and FC removal after flocculation–coagulation

The sludge volume obtained after the Fl/Co was four times smaller in average, when the pH of the MWW was initially adjusted to 7.0 (see Fig. 7.10). This result was independent of the Fl/Co agent (biopolymer or salt). Contrarily, the volume of sludge increased by four times when the pH was adjusted to 11. In the presence of $FeCl_3$ the sludge volume increased 2.5 times at the pH of 7.0 and of 1.3 times at the pH of 11.0, compared with the HPTAC-guar. The biopolymer produced a smaller volume of the sludge. On the other hand, the variation of the Fl/Co agent concentration had no effect on the sludge volume.

In the case of the removed COD, the strong effect of the pH was observed. At pH = 7, the salt was more effective (70%, to be compared with 35%). But the increases of pH to 11.0 yields a COD removal of 60–65% in the presence of the HPTAC, which is almost the same as obtained with a salt at a pH of 7. However, the salt at a pH of 11 provides only 55% of the COD removing twice its concentration (Fig. 7.11).

A basic pH promotes the increment of the sludge volume, because it stabilizes the flocs structure. This fact has been proven in a preliminary study (Carpinteyro-Urban et al., 2012). The variations of the Z-potential served to

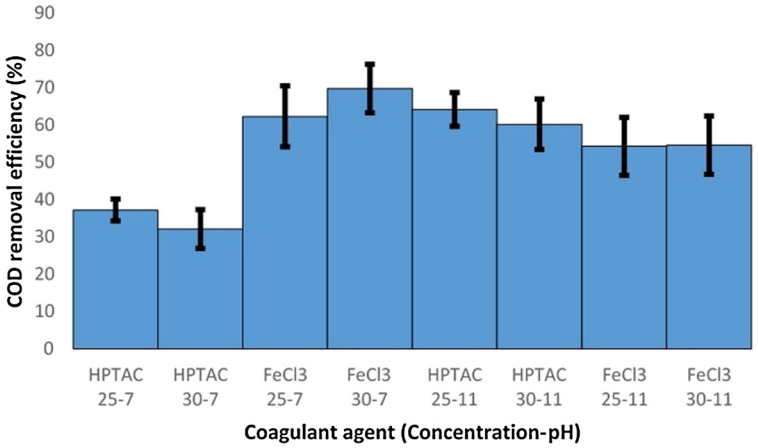

■ **FIGURE 7.11** Effects of the coagulant concentration and the pH on the removed COD.

establish how the pH increment can increase the sludge volume. The weak dipole charge of the HPTAC-guar, as compared to $FeCl_3$, leads to a decrease of the sludge volume.

The turbidity is removed by 35% independently of the concentration of the natural gum. This value is 3.5 times higher than the one obtained with the $FeCl_3$.

The TC and FC coliforms were evaluated at the end of the flocculation/coagulation. The presence of the HPTAC-guar produced the highest TC elimination. At a HPTAC concentration of 25 mg L^{-1}, the TC was removed up to 67%, while the $FeCl_3$ at the same concentration led only to 40%. If the concentration of the coagulant agent was increased to 30.0 mg L^{-1}, the TC was removed up to 98.0% with the FeCl, while HPTAC-guar guarantees a 100.0% removal. A preliminary study showed that biopolymer formed an internal net in the MWW that trapped the TC, as well as the FC. In the presence of salt, this kind of biopolymer net was not formed (Zamudio-Pérez et al., 2014).

7.3.3.3 COD, turbidity, TC, and FC removal in ozonation without preliminary flocculation–coagulation

The COD removal was more efficient in conventional ozonation, where the ozone concentration was the most important parameter. As one can see in Fig. 7.12, the COD removed was around 70% at two pH values (7 and 11) when the ozone concentration was 30.0 mg L^{-1}. The decrease of the ozone concentration to 15 mg L^{-1} leads to the decrease of the COD removal to 35.0%, on average, at the two pH values of 7.0 and 11.0. The COD removal

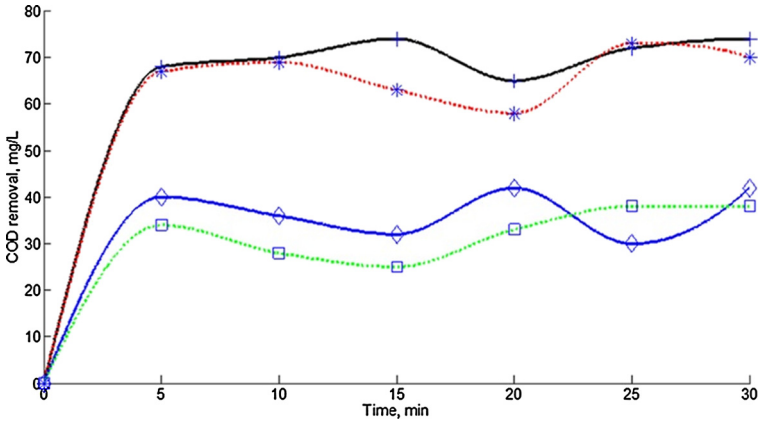

■ **FIGURE 7.12** Effects of the pH and the ozone concentration on the COD removal: pH $= 7.0$ and $[O_3] = 15.0\,\text{mg}\,\text{L}^{-1}$ (green, □), pH $= 7.0$ and $[O_3] = 30.0\,\text{mg}\,\text{L}^{-1}$ (red, ∗), pH $= 11.0$ and $[O_3] = 15.0\,\text{mg}\,\text{L}^{-1}$ (blue, ◇) and pH $= 11.0$ and $[O_3] = 30.0\,\text{mg}\,\text{L}^{-1}$ (black, +).

changed significantly in the first 5 min of ozonation for all the studied cases, and after this time the COD value almost did not change. This means that the dissolved organic matter is more reactive with ozone and it is removed during the first 5 min.

It is well recognized that a basic pH promotes better organic matter removal. The same removal of the COD, observed at pH values of 7 and 11.0, at two ozone concentrations, can be considered a consequence of the free radical scavengers, such as phosphates or sulfates, which are usually detected in real waste waters. Therefore, the effect of the pH was not observed. This phenomenon is described in Zamudio-Pérez et al. (2014).

The behavior of the turbidity in ozonation depends on the pH and almost does not depend on the ozone concentration. Namely, it is reduced by 70.0% at a pH of 7.0 at two ozone concentrations during the first 5.0 min and then it remains almost constant. At pH $= 11.0$, the turbidity was removed only by 45.0%.

The conventional ozonation is very effective in the disinfection that has been confirmed by the excellent results of the TC and the FC deleting. At the pH of 7.0 (the pH of MWW), the TC and FC removals are close to 100%. After 20 min of ozonation, the average removal was 99.88% for the TC and 97.83% for the FC. After 30 min of ozonation, all the averaged parameters reached 99%. This phenomenon was explained by the high sensibility of the TC to oxidation by ozone. This result coincides with the ones reported in Bustos et al. (2010); Orta de Velasquez et al. (2008); Xu et al. (2002).

Table 7.14 Effect of the ozone concentration on the removal of the TC and the FC at a pH of 7.0.

Reac. time (min)	TC		FC	
	Ozone concentration $\left(\frac{mg}{L}\right)$			
	15	30	15	30
5	99.91 ± 0.09	99.90 ± 0.05	100.00 ± 0.00	96.50 ± 3.54
10	99.91 ± 0.12	99.88 ± 0.06	93.75 ± 1.77	99.00 ± 1.41
15	99.66 ± 0.10	100.00 ± 0.00	97.00 ± 2.83	100.00 ± 0.00
20	99.92 ± 0.11	100.00 ± 0.00	98.50 ± 0.71	100.00 ± 0.00
25	99.98 ± 0.01	100.00 ± 0.00	99.79 ± 0.11	100.00 ± 0.00
30	99.97 ± 0.00	100.00 ± 0.00	99.91 ± 0.02	100.00 ± 0.00

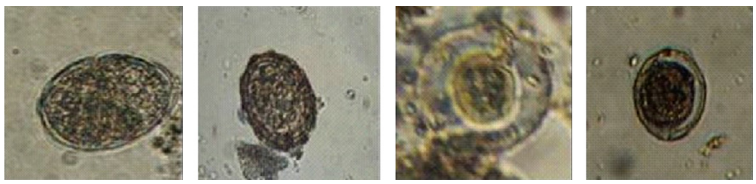

■ **FIGURE 7.13** Microphotographs of the helminth eggs in the MWW (A) and the effect of ozone concentration on their morphology: 6.0 mg L^{-1} (B), 15.0 mg L^{-1} (C), and 30 mg L^{-1} (D).

Table 7.14 demonstrates the removal of the TC and the FC with both concentrations of ozone.

As can be seen, even at an ozone concentration of 15.0 mg L^{-1}, the removal of these indicators is very high; for the FC it is 99.98% and 99.81% for the TC. If the ozone concentration was increased up to 30 mg L^{-1}, the removal of FC and TC was 100.00%. Both microbial factors were also removed completely (100.0%) at pH = 11. This positive result is explained by the simultaneous effect of two processes: the oxidation by ozone and the low biomass accumulation for the TC and the FC.

The HE removal is 82%, 85%, and 99% on average at the ozone concentrations of 6, 15, and 30 mg L^{-1}, respectively. The direct microscopy analysis confirmed the destruction of the membrane of the HE by ozone (Fig. 7.13), where also the effect of the ozone concentration on the intensity of the destruction can be observed.

Fig. 7.13A shows the original photograph of one HE. Fig. 7.13B shows how the membrane of the HE was destroyed by ozone, when its concentration was 6.0 mg L^{-1} and at a pH of 7, where one can see how the intracellular material was released to the external media. Fig. 7.13C demonstrates a wider region of the membrane destroyed by ozone for a concentration of

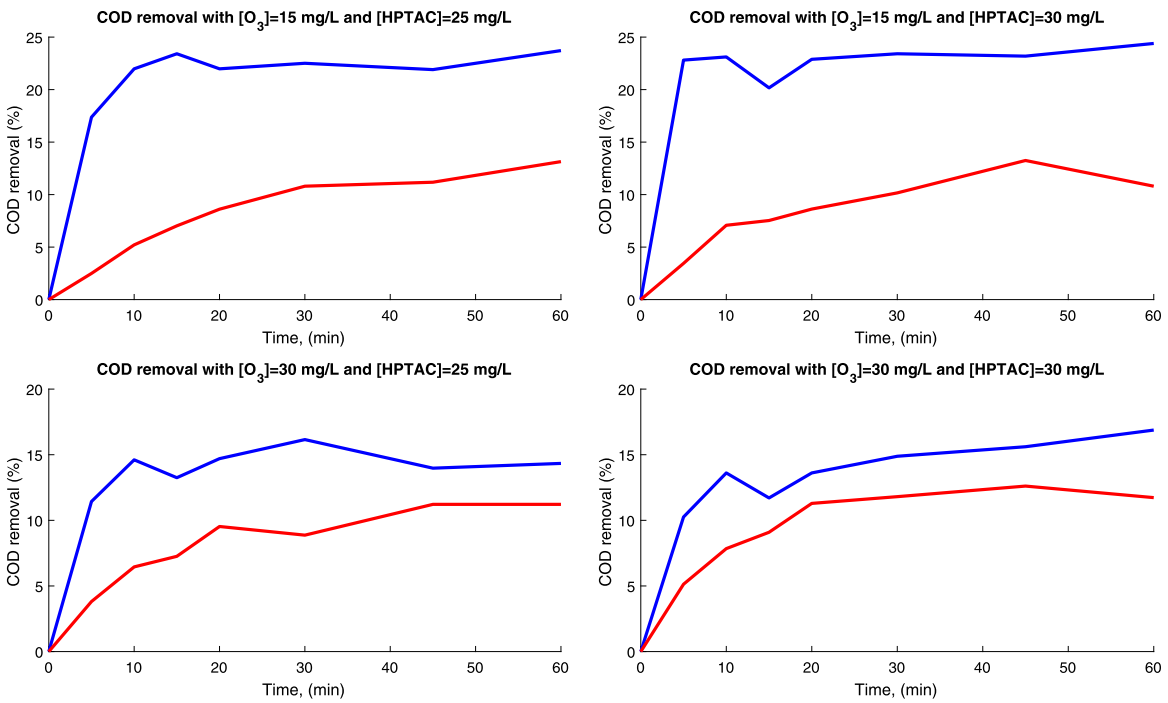

■ **FIGURE 7.14** COD removal during the ozonation, at a pH of 7.0 with different ozone, biopolymer (upper-blue line) and $FeCl_3$ (lower-red line) concentrations. (Note: The color figures will appear in color in all electronic versions of this book.)

15 mg L^{-1}. Finally, at the ozone concentration of 30 mg L^{-1} the cell membrane is completely destroyed (Fig. 7.13D).

7.3.3.4 COD, turbidity, TC, FC, and HE removals by the combination of flocculation–coagulation and ozonation

Fig. 7.14 shows the COD removal at the pH = 7 for both ozone concentrations and two HPTAC concentrations. These data are reported just for the ozonation, but considering the concentration of the HPTAC used in the preliminary Fl/Co process.

In all the cases at pH = 7, the ozonation showed a superior effectivity after the flocculation–coagulation in the presence of the HPTAC (23%) that improved the COD removal by 1.5–2.0 times compared to the $FeCl_3$ as the flocculant–coagulant agent (13%).

At an ozone concentration of 15.0 mg L^{-1}, a positive effect of the HPTAC concentration on the rate of the COD removal was also observed. Namely, the insignificant increase of the HPTAC concentration from 25 to 30 mg L^{-1}

leads to a significant decrease of the maximum COD removal time (from 15 to 5 min).

Notice that this tendency is not preserved at an ozone concentration of 30 mg L^{-1}. In that case the COD removal decreased to 15.0% for both HPTAC concentrations, and to 10% for both concentrations of the $FeCl_3$. In general, the application of the inorganic salt at the preliminary stage of the treatment is less efficient for the COD removal.

These results indicate that the ozone concentration has the most relevant effect on the COD removal, despite the coagulant concentration, but its increment reduces the COD removal. The increment of the HPTAC concentration has no evident COD removal effect. On average, the COD removal increased 5%, if the ozone concentration was reduced from 30 to 15 mg L^{-1}. This small increment might be a consequence of the reaction between ozone and HPTAC, which may reduce the biopolymer concentration.

Fig. 7.15 shows the COD removals at pH = 11.0, where a stronger effect of the concentration of the flocculant–coagulant agents on the COD removal efficiency can be observed. If their concentrations are 25 mg L^{-1}, the COD removal with the $FeCl_3$ is even more effective than with the biopolymer (15.0% vs. 8.0% and 8.0% vs. 6.0% at the ozone concentrations of 15.0 and 30.0 mg L^{-1}, respectively).

If the concentration of flocculant–coagulant agent increases to 30 mg L^{-1}, higher COD removals are obtained with the biopolymer (23% during only 5 min) at an ozone concentration of 15 mg L^{-1}. At an ozone concentration of 30 mg L^{-1}, the COD removal decreases to 13% with the biopolymer and to 8% with the salt. Based on the obtained results, one may can conclude that in the combined treatment the effect of the coagulant nature and its concentration is stronger than the ozone concentration. On the other hand, at a smaller ozone concentration, the best result of the global treatment has been obtained.

In the case of the turbidity, the effect of the coagulant concentration is also very strong. The tendency of the turbidity removal is similar to the COD behavior. At a pH of 7 and at an ozone concentration of 15 mg L^{-1} and a coagulant concentration of 25 mg L^{-1}, the difference between the two coagulants was not significant. However, the increase of the coagulant concentration to 30 mg L^{-1} provides significant changes of the turbidity behavior (60% with the HPTAC vs. 20% with the salt) (Fig. 7.16).

The two-fold increment of the ozone concentration leads to changes of the turbidity behavior. At a coagulant concentration of 25 mg L^{-1}, the turbidity removal decreases to 40% with the HPTAC and to 20% with the $FeCl_3$,

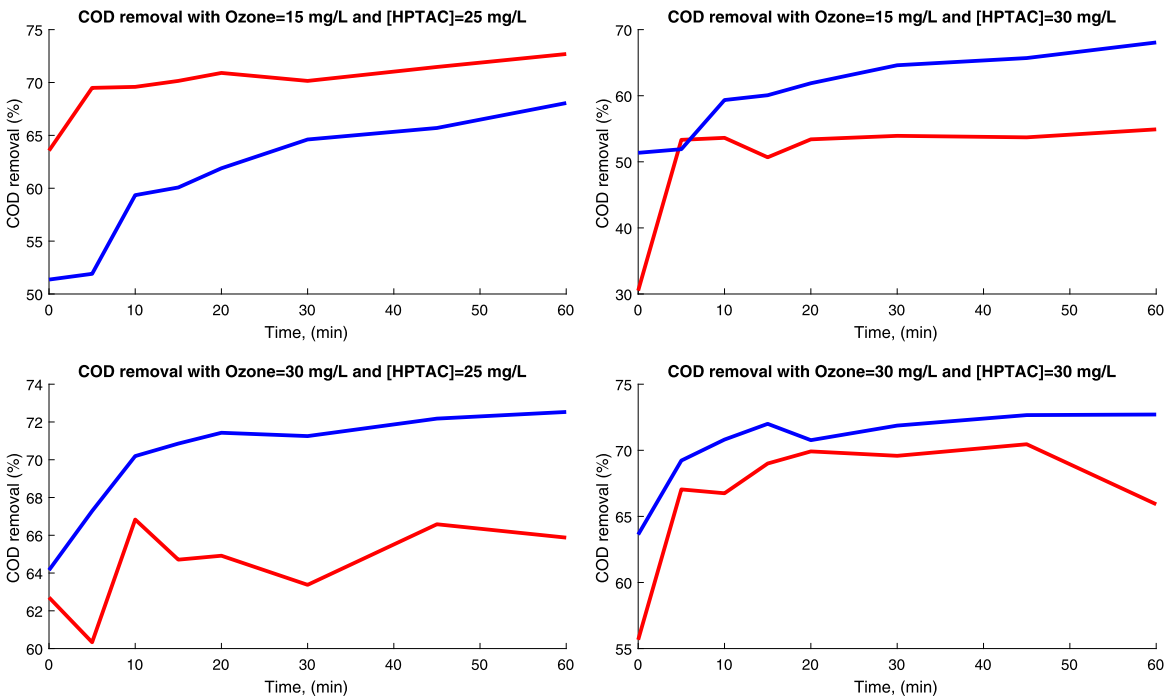

■ **FIGURE 7.15** COD removal during the ozonation, at a pH of 11.0 under different ozone, biopolymer (blue line in the electronic version) and $FeCl_3$ (red line in the electronic version) concentrations.

proving that the biopolymer is more effective. On the contrary, with the coagulant concentration of 30 mg L^{-1}, the best result is obtained with the salt (32%), to be compared to 12% with the biopolymer. The augment of the pH up to 11 totally changes the behavior of the turbidity (Fig. 7.17).

In this case, there is a noticeable relation between the ozone concentration, the coagulant concentration and the turbidity. However, the behavior of the last parameter is absolutely different. At the ozone concentration of 15 mg L^{-1}, the insignificant increase of the coagulant concentration to 30 mg L^{-1} increases the turbidity removal from 13% for the biopolymer to 60% and it is not occurring in the case of the salt (30% for both concentrations). The two-fold increase of the ozone concentration demonstrates almost the same effect for both coagulants (20% in the first 20 min) at their concentrations of 25 mg L^{-1}, and the significant augment for the biopolymer (58% in the first 10 min) at the coagulants concentrations of 30 mg L^{-1}. The influence of the $FeCl_3$, in the last case, remains the same. Figs. 7.18–7.19 show the variation of UV absorbance (with respect to time and wavelength) in ozonation under the different experimental conditions: the concentration of ozone and of the biopolymer. This permits one to control the elimination of the organic matter in the combined treatment. In

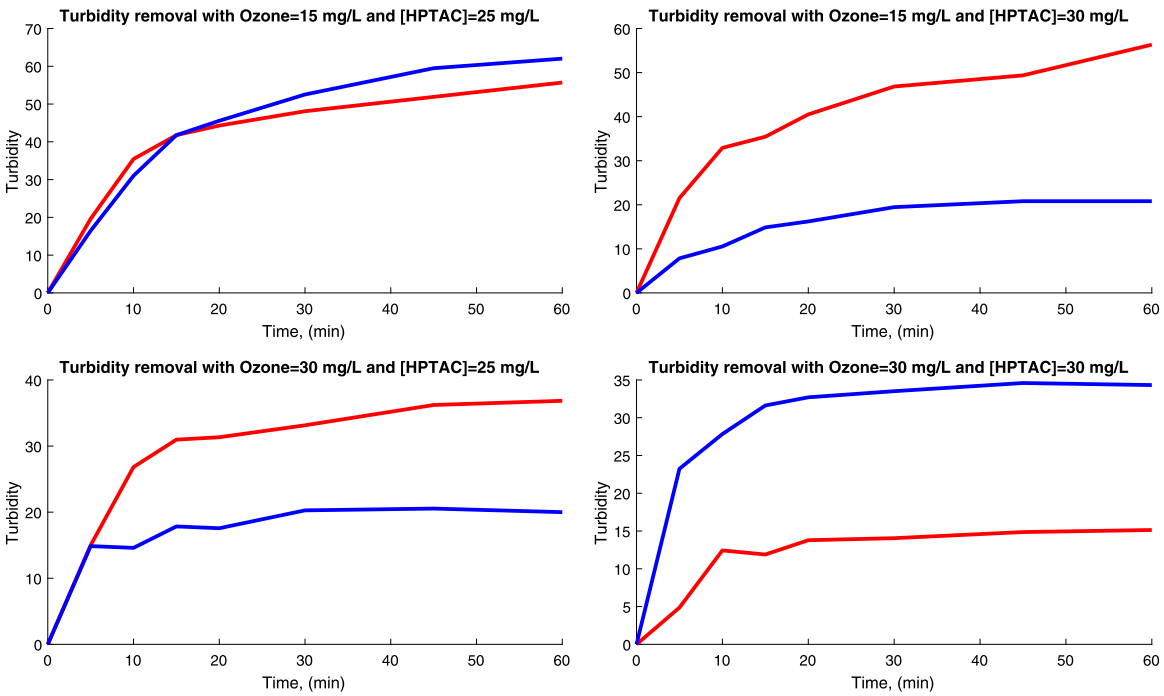

■ **FIGURE 7.16** Turbidity removal during the ozonation, at a pH of 7.0 under different ozone, biopolymer (blue line), and $FeCl_3$ (red line) concentrations.

general, at an ozone concentration of 15.0 mg L^{-1}, despite the biopolymer concentration, the absorbance behavior demonstrates the predominance of the direct mechanism of the reaction between ozone and the organic matter.

If the ozone concentration increases to 30.0 mg L^{-1}, the absorbance is reduced. Moreover, the spectrum seems to be flat after 30.0 min of ozonation. This tendency is more evident at a biopolymer concentration of 30 mg L^{-1}. This confirms the presence or the accumulation of compounds slowly reacting with ozone such as alcohols, aldehydes, and simple organic acids.

7.3.3.5 TC and FC removal

The upper subfigure in the left of Fig. 7.20 shows the TC removal (when pH = 7.0) at the ozone concentration of 15 mg L^{-1}, and the gum concentration of 25 mg L^{-1}. The upper figure in the right of Fig. 7.20 shows the TC removal at the ozone concentration of 15 mg L^{-1}, and the gum concentration of 30 mg L^{-1}. The lower figure in the left of Fig. 7.20 shows the TC removal at the ozone concentration of 30 mg L^{-1}, and the gum concentration of 25 mg L^{-1}: The lower figure in the right of Fig. 7.20 shows the TC removal at the ozone concentration of 30 mg L^{-1}, and the gum concentration of 30 mg L^{-1}.

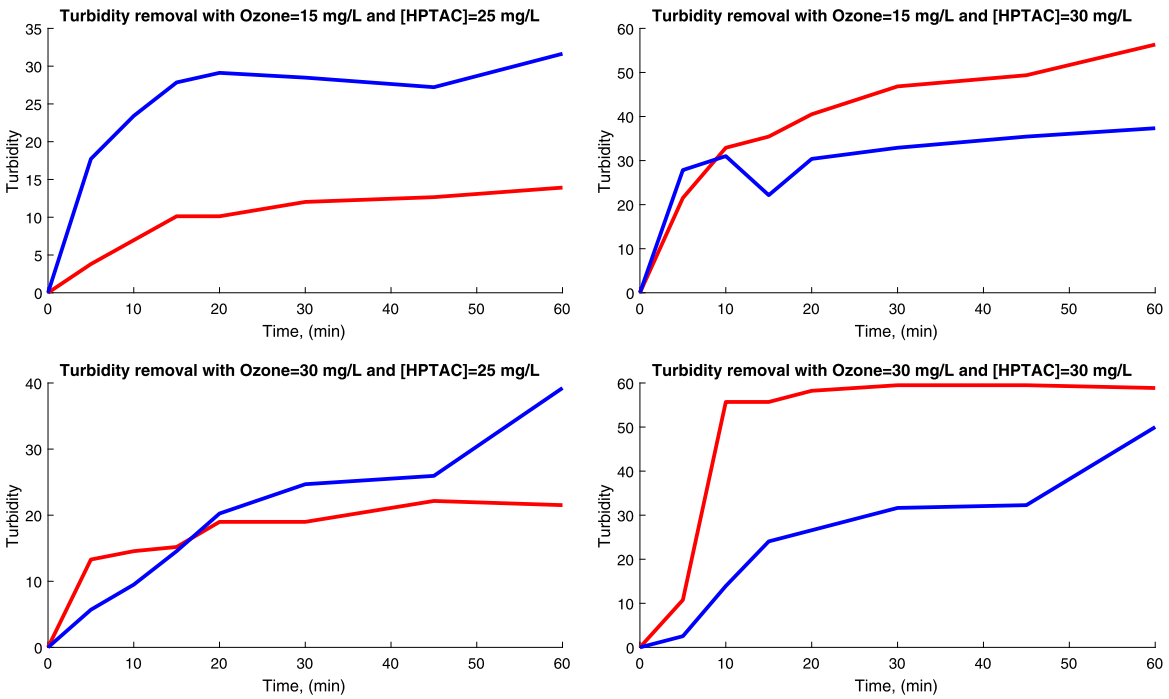

■ **FIGURE 7.17** Turbidity removal during the ozonation, at a pH of 11.0 under different ozone, biopolymer (blue line), and $FeCl_3$ (red line) concentrations.

The upper subfigure in the left of Fig. 7.21 shows the TC removal (when pH = 11.0) at the ozone concentration of 15 mg L^{-1}, and the gum concentration of 25 mg L^{-1}. The upper figure in the right of Fig. 7.21 shows the TC removal at the ozone concentration of 15 mg L^{-1}, and the gum concentration of 30 mg L^{-1}. The lower figure in the left of Fig. 7.21 shows the TC removal at the ozone concentration of 30 mg L^{-1}, and the gum concentration of 25 mg L^{-1}. The lower figure in the right of Fig. 7.21 shows the TC removal at the ozone concentration of 30 mg L^{-1}, and the gum concentration of 30 mg L^{-1}.

7.4 FLOCCULATION–COAGULATION WITH BIOPOLYMER AND CATALYTIC OZONATION

7.4.1 Vinasse waste water

Vinasse waste water is an example of a different combination of the Fl/Co and heterogeneous catalytic ozonation systems that can be applied to the treatment of the vinasse waste water in the tequila production. In the pretreatment by the coagulation–flocculation we compared six biopolymers to decrease the insoluble organic matter and the color. Chitosan is the most

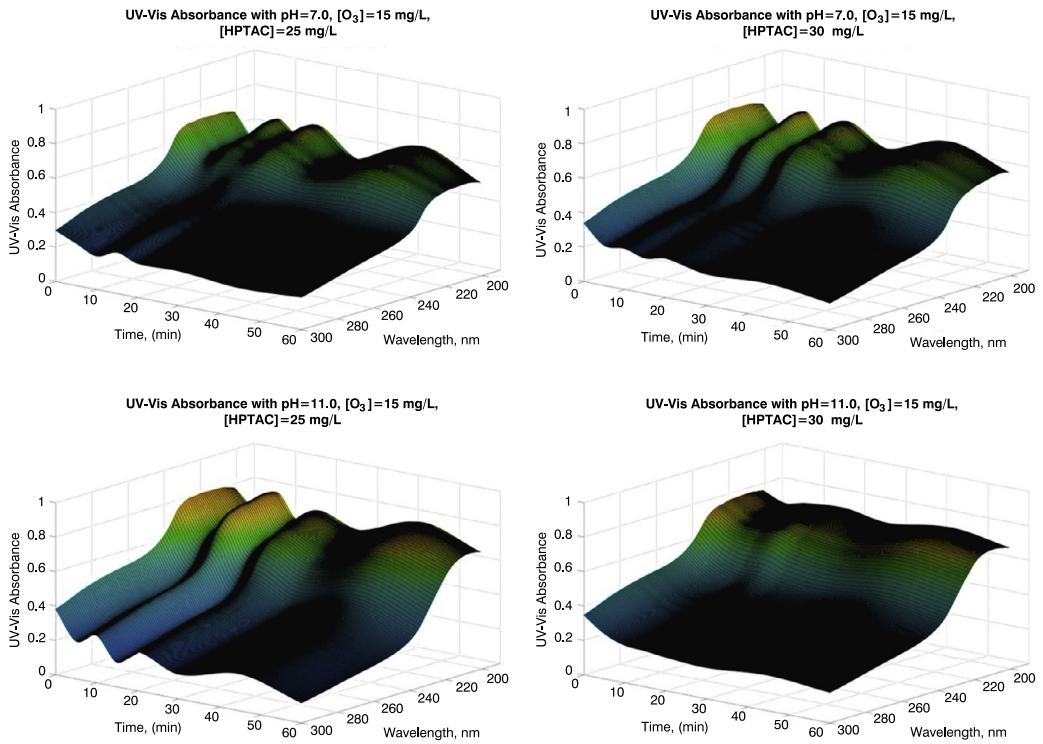

■ **FIGURE 7.18** Variation of the UV-spectra of the treated water at two concentrations of ozone and HPTAC at a pH of 7.

efficient biopolymer to maximal remove the COD (84.0%). Nickel oxide (100 mg L^{-1}) is used as a catalyst in ozonation. Additionally, to optimize the conditions of the coagulation–flocculation and the subsequent ozonation, the DNN technique was applied.

Due to the growing popularity of tequila in many countries all over the world, its production is increasing many times each year. The tequila raw material is blue agave (*Agave tequilana*), which is processed to extract aguamiel, a kind of a natural sugared beverage that then is boiled and fermented. A fermentation broth is distilled and we get two main contaminants:

a) residual solid of agave (bagasse) and

b) liquid (vinasse) (López-López et al., 2010).

Due to the low conversion of sugar to alcohol, 10–12 L of vinasse per liter of tequila is produced. The lack of the standards and the technology of the tequila waste water treatment causes an environmental crisis in the producer regions. Vinasses are merged into rivers, lakes, and soil without any treatment (Íñiguez-Covarrubias and Peraza-Luna, 2007). In general, physic-

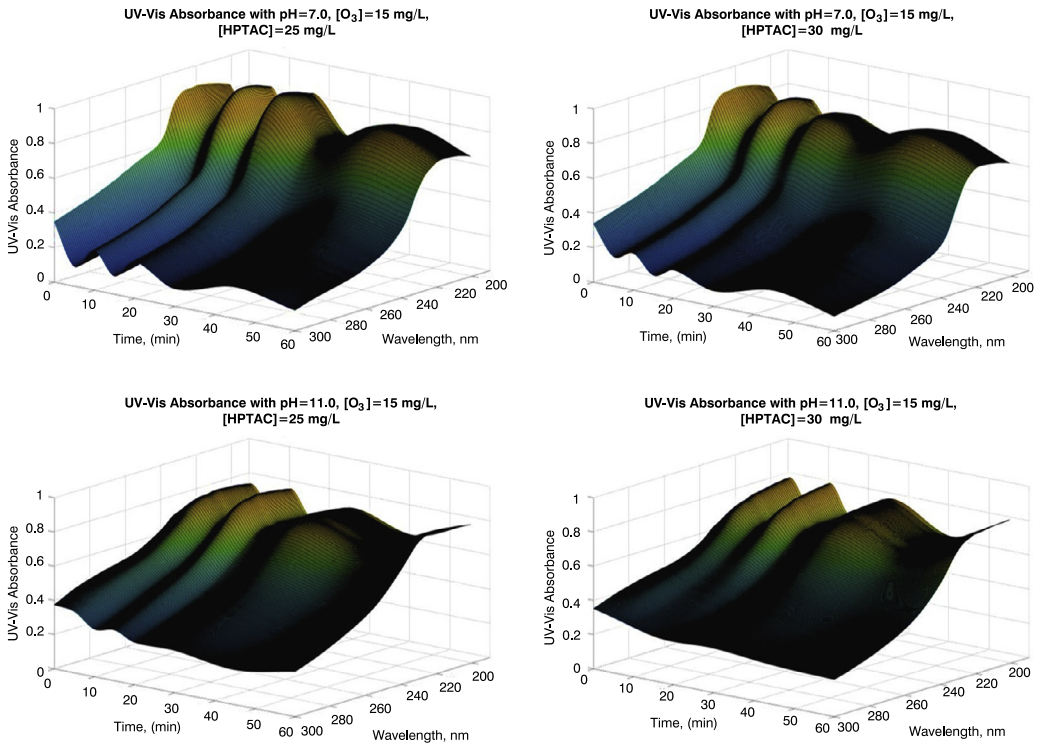

■ **FIGURE 7.19** Variation of the UV-spectra of the treated water at two concentrations of ozone and HPTAC at a pH of 11.

ochemical characteristics of vinasses are the low pH, the high COD, and a dark brown coloration. This last feature can lead to a serious environmental problem, namely, to water acidification and an increasing soil salinity (Zayas et al., 2007). The several treatment methods are proposed to eliminate the vinasses. Among others, physicochemical treatments, biodegradation, and AOPs have been considered as successful options (López-López et al., 2010). Anaerobic digestion provides a significant removal of organic matter; however, it cannot remove the vinasses color (Zayas et al., 2007). The best result obtained for the COD removal was 90–95% (Méndez-Acosta et al., 2010). As an alternative, the combination of different treatments can remove the COD and the humic and fulvic acids, which is responsible for the color of vinasses. For example, coagulation–flocculation can provide the removal of colloidal solids by 20–30%. Metallic salts and synthetic polymers are used as coagulants. In López-López et al. (2010), a color removal of 70% using $Al_2(SO_4)_3$ was obtained. However, the COD removal is only 37%. As a substitute for inorganic salts, biopolymers, such as locust bean gum, cactus mucilage, guar gum, and mesquite gum were investigated. This alternative takes advantage of biopolymers, since they are more environment friendly than inorganic salts (Carpinteyro-Urban et al., 2012). The applica-

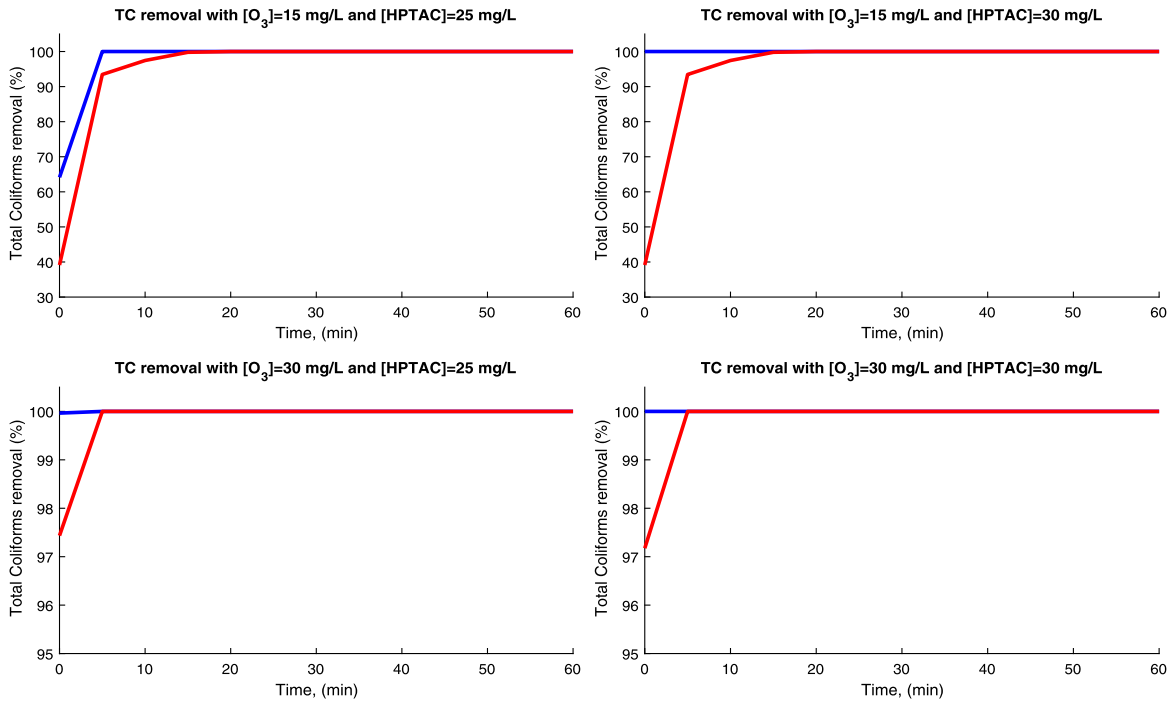

■ **FIGURE 7.20** TC removal during the ozonation process when the initial mixture has a fixed pH of 7.0 under different ozone and gum concentrations. Top left corner: $[O_3] = 15$ mg/L and [HPTAC] = 25 mg/L. Top right corner: $[O_3] = 15$ mg/L and [HPTAC] = 30 mg/L. Bottom left corner: $[O_3] = 15$ mg/L and [HPTAC] = 30 mg/L. Bottom right corner: $[O_3] =$ 30 mg/L and [HPTAC] = 30 mg/L. The solid line corresponds to the results of experiments executed with a natural gum, while the dashed line describes the COD removal when $FeCl_3$ was used as flocculant–coagulant.

tion of biopolymers for the cosmetic industry waste water treatment permits one to remove 67.8% and 38.6% for turbidity and the COD, respectively. The work presented by Torres et al. (2012) addressed the application of biopolymers, such as locust bean gum, cosmetics guar gum, mucilage cactus, mesquite seed gum, and $FeCl_3$, as a reference, in municipal waste water treatment. The authors proved that mesquite bean gum has a COD removal efficiency of 90% and cactus mucilaget of 65% at a pH value of 10. Reference Ferral-Pérez et al. (2016) proposed the use of the polyglutamic acid, which is the main component of cactus mucilage, as the coagulant agent in the treatment of tequila vinasses. If this biopolymer is mixed with the sodium hypochlorite and then sand filtered, a turbidity removal by 70% and the COD by 79.5% is obtained.

Ozonation is an attractive method for the treatment of vinasses, because ozone may decompose itself to form different free radicals, such as $^{\cdot}OH$ (hydroxyl), HO_3^-, HO_4^-, and O_2^- (superoxide) (Westerhoff et al., 1999). These free radicals are unselective and react fast with the organic contaminants dissolved in water, such as dyes, phenols, pesticides, organochlorides, and ammonium (Siles et al., 2011). The work of Lucas et al. (2009) developed a winery waste water treatment, based on ozone in a pilot-scale bubble col-

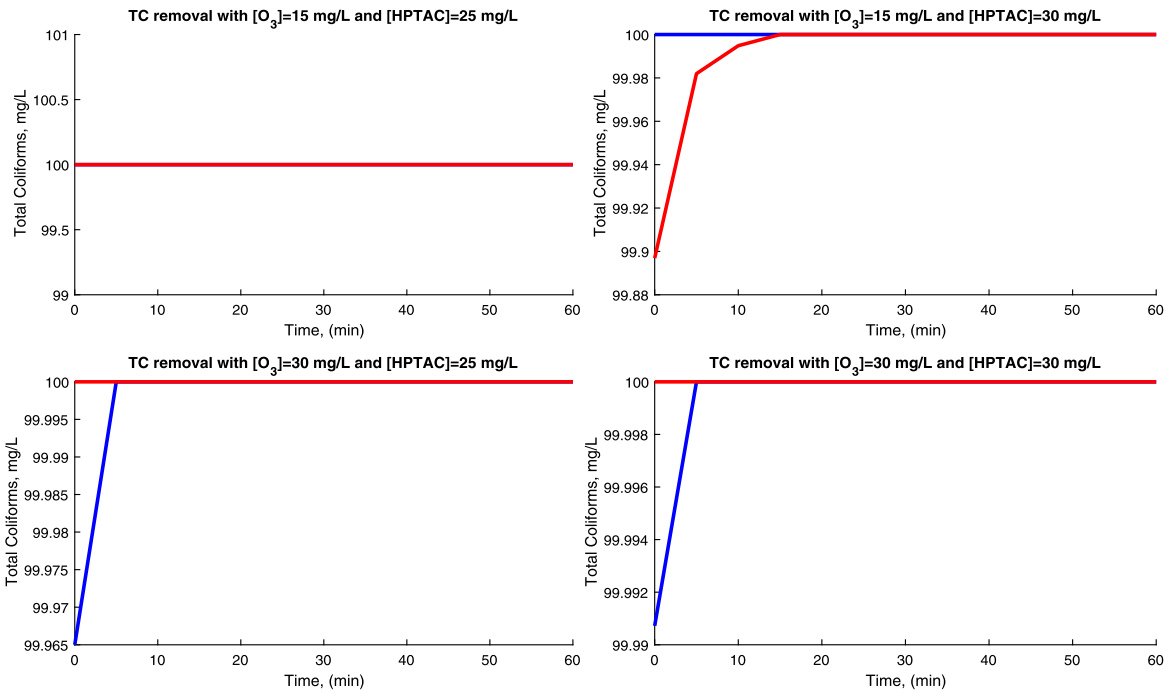

■ **FIGURE 7.21** TC removal during the ozonation when the initial mixture has a fixed pH 11.0 under different ozone and gum concentrations. Top left corner: $[O_3] = 15\ mg\ L^{-1}$ and [HPTAC] = $25\ mg\ L^{-1}$. Top right corner: $[O_3] = 15\ mg\ L^{-1}$ and [HPTAC] = $30\ mg\ L^{-1}$. Bottom left corner: $[O_3] = 15\ mg\ L^{-1}$ and [HPTAC] = $30\ mg\ L^{-1}$. Bottom right corner: $[O_3] = 30\ mg\ L^{-1}$ and [HPTAC] = $30\ mg\ L^{-1}$. The solid line corresponds to the results of experiments executed with the natural gum, while the dashed line describes the COD removal with $FeCl_3$.

umn at different pH values, reaching an aromatic compound degradation by 70% at a pH of 10 during 60 min. However, the maximum COD degradation is only 20% after 180 min. The same authors applied different AOPs (O_3, O_3/UV and $O_3/UV/H_2O_2$) to the treatment the winery waste water (Lucas et al., 2010). At a pH of 4.0, the effectiveness of each AOPs followed the sequence

$$UV - C < O_3 < O_3/UV < O_3/UV/H_2O_2.$$

The economic analysis of the operating costs of the AOPs revealed that $O_3/UV/H_2O_2$ is the cheapest scheme to treat the winery waste waters. Despite the remarkable results obtained, there are several deficiencies in this kind of treatment that cannot be neglected. In particular, the expense has been recognized as its primary negative aspect, but also its insufficient capacity to decompose some particular type of organic matter, such as organic acids, aldehydes, alcohols, etc. This is the main reason for developing new combined waste water treatments (Oller et al., 2011), which will show a significant efficiency over their individual treatments (García-Peña et al., 2012). For rum vinasses, Zayas et al. (2007) reported the application of anaerobic degradation with the Fl/Co (with $FeCl_3$). In this mixed treatment,

a COD reduction by 75.2%, a color removal by 99.6%, and a turbidity removal by 99.8% were attained. The work of Meza et al. (2004) studied the anaerobic digestion with Fl/Co, using $FeCl_3$ and $Al_2(SO_4)_3$ as coagulants, and KMnO4 as oxidant agent to treat tequila vinasses. This complex treatment achieved a high removal (above 85%) of the color and the turbidity (Sangave et al., 2007). The same combined scheme was used for the distillery waste water treatment, where a COD removal by 79% and an effluent discoloration during 4 h of ozonation and 30 min of biodegradation were obtained.

In the case of anaerobic oxidation, the results obtained in Siles et al. (2011) proved the enhancement of the digestion of vinasses in the ethanol production, when the ozonation was used as the pretreatment for 15 min. This mixed treatment produced methane with a yield of 13.6% and an increase of the rate of the methane production of 41.16%.

In Benitez et al. (2000), wine vinasses are treated independently by two methods: ozonation or biodegradation by an activated sludge. The sequential treatment was also tested: it consisted of an aerobic pretreatment followed by ozonation, in continuous reactors. The combined process reveals an improvement of the efficiency of the ozonation due to the previous aerobic oxidation. An inverse scheme (ozonation as pretreatment) also evaluated the decomposition of organic matter in the mixed waste water of the wine distillery and the domestic sources. The preozonation improved both the COD and the TOC removals; moreover, also it enhanced the nitrogen removal in the biological nitrification step and in settling the properties of the sludge (Beltrán et al., 2000). In Sangave et al. (2007) the effect of ozone before and after aerobic biodegradation to treat vinasses from sugar cane was studied. In the pretreatment step, ozone removed 27% of the COD. In the combined process, the preozonation leads to enhanced rates of biological oxidation.

7.4.2 Materials and methods

7.4.2.1 Vinasses

The vinasse samples were obtained from the *El Patron* tequila distillery, Jalisco, Mexico. Vinasses were characterized by the following Mexican normativity: acidity, COD, pH, turbidity, color degree, the content of phenols, oil and tars, and, additionally, heavy metals.

7.4.2.2 Coagulation–flocculation

The efficiency of coagulation–flocculation was determined by the Jar tests in six parallel jars equipment (Phipps and Bird, USA). The coag-

Table 7.15 Characteristics (averaged) of the VWW samples.

Parameters	Values
pH	3.9
Turbidity (Abs 620 nm)	0.5
Color [PtCo]	4066.7
BOD [mg L^{-1}]	15,076.0
COD [mg L^{-1}]	37,000.0
Total solids [mg L^{-1}]	16,920.0
Total nitrogen [mg L^{-1}]	243.0
Conductivity [μs]	4.1
Phenols [mg L^{-1}]	602.7
Methanol [mg L^{-1}]	75.5
Propanol [mg L^{-1}]	128.4
s-Butanol [mg L^{-1}]	22.72
i-Amilico [mg L^{-1}]	2413.0

ulant reagents were a chitosan solution (1%) with two concentrations (200 mg L^{-1} and 300 mg L^{-1}), Cosmedia Guar (700 mg L^{-1}), Algarrobo seed (1000 mg L^{-1}), guar gum (1100 mg L^{-1}), and the ferric chlorine (500 mg L^{-1}). The best conditions for coagulation–flocculation were determined by Box-Behnken as in Zamudio-Pérez et al. (2014). Independent variables were the chitosan concentration, the initial COD, and the reaction time.

7.4.2.3 Vinasses characterization

The characterization of the physicochemical and microbiological parameters of the vinasse waste water (VWW) was developed by the certificated laboratory of the Universidad Autónoma Metropolitana, Campus Azcapotzalco (Table 7.15)

As one can see in Table 7.15 the pH is acid, the COD of 37,000.00 mg L^{-1} is twice larger than other waste waters of the same source, and there is a high level of color.

7.4.3 Results and discussion

7.4.3.1 Determination of flocculation/coagulation optimum conditions

The selection of the biopolymer was made by the methodology proposed in Torres et al. (2012), namely, all the six different biopolymers were evaluated, and the pH and the biopolymer concentration. The best results of the

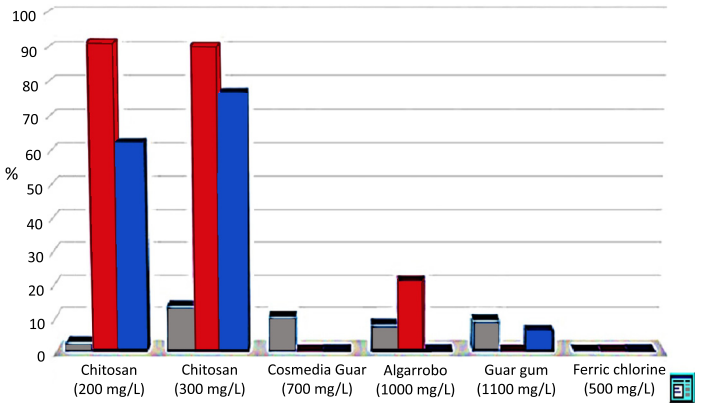

■ **FIGURE 7.22** Effect of the biopolymers in VWW treatment to remove the COD (gray), the turbidity (red), and the color (blue).

Table 7.16 Box-Behnken experimental design to determine attainable optimum reaction conditions.

Ranges	Chitosan mg L^{-1}	Initial COD mg L^{-1}	Time min
−1	200	22,200.00	20
0	300	29,600.00	40
1	400	37,000.00	60

color removal, the turbidity, and the COD were obtained for the chitosan with the concentration of 300 mg L^{-1}: 75%, 90% and 13.55%, respectively. Moreover, the decrease of the chitosan concentration to 200 mg L^{-1} led to the best results (Fig. 7.22).

Table 7.16 demonstrates the parameters used to characterize the efficiency of the Fl/Co. The chitosan concentrations were obtained from the results of the process optimization. A similar strategy was followed to determine the time of ozonation. The different initial CODs of 100%, 80%, and 60% were obtained from three different fractions of the VWW after a biological treatment and dilution (Méndez-Acosta et al., 2010).

7.5 EXPERIMENTAL EVALUATION OF THE NEURAL NETWORK

Two sets of the experimental data were used to test the application of the DNNO method for the combined treatment presented in this chapter. The first one uses the relative variation of components included in each group of compounds demonstrated in Section 7.3. The second one deals with the

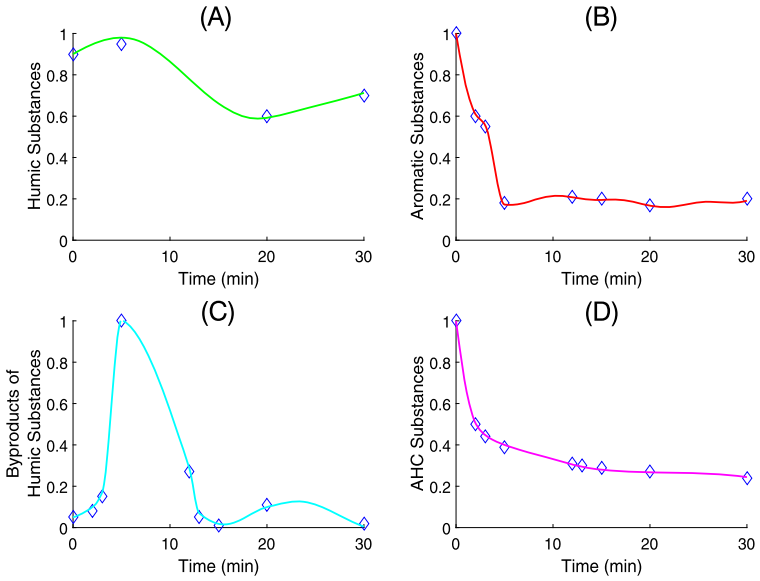

■ **FIGURE 7.23** Comparison of the experimental data (◇), with the states of DNNO (solid lines).

evolution of the wavelength absorbance with respect to time, when each element is considered as the state of an uncertain system. These two examples demonstrate the ability of the observer to reconstruct relevant information for highly complex systems with related elements.

7.5.1 First test

Fig. 7.23 demonstrates the comparison of the experimental data obtained from the ozonation of leachates with the estimated trajectories produced by the DNNO (Eq. (4.10)) using the learning laws (Eq. (4.11)).

Notice that all groups of compounds were reconstructed based only on the information obtained from the ozonogram presented in Fig. 7.8. Fig. 7.23A describes the variation of humic substances, which are slightly affected by ozone. Fig. 7.23B depicts the decomposition of aromatic compounds, which are decomposed during the first 5 min of ozonation in 80%. Fig. 7.23C shows the accumulation and decomposition of byproducts formed by the interaction between ozone and the humic substances. Fig. 7.23D describes the decomposition of AHC, which decreased 20% during 30 min.

The noising data observed in the ozone concentration in the gaseous phase affected the estimation quality. Therefore, a first order low-pass filter is implemented to clean up the data that appear in Fig. 7.23.

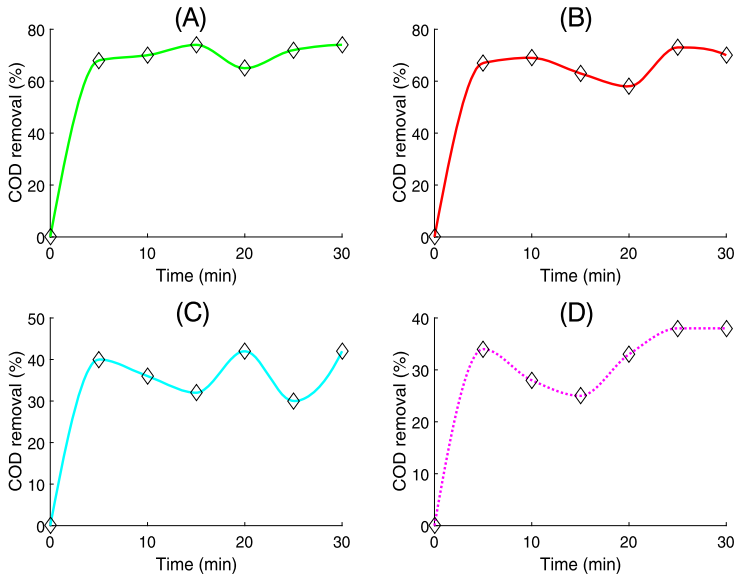

■ **FIGURE 7.24** Comparison of the experimental data of COD removal (◇) with the states of DNNO (solid lines).

7.5.2 **Second test**

Fig. 7.24 shows the COD variation obtained during the ozonation, when the waste water was previously treated with Fl/Co. These results confirm that in all cases the DNNO with exponential term reconstructs the information, which cannot be obtained online. Fig. 7.24A depicts the variation of COD, when pH = 7.0 and $c_{in,g} = 15.0$ mg L^{-1}. Fig. 7.24B demonstrates the COD modification, when pH = 7.0 and $c_{in,g} = 30.0$ mg L^{-1}. If the pH is augmented to pH = 11.0 and the input ozone concentration is fixed at $c_{in,g} = 30.0$ mg L^{-1}, the corresponding variation of COD appears in Fig. 7.24C. The experimental COD change, when pH = 11.0 and $c_{in,g} = 30.0$ mg L^{-1} appears in Fig. 7.24D.

7.6 **CONCLUSIONS**

The conclusions of this chapter are:

1. The previous precipitation of the diluted samples with sulfuric acid decreases the initial color by 96% and the formed sludge by 90%.
2. The coagulated sludge contains a sulfolignin complex, which may be obtained in the precipitation with the sulfuric acid.

3. In the decomposition of the lignin derivatives dissolved in the filtered water with ozone during 25 min and formed a mixture of the simple acids (fumaric, maleic, malonic and formic).
4. The precipitation pH has a significant effect on the efficiency of the sulfolignin formation, as well as on the lignin decoloration kinetics. It is feasible that different compositions of the dissolved contaminants are formed in the precipitation stage depending on the pH. The decoloration rates have the following order:
   – $pH = 12 > pH = 1 > pH = 8$ for the precipitation at $pH = 1$.
   – $pH = 8 > pH = 3 > pH = 12$ for the precipitation at $pH = 3$.
5. The biodegradability of the lignin decomposition products increased in ozonation (during 25 min) at the four pH values (1, 3, 8, and 12) from 0.066 up to 0.24–0.29.
6. The application of Fl/Co used a biopolymer to reduce the toxicity of effluents obtained from the former physicochemical process. Non-dissolved COD was removed by 92.0% using 30.0 mg L^{-1} as the initial concentration of biopolymer.
7. The variation of pH was also evaluated as a cofactor in the ozonation considering the reaction mechanism (direct and indirect).
8. Independently of the ozone concentration, the sequential treatment removed more than 99.0% of TC and FC after 25 min of reaction. In the case of HE, the removal percentage was 85% and 99%, when the ozone concentration was 15.0 and 30.0 mg L^{-1}. Therefore, the disinfection of the residual MWW was completed (according to the national regulations), by the Fl/Co and ozonation during 30 min.
9. Dissolved COD after Fl/Co was removed up to 30%, on average. Therefore, the total COD removal was above 93% at an ozone concentration of 30.0 mg L^{-1} and a pH of 11.0.

Chapter 8

Automatic control of ozonation systems in liquid phase

CONTENTS

Ozonation and Biodegradation in Environmental Engineering
https://doi.org/10.1016/B978-0-12-812847-3.00018-4

ABSTRACT

This chapter describes the application of two different automatic controllers for the ozonation of contaminated water. The first approach uses the new method to design a local optimal controller for ozonation. The online solution of the adaptive gains adjusting a linear control form yields the calculus of the suboptimal controller. A special performance index, meant to solve the transient evolution of such systems, is proposed. The class of systems considered in this study is highly uncertain: some components of chemical reactions are not measurable online, and then they cannot be used in the controller realization. The recovering of this information was executed by a differential neural network (DNN) structure. The ozonation process of a single contaminant (as a particular example of ozonation) is evaluated in detail using the control design proposed here. The second controller uses a trajectory tracking adaptive controller based on DNN to control the ozonation system. This approach uses a nonlinear transformation of the ozonation model to obtain a chain-of-integrators equivalent form. This controller was applied on the simple ozonation model with only one contaminant. The numerical and experimental validation of the tracking controller justifies both designs.

8.1 WHAT DOES IT MEAN TO OPTIMIZE AN OZONATION?

The determination of the optimal equipment sizes and the regimes of chemical processes in general and ozonation in particular, which guarantee the robustness of these processes under several uncertain factors, constitutes the basic optimization problem considered below in this chapter. Optimization problems of dynamic processes, with states varying in time, are typically quite challenging for real-time applications. Moreover, online applications with demanding real-time state constraints are challenging. Many systems in chemical engineering are difficult to optimize, using gradient-based algorithms usually applied to static chemical models in stationary regimes, since in real practice most of all chemical processes deal with multimodal objective functions and discontinuities.

To realize successfully the optimization of ozonation process the following topics (among others) should be considered here:

– flow-sheet synthesis,

– mass and energy balances,

– equipment sizing,

– process simulation,

– and controller designing which provides the fulfilling of some (usually several) objective aims.

Sometimes, some cost and economic evaluations are required additionally. The model quality is crucial for achieving good economical performance, but here we will not to touch on these aspects.

The objective of this chapter is to develop tools for feedback control designing in ozonation processes which are modeled by nonlinear (in fact, bilinear) differential equations with some algebraic relations between admissible control actions. We will refer below to the optimal synthesis of operations for ozone water treatment as **the optimization of ozonation processes**.

8.1.1 Variables which can be considered as control actuators

Recall that the mathematical model of ozonation in the presence of several contaminants is given by the collection of ordinary differential equations (2.15). Reconstruction of non-measurable variables $Q(t)$ and $c_i(t)$ is realized by the application of the differential neural network observers (DNNO) (4.15). In ODE (2.15) the main parameters, which can significantly change the behavior of the process and, therefore, can be considered as the *principal control actions,* are the following:

– W_g is the gas flow-rate (L s^{-1}) in the ozone reactor, so that

$$v_1 := W_g, \tag{8.1}$$

– c^g_{entr} is the ozone concentration at the reactor input (mol/L), that is,

$$v_2 := c^g_{in}. \tag{8.2}$$

Notice also that in the model of the process (2.15) both control variables v_1 and v_2 participate as a joint bilinear term,

$$W_g \left(c^g_{in} - c^g(t)\right) = v_1 v_2 - c^g(t) v_1. \tag{8.3}$$

To work with this model in a more simple linear format, let us introduce the new control variables

$$u_1 := v_1 = W_g \tag{8.4}$$

and

$$u_2 := v_1 v_2 = W_g c^g_{in} \tag{8.5}$$

In terms of these new control variables the bilinear control term (8.3) becomes linear:

$$W_g\left(c_{in}^g - c^g(t)\right) = v_1 v_2 - c^g(t) v_1 = u_2 - c^g(t) u_1.$$

That is why the model (11.3), which now may be considered as a *controlled model*, can be represented as follows:

$$\left.\begin{aligned} \frac{d}{dt}c^g(t) &= -V_g^{-1}\left[c^g(t)u_1 - u_2 + k_{sat}(Q_{\max} - Q(t)) - Q(t)\sum_{i=1}^{N} k_i c_{i,t}\right], \\ \frac{d}{dt}Q(t) &= k_{sat}(Q_{\max} - Q(t)) - Q(t)\sum_{i=1}^{N} k_i c_{i,t}, \\ \frac{d}{dt}c_{i,t} &= -k_i \frac{Q(t)}{V_{liq}} c_{i,t} \quad i = \overline{1,N}, \end{aligned}\right\} \tag{8.6}$$

with the measured online output

$$y(t) = c^g(t). \tag{8.7}$$

8.1.2 Available information which can be used for the design of controllers

8.1.2.1 A priori known parameters of ozonation process

Traditionally, researchers possess a priori information on the following process parameters:

- V_g, the volume of the gas phase (L),
- k_{sat}, the saturation constant of ozone in water (s^{-1}),
- $Q_{\max}$, the maximum amount of ozone in the saturation state of the liquid phase at a fixed temperature (mol),
- $Q_{t=0} = Q_0$, the initial amount of ozone in liquid phase (mol).

Remark 8.1. *Usually, we deal with the start situation when*

*– **the liquid is free of ozone**, i.e.,*

$$Q_0 = 0,$$

*or **the liquid is saturated by ozone**, i.e.,*

$$Q_0 = Q_{\max}.$$

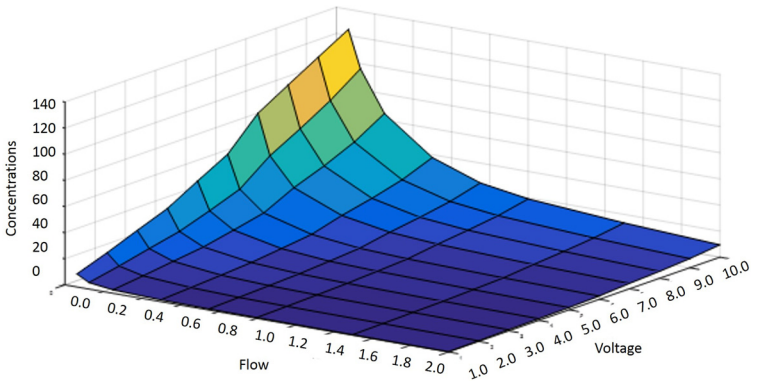

■ **FIGURE 8.1** Ozone concentration depending on the inner voltage and the oxygen flow.

8.1.2.2 Admissible set of control actions

In practice, researchers run into the two following situations:

1. Fixing the gas flow-rate $W_g = u_1$ (L/s) in the ozone reactor, the desired ozone concentration $c^g_{entr} = u_2/u_1$ at the reactor input can be obtained by the corresponding selection of the discharge voltage u_0 (kilovolt) of the ozone generator (see Chapter 1 of this book), that is,

$$u_2 = u_1 c^g_{in}(u_0, u_1) = \varphi(u_0, u_1)\, u_1, \tag{8.8}$$

   where the function φ is a specific mapping for each individual ozone generator,

$$\varphi(u_0, u_1) := c^g_{in}(u_0, u_1).$$

2. Fixing the discharge voltage u_0 and, hence, fixing the desired ozone concentration $c^g_{entr}(u_0, u_1) = u_2/u_1$ one can change the properties of the ozone reactions varying the gas flow-rate $W_g = u_1$, i.e.,

$$u_1 = u_2/c^g_{in}(u_0, u_1). \tag{8.9}$$

Examples of the function $\varphi(u_0, u_1)$ are depicted in Fig. 8.1.

Notice also that the admissible set of possible control variables $u_1 = W_g$ and $u_2/u_1 = c^g_{entr}$ are a priori given and usually are as follows:

$$0.1\ (\text{L/min s}) := W_g^- = u_1^- \le u_1 = W_g \le u_1^+ = W_g^+ := 0.5\ (\text{L/min})$$

and

$$\varphi^{-}(u_1) := c_{in}^{g-}(u_1) \le \varphi(u_0, u_1) := c_{in}^{g}(u_0, u_1) \le c_{in}^{g+}(u_1) := \varphi^{+}(u_1).$$

So, finally, we have

$$\left.\begin{array}{c} u_1^{-} \le u_1 \le u_1^{+}, \\ u_2^{-} := \max\limits_{u_1} u_1 \varphi^{-}(u_1) \le u_1 c_{in}^{g}(u_0, u_1) \\ = u_2 \le \max\limits_{u_1} u_1 \varphi^{+}(u_1) := u_2^{+}. \end{array}\right\} \tag{8.10}$$

By physically the two low constraints are equal to zero, that is,

$$u_1^{-} = u_2^{-} = 0.$$

8.1.3 Ozonation system as an uncertain plant

To realize directly the optimization of the ozonation process, given by the mathematical model (8.6), ozonation processes turn out to be impossible because of two factors:

- **first**, we do not know the kinetic parameters k_i $\left(i = \overline{1, N}\right)$,
- **second**, the measured online output of the system is $y(t) = c^{g}(t)$ (8.7).

These factors necessitate us to consider ozonation as *an uncertain plant* whose mathematical model contains both uncertain parameters k_i $(i = \overline{1, N})$ and unmeasurable states $Q(t)$ and $c_{i,t}$ $\left(i = \overline{1, N}\right)$. In view of that, the corresponding state reconstruction method (4.15) is required. In view of the close approximations

$$\hat{Q}(t) \simeq Q(t) \text{ and } \hat{c}_{i,t} \simeq c_{i,t} \ \left(i = \overline{1, N}\right)$$

instead of the original model (8.6) we can consider its DNN-approximative version (4.14):

$$\left.\begin{array}{c} \dfrac{d}{dt}\hat{c}^{g}(t) = A_g(t) + B_{1,g}(t)\, u_1(t) + B_{2,g}(t)\, u_2(t), \\ \dfrac{d}{dt}\hat{Q}(t) = A_Q(t) + B_{1,Q}(t)\, u_1(t) + B_{2,Q}(t)\, u_2(t), \\ \dfrac{d}{dt}\hat{c}_i(t) = A_{c_i}(t),\ i = \overline{1, N}, \end{array}\right\} \tag{8.11}$$

where

$$\left.\begin{array}{c} A_g(t) = a_{1,1}\hat{c}^g(t) + a_{1,2}\hat{Q}(t)/V_{liq} + \sum\limits_{i=1}^{N} a_{1,2+i}\hat{c}_i(t) + \\ \sum\limits_{s=1}^{W_1} W_{1:1,s}(t)\,\sigma_s(V_{1,l}(t)\,\hat{x}(t)) + L_{1,1}e(t) + \\ L_{2,1}\mathrm{sign}(e(t)) + L_{3,1}[e(t) - e(t-h)], \\ B_{1,g}(t) = \sum\limits_{s=1}^{W_2} W_{2:1,s}(t)\phi_{s,1}(V_{2t}\hat{x}(t)), \\ B_{2,g}(t) = \sum\limits_{s=1}^{W_2} W_{2:1,s}(t)\phi_{s,2}(V_{2t}\hat{x}(t)), \end{array}\right\} \quad (8.12)$$

$$\left.\begin{array}{c} \frac{1}{V_{liq}}A_Q(t) = a_{2,1}\hat{c}^g(t) + a_{2,2}\hat{Q}(t)/V_{liq} + \sum\limits_{i=1}^{N} a_{2,2+i}\hat{c}_i(t) + \\ \sum\limits_{s=1}^{W_1} W_{1:2,s}(t)\,\sigma_s(V_{1,l}(t)\,\hat{x}(t)) + L_{1,2}e(t) + \\ L_{2,2}\mathrm{sign}(e(t)) + L_{3,2}[e(t) - e(t-h)], \\ B_{1,Q}(t) = \sum\limits_{s=1}^{W_2} W_{2:2,s}(t)\phi_{s,1}(V_{2t}\hat{x}(t)), \\ B_{2,Q}(t) = \sum\limits_{s=1}^{W_2} W_{2:2,s}(t)\phi_{s,2}(V_{2t}\hat{x}(t)), \end{array}\right\} \quad (8.13)$$

and for $i = \overline{1, N}$

$$\left.\begin{array}{c} A_{c_i}(t) = a_{2+i,1}\hat{c}^g(t) + a_{2+i,2}\hat{Q}(t)/V_{liq} + \\ \sum\limits_{s=1}^{N} a_{2+i,2+s}\hat{c}_s(t) + \sum\limits_{s=1}^{W_1} W_{1:2+i,s}(t)\,\sigma_s(V_{1,l}(t)\,\hat{x}(t)) + \\ L_{1,2+i}e(t) + L_{2,2+i}\mathrm{sign}(e(t)) + L_{3,2+i}[e(t) - e(t-h)]. \end{array}\right\} \quad (8.14)$$

So, below we will work with the DNN-approximative model (8.11).

8.2 INTEGRAL OPTIMIZATION METHOD

8.2.1 Main optimization criteria for the control design of ozonation processes

Optimal control theory has received great attention since the 1950s in many fields in science and engineering. It deals with the problem of finding a

control law for a given system such that a certain optimality criterion is achieved. It is an extension of the calculus of variations, and represents a mathematical optimization method for deriving control policies (see, for example, Chapters 1–4 in Boltyanski and Poznyak, 2012). The basic problem considered in this theory consists in the optimization of a given cost functional, usually characterizing integral losses of the system within some given time-interval. Classical optimal control theory deals with *exact (non-approximative) models of the processes* to be optimized with the final aim to derive a feedback or program-type control law realizing the extremum (minimum) of the considered cost functional. It cannot be applied in our case directly to the model (8.6): we should work only with a DNN-approximative model (8.11).

That is why we will use here the so-called *local optimal control method* (Kelmans et al., 1981, 1982; Poznyak et al., 2001), which is much more simple than (but not as exact as) the classical optimal control and admits a well-treated practical realization.

Besides the uncertainty problems we face the *multi-criterion character* of the desired optimization process: by the control action designing we wish to realize simultaneously two properties of ozonation reactions, namely:

- *maximal contaminants decomposition*, corresponding to the most complete decomposition effect in the ozonation reactor,
- and *minimal ozone concentration at the rector output*, realizing the most effective regime of ozonation with minimal portion of "unused" ozone which may also contaminate the atmosphere presenting a dangerous place for working personnel.

So, in the next sections we will consider in detail both local criteria mentioned above.

8.2.2 Joint weighted optimization functional, represented in DNN format, and local optimal controller

For each time $t \geq 0$ define the *joint weighted "loss" function*

$$F\left(\hat{c}^g(t), \hat{c}(t)\right) := \frac{1}{2}\left(\lambda_0\left[\hat{c}^g(t)\right]^2 - \sum_{s=1}^{N}\lambda_s\left(\left[\hat{c}_s(t)\right]^2 - \left[\hat{c}_s(0)\right]^2\right)\right) + \rho, \tag{8.15}$$

where $\rho > 0$ and $\lambda_i \ \left(i = \overline{0, N}\right)$ are weighting parameters, characterizing the "importance" of the corresponding component in the optimization process

and satisfying the so-called simplex-conditions:

$$\sum_{s=0}^{N} \lambda_s = 1,\ \lambda_i \geq 0\ \left(i = \overline{0, N}\right). \tag{8.16}$$

Since the initial contaminant concentrations $\hat{c}_s(0)$ are always higher than the concentrations $\hat{c}_s(t)$ after the destruction it follows that for all $t \geq 0$

$$F\left(\hat{c}^g(t), \hat{c}(t)\right) \geq \rho > 0. \tag{8.17}$$

Remark 8.2. *Notice that our local aims are:*

– to minimize the term $\left[\hat{c}^g(t)\right]^2$*, which corresponds to a minimal quantity of unused ozone in the output of the reactor,*

– to maximize the term $\sum_{s=1}^{N} \lambda_s \left[\hat{c}_s(t)\right]^2$*, or equivalently, minimize*

$$\left(-\sum_{s=1}^{N} \lambda_s \left[\hat{c}_s(t)\right]^2\right)$$

providing the maximal contaminant decomposition effect.

The global criterion of the averaged losses minimization on the time-interval $[0, T]$ can be formulated as follows:

$$\begin{gathered} J(u(\cdot)) := \limsup_{t\to\infty} J(t)(u(\cdot)), \\ J(t)(u(\cdot)) = \frac{1}{t+\varepsilon} \int_{\tau=0}^{t} F\left(\hat{c}^g(\tau), \hat{c}(\tau)\right) d\tau,\ \ \varepsilon > 0. \end{gathered} \tag{8.18}$$

Optimal control actions $u^*(t) = \left(u_1^*(t),\ u_2^*(t)\right)^{\mathsf{T}}$ will correspond to the solution of the following optimization problem:

$$J(u(\cdot)) \to \min_{u^*(t)\in U_{adm}}, \tag{8.19}$$

where

$$U_{adm} = \left\{u \in \mathbb{R}^2 : u_1^- \leq u_1 \leq u_1^+,\ u_2^- \leq u_2 \leq u_2^+\right\} \tag{8.20}$$

is the admissible set of all possible control action and the variables $\hat{c}^g(t)$, $\hat{c}(t)$ are given by the dynamic equations (8.11).

8.2.3 Local loss minimization

The exact solution of the problem (8.18) requires the application of the *optimal control methods* (see, for example, Boltyanski and Poznyak, 2012) which solution is too complex from the mathematical and practical points of view. That is why instead of minimizing (8.18) we now minimize the local losses $F(\hat{c}^g(t), \hat{c}(t))$ (8.15) within a given class of controllers, namely, linear controllers with a time-varying gain parameter.

Calculating the time-derivative of the local cost-functional $F\left(\hat{c}^g(t), \hat{c}(t)\right)$ (8.15), we get

$$\left.\begin{aligned} \frac{d}{dt}F\left(\hat{c}^g(t), \hat{c}(t)\right) &= \lambda_0 \hat{c}^g(t)\frac{d}{dt}\hat{c}^g(t), \\ -\sum_{s=1}^{N}\lambda_s \hat{c}_s(t)\frac{d}{dt}\hat{c}_s(t) &= \\ \lambda_0 \hat{c}^g(t)\left[A_g(t) + B_{1,g}(t)u_1(t) + B_{2,g}(t)u_2(t)\right] & \\ -\sum_{s=1}^{N}\lambda_s \hat{c}_s(t)A_{c_i}(t). & \end{aligned}\right\} \tag{8.21}$$

We select the applied controllers $u_1(t)$, $u_2(t)$ such that they fulfill the relations

$$\left.\begin{aligned} \lambda_0 \hat{c}^g(t)B_{1,g}(t)u_1(t) &= -k_1\lambda_0\left[\hat{c}^g(t)\right]^2, \ k_1 > 0, \\ \lambda_0 \hat{c}^g(t)A_g(t) + \lambda_0 \hat{c}^g(t)B_{2,g}(t)u_2(t) - \sum_{s=1}^{N}\lambda_s \hat{c}_s(t)A_{c_i}(t) & \\ = \frac{k_1}{2}\sum_{s=1}^{N}\lambda_s\left(\left[\hat{c}_s(t)\right]^2 - \left[\hat{c}_s(0)\right]^2\right) + \rho. & \end{aligned}\right\} \tag{8.22}$$

Such control actions, realizing the local optimal control, are as follows:

$$\left.\begin{aligned} u_1(t) &= -\frac{k_1}{2}B_{1,g}^{-1}(t)\hat{c}^g(t), \\ u_2(t) &= \begin{cases} v_2(t) & \text{if} \quad v_2(t) \le u_2^+, \\ u_2^+ & \text{if} \quad v_2(t) > u_2^+, \end{cases} \end{aligned}\right\} \tag{8.23}$$

where

$$v_2(t) := \frac{\sum_{s=1}^{N}\lambda_s \hat{c}_s(t)\left[\frac{k_1}{2}\hat{c}_s(t) + A_{c_i}(t)\right]}{\lambda_0 \hat{c}^g(t)B_{2,g}(t)} - \frac{A_g(t)}{B_{2,g}(t)}. \tag{8.24}$$

Usually we are working within the regime when $v_2(t) \le u_2^+$.

With this controller selection in view of (8.17) we have

$$\frac{d}{dt}F\left(\hat{c}^g(t),\hat{c}(t)\right)=-k_1F\left(\hat{c}^g(t),\hat{c}(t)\right)\leq-k_1\rho<0,$$

which means that the local loss function $F\left(\hat{c}^g(t),\hat{c}(t)\right)$ monotonically decreases, tending to its minimal value.

To fulfill the constraint $0=u_1^-\leq u_1\leq u_1^+$ it is sufficient to take

$$k_1=\frac{2u_1^+}{\left(\left|B_{1,g}^{-1}(t)\right|+\varepsilon\right)W_g^+},\ \varepsilon>0. \tag{8.25}$$

8.2.4 Numerical results

The resulting system of ordinary equations gathers both the ozone mass transfer and its kinetic reaction with the initial contaminants, their byproducts formed and decomposed along the ozonation. In this particular process, the ozone dissolved in the aqueous phase is Q (mol), which is transferred from the gaseous phase (with a given ozone concentration c_g). This Q is consumed by the reaction with the contaminants as well as the corresponding byproducts. The initial contaminants (c_j (mol L^{-1}), $j\in[1,N]$) are decomposed by the reaction with the dissolved ozone.

The vector $u\in\mathbb{R}^2$ describes the variables used to represent the control elements that adjust the ozonation dynamics, that is, $u=[u_1,u_2]^\top$ is formed by the ozone flow injected into the reactor and gas concentration fixed at the reactor's input produced by the ozone generator. A more realistic model must consider the presence of external perturbations that may affect the ozonation and that cannot be included as part of the reactions occurring in the reactor. In the nominal model (8.6), the mapping f can be represented as follows:

$$f=\begin{bmatrix}-V_g^{-1}\left[u_2-c^gu_1+k_{sat}(Q_{\max}-Q)-Q\sum_{i=1}^{N}k_ic_i\right]\\ k_{sat}(Q_{\max}-Q)-Q\sum_{i=1}^{N}k_ic_i\\ -k_1\dfrac{Q}{V_{liq}}c_1\\ \vdots\\ -k_N\dfrac{Q}{V_{liq}}c_N\end{bmatrix}. \tag{8.26}$$

The model (8.6) possesses several characteristics that may be considered in the observer design:

a) the assumption of bilinear interaction with respect to the components of the state vector,

b) not all the parameters of this model are known,

c) the contaminants concentrations can be measured using special and expensive laboratory equipment such as a UV-Vis spectrophotometer, high performance liquid chromatography, infrared spectroscopy, nuclear magnetic resonance, and

d) only some of components (frequently only one) of the state vectors can be measured during the process: in the case of ozonation it is the current concentration c_g of ozone in the gas phase, $y(t) = c^g(t)$.

Notice that the control actions are bounded and measurable. Also, the function f is locally Lipschitz, which is a technical issue that must be taking into account. Also, the chemical nature of the states justifies the assumption that all of them are bounded from above.

8.2.5 Variables which can be considered as control actuators

Recall that the mathematical model of ozonation in the presence of several contaminants is given by the collection of ordinary differential equations (8.6). Reconstruction of the non-measurable variables $Q(t)$ and $c_j(t)$ is realized by the application of the DNN observers (DNNOs) (8.13) and (8.14). In ODE (8.6) the main parameters, which may significantly change the behavior of the process and, therefore, can be considered as the *principal control actions*, are as follows: W_g is the gas flow-rate (L s^{-1}) in the ozone reactor, so that $v_1 := W_g$, c^g_{in} is the ozone concentration at the reactor input (mol L^{-1}), that is, $v_2 := c^g_{in}$. Notice also that in the model of the process (8.6) both control variables v_1 and v_2 participate as the bilinear form proposed in the introduction section, that is,

$$u_1 := v_1 = W_g \text{ and } u_2 := v_1 v_2 = W_g c^g_{in}.$$

In these new control variables, the bilinear control term becomes linear:

$$W_g \left(c_{g,in} - c_g\right) = v_1 v_2 - c_g v_1 = u_2 - c_g u_1.$$

Then, the DNN form, proposed for the function $\hat{f}$, is clearly justified.

8.2.6 Numerical simulations

Traditionally, researchers possess a priori information on the following process parameters:

a) $V_g = 0.3$ L, the volume of the gas phase,

b) $k_{sat} = 0.2\ s^{-1}$, the saturation constant of ozone in water,

c) $Q_{\max} = 0.05$ mol, the maximum amount of ozone in the saturation state of the liquid phase at a fixed temperature and

d) $Q_0 = Q_0$ mol, the initial amount of ozone in liquid phase.

Below, only one contaminant was considered and the constant reaction rate was ($k_1 = 1934.0\ L\ mol^{-1}\ s^{-1}$). This rate constant corresponds to the result obtained for phenol in Poznyak et al. (2008).

Fig. 8.2A demonstrates the variation of ozone gas concentration c^g, Fig. 8.2B shows the variation of the ozone dissolved in the liquid phase, while Fig. 8.2C depicts the variation of the contaminant concentration. These variables correspond to the lower lines showed in each subfigure. The comparison of all the variables with respect to the values obtained when both controllers used the common constant values $u_1 = 0.5\ L\ s^{-1}$ and $u_2 = 15.0\ mg\ L^{-1}$. These variations correspond to the upper lines in each subfigure.

In Fig. 8.2 the lines in blue represent the variables obtained with fixed values of the controllers and the lines in red correspond to the variables obtained with the suboptimal controller.[1]

8.3 CONTROL OF OZONATION SYSTEMS AS TRACKING TRAJECTORY PROBLEM

Artificial neural networks (ANNs) have shown relevant properties to obtain a reliable nonparametric modeling approximation for uncertain systems (Chairez et al., 2008). So far, the developments, involving ANNs, include signal processing (Alotaiby et al., 2014), signal classification applications (Alfaro et al., 2016) and identification and estimation solutions oriented to control challenges (Poznyak et al., 2001). As regards the estimation and control problems, dynamic neural networks are more suitable to deal with them because of the feedback included in their structure (Poznyak et al., 1998), (Delgado et al., 1995). This kind of dynamic algorithms, recurrent neural networks (RNNs) (Sanchez et al., 2008), (Salgado and Chairez, 2009) and

[1] Note: The color figures will appear in color in all electronic versions of this book.

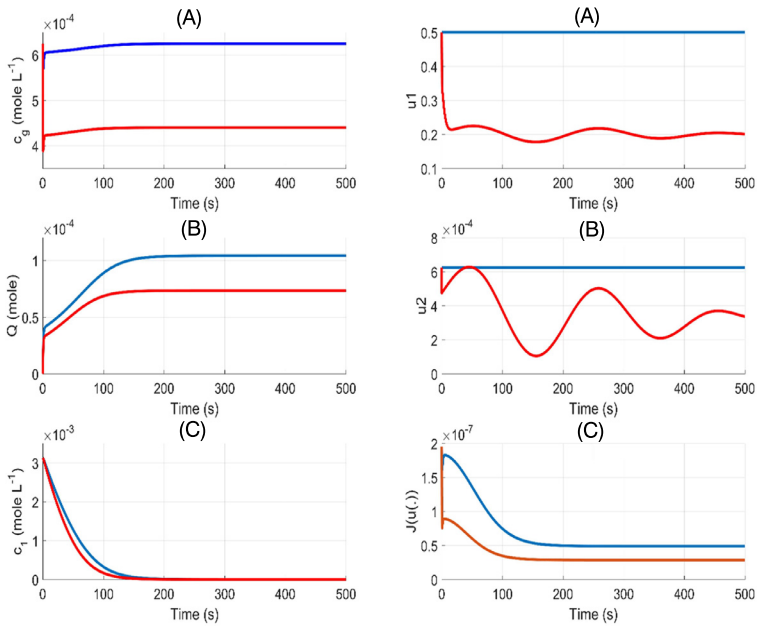

■ **FIGURE 8.2** The states c_g, Q and c in the system (8.6) and the evaluation of the control actions u_1, u_2, and the performance index J.

differential neural networks (DNNs) for discrete-time and continuous time, respectively, are commonly analyzed in the framework of Lyapunov stability theory (Khalil, 2002). *Lyapunov control functions* (LCFs) are an efficient tool to develop updating laws for DNN, prove the DNN stability and even to design closed-loop control strategies for nonlinear systems. As an example, the work of Poznyak et al. (2001) describes a complete study of the DNN dealing with the problems of identification, state estimation, and control, applying the LCF. The counterpart in discrete-time systems is described in Salgado and Chairez (2014).

One of the most remarkable problems in control theory is the stabilization of a disturbed chain of integrators (Sira-Ramirez et al., 2010). This normal form is not a restriction in the class of nonlinear systems to deal with and it is usually obtained from systems with full relative degree (Khalil, 2002) or differential flat systems (Aranda-Bricaire et al., 1995). In most of the cases, the disturbance signal is a lumped function containing non-modeled dynamics and perturbation functions. Classical control techniques like PD controllers include the compensation of the disturbance by observation algorithms (Luviano-Juárez and Chairez, 2013), (Khalil, 2002). Observer techniques that estimate the unknown disturbance in order to in-

troduce it in the control law are commonly referred as Active Disturbance Rejection Control (ADRC) (Gao, 2006).

Among other alternatives, the *Generalized Proportional Integral* (GPI) observers provide a linear estimation of the unknown perturbation (Sira-Ramirez et al., 2010). The estimation applies the concept of a polynomial approximation (Taylor series) and high gain observers. Noise in the available output is probably the main disadvantage of high gain observers and therefore for the GPI observers (Khalil, 2002).

In this section, the proposed DNN observer estimates the non-measurable states of a nonlinear system described by a chain of integrators but affected by a nonlinear perturbation in the last equation. The available measurement, that is, the first state in the chain of integrators, is considered corrupted by bounded noises. The DNN observer simultaneously estimates the unknown disturbance and then, the control strategy introduces the estimated disturbance to enhance the tracking performance. The control design incorporates an optimization algorithm based on the attractive ellipsoid method (AEM) (Poznyak et al., 2011) to reduce the zone of convergence for the tracking and estimation errors despite the presence of noises affecting the measured signal. Numerical simulations compare the implementation of the DNN observer with classical Luenberger observers but using a similar control structure (with different gains).

8.3.1 Problem statement in mathematical form

All the ozonation systems presented in previous chapters admit a nonlinear transformation, $z = T(x)$, where $x \in \mathbb{R}^n$ is the vector of variables corresponding to the ozonation system, and $z \in \mathbb{R}^n$ defines the vector of auxiliary variables obtained as a result of the application of the nonlinear transformation $T : \mathbb{R}^n \to \mathbb{R}^n$. This transformation is a diffeomorphism, that is, it is invertible and it is differentiable in the domain of x. The dynamics of the variable z satisfies

$$\left.\begin{aligned} \dot{z}(t) &= Az(t) + b\left[f(z(t) + g(z(t))u(t) + \xi(z(t), t)\right], \\ y(t) &= C^{\top} z(t) + \eta(t), \end{aligned}\right\} \tag{8.27}$$

where

$$A = \begin{bmatrix} 0 & 1 & 0 & \cdots & 0 \\ 0 & 0 & 1 & \cdots & 0 \\ \vdots & \vdots & \vdots & \ddots & \vdots \\ 0 & 0 & 0 & \cdots & 1 \\ 0 & 0 & 0 & \cdots & 0 \end{bmatrix}, \quad b = \begin{bmatrix} 0 \\ 0 \\ \vdots \\ 0 \\ 1 \end{bmatrix}, \quad C = \begin{bmatrix} 1 \\ 0 \\ \vdots \\ 0 \\ 0 \end{bmatrix}.$$

Here

$z \in \mathbb{R}^n$ is the state vector,

$f : \mathbb{R}^n \to \mathbb{R}$ is a function representing the known dynamics of system (8.27),[2]

$g : \mathbb{R}^n \to \mathbb{R}$ is an input function associating the control input $u \in \mathbb{R}$ with the state dynamics, $g = V_g^{-1}$,

and $\xi : \mathbb{R}^n \times \mathbb{R} \to \mathbb{R}^n$ represents a function that includes external disturbances and no modeled dynamics.

Let us assume that the disturbance $\xi(z(t), t)$ is bounded and has bounded finite derivatives. The output function $g(z)$ satisfies the following condition:

$$0 < g^- \leq |g(z)| \leq g^+ \tag{8.28}$$

with $g^-, g^+ \in \mathbb{R}^+$, $\forall x \in \mathbb{R}^n$, to guarantee the controllability of system (8.27). The uncertain function satisfies

$$\|\xi(z(t), t)\|^2 \leq \beta_1 + \beta_2 \|z\|^2$$

with β_0 and β_1 positive scalars. The output noise is bounded inside of a known ellipsoidal set (Poznyak et al., 2011) defined by

$$\eta^\top(t) Q_\eta \eta(t) \leq 1.$$

8.3.1.1 Desired dynamics

Let us assume that the next differential equations describe the desired system trajectories:

$$\left.\begin{aligned} \dot{z}^*(t) &= Az^*(t) + bh(z^*(t)), \\ y^*(t) &= C^\top z^*(t). \end{aligned}\right\} \tag{8.29}$$

The system (8.29) is usually referred to as *the reference model*. Here $z^* \in \mathbb{R}^n$ is the state vector of the objective system, $h(z^*) : \mathbb{R}^n \to \mathbb{R}$ is a function uniformly continuous on t satisfying the Lipschitz condition

$$\|h(z_1) - h(z_2)\|^2 \leq L_h \|z_1 - z_2\|^2, \qquad z_1, z_2 \in \mathbb{R}^n. \tag{8.30}$$

In the case of ozonation reactions we have $z_0^* = c^g(t)$ and $z_i^* = c_{i,t}$ $\left(i = \overline{1, N}\right)$. The desired dynamics x^* in our case is given by the following

[2]The function f is usually assumed to be Lipchitz (Khalil, 2002).

models:

$$\dot{x}^*(t) = \begin{bmatrix} -V_g^{-1}\left[u_2^*(t) - c^g(t)\,u_1^*(t) - Q^{\max}\sum_{i=1}^{N} k_i c_i(t)\right] \\ -Q^{\max}\sum_{i=1}^{N} k_i c_i(t) \\ -k_1\dfrac{Q^{\max}}{V_{liq}}c_1(t) \\ \vdots \\ -k_N\dfrac{Q^{\max}}{V_{liq}}c_N(t) \end{bmatrix}. \quad (8.31)$$

The main problem considered here is to design an output-feedback controller that forces the states $x(t)$ of our controlled system to track the desired reference vector trajectory $x^*(t)$ despite the presence of additive external disturbances and bounded measurement noise restricting the tracking output error $y(t) - y^*(t)$ inside a neighborhood of the origin.

8.3.2 The existing solutions

This section describes the results available in the literature. These approaches include a complete feedback linearization and the GPI technique. The advantages and disadvantages are pointed out.

8.3.2.1 Output-feedback linearization

The following controller linearizes system (8.27):

$$u_1(t) = \frac{1}{g(z(t))}\left(-\xi(z(t),t) - f(z(t)) + h(z^*)\right) - \frac{1}{g(z(t))}\left(\sum_{j=1}^{n} k_j\left(z_j(t) - z_j^*(t)\right)\right),$$
$$u_2(t) := u_1(t)c_{g,in}(t),$$

and produces asymptotic convergence of $z(t)$ to $z^*(t)$. However, the main disadvantages of this controller are the necessity of measuring the entire state vector z and the perfect knowledge of the signal perturbation $\xi(z(t),t)$. Moreover, the available output must be a free-noise signal (Spong and Vidyasagar, 1989).

8.3.2.2 GPI observer

The so-called GPI observer estimates the unknown disturbance signal $\xi(x(t), t)$. The GPI observer is an extension of classical Luenberger observers (Aranda-Bricaire et al., 1995; Sira-Ramirez et al., 2010) and it is given by

$$\begin{bmatrix} \frac{d}{dt}\hat{z}(t) \\ \dot{\hat{\rho}}(t) \end{bmatrix} = \begin{bmatrix} A_{11} & A_{12} \\ 0 & A_{22} \end{bmatrix} \begin{bmatrix} \hat{z}(t) \\ \hat{\rho}(t) \end{bmatrix} + \begin{bmatrix} b\left(f(\hat{z}(t)) + g(\hat{z}(t))\right)u(t) \\ 0 \end{bmatrix} + \Gamma e(t),$$

$$e(t) = y(t) - \hat{y}(t),$$

where

$\hat{x} = \begin{bmatrix} \hat{z}_1, & \ldots, & \hat{z}_n \end{bmatrix}^\top$ is the estimated state vector,

$\rho = \begin{bmatrix} \rho_1, & \cdots, & \rho_m \end{bmatrix}^\top$ is the set of extended states used to estimate the unknown disturbance $\xi(z(t), t)$ by means of the Taylor series expansion

$$\xi(z(t), t) = \sum_{i=1}^{m-1} \tilde{c}_i t^i + \tilde{r}(t).$$

In the last equation $\tilde{c}_i \in \mathbb{R}$ and $\tilde{r}(t)$ denotes the set of high order terms to complete the series.

The vector $\Gamma = \begin{bmatrix} \gamma_1, & \ldots, & \gamma_{n+m} \end{bmatrix}^\top$ defines the gains designed to force the estimation error convergence to the origin. The matrices A_{11}, A_{12}, and A_{22} are as follows:

$$A_{11} = A, \qquad A_{12} = \begin{bmatrix} 1 & 0 & \cdots & 0 \\ 0 & 0 & \cdots & 0 \\ \vdots & \vdots & \ddots & \vdots \\ 0 & 0 & \cdots & 0 \end{bmatrix}, \qquad A_{22} = A.$$

The structure of matrix A_{22} is the same as matrix A. Regardless of the benefits achieved by the method, the convergence region of the observer depends on possible high values of the gain vector Γ, which may have problems in the presence of noisy signals, or some peaking effects by an incorrect gain tuning (Liu et al., 2014).

8.3.3 DNN Observer and perturbation estimation

This section addresses the case of a DNN working as a state estimator for system (8.27). The adaptive structure provides an estimation of the unknown perturbation $\xi(z(t), t)$.

8.3.3.1 Neural network representation

Notice that system in (8.27) can be represented as

$$\begin{aligned}\dot{z}(t) &= Az(t) + b\left(f(z(t)) + g(z(t))u(t)\right) \\ &\quad + b\left(\xi_0(z|\Theta) + \tilde{\xi}(z, t|\Theta)\right), \\ \tilde{\xi}(z, t|\Theta) &= \xi(z(t), t) - \xi_0(z|\Theta),\end{aligned}$$

where

$\xi_0 : \mathbb{R}^n \times \mathbb{R} \times \mathbb{R}^m \to \mathbb{R}$ represents a *nominal dynamics* (8.31) of the signal perturbation ξ, which can be selected arbitrarily (according to the designer desires) and

$\tilde{\xi}$ is a vector field corresponding to the modeling error of ξ.

Define the parameters $\Theta := \left[W^*\right]^\top$ ($\Theta \in \mathbb{R}^m$) that will be adjusted to enforce the convergence of the DNN to the trajectories of system (8.27). According to the DNN approach (Poznyak et al., 2001), we define the nominal dynamics as

$$\xi_0(z|\Theta) = (W^*)^\top \sigma(z) \tag{8.32}$$

where $\sigma : \mathbb{R}^n \to \mathbb{R}^m$ corresponds to the vector of activation functions $\sigma(\cdot) := [\sigma_1(\cdot), \ldots, \sigma_m(\cdot)]^\top$. In this study, sigmoid functions constitute the vector σ (Chairez, 2009), that is,

$$\sigma_j(z) := \frac{a_j}{1 + b_j e^{-c_j^\top z}}, \quad j = 1 : m, \quad a_j, b_j \in \mathbb{R}, \qquad c_j \in \mathbb{R}^n,$$

which satisfy the sector condition

$$\|\sigma(z) - \sigma(z')\| \le L_\sigma \|z - z''\| \quad z, z'' \in \mathbb{R}^n. \tag{8.33}$$

Here $L_\sigma \in \mathbb{R}^+$ ($\mathbb{R}^+$ is the set of positive real numbers). By this property the activation function $\sigma_j(x)$ fulfills

$$\|\sigma(z)|^2_{\Lambda_{W^*}} \le \sigma^+, \qquad 0 < \Lambda_{W^*} = \Lambda_{W^*}^\top \in \mathbb{R}^{m \times m}. \tag{8.34}$$

The class of parametric uncertainties are assumed bounded, that is,

$$\|\tilde{\xi}(z, t|\Theta)\|^2_{\Lambda_\xi} \le \tilde{\xi}^+, \qquad \Lambda_\xi = \Lambda_\xi^\top > 0, \tag{8.35}$$

with $\tilde{\xi}^+ \in \mathbb{R}^+$ and $\|S\|^2_{\Lambda_\xi} := S^\top \Lambda_\xi S$ for a vector $S \in \mathbb{R}^p$ and $\Lambda_\xi \in \mathbb{R}^{p\times p}$ (being a positive definite symmetric matrix). In general, the weights W^* are unknown. However, it is usual to consider that they are bounded with known parameters, that is,

$$(W^*)^\top \Lambda_W^{-1} W^* \leq \bar{W} \tag{8.36}$$

where $\Lambda_W \in \mathbb{R}^{n\times n}$ is a known positive definite and symmetric matrix and $\bar{W} \in \mathbb{R}^{n\times n}$ is a given matrix.

8.3.3.2 DNN observer and control design

Following the development proposed in Poznyak et al. (2001) (see also Chapter 4 of this book) we define the DNN observer as

$$\left.\begin{aligned} \frac{d}{dt}\hat{z}(t) = A\hat{z}(t) + b\left(f(\hat{z}(t)) + g(\hat{z}(t))u(t)\right) \\ + bW^\top(t)\sigma(\hat{z}(t)) + L(y(t) - \hat{y}(t)), \\ \hat{y}(t) = C^\top \hat{z}(t). \end{aligned}\right\} \tag{8.37}$$

The free parameters W are supplied with a special *updating* (learning) law $\Phi(W, y|W^{Id})$, W^{Id} are the weights obtained from an offline training adaptation if there are some available data to train the DNN (Chairez et al., 2008), (Chairez, 2014).

8.3.4 Learning law for the observer

Let the estimation error be defined by $e = y - \hat{y}$. Then, the adaptive learning law $\Phi(W, y|W^{Id})$ for the free parameters W is

$$\left.\begin{aligned} \dot{W} = -ke^\top(t)C^\top N_\mu P_1 b(1-\bar{g})\sigma^\top(\hat{z}) \\ -\mu(1-\bar{g})b^\top P_1 \Lambda_W P_1 b(1-\bar{g})\tilde{W}\sigma(\hat{z})\sigma^\top(\hat{z}), \\ \bar{g} = \frac{g^+ - g(\hat{z})}{g(\hat{z})}. \end{aligned}\right\} \tag{8.38}$$

In Eq. (8.38), $W(0) = W_0$ defines the initial condition of the learning law. The values of $\tilde{W}(t) = W - W^{id}$ (W^{id} are the weights obtained from the offline training) are approximated by an offline training algorithm. The value of k is the learning coefficient of the DNN observer and the matrix P_1 satisfies the following matrix inequality:

$$M = \begin{bmatrix} P_1\tilde{A} + \tilde{A}^\top P_1 + P_1 R P_1 + \tilde{Q}_1 & -P_1 b\bar{g}^+ K \\ -K^\top \bar{g}^+ b^\top P_1 & P_2 A_c + A_c^\top P_2 + Q_2 \end{bmatrix} < 0 \tag{8.39}$$

where

$$\tilde{A} = A - LC^{\top}, \qquad A_c = A - bK$$
$$R := \Lambda_f + \bar{W} + LC^{\top}\Lambda_\eta CL^{\top} + 2\mu N_\mu^{\top}\Lambda_\eta N_\mu + \bar{g}^{+}b^{\top}\Lambda_W^{-1}b\bar{g}^{+}$$
$$\tilde{Q}_1 = L_f b^{\top}\Lambda_f^{-1}b + L_\sigma\Lambda_W^{-1} + Q_1, \quad Q_0 = Q_0^{\top} > 0, \quad Q_1 = Q_1^{\top} > 0,$$
$$Q_2 = Q_2^{\top} > 0, \quad K^{\top} \in R^n, \quad 0 < P = P^{\top} \in R^{n\times n}$$
$$N_\mu = (\mu I_{n\times n} + CC^{\top})^{-1} \qquad \mu \in R^{+}.$$

Here Λ_f, Λ_η, Λ_W are positive definite matrices. The value of $\bar{g}^{+}$ is defined as

$$\bar{g}^{+} := \frac{g^{+} - g^{-}}{g^{-}} > 0. \tag{8.40}$$

The offline training allows one to define (Chairez, 2014)

$$\tilde{W} = W - W^{Id} + W^{Id} - W^{*}. \tag{8.41}$$

We can ensure the existence of an upper bound for the difference $W^{Id} - W^{*}$, that is,

$$\|W^{Id} - W^{*}\|_W \leq W^{+}.$$

The value of the norm $\|\cdot\|_W$ can be selected as any matrix norm, such as

$$\|Z\|_W = \sqrt{\mathrm{tr}(Z^{\top}WZ)}.$$

This upper value is introduced directly in the matrix inequality in (8.39).

8.3.4.1 Main property of the DNN estimation process

The next proposition summarizes the main theoretical result concerning the state estimation and tracking problems.

Proposition 8.1. *If for the nonlinear system (8.27) the DNN observer is given by (8.37) with the learning law (8.38) and the control*

$$\left.\begin{aligned} u_1(t) = \frac{1}{g(\hat{z})}\left(-f(\hat{z}) - W(t)\sigma(\hat{z}) + h(x^{*}) - K\delta(t)\right), \\ \delta := \hat{z} - z^{*}, \end{aligned}\right\} \tag{8.42}$$

where the control gain K and the observer gain L are chosen in such a way that the matrix inequality (8.39) is feasible for some positive definite matrices P_1 and P_2, then the trajectories of the tracking and estimation error (δ and $\Delta = z - \hat{z}$) converge to a neighborhood r around the origin:

$$r := \lambda_{\min}\{Q\}\gamma$$

with

$$\gamma := f^+ + h^+ + \eta^+ + \sigma^+, \; Q = \begin{bmatrix} Q_1 & 0 \\ 0 & Q_2 \end{bmatrix}.$$

$f^+, h^+, \eta^+, \sigma^+$ are positive constants and Q_1 and Q_2 are defined in (8.39).

8.4 NUMERICAL SIMULATIONS

Consider the following third order system, which can represent the dynamics of the transformed conventional ozonation system (with a single contaminant) that yields a third order system transformed into its Brunovski form (Khalil, 2002):

$$\dddot{y}(t) = f(y(t), \dot{y}(t), \ddot{y}(t)) + g(y(t), \dot{y}(t), \ddot{y}(t))u(t) + \omega(t) \tag{8.43}$$

with the following function definitions:

$$\left.\begin{aligned} f(y(t), \dot{y}(t), \ddot{y}(t)) &= (a_0 + a(t))^\top \begin{bmatrix} y \\ \dot{y}(t) \\ \ddot{y}(t) \end{bmatrix}, \\ g(y(t), \dot{y}(t), \ddot{y}(t)) &= 2, \\ a_0(t) = \begin{bmatrix} -2.3 \\ -1.5 \\ -4.2 \end{bmatrix}, \qquad a(t) &= \begin{bmatrix} 0.29\sin(8\pi t) \\ 0.16\sin(\pi t) \\ 0.23\sin(2.4\pi t) \end{bmatrix}, \\ \omega &= \cos(60\pi t). \end{aligned}\right\} \tag{8.44}$$

In the last system, the total function $f(y(t), \dot{y}(t), \ddot{y}(t))$ is unknown. The approximated DNN observer developed in the previous section estimates the unknown function to be injected in the system. Defining the state vector $z = \begin{bmatrix} y & \dot{y} & \ddot{y} \end{bmatrix}^\top$ the system in Eq. (8.43) becomes

$$\begin{aligned} \dot{z}(t) &= Az(t) + b\left[(a_0 + a(t))z(t) + g(z(t))u(t) + \omega(t)\right], \\ y(t) &= C^\top z(t). \end{aligned} \tag{8.45}$$

The next state equation describes the objective system to be tracked:

$$\left.\begin{aligned} \dot{z}^*(t) &= A^* z^*(t) + bv(t), \\ A^* = \begin{bmatrix} 0 & 1 & 0 \\ 0 & 0 & 1 \\ -0.10 & -0.99 & -0.22 \end{bmatrix}, \qquad v(t) &= 2\sin(2\pi t). \end{aligned}\right\} \tag{8.46}$$

Table 8.1 Parameters implemented in the DNN observer simulation.

Parameter	Value	Parameter	Value
P	$0.2 \times I_{3\times 3}$	Learning coeff.	$k = 0.55$
$\sigma(\hat{x})$	$a = 2$ $b = 5.5$ $c = 5 \times \begin{bmatrix} 1 & 1 & 1 \end{bmatrix}$	μ	0.01
N_μ	$I_{3\times 3}$	Λ_W	$I_{3\times 3}$

8.4.1 Estimation of the unknown disturbance by the DNN approach

The subsequent equations have been renumbered and their corresponding citations have also been changed throughout the text.

This subsection describes the application of the DNN in the estimation of the unknown disturbance $\xi(z(t), t)$. The objective of including just the state estimation without the tracking objective is to provide a better understanding on how the parameters of the DNN have to be adjusted. For this task, the learning law in (8.38) has to be modified to

$$\dot{\hat{W}}(t) = -ke^{\top}(t)C^{\top}N_{\mu}P_1 b\sigma^{\top}(\hat{z}) - \mu b^{\top}\Lambda_W b\tilde{W}\sigma(\hat{z})\sigma^{\top}(\hat{z}). \tag{8.47}$$

Eq. (8.47) is obtained with the Lyapunov candidate function given by

$$V(\Delta, \tilde{W}) := \Delta^{\top}P_1\Delta + k^{-1}tr\left[\tilde{W}^{\top}\tilde{W}\right].$$

Moreover, notice that this learning law has the same structure as the one presented in (8.38) without the value of $\bar{g}$. Table 8.1 summarizes the parameters used in simulation for the DNN observer. The observer gain L was the result of applying the Ackerman formula with desired eigenvalues of the matrix $A - LC^{\top}$ in $\begin{bmatrix} -2.8 & -2.1 & -2.5 \end{bmatrix}^{\top}$. The numerical results include a comparison with a classical Luenberger observer to appreciate the advantages provided by the DNN approach. The gain in the Luenberger observer is calculated from the Ackerman procedure with eigenvalues located in $\begin{bmatrix} -5.8 & -6.1 & -7.5 \end{bmatrix}^{\top}$. The control injected to each observer was $u(t) = \sin(t)$. The difference in the gains are the consequence of the energy needed in the correction terms for each observer. The adaptive observer based on DNN requires less energy to estimate the unknown states.

Fig. 8.3 shows the evolution in time of the states x against the estimated $\hat{x}$. The convergence of the Luenberger observer is faster than the DNN due to the learning time used by the DNN to estimate the unknown states. The convergence is almost the same in the first and second states $(\hat{x}_1, \hat{x}_2)$ because these states are not affected directly by the uncertainty. However, in

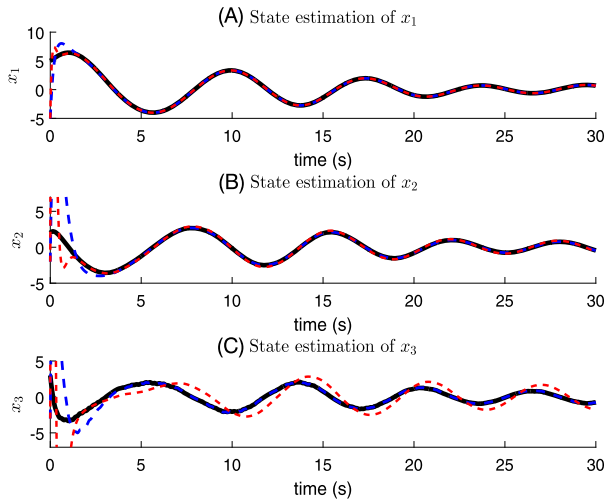

■ **FIGURE 8.3** State estimation of z. The black line is for the real trajectories.

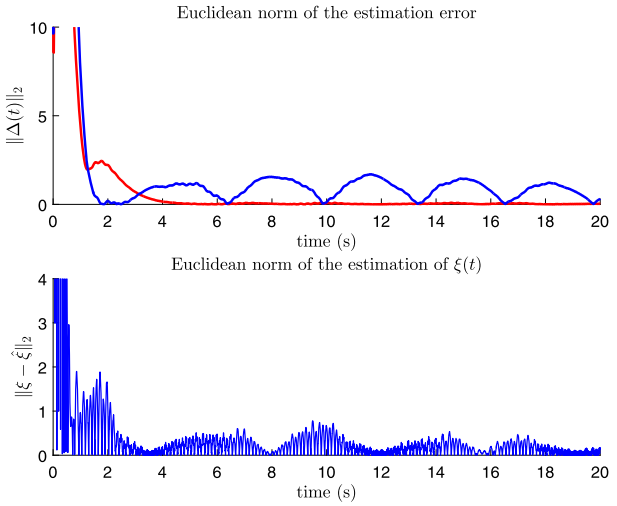

■ **FIGURE 8.4** The Euclidean norm of the estimation error.

the estimation of the third state, the linear observer does not reach the real trajectories as well as the DNN observer.

Fig. 8.4 describes the uncertainty estimation. The DNN observer takes less than 3 s to learn and to estimate the unknown disturbance. Finally, the performance index for each observer selected as the Euclidean norm of the estimation error Δ shows better estimation properties in the steady state for

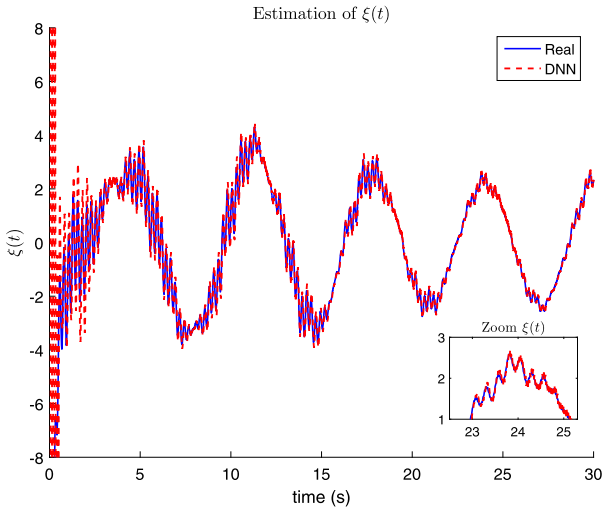

■ **FIGURE 8.5** Estimation of the disturbance.

the adaptive observer (see Fig. 8.5). It shows a closer view to appreciate the convergence of the DNN to the high frequency dynamics in the perturbation signal $\xi(t)$.

In Fig. 8.3, the solid (blue in the electronic version) line (with oscillations) represents the trajectory provided by the DNN observer and the thin (red in the electronic version) flat line is the trajectory obtained by a Luenberger observer. In Fig. 8.4, the oscillating (blue in the electronic version) line is provided by the Luenberger observer and the converging (red in the electronic version) line is the Euclidean norm obtained by the DNN observer.

In Fig. 8.5 the solid line (blue in the electronic version) is the real trajectory. The dotted line (red line in the electronic version) is the trajectory provided by DDN observer.

8.4.2 Tracking performance by the DNN approach

An output-feedback controller based on the Luenberger observer was designed to compare it with the DNN observer.

The gain matrix applying to the DNN was $K = -10 \times \begin{bmatrix} 80 & 63 & 55 \end{bmatrix}$ and for the output-feedback controller based on the Luenberger observer the gain matrix was $K = -15 \times \begin{bmatrix} 80 & 63 & 55 \end{bmatrix}$. That means that the output-feedback controller based on the Luenberger observer requires 50% more energy to obtain an acceptable tracking performance. If these gains are modified to the ones applied in the DNN observer, the tracking error in

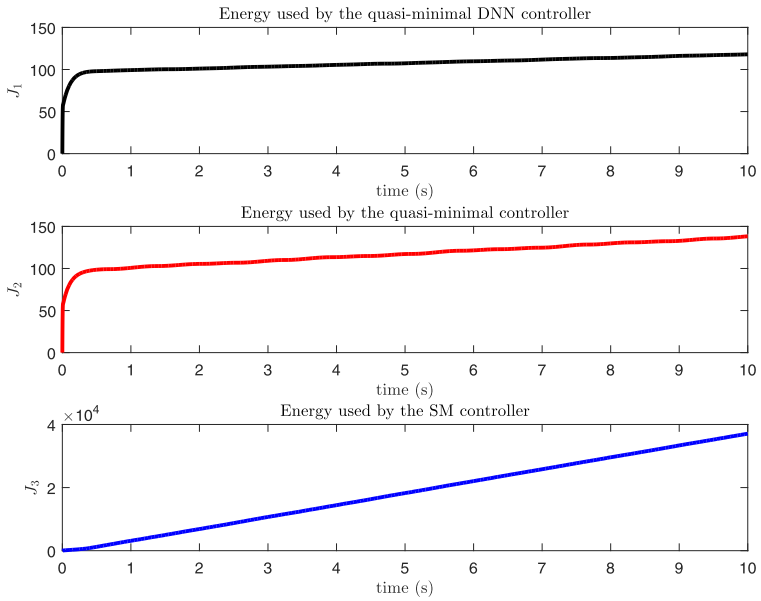

■ **FIGURE 8.6** Tracking performance of the model reference.

the Luenberger output-feedback approach does not converge to zero. Even with this increment in the control gain, the active control rejection provides a better tracking performance.

Fig. 8.6 shows the trajectories of the real system against the reference model described in Eq. (8.43). In this figure,

$$\begin{aligned} J_1(t) &= \int_0^t \|u_{DNN}(\tau)\|^2 d\tau, \\ J_2(t) &= \int_0^t \|u_L(\tau)\|^2 d\tau, \\ J_3(t) &= \int_0^t \|u_{SM}(\tau)\|^2 d\tau. \end{aligned} \tag{8.48}$$

The control based on DNN takes less than 7 s in simulation to reach the desired trajectories. Notice that the linear approach does not reach the desired trajectories. The performance (the Euclidean norm of the tracking error $\delta(t)$) for the proposed controller remains in a smaller region around the origin than the one produced by the linear controller (see Fig. 8.7).

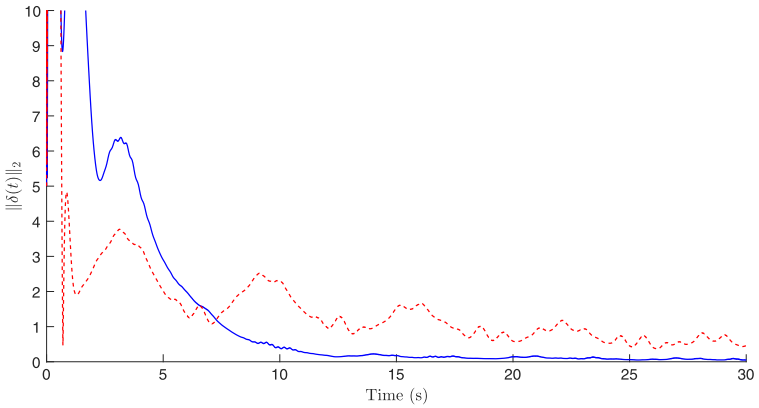

■ **FIGURE 8.7** Euclidean norm of the tracking error.

In Fig. 8.6 (J_1), the black continuous line is the real trajectory to be followed; in Fig. 8.6 (J_2) (blue in the electronic version) line is the tracking obtained by the DNN active rejection control and the trajectories represented in Fig. 8.6 (J_3) (red in the electronic version) line are produced by the output-base controller with a linear observer. In Fig. 8.7 the DNN active rejection control produces the solid (blue in the electronic version) trajectory and the output-based control with a Luenberger observer provides the dashed (red in the electronic version) trajectory.

8.5 CONCLUSIONS

Notice that the controllers, developed here, may be applied to vary the ozone concentration and its flow only. These two operation variables must be adjusted in the ozone generator. The local optimal control, developed in this chapter, minimizes the performance index, designed specially for the ozonation. The linear controllers with the special adaptive gains are shown to enforce the optimization. A new adaptive observer, using the structure of DNN with additional linear, discontinuous and error delayed correction terms, successfully recuperate the behavior of the non-measurable states of the ozonation system. Based on the application of the reconstructed states, the evaluation of LOC with DNN observations has been successfully applied in numerical simulation. The second controller, proposed here, considered the application of an extended observer to solve the ozonation control within the tracking trajectory framework.

Part 3

Ozonation in Solid and Gaseous Phases

Chapter 9

Ozonation modeling in solid phase

CONTENTS

Ozonation and Biodegradation in Environmental Engineering
https://doi.org/10.1016/B978-0-12-812847-3.00020-2

ABSTRACT

This chapter proposes the mathematical modeling of ozonation in solid phase whereas the example of the decomposition the phenanthrene, adsorbed in the model (sand) and the real soil (agricultural soil), is taken. The modeling scheme includes ordinary differential equations with time varying coefficients. This model deals with the adsorbed ozone and ozone, reacted with the contaminant, and the phenanthrene concentration in the soil. The main parameters, involved in the mathematical model, include the time varying ozone saturation function $k_{sat}(t)$ and reaction constants k_r. These parameters are calculated using the ozone concentration variation at the reactor output, and the phenanthrene decomposition by ozone. To validate the model we realized two series of experiments: soil, saturated with ozone in the absence of the contaminant, and soil with phenanthrene. Also, this chapter discusses the possibility of the conventional ozonation in the solid phase in a two-phase system (soil–ozone) and a three-phase system (soil–water–ozone) to eliminate Polyaromatic Hydrocarbons (PAHs) from the contaminated model and real soil samples. Because the ozone is a gas, it preserves the oxidative potential not only in the liquid phase (water), but also in the solid phase (soil). It is very important to notice that the ozonation kinetics practically is not different for both phases. The application of the DNN technique permits one not only to assess the ozonation kinetics, but to realize the reconstruction of the decomposition profiles of the intermediates of ozonation. Below, we describe the different examples of the decomposition of PAHs in solid phase.

9.1 INTRODUCTION

The successful applications of ozone in a water treatment motivated the investigation of its potential application for cleaning the contaminated soil (Pierpoint et al., 2003), particularly, to eliminate polycyclic aromatic hydrocarbons (PAHs). However, this treatment method has not been extended for solid phase, considering the number of open questions regarding the interaction mechanism between ozone and contaminants adsorbed on the soil surface. The mathematical modeling of soil ozonation may contribute to the understanding of these interactions. The optimization of the soil remediation by ozone, based on mathematical models, remains an active field in the environmental researching. As in the water case, in the solid phase it is possible to use the mathematical modeling of the ozone mass transfer and the decomposition of the contaminant or the mixture of contaminants by ozone.

The mathematical modeling of ozonation in solid phase is a tough task. The heterogeneous soil composition, the variety of the particle geometry, the combination of the solid and gaseous phases (two-phase system), or also with the liquid phase (three-phase system) provoke some difficulties to the modeling process. Moreover, the modeling complexity is strongly augmented in the case of the presence of pollutants adsorbed in the soil. In this case, it is necessary simultaneously to take into account the contaminant decomposition dynamics and the ozone mass transfer (Choi et al., 2002; Dong et al., 2008a,b; Kim and Choi, 2002; Kulik et al., 2006; Shin et al., 2004). During modeling the presence on the soil surface some the natural organic matter, metals, metal oxides, and moisture, should be also considered, since these components affect severely the ozonation kinetics (Chiang et al., 2002; Dong et al., 2008a,b; Haapea and Tuhkanen, 2006; Lim et al., 2002). As may be expected, all the previous models describing ozone mass transfer in soil simultaneously with the pollutant degradation are represented by partial differential equations (Luster-Teasley et al., 2009).

In this chapter, the mathematical modeling of the phenanthrene decomposition in soil by ozone is designed where time-varying parameters are used in a system of ordinary differential equation. Here the proposed mathematical model is used for the characterization of phenanthrene decomposition kinetics.

9.2 MATHEMATICAL MODELING

The considered model deals with the packed reactor (column) similar to the one, reported in O'Mahony et al. (2006) and many others, which are summarized in the report of Kulik et al. (2006). Here we consider the ozone

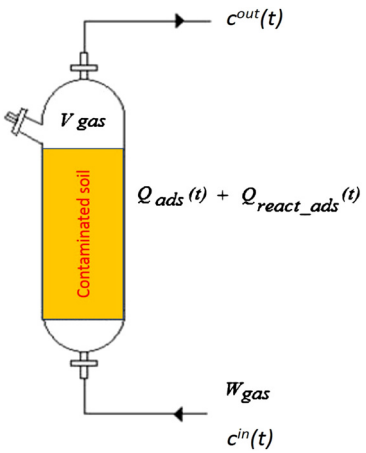

■ **FIGURE 9.1** Ozonation scheme in the solid phase.

mass-transfer into the soil in the presence of the pollutant. The proposed model is obtained from the ozone mass balance in the packed column with the phenanthrene (Fig. 9.1) using ordinary differential equations.

It is important to notice that the equation of the ozone mass balance is based on the assumptions of *a homogeneous distribution of ozone in the reactor*.

In the case contaminant is absent, the model can be also used to characterize different types of soil by the identification of the time varying parameter $k_{sat}(t)$ characterizing the ozone saturation process. This time dependent function $k_{sat}(t)$ can be obtained using the experimental measurements of the ozone concentration at the reactor output (ozonogram) (Poznyak et al., 2007). To provide a detailed study on the model validity, all the parameters in the ozonation model are identified.

9.2.1 Mass balance analysis

The mass balance of ozone, flowing through the reactor, can be described in the following integral form:

$$\int_{\tau=0}^{t} W_{gas} c^{in}(\tau) d\tau = \int_{\tau=0}^{t} W_{gas} c^{out}(\tau) d\tau + V_{gas} c^{out}(t) + Q_{r,ads}(t) + Q_{ads}(t), \tag{9.1}$$

where:

– c^{in} and $c^{out}(t)$ are the ozone concentration in the gas phase at the input (constant for all the experiments) and output of the reactor [mol L^{-1}];

– W_{gas} is the gas flow [L s^{-1}];

– V_{gas} is the gas phase volume [L] (empty reactor space);

– $Q_{ads}(t)$ is the quantity of ozone adsorbed in the solid phase [mol];

– $Q_{r,ads}(t)$ is amount of adsorbed ozone reacting with the phenanthrene [mol].

The mass balance considers the variety of the ozone interaction within the reactor. Therefore, in the proposed model we focus on the global variation of the ozone mass transfer and of the contaminant concentration. This model also takes into account the contaminant degradation described by the *Langmuir–Hinshelwood mechanism* (Luster-Teasley et al., 2009; Current State of Soil Science, 1978), implying that ozone adsorption on the soil particle is the limiting stage in the phenanthrene ozonation. The time derivative of (9.1) leads to

$$W_{gas}c^{in} = W_{gas}c^{out}(t) + V_{gas}\dot{c}^{out}(t) + \dot{Q}_{r,ads}(t) + \dot{Q}_{ads}(t). \tag{9.2}$$

Eq. (9.3) is obtained by a different arrangement of (9.2). This differential equation represents the change rate of the ozone concentration at the reactor output:

$$\frac{d}{dt}c^{out}(t) = V_{gas}^{-1}\left[W_{gas}c^{in}(t) - W_{gas}c^{out}(t) - \dot{Q}_{r,ads}(t) - \dot{Q}_{ads}(t)\right]. \tag{9.3}$$

Eq. (9.3) involves all parameters of the model and one measurable variable $c^{out}(t)$. The parameters W_{gas}, V_{gas}, and c^{in} are constant during the experiments, and $c^{out}(t)$ is measured online. The terms related to the time derivatives of $Q_{ads}(t)$ and $Q_{r,ads}(t)$ are analyzed independently.

First, the following expression for the change rate of $Q_{ads}(t)$ is

$$\dot{Q}_{ads}(t) = k_{sat}(t)\left[Q_{ads}^{\max} - Q_{ads}(t)\right], \tag{9.4}$$

where:

– $k_{sat}(t)$ is the time varying ozone saturation function [s^{-1}] for the solid phase;

– $Q_{ads}(t)$ is the current adsorbed amount of ozone in the solid phase [mol];

– $Q_{ads}^{\max}$ is the maximum amount of ozone that can be adsorbed on the solid phase without contaminant [mol].

The function $k_{sat}(t)$ depends on many factors such as porosity, superficial area, and the particle size distribution. The experimental determination of this parameter is explained in the next section.

On the other hand, the time varying change of $Q_{r,ads}$ is given by

$$\dot{Q}_{r,ads}(t) = k_{sat,r}(t)\left[Q^{\max}_{r,ads}(t) - Q_{r,ads}(t)\right]. \tag{9.5}$$

Here:

– $Q_{r,ads}(t)$ is the amount of ozone in the solid phase [mol] that reacted with the contaminant until the current t;

– $Q^{max}_{r,ads}(t)$ is the maximum amount of ozone that reacts with the contaminant up to its decomposition;

– $k_{r,sat}$ is a parameter depending on the physicochemical properties of soil and the contaminant adsorption on the particle.

The ozone reaction with the contaminant is described by

$$\dot{c}(t) = -k_r G^{-1} c(t) Q_{r,ads}(t),\ k_r > 0. \tag{9.6}$$

9.2.2 The complete mathematical model

The complete mathematical model of the contaminant ozonation (CO) is described by the system of equations (9.3)–(9.6):

Model CO

$$\left.\begin{aligned}
\dot{c}^{out}(t) &= V_{gas}^{-1}\left[W_{gas}c^{in}(t) - W_{gas}c^{out}(t)\right] \\
&-V_{gas}^{-1}k_{sat}(t)\left[Q^{\max}_{ads} - Q_{ads}(t)\right] - \\
&V_{gas}^{-1}k_{sat,r}(t)\left[Q^{\max}_{r,ads}(t) - Q_{r,ads}(t)\right], \\
\dot{Q}_{ads}(t) &= k_{sat}(t)\left[Q^{\max}_{ads} - Q_{ads}(t)\right], \\
\dot{Q}_{r,ads}(t) &= k_{sat,r}(t)\left[Q^{\max}_{r,ads}(t) - Q_{r,ads}(t),\right] \\
\dot{c}(t) &= -k_r G^{-1} c(t) Q_{r,ads}(t).
\end{aligned}\right\} \tag{9.7}$$

In the case that there is no contaminant ($c(t) = 0$), the **model CO** is reduced to the model of ozonation without contaminant (**OWC**):

$$\left.\begin{array}{c} \textbf{Model OWC} \\ \dfrac{d}{dt}c^{out}(t) = V_{gas}^{-1}\left[W_{gas}c^{in}(t) - W_{gas}c^{out}(t)\right. \\ \left. -k_{sat}(t)\left[Q_{ads}^{\max} - Q_{ads}(t)\right]\right], \\ \dfrac{d}{dt}Q_{ads}(t) = k_{sat}(t)\left[Q_{ads}^{\max} - Q_{ads}(t)\right]. \end{array}\right\} \tag{9.8}$$

The model OWC characterizes the mass transfer of ozone in the absence of contaminant, where only one parameter $k_{sat}(t)$ and its variations are unknown. The next section deals with the experimental validation of the proposed mathematical models.

9.3 PARAMETER IDENTIFICATION

9.3.1 Parameter calculation procedure for model OWC

In **model OWC** (in the absence of contaminant) the main parameter is $k_{sat}(t)$, which can be derived from (9.4), as the expression for its calculation,

$$k_{sat}(t) = \begin{cases} \dfrac{\dot{Q}_{ads}(t)}{Q_{ads}^{max} - Q_{ads}(t)} & \text{if} \quad Q_{ads}(t) < Q_{ads}^{max}, \\ 0 & \text{if} \quad Q_{ads}(t) = Q_{ads}^{max}. \end{cases} \tag{9.9}$$

As may be seen in Eq. (9.9) one needs to consider a zero value, when soil is completely saturated with ozone. This is achieved by the adsorption, which already finished at that time. The calculation of $k_{sat}(t)$ demands the knowledge of $Q_{ads}(t)$, the rate of the change of $Q_{ads}(t)$, and Q_{ads}^{max}, which can be obtained experimentally.

Notice first that to realize the identification process the ozone saturation in the empty reactor (without solid phase) should be obtained. Then the ozonogram, which corresponds to $c_r^{out}(t)$, must be measured. After the stripping of ozone by an oxygen flow, the reactor should be packed with a solid phase (without contaminant). The measured online data correspond to the variation of $c_{solid}^{out}(t)$. By these values we derive $\dot{Q}_{ads}(t)$ using Eq. (9.10):

$$\frac{d}{dt}Q_{ads}(t) = W_{gas}\left(c_{ror}^{out}(t) - c_{solid}^{out}(t)\right). \tag{9.10}$$

Integrating (9.10) at each time allows one to obtain the integral representation for $Q_{ads}(t)$:

$$Q_{ads}(t) = \int_0^t \left(c_r^{out}(\tau) - c_{solid}^{out}(\tau)\right) d\tau. \tag{9.11}$$

The final integration time is $T > 0$ in such a way that $c_r^{out}(T) = c_{solid}^{out}(T) = c^{in}$. Eq. (9.11) produces the calculation of the area between this pair of ozonograms, weighted by the flow magnitude, in order to obtain the quantity of adsorbed ozone at each integration time. The quantification of the total integral in (9.3) until the final time T yields Q_{ads}^{max} by the following integral equation:

$$Q_{ads}^{max} = \int_0^T \left(c_r^{out}(\tau) - c_{solid}^{out}(\tau)\right) d\tau. \tag{9.12}$$

The results obtained from (9.10), (9.11), and (9.12) are substituted in (9.9) to determine the time varying parameter $k_{sat}(t)$.

9.3.2 Parameters calculation for the model CO

Eqs. (9.4), (9.5), and (9.6) use the unknown parameters: $k_{sat}(t), k_r$, and $k_{sat,r}$, respectively. The previous section points out the calculation of the first parameter, when no contaminant presence is considered. However, the calculation of $Q_{ads}(t)$ and its change rate, involved in Eq. (9.7), has to be done in the presence of the contaminant. In this case, the next steps to determine $Q_{ads}(t)$ and $Q_{r,ads}(t)$ should be fulfilled.

The saturation of the empty reactor (without solid) must be forced while acquiring the ozonogram that corresponds to $c_{ror}^{out}(t)$. After the saturation, the ozonogram must be acquired when the ozonation of the contaminated soil is performed ($c_{conta,solid}^{out}(t)$). Due to the fact that the adsorption of ozone and the reaction of the adsorbed ozone are simultaneous processes, let us introduce the terms

$$Q_{ads}(t) = (1-\alpha)\, Q_{total}(t) \tag{9.13}$$

and

$$Q_{r,ads}(t) = \alpha\, Q_{total}(t) \tag{9.14}$$

where $0 < \alpha \leq 1$ and $Q_{total}(t)$ may be calculated by the following ordinary differential equation:

$$\frac{dQ_{total}(t)}{dt} = W_{gas}\left(c_r^{out}(t) - c_{conta,solid}^{out}(t)\right). \tag{9.15}$$

Integrating (9.15) from 0 to T, we get

$$Q_{total}(t) = \int_0^t \left(c_r^{out}(\tau) - c_{conta,solid}^{out}(\tau)\right) d\tau. \tag{9.16}$$

However, it is known that there exists a maximum value for ozone adsorbed on soil (Q_{ads}^{max}). This constraint must be considered (when data from ozonograms are processed to calculate the experimental $Q_{ads}(t)$ and $Q_{r,ads}t(t)$):

$$Q_{ads}(t) = \begin{cases} (1-\alpha)Q_{total}(t) & \text{if} \quad Q_{ads}(t) < Q_{ads}^{max}, \\ Q_{ads}^{max} & \text{otherwise,} \end{cases} \tag{9.17}$$

and

$$Q_{ads,r}(t) = \begin{cases} \alpha Q_{total}(t) & \text{if} \quad Q_{ads}(t) < Q_{ads}^{max}, \\ Q_{total}(t) & \text{otherwise.} \end{cases} \tag{9.18}$$

The time derivatives of Eqs. (9.12) and (9.13), in view of the restrictions, given by (9.17) and (9.18), complete the necessary information to calculate the unknown parameters:

$$\frac{dQ_{ads}(t)}{dt} = \begin{cases} (1-\alpha)\dfrac{dQ_{total}(t)}{dt} & \text{if} \quad Q_{ads}(t) < Q_{ads}^{max}, \\ 0 & \text{otherwise,} \end{cases} \tag{9.19}$$

and

$$\frac{dQ_{ads,r}(t)}{dt} = \begin{cases} \alpha\dfrac{dQ_{total}(t)}{dt} & \text{if} \quad Q_{ads}(t) < Q_{ads}^{max}, \\ \dfrac{dQ_{total}(t)}{dt} & \text{otherwise,} \end{cases} \tag{9.20}$$

where $k_{sat}(t)$ is calculated from Eq. (9.9), considering also (9.15) and (9.19). To calculate k_r, we may use the standard least-square estimate k_r^* (Poznyak et al., 2005, 2007):

$$k_r^*(t) = \arg\min_{k_r} \int_0^t \left(\frac{d}{d\tau}c(\tau) + k_r G^{-1} c(\tau) Q_{ads,r}(\tau)\right)^2 d\tau, \tag{9.21}$$

which has been solved as

$$k_r^*(t) = G\frac{\int_0^t \left(c(\tau)Q_{ads,r}(\tau)\frac{d}{dt}c(\tau)\right)d\tau}{\int_0^t \left(c(\tau)Q_{ads,r}(\tau)\right)^2 d\tau + \gamma} > 0. \tag{9.22}$$

In Eq. (9.22), one needs the time variation of $c(t)$, $Q_{r,ads}(t)$, and their rates of change; the function $c(t)$ is represented by a regression model of double exponential, which is obtained from the set of punctual extractions of the phenanthrene. The remaining data are obtained from (9.14). The small parameter $\gamma > 0$ is used to avoid any possible division by 0. To determine $k_{sat,r}(t)$, a similar procedure to that described for $k_{sat}(t)$ is used. This value is the solution of the following pair of equations:

$$k_{sat,r}(t) = \begin{cases} \dfrac{\dfrac{d}{dt}Q_{r,ads}(t)}{\left[Q_{r,ads}^{max} - Q_{r,ads}\right]} & \text{if} \quad Q_{r,ads}(t) < Q_{r,ads}^{max}, \\ 0 & \text{if} \quad Q_{r,ads}(t) = Q_{r,ads}^{max}. \end{cases} \tag{9.23}$$

Taking into account Eqs. (9.18) and (9.20), one gets enough information to obtain the function values of (9.23).

9.4 EXPERIMENTAL VALIDATION

In an ozonogram is the key information needed to validate the mathematical models presented above. Therefore, a brief study of sensor sensitivity is proposed below to differentiate the ozonogram of each solid phase without overlapping. The comparison is carried out after applying a simple first-order low pass filter over all data sets. The procedure assumes each solid phase to be exposed to ozone. Then, the corresponding ozonograms are recorded and filtered. In the last step we used the set of experimental data that are adjusted according to the following sigmoidal equation:

$$c^{out}(t) = c^{in} - \frac{c^{in}}{1 + d^{-1}e^{(t-t_0)}}. \tag{9.24}$$

The unknown parameters t_0 and d are calculated by means of the nonlinear regression techniques that are implemented in the software OriginPro (version 7.0). The values of these parameters with confidence intervals are compared ($p = 0.05$) in Table 9.1.

It is worth to remark that this associated statistical model for the ozonogram, represented by (9.24), is employed only to analyze the sensitivity of the proposed experimental method, and it is not considered in the structure of the proposed mathematical models OP and OWP.

Table 9.1 Values of the parameters t_0 and d with their confidence intervals.

Phase	t_0	Confidence interval ($p = 0.05$)	d	Confidence interval ($p = 0.05$)
Empty reactor	42.00	41.976–42.024	5.87	5.855–5.897
Sand	46.95	46.914–46.991	7.43	7.406–7.473
Soil I	47.63	47.595–47.664	7.16	7.136–7.198
Soil II	68.69	68.654–68.735	9.78	9.745–9.816

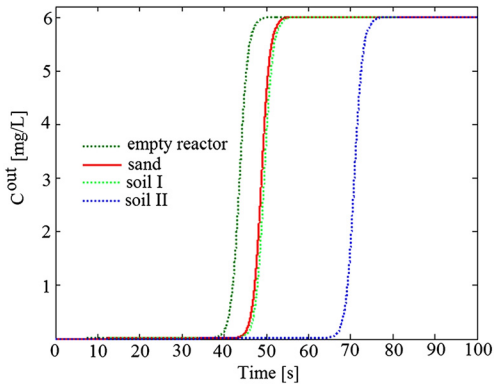

■ **FIGURE 9.2** Ozonograms of different solid phases approximated by the sigmoidal model.

9.5 RESULTS AND DISCUSSION

9.5.1 Experimental validation of the mathematical models

Table 9.1 depicts the calculated parameters t_0 ($R^2 = 0.9998$) and d, involved in the model, given by (9.24) for each one of the soils. As one may notice, there is no overlapping between the confidence intervals. This condition implies that at least, for the fixed experimental conditions, it is possible to ensure that each ozonogram is specific for each phase. Furthermore, the ozone sensor possesses enough sensibility to characterize them. It is not possible to guarantee this situation under any other experimental conditions. Fig. 9.2 depicts the evaluation of the regression model (9.24) with the parameters as in Table 9.1.

As one can see, the ozonogram profiles of sand and soil (CO) are almost the same. However, the obtained parameters turned out to be different. This can be explained by the similar selected particle sizes of the two soils. It should be noticed that data used for the comparison purposes came from a

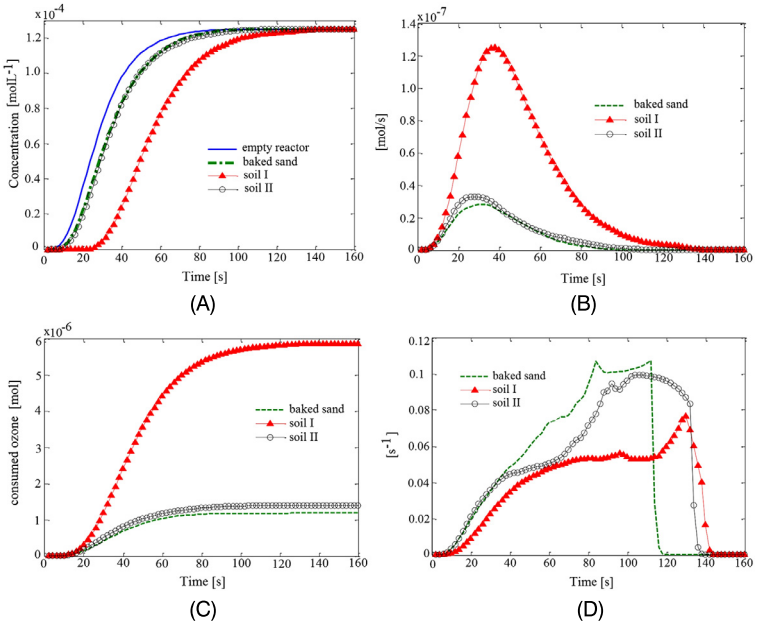

■ **FIGURE 9.3** Ozonogram comparison of the empty reactor, sand, soil I, and soil II (A); the experimental rate of change of $Q_{ads}(t)$, $\frac{d}{dt}Q_{ads}(t)$ from the equation (B); behavior of the adsorption $Q_{ads}(t)$ for different solids (C); $k_{sat}(t)$ evolution (D).

different experiment from those used in the parametric identification method described above.

9.5.1.1 Parameter calculation and simulation of model OWC

Fig. 9.3 depicts the ozonogram for the empty reactor and all three soils. In all cases, the ozone concentration reached the initial ozone concentration in a period of time smaller than 1000 s.

Fig. 9.3A shows the rate of change of the amount of ozone adsorbed on the solid ($dQ(t)/dt$) and calculated from (9.10) and the information coming from ozonograms. Integrating with respect to time $dQ(t)/dt$ (Runge–Kutta fourth order with integration step of 0.01 s) and by Eq. (9.11), it is possible to derive the current adsorption $Q_{ads}(t)$ (Fig. 9.3C). Fig. 9.3D depicts the $k_{sat}(t)$ evolution calculated from Eq. (9.9) and the data in Fig. 9.3B, C. Recalling that $k_{sat}(t)$ is proportional to the saturation rate of $dQ_{ads}(t)/dt$ and inversely proportional to the difference between maximum amount of ozone and the current amount of ozone accumulated in the soil, it is possible to appreciate that $k_{sat}(t)$ has a completely different behavior for each soil

Table 9.2 Characteristic parameters calculated for each soil without the contaminant.

Solid	Q_{ads}^{max} [mol]	$\max dQ_{ads}/dt$ [mol/s]	k_{sat}^{max} [s^{-1}]
Sand	$1.18 \cdot 10^{-6}$	$2.83 \cdot 10^{-8}$	$10.91 \cdot 10^{-2}$
Soil I	$5.87 \cdot 10^{-6}$	$1.25 \cdot 10^{-7}$	$7.92 \cdot 10^{-2}$
Soil II	$1.38 \cdot 10^{-6}$	$3.30 \cdot 10^{-8}$	$9.97 \cdot 10^{-2}$

studied. This can be explained by the different physicochemical characteristics of the soils, such as permeability and porosity.

Even when the ozonograms depicted in Fig. 9.3A for sand and soil OWP samples seem to be equal, their identified parameters point to true mutual differences. In particular, the time varying function $k_{sat}(t)$ quantifies such differences without the complete knowledge of their physicochemical characteristics accurately. However, an extensive study considering the control of the specific geometric parameters must be carried out, in order to establish the correlation with the $k_{sat}(t)$ behavior. The acceptable correspondence (percentage relative means square error less than 5%) between simulated $c^{out}(t)$ and the ozonograms for each solid confirms the high representativeness of the function $k_{sat}(t)$ to characterize the type of the soil.

Table 9.2 summarizes the maximum values of $Q_{ad}s(t)$, $dQ_{ads}(t)/dt$, and the calculated $k_{sat}(t)$ for each model soil in the absence of phenanthrene.

The calculated $k_{sat}(t)$ is tested by the numerical solution of the model OWC for each soil. The comparison of the simulation results with the experimental data is shown in Fig. 9.4A, B. These figures compare the experimental and calculated ozonograms for baked sand, soil CO, and soil OWC. The closeness between the experimental ozonograms and the simulation results is shown in Fig. 9.4B. The mean square error is $3.56 \cdot 10^{-6}$.

9.5.1.2 Parameter calculation and simulation of model CO

Fig. 9.5A shows the experimental ozonograms of the baked sand without and with the phenanthrene in the comparison with the empty reactor. The high degree of the similarity between the profiles of ozonograms for the empty reactor and the baked sand demonstrates that this information can be used to characterize the soils. This fact can explained by the small absorbance of ozone on the surface of baked sand due its low porosity.

Based on the UV-Vis absorbance variation at 254 and 292 nm of the phenanthrene extracts in methanol (results not shown), the complete contaminant decomposition is obtained during the period of the time, when ozonation is carried out (Fig. 9.5B). The experimental data of the phenanthrene decom-

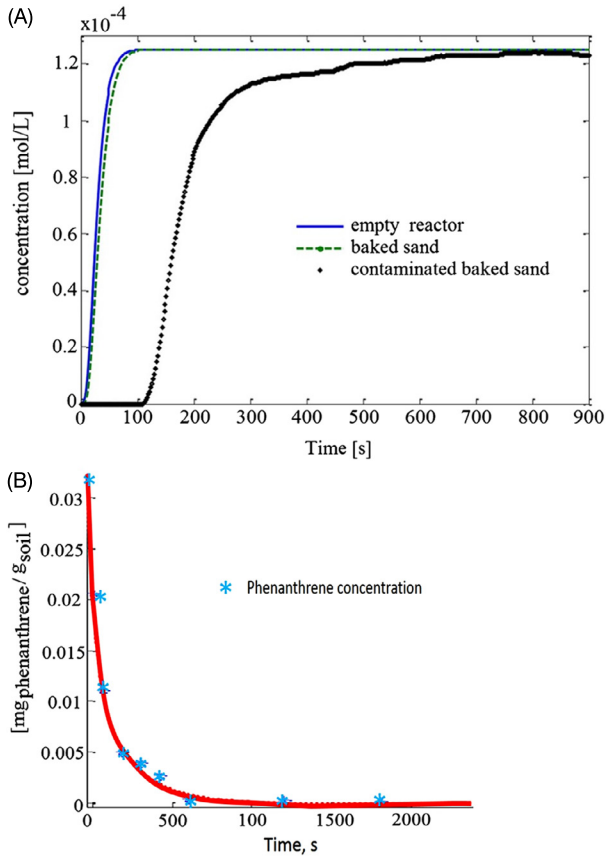

■ **FIGURE 9.4** Experimental and regression model data for the ozone concentration (A) and the phenanthrene degradation (B).

position c_{ph} are adjusted by the following equation:

$$c_{ph}(t) = ae^{bt} + ce^{dt}. \tag{9.25}$$

The calculated parameters obtained by the proposed method ($R^2 = 0.9996$) are presented in the second and third columns of Table 9.3.

The fourth and fifth columns of 9.3 summarize the calculated parameters from experimental data to characterize the **model CO**, considering $b = 0.5$, and $Q_{ads}(t)$; it is presented in Table 9.2 ($R^2 = 0.994$).

The simulation of the phenanthrene decomposition in the soils is carried out using the data presented in Table 9.3. Fig. 9.5 depicts the results for each of the involved variables in **model CO**. There are small differences

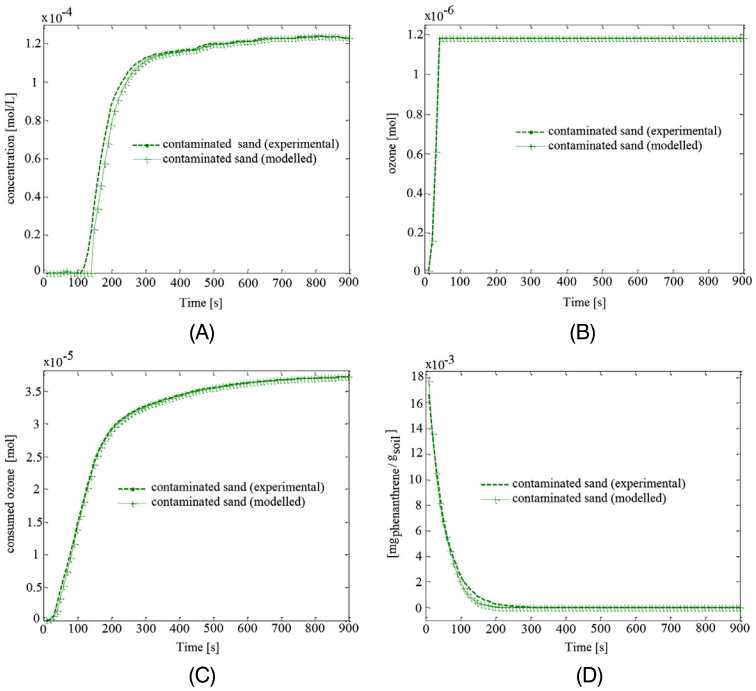

■ **FIGURE 9.5** Comparison between the simulation (model CO) and the experimental data of the baked sand: $c^{out}(t)$ (A), $Q_{ads}(t)$ (B), $Q_{r,ads}(t)$, (C), and $c(t)$ (D).

Table 9.3 Parameters calculated for the decomposition of the phenanthrene.

Parameter	Value	Confidence interval ($p = 0.05$)	Value	Deviation
A	0.009	$(-0.001, 0.020)$	0.010	± 0.001
B	-1.248	$(-2.893, 0.395)$	4.430	± 0.016
C	0.010	$(0.001, 0.022)$	0.010	± 0.065
D	-0.245	$(-0.441, -0.049)$	0.721	± 0.012

between the experimental values and the numerical simulation for $c^{out}(t)$, particularly (Fig. 9.5A).

We can assume that one of the main cause for this difference is the byproduct formation through phenanthrene ozonation; however, this phenomenon is not considered in the modeling, but the presence provokes the increment of the consumed ozone. In spite of this situation, the convergence of the model is highly acceptable. One should consider that the assumed condition

of $b = 0.5$ implies that the adsorption of ozone and its reaction is happening at the same rate of change until $Q_{ads}(t)$ achieves its maximum value.

All the parameters needed to perform the calculation of the reaction rate constant k_r between ozone and phenanthrene is already obtained by (9.22). This constant must characterize the phenanthrene decomposition by ozone in the baked sand and the soil. The obtained constant is $k_r = 14.01 \times 10^4$ g mg^{-1} s^{-1}. This value is twice larger than that found by the authors for the anthracene, 6.10×10^4 g mg^{-1} s^{-1} (Poznyak et al., 2007). This difference is expected, because phenanthrene is more reactive with ozone according to its chemical structure. The same difference is achieved, when we consider the contaminants decomposed in water by ozone.

9.6 PROJECTIONAL OBSERVERS

It seems to be very important to keep the generated state estimates $\hat{x}(t)$ always remaining within a given compact set X, that is,

$$\hat{x}(t) \in X.$$

Indeed, if the state estimates are supposed to be used in some (in fact, feedback) control construction, for example, $u(t) = K\hat{x}(t)$, then any changing of a sign in $\hat{x}_t$ may lead to a significant instability effect of the corresponding closed-loop dynamics.

Let us consider the following projectional observer ($t \geq h$):

$$\hat{x}(t) = \pi_X \left\{ \hat{x}(t-h) + \int_{\tau=t-h}^{t} F\left(\tau, \hat{x}_\tau, y_{s\in[0,\tau]}\right) d\tau \right\}. \tag{9.26}$$

Here $\pi_X\{\cdot\}$ is the projector to the given convex compact X satisfying the condition

$$\|\pi_X\{x\} - z\| \leq \|x - z\| \tag{9.27}$$

for any $x \in \mathbb{R}^n$ and any $z \in X$.

Remark 9.1. *Notice that the trajectories* $\left\{\hat{x}_t\right\}$ *are not differentiable for any* $t \geq h > 0$ *but still continuous.*

Based on the arguments presented above we wish to demonstrate the ability of the *projectional observer* (9.26) to reconstruct the non-measurable states, if the output error injection function $\Psi(e)$ satisfies

$$\Psi(e) = Ke, \quad K \in \mathbb{R}^{n\times m}, \tag{9.28}$$

(which corresponds to the standard Luenberger filter with a linear correction term). The proof of this ability is based on the application of the non-standard Lyapunov candidate function described by

$$V_t := \int_{\tau=t-h}^{t} \left\| \hat{x}(\tau) - x(\tau) \right\|^2 d\tau \quad \forall t \geq h \tag{9.29}$$

(which is, in fact, a class of Lyapunov–Krasovski functionals) instead of the standard Lyapunov function $V_t = \frac{1}{2} \left\| \hat{x}_t - x_t \right\|^2$ which is not differentiable on the trajectories of the *projectional observer* (9.26).

In this section:

– we found the upper bound for the averaged observation error corresponding to (9.26) with (9.28);

– to show the effectiveness of the suggested observer we have presented the illustrative example of the chemical reactor (ozonation of contaminated soil) where two observers have been compared: without projection (4.4) and with projection (9.26). In this section, the *projectional observer* (9.26) shows significant advantages.

An advanced oxidation process employing ozone is one of the most recent approaches in the contaminated soil treatment by chemical agents such as polyaromatic hydrocarbons. The next simplified model describes the ozonation process, when a contaminant is present in a soil just with solid and gas phase involve (without water presence):

$$\left.\begin{aligned} V_{gas}\dot{x}_1(t) = V_{gas}^{-1}\left[W_{gas}c^{in}(t) - W_{gas}x_1(t) - \right. \\ \left. k_1 S_1 x_4(t) x_3(t) - K^{abs}(t)\left(Q_{\max}^{free\_abs} - x_2(t)\right)\right], \\ \dot{x}_2(t) = K^{abs}(t)\left(Q_{\max}^{free\_abs} - x_2(t)\right), \\ \dot{x}_3(t) = k_1 S_1 x_4(t) x_3(t), \\ \dot{x}_4(t) = -k_1 x_4(t) x_3(t). \end{aligned}\right\} \tag{9.30}$$

In (9.30)

$$y_t = x_1(t) + \eta(t)$$

is the ozone concentration at the output of the reactor and is assumed to be measurable, $x_2(t)$ is the amount of ozone absorbed by the soil which is not reacting with the contaminant, $x_3(t)$ is the amount of ozone absorbed by the soil and reacting with the contaminant, and $x_4(t)$ is the current contaminant concentration. The term $K^{abs}(t)$ represents the time dependent saturation parameter characterizing the ozone transfer to the solid phase. Figs. 9.6, 9.7, and 9.8 represent the results of the state recuperation.

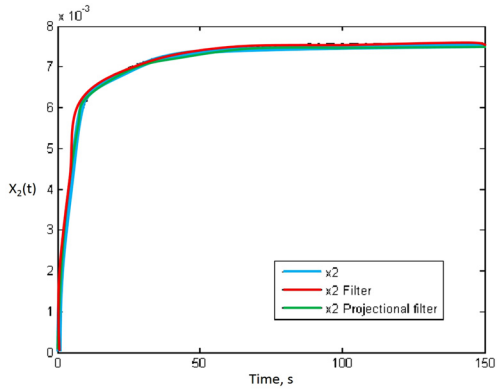

■ **FIGURE 9.6** Reconstruction of the variable $x_2(t)$.

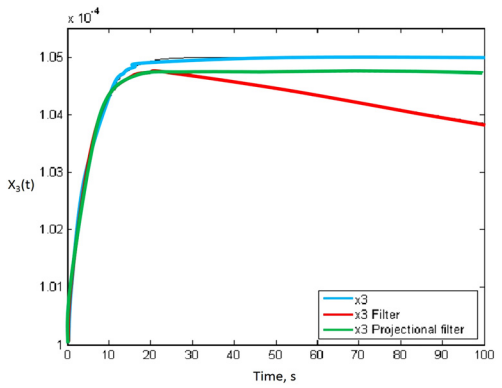

■ **FIGURE 9.7** Reconstruction of the variable $x_3(t)$.

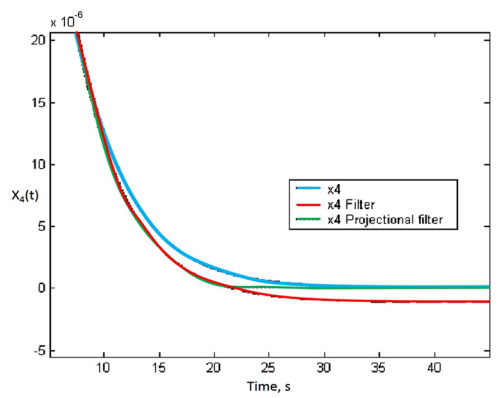

■ **FIGURE 9.8** Reconstruction of the variable $x_4(t)$.

From the curves presented above we may conclude that for the projectional filters suggested here we have a significantly better quality of state estimation especially in the beginning of a process as compared with traditional (non-projectional filters) filters.

9.7 CONVENTIONAL OZONATION IN SOLID PHASE TO ELIMINATE POLYAROMATIC TOXIC COMPOUNDS IN CONTAMINATED SOIL

9.7.1 Anthracene decomposition in soils by conventional ozonation

The Polycyclic Aromatic Hydrocarbons (PAHs) are byproducts of the pyrolysis of petroleum at high temperatures, as well as in acetylene synthesis from natural gas, refinery operations, etc. (Fouillet et al., 1991). The presence of PAHs in air, water, and soil has been detected. In some cases, concentrations of these contaminants of more 10 g/kg were found (Lundstedt, 2003). The PAHs are characterized by their hydrophobic nature; therefore they tend to be adsorbed on solid particles and this characteristic converts them into an important soil pollutant. Due to their low solubility in water, the PAHs can be adsorbed in the surface of soil, and then to realize their biodegradation is a difficult task, because they are highly hydrophobic and strongly interact with the soil (Cerniglia, 1992; Hansen et al., 2004; Luthy et al., 1994; Mulder et al., 2001). Some attempts to study the local and global distribution of the PAHs in soil have found a pattern determined by background conditions and we have a direct impact by the atmospheric deposition of the anthropogenic emissions (Ünlü and Alpar, 2006; Wilcke, 2007). Many studies show that the presence of these compounds has a toxic effect on living beings (W. H. Organization, 2004). Among the available soil remediation technologies, there exist *in situ* and *on site* techniques (Thakuria et al., 2004). For the elimination of the PAHs from soils there two kinds of technologies:

1. *Physical treatment*: extraction with subcritical and supercritical fluids, surfactants, vegetable oil, solvents, etc.

2. *Chemical treatment*: oxidation, where ozone and/or hydrogen peroxide (with or without iron ions) are/is employed.

It is worth to notice that most of the PAHs are non-volatile, and not biodegradable, which explains why conventional methods, such as the extraction by vapor and bioventing, are non-efficient (Choi et al., 2001; Goi and Trapido, 2004). Consequently, these techniques must be combined with

chemical oxidation by the *Fenton reaction* and ozone (Derudi et al., 2007; Haapea and Tuhkanen, 2006; Kulik et al., 2006; Stehr et al., 2001).

According to many investigations, ozonation presents some advantages over other methods (Lee and Kim, 2002; O'Mahony et al., 2006); among others are reported the byproducts formation in ozonation of PAHs in two-phase systems (gas–solid phase), and there are a few studies of kinetics too (Kwamena et al., 2006). In the majority of these works, the efficacy of the treatment is controlled through the measurement of the initial compound concentration. The anthracene decomposition by ozone with the 9,10-anthraquinone formation, as the main ozonation byproduct in sand, as model soil was reported in Zhang et al. (2005), or the anthrone and 9,10-anthraquinone production in silica, as the solid phase in Perraudin et al. (2007). Each of these processes have influence on some operations parameters: organic matter, soil particle size, concentration of oxidant, etc. (Gómez-Alvarez et al., 2012). Some studies show that the PAHs oxidation byproducts are more biodegradable than initial compounds, and therefore ozonation can be combined with biodegradation (Goi and Trapido, 2004; Kulik et al., 2006; Nam and Kukor, 2000; Zeng and Hong, 2002). Moreover, the soil treatment by ozonation is an attractive technology, because it can be applied *in situ* (United States Solid Waste and EPA, 2002).

In the first stage, the anthracene decomposition in different soils (model and real) by ozonation is studied, because this is one of the most abundant PAHs in the contaminated soils and has a high reaction rate constant with ozone (Poznyak et al., 2007). Here we are focused on the effect of water, the kind of soil, and the presence of the organic matter on the anthracene decomposition, and on the partial composition of byproducts of ozonation on the base of their identification.

9.7.2 Materials and methods

9.7.2.1 Preparation of the model contaminated soil

The sand with distilled water (during 0.5 h) and with ethanol (0.5 *h*) preliminarily is washed under continuous mixing. To eliminate the organic matter the agricultural soil with hexane, ethanol, and water is washed and calcined to 500°C of 24 h. The washing efficiency is controlled by the UV-spectra of the filtrates. In 40 g of dry sand is added, the anthracene solution in the ethanol (40 mL) with a concentration of 2000.0 mg L^{-1}, and then after mixing (0.5 h) the ethanol is evaporated at 70°C were added. The anthracene distribution and its concentration in the sand surface is controlled by the UV-spectrum of the anthracene extracted in ethanol from the soil contaminated (1 g of soil) by the Soxhlet (in 20 mL of ethanol) during 3 cycles.

Table 9.4 Physiochemical characteristics of soils.

		Sand	Calcinated soil	Natural soil
Particle size (mm)	< 0.1490	4.7%	4.6%	2.1%
	0.1490	14.2%	4.6%	17.6%
	0.1770	73.8%	37.5%	64.0%
	0.4190	7.3%	53.3%	16.30%
Density (g mL^{-1})		1.7	1.0	1.1
OM content (%)		0.50	0.0	9.11
pH		7.30	8.2	7.8

The model soils with anthracene has an initial anthracene concentration of 2.0 mg g^{-1}. In the case of moisted sand, 20% w/w of water is added to the contaminated baked sand. Table 9.4 gives the characteristics of the used soil.

9.7.2.2 Soil ozonation

The ozonation of the contaminated soils (baked sand, moist sand, and real soil) was carried out in the reactor by the "fluid bed" principle ($12 \cdot 3.0$ cm) with a 40 g of sample, during the time: 2, 5, 10, 15, 20, 30, 60 and 90 min. The initial ozone concentrations were 16 mg L^{-1} and 40 mg L^{-1}, and the gas flow of 0.5 mL/min. To measure the degree of anthracene stripping, the blank test of the contaminated soil during 25 min with oxygen flow only was realized. This parameter was calculated by a comparison of the UV spectrum of its extracts in ethanol.

9.7.2.3 Analytical methods

To obtain the summary information on the anthracene decomposition, all soil samples were extracted in ethanol and then extracts were analyzed by UV-Vis spectrophotometry at 190–400 nm by a spectrophotometer (Perkin-Elmer Lambda 2B). The control of the anthracene decomposition, as well as the intermediates and final products identification was realized by High Performance Liquid Chromatography (HPLC) using three systems:

1. The first, by Perkin-Elmer series 200 with a automatic UV-Vis detector and the chromatographic column Nova Pack C-18, 250 × 4.6 mm with a mobile phase of water : acetonitrile : phosphoric acid mixture (70:29.9:0.1) for anthracene.

2. The second, by an Varian equipment: pump 9010, detector UV-Vis 9050, and an integrator HP 3393A with the column Interstil C-18, 250 × 4.6 mm with a mobile phase acetonitrile : water (53:47) for partial identification of the byproducts.

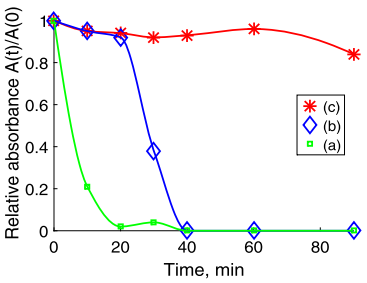

■ **FIGURE 9.9** Anthracene decomposition by ozonation in: baked sand (A), moisten sand (B), and agriculture soil (C).

3. The third, by the equipment LDC Analytical Consta Metric 3500 solvent delivery system with a SP TP Spectro monitor 3200 as UV-Vis detector and a SP TP Chromjet Integrator with a Alltech column C-18, 150 × 3.9 mm with a mobile phase acetonitrile : water (53:47) also for byproduct identification.

For all systems, the injected sample volume was 20 μL and the wavelength was 254 nm with flows of 0.8 mL min^{-1} and 1.0 mL min^{-1}. In the HPLC-MS/MS analysis an equipment 3200Q TRAP quadrupole mass spectrometer (Applied Biosystem MDS SCIEX) with electrospray ionization was used. From the extract in ethanol of ozonated sand (after 30 min of ozonation) the solvent was evaporated from each sample and then dissolved in acetonitrile; then these samples were injected to HPLC-MS/ MS. To identify the ozonation products, the 9,10-anthraquinone, the anthrone, and the phthalic acid were used as the standards. The ESI parameters were ion spray (IS) voltage (4500 V), and source temperature (TEM) 100 C. DP 210 V, EP 10 V, CEP 14 V, CE 0e130 V, CXP 3.25 V.

9.7.3 Results and discussion

9.7.3.1 Anthracene decomposition in baked sand

The two-phase ozonation is suggested to be applied for the anthracene decomposition in the baked sand and the real soil at the native pH. The loss of anthracene through stripping during ozonation is negligible. The obtained results confirm that the anthracene may be completely decomposed by the conventional ozonation. Based on the HPLC analysis of the anthracene extracted in ethanol (Fig. 9.9), we may conclude that the anthracene is decomposed during 12 min by 80%.

In the beginning of ozonation (Fig. 9.10A, B), seven compounds were accumulated during 30 min and then decomposed. By the comparison

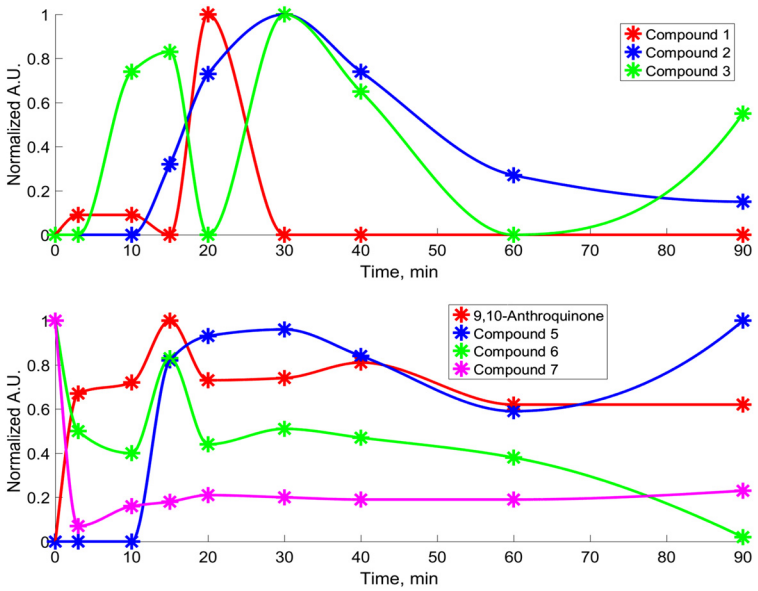

■ **FIGURE 9.10** Byproduct formation–decomposition obtained by the HPLC technique: method 2 (A), method 3 (B) (ozone concentration of 16 mg L^{-1}).

Table 9.5 Mass spectra of the identified products in ozonation of anthracene in baked sand.

Compound	Molecular weight MW	m/z relative abundance
Phthalic acid	167.0	152.1, 139.1, 127.8, 113.2, 101.8
Anthrone	195.0	180.2, 165.3, 152.1, 138.0, 128.3, 115.0, 101.9, 89.2, 76.8, 65.0
9,10-Anthraquinone	209.2	193.1, 178.0, 165.2, 151.8, 140.2, 128.3, 114.9, 89.0, 77.3, 63.0, 51.3

of mass spectra of standards, only three compounds may be identified: 9,10-anthraquinone, anthrone, and phthalic acid (Table 9.5).

9.7.3.2 Anthracene decomposition in moist sand

To study the effect of the water, the three-phase ozonation (ozone–sand–water) was carried out for the anthracene decomposition in moist sand (Fig. 9.9). The total anthracene decomposition was achieved during 30 min of ozonation. As one can see, in the first 15 min of ozonation the anthracene does not degrade. This may be the effect of the presence of water. The sand

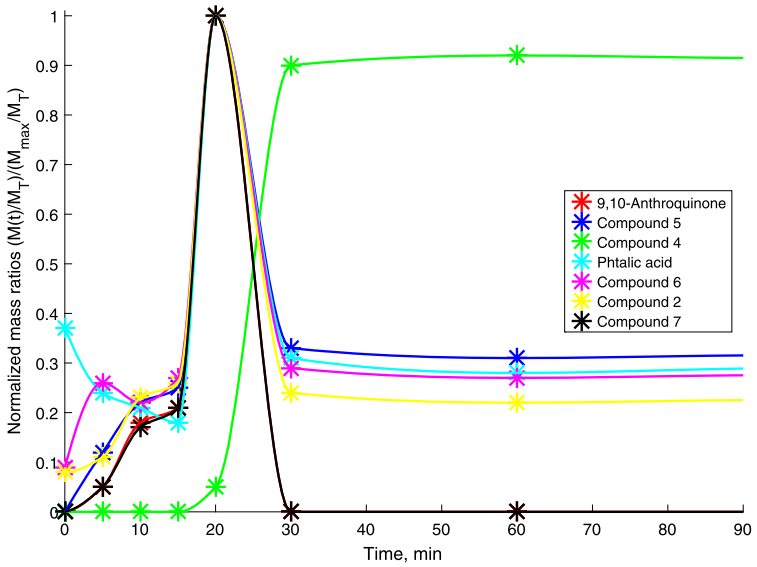

■ **FIGURE 9.11** Formation–decomposition of the intermediates in ozonation of the moist sand (20%) (ozone concentration of 16 mg L^{-1}).

particles with anthracene are surrounded by a film of water, which is a barrier to the mass transfer of ozone. So, ozone should be dissolved in water and then react with the anthracene. In addition, ozone is decomposed in water to generate OH radicals, which also attacks the anthracene (Rivas, 2006). After the first 15 min and during the next 17 min anthracene is decomposed completely; however, the byproduct dynamics is also changed. The intermediates have a similar dynamics of formation and decomposition (Fig. 9.11).

As was observed, these compounds were accumulated within 20 min, and after this time they tended to decompose by 60–100% of their maximum concentration. The presence of the water favors the formation of ·OH radicals, which are not selective, and their reaction rate constant with organic compounds is greater than the molecular ozone. This leads to a higher and similar decomposition dynamics of all byproducts (at least after 10 min). One compound (No. 4 in Fig. 9.11) tends to be formed after 20 min of ozonation and it is accumulated over the next 15 min. Likely that this compound was formed during the reaction of the same intermediates with ozone, and it can be classified as final product. Compared to the experiment with the baked sand, we may conclude that the presence of water promotes the decomposition of anthracene, as well as of the byproducts formed during the ozonation. Moreover, it was observed that in the last experiment the phthalic

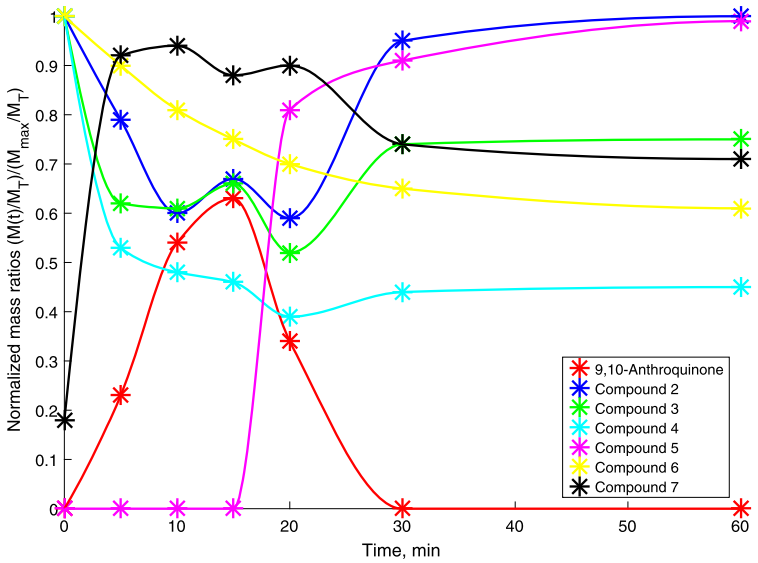

■ **FIGURE 9.12** Formation–decomposition of the intermediates in ozonation of the calcinated soil (ozone concentration of 16 mg L^{-1}).

acid was formed in a shorter time (20 min vs. 120 min), and the formation of the anthrone not observed absolutely.

9.7.3.3 Anthracene decomposition in the calcinated and agricultural soil in the presence of OM

To study the effect of the presence of organic matter (OM) in the agricultural soil on the degradation of the anthracene, the soil was calcinated to remove organic matter and then was treated by ozone with and without OM (Fig. 9.12). The OM content in soil before and after the calcination is presented in Table 9.1. The experiment with calcinated soil, contaminated with anthracene, was carried out under an ozone concentration of 40 mg L^{-1}. The obtained results are as follows:

– the complete degradation of anthracene after 5 min of ozonation and

– the decomposition of byproducts is required at least 3 h of treatment.

This could be associated with the calcinated soil, which is more porous (less dense soil) than sand. It was verified the presence of 9,10-anthraquinone as one of the main byproducts of ozonation, including six unidentified byproducts (Fig. 9.12). Agricultural soil in the decomposition of anthracene is very slow compared to the baked sand, moist sand, and calcinated soil (Fig. 9.9). It was observed that after 90 min of treatment with ozone, the achieved an-

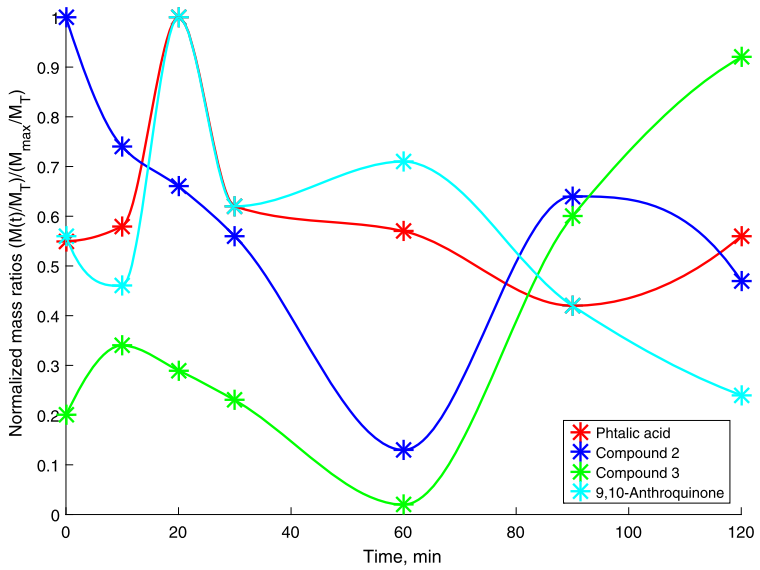

■ **FIGURE 9.13** Formation–decomposition of byproducts in ozonation of the agricultural soil at the ozone concentration of 40 mg L^{-1}.

thracene decomposition is only 30% of the initial concentration. This might be due to the effect of the OM presence by two factors:

– First, the OM may be more reactive with ozone or its content is more reactive than the anthracene.

– Second, anthracene can be found inside of the OM and ozone must react with anthracene and organic matter simultaneously to decompose both of them.

In this case, the ozone consumption related to the reactions with the OM or other compounds contained in it or dissolved in the water film. The identified ozonation byproducts are 9,10-anthraquinone and phthalic acid, including two unidentified compounds (Fig. 9.13).

Comparing the four studied cases (baked sand, moist sand, calcinated soil and agricultural soil), the principal byproducts of the anthracene decomposition in the solid are 9,10-anthraquinone, phthalic acid, and anthrone. In some studies of the anthracene decomposition by ozone in organic media (Bailey, 1958; Razumovskii et al., 1984), and in soil (Kwamena et al., 2006; Perraudin et al., 2007) similar oxidation products were found. In the case of the aqueous solution, also the formation of the simple organic acids was proven (Santillan et al., 2010). Some studies have shown that the oxidation products of anthracene, such as 9,10-anthraquinone, were less toxic than the

anthracene itself for several animal and plant cells (Choi et al., 2001) and some green algae (Tukaj and Aksmann, 2007). So, the application of ozone is an alternative for the remediation of the soils contaminated with PAHs.

To investigate the decomposition degree of the organic matter in agricultural soil, the ozonation was carried out during 120 min. The extraction of the OM fractions with different solvents (benzene, chloroform: methanol, and hexane) permits us to separate the aromatic, polar, and aliphatic fractions of the organic matter (Poznyak et al., 2008). Then, three fractions may be analyzed by UV-Vis spectrophotometry and the HPLC at the two wavelengths of 254 and 280 nm. Fig. 9.14 represents the variation of the organics composition in the different OM fractions.

Based on these results, we may conclude that the composition of the organic compounds in the OM is very complete, and they are reactive with ozone. In three fractions of the organic matter after ozonation, other compounds appear, which are interpreted as the products of the reaction with ozone. It was found that the aromatic fraction was more reactive ($\leq$ 90% of aromatic compounds degraded) than the fraction in hexane ($\leq$ 50% of compounds decomposed), and, finally, the polar fraction. In this case, the ozone consumption was justified due to the competition in the reaction with the anthracene and the OM.

9.8 EFFECT OF MORPHOLOGICAL AND PHYSICOCHEMICAL SOIL PROPERTIES ON THE PHENANTHRENE DEGRADATION BY OZONE

Based on the results obtained above, the necessity is obvious of a more profound study of the influence of the morphological and the physicochemical properties of soil on the mechanism, kinetics, and efficacy of ozonation of the PAHs, particularly, of phenanthrene. The effect of soil physicochemical properties, such as texture, bulk density, particle density, porosity, elemental composition, permeability, surface area, and pore volume are evaluated here. Additionally, the more profound identification of the intermediates and the final accumulated products formed by the phenanthrene decomposition in ozonation is carried out.

In Mexico, in 2010 around 161 sites were identified as potentially contaminated, and a third of all these sites (55) are polluted by the toxic compounds derived from petroleum. The local petroleum company (PEMEX) reported that 8031 tons of hydrocarbons (oil, diesel, and gasoline) were spilled in soil of four pipeline sectors of the country (Mexicanos, 2001; Vega et al., 2012). Among PAHs, phenanthrene is the toxic compound which has larger

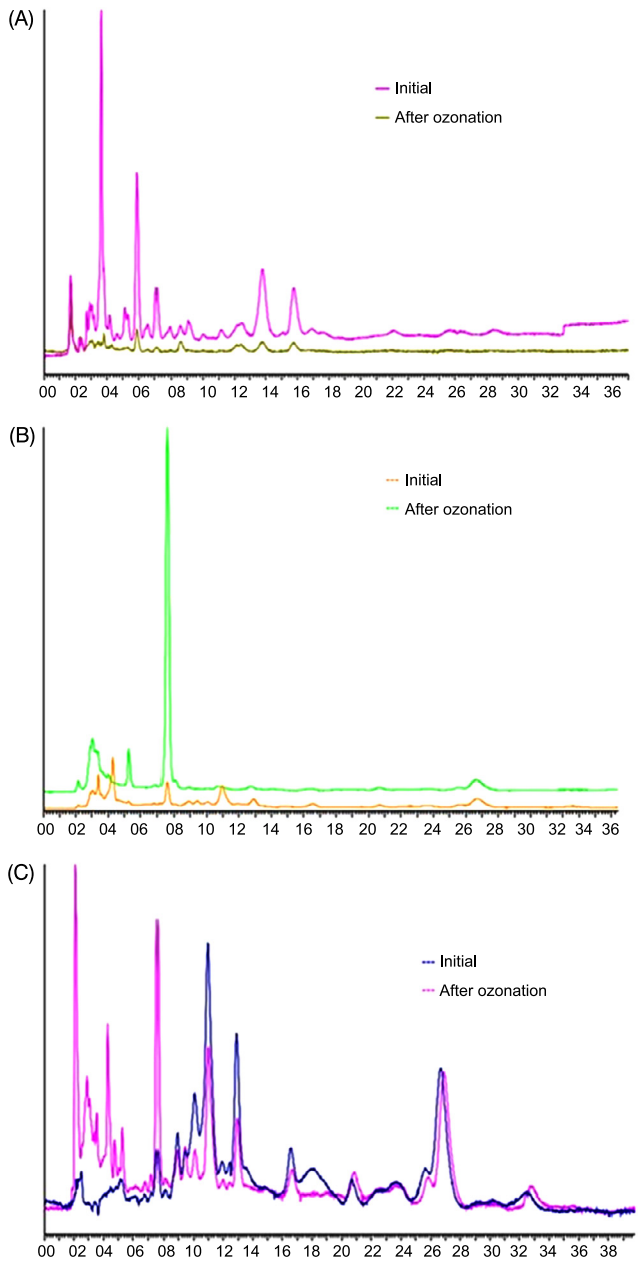

■ **FIGURE 9.14** Variation of the OM composition in agricultural soil in the different fractions after ozonation during 120 min: the aromatic fraction (280 nm) (A); the polar fraction (254 nm) (B); the fraction in hexane (254 nm) (C).

reactivity with ozone than anthracene. For this reason, this compound is selected as the example of the PAHs to study the effect of the morphological and physicochemical properties of soils and the presence of the organic matter on its decomposition dynamics by ozone, as well as on the distribution of the ozonation byproducts.

9.8.1 Materials and methods

9.8.1.1 Soil characterization

The sand used as the model soil is commercial and has been donated by the Mexican Petroleum Institute. Agricultural land was obtained from a farming site located in the municipality of Allende, Cuernavaca, Morelos, Mexico. This site is exclusively used for the organic cultivation of agave (without pesticides or some other chemicals), and therefore, it can be considered to be free of other contaminants. The soil characterization was carried out by the determination of the following physicochemical properties: granulometry, apparent and real density, moisture, permeability, morphology, texture, porosity, pH, conductivity, BET area, and the content of heavy metals and organic matter. The SEM technique and the scanning electron microscope JSM-6300 JEOL were used to analyze the particle size, morphology, and the distribution of the soil aggregates. The coating of the porous media was prepared with a carbon film or metal (gold or platinum) to provide sufficient electrical conductivity in the system.

To determine the mineralogical and elemental composition of the soil samples, the XRD technique are employed using the two equipments of X-ray spectroscopy and Energy Dispersive Spectroscopy (Brand NORAN 2000). To determine the heavy metals content the technique reported in Cresser and Hargitt (1976); Gao et al. (2006) by Atomic Absorption (model Perkin-Elmer, Series 2380) was used (Table 9.6).

9.8.1.2 Preparation of the contaminated soil

The sand was washed with distilled water (during 0.5 h) and then with ethanol (0.5 h) under continuous mixing. The organic matter was removed from the agricultural soil by washing with hexane, ethanol, and water. The soil samples were dried at a temperature of 500°C for 24 h. The washing degree with the distilled water was controlled by the UV spectra of the filtrated solvent. A volume of 400 mL of the phenanthrene solution in methanol was added to 400 g of calcinated sand or soil. Then, the methanol was evaporated at ambient temperature. The phenanthrene concentration in the sand and soil was controlled by the UV-spectra of the phenanthrene extracts in the methanol from the contaminated soil (1.0 g of soil in 30 mL of methanol).

Table 9.6 Physicochemical properties of soils.

Parameter	Sand	Agricultural Soil	
		Before calcination	After calcination
Specific gravity,[a] kg m^{-3}	1701.38	999.52	1105.67
Real density, kg m^{-3}	2492.50	2673.55	2581.88
Permeability (k, cm s^{-1})	0.075	0.0049	0.0059
Porosity, %	31.71	57.14	57.14
Moisture, %	0.016	0.42	–
Texture	sandy	sandy	sandy
Composition,[b] %			
Sand	99.33	94.77	–
Clay	0.063	5.012	–
Slime	0.004	0.011	–
Conductivity, µS	525.51	307.69	289.16
pH	10.19	7.88	6.97
BET surface area (m^2 g^{-1})	7.87	34.92	13.027
Pore volume (cm^3 g^{-1})	0.0036	0.0160	0.0059

[a] *Standard method ASTM D 854.*
[b] *Standard method ASTM D 422a.*

The extraction was realized in the Soxhlet during three cycles. The initial concentration of the contaminant was 1.5 mg g^{-1}.

9.8.1.3 Soil ozonation

The ozonation of the contaminated soils (sand and agricultural soil) was carried out in a glass reactor (12.0 cm · 3.0 cm) by the *fluid bed* principle with a 30 g of sample. Ozonation was carried out during the different times: 2, 5, 10, 15, 20, 30, 60, 90, and 120 min. All the experiments were triplicated. To measure the phenanthrene stripping, a blank test of the contaminated soil with only the oxygen flow during 25 min was realized.

9.8.1.4 Analytical methods

To obtain the summary information of the phenanthrene decomposition, the extracts in methanol were analyzed by the UV-Vis spectrophotometer (Perkin-Elmer Lambda 2). The control of contaminant decomposition and the intermediate and final product identification were made by the HPLC (Liquid chromatograph Perkin-Elmer, series 200), with the chromatographic column Nova Pack C-18, 250 · 4.6 mm, with the mobile phase of water : acetonitrile : phosphoric acid mixture (70:29.9:0.1); a sample vol-

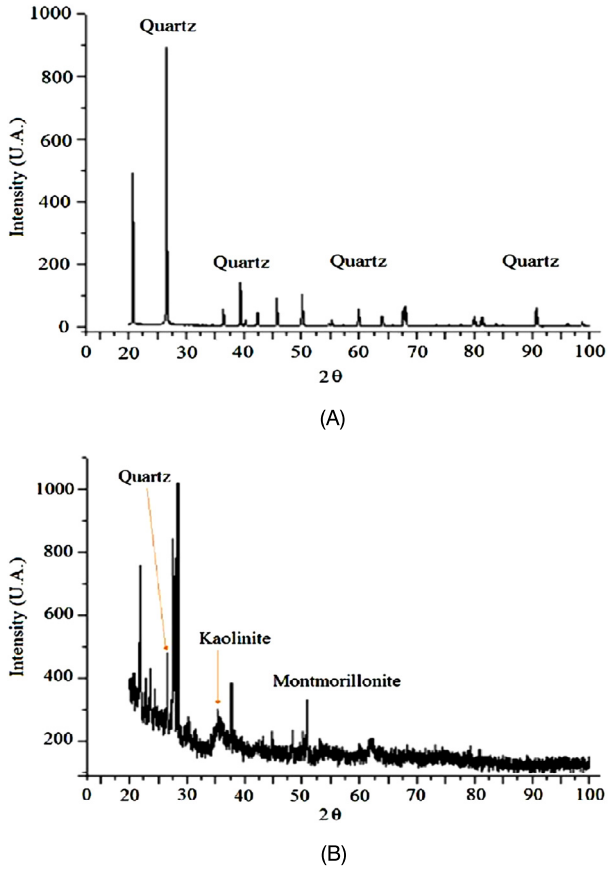

■ **FIGURE 9.15** Diffractograms of sand (A) and agricultural soil (B).

ume of 30 μL; the wavelength was 251 nm and the mobile phase flow of 1.0 mL min^{-1}. All the analytical tests were duplicated.

9.8.2 Results and discussion

9.8.2.1 Morphological analysis

Fig. 9.15 represents the micrographs of sand and agricultural soil without the contaminant, and after the treatment, respectively. The morphology of the soil samples is characterized by the SEM technique. The sand has a smooth surface (Fig. 9.15A), which confirms the absence of cavities and/or pores in these samples. The agricultural soil has a wide distribution of particle size (Fig. 9.15B), which agrees with a possible increment of porosity and the decrease of permeability.

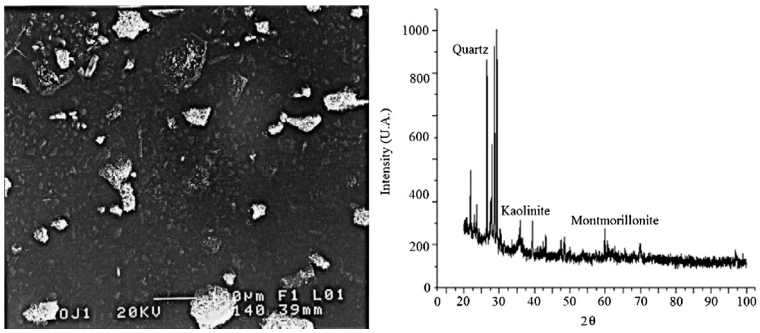

■ **FIGURE 9.16** Micrograph (A) and diffractogram (B) of the calcinated soil.

In general, if the soil is highly porous and in it pits are present, and fissures or cracks in each particle, the phenanthrene may be adsorbed. Indeed, the contaminant crystals acquire the size of the pore, crack, void or the space available for the occupancy. This leads to the formation of the crystals of different sizes, which increases the pollution and provides difficulties for the contaminant degradation.

9.8.2.2 Changes of physicochemical properties of agricultural soil after calcination

Table 9.6 shows the physicochemical properties of the sand and the agricultural soil before and after the calcination. The specific density increased around 10% due to the effect of removing of the organic matter (OM). The calcination reduces the density (4%) and the porosity (8%). The BET area decreases about 63%, which leads to a decrease of the ozone adsorption (saturation) (Ramaroson et al., 2009). SEM and XRD analyses confirmed the changes of the physicochemical characteristics and the structure of the soil particles due to their dehydroxylation (550°C), according to Rodriguez et al. (2017).

Fig. 9.16A shows the micrograph of the ozonated agricultural soil. The effect of the particle size on their breaking degree may be observed, therefore, the significant change of the available surface can be explained by the degradation of the OM. The diffractogram in Fig. 9.16B confirms that the characteristic peak of SiO_2 is not affected by the ozonation. Kaolinite and montmorillonite also remained without undergoing morphological changes. This confirmed that recrystallization or the transformation did not happen in the system.

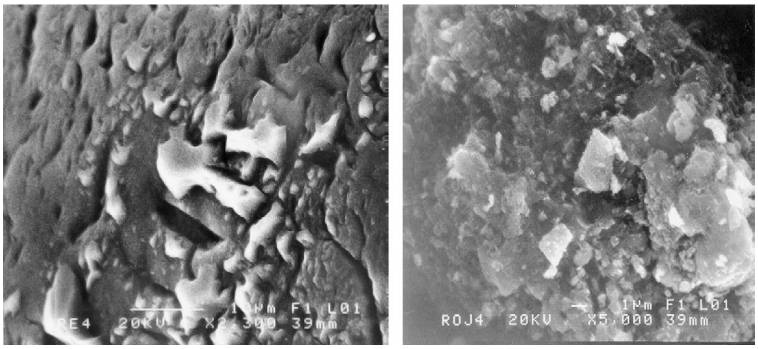

■ **FIGURE 9.17** Micrographs of contaminated sand (A) and agricultural soil (B).

9.8.2.3 Distribution of the phenanthrene in soils

The information of the phenanthrene crystal shape in each soil after contamination and the evaporation of the solvent was obtained by the SEM analysis (Fernández Linares and Linares, 2006). To ensure the representativeness of the sample, the average value of all the measurements, obtained from collected samples, was calculated at three different regions of surface. Fig. 9.17 shows the micrographs of the contaminated sand and agricultural soil, showing that the distribution of the phenanthrene strongly depends on the soil morphology. In the case of contaminated sand, phenanthrene is mainly deposited on the surface (forming clusters or crystals) in the greater proportion than the one observed within the pores (Fig. 9.17A). The size of the crystals formed on the surface and in the pores is between 1 and 100 μm. In the case of the contaminated agricultural soil, the phenanthrenes were adsorbed on the surface with a greater proportion than the one observed in the sand. The higher porosity of the agricultural soil with respect to the baked sand is the key factor explaining this difference (Fig. 9.17B). The phenanthrene was deposited on the surface of the particles and in the pores or cavities in equal proportion. The presence of the pores of the different volume causes the formation of the phenanthrene crystals of the different sizes, thereby facilitating a more effective interaction between ozone and contaminant.

9.8.2.4 Phenanthrene degradation in soils

Fig. 9.18A illustrates the ozonograms of phenanthrene in the sand and agricultural soil, the profiles of which are different. The ozonogram of the sand demonstrates a fast soil saturation in less than 120 s. On the other hand, the degradation was carried out during 30 min with an efficiency of the phenanthrene decomposition of 74% and during the rest of time (2 h) by 80%

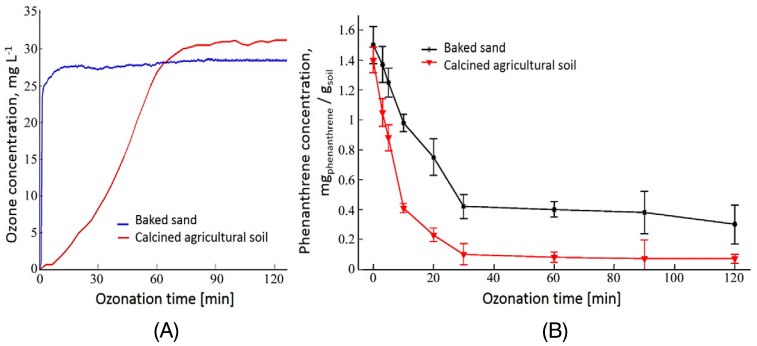

■ **FIGURE 9.18** Ozonograms of the phenanthrene in the sand and the agricultural calcinated soil (A); decomposition of phenanthrene (B). Bars depict the standard deviation obtained as a result of the three experiments.

(Fig. 9.18B). The result obtained is related to several factors: the adsorption of both the gas and the contaminant on the sand, the distribution, and the size of the crystals.

In the case of agricultural soil, the better contaminant removal (95%) is obtained during the very fast time of 30 min due to the clear difference between the physicochemical properties of soils related to the porosity, which is higher in the agricultural soil.

9.8.2.5 Partial identification of intermediates and final products of phenanthrene ozonation

Using the HPLC the following decomposition byproducts were identified: 9,10-phenanthraquinone, 9,10-hydroquinone, phenol, and diphenic acid. At the latter stages of the reaction, the accumulation of the phthalic and the oxalic acids was observed, which confirms the breaking of the aromatic rings. Fig. 9.19A shows the formation and the decomposition of the main identified products. Most of them were accumulated during the first 20 min. After this time, all compounds were degraded. These data confirm that 20 min of the ozonation, under the experimental conditions, are sufficient to degrade the phenanthrene by 80%.

In the case of calcinated agricultural soil, the following products were identified: 9,10-phenanthroquinone, catechol, phenanthrol, and diphenic acid. All of them had the concentration of 2–10 mg kg^{-1} (Fig. 9.19B). Most of the identified compounds are identical to the ones obtained in the case of calcinated sand. The main difference is the removal efficiency.

Based on the literature data (Kim et al., 2006; Sturrock et al., 1963; Traczewska, 2000), it is possible to deduce that ozone has a major affin-

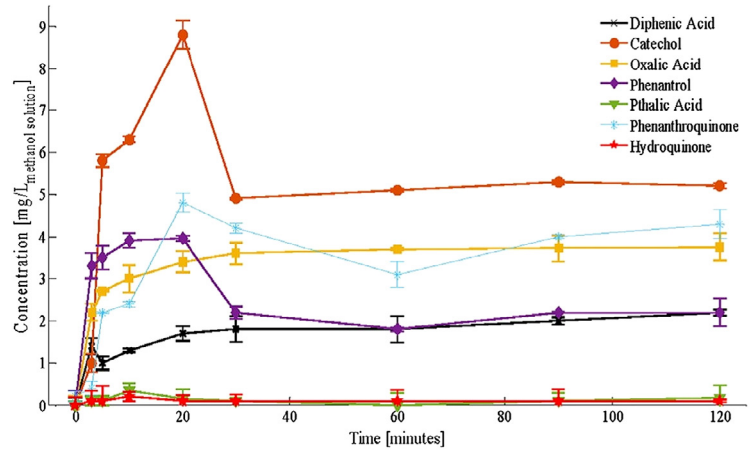

(A)

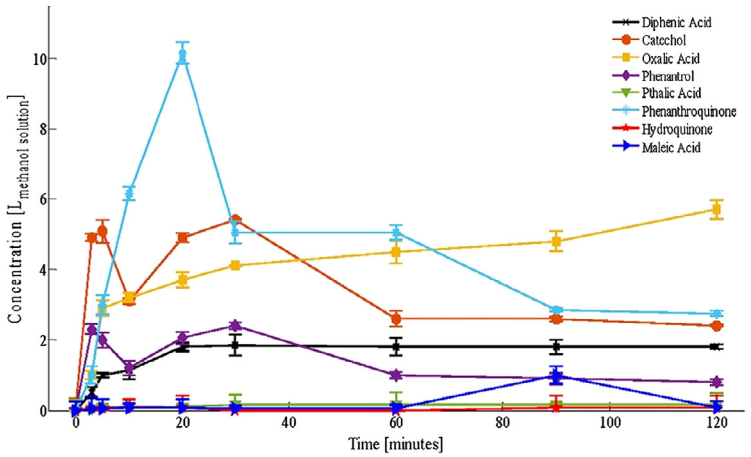

(B)

■ **FIGURE 9.19** Behavior of the identified products of the phenanthrene decomposition in the calcinated sand (A) and the calcinated agricultural soil (B). Bars depict the standard deviation.

ity to attack carbons 9 and 10 in a molecule of phenanthrene, where at the place of the double bond (>C=C<) a reaction similar to the reaction of ozone and alkenes occurs, which produces unstable primary ozonides (Stingley et al., 2004). As a result, the formed organic acids, such as phthalic, maleic, and oxalic acids, may facilitate the total mineralization by the subsequent biodegradation. Based on the results of the partial identification of the phenanthrene ozonation products and the results of the previous investigations, a possible decomposition pathway of the phenanthrene (Fig. 9.20) is proposed.

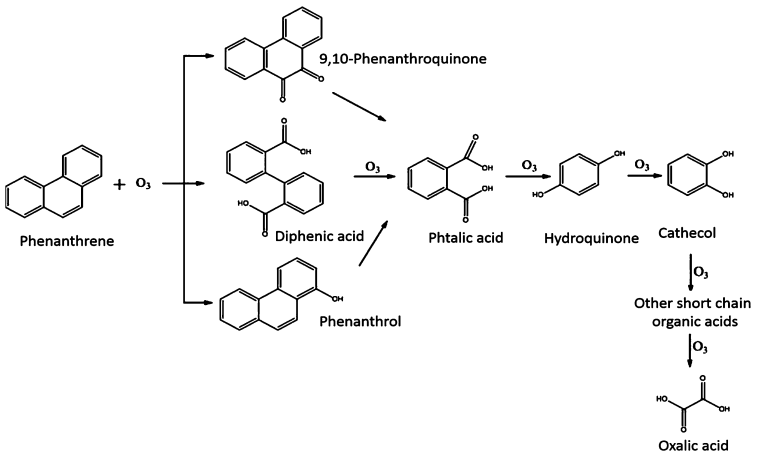

■ **FIGURE 9.20** Proposed degradation pathways of the phenanthrene in ozonation.

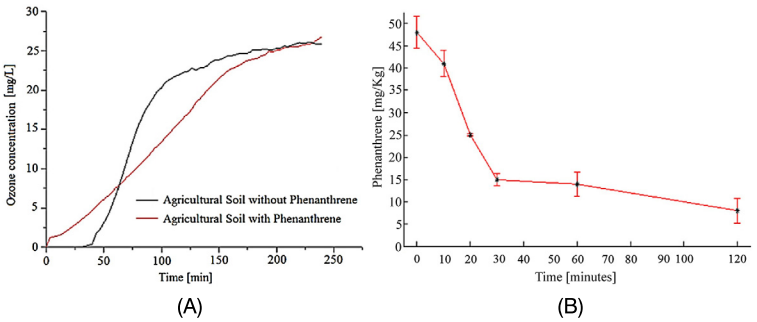

■ **FIGURE 9.21** Ozonograms of agricultural soil without and with phenanthrene. Phenanthrene decomposition in the presence of the OM.

According to the results obtained in the degradation of phenanthrene in the two soils, ozonation can be considered as an excellent alternative, especially when the treatment is proposed to be performed *in situ*.

9.8.2.6 Effect of OM in agricultural soil applied to the phenanthrene decomposition

The presence of the OM plays an important role in the physicochemical properties of soil, and their variation directly reflects in the saturation with ozone, the phenomenon of adsorption, and the ability of the removal of different contaminants. In ozonation of the natural agricultural soil with the OM, the ozone consumption was considerably increased due to the degradation of the phenanthrene, as well as the OM (Fig. 9.21).

According to Wang et al. (2012) the OM, present in soil, is also an important ozone consumer, since it is a complex mixture of organic compounds, such as dissolved organic matter (DOM), alkaline extractable organic matter (humic acid and fulvic acid), and non-extractable organic matter (Humin or HM). All these groups of organics can react with ozone with a different rate, depending on their chemical structure (Razumovskii et al., 1984). The content of OM decreases during ozonation, and its composition and characteristics also change. Indeed, the decomposition kinetics of the OM is different, compared to the phenanthrene degradation. The ozonograms were changed significantly, which confirms the effect of the OM on the ozone transfer in the soil; however, the phenanthrene decomposition remains dominant, leaving in second place the degradation of the OM. This phenomenon was confirmed by its decomposition dynamics (Fig. 9.21). The behavior of the phenanthrene decomposition with and without OM is practically the same: 70% after the first 30 min and the rest of it during the next 90 min. In this particular case, the efficiency of the phenanthrene degradation was 80%.

9.9 NUMERICAL RECONSTRUCTION BY PROJECTIONAL DNNO BASED ON EXPERIMENTAL DATA

Using the ozonation mathematical model and applying the DNNO, we can obtain the anthracene decomposition dynamics in model soil, based only on the monitoring data $c_{gas}(t)$.

9.9.1 Results of the DNNO training

Fig. 9.23 depicts the modeled and identified trajectories for the ozone concentration at the output of reactor (c_{gas} and c_{ads}) (A), for the absorbed ozone (B), for the reacting ozone (C). The evolution in time of the estimated $\hat{c}_1$ and the modeled dynamics c_1 for the anthracene concentration are given in Fig. 9.23. The DNNO parameters are shown in Table 9.6.

9.9.2 Dynamics of the anthracene decomposition (experimental data)

From the data shown in Fig. 9.22, the total anthracene decomposition was completed after 20 min of ozonation. As is seen from these data, the anthracene decomposition was carried out during 20 min of ozonation. After 15 min of ozonation the formation of byproducts was also observed. Fig. 9.22 represents also the byproducts summary concentration variation

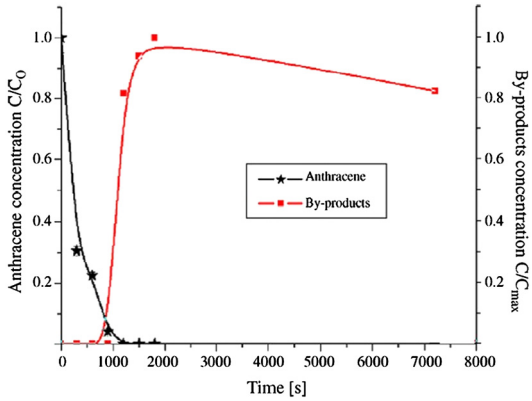

■ **FIGURE 9.22** Comparison of the experimental data (anthracene (∗, black) decomposition and byproducts (■, red) formation–decomposition) and reconstructed states by the projectional DNNO (lines).

during ozonation. From these data we can see that these compounds are accumulated from 15 to 30 min of ozonation, and start to be decomposed after 30 min. The phtalic acid formation during ozonation is also observed.

This compound is interpreted as a final product of ozonation. If we take into account that the initial anthracene concentration is high (3.24 mg g^{-1}) and the initial ozone concentration is comparatively small (16 mg L^{-1}), the contaminant decomposition degree may be treated at the adequate time by the increasing of the initial ozone concentration.

9.9.3 Anthracene decomposition reconstruction

Fig. 9.23 depicts the ozone concentration at the reactor outlet (ozonogram) for three cases:

– when the reactor is completely empty,

– when the reactor contains the model soil (sand),

– when the reactor is fulfilled with the contaminated model soil.

Notice that the upper area, bounded by each one of the ozonograms, corresponds in the first case to the ozone quantity completely filling the reactor. In the second case, this area corresponds to ozone absorbed by the soil, and, in the third case (which involves the two previous cases), it corresponds to the ozone quantity reacting with the anthracene and its byproducts. In the first two cases, the ozone output concentration attains the input concentration in a short time. Meanwhile, in the third case, the existence of anthracene and the byproducts provokes an ozone consumption, which is why the current

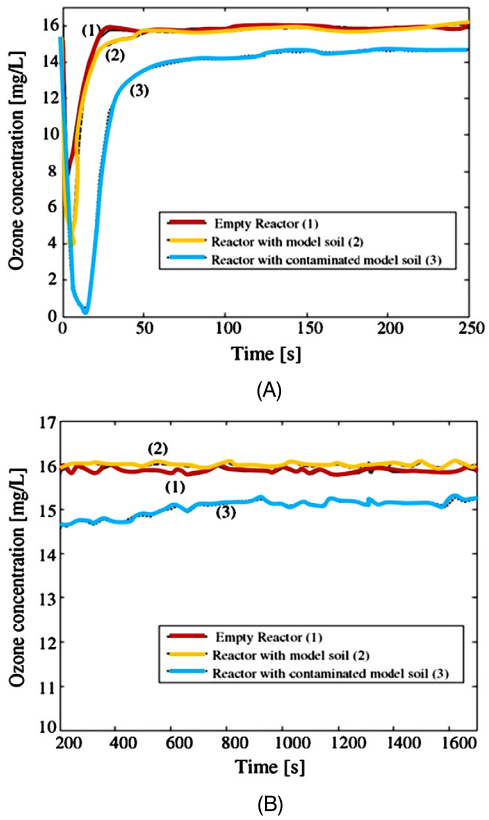

■ **FIGURE 9.23** Ozonograms of: (1) empty reactor (blank test), (2) model soil, and (3) contaminated model soil: (A) 0 to 250 s and (B) 250 to 1700 s.

ozone concentration does not return back at all to the input (initial) value (Fig. 9.23B).

Employing the monitored ozone concentration variation in the gas phase in the reactor outlet (Fig. 9.23 ozonogram (3)) and the trained DNNO, we can estimate the decomposition dynamics of the anthracene and make a comparison with the experimental data obtained by HPLC technique (Fig. 9.22). We can observe the good correspondence between the experimental data and the ones estimated by DNNO (Fig. 9.24) with the average estimation error of -0.02 ± 0.0795.

Comparing the anthracene decomposition and the corresponding ozonogram (Fig. 9.25), one can detect two different parts in the ozonogram and in the decomposition curve of anthracene:

– part I corresponds to the kinetic regime of anthracene ozonation,

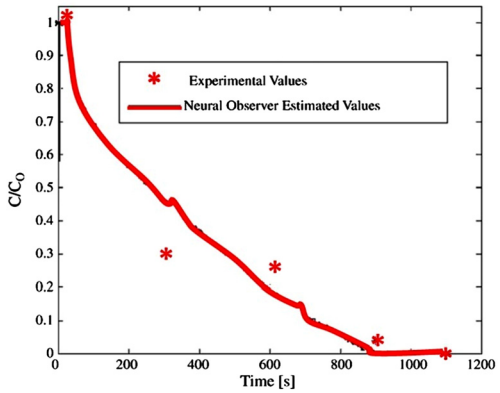

■ **FIGURE 9.24** Anthracene decomposition in ozonation and DNNO estimation.

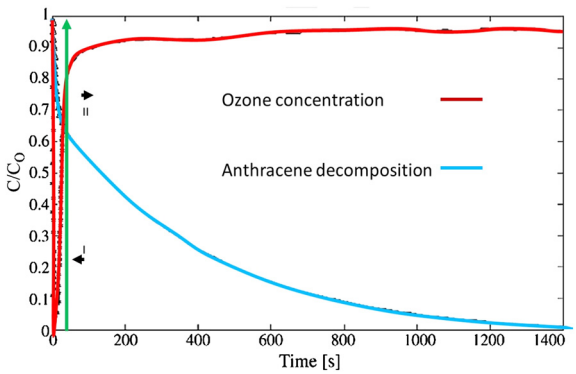

■ **FIGURE 9.25** Anthracene degradation and the corresponding ozonogram.

– part II corresponds to the diffusion regime of the reaction ozone with anthracene.

Based on these data, we may conclude that the anthracene ozonation in solid phase is carried out in two regimes: the kinetic and diffusion regimes.

9.10 CONTAMINANTS RECONSTRUCTION BY DNNO

In this section, the estimation of states in ozonation of contaminants adsorbed in solids is solved by DNNs (Chairez et al., 2006). Only asymptotic DNNO based state estimators have been developed for ozonation systems. These estimators are technically sound, but they do not show one major characteristic of ozonation systems: conventional ozonation has predefined periods of time of execution. Therefore, there is a theoretical contradiction

in these two sets of results. This was a major motivation to develop the new type of observer proposed in this section. It deals with the state estimation of ozonation systems for treatment of contaminated soil based on DNNO with discontinuous learning laws. The DNNO uses a variant of the supertwisting algorithm (Levant, 2007). A Lyapunov-based stability analysis yields the discontinuous learning laws that adjust the weights in the DNN observer. To the best of the author's knowledge, the adaptive observer with discontinuous laws to adjust the time dependent parameters has not been commonly developed in the literature. Moreover, the superior characteristics of the supertwisting algorithm are exploited within the DNN observer structure to reduce the chattering amplitude that may appear by the implementation of the class of sliding mode-based observers (Fridman and Levant, 1996).

The DNN observer (4.8)–(4.9) is modified in this study to be represented by the following set of ordinary differential equations:

$$\begin{aligned}\frac{d}{dt}\hat{x}(t) &= A\hat{x}(t) + W(t)\Gamma(\hat{x}(t), u(t)) - K_1\Phi_1(e(t)),\\ \Gamma\left(\hat{x}, u\right) &= \left[\sigma\left(V_1\left(t\right)\hat{x}(t)\right)^{\top}, \left(\phi\left(V_2\left(t\right)\hat{x}(t)\right)u(t)\right)^{\top}\right]^{\top}.\end{aligned} \tag{9.31}$$

Here $\hat{x} \in \mathbb{R}^n$ is the state vector of the DNNO representing the current estimates of the real process states, $\hat{y} = C\hat{x} \in \mathbb{R}$ is the output of the DNN. The external and internal layer weights are tuned by an online *learning* procedure (Poznyak, 2004a) given by the following differential equations:

$$\begin{aligned}\frac{d}{dt}W_j(t) &= -K_{2,j}PN_{\delta}\Phi_{2,j}(e(t))\Gamma_j^{\top}(\hat{x}(t), u(t))\\ &\quad + \frac{K_{2,j}}{2}PN_{\delta}C^{\intercal}e(t)\hat{x}(t)^{\intercal}V_j(t)D_j(t)\\ &\quad - \frac{K_{2,j}}{2}PN_{\delta}\Pi_{1,j}N_{\delta}P\tilde{W}_1\left(t\right)\Gamma_j(\hat{x}(t), u(t))\psi_j^{\intercal}\left(\hat{x}(t)\right),\\ \Gamma_1(\hat{x}(t), u(t)) &= \sigma\left(V_1\left(t\right)\hat{x}(t)\right),\\ \Gamma_2(\hat{x}(t), u(t)) &= \phi\left(V_2\left(t\right)\hat{x}(t).\right.\end{aligned} \tag{9.32}$$

The functions Φ_1 and Φ_2 are defined as follows:

$$\begin{aligned}\Phi_1(e) &= \lambda_1 \mathrm{diag}\left(|e|^{1/2}\right)\mathrm{Sign}(e) + \lambda_1 e,\\ \Phi_{2,j}(e) &= \lambda_{1,j}^2\mathrm{Sign}(e) + \lambda_{2,j}^2 e +\\ &\quad 1.5\lambda_1\lambda_{2,j}\mathrm{diag}\left(|e|^{1/2}\right)\mathrm{Sign}(\Delta),\end{aligned} \tag{9.33}$$

where the square positive definite matrices $\lambda_1 \in \mathbb{R}^{n\times n}$ and $\lambda_2 \in \mathbb{R}^{n\times n}$ are the free parameters that must be adjusted to enforce the convergence of Δ

at the origin. The functions $|e|^{1/2}$ and $S(e)$ satisfy

$$|e|^{1/2} = \left[|e_j|^{1/2}\right]_{j\in\{1,2,\ldots,n\}},$$
$$\text{Sign}(e) = \left[\text{sign}\left(e_j\right)\right]_{j\in\{1,2,\ldots,n\}}.$$

9.10.1 Numerical example

This section describes the application of the DNNO described above to estimate the states of the model (9.7). Also, this numerical evaluation may serve as a training process for the experimental evaluation presented in the next section.

9.10.1.1 DNNO simulation

The observer proposed above was simulated in the Matlab-Simulink platform. This simulation used the integration algorithm Runge–Kutta ODE 4 with an integration step of 0.001 s. The ozonation mathematical model (9.7) served as data generator to test the observer. The parameters used to simulate the model were $c^{in} = 6.2500 \cdot 10^{-4}$ mol L^{-1}, $W_{gas} = 0.1$ L s^{-1}; $V_{gas} = 0.1$ L, $Q_{ads}^{\max} = 1.0417 \cdot 10^{-5}$ mol; $Q_{r,ads}^{\max} = 0.7417 \cdot 10^{-5}$ mol, $k_r = 9600$ L mol^{-1} s^{-1}. This corresponds with the estimated reaction constant for the anthracene. The parameters used to execute the numerical simulation of the DNNO were

$$A = \text{diag}(-2.5, -2.5, -1.8, -1.9),$$
$$P = \text{diag}(0.5794, 1.4697, 2.9859, 3.2247),$$
$$Q = \text{diag}(2, 5, 7, 8), \quad R = \text{diag}(12, 15, 17, 18),$$
$$\lambda_1 = 0.01 \cdot I_{4\times4}, \ \lambda_2 = 0.07 \cdot I_{4\times4},$$
$$K_1 = 20 \cdot I_{4\times4},$$
$$K_{2,1} = 0.05 \cdot I_{4\times4}, K_{2,2} = 0.03 \cdot I_{4\times4},$$
$$K_3 = 12 \cdot I_{4\times4}, K_4 = 13 \cdot I_{4\times4}.$$

9.10.1.2 Reconstruction of the variables in the anthracene ozonation

Fig. 9.26 depicts the ozone concentration at the reactor outlet (ozonogram) measured directly by an ozone sensor. This measuring device was connected to an acquisition board and the ozone concentration was recorded. This information is highly noisy. Therefore, the observer testing needs the preliminary implementation of a first-order low pass filter. This filter is ex-

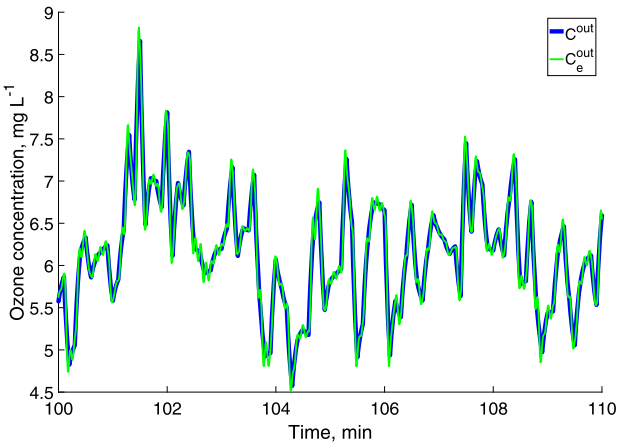

■ **FIGURE 9.26** Comparison of experimental c^{out} and its estimate obtained by the DNNO with discontinuous learning law.

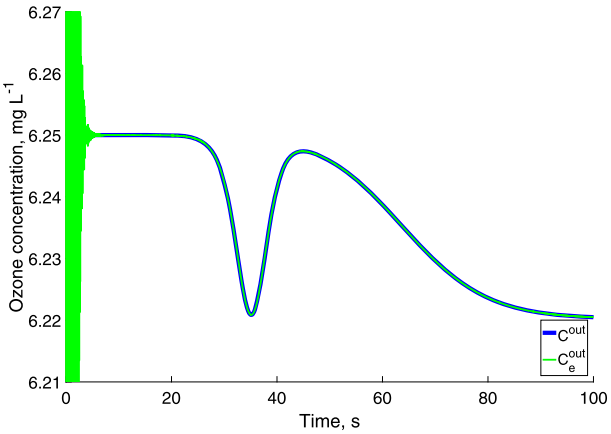

■ **FIGURE 9.27** Comparison of experimental ozone concentration at the reactor's output (c^{out}) and the reconstructed by the DNNO (c_e^{out}).

ecuted as software code in Matlab. Fig. 9.26 shows a comparison of the original and filtered signals.

The filtered information is injected into the DNNO, which is able to reconstruct the experimental variables of the anthracene ozonation. Fig. 9.27 depicts the modeled and identified trajectories for the ozone concentration at the output of reactor (c^{out} and $\hat{x}_1$). The time evolution of the modeled variable helps to represent accurately the variation observed in experiments considered for the treatment of contaminated solid phase.

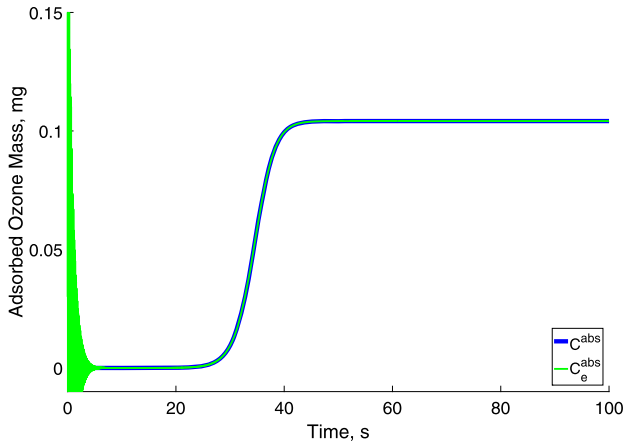

■ **FIGURE 9.28** Comparison of experimental adsorbed ozone (Q_{ads}) and the reconstructed by the DNNO ($Q_{ads,e}$).

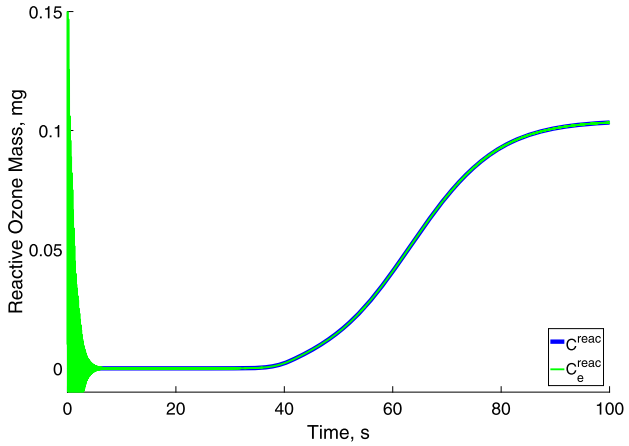

■ **FIGURE 9.29** Comparison of experimental adsorbed ozone that reacts with the contaminant ($Q_{r,ads}$) and the result reconstructed by the DNNO ($Q_{r,ads,e}$).

Fig. 9.28 shows the modeled ozone mass adsorbed on the soil surface and its corresponding identified trajectory (Q_{ads} and $\hat{x}_2$). Fig. 9.29 demonstrates the comparison of modeled and estimated ozone mass that reacts with the contaminant ($Q_{r,ads}$ and $\hat{x}_3$). These two figures confirm the representativeness of the model with respect to the ozone mass transfer in solid phase.

Employing the monitored ozone concentration variation in the gas phase of the reactor (Fig. 9.26) and the trained DNNO (the same as in the numerical simulations), the dynamics decomposition of anthracene can be estimated.

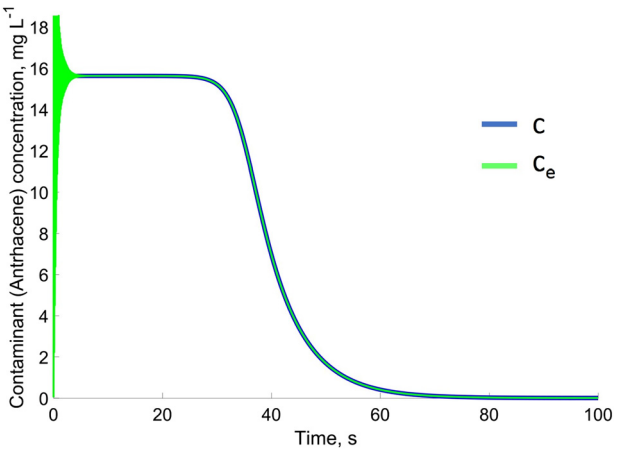

■ **FIGURE 9.30** Comparison of experimental contaminant concentration c_1 (corresponding to anthracene) and its estimate obtained by the DNN with discontinuous learning law.

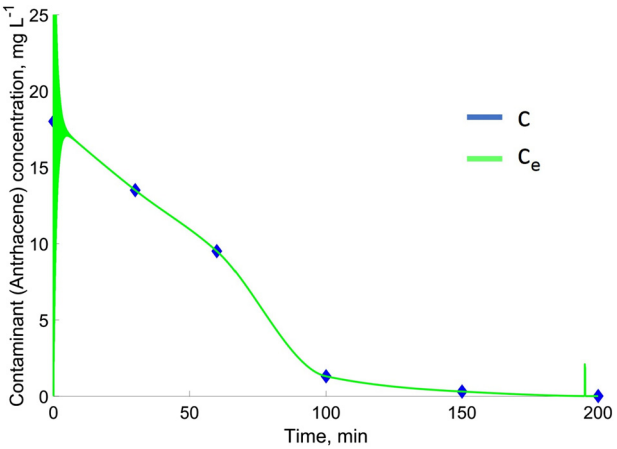

■ **FIGURE 9.31** Comparison of experimental anthracene concentration (c) and the reconstructed result by the DNNO (c_e).

The comparison of experimental data obtained by the HPLC technique and the estimated information provided by the DNNO appears in Fig. 9.30. In this case, the experiments were carried out using the soil without OM. This provides a good correspondence between the experimental data and the estimated ones by DNNO.

Fig. 9.31 depicts the variation of contaminant concentration on the soil surface and its estimated variable. These experimental data were obtained in the ozonation of soil with OM. The DNNO with discontinuous learning

laws reconstructs the variables of the anthracene ozonation. Moreover, the reconstruction used a stronger theoretical fundamental which can justify the finite-time convergence of the estimation error to a bounded region near the origin.

The reconstruction results obtained for both the soil with and without OM was successful. This claim is justified by the correspondence between the experimental data and the reconstructed trajectories.

Remark 9.2. *Notice that the trajectories produced by the DNNO shows sufficiently high amplitude oscillations during the first instants. This is a consequence of the DNNO adaptation induced by the learning procedures (training) and the discontinuous learning laws. After that, the trajectories of DNNO practically coincide with the experimental data.*

9.11 CONCLUSIONS

Based on the results described in this chapter, it is possible to conclude that:

– The decomposition of the anthracene depends on the physicochemical characteristics of the soil and the content of the water and organic matter. As the degradation efficiency of anthracene decreases, model soils have the following order: baked sand, burned soil, moist sand, and agricultural soil.

– In baked sand, the anthracene was completely decomposed during 20 min. The identified ozonation products are 9,10-anthraquinone, anthrone, and phthalic acid, with four products unidentified.

– In moist sand, the total decomposition of anthracene is achieved up to 40 min; however, during the first 20 min any changes were not observed, and after this time during the same next 20 min this compound decomposed by 100%. The last coincides with the result obtained in the baked sand, but with the different dynamics. This lag can be explained by the dissolution of ozone in water, which leads to the formation of $^{\cdot}$OH radicals. This fact is confirmed by the very similar decomposition dynamics of all intermediates (9,10-anthraquinone and phthalic acid, with five intermediates unidentified), which were practically decomposed in 30 min.

– In burned soil the anthracene degradation is carried out during 5 min, which could be attributed by the more porosity (less density) of the burned soil. The presence of 9,10-anthraquinone together with six unidentified products is confirmed.

– In an agricultural soil the degradation of anthracene proceeds more slowly than in the three previous cases. Only 30% of the anthracene degraded during 90 min of ozonation due the presence of the OM which consumed ozone.

The order of the reactivity of the OM fractions is as follows: aromatic $\Longrightarrow$ aliphatic $\Longrightarrow$ polar.

– Physicochemical properties of the sand and the soil allowed the transfer of ozone. On the other hand, the porosity of the soil and the pore volume are directly related to the phenomenon of phenanthrene adsorption, as well as to the formation of the different sizes of the crystal from 1 nm to 1000 nm. The larger crystal size of phenanthrene made it more difficult to oxidize with ozone than with the small size. This is confirmed by the time of the decomposition by 70% in the sand (30 min) and in the calcinated soil (10 min). The presence of the OM in the soil practically does not change the decomposition dynamics of the phenanthrene, which can be explained by the parallel oxidation of the contaminant and the OM.

– The proposed treatment of soils by ozone is very attractive, because it has a better efficiency in the decomposition of phenanthrene (by 80%), with respect to the ozonation time (120 min) for the sand and for the agricultural soil, in the presence of OM, after 30 min of treatment with ozone, 70%. In the case of sand, after 2 h of ozonation, just a residual contaminant concentration remained (above 0.0836 mg/g), which corresponds to the permissible limits of phenanthrene in soil (the Mexican Official Standard (NOM-138 SEMARNAT/SS-2003)).

– Two DNNOs (one with projection operator and one with discontinuous learning law) served to recuperate the variation of unmeasured contaminants in the ozonation of contaminated solid samples. Even when two different methods to adjust the weights were used, the quality of estimation, measured in terms of the mean square of the estimation error, was practically similar.

Chapter 10

Ozonation in the gaseous phase

CONTENTS

ABSTRACT

In this chapter we discuss the ozonation in the gas phase in a tubular reactor to demonstrate the possibility of decomposing of the contaminants by ozone, in the same way as in the liquid and solid phases As we shall see below, the ozonation obeys the direct mechanism as it is realized in the liquid and solid under some specific conditions. The proposed mathematical model of ozonation is based on the material balance as in the previous cases. The emission of Volatile Organic Compounds (VOCs), particularly benzene, toluene, ethylbenzene, and xylene (BTEX) or Unsaturated Organic Compounds (UOCs) is one of the most important contributions to

Ozonation and Biodegradation in Environmental Engineering
https://doi.org/10.1016/B978-0-12-812847-3.00021-4

atmospheric pollution, which leads to the decreasing of the air quality. The individual identification of the Unsaturated Hydrocarbon Pollutants (UHPs) was realized by a comparison of the FID-chromatogram and the ozonogram. A novel simple mathematical method was developed allowing one to calculate the ozonation constants for the different UHPs. A second mathematical model described the ozonation of the BTEX in the gaseous phase considering the spatial and temporal distribution of the contaminants and the ozone concentration. The model deals with the reaction between ozone and an organic volatile compound in the tubular reactor. This interaction is described by two second order Partial Differential Equations (PDEs). The identification problem is solved using the exact expression for the weights dynamics, based on the DNN properties for PDE. A numerical example is addressed considering two practical scenarios: ozone and benzene are injected into the reactor directly and, second, one assumes that benzene was added to the reactor by stripping from contaminated water.

10.1 MATHEMATICAL MODELS OF OZONATION IN THE GASEOUS PHASE

Ozonation in the gaseous phase was carried out in the tubular reactors of different lengths depending on the objective of the study (Zienkiewicz et al., 1977). Most studies regarding the tubular reactors are based on mathematical models, describing the organics dynamics inside the reactor. Some of these mathematical models are described by ordinary differential equations, assuming that organics movement inside the reactor depends only on time, but ignoring diffusion, convection, and advection processes. To describe more complex and informative processes, it is necessary to use a system of partial differential equations (PDEs).

The tubular reactor models are usually given by linear second order parabolic PDEs. Indeed, this class of PDEs appear in time dependent compounds mass transfer, such as the gas flow in the reactor. Even linear PDEs seem to be a good choice to describe the organics dynamics in the reactor. There is a degree of uncertainty regarding the parameters involved in the model, nonlinear relationships between mass transfer and chemical reaction. The uncertainties considered here can be treated using a numerical approximation to solve the PDEs. This assumption is valid when the relative size of the aforementioned uncertainties is small (compared with the numerical accuracy used for the algorithm to solve the PDE) or when the model uncertainties are not well defined.

10.2 SIMPLE MATHEMATICAL MODEL OF OZONATION IN THE GASEOUS PHASE

The material ozone balance in the tubular reactor is expressed in the following integral form:

$$\int_{s=0}^{t} W_g(s)\, c_o^g ds = \int_{s=0}^{t} W_g(s)\, c^g(s)\, ds + \int_{s=0}^{t} W_g\left(c^{in}(s)\frac{W_0}{W(s)} - c^{out}(s)\right) ds \tag{10.1}$$

where

$c_0^g = \text{const}$, $c_s^g (0 \le s \le t)$ are the ozone concentrations in the input and output of the reactor (mol L^{-1});

$W_0(t)$, $W_g(t)$ are the gas-carrier (oxygen) and the ozone–oxygen mixture flow (L s^{-1});

$W(t) = W_g(t) + W_0$;

$c^{in}(t)$, $c^{out}(t)$ are the UHP concentrations in the input and output of the reactor at time s, respectively.

The initial concentrations of ozone and the UHP are $c_0^g \frac{W_g}{W}$ and $c_0^{in}\frac{W_0}{W}$, respectively.

The kinetic equation of the ozonation considered at the contact time

$$\tau = \frac{V_r}{W}$$

(V_r is the reactor volume L), is given by Poznyak (2000)

$$\frac{d}{dt}c^{out}(t) = -kc^{out}(t)c^g(t) \tag{10.2}$$

where k is the ozonation constant (L mol^{-1} s^{-1}). The differential form of (10.1) together with (10.2) leads to the following expressions:

$$\left.\begin{aligned} c_t^{out} &= c_0^{in}\frac{W_0\left(W_g c_0^g - W_0 c_t^{in}\right)}{W\left(W_g c_0^g e^{\{W^{-1}k_t(W_g c_0^g - W_0 c_t^{in})\}} - W_0 c_t^{in}\right)}, \\ c_t^g &= \frac{\left(W_g c_0^g - W_0 c_t^{in}\right)}{W\left(1 - \frac{c_t^{in}W_0}{c_0^g W^g}e^{\{W^{-1}k_t(W_g c_0^g - W_0 c_t^{in})\}}\right)}. \end{aligned}\right\} \tag{10.3}$$

Taking into account that the value c_t^{in} can be well enough approximated by the following impulse signal:

$$c_t^{in} \cong f(t)' = \frac{1}{t'} \int_{s=\tau-t'/2}^{\tau+t'/2} c_s^{in} ds, \tag{10.4}$$

where t' is the width of the individual peak in the time units (s), and substituting (10.4) into (10.3), we finally derive

$$c_t^g \cong \frac{\left(W_g c_0^g - W_0 f(t)'\right)}{W\left(1 - \frac{f(t)' W_0}{c_0^g W_g} e^{\{W^{-1} k_t (W_g c_0^g - W_0 f(t)')\}}\right)}. \tag{10.5}$$

Using the measurable selective signal c_t^g from the ozonogram, the ozonation rate constant k can be calculated by the following formula, obtained from (10.3):

$$k = \frac{W^2}{V\left(W c_0^g - W_0 c_t^{in}\right)} \ln\left(\frac{c_t^{in} c_t^g W W_0}{W_g c_0^g \left(W c_t^g + W_0 c_t^{in} + W_g c_0^g\right)}\right). \tag{10.6}$$

First, the proposed simple mathematical model of ozonation in gaseous phase in the tubular reactor is used to optimize ozonation in the microreactor, which is used in the special analytical system on the base of the gas chromatograph with the FID and the ozone detector, which is selective for unsaturated organic compounds (Poznyak, 2000).

From the data of the US-EPA, it is seen that the air of Mexico City is a very complex mixture containing 200–300 compounds, with 16 species accounting for nearly 60%. The VOCs contain 43 paraffins, 18 olefins, and 14 aromatic compounds. The more abundant compounds are propane, n-butane, toluene, iso-pentane, n-pentane, acetylene, ethylene, m- and p-xylene, 2-methyl-pentane, n-hexane, MTBE, benzene, ethane, and b-propylene.

It is well known that unsaturated hydrocarbon pollutants (UHPs) in air can have a strong toxic effect on human health (Intergubernamental, 1990). Thus, the analysis of these UHPs in air is very important, as is the development of their elimination methods. Their identification and quantification are typically realized by gas chromatography with flame ionization detection (GC-FID). However, the sensitivity of this method is insufficient to identify small concentrations of UHP in air, because the corresponding chromatographic peaks can be disturbed or completely obliviated by other organic pollutants with similar retention times. These problems can be effectively overcome by the implementation of the selective detection of the

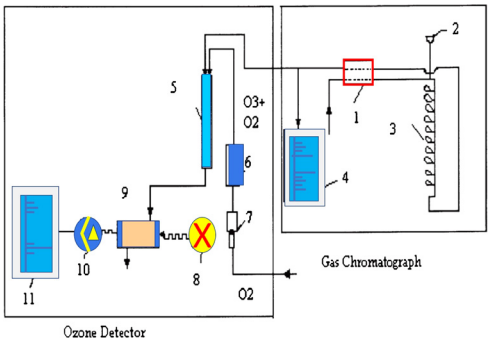

■ **FIGURE 10.1** Block scheme of the chromatograph with ozone detector: 1 = FID, 2 = sample injection, 3 = capillary column, 4 = recorder, 5 = ozone reactor, 6 = ozone generator; 7 = gas flow regulator; 8 = UV-source; 9 = measuring cell, 10 = photocell and 11 = recorder.

Unsaturated Organic Compounds (UOCs) in complex mixtures, based on their interaction with ozone in the gas phase (Poznyak, 2000; Razumovskii et al., 1984).

The proposed mathematical model is successfully used for the optimization of the reaction conditions to provide UOC detection by the capillary gas chromatography. An accelerated method is proposed for the individual identification of UH substances in air by the calculation of the ozonation rate constants of the corresponding UHPs, and by a comparison of the FID-chromatogram and the ozonogram.

The block scheme shows the principle of this chromatograph with selective detector (Fig. 10.1). First, oxygen passes into an ozone-generator and through a reduction gear. Afterwards, the ozone–oxygen mixture is delivered to the ozone reactor, where it reacts with UHP. The UV-detector, which includes the UV-source (8), the measuring cell (9) and the photocell (10), determines the ozone spent during the reaction in the gas phase and registers it in the form of an ozonogram (Fig. 10.2).

The necessary condition for the quantitative analysis is the selection of the optimal size of the micro-tubular reactor ($V_r = 1.25$ cm^3, $l_r = 10$ cm, $d_r = 2$ mm). These optimal parameters, obtained with the use of the mathematical model discussed above, provide a UHP conversion of more than 95% during the very small time of less than 1 s.

10.2.1 The air sample analysis

The proposed analytical system includes the LHM-80 gas chromatograph application with the detector of ozone. The scheme of the ozone detector is presented in Poznyak et al. (2003). The conditions of the chro-

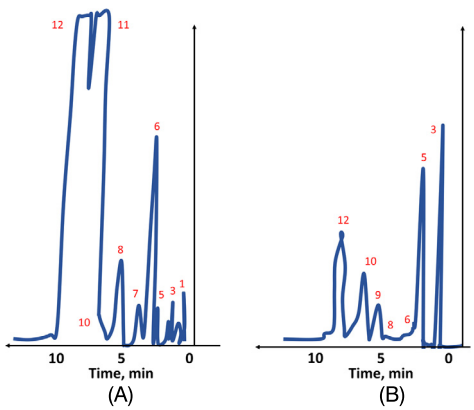

■ **FIGURE 10.2** Chromatogram (A) and ozonogram (B) of the C_2–C_5 hydrocarbon fraction. 1, 2, 4, 6–8, 11, 12 = alkanes and iso-alkanes; 3, 5, 9, 10, 12 = alkenes.

matographic analysis are: capillary metallic column (50 m, 0.25 mm with OV-17). The column temperature is 30°C; the evaporator temperature is 50°C; the ozone-detector temperature is 30°C. The gas-carrier (helium) flow is 1.5 mL min^{-1}; the ozone–oxygen mixture flow is 1.5 mL min^{-1}. The gas sample volume is 0.2 mL. The ozone concentration in the input of the reactor is $c_o^g = 2.5 \cdot 10^{-5}$ mol L^{-1}, the UHP initial concentration is $4 \cdot 10^{-6}$ mol L^{-1}.

10.2.2 Optimization of ozonation in the gaseous phase

The suggested mathematical model permits one to select the optimal reactor size and ozone–oxygen flow, which provides a UHP conversion of greater than 95% during a reaction time t of less than 1 s. The increasing of the initial reaction rate minimizes the error of the selective detector error. The corresponding expression for the initial reaction rate is as follows:

$$\frac{d}{dt}c^{in}(t) = -k\frac{c_0^g W_g}{W}\frac{c_t^{in} W_0}{W} = -k\frac{c_t^{in} c_0^g W_g W_0}{W^2}. \qquad (10.7)$$

In view of the fact that the gas-carrier flow and the initial UHP concentration cannot be varied, the unique way to increase the initial reaction rate is the variation of the ozone–oxygen flow. The effect of the gas flow ratio ($b = \frac{W_g}{W_0}$) on the initial reaction rate (S) is shown in Fig. 10.3.

This dependence is maximal for $b = 1$. If it is impossible to attain this condition, the gas flow ratio can be varied in the region $0.5 \le b \le 2.5$, which guarantees that the initial reaction rate is decreased by no more than 10%.

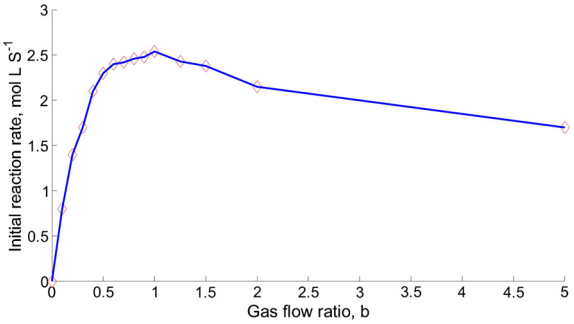

■ **FIGURE 10.3** Effect of the gas flow ratio on the initial reaction rate.

10.2.3 Calculation of the ozonation constants to identify the UHP

Applying the Internal standard (IS) with the known ozonation constant for the standard condition (k_{sta}), from Eq. (10.6) one deduces

$$k = k_{sta}\frac{\left(W_g c_0^g - W_0 c_{t,st}\right)}{\left(W c_0^g - W_0 c_t^{in}\right)}\frac{\ln\left(\dfrac{c_t^{in} c_t^g W W_0}{W_g c_0^g \left(W c_t^g + W_0 c_t^{in} - W_g c_0^g\right)}\right)}{\ln\left(\dfrac{c_{t,st}^{in} c_{t,st}^g W W_0}{W_g c_0^g \left(W c_{t,st}^g + W_0 c_{t,st}^{in} - W_g c_0^g\right)}\right)}, \tag{10.8}$$

where $c_{t,st}^{in}$ is the standard concentration in the input of the reactor, $c_{t,st}^g$ is the ozone concentration obtained from the ozonogram for the given standard (mol L^{-1}), and k_{sta} is the reaction rate constant for the standard concentration. If we take $c_t^{in} = c_{t,st}^{in}$ and realize the condition

$$W_g c_0^g \left(c_t^{in} W_0 - W_g c_0^g\right) << W_g c_0^g W c_t^g, \tag{10.9}$$

Eq. (10.8) may be simplified to

$$k = k_{st}\frac{\left(c_{t,st}^g c_0^g + 2c_t^g\right)}{\left(c_t^g c_0^g + 2c_{t,st}^g\right)}. \tag{10.10}$$

So, satisfying the condition in Eq. (10.9) and applying Eq. (10.10), we can calculate the ozonation constant for different UHPs, using ethylene as the IS. Table 10.1 presents the ozonation constants obtained for different UHPs and their comparison with the bibliographic data (Bérces and Dombi, 1980; Hanst et al., 1958; Martinez-Guerra et al., 2000; Vrbaski and Cvetanović, 1960).

Table 10.1 Ozonation constants obtained for different UHP.

UHP	k (L mol^{-1} s^{-1})[b]	k (L mol^{-1} s^{-1})[c]
Ethylene[a]	$0.5 \cdot 10^3$	$1.6 \cdot 10^3$
		$1.02 \cdot 10^3$
		$0.8 \cdot 10^3$
Propylene	$2.1 \cdot 10^3$	$7.1 \cdot 10^3$
Butene-1	$4.5 \cdot 10^3$	$6.0 \cdot 10^3$
		$3.9 \cdot 10^3$
Trans-butene-2	$9.2 \cdot 10^3$	$13 \cdot 10^3$
1,3-Butadiene	$1.35 \cdot 10^3$	$4.5 \cdot 10^3$

[a] *Internal standard.*
[b] *This work.*
[c] *Literature.*

10.3 MODELING OF OZONATION IN GASEOUS PHASE USING DNN

The spatial distribution of the mass, energy and concentrations in this type of reactor requires the usage of the models given by PDEs. The reaction between benzene and ozone in a tubular reactor is an example of such models as are discussed here. The DNN technique permits one to convert the task of the mathematical modeling of ozonation in the tubular reactor containing an uncertain (not well-defined) dynamics to a non-parametric identification problem. The coincidence between the benzene and ozone concentrations variation calculated by the suggested DNN-algorithm and those generated by a kinetic model is shown to be good enough.

The main disadvantage of the PDE-based modeling is the difficulty to find their exact solutions. The classical methods, such as the variable separation or series schemes, are not more applicable, when the mathematical description of PDEs has any uncertainty degree (Haykin, 1994), (Slotine, 1984). Neural Networks (NNs) seem to be a good tool to obtain numerical analogs of the nonlinear PDEs. Using this method, we can avoid the necessity of the description of the mathematical model.

A strategy, based on the DNN for the trajectory identification in a mathematical model, described by the PDEs, is proposed. The idea is to reproduce the concentration profiles of ozone and benzene along the reactor and during the ozonation time. The identification problem is reduced to finding an exact expression for the weights dynamics, based on the DNN properties. To investigate the qualitative behavior of the suggested methodology, the non-parametric modeling problem for a distributed parameter plant is considered (Dissanayake and Phan-Thien, 1994), (He et al., 2000), (Krstic et al., 1995). The model tackles the reaction between ozone and benzene in the gas

phase in the tubular reactor, where this interaction is represented by two second order PDEs. A numerical example is realized considering two practical scenarios: ozone and benzene are injected into the reactor in gaseous form and, second, one performs the benzene's stripping from contaminated water. The contributions to the development of a non-parametric identifier for uncertain systems are described by partial differential equations. The method produces an artificial mathematical model that is able to describe the partial differential equations dynamics. The required numerical algorithm to solve the non-parametric identifier is also developed as an additional part.

10.4 DNNO MODELING OF CHEMICAL REACTIONS IN GASEOUS PHASE

The identification problem requires the proposal of a non-parametric identifier based on DNN. The problem here may be treated within the PDEs framework. Therefore, this section introduces the DNN approximation characteristics to reconstruct the trajectory profiles for a family of parabolic PDEs. Let assume that an ozone–benzene reaction was realized in the tubular reactor, which is given by a set of second order parabolic PDEs with uncertain structure and disturbed by unknown, but bounded perturbations. In general, this reaction may be described as follows:

$$u_t = f\left(u(x,t), u_x(x,t), u_{xx}(x,t)\right). \tag{10.11}$$

Here u has n components ($u \in \mathbb{R}^n$) defined in a domain given by $x \in [0,1]$, $t \geq 0$. The variables u_t, u_x, and u_{xx} correspond to u;

$$_t = \frac{\partial u(x,t)}{\partial t}, \quad u_x = \frac{\partial u(x,t)}{\partial x}, \quad u_{xx} = \frac{\partial^2 u(x,t)}{\partial x^2}.$$

Considering the reaction conditions, the set of PDEs (10.11) is armed with the boundary (Neumann and Dirichlet) and initial conditions given by

$$u(0,t) = 0 \in \mathbb{R}^n, \; u_x(0,t) = u_0 \in \mathbb{R}^n, \; u(x,0) = c \in \mathbb{R}^n. \tag{10.12}$$

The main idea behind the application of DNN (Poznyak et al., 2001) to approximate the PDE solution is to use a class of modified finite-difference methods for uncertain nonlinear functions. Thus, it is necessary to construct an interior set (commonly called grid or mesh) that divides the domain $x \in [0,1]$ in N equidistant sections (Fig. 10.4) defined as x_i in such a way that $x_0 = 0$ and $x_N = 1$. Using this mesh-based description one can introduce

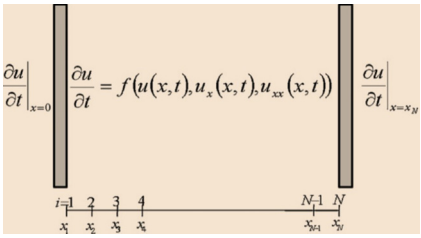

■ **FIGURE 10.4** Equidistant distribution of the space domain of the PDE.

the following definitions:

$$\left.\begin{aligned} u_i(t) = u(x_i, t), \quad u_{i,t}(t) = \frac{\partial}{\partial t} u(x,t)\|_{x=x_i}, \\ u_{i,x}(t) = \frac{\partial}{\partial x} u(x,t)\|_{x=x_i}, \quad u_{i,xx}(t) = \frac{\partial^2}{\partial x^2} u(x,t)\|_{x=x_i}. \end{aligned}\right\} \tag{10.13}$$

Now, applying the finite-difference approximation:

$$\left.\begin{aligned} u_{i,x}(t) = \Delta_x^{-1}\left(u_i(t) - u_{i-1}(t)\right), \\ u_{i,xx}(t) = \Delta_x^{-1}\left(u_{i,x}(t) - u_{i-1,x}(t)\right), \end{aligned}\right\} \tag{10.14}$$

we obtain the so-called Δ_x-approximation of the nonlinear PDE (10.11) that can be expressed as

$$\begin{aligned} \frac{d}{dt} u_i = u_{i,t} = f\left(u_i(t), \Delta_x^{-1}\left(u_i(t) - u_{i-1}(t)\right),\right. \\ \left.\Delta_x^{-1}\left(u_{i,x}(t) - u_{i-1,x}(t)\right)\right). \end{aligned} \tag{10.15}$$

In view of Eq. (10.15), it is feasible to introduce an uncertain function Φ such that

$$\frac{d}{dt} u_i = \Phi\left(u_i(t), u_{i-1}(t), u_{i-2}(t)\right). \tag{10.16}$$

Based on the neural network methodology, by simply adding and subtracting the corresponding terms, one can represent the previous equation as

$$u_t(x,t) = Au(x,t) + V_1\sigma(x) + V_2\phi(x) + V_3\gamma(x) + \tilde{f}(x,t), \tag{10.17}$$

where we have introduced A, V_1, V_2, V_3. The term $\tilde{f}(x,t)$ represents the modeling error provided by the ANN approximation, so that

$$\tilde{f}(x,t) = u_t(x,t) - Au(x,t) - V_1\sigma(x) - V_2\phi(x) + V_3\gamma(x). \tag{10.18}$$

The set of functions $\sigma(x)$, $\phi(x)$, $\gamma(x)$ are usually referred to as activation functions. Following the DNN ideas, introduced in Poznyak et al. (2001),

and applying the same representation to (10.3), we get for each $i \in (1, ..., N)$

$$\left.\begin{aligned}\frac{d}{dt}u_i(t) = A_i u_i(t) + \left[W_1^i\right]^\top \sigma(x_i) + \left[W_2^i\right]^\top \phi(x_i)u_{i-1}(t) \\ + \left[W_3^i\right]^\top \gamma(x_i)u_{i-1}(t) + \tilde{f}^i(t),\end{aligned}\right\} \tag{10.19}$$

where

$$\left.\begin{aligned}\tilde{f}_i(t) = \frac{d}{dt}u_i(t) - A_i u_i(t) - \left[W_1^i\right]^\top \sigma(x_i) - \\ \left[W_2^i\right]^\top \phi(x_i)u_{i-1}(t) - \left[W_3^i\right]^\top \gamma(x_i)u_{i-1}(t).\end{aligned}\right\} \tag{10.20}$$

10.4.1 DNN approximation for uncertain PDEs

The differential form of the neural-identifier, based on DNN, is as follows:

$$\left.\begin{aligned}\frac{d}{dt}\hat{u}_i(t) = A_i \hat{u}_i(t) + \left[W_1^i\right]^\top (t)\,\sigma(x_i) + \\ \left[W_2^i(t)\right]^\top \phi(x_i)\hat{u}_{i-1}(t) + \left[W_3^i(t)\right]^\top \gamma(x_i)\hat{u}_{i-1}(t),\end{aligned}\right\} \tag{10.21}$$

where

$A_i \in \mathbb{R}^-$ $(i \in [1, n])$, $W_1^i(t) \in \mathbb{R}^{s_1}$, $W_2^i(t) \in \mathbb{R}^{s_2}$, $W_3^i(t) \in \mathbb{R}^{s_3}$ are the parameters or weights that should be adjusted to ensure a good neural network approximation;

$\sigma(x_i)$, $\phi(x_i)$ and $\gamma(x_i)$ are three vector fields composed with standard sigmoid functions as described above;

$\hat{x}(t)$ is the state vector of the neural-identifier of the reaction parameters.

An adequate learning procedure for the neural-identifier (10.21) provides a sufficiently small upper level (in the sense of an averaged value) for the estimation error $\Delta(t) = \hat{u}(t) - u(t)$. The procedure of learning is given for the variable in the time weight matrices:

$$\left.\begin{aligned}\dot{W}_s^i(t) = -2k_s^{-1}\sum_{i=1}^{N}\left[\Delta_i^\top(t)\,P_i\psi_s(u_i(t))\right. \\ -\Delta_{x,i}^\top(t)\,S_i\nabla_x(\psi_s(u_i(t))) \\ \left.+\hat{u}_i^\top(t)\,T_i\psi_s\left(\hat{u}_i(t)\right) - 2k_s^{-1}\alpha_{i,m}\tilde{W}_s^i(t)\right].\end{aligned}\right\} \tag{10.22}$$

The matrices P_i, S_i and T_i are solutions for a set of three uncoupled Riccati equations (Krstic et al., 1995). If these solutions exist and they are positive definite, then the parameter adjustment schemes (10.22) are valid. Here it

should be noticed that the identifier (10.11) does not use any information on the PDE structure. This means that no dynamic model is necessary to develop the preidentification DNN-algorithm. In this sense, the suggested technique is treated as an identifier for model uncertainties. Considering the identifier defined in Eq. (10.21) with the nonlinear adjustments laws (10.22) to tune the weights, it is possible to ensure an upper limit for the identification process depending on the power of the noises.

10.4.2 PDE identification

The state identification (estimation) problem for the nonlinear uncertain PDEs (10.11), could be now formulated as: to analyze the quality of the DNN-identifier (10.21) supplied with the adjustment (learning) laws (10.22), providing a small enough identification error

$$\delta := \limsup_{t\to\infty} \sum_{i=0}^{N} \left\| \hat{u}_i\,(t) - u_i(t) \right\|_{P_i}^2 . \tag{10.23}$$

One additional problem, if possible, is to reduce the estimation error to its lowest possible value. The minimization of δ may be realized by the selection of the free parameters participating in the DNN-identifier.

Consider the nonlinear model (10.11), given by the system of PDEs with uncertainties (perturbations) in the states and the outputs, under the border conditions (10.12). The DNN-identifier is given by (10.21), of which the parameters are adjusted by the learning laws (10.22) with positive parameters $\alpha_{i,m}$, $(i = 0, ..., N)$, providing for all $i = 0, ..., N$ the following upper μ bound for the adaptive identification problem:

$$\delta := \limsup_{t\to\infty} \sum_{i=0}^{N} \left\{ \left\| \hat{u}_i\,(t) - u_i(t) \right\|_{P_i}^2 + \left\| \hat{u}_{i,x}\,(t) - u_{i,x}(t) \right\|_{S_i}^2 \right\} \le \mu$$

which is ensured with

$$\mu_0 = \sqrt{N} \left[\min_i \left(\alpha_{i,m} \right) \right]^{-1/2}$$

and

$$\mu = \mu_0 \sqrt{\max_i \left(\lambda_{\max} \left\{ \Lambda_{i,P}^{-1} \right\} F_{i,1} \right)} + \mu_0 \sqrt{\max_i \left(\lambda_{\max} \left\{ \Lambda_{i,S}^{-1} \right\} F_{i,2} \right)} + \mu_0 \sqrt{\max_i \left(\lambda_{\max} \left\{ \Lambda_{i,T}^{-1} \right\} F_{i,3} \right)},$$

where $\Lambda_{i,P}$, $\Lambda_{i,S}$ and $\Lambda_{i,T}$ are positive definite matrices of appropriate dimensions and $F_{i,1}$, $F_{i,2}$, and $F_{i,3}$ are positive constants that characterize the upper bounds for $\|u_i\|^2$, $\|u_{i,x}\|^2$, and $\|u_{i,t}\|^2$. This means that the reconstructed trajectories involved in the chemical benzene–ozone reaction inside the reactor tube are so close to their real values and are as small as the disturbances are affecting the state. To guarantee that the identification error be as small as possible, the DNN parameters (10.11) must be chosen carefully. There are two major ways to solve the training (Dissanayake and Phan-Thien, 1994):

1. Using the simplified reaction model of benzene with ozone. This model is applied to generation of an idealized set of best fitted weight values. This set of best fitted weights is employed in the correction of the DNN parameters and it is used in the selection of the identifier initial conditions.
2. Using a set of experimental data to produce the best fitted weights values required in the DNN-identifier. Here it is important that the training is only made once, and then the neural-identifier could be used without the information of the reaction conditions.

10.4.3 Mathematical model of reaction of benzene with ozone

Previously, it has been settled that the benzene is feeding by its liberation from contaminated water (by stripping, Fig. 1.2). The solution for the mathematical model of PDEs describing the reaction between ozone and benzene is not well defined and it is necessary to make a big effort to estimate the stoichiometric coefficient.

The more common hypothesis is to suppose that the gas flow through the reactor is uniform or laminar (Fuentes et al., 2009); the molecules are diffused at a specific rate, depending on the position inside the tubular reactor and a chemical reaction between two gases is occurring. Therefore, there are a lot of possible sources of uncertainties, when the reaction is modeled. DNN adjustment demands a large set of experimental data to obtain enough information for the second training method described above. This is the main reason to present a simplified PDEs model, describing the reaction between benzene and ozone.

Besides, an isothermal reaction is assumed to avoid the presence of an extra parabolic PDE. The mathematical description of aforementioned coupled

system is as follows:

$$\left.\begin{aligned}
\frac{\partial c_v}{\partial t} &= D_{c_v}\frac{\partial^2 c_v}{\partial x^2} + u_v\frac{\partial c_v}{\partial x} + \\
& g_{t,v}\left(Hc_l - c_v\right) - k_c^{gas} c_v^{m_1}\left(c_{O_3}^{gas}\right)^{n_1}, \\
\frac{\partial c_{O_3}^{gas}}{\partial t} &= D_{O_3}\frac{\partial^2 c_{O_3}^{gas}}{\partial x^2} + u_{O_3}\frac{\partial c_{O_3}^{gas}}{\partial x} + \\
& g_{t,O_3}\left(Hc_{l,O_3} - c_{O_3}^{gas}\right) - k_c^{gas} c_v^{m_1}\left(c_{O_3}^{gas}\right)^{n_1}, \\
\frac{dc_l}{dt} &= -g_t\left(Hc_l - c_v\right).
\end{aligned}\right\} \tag{10.24}$$

The first equation describes the decomposition dynamics of gas reacting (c_v, mol/L) with ozone in gaseous phase. This equation considers diffusion ($D_{c_v}\frac{\partial^2 c_v}{\partial x^2}$), dragging ($u_v\frac{\partial c_v}{\partial x}$) processes, the decomposition produced by reaction with ozone ($k_c^{gas} c_v^{m_1}\left(c_{O_3}^{gas}\right)^{n_1}$), and the contribution produced by contaminant stripped from water ($g_{t,v}\left(Hc_l - c_v\right)$). The second equation is similar, but in this case, it describes the ozone dynamics ($c_{O_3}^{gas}$, mol L^{-1}). The last pair of equations considers contaminant decomposition (c_l, mol/L) in water and dissolved ozone dynamics (c_{l,O_3}, mol), respectively. Parameters involved in this process are as follows:

– D_{c_v} is the contaminant's diffusion coefficient,

– D_{O_3} is the ozone's diffusion coefficient,

– u_v is the velocity of injected contaminant,

– u_{O_3} is the velocity of injected ozone,

– k_c^{gas} is the reaction rate constant of ozone and contaminant in gas phase,

– $g_{t,v}\left(Hc_l - c_v\right)$ refers to the stripping of dissolved benzene.

This model uses the Henry law constant H. Here, the ozonation is only considered in the gas phase. Using the previous model, it is possible to get numerical results for the benzene's ozonation (Fuentes et al., 2009; Poznyak et al., 2005).

10.5 NUMERICAL RESULTS

To realize an identification of good quality, the neural network parameters equation (10.12) must be chosen very carefully. The parameter A is adjusted

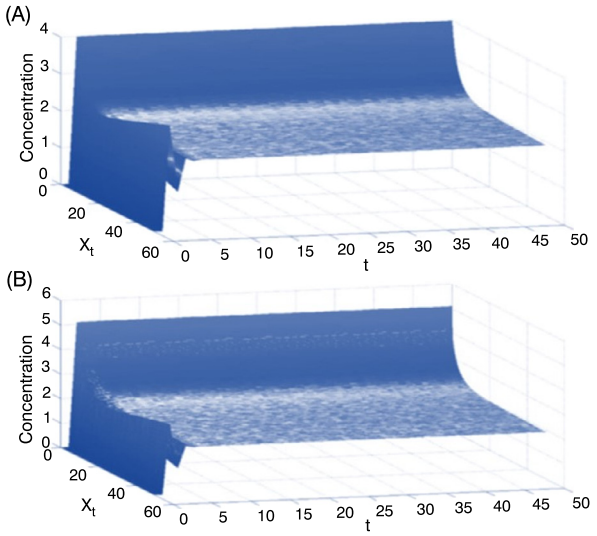

■ **FIGURE 10.5** Comparison between the benzene concentration (mol L^{-1}) simulated using the model (10.24) (A) and reconstructed by the DNN-identifier (B).

offline by a trail-and-error procedure. It is assumed that it is possible to measure the benzene concentration along the reactor in specific sites (Fig. 10.5).

This section discusses a pair of reaction conditions. In the first case, the main supposition is that benzene is feeding as gas with a constant initial concentration. The second case considers that benzene is stripped from contaminated water (200 mg/L). In the last case, a moving boundary problem is obtained, which is not a simple task in the framework of classical methods.

10.5.1 Tubular reactor feeding without the benzene stripping

A numerical reconstruction of the compounds variation for the benzene and ozone concentrations, created by the DNN, provides a close correspondence to the trajectory obtained by the mathematical model (see Figs. 10.4, 10.5 and 10.6). The proposed algorithm to adjust the identifier allows for an almost complete trajectory reconstruction in short time (all identification cases were finished before 2 s of numerical simulation), whereas the profiles of gases concentrations agreed with the data obtained from the ozonation mathematical model. The correspondence between these variations, generated by the model (10.24) and those based on DNN, is acceptable considering the identification error obtained along the whole domain in x and t (Fig. 10.7).

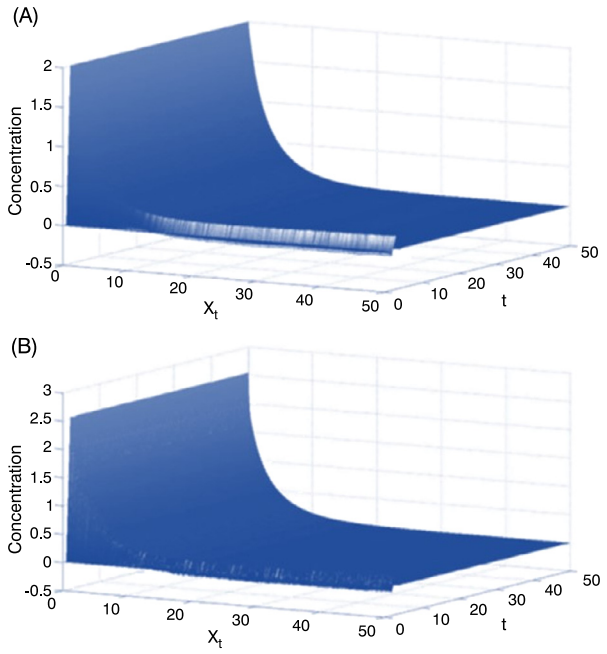

■ **FIGURE 10.6** Comparison between the ozone concentration (mol L^{-1}) simulated using the model (10.24) (A) and reconstructed by the DNN-identifier (B).

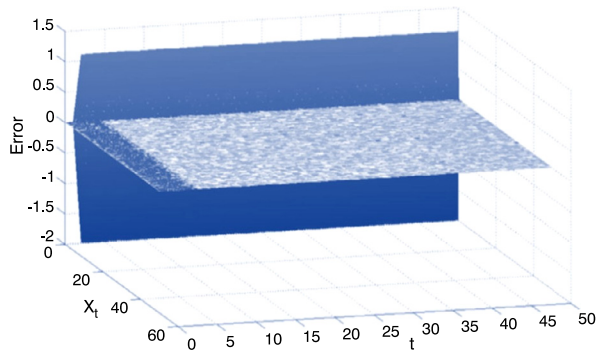

■ **FIGURE 10.7** Error between the modeled benzene concentration and its estimation obtained by the DNN-identifier.

Fig. 10.7 demonstrates the efficient estimation of the benzene concentration by the the DNN-identifier. These numerical simulations demonstrate the DNN capability to approximate the trajectories of uncertain PDEs. Moreover, the correspondence between the two figures is presented not only for the PDEs solution, but also for their derivatives with respect to t and x. Even

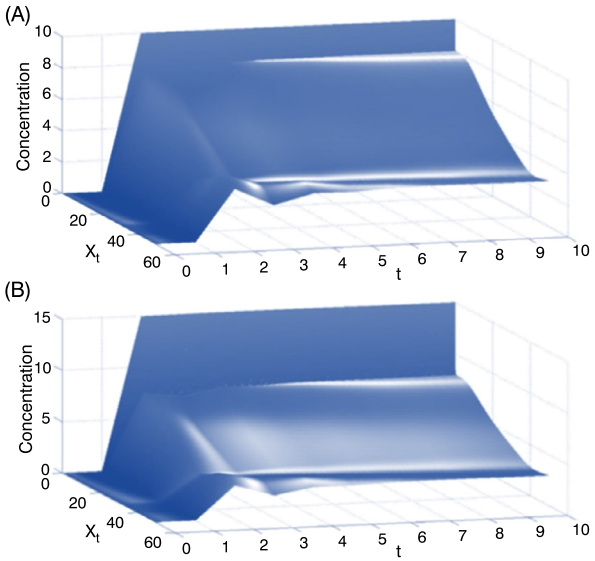

■ **FIGURE 10.8** Comparison between the benzene concentration (mol L^{-1}) simulated using the model (10.24) (A) and reconstructed by the DNN-identifier (B) in the case of benzene stripping.

when the two simulations are almost equivalent, there is a zone when x and t are close to zero where a big difference between real and estimated trajectories is observed. This dissimilarity is dependent on the learning period (approximately 2 s) that is required to adjust the DNN-identifier. This result shows the efficiency of the identification provided by the DNN-algorithm.

10.5.2 Tubular reactor feeding by the benzene stripped from contaminated water

The more complex problem discussed here arises when benzene was stripped from the contaminated water. The reconstruction of the benzene concentration was solved successfully as can be seen in Fig. 10.8. In this case, the closeness between both trajectories is again evident. The main characteristics described in the previous case remain valid for this more complex case.

Figs. 10.8 and 10.9 demonstrate the quality achieved by the proposed methodology based on the DNN-identifier. As one can understand, it is quite difficult to observe some details in the error graphics presented in 2D. However, Fig. 10.9 includes the norm of the error throughout the time. This graphic is one-dimensional and can show the convergence of the proposed method based on DNN.

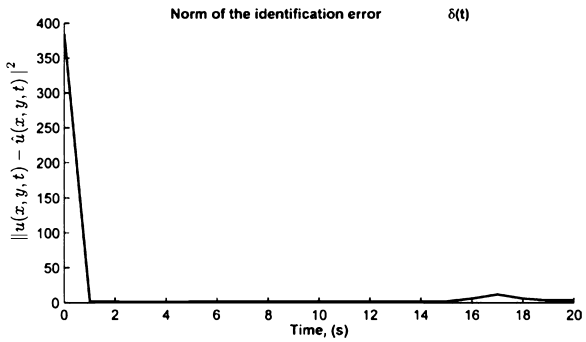

■ **FIGURE 10.9** Time evolution of the norm calculated for the identification error.

10.6 BTEX DECOMPOSITION IN GASEOUS PHASE BY OZONE

Nowadays, the air organic pollutants, coming from different sources, are becoming into the main cause of serious human illness. Particularly, benzene, toluene, ethylbenzene, and xylene (BTEX) are getting more and more attention due to the high level of their volatilization and toxicity. The decomposition of these compounds by ozone in the gaseous phase is proposed as the possible alternative treatment of these VOCs, liberated from water by their stripping. The experiments were carried out in a tubular reactor with fixed length (1.5 m) and diameter (2.5 cm) in two stages. In the first one, BTEX were ventilated by an oxygen flow and they were liberated in the gaseous phase. Second, the liberated BTEX were decomposed by ozone in the gas phase in the reactor. The ozonation efficiency was determined by the measurement of the VOCs concentration at the output and input of the tubular reactor. Also, the dynamic relationship between the degradation and the liberation of the BTEX was studied and characterized. The results obtained confirm the possibility to use ozone for the VOCs decomposition in the gaseous phase.

Air emissions, coming from a variety of industries, contain big amounts of VOCs and have been subject to increasingly stringent environmental regulations over last three decades (Park et al., 2011). For example, benzene, toluene, ethylbenzene, and xylene (BTEX) and methyl-tert-butyl-ether (MTBE) are considered as the predominant pollutants in areas near large cities or the industrial zones (Epa, 2004). Many VOCs are emitted to the environment from an extensive variety of sources including combustion products of wood and fuels, industrial production, adhesives preparation, and use of degreasing agents and aerosols (Shih and Li, 2008). The presence of VOCs in the atmosphere causes severe health problems. Even when not all VOCs pose a direct risk to human health, many of them can partici-

pate in a photochemical smog cycle, which is also a source of health danger. Besides, human exposition to VOCs occurs by ingestion (consuming contaminated water or food), inhalation or absorption through the skin, etc. (Sarafraz-Yazdi et al., 2009). The main problem with this kind of contaminants is that their degradation products are known or suspected carcinogens. Therefore, the development of the effective treatments is necessary to remove these organics (Jia et al., 2008a,b). The variety of technologies of air pollution control (APC), including adsorption, absorption, thermal oxidation, catalytic oxidation, and chemical scrubbing, are technically capable to recover or destroy VOCs from industrial emissions (Beltrán et al., 2002a). However, the applications of these conventional APC technologies generally have disadvantages in the treatment of dilute industrial VOC emissions. A number of methods was suggested to remove VOCs in the gaseous phase, such as biofiltration, incineration, stripping, scrubbing, and physical adsorption (Devinny et al., 1998; Iranpour et al., 2005; Jia et al., 2008a,b; Mascolo et al., 2008; Saravanan and Rajamohan, 2009). All these methods have advantages and disadvantages that serve for the adequate selection of the treatment method of the VOCs remediation. One common method is their adsorption in activated carbon (Shih and Li, 2008). This method has a high removal efficiency and low cost; however, it requires the disposal or a secondary treatment to decompose the adsorbed VOCs (Ambrożek, 2008).

The biological filtration (or biofiltration) is based on the biological oxidation of the VOCs using microorganisms, but this method has been widely used, when the VOC concentration in air was relatively low (0.6–2.85 mg L^{-1}). In addition, this method can also be limited by the biological reaction rate in the case of poorly biodegradable and/or toxic pollutants. Interestingly, some poorly biodegradable VOCs, such as the MTBE, require a long start-up phase (months rather than days) before significant removal (Cai et al., 2007; Iranpour et al., 2005).

Additionally, there exists the problem of the ground and residual water treatments, as well as contaminated soil with high content of VOCs, because of their stripping to atmosphere by the liberation of the VOCs from treated water or soil into the gaseous phase, using the gas inflow as carrier. Indeed, some treatments are proposed to recover the stripped contaminants with different technologies (Ambrożek, 2008; Budzianowski and Koziol, 2005; Budzianowski and Miller, 2008). This stripping may provoke air contamination, in the case of the incomplete decomposition of the VOCs in the liquid and solid phases. When the water is extracted from underground (to develop any possible on-site treatment), there is a possibility to lose VOCs (until 99.9% for low-weight volatile compounds) into the atmosphere without any previous treatment (Shah et al., 1995). These two aspects may serve

as a justification to treat the dissolved VOCs in liquid phase and to treat the stripped compounds in gaseous phase. In the latter case, chemical oxidation is an alternative method to decompose hazardous contaminants to less toxic compounds (Beltrán et al., 1999c). The treatment by ozone of the contaminated water (Beltran, 2003) and soil (Rivas, 2006; Rivas et al., 2009) was deeply studied. Nevertheless, the ozone application to groundwater remediation still shows similar problems to stripping. One possible option is the reaction between ozone and volatile organics in the gaseous phase (Razumovskii et al., 1984).

Here, the decomposition of the model BTEX, dissolved in water and then stripped by oxygen from it, and decomposed by ozone in the gaseous phase, was realized. The treatment was performed in a tubular reactor with fixed length (1.5 m) and diameter (2.5 cm), at different gas flow and reagents concentration. The BTEX decomposition efficiency in ozonation was determined by the relationship of concentrations of the compounds in the input and the output of the tubular reactor as measured using liquid chromatography (HPLC) (Bin and Roustan, 2000).

10.6.1 Ozonation of the BTEX

The ozonation was conducted in two stages. In the first stage, the oxygen was injected into an aqueous solution (250 mL) that contained the dissolved BTEX. This injection was performed using the diffuser at the reactor bottom (500 mL). The oxygen flow provokes the BTEX stripping from the aqueous solution in the reactor. The initial concentration of the VOCs is 200 mg L^{-1} for benzene, toluene, and xylene, and 150 mg L^{-1} for ethylbenzene. The oxygen flow used to the stripping was 0.5 and 0.2 L min^{-1}. The liberated BTEX were adsorbed on the granular activated carbon (GAC) (1.0 g), that was placed in a small glass tube ($10.0 \cdot 1.0$ cm). To study BTEX stripping, the water samples were analyzed after different times (2, 5, 10, 15, 20, 30, until 60 min).

At the second stage, the stripped BTEX passed through a tubular reactor, where the BTEX ozonation was carried out with the different ozone concentrations (30 and 15 mg L^{-1}) and the gas flow (0.2 and 0.5 L min^{-1}). The residual ozone, byproducts, and final products of ozonation were adsorbed in GAC. All experiments were evaluated at ambient temperature. Fig. 1.2 shows the experimental set-up (Álvarez et al., 2008).

10.6.2 Analytical methods

The intermediates and final products, obtained in ozonation in the gaseous phase, were adsorbed on the GAC. The samples of the GAC were analyzed

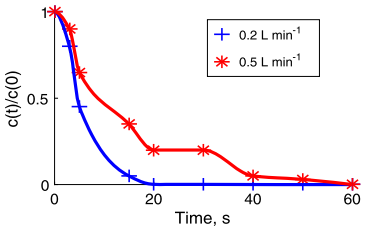

■ **FIGURE 10.10** Stripping of benzene at a gas flow of 0.2 and 0.5 L min^{-1}.

using the Soxlhet method (Wang et al., 2012): the adsorbed compounds were extracted in methanol (30 mL per 0.5 g of the GAC). The extracts were analyzed by the high performance liquid chromatography (HPCL). The HPLC analysis were performed by a liquid chromatograph Perkin-Elmer series 40 with the UV-Vis detector and a chromatographic column Nova Pack C-18, 250 × 4.6 mm, with the mobile phase of water: acetonitrile (30.0:70.0) with a flow of 0.5 mL min^{-1}. The injected sample volume was 30 μL. The used wavelengths were 264 nm for benzene, 250 nm for toluene, 262 nm for ethylbenzene, and 249 nm for xylene. For the simple organic acids, the selected wavelength was 211 nm. The mobile phase, in the last case, was not modified.

The results are presented in two parts: the first one describes the stripping of the BTEX and their adsorption onto the GAC; the second one the evaluation of the BTEX decomposition degree in ozonation in the gaseous phase at different operating conditions.

10.6.3 BTEX stripping and adsorption on GAC

Fig. 10.10 depicts the BTEX stripping, while its adsorption is presented in Fig. 10.11 at two gas flow. The adsorption behavior is similar for toluene, ethylbenzene. and xylene. For the oxygen flow of 0.5 L min^{-1}, toluene and ethylbenzene are stripped before 10 min and benzene and xylene during 15 and 30 min, respectively (Figs. 10.12–10.14). The decrease of the oxygen flow to 0.2 L min^{-1} increases the stripping time for all compounds to 20–40 min. The liberation rate of the VOC depends on the properties of the organics, the vapor pressures, and the water solubility, as well as on the operating conditions.

The mass-transfer between the two phases (liquid and gaseous) may be characterized by the Henry coefficient. To characterize the dependence of the BTEX stripping on their properties, we calculated the constants of their liberalization at the two gas flows (Table 10.2).

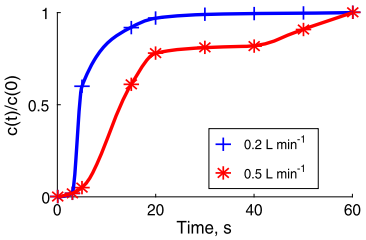

■ **FIGURE 10.11** Absorption of benzene at a gas flow of 0.2 and 0.5 L min^{-1}.

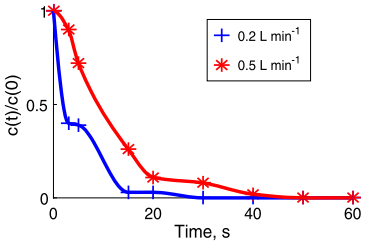

■ **FIGURE 10.12** Stripping of toluene at a gas flow of 0.2 and 0.5 L min^{-1}.

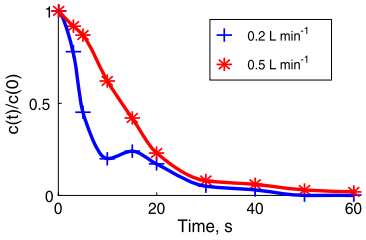

■ **FIGURE 10.13** Stripping of xylene at a gas flow of 0.2 and 0.5 L min^{-1}.

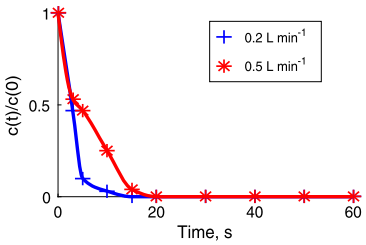

■ **FIGURE 10.14** Stripping of ethylbenzene at a gas flow of 0.2 and 0.5 L min^{-1}.

As can be observed, the calculated values of the stripping constants are not correlated with the values of the Henry coefficient and the vapor pressure. We may conclude that the Henry coefficient is a better predictor of the strip-

Table 10.2 Henry coefficient, liberated constants of BTEX at two different flows (k, min^{-1}).

Compound	Vapor pressure kPa at 20°C	Henry's coefficient $\frac{atm\ m^3}{mol}$	k [min^{-1}]	
			0.2 L min^{-1}	0.5 L min^{-1}
Benzene	10.0	$5.49 \cdot 10^{-3}$	$6.2 \cdot 10^{-2}$	$8.7 \cdot 10^{-2}$
Toluene	2.9	$6.44 \cdot 10^{-3}$	$5.1 \cdot 10^{-2}$	$8.8 \cdot 10^{-2}$
Ethybenzene	0.9	$8.43 \cdot 10^{-3}$	$5.7 \cdot 10^{-2}$	$21.1 \cdot 10^{-2}$
Xylene	0.8		$3.9 \cdot 10^{-2}$	$5.4 \cdot 10^{-2}$

ping behavior. The last statement coincides with the observations of other researchers (Deshusses and Johnson, 2000). In addition, we notice that the stripping time of VOCs is the same as the adsorption time.

10.6.3.1 Decomposition of BTEX

The proposed experimental scheme leads to the dilution by oxygen of the ozone and the contaminant concentrations in the tubular reactor. According to the results obtained, the BTEX degradation starts just after their contact with ozone in the input of the reactor; however, with different reaction rates or ozonation constants (Fig. 10.15A–D).

It can be seen that the xylene was decomposed faster (during < 2 min). On the other hand, benzene was not decomposed completely at a gas flow of 0.5 L min^{-1} and the initial ozone concentration of 15 mg L^{-1}; however, it was decomposed, with a gas flow of 0.2 L min^{-1} during 15 and 30 min, at the ozone concentrations of 35 and 15 mg L^{-1}, respectively (Fig. 10.15A).

In the case of toluene ozonation at a gas flow of 0.2 L min^{-1} and an ozone concentration of 35 mg L^{-1}, it was decomposed during 10 min with an efficiency of 100% (Fig. 10.15B). The ethylbenzene at a gas flow of 0.5 L min^{-1} and the ozone concentration of 15 mg L^{-1} was decomposed only 30%. Nevertheless, if the ozone concentration increased up to 35 mg L^{-1} and the gas flow decreased to 0.2 L min^{-1}, it was completely degraded during 10 min. This is very important, considering that the ethylbenzene is stripped faster, during 10 and 15 min, compared with other VOCs (Fig. 10.15C).

The ratio c_t/c_0 (Figs. 10.15A–D), is different for each compound. This ratio was obtained using the same extraction method as presented in the previous section. This relationship is valid considering that the two concentrations are measured on the GAC. The initial concentration is obtained by only stripping with the oxygen flow. Ozone is effective to decompose xylene. If the ozone concentration is low (15 mg L^{-1}) and when the gas flow is higher

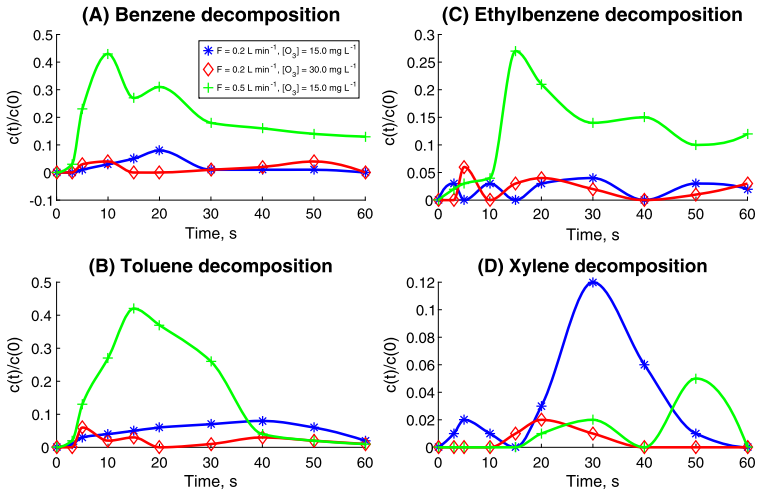

■ **FIGURE 10.15** Decomposition dynamics of benzene (A), toluene (B), ethylbenzene (C), and xylene (D).

(0.5 L min^{-1}), the xylene is completely decomposed. This result coincides with others dealing with xylene ozonation (Kasprzyk-Hordern et al., 2005).

The concentrations of BTEX, adsorbed on the GAC, are obtained by the extraction, described above. Even when the BTEX concentration in the gas phase was reduced to zero, on the GAC surface still the traces persist of these compounds (as shown in Fig. 10.15), because they cannot be eliminated completelly by simple ozonation.

10.6.3.2 Identification of intermediates and final products of the BTEX ozonation

To identify intermediates and final products of the BTEX decomposition in ozonation, the HPLC analysis was applied. Table 10.3 presents all the compounds, obtained in the BTEX ozonation with their concentration in the extract with methanol and in the gaseous phase in the tubular reactor.

10.7 CONCLUSIONS

It may be concluded that intermediates and final products are presented in the gaseous phase as the traces (less than 2.0 mg L^{-1}), except formic acid in the benzene decomposition, oxalic acid in the toluene decomposition, benzoic acid in the ethylbenzene decomposition, and malonic acid in the xylene decomposition with concentrations in the range of 3.0–15.0 mg L^{-1}. Comparing all experimental conditions, the best results in the efficiency of the degradation of the BTEX and intermediaries were obtained at the flow of

Table 10.3 Intermediates and final products obtained in the BTEX ozonation at the different operating conditions (extracted in methanol from the GAC sample, as well as at the reactor's head-space): B = Benzene, T = toluene, E = ethylbenzene, X = xylene, BA = benzoic acid, OA = oxalic acid, FA = formic acid, FuA = fumaric acid, MA = malonic acid.

BTEX	Products	Concentration $[O_3]$ mg L^{-1}	In methanol	Gaseous phase
	Flow	0.5 L min^{-1}	0.2 L min^{-1}	0.2 L min^{-1}
		15	15	35
B	BA	3.7(0.3)	1.0(0.1)	1.6(0.1)
	OA	4.0(0.3)	6.4(0.5)	9.0(0.7)
	FA	146.0(11.0)	0.3(0.03)	36.0(3.0)
T	B	17.0(1.4)	ND	5.0(0.4)
	BA	1.0(0.1)	ND	6.4(0.5)
	FuA	ND	0.4(0.03)	ND
	MA	ND	28.0(2.0)	ND
	OA	97.0(8.0)	12.0(0.9)	ND
	FA	ND	1.9(0.2)	ND
E	BA	119.0(9.0)	35.0(3.0)	3.0(0.25)
	MA	8.0(0.7)	3.0(0.3)	ND
X	B	ND	0.5(0.04)	ND
	MA	188.0(15.0)	44.0(3.5)	19.0(1.5)
	OA	0.5(0.04)	4.0(0.3)	ND
	FA	2.5(0.2)	1.3(0.1)	ND

0.2 L min^{-1} and the ozone concentration of 35 mg L^{-1}, which corresponds to the maximal contact time of the BTEX and ozone. However, in the case of the intermediate decomposition, depending on their reactivity with ozone, the optimal experimental conditions can be varied in time. On the other hand, the optimal conditions can be supported automatically, using the DNN and the corresponding algorithms of the control that have been discussed in Chapter 8.

Part 4

Combination of Ozonation and Biodegradation

Chapter 11

Biodegradation

CONTENTS

ABSTRACT

This chapter describes the general characteristics of biodegradation systems. The specific details of aerobic and anaerobic cultures are explained and the technical details of bioreactor operation are also discussed. The modeling describing the dynamics of microbial cultures is developed. The concept of variable reconstruction based on state observers with discontinuous correction terms is analyzed. The observer is based on the application of the supertwisting algorithm structured in a step-by-step structure. A biodegradation system is considered to test the estimation capacities of the observer. The numerical results confirmed the observer workability to estimate the non-measurable states accurately enough.

Ozonation and Biodegradation in Environmental Engineering
https://doi.org/10.1016/B978-0-12-812847-3.00023-8

11.1 INTRODUCTION

Biodegradation is the decay or breakdown of materials that occurs, when microorganisms use an organic substance as a source of carbon and energy. For example, the activated sludges are used to treat sewage flows in a waste water treatment plant to biotransform the organic compounds up to get their complete mineralization. The recalcitrant materials, which are hard to break down, may enter the environment as contaminants. This is a major motivation to use biodegradation.

The microorganisms need energy plus carbon, nitrogen, oxygen, phosphorus, sulfur, calcium, magnesium, and several metals to grow and reproduce. The oxidation of organic substances to carbon dioxide and water is an exothermic (heat-releasing) process. For each mole of oxygen, used as electron acceptor (oxidant), about 104 kilocalories (435 kJ) of energy is potentially available. All organisms make use of some part of this energy. The rest is lost as heat. This can be observed in composting, when the compost becomes hot. Biodegradation can occur under aerobic conditions, where oxygen is the electron acceptor, and under anaerobic conditions, where nitrate, sulfate, or another compound is the electron acceptor.

Bacteria and fungi, including yeasts and molds, are the microorganisms responsible for biodegradation. In the environment, the biodegradation can be used to treat water and soil and also to preserve food, wood and agricultural products.

11.2 MICROBIAL ACTIVITY IN DEGRADATION OF CONTAMINANTS

The presence of microorganisms with the appropriate metabolic capabilities is the most important requirement for oil spill bioremediation according to Venosa et al. (2002). The microbial consortia, which are exposed to hydrocarbons, get adapted, exhibiting selective enrichment and genetic changes (Atlas, 1984; Leahy and Colwell, 1990). The adapted microbial consortia may react with the contaminants within hours and exhibit higher biodegradation rates than the non-adapted consortia (Leahy and Colwell, 1990). So, the ability to isolate high numbers of certain oils, degrading microorganisms from an environment is taken as the evidence that those microorganisms are the most active in the environment and can be used in the bioremediation of contaminated sites. Since crude oil is made of a mixture of compounds, and since individual microorganisms have only specialized metabolic activity, biodegradation of petroleum hydrocarbon requires the application of microbial consortia (Esmaeil et al., 2009). The activity of the consortia depends

on the availability of nutrients and the optimal presence of other factors that support their biological functions.

These factors are as follows.

- *Contaminant concentrations*: they have a direct influence on the microbial activity. If the concentrations are very high, the contaminants may have toxic effects on the bacteria. Contrarily, a low contaminant concentration may prevent the induction of bacterial degradation enzymes.
- *Contaminant bioavailability*: it depends on the degree to which they sorb to solids or are sequestered by molecules in contaminated media, or are diffused in macropores of soil or sediment, and other factors (such as the presence of other contaminants) are present in non-aqueous phase liquid (NAPL) form. Bioavailability for microbial reactions is lower for contaminants that are more strongly adsorbed to solids, enclosed in matrices of molecules in contaminated media, more widely diffused in macropores of soil and sediments, or are present in NAPL form.
- *Site characteristics*: they have a significant impact on the effectiveness of any bioremediation strategy. The environmental conditions are important for bioremediation applications, including an optimal pH range of 6–8, temperature, water content, nutrient availability, and redox potential.
- *Redox potential and oxygen content*: they typify oxidizing or reducing conditions. The redox potential is influenced by the presence of electron acceptors, such as nitrate, manganese oxides, iron oxides, and sulfate.
- *Nutrients*: they are needed for microbial cell growth and division. Suitable amounts of trace nutrients for microbial growth are usually present, but nutrients can be added in a usable form or via an organic substrate amendment (Piehler et al., 1999), which also serves as an electron donor, to stimulate bioremediation.
- *Moisture content*: microbial growth requires an optimum presence of water in the environmental matrix. For optimal growth and proliferation, the microorganisms require 12 to 25% of moisture (Mukherjee and Das, 2005).
- *Temperature*: it directly affects the rate of microbial metabolism and consequently microbial activity in the environment. The biodegradation rate increases with increasing temperature and slows down with decreasing temperature.

11.3 AEROBIC AND ANAEROBIC BIODEGRADATION SYSTEMS

Aerobic biodegradation is the breakdown of organic contaminants by microorganisms, when oxygen is present. More specifically, it refers to the occurrence of oxygen or microorganisms can live only in the presence of oxygen; therefore, the chemistry of the system, environment, or an organism is characterized by oxidative conditions. Many organic contaminants are rapidly degraded under aerobic conditions by aerobic bacteria, called aerobes.

Aerobic bacteria (aerobes) have an oxygen-based metabolism. Aerobes, referred to by their cellular respiration, use oxygen to oxidize substrates (for example, sugars and fats) in order to obtain energy.

Before the cellular respiration begins, the glucose molecules are broken down into two smaller molecules. This happens in the cytoplasm of the aerobes. Then these smaller molecules enter a mitochondrion, where aerobic respiration takes place. Oxygen is used in the chemical reactions that break down the small molecules into water and carbon dioxide. The reactions also release energy. An aerobic process, unlike anaerobic digestion, does not produce pungent gases. The aerobic process results in a more complete digestion of waste solids, reducing the buildup by more than 50% in most cases. The aerobic process also improves the environment of the workers and the animals and helps to keep pathogens in check.

Anaerobic digestion occurs when the anaerobic microbes are dominant over the aerobic microbes. Biodegradable waste in landfill degrades in the absence of oxygen through the process of anaerobic digestion. Paper and other materials, which normally degrade in a few years, degrade more slowly over longer periods of time.

Biogas contains methane, which has approximately 21 times the global warming potential of carbon dioxide. In a cradle this biogas is collected and used for eco-friendly power generation.

Anaerobic digestion is a series of processes, where microorganisms break down biodegradable material in the absence of oxygen. It is widely used to treat waste water sludge and biodegradable waste because it provides volume and mass reduction of the input material.

As part of an integrated waste management system, the anaerobic digestion reduces the emission of landfill gas into the atmosphere. Anaerobic digestion is a renewable energy source because the process produces methane and carbon dioxide rich biogas suitable for energy production, helping replace fossil fuels. Also, nutrient-rich solids, left after digestion, can be used

as fertilizer. The digestion process begins with bacterial hydrolysis of the input materials in order to break down insoluble organic polymers, such as carbohydrates, and make them available for other bacteria. Then acetogen converts the sugars and amino-acids into carbon dioxide, hydrogen, ammonia, and organic acid. After that acetogenic bacteria convert these resulting organic acids into acetic acid, along with additional ammonia, hydrogen, and carbon dioxide. Finally, methanogens are able to convert these products to methane and carbon dioxide.

There are a number of bacteria involved in the anaerobic digestion, including the acetic acid-forming bacteria and the methane-forming bacteria. These bacteria feed upon the initial feedstock, which undergoes a number of different processes converting it to intermediate molecules, including sugars, hydrogen, and acetic acid, before the final conversion to biogas.

There are five key biological and chemical stages of anaerobic digestion:

- hydrolysis,
- acidogenesis,
- acetogenesis,
- methanogenesis,
- hydrolysis.

In the most cases, the biomass is made up of large organic polymers. In order to access the energy potential of the material for the bacteria in anaerobic digesters, these chains must first be broken down into their smaller constituent parts. These constituent parts or monomers, such as sugars, are readily available by other bacteria. The process of breaking these chains and dissolving the smaller molecules into solution is called *hydrolysis*. Therefore, the hydrolysis of these high molecular weight polymeric components constitutes the necessary first step in anaerobic digestion.

Through hydrolysis complex organic molecules are broken down into simple sugars, amino acids, and fatty acids. Acetate and hydrogen, produced in the first stages, can be used directly by methanogens. Other molecules, such as *volatile fatty acids* (VFAs) with a chain length greater than acetate, must first be catabolized into compounds that can be directly utilized by methanogens.

Acidogenesis is a biological process, in which the further breakdown of the remaining components by acidogenic (fermentative) bacteria takes place. Here VFAs are created along with ammonia, carbon dioxide, and hydrogen sulfide, and other byproducts. The process of acidogenesis is similar to the way that milk sours.

Acetogenesis is the third stage anaerobic digestion. Here simple molecules created through the acidogenesis phase are further digested by acetogens to produce largely acetic acid, carbon dioxide, and hydrogen.

Methanogenesis, as a biological process, constitutes the final stage of the anaerobic digestion. Here methanogens utilize the intermediate products of the preceding stages and convert them into methane, carbon dioxide, and water. They are the main components making up the majority of the biogas emitted from the system.

11.4 METABOLIC MECHANISMS IN BIODEGRADATION

Microbial community structure and diversity likely defines the metabolic potential of contaminant-degrading communities (Head et al., 2006). Thus, it is critical to understand the relationships between microbial community structure and the metabolic activity of organics-degrading microbial consortia. Remarkable progress has been made to determine the response of specific microbial taxa to the presence of diverse contaminants in environments. Nowadays, the majority of studies of the organic-degrading microorganisms have been conducted in laboratory cultures.

Biodegradation showed to be successful in naturally remediating contamination, associated with several spills that impacted natural environments (Atlas, 1984; Head et al., 2006). There are several studies evaluating the environmental conditions (oxygen availability, nutrient levels, organics chemistry), controlling biodegradation in different ecosystems with experimental and modeling approaches. There is a particular interest in developing biodegradation studies, when the contaminants are hydrocarbons. Under aerobic conditions, Shing-Lee et al. (2014) studied the kinetic parameters of crude oil-degrading microbial communities in response to nutrient and oil loading in beach sand microcosms. High nutrient levels are shown to select for members of the hydrocarbonoclastic genus, *Alcanivorax*, while selecting against aromatic-degrading *Cycloclasticus* sp. (Bose et al., 2013) quantifies oxidation rates of short chain alkanes under sulfate-reducing conditions and explores the use of stable C isotopes to trace biodegradation activity in microcosms of cold seep sediments. Capping and *in situ* aeration are shown to effectively remediate and detoxify buried oil in anaerobic marine sediments by Genovese et al. (2014). Torlapati and Boufadel (2014) present a numerical model that employs genetic algorithms to predict biodegradation kinetics for oil entrapped in sediments.

11.5 BIOREACTORS USED IN BIODEGRADATION

Fermentation technology could be defined simply as the study of the fermentation, techniques and its application. Fermentation should not be seen merely as a process that is entirely focused on the happenings occurring in the fermenter alone! There are many activities that occur upstream leading to the reactions taking place within the bioreactor or fermenter, despite the fermenter being regarded as the heart of the fermentation.

Fermentation technology is the whole field of study which involves controlling and optimizing the fermentation right up from upstream activities, mid stream and downstream or postfermentation activities. The study of fermentation technology requires essential inputs from various disciplines, such as biochemistry, microbiology, genetics, chemical and bioprocess engineering, and even a scatter of mathematics and physics.

The function of the fermenter or bioreactor is to provide a suitable environment, where an organism can efficiently produce a target product. The target product might be cell biomass, metabolite, and a bioconversion product. It must be so designed that it will allow for supporting the growth of the microorganisms.

The choice of microorganisms to be used in the fermentation studies is diverse. Bacteria, unicellular fungi, virus, and algal cells have been cultivated in fermenters. Now more and more attempts are tried to cultivate single plant and animal cells in fermenters. It is very important for us to know the physical and physiological characteristics of the type of cells which we use in the fermentation. The fermentation vessel must fulfill certain requirements, some of them are: the agitation speed, the aeration rate, the heating intensity or cooling rate, the nutrient feeding rate, and the acid or base valve. The precise environmental control is of considerable interest in fermentations, since oscillations may lower the system efficiency, increase the plasmid instability, and produce undesirable end products.

Bioreactors are commonly cylindrical vessels with hemispherical top and/or bottom, ranging in size from some liter to cube meters, and they are often made of stainless steel and glass. The sizes of the bioreactor can vary over several orders of magnitudes. The microbial cell (few mm^3), shake flask (100–1000 mL), laboratory fermenter (1–50 L), pilot scale (0.3–10 m^3) to plant scale reactors (2–500 m^3) are examples of bioreactors.

The design and mode of operation of a fermenter mainly depends on the production organism, the optimal operating condition, required for target product formation, product value, and scale of production. The design also takes into consideration the capital investment and running cost:

- Large volume and low value products like alcoholic beverages need a simple fermenter and do not need aseptic conditions.
- High value and low volume products require a more elaborate system of operation and aseptic conditions.

The key differences between chemical reactors and bioreactors are the selectivity and the rate. In bioreactors, we have a higher selectivity, that is, the measure of the system's capability to produce the preferred product (over other outcomes) is of primary importance. In fact, selectivity is especially important in the production of relatively complex molecules, such as antibiotics, steroids, vitamins, proteins, and certain sugars and organic acids. Frequently, the activity and desired selectivity was guaranteed in a substantially smaller range of conditions than present in conventional chemical reactors. Further, the deactivation of the biomass often provokes more severe consequences.

11.6 FUTURE TRENDS IN BIOREMEDIATION

The use of certain genetically engineered microorganisms to use their ability to utilize specific contaminants, such as hydrocarbons and pesticides, is gaining grounds. This technique in early times was mentioned in the late 1980s and early 1990s. The ability to engineer microorganisms to improve degradative properties is based on the possibility to explore genetic diversity and metabolic versatility of microorganisms (Fulekar et al., 2009).

The blueprint, necessary for gene encoding for biodegradative enzymes, is present in chromosomal and extrachromosomal DNA of such microbes. Recombinant DNA techniques explore the ability of an organism to metabolize a xenobiotic by detecting the presence of degradative genes and transforming them into appropriate hosts through a suitable vector within a controlled setting. This technology explores *Polymerase Chain Reactions* (PCRs), the anti-sense RNA technique, site directed mutagenesis, electroporation, and particle bombardment techniques.

The first step in *Genetically Modified Microorganism* (GMM) construction is the selection of a suitable gene or suitable genes; next, the DNA fragment to be cloned is inserted into a vector and introduced into host cells. The modified bacteria are called *recombinant cells*. The next step is the production of multiple gene copies and selection of cells containing recombinant DNA. The final step includes screening for clones with desired DNA inserts and biological properties.

Since the possibility of conferring new properties into existing organisms abound, researchers have studied the ability of modified organisms to de-

grade petroleum hydrocarbons or hydrocarbon-based compounds. For example, in Fulekar et al. (2009) the authors studied the transfer of plasmid pJP4 from two introduced donors, natural host *R. eutropha* (JMP134) and a laboratory-constructed strain *Escherichia coli* (D11), to indigenous microbes in soil, contaminated with 2,4-D. A key difference between donors was their ability (*R. eutropha*) or inability (*E. coli*) to mineralize 2,4-D. Additionally, they studied the transconjugant occurrence, their identification, and the plasmid persistence. Both inoculated donors were detectable and they transferred plasmid pJP4 to indigenous recipients to different extents. In the first experiment 2,4-D was degraded significantly faster (28 days) in soil, inoculated with *R. eutropha* JMP134, and was compared with soil inoculated with *E. coli* (D11) (49 days). Interestingly, a greater number of transconjugants was detected in *E. coli* (D11)-inoculated soil and they were members of the *Burkholderia* and *Ralstonia* genera. After reamendment 2,4-D was degraded more rapidly in the soil with *E. coli* (D11)-inoculants than in *R. eutropha* (JMP134)-inoculated treatments. These results indicate that the choice of donor microorganism is a crucial factor to be considered for a bioaugmentation approach.

In an earlier study, the University of Tennessee in collaboration with Oak Ridge National Laboratory performed research in the field, based on bioremediation, using genetically modified microorganisms. The organism involved was a *Pseudomonas fluorescens* strain, designated HK44, released into a hydrocarbon contaminated environment. The original parental strain with the strain HK44 was derived and isolated from a manufactured gas plant, heavily contaminated with polyaromatic hydrocarbons (PAHs). The naphthalene catabolic plasmid (PUTK21) was introduced into the strain to form *P. fluorescens* (HK44). Upon the introduction of the modified organism to naphthalene (or the intermediate metabolite salicylate) there was an increased catabolic gene expression, naphthalene degradation, and a coincident bioluminescent response.

Because of the well-established tools from metabolic engineering and biochemistry it became possible to infuse different pathways into a "*designer*" microbe. This technique is a very powerful instrument for enhancing petroleum hydrocarbon biodegradation. Very often, these pathways are combined with existing pathways to enable complete biodegradation. The construction of a hybrid strain, which would be capable to mineralize components of a mixture of benzene, toluene, and p-xylene simultaneously was attempted by redesigning the metabolic pathway of *Pseudomonas putida*. A hybrid strain expressing both the Todd and the toll pathways was constructed and was found to mineralize a benzene, toluene, and p-xylene mixture without accumulation of any metabolic intermediate (Chen et al., 2015).

Irrespective of the glowing prospects of genetic engineering to confer new properties on microbes and subsequently improve their abilities on the field, the practice is faced with some constraints. Sayler and Ripp (2000) report that there is difficulty in deducing the exact extent of the microbe under modification, which actually contributes to the degradation process, recognizing that several factors (such as volatilization and chemical transformation) simultaneously occur within a reactor system.

In using GMM, it can be problematic to distinguish between GMM specific degradation and biodegradation due to the presence of indigenous microbial consortia. Another obstacle is the inability to statistically conclude on bioremediation efficiency because of the highly heterogeneous distribution of the contaminants.

Sample–sample chemical analyses can typically vary by up to 200%, making valid conclusions blurred. To buttress this, in an experiment using *P. fluorescens* HK44 lysimeter release, soil PAH concentrations were dispersed heterogeneously ranging from 0.04 to 192 ppm spatially. Consequently, a precise evaluation of the effectiveness of P. flurescens HK44 in the overall process could not be adequately determined. Statistical models that can incorporate chemical heterogeneity kinetics into the entire design are required before valid efficacy assessments can be obtained.

Another impediment to actualizing field release studies is the securing of the required governmental permission, which is often a difficult and lengthy endeavor. Although necessary to ensure environmental and public health safety, the process often leads to an overall aversion to GEM implementation in environmental systems, especially with researchers, concentrating rather on the optimization and commercial development of naturally occurring (intrinsic) microbial degradation. Also, during the approval process the GEM might undergo significant refinement and genetic restructuring in the hands of researchers, making the originally proposed release microorganism somewhat obsolete. This unfortunately prevents the integration of state-of-the-art engineered microbes into field release studies.

11.7 STATE RECONSTRUCTION FOR BIOREACTORS

11.7.1 Characterization of nitrogen substrate limitation on *Escherichia coli's* growth by DNNO

Nitrogen is an essential element to all microorganisms. In the case of *Escherichia coli (E. coli)*, nitrogen is coupled to the carbon metabolism by the Krebs cycle, where alpha-cetoglutarate is used to produce glutamate and

glutamine, which are the fundamental compounds to synthesize all other amine-acids and proteins (Reitzer, 2003; van Heeswijk et al., 2013).

In several microorganisms with industrial applications, a nitrogen-limited batch or continuous microbiological cultures allow for the control of the cell growth by maintaining a sub-optimal nitrogen level and prevent the cells to become starved and to stop growing (Falkowski and Raven, 2007).

For example, nitrogen limitation has showed to be a relevant condition to promote efficient neutral lipid accumulation in microalgae or increase the hydrogen rate production in photobacteria (Zhang et al., 2014). Other groups have also demonstrated that *S. cerevisiae* increases ethanol yield under nitrogen limitation (Niessen et al., 2006).

Despite the substrate concentration, feed flow rate and carbon bio-disponibility are well-known relevant issues that affect the microorganism metabolism. The carbon to nitrogen ratio (CNR) in the microorganism's culture media has started to be considered also as a critical aspect that can modify entirely the microorganism behavior (Baez et al., 2011).

In particular, aerobic and anaerobic cultures of *E. coli*, where the nitrogen source is ammonia (NH_4), are characterized by the biomass growth with the corresponding carbon dioxide (CO_2) and formation of byproducts, such as acetate, formate, lactate, and ethanol, among others. However, in aerobic cultures, as soon as the nitrogen source is completely consumed, the microorganism growth is stopped, but the remaining cells continue consuming glucose to produce CO_2 and water. On the other hand, in anaerobic conditions, the metabolism is redirected to produce only byproducts, such as acetate, formate, lactate, and ethanol.

Similar conditions (with a different distribution of byproducts) have been observed in some other microorganisms such as *Salmonella typhimurium* (Ikeda et al., 1996), *Saccharomyces cerevisiae* (Larsson et al., 1997), etc.

The simplest model to describe the growth of a microorganism limited by nitrogen is the Droop model. This model assumes that the growth rate depends on the intracellular concentration of nitrogen. More accurate models have been proposed to deal with the coupling between nitrogen and carbon assimilation under several conditions of light radiation (Faugeras et al., 2004; Geider et al., 1998; Pahlow et al., 2013).

However, complete understanding of the CNR effect on the microorganism metabolite and genetic response requires long experiments and significant amounts of resources. In this sense, mathematical modeling may simplify the conceptual study of the relevance of CNR for each particular microorganism, and save time and resources.

The model complexity must be the result of a tradeoff between realism (in order to accurately represent the key variables of the process) and simplicity, so that it can be mathematically tractable to solve control and optimization problems (Bernard and Queinnec, 2008).

Even more important is the concept that any mathematical model can be considered useless, if it is not describing the behavior well of the particular microorganisms. Therefore, a detailed kinetic study and the associated parametric identification scheme are mandatory to evaluate the model. If this set of tasks can be successfully solved, then the prediction of the behavior of microorganisms and optimization analysis can easily be proposed without important resource investments. There are many examples where some application of well-characterized models have been key elements of improving the productiveness of metabolites, feeding strategies, scale-up designs, and control methods designs.

The main objective of the sections below was to obtain a parametric characterization of a simplified dynamical model able to predict the biomass and the metabolites productivity under the nitrogen stress. The model was obtained considering the following facts:

- Biomass growth depends on both nitrogen and glucose.
- There is a proportional time invariant relationship between carbon and nitrogen consumption rates.
- Byproduct generation is closely related to biomass growth.
- Byproduct formation is related to biomass accumulation.
- The dilution rate is considered constant.

The model is developed based on the experiments carried out in various nitrogen conditions (replete and starvation) with *Escherichia coli,* testing microorganism under aerobic conditions.

11.7.1.1 Mathematical model of microorganisms culture under the nitrogen limitation

According to van Heeswijk et al. (2013), the nitrogen limitation condition in microbiological reactors can be modeled with the application of a modified specific growth rate. The mathematical model studied below was proposed to support an optimization strategy and to guide the tradeoff between growth and nitrogen effects on the metabolite accumulation.

The proposed model must keep complexity at a minimal level to be mathematically tractable. Therefore, the number of variables was limited to the most important ones: biomass growth, substrate consumption, and main

byproduct accumulation. The model was designed to consider the relationship between all above-mentioned variables.

This study focuses on the growth of *E. coli*, whose biomass, in terms of organic carbon, is denoted as X (g L^{-1}). This growth was supported by the injection of the substrate denoted by S (g L^{-1}). Metabolites produced by *E. coli* were represented as P_j (g L^{-1}) with $j = 1, ..., N$.

Two different scenarios were considered: the first one considers *E. coli* cells, limited by a CNR source, and a second one no longer considers this limitation with the corresponding increasing of CNR. In line with Ross and Geider (2009), the assumption on organic carbon, which can be split into functional and storage pools, is still holding. Despite the considered scenario to analyze the CNR effect on the microorganism growth, the compartmental method was the theoretical basement to develop this model.

The functional compartment (f) includes the biosynthetic apparatus (proteins and nucleic acids) and the structural material (membranes mainly made of glycolipids and phospholipids). In several microorganisms, the nutrient uptake and the biomass growth are known to be uncoupled processes for microalgae (Chisti, 2007; Christenson and Sims, 2011), leading thus to variations in the internal quota of nutrient. However, this is not the case for *E. coli*. Therefore, the biomass growth rate should include both effects simultaneously.

The model was based on the usual continuous stirred tank reactor with a two-factor specific growth reaction rate (Thamsiriroj and Murphy, 2011), (Boe and Angelidaki, 2009), (Gibon-Fargeot et al., 2000). This was constructed as a function of both carbon and nitrogen sources. In addition, the model considered the consumption of some key byproducts, once the nitrogen or substrate were completely consumed. This fact was modeled as a hybrid system considering a reference value N^* that can be identified by experimental analysis. Also, the model that considers the fact described above can be characterized by the following set of ordinary differential equations:

$$\frac{d}{dt}C(t) = F(C(t), u(t)) + \chi(N(t))F_N(C(t)) \tag{11.1}$$

where $C = [X, S, P_1, ..., P_N]^\top$ and the vector field F is defined by

$$F(C(t), u(t)) = \begin{bmatrix} \mu(X, S(t))X(t) - D(t)X(t) \\ D(t)\,(u(t) - S(t)) - \rho(S)X(t) \\ \mu_{P,1}X(t) \\ \vdots \\ \mu_{P,N}X(t) \end{bmatrix} \tag{11.2}$$

with $N(t) = \alpha S(t)$, $0 < \alpha < 1$. The time varying parameters $\rho\,(s\,(t))$ and $\mu\,(Q_N\,(t))$ are described by the Monot-like relations:

$$\rho\,(S(t)) = \rho_m \frac{S(t)}{S(t) + K_S},$$
$$\mu\,(S(t), N(t)) = \bar{\mu}\left(\frac{S(t)}{K_S + S(t)}\right)\left(\frac{N(t)}{K_N + N(t)}\right).$$

The biomass concentration is denoted X [g L^{-1}], and the substrate concentration S [g L^{-1}]. The variation of the different product concentrations is denoted by P_i [g L^{-1}]. The substrate uptake rate is represented as ρ [1/h], while μ [1/h] is the specific growth rate and D [1/h] is the constant dilution rate calculated as $D = Q_{in}/V$, where Q_{in}, (L/h) and V, L are the input flow of external substrate and volume in the reactor, respectively.

The vector $F_N(C(t))$, presented in (11.2), characterizes the effect of substrate (either glucose or nitrogen) on the reaction dynamics. Indeed, it models the utilization of organic acids as the carbon source to keep the biomass growth continuing. Simultaneously, this part of the model highlights the effect of the nitrogen limitation condition. In particular, this effect is evidenced in ethanol dynamics. This condition has been observed in some studies. The vector field $F_N(C(t))$ is defined as

$$F_N(C) = \begin{bmatrix} \mu_{N,1} P_1 + \mu_{N,2} P_2 \\ 0 \\ -\bar{\mu}_{P,1} X \\ \vdots \\ \mu_{P,N} X \end{bmatrix}. \tag{11.3}$$

This term has been introduced in the model (11.1) to justify the evidence of byproduct consumption, as a secondary substrate. In El Mansi and Holms (1989), the initial substrate, formed by glucose (50.0 g L^{-1}) and ammonia (1.0 g L^{-1}), evidenced the consumption of the organic acids, produced by the fermentation process. This fact was explained by the fastest complete consumption of the nitrogen source that yield a reduction of the growth of the microorganism. Therefore, despite glucose being still consumed after the nitrogen source was entirely consumed, lactate and acetate were used as the substrate to satisfy the pyruvate and acetyl-coenzyme A demands, which serve as key intermediates in many different metabolic mechanisms. The function χ serves to indicate if the alternative substrate sources should be used depending on the nitrogen presence in the medium. This term is used to introduce the hybrid nature of the metabolism if nitrogen is consumed.

Then

$$\chi(N) = \left\{ \begin{array}{lll} 1 & if & N \geq N^*, \\ 0 & if & N < N^*, \end{array} \right]$$

where N^* is the minimum nitrogen concentration needed to keep glucose as the main substrate for the microorganism.

A set of aerobic experiments, discussed below, were executed by triplicate. These experiments were carried out with two different C/N ratios. Under these conditions, biomass, substrate and some metabolites were analyzed. These elements were used to characterize the *E. coli* growth and its secondary metabolic evolution.

These data were applied to characterize the effect of the C/N ratio by parametric identification methods. Based on the variations of the parameters, involved within the model presented in (11.2), the nitrogen limitation over *E. coli* growth is discussed in details in the next subsections.

11.7.1.2 Biological and chemical materials

The bacterial strain, used to perform all experiments, is *E. coli* K-12. The inoculation of the microorganisms was prepared by a preliminary culture of 12 h at 37°C and 200 rpm in a controlled incubator.

This inoculum was cultured in several seed lab-scale baffled reactors with a volume of 0.5 L. The fermentation medium was based on M9 commercial solution (3.0 g L^{-1} of KH_2PO_4, 6.0 g L^{-1} of Na_2HPO_4, 0.5 g L^{-1} of NaCl, 1.0 g L^{-1} of NH_4Cl, 0.49 g L^{-1} of $MgSO_4 7H_2O$, and 0.11 g L^{-1} of $CaCl_2$) supplemented with glucose (2.0 g L^{-1}). The inoculation process used 200.0 mL of two different seed reactors (100.0 mL from each one).

All solvents and reagents were HPLC analytic grade. Glucose, acetic acid, lactic acid, and ethanol were purchased from Sigma-Aldrich (Sigma-Aldrich, USA). The concentrated sulfuric acid was purchased from Fermont (Mexico). Standard solutions were used to determine the variation of substrate and byproducts during the fermentation. A primary stock solution of glucose, acetic acid, lactic acid, and ethanol (10 g L^{-1}) was prepared in distilled water, and stored at 4°C. Intermediate working solutions (0.01, 0.05, 0.1, 0.2, 0.5, 1, and 2 g L^{-1}) were obtained through dilutions of this primary stock solution with distilled water and filtered through a 0.22 μm filter before the injection into the chromatographic column.

11.7.1.3 Fermentation

All fermentation experiments were evaluated in 3.0 L Bioflo reactors. The culture media was an M9 commercial solution supplemented with glucose

(10.0 and 50.0 g L^{-1}) and yeast extract (3.0 g L^{-1}). The initial pH was adjusted to 7.0 using either NaOH 2.0 N or H_2SO_4 2.0 N, when necessary. The reactor temperature was controlled to the constant value of 37°C by a water bath. The dissolved oxygen was fixed (by an external controller) at 20% above the air saturation level. Air inject velocity was fixed at 0.5 vvm.

Samples were withdrawn from the reactor during 24.0 h at fixed intervals of 2.0 h. The sample volume was 20.0 mL. These samples were centrifuged in 50.0 mL Falcon tubes at 6000.0 rpm, 4.0°C during 15.0 min. Cells separated by this process were diluted in 20.0 mL of distilled water. This process was used to obtain the dry weight of samples.

The CNR effect on *E. coli* under aerobic conditions was evaluated by running two different sets of reactions, where the initial glucose concentration was 50.0 g L^{-1}, while the ammonia concentration was 1.0 g L^{-1}. In the second set, the glucose concentration was 10.0 g L^{-1} with the same concentration of the nitrogen source. Experiments were executed by triplicate.

11.7.1.4 Methods

11.7.1.4.1 Optical density analysis

Microorganisms growth was determined by the regular optical density method measured at 600 nm by UV-Vis spectrometer. A 3.0 mL sample was withdrawn from the reactor to complete this analysis. The sample was diluted until reaching the adequate absorbency value within the 0.1 to 1.0 range. Dilution ratios were 1:3, 1:5, and 1:10, depending on the fermentation time.

11.7.1.4.2 Dry weight analysis

Extra 5.0 mL samples were dried in oven with fixed temperature at 60°C. This process was executed for a period of 48 h. This condition ensured a constant weight for the dried sample.

11.7.1.4.3 HPLC analysis

HPLC (RI detector, Smartline, KNAUER, Germany) analysis was proposed to characterize the metabolite time evolution throughout the fermentation. A set of operation conditions was realized to obtain the alcohol and organic acid variation, respectively. A 2.0 mL filtered (0.22 μm membrane) sample was diluted 1:5 with a distilled water previous HPLC analysis (Table 11.1). The mobile phase was 0.005 N of H_2SO_4.

Table 11.1 HPLC analysis conditions.

Condition	Value
Column	Rezex Roa Org Aci H+ (8%), Phenomenex, USA
Dimensions	$300 \cdot 7.8$ mm
Oven temperature	60°C
Flow	0.6 mL min^{-1}
Carrier phase	0.005 N H_2SO_4
Detector	Refraction index
Injection volume	20 µL
Analysis period	30 min

11.7.1.4.4 Ammonia detection method

The method known as phenol-hypochloride was applied to characterize the ammonia ion. NH_4Cl and $(NH_4)_2SO_4$ were used as standard compounds. The method was executed by using the supernatant of samples, taken periodically from the bioreactor. Each sample was diluted 1:10. A volume of 20 µL was mixed with 5 mL of solution A during 5 min of continuous agitation. Then 5 mL of solution B was added with continuous agitation by 5 more minutes. The mixed samples were incubated by 30 min. The incubated samples were measured by the spectrophotometer at 625 nm. Solution A was prepared by 10 g L^{-1} of phenol and 50 mg L^{-1} of sodium nitroprusside, while solution B was prepared by 5 g L^{-1} of NaOH and 8.4 mL/L of sodium hypochloride.

11.7.2 Results and discussion

The biomass growth and the substrate consumption are depicted in Figs. 11.1 and 11.2. If no nitrogen limitation was the condition in the reactor (CNR 5:1), glucose was used as a main carbon source (Fig. 11.2). Indeed, the substrate was eliminated after 6.21 h of reaction. The nitrogen source remained in the reactor with a final concentration of 0.2 g L^{-1}. The final biomass concentration reached 4.53 g L^{-1} measured as dried weight. The biomass/substrate yield was 0.45.

In the case of the 1:1 CNR ratio (Fig. 11.2), ammonia was not detected in the reactor after 6.0 h. However, the biomass concentration at that moment was 6.4 g L^{-1} (35% higher than the case when nitrogen was not the limiting reagent). Nevertheless, after nitrogen was eliminated completely from the reactor, the biomass concentration decreased continuously until reaching 5.1 g L^{-1}. Moreover, the glucose consumption velocity changed from its expected exponential form to an almost linear condition.

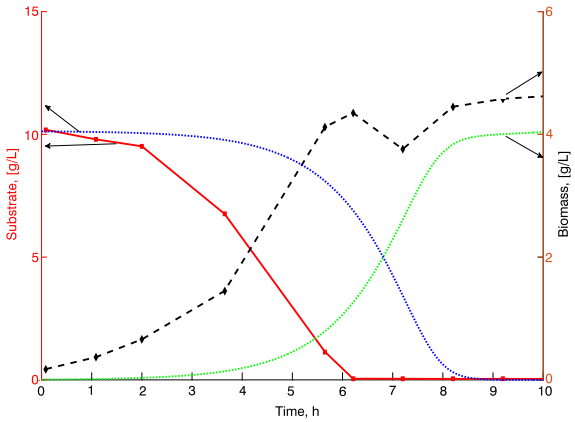

■ **FIGURE 11.1** Comparison of the biomass and the substrate evolution at two different CNRs: 5:1 and 1:1.

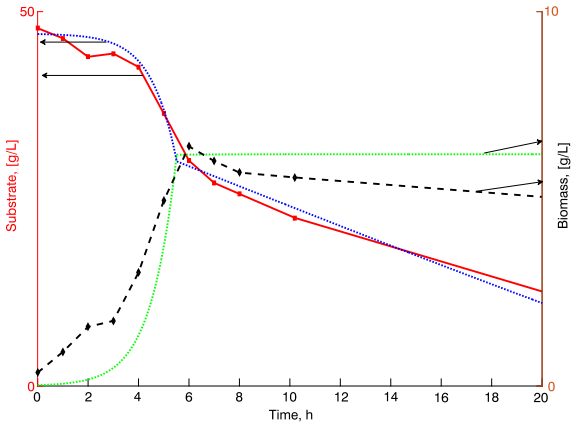

■ **FIGURE 11.2** Comparison of the biomass and the substrate evolution at two different CNR: 5:1 and 1:1.

Figs. 11.1, 11.3, and 11.5 show the trajectories of the model simulated with the parameters presented in Table 12.1, which corresponds to both CNR. These figures show the time evolution of biomass, substrate, acetate, ethanol, and lactate if the CNR ratio was 1:1 and 5:1. The parameter estimation method was also executed, when both CNR ratios were considered in the reaction (data corresponding to CNR were 5:1). In both cases, the simulated model yields the correct correspondence between the estimated and experimental concentrations of all compounds. Once more, in all cases, solid and dashed lines were used to represent the original states. Dotted lines represent the simulated states, when the estimated parameters were set.

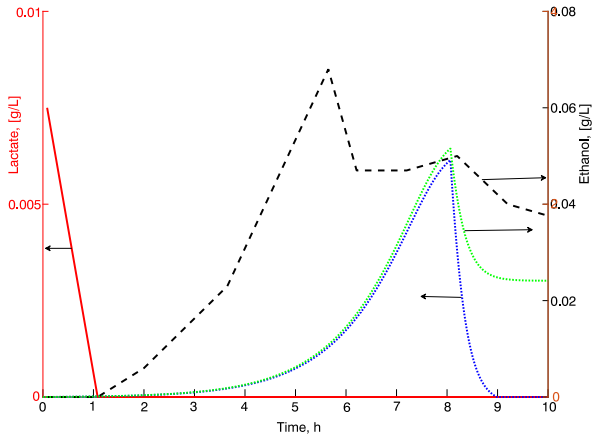

■ **FIGURE 11.3** Comparison of the lactate and the ethanol evolution at two different CNR: 5:1 and 1:1.

If the 5:1 CNR was evaluated, acetate was also used as carbon source after glucose disappeared (Fig. 11.5) and lactate was consumed during the first 1.5 h of the reaction (Fig. 11.3). The biomass concentration did not diminish, because acetate was set as the carbon source (Fig. 11.1).

If the 1:1 CNR was evaluated, biomass followed the same pattern during the first 5 h of culture. After the nitrogen was detected in the reactor (below the limiting detection), the biomass concentration decreased because the main substrate was not usable anymore (Fig. 11.2). Lactate was accumulated during the first 6 h (before the nitrogen source was completely consumed). After that moment, this byproduct was used as an alternative carbon source, because it was consumed during the next 6 h (Fig. 11.4). A similar condition was observed for the case of acetate (Fig. 11.6), which also was consumed since the moment that nitrogen was no longer detected.

It is noticeable that in both CNR experiments, acetate was preferably applied as the substituting carbon source of glucose. This fact was confirmed indirectly by the velocity consumption, showed under both conditions (lower and higher CNR). Then acetate and lactate were also used as carbon source considering that they both were consumed after nitrogen source was not detected. Nevertheless, glucose was also consumed during that period of the reaction, but less efficiently compared to the case that nitrogen was still detected in the reactor. Thus, the presence of nitrogen can be characterized as a regulator of the efficiency of the substrate consumption.

The final byproduct, ethanol, was accumulated in both cases (lower and higher CNR) (Figs. 11.3 and 11.4). Nevertheless, when nitrogen was not limited, ethanol decreased after glucose was consumed (Fig. 11.3). One fea-

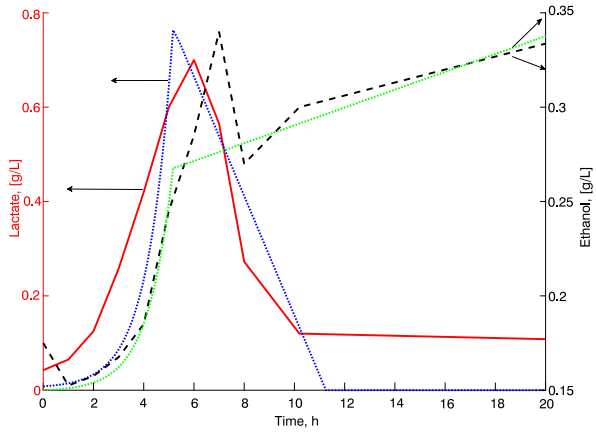

■ **FIGURE 11.4** Comparison of both lactate and ethanol evolution when two different CNR conditions were evaluated: 5 to 1 (A) and 1 to 1 (B). Experimental results and states of the model presented in Eq. (11.2) executed with estimated parameters are also compared.

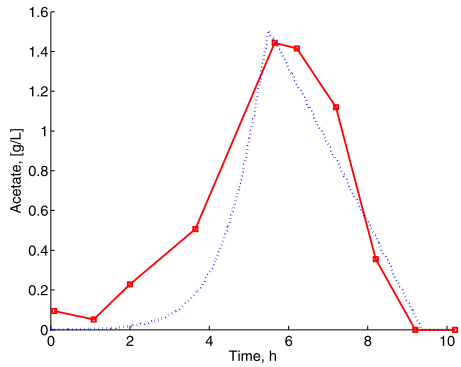

■ **FIGURE 11.5** Comparison of the acetate evolution at two different CNR: 5:1 and 1:1.

sible explanation considers the evaporation condition after it was not longer produced and the reactor temperature, which is slightly above the evaporation temperature of alcohol. When nitrogen was eliminated from the reactor, in the case of the smaller CNR, ethanol was accumulated slower after the nitrogen was consumed, but still its concentration continued accumulating (Fig. 11.4).

This part of the section shows the estimated parameters, obtained in the experiments under predefined different CNR. The similarities between trajectories were obtained as a result of the experimental information and the simulated model with the estimated parameters, representing a promising condition to validate the model. However, several additional experiments

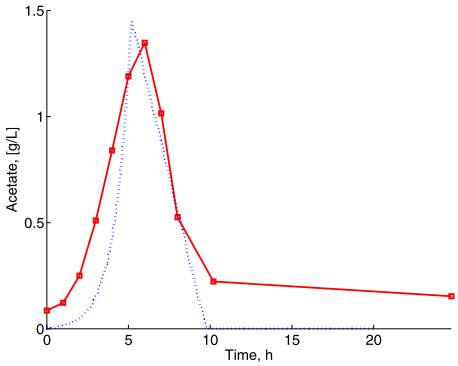

■ **FIGURE 11.6** Comparison of the acetate evolution at two different CNR: 5:1 and 1:1.

were done, where some other experimental conditions must be changed in order to verify the generalization capacity of the model proposed here (Figs. 11.5 and 11.6).

The mean square error for the estimation process was calculated for evidencing the exact convergence of the proposed parameter identification method. Even when the values at this figure seem to be very high, compared with the values of the states presented in Figs. 11.1–11.6, they are, in fact, relatively low. The similarities between experimental information and the model variables, obtained with the parameters recovered by the proposed algorithm, explain why the solution, proposed here, can be used to characterize the CNR effect on *E. coli*. Eventually, this tool can be modified to include the effect of some other substrates.

11.7.3 Microalgae culture

Microalgae are sunlight-driven cell biological factories that convert carbon dioxide to potential biofuels, foods, feeds, and high value bioactivities. In addition, they can be used in bioremediation applications and as nitrogen fixing biofertilizers (Chisti, 2007). Microalgae are prokaryotic or eukaryotic photosynthetic microorganisms that can grow rapidly and live under harsh conditions due to their unicellular or simple multicellular structure (Mata et al., 2010).

The term algae has no formal understanding of taxonomy, as it is routinely used to indicate a set of photosynthetic organisms artificially attached polyphyletic and not cohesive. This classification includes the organisms, which do not share their origin, but continue multiple or independent lines of evolution. Moreover, there are relevant morphological similarities between them (Barsanti and Gualtieri, 2006).

Microalgae are considered as primitive plants (thallophytes), i.e., lacking roots, stems and leaves, which have no sterile covering of cells around the reproductive cells and have chlorophyll as their primary photosynthetic pigment. Microalgae structures are primarily focused on energy conversion without any development beyond cells, and their simple development allows them to adapt to prevailing environmental conditions and prosper on the long term (Brennan and Owende, 2010).

Recently, microalgae have been exploited in different areas, such as biofuels production, waste treatment, food supplements, carbon dioxide (CO_2) abatement, production of fine chemicals, immobilized systems for production of some extracellular compounds and biosorption of heavy metals (Ugwu et al., 2008). Despite the large number of applications where microalgae are applied, there are some challenges that must be solved before they can represent a true solution in many industrial processes.

As noticed, microalgae have a lot of potential utilities. However, in recent years one of the most studied applications has become biofuel production. Fossil fuels are widely used in daily life and their consumption is increasing every day, especially in transportation industry. However, they are a nonrenewable energy source, so they are becoming scarcer causing the price to rise by high demand and limited supply. Added to this, the use of these resources leads to increased emissions of air pollutants from different sources, from oil refining to fuel application.

To overcome the problems associated with the use of fossil fuels, some people have sought new forms of energy, in particular for biofuels, which are capable of reducing production costs, plus they can contribute to reducing CO_2 emissions from the transportation industry and the v of private cars (Timilsina and Sherestha, 2011).

Based on the feedstock, used for production and the technologies, and applied to convert feedstock into fuel, biofuel technologies can be classified into two groups: biofuels of the first and of the second generation. Technologies that normally utilize the sugar or starch fraction of plants as feedstock to produce ethanol and those applied for oilseed crops to produce biodiesel, are known as first-generation biofuels. On the other hand, biofuels produced using technologies, converting lignocellulosic biomass, are referred to as the second-generation biofuels. These are biofuels produced from advanced feedstock (Timilsina and Sherestha, 2011).

Nowadays, increasing interest in second-generation biofuels is observed. For example, second-generation ethanol is produced through the conversion of lignocellulosic biomass, which their sources can be waste seed husks, stalks, and fast-growing grasses and trees. Making use of those sources,

its production does not compete with food supply. Lignocellulosic biomass is comprised of polysaccharides, which are converted into carbohydrates through hydrolysis or other chemical process. The sugars are then fermented into ethanol using existing fermentation technology.

Besides, the production of high added-value products, such as carotenoids, phycobilins, fatty acids, medication delivery platforms, pharmaceuticals, and bioplastics can be conducted in microalgae. These organisms are promising sources considering that they represent a safe way to develop these products, because microalgae are innocuous. However, there are some challenges as to the way that they are produced and harvested.

As one can notice, there are different algae applications that have remarkable diverse characteristics. Therefore, the required conditions to reproduce or grow them are varied, including aspects; the type and amount of nutrients, the lighting conditions, the medium pH, turbidity, salinity, and the temperature, among others. So, one of the main challenges in the cultivation of microalgae is the choice of the most suitable system to grow microalgae. These systems are known as photobioreactors and there are mainly two types: closed and open systems.

To accomplish the growing needs of each microalgae, it is important to develop a particular system, required to keep regulated the conditions to promote their growth. Photobioreactors are considered a specific class of bioreactors, which are devices designed and constructed to support a biologically active environment. In particular, these photobioreactors consider the light as a variable to be controlled in order to optimize the microalgae growth.

Photobioreactors classified as open show poor mass transfer rates yielding low biomass productivity (Ugwu et al., 2008). Different forms of open photobioreactors can be distinguished: these may be natural waters such as lakes and ponds, waterfall type inclined, circular ponds, and rough raceways systems (Borowitzka and Moheimani, 2013). Open systems can easily be constructed and operated. These are the two major reasons because they are the most widely used commercially. However, they tackle also some important problems such as poor light utilization by cells, evaporative losses of liquid medium, diffusion of CO_2 to the atmosphere, requirement of large areas of land, contamination by predators. and other fast-growing heterotrophs.

Closed systems reduce contamination risks and increase the possibility of implementing control systems under the culture conditions. They can be found as flat plate systems, bubble columns, air-lifts, stirred tanks, and toroidals, among others. In these photobioreactors, several different in-

struments can be set up to promote the culture medium recirculation, the exchange of CO_2, etc. Since the illumination is essential for growing microalgae, closed photobioreactors are designed with transparent containers. Despite all their aforementioned benefits, closed systems have the major disadvantage of the high cost of construction and of operation and maintenance.

Independently of the class of bioreactors, used for the microalgae culture, the regulation of their operation conditions is very important for increasing the biomass concentration with respect to the one that can be obtained in nature. This seems to be a relevant factor because when a microalgae method is applied for biodiesel production, the most important challenges include the large-scale implementation of an integrated algae production system and the harvesting of algae in such a way that downstream processing to produce bioproducts of high added value is enforced (Christenson and Sims, 2011).

This regulation must consider the type of photobioreactor to be used: the operation conditions of open systems are more difficult to regulate since these reactors are exposed to contaminants or external factors such as dust or rain. On the opposite, in a closed system, the variable regulation is easier, however, the technical/economical ratio might be less attractive.

One of the main factors that increases the reactor operation cost are the measurement systems. Photobioreactors usually work in very specific and time varying conditions. This fact underlies the necessity of having specific and reliable sensors to monitor different variables. These sensors must have a wide operating range, which usually simply increases the cost of each sensor, but such sensors do not exist at all. One possibility for decreasing costs of a closed or open system is through the usage of virtual sensors which allow one to estimate variables that can result in economic (costly or technically) measurements, from the measurements that are feasible to obtain.

In terms of control engineering, virtual sensors are referred to as state estimators or observers. One of the most attractive aspects of using state observers is the possibility of virtually measuring internal variables of the photobioreactor, i.e., substrate concentrations, a subproduct or an intermediate compound of the reaction. These measurements can be obtained as a result of a computer algorithm using reduced information from the photobioreactor: available information regarding the microorganism metabolism, such as biomass and the input used to feed the reactor.

State estimation recuperation for bioreaction systems has been an active field for many years (Gauthier et al., 1991), (Luenberger, 1979), (Drakunov,

1992). Many different methodologies were proposed to solve this problem in the last decades (Lafont et al., 2011), (Mihoub et al., 2011), (Zhang and Guay, 2002). In general, these processes are defined by the concentration of several compounds of a chemical or biochemical nature that usually cannot be measured directly or that cannot be measured independently (Theilliol et al., 2003). Moreover, the majority of state observers for bioreactors have been designed to converge asymptotically. An additional limiting issue of this class of observers is the approximate estimation of actual states due to the effect of uncertainties and disturbances that may affect the dynamics of the photobioreactor.

11.7.3.0.1 Mathematical model for microalgae culture

The Droop model (Droop, 1968) is a simple and widely used model that can represent the growth of microalgae. This model describes the dynamic evolution of biomass, so that the internal quota of nitrogen and the substrate is used to feed microalgae. The model is formally represented by

$$\left.\begin{aligned} \dot{x}(t) &= x(t)\left(\mu\left(Q_N(t)\right) - D\right), \\ \dot{Q}_N(t) &= \rho\left(s(t)\right) - \mu\left(Q_N(t)\right) Q_N(t), \\ \dot{s}(t) &= D\left(s^{in}(t) - s(t)\right) - \rho\left(s(t)\right) x(t), \end{aligned}\right\} \tag{11.4}$$

where the time varying parameters $\rho\left(s(t)\right)$ and $\mu\left(Q_N(t)\right)$ are

$$\rho\left(s(t)\right) = \rho_m \frac{s(t)}{s(t) + K_s},$$
$$\mu\left(Q_N(t)\right) = \bar{\mu}\left(1 - \frac{K_Q}{Q_N(t)}\right).$$

The biomass concentration is denoted by x [µmol L^{-1}], the internal quotum Q_N [µmol L^{-1}] is defined as the quantity of intracellular nitrogen per unit of biomass, and s [µmol L^{-1}] is the substrate concentration. The substrate uptake rate is represented as ρ [L μm^{-3} d^{-1}], while μL [μm^{-3} d^{-1}] is the specific growth rate, and D [d^{-1}] is the constant dilution rate.

The selection of x and s_{in} as output and input, respectively, provides the full relative degree equal to 3 according to the procedure described in Isidori (1995). Therefore, using the results given in the same reference, there exists a nonlinear transformation $z = T(X_b, S, O)$ ($z^\top = \left[z_1, z_2, z_3\right]$) given by

$$\left.\begin{aligned} z_1 &= y = x, \\ z_2 &= \dot{x} = x\left[\bar{\mu}\left(1-\frac{K_Q}{Q_N}\right)-D\right], \\ z_3 &= x\left[\frac{\bar{\mu}K_Q}{Q_N^2}\left(\frac{\rho_m s}{s+K_s}-\mu Q_N\right)\right]+ \\ &\left\{x\left[\bar{\mu}\left(1-\frac{K_Q}{Q_N}\right)-D\right]\right\}\bar{\mu}\left(1-\frac{K_Q}{Q_N}\right), \end{aligned}\right\} \tag{11.5}$$

such that the new variables z obey the following dynamics:

$$\begin{aligned} \frac{d}{dt}z_1(t) &= z_2(t), \\ \frac{d}{dt}z_2(t) &= z_3(t), \\ \frac{d}{dt}z_3(t) &= f(z(t)) + g(z(t))\,u(t), \end{aligned} \tag{11.6}$$

where the nonlinear function $f(z)$ is given by

$$\left.\begin{aligned} f(z) = \bar{\mu}K_Q\frac{z_1}{Q_N}&\left[\frac{-\rho_m s\dot{Q}_N}{Q_N^2(s+K_s)}-\frac{\bar{\mu}K_Q\dot{Q}_N}{Q_N^2}\right]+ \\ &\frac{z_2\bar{\mu}K_Q\dot{Q}_N}{Q_N^2}+z_3\left[\bar{\mu}\left(1-\frac{K_Q}{Q_N}\right)-D\right]- \\ &\frac{\bar{\mu}K_Q K_s\rho_m z_1}{Q_N^2(s+K_s)^2}\left(Ds+\frac{\rho_m s x}{s+K_s}\right). \end{aligned}\right\} \tag{11.7}$$

Additionally, the input-associated function $g(z)$ has the following structure:

$$g(z) = \frac{\bar{\mu}K_Q K_s\rho_m D z_1}{Q_N^2(s+K_s)^2}. \tag{11.8}$$

The nonlinear functions $Q_N(z)$ and $s(z)$ are described by

$$\left.\begin{aligned} Q_N(z) &= \frac{-\bar{\mu}K_Q}{\frac{z_1}{z_2}-\bar{\mu}+D}, \\ s(z) &= \frac{\beta(z)\,Q_N(z)\,K_s}{\rho_m-\beta Q_N(z)}, \\ \beta(z) &= \frac{z_3-z_2\left[\bar{\mu}\left(1-\frac{K_Q}{Q_N(z)}\right)-D\right]}{z_1\left(\frac{\bar{\mu}K_Q}{Q_N(z)}\right)} \\ &\quad+\bar{\mu}\left(1-\frac{K_Q}{Q_N(t)}\right). \end{aligned}\right\} \tag{11.9}$$

In general, measuring the internal quotum and substrate is considered as an expensive and time-consuming procedure. However, the existence of the so-called *full relative degree condition* allows one to use biomass as the sole required information to design an observer or software sensor. Therefore, here we are focusing on the development of an algorithm serving as a software sensor to reconstruct the concentrations of Q_N and s (Martínez-Fonseca et al., 2014). As one can understand, microalgae biomass can be straightforwardly estimated by a simple optoelectronic sensor using a red light emitting led and the corresponding photodiode.

11.8 VARIABLES RECONSTRUCTION OF MICROALGAE CULTURE

The proposed observer is defined by the following differential equations:

$$\left.\begin{array}{c} \frac{d}{dt}\hat{z}_1(t) = \tilde{z}_2(t) + k_{11}\phi_{11}\left(e_1(t), \alpha_1\right), \\ \frac{d}{dt}\tilde{z}_2(t) = k_{12}\phi_{21}\left(e_1(t), \alpha_1\right), \\ \frac{d}{dt}\hat{z}_2(t) = E_2\left(\tilde{z}_3(t) + k_{21}\phi_{12}\left(e_2(t), \alpha_2\right)\right), \\ \frac{d}{dt}\tilde{z}_3(t) = E_2\left(k_{22}\phi_{22}\left(e_2(t), \alpha_2\right)\right), \\ \frac{d}{dt}\hat{z}_3(t) = E_3\left(f\left(\hat{z}(t)\right) + g\left(\hat{z}(t)\right)u(t)\right) + \\ E_3\left(\sum_{i=1}^{3} K_i e_i(t) + K_{SM}\,\mathrm{sign}\left(e_3(t)\right)\right), \end{array}\right\} \tag{11.10}$$

with

$$e_i = \hat{z}_i - \tilde{z}_i, \quad i \in \{1, 2, 3\}. \tag{11.11}$$

The set of variables $\hat{z}_i$ represents the corresponding estimated trajectories of z_i. In particular, $\tilde{z}_1 = z_1$.

The observer gains represented by k_{11}, k_{12}, k_{21} and k_{22} are positive scalars that must be adjusted to force the convergence of the observer trajectories to the states of the uncertain system. The indicator function $E_i(t)$ is given by

$$E_i = \begin{cases} 0 & t < t_i^*, \\ 1 & t \geq t_i^*. \end{cases} \tag{11.12}$$

The switching time t_i^* is found as a result of the fixed time convergence obtained by the observer. The nonlinear functions $\phi_{1j}\left(e_j, \alpha_j\right)$ and $\phi_{2j}\left(e_j, \alpha_j\right)$

$(j = 1, 2)$ were designed in agreement with the proposal given in Cruz-Zavala et al. (2011b). Then they are defined as

$$\left.\begin{aligned} \phi_{1j}\left(e_j, \alpha j\right) &= \left|e_j\right|^{1/2} \operatorname{sign}\left(e_j\right) + \alpha_j \left|e_j\right|^{3/2} \operatorname{sign}\left(e_j\right), \\ \phi_{2j}\left(e_j, \alpha_j\right) &= \frac{1}{2}\operatorname{sign}\left(e_j\right) + 2\alpha_j e_j + \frac{3}{2}\alpha_j^2 \left|e_j\right|^2 \operatorname{sign}\left(e_j\right), \end{aligned}\right\} \tag{11.13}$$

where α_1 and α_2 are positive constants.

The following subsection describes the numerical implementation of the observer using the Droop model presented in (11.4) as data generator.

11.8.0.0.1 Numerical results

The model of the photobioreactor is simulated using the following parameters:

Parameter	Value	Units
D	1.3	d^{-1}
ρ_m	9.3	$\mu mol\ \mu m^{-3}\ d^{-1}$
$\bar{\mu}$	2.0	d^{-1}
s^{in}	100.0	$\mu mol\ L^{-1}$
K_s	0.105	$\mu mol\ L^{-1}$
K_Q	1.8	$\mu mol\ \mu m^{-3}$

These parameters were taken from Khaksar Toroghi et al. (2013). Under the selected set of parameters, the simulated microorganism growing was not inhibited neither by the substrate nor the product. These conditions are usually considered in observer design for bioreactors. The transformation (11.5) of the system (11.4) presented in this study is simulated in Matlab/Simulink. The simulation is executed using a fixed step numerical integration algorithm (ODE1-Euler) with an integration step of 0.0001 h.

Fig. 11.7 shows the performance of the observer in the z-coordinates. The trajectories depicted in this figure are obtained by using the set of discontinuous system described in (11.6). Each individual figure (one is used for each variable of the transformed system) shows also the step-by-step convergence of all the states. The first state z_1 converges before z_2, which in turn converges before z_3. The convergence of all the states was achieved in finite time and the estimation error converged before 0.65 h. This value almost coincides with the predicted time T (0.69 h), which is relatively small with respect to the period of simulation (10.0 h).

For comparison purposes, a *high-gain observer* is also simulated. This observer structure is adapted from the results presented in Hadj-Sadok and

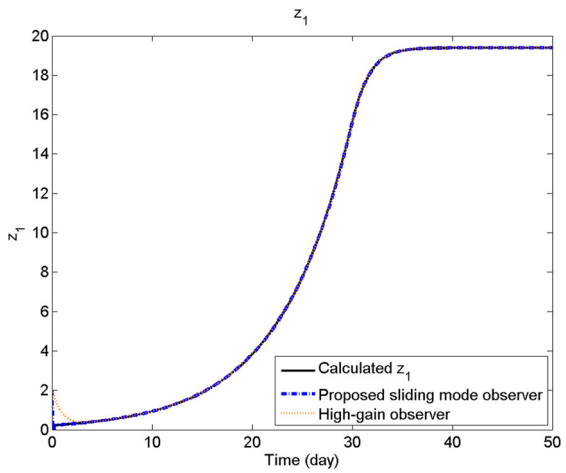

■ **FIGURE 11.7** Comparison of the trajectories obtained for the transformed system, the observer proposed in this study, and the high-gain state estimator for the variable z_1.

Gouzé (2011):

$$\left.\begin{aligned} \frac{d}{dt}\hat{z}_1(t) &= \hat{z}_2(t) + l_1 e_1(t), \\ \frac{d}{dt}\hat{z}_2(t) &= \hat{z}_3(t) + l_2 e_1(t), \\ \frac{d}{dt}\hat{z}_3(t) &= f(\hat{z}(t)) + g(\hat{z}(t))u(t) + l_3 e_1(t). \end{aligned}\right\}$$

The high-gain observer gains are selected following the method presented in Gauthier et al. (1991): $l_1 = 5000$, $l_2 = 10{,}000$, and $l_3 = 100{,}000$. The trajectories of this alternative observer converged to the true values of the system (11.4). However, the convergence is achieved asymptotically in this case. The transient process exhibited oscillations with big amplitude (Figs. 11.7–11.9). As for the uniform observer states the convergence is completed after 0.65 h. Figs. 11.10–11.12 show a detailed view of the trajectories of z_1, z_2, and z_3, obtained from the numerical simulation of the transformed system and its comparison with the estimated values, obtained from the trajectories of the observer proposed here, and the high-gain and first order sliding mode versions. This figure is showing high amplitude oscillations around the true trajectory; this is an effect of the scale. Moreover, one can notice that all the three variables are not reached by the estimated states generated by the high-gain observer.

The convergence of the estimated states in the z-coordinates forces the corresponding fixed-time estimation of biomass and substrate. These values

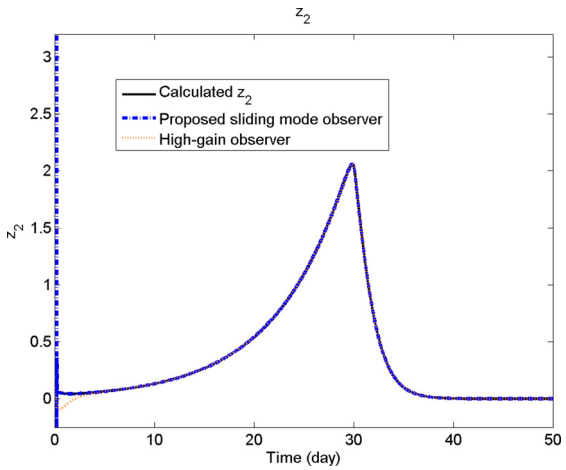

■ **FIGURE 11.8** Comparison of the trajectories obtained for the transformed system, the observer proposed in this study, and the high-gain state estimator for the variable z_2.

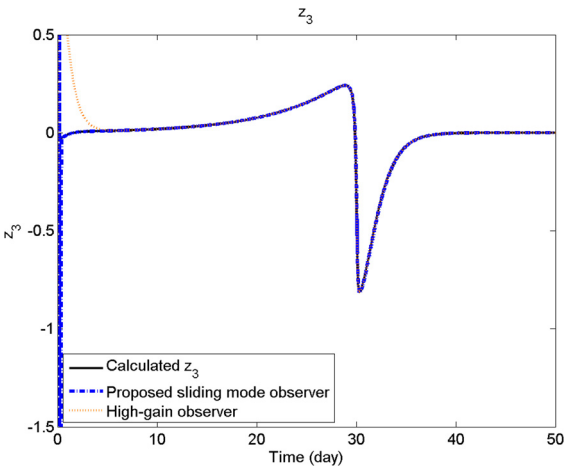

■ **FIGURE 11.9** Comparison of the trajectories obtained for the transformed system, the observer proposed in this study, and the high-gain state estimator for the variable z_3.

are obtained as a solution of the inverse transformation presented in (11.9). Figs. 11.13–11.15 shows the trajectories of both, the bioreaction system described in (11.4) and the observer obtained as the solution of the inverse transformation applied over the trajectories of (11.6).

The reconstructed biomass is showed in Fig. 11.13. One may notice that there is no evident difference between both trajectories, the biomass time evolution, and the estimated state. The substrate is estimated some minutes

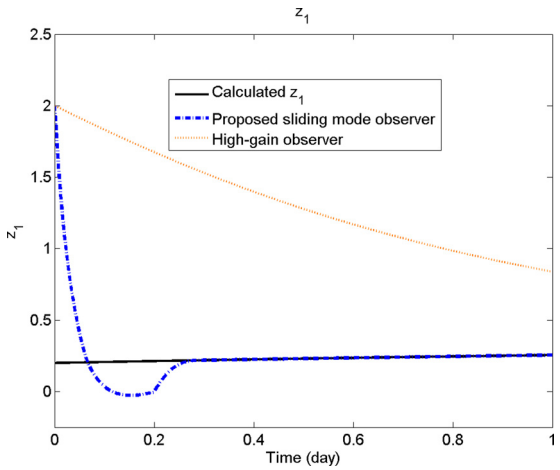

■ **FIGURE 11.10** Detailed view of comparison of the trajectories obtained for the transformed system, the observer proposed in this study, and the high-gain state estimator for the variable z_1.

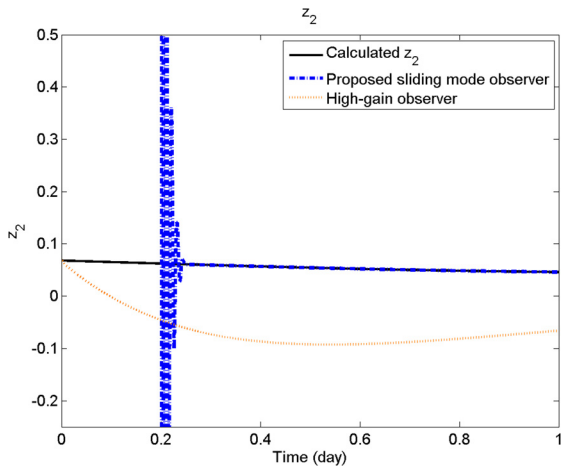

■ **FIGURE 11.11** Detailed view of comparison of the trajectories obtained for the transformed system, the observer proposed in this study, and the high-gain state estimator for the variable z_2.

after the biomass is fully reconstructed. This is an expected behavior considering the step-by-step nature of the observer.

Fig. 11.14 demonstrates the true substrate trajectory produced by the model (11.4) and the estimated substrate produced by the observer (11.10). Finally, Fig. 11.15 demonstrates the corresponding comparison between the actual Q_N and their corresponding estimates produced by the fixed time proposed here and the high-gain version.

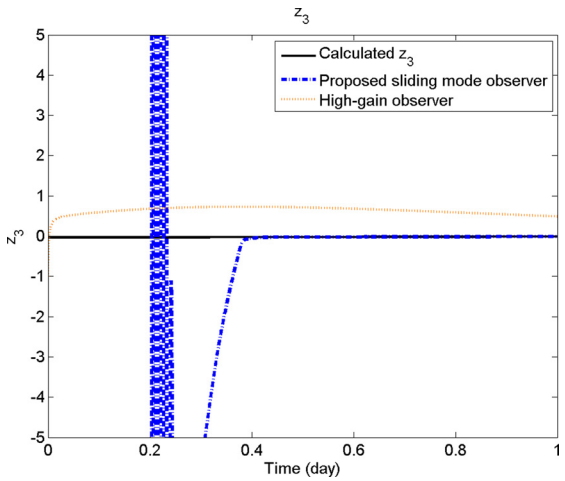

■ **FIGURE 11.12** Detailed view of comparison of the trajectories obtained for the transformed system, the observer proposed in this study, and the high-gain state estimator for the variable z_3.

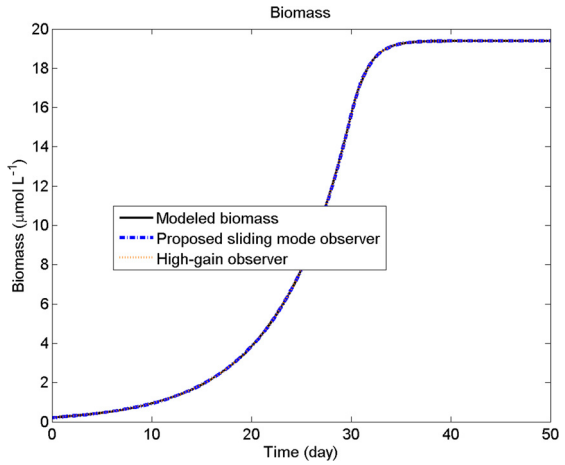

■ **FIGURE 11.13** Comparison of the trajectories obtained for the bioreactor system, the observer proposed in this study, and the high-gain state estimator for the variable X.

In the same figure, the corresponding trajectories for the high gain are also shown. In both cases, the proposed observer showed a lower level of oscillations around the true trajectories of the bioreactor system and smaller convergence time. In particular, one may notice the big oscillations demonstrated by the estimated variable associated to the substrate. This is a consequence of the ladder structure of the transformed system. A feasible solution to reduce these oscillations is to adapt the gain of the fixed-time observer.

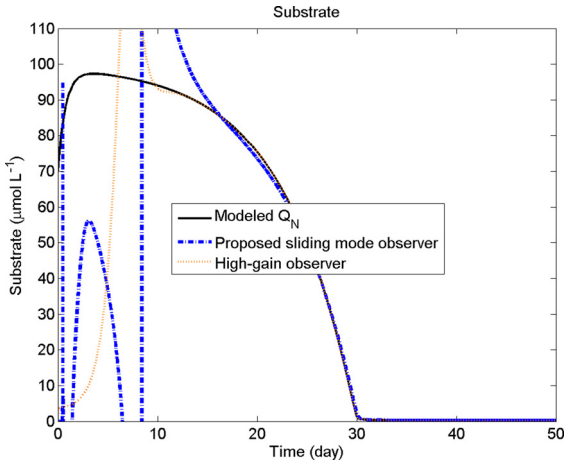

■ **FIGURE 11.14** Comparison of the trajectories obtained for the bioreactor system, the observer proposed in this study, and the high-gain state estimator for the variable S.

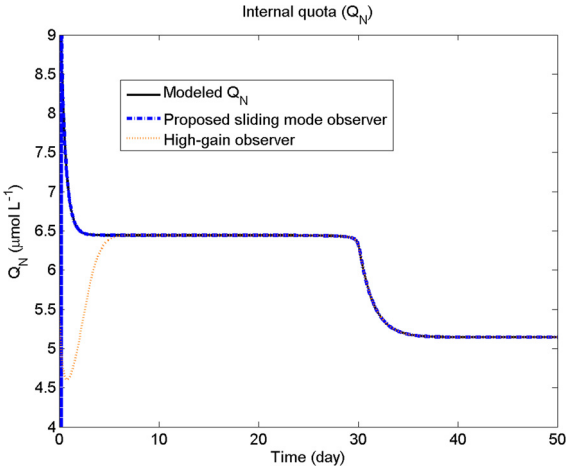

■ **FIGURE 11.15** Comparison of the trajectories obtained for the bioreactor system, the observer proposed in this study, and the high-gain state estimator for the variable Q_N.

Figs. 11.16–11.18 depict detailed views of the biomass evolution obtained from the model (11.4), its estimate produced by the fixed-time observer, and the state generated by the high-gain observer. One must notice that in this figure only the true trajectory of the model and the one obtained with the fixed-time observer appeared. This is additional confirmation of the superior performance obtained by the proposed observer. Moreover, any possible application of the high-gain observer to construct an output closed-loop con-

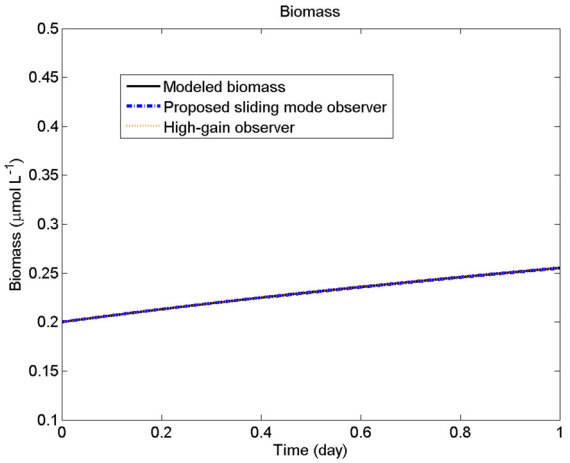

■ **FIGURE 11.16** Detailed view of the comparison for the trajectories obtained for the bioreactor system, the observer proposed in this study, and the high-gain state estimator for the biomass.

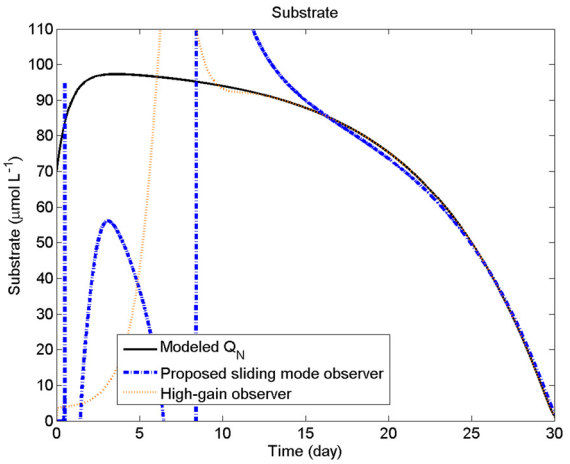

■ **FIGURE 11.17** Detailed view of the comparison for the trajectories obtained for the bioreactor system, the observer proposed in this study, and the high-gain state estimator for the substrate.

troller may present relevant failures over the reactor as the consequence of big amplitude oscillations in the estimation process.

The mean square error for the estimation process was calculated for evidencing the fixed-time convergence of the proposed observer and its comparison with the high-gain and the first order sliding mode observers. The time evolution of the error is depicted in Fig. 11.19.

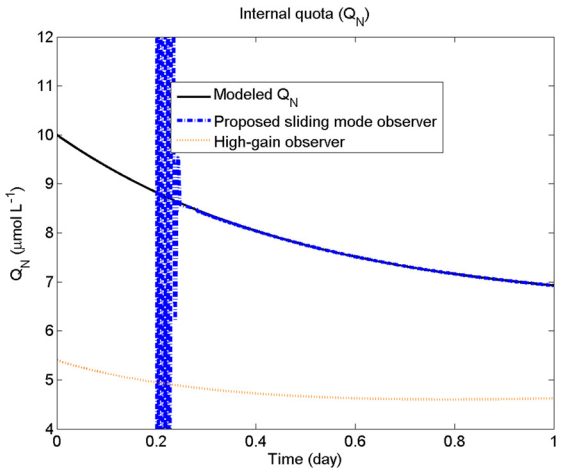

■ **FIGURE 11.18** Detailed view of the comparison for the trajectories obtained for the bioreactor system, the observer proposed in this study, and the high-gain state estimator for the nitrogen quota.

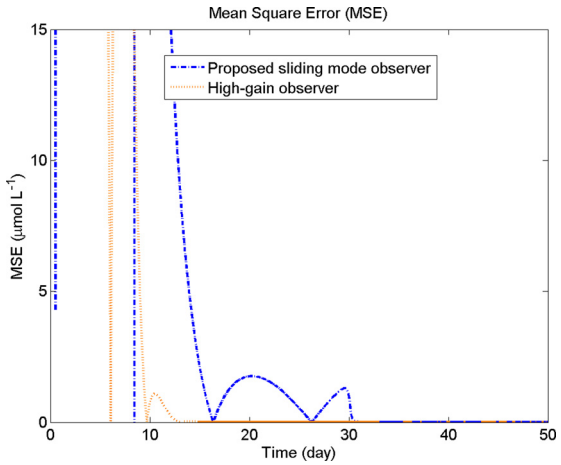

■ **FIGURE 11.19** Comparison of the mean square error evaluated over the estimation error generated by the observer proposed in this study and the high-gain state estimator.

11.8.1 Numerical algorithm for the variables reconstruction

The last stage of designing and applying the proposed state observer deals with the problem of how to implement it in actual photobioreactors. Considering the class of solutions presented in this chapter, the problem can be solved as follows:

a) One should develop an online sensor for the microalgae biomass. This can be done by a simple optoelectronic device that can measure the absorbance of a sample derived from the main flow of the reactor.

b) The absorbance value can be acquired by a digital device, which can implement the corresponding function, transforming the absorbance value into the corresponding biomass concentration. This can be done using the standard calibration procedure.

c) The biomass concentration can be injected into a discretized version of the observer that can be implemented using a first order Euler approximation of the observer (11.10), namely,

$$\left.\begin{array}{c}
\hat{z}_1\left((k+1)T_s\right) = \hat{z}_1(kT_s) + T_s\tilde{z}_2(kT_s) + T_s k_{11}\phi_{11}\left(e_1(kT_s), \alpha_1\right), \\
\tilde{z}_2\left((k+1)T_s\right) = \tilde{z}_2\left(kT_s\right) + T_s k_{12}\phi_{21}\left(e_1\left(t\right), \alpha_1\right), \\
\hat{z}_2\left((k+1)T_s\right) = \hat{z}_2\left(kT_s\right) + T_s E_2\left(\tilde{z}_3\left(t\right) + k_{21}\phi_{12}\left(e_2\left(t\right), \alpha_2\right)\right), \\
\tilde{z}_3\left((k+1)T_s\right) = \tilde{z}_3\left(kT_s\right) + T_s E_2\left(k_{22}\phi_{22}\left(e_2\left(t\right), \alpha_2\right)\right), \\
\hat{z}_3\left((k+1)T_s\right) = \hat{z}_3\left(kT_s\right) + T_s E_3\left(f\left(\hat{z}\left(t\right)\right) + g\left(\hat{z}\left(t\right)\right)u\left(t\right)\right) + \\
T_s E_3\left(\sum_{i=1}^{3} K_i e_i + K_{SM}\,\mathrm{sign}\left(e_3\right)\right),
\end{array}\right\}$$

where T_s is the sampling time forced by the digital device and k is the discrete counter used to update the observer algorithm.

These three simple stages yield a real time implementation of the proposed observer.

11.9 CONCLUSIONS

The main characteristics of biodegradation systems were described. The application of aerobic and anaerobic cultures for the degradation of different contaminants was explained. The bioreactor and its main technical characteristics were associated with the microbial culture to eliminate complex organics. The mathematical models of bacteria and microalgae cultures were discussed and simulated. The suggested models were validated using experimental information.

Chapter 12

Ozonation and biodegradation as complementary treatments

CONTENTS

Ozonation and Biodegradation in Environmental Engineering
https://doi.org/10.1016/B978-0-12-812847-3.00024-X

ABSTRACT

This chapter deals with the sequential combination of ozonation and biodegradation of toxic compounds in different synthetic and real effluents. In general, after the adequate ozonation time, the relevant amount of initial toxic contaminants decreased, which then were transformed into non-toxic organic acids that were easily degraded by biodegradation. If the ozonation is not considered as pretreatment, the biodegradation system is not able to decompose the high concentration contaminants. Additionally, the acclimation of microorganisms plays a relevant role in the contaminants degradation effectiveness. This fact was confirmed by the kinetics of the microorganism growth, which showed an increment of the specific growth velocity, when the ozonation was used as pretreatment. The entire set of variables, describing the sequential process, was efficiently estimated by a variant of DNNO with discontinuous learning laws.

12.1 INTRODUCTION

In developing countries, pollution caused by population growth and high industrial activity has spurred interest in finding more efficient technologies for waste water treatment. Aromatic compounds constitute ubiquitous pollutants due to their extensive use. Among others, phenol (Ph) is an aromatic compound commonly found as a pollutant in industrial effluents, including pulp paper bleach, textiles, pesticides, tannery, oil, and petrochemical products (Banerjee and Ghoshal, 2010; Beltrán et al., 1997; Grau, 1991). This compound is recognized to be one of the most toxic and regular pollutants (Epa, 2004; Saravanan et al., 2008; Wei et al., 2008) by the Mexican regulation, which defines the permissible levels smaller than 0.3 mg L^{-1} (Mexicana, 1994).

Many methods to eliminate phenol and its derivatives using chemical and biological systems have been studied. Biological systems are environmentally friendly, low-cost technologies that can be successfully used to remove phenols by using different microbial strains, but with pure cultures (Abuhamed et al., 2004; Banerjee and Ghoshal, 2010; Jiang et al., 2006; Kumar et al., 2005; Wei et al., 2008). The reports of phenol removal by mixed cultures are still scarce (Bajaj et al., 2009; Saravanan et al., 2008; Zhao et al., 2009a); however, it is well known that a mixed microbial consortium is needed to attain the complete mineralization of mixtures of pollutants in wastewater. Additionally, some studies have been conducted to evaluate the rate and the extent of degradation as these data may be useful in the design and optimization of biological reactors to treat phenolic wastes (Kumar et al., 2005). According to some authors, it is possible to degrade phenol at high concentrations (less than 1000 mg L^{-1}) (Chen et al., 2002; Yan et al.,

2005) in batch or continuous reactors and in the presence of catechol and 2,6-dimethoxyphenol (Stoilova et al., 2006).

On the other hand, many industrial effluents contain phenol, chlorinated phenols (CPhs), and/or other contaminants (Stoilova et al., 2006). This may result in higher toxicity compared to phenol alone. The toxic effects of CPhs increase with a higher degree of chlorination and with its concentration in the waste water effluent (Kargi and Eker, 2005). Consequently, CPhs are difficult to eliminate by traditional biological treatments. Therefore, two major factors play an important role as regards the generalized application of biological treatments to degrade complex mixtures containing phenols and chlorinated phenols:

– the long period of time required to eliminate the complex mixture and

– the constrained efficiency of biological systems to reduce the concentration of such complex mixtures, when their toxicity and/or concentrations are very high.

To overcome the reduction in microbial activity due to the high initial concentration of phenol, many strategies have been proposed. Microbial immobilization is an interesting alternative (El-Naas et al., 2010; Prieto et al., 2002). In general, systems with immobilized bacterial cells are more stable during phenol degradation compared with those operated using free cells (Adav et al., 2007; Godjevargova et al., 2006; Nair et al., 2007). Even when the immobilization improves the performance achieved by microbial strains to eliminate phenols and their derivatives, the correspondent increase of initial concentration, which can be eliminated is not significant.

Despite the fact that immobilized microorganism showed better results than free cells in removing high pollutants concentrations, the high toxicity of some compounds could not be solved completely using this strategy. An interesting option to decompose high concentrations of phenols and chlorinated phenols consists of using the pretreatment of this mixture based on chemical methods. Phenol and chlorophenols could be pretreated by chemical oxidation to reduce their toxicity. The combination of chemical oxidation and biodegradation results in less toxic compounds, thus enhancing the overall treatment efficiency and reducing the treatment time and cost (Beltran-Heredia et al., 2000; Dong et al., 2008c; Edalatmanesh et al., 2008).

Several mixed processes have been proposed recently. Some of them have included a chemical process, based on chemical oxidatiion plus a biologically based decomposition.

Among others, oxygen injected with high pressure, ozonation, catalytic and photocatalytic processes, and others have been tested to perform the developed chemical decomposition. Most of these treatment methods have important advantages, but also have important drawbacks.

These problems can be classified in two main areas:

– the first one contains all economic aspects associated with the high cost required to implement these treatments;

– the second one includes all troubles associated with the resources needed to complete the transformation from very toxic compounds to simpler chemical forms that can be considered as nontoxic and nonhazardous.

Exactly these drawbacks may be resolved by biologically based treatments. In particular, chemical oxidation by ozone resulted in very efficient removal of phenols and chlorophenols, as well as of phenol mixtures (Chaichanawong et al., 2010; Hong and Zeng, 2002; Khokhawala and Gogate, 2010; Nam and Kukor, 2000; Poznyak and Vivero, 2005; Poznyak et al., 2005). The combination of biodegradation with either preliminary or postchemical oxidation or ozonation for waste water treatment has drawn attention (Aparicio et al., 2007; Benitez et al., 2003; Contreras et al., 2003; Derudi et al., 2007; Nam et al., 2001). During ozonation, mixtures of simple nontoxic organic acids are obtained.

These acids cannot be completely mineralized during the same process. However, they could be degraded by a suitable bioprocesses. Beltran-Heredia et al. (2000) reported that combined ozonation and aerobic treatment increased the removal efficiency from 82 or 76% for the chemical oxygen demand (COD) or the total phenolic content, respectively. Benitez et al. (2003) demonstrated that the COD removal for wine vinasses containing organic matter and aromatic compounds was enhanced (from 27.7 to 39.3%), when a combined ozonation and biological process was used. Aparicio et al. (2007) reported the use of a combined waste water treatment setup in a resin-producing factory. After biological treatment of the ozonated effluent, the organic carbon and nitrogen removal was increased from 27% to 97% and from 27% to 80%, respectively.

The possible benefits coming from the combination of pretreatment based on ozone and a sequential bioprocesses are almost evident. However, there are still several questions concerning this procedure. For example, what time is adequate to change the mixture from the ozonation reactor to the biological one or what conditions should be set up for both reactions still remain as open problems. Another important issue that must be explained is what conditions must fulfill the microorganism strains to handle the mixture

produced by the preliminary ozonation. This is a very important aspect conditioned on the composition of the mixture supplied to microorganism that can modify dramatically the efficiency of the organics elimination provided by the biological procedure. Moreover, there is only little work describing what type of microorganisms are responsible for the elimination of residual compounds after ozonation. Just to give an example, in recent reports, several details have been given about byproducts obtained after using phenol and its chlorinated derivatives (Contreras et al., 2003; Derudi et al., 2007; Nam and Kukor, 2000; Nam et al., 2001; Poznyak and Vivero, 2005; Poznyak et al., 2005). In that work, catechol, hydroquinone, and several low weight organic acids have been recognized as the main byproducts. Nevertheless, what relative concentration of each byproduct is most adequate to construct a combined process including ozonation and biological reaction has not been determined yet.

The aims of this chapter are:

- the evaluation of the effect of the initial concentration of phenol and chlorinated phenols (4-chlorophenol, 4-CPh, 2,4-dichlorophenol 2,4-DCPh) on bacterial growth and aerobic removal by free and immobilized cells;
- the determination of the effect of the pH and the ozonation time on the byproducts obtained during the ozonation;
- the definition of the feasibility of applying biodegradation after the preozonation of chlorinated phenols including the selection of the adequate operation conditions.

12.2 MATERIAL AND METHODS

12.2.1 Microbial culture, mineral media, and packing material

The mineral media, used for all experiments, have contents (in grams per liter) as follows:

$$3(NH_4)2SO_4,\ 0.6KH_2PO_4,\ 2.4K_2HPO_4,$$
$$1.5MgSO_4{\cdot}7H_2O,\ 0.15CaSO_4,\ 0.03FeSO_4.$$

Lava rock was used as packing material for the *trickling packed-bed reactor* (TPBR) experiments. A mixed microbial culture from a biofilter used to remove aromatic compounds and gasoline vapors (Dr Revah's Laboratory, Universidad Autonoma Metropolitana Iztapalapa, Mexico) was independently adapted for 3 months to phenol (100 mg L^{-1}) and to organic acids (100 mg L^{-1}) in mineral media.

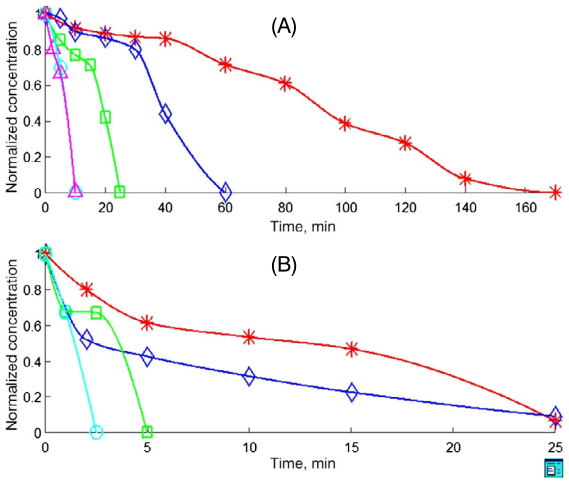

■ **FIGURE 12.1** Phenol degradation in batch culture at different concentrations: (A) 120 (red, ∗), 250 (dark blue, ◇), 500 (green, □), 800 (light blue, ○), and 1000 (purple, △) mg L^{-1}; (B) phenol degradation in the TPBR at different concentrations: 250 (red, ∗), 500 (green, □), 1000 (dark blue, ◇), and 1500 (light blue, ○) mg L^{-1}.

The mixed culture was cultivated in an Erlenmeyer flask of 1 L with 500 mL of mineral media. These compositions were inoculated with 50 mL of the microbial mixture. The system was kept at temperature of 25°C under continuous stirring and aeration. To allow for microbial population growth based on the phenol consumption and ensuring mineral media supply, 200 mL of exhausted media was replaced with fresh media every week. Phenol (100 mg L^{-1}) was fed periodically once it was consumed (approximately every 2 or 3 days) as shown in Fig. 12.1. The cultures were harvested between 24 and 30 h, corresponding to the exponential growth phase and then used for the degradation experiments of Ph, CPhs, and ozonation products (catechol, hydroquinone, and organic acids).

12.2.2 Microbial identification

Recently, the research activity has been focused on the isolation and identification of strains able to degrade high pure phenol concentration (Banerjee and Ghoshal, 2010; Essam et al., 2010). The recently isolated *Alcaligenes* strain TW1 has been found to show a high phenol tolerance and capacity to degrade polycyclic aromatics. This strain is able to completely mineralize up to 1200 mg L^{-1} phenol. Microbial growth was inhibited at 1300–1500 mg L^{-1} of phenol and no growth was observed at concentrations higher than 1500 mg L^{-1} (Essam et al., 2010). Other authors have reported that the degradation efficiency was low, when the effluent contain-

ing high concentrations of these pollutants and that higher retention times were required, because substrate inhibition resulted in reduced microbial activity (El-Naas et al., 2010; Zhao et al., 2009a). Phenol has been shown to significantly inhibit the growth of the microorganisms, when a higher concentration is present (Kumar et al., 2005; Stoilova et al., 2006).

In Adav et al. (2007), the use of aerobic granules in a column-type sequential reactor to degrade phenol (50–1000 mg L^{-1}) was studied. This study showed that the *Acinetobacter* strain has high potential for phenol biodegradation. It was found that the strain had the ability to attach to a sterilized sponge to form biofilms that survived, and this microorganism was able to degrade phenol at a high concentration in water (1500 mg L^{-1}). More recently, Zhao et al. (2009a) reported enhanced phenol degradation using a mixed culture immobilized in a two-phase bioreactor. All this work has considered the presence of one single microorganism species. However, most successful decomposition efficiencies are obtained when a consortium (a set of several microorganisms with different species) is working together to decompose complex organic mixtures or high toxicity compounds. Here, the biological media are composed by a complex consortium. One of the most important aims of the previous works deals with the identification of the consortium.

To complete this part of the study, DNA samples of the microbial consortium (previously adapted to phenol or organic acid, 500 µL) were extracted using an Easy-DNATM Kit (Invitrogen, USA) following the manufacturer's instructions. The 16 S rRNA gene was amplified using the following universal bacterial primers: forward primer F-GC Clamp

5'CGCCCGCCGCGCGCGGCGGGCGG
GGCGGGGGCACGGGGGGCCTACXX ctcctacgggaggcagcag3'

and reverse primer R

5'TCCCGCAACGAGCGCAACCC3'

An 800-bp PCR product was obtained corresponding to the nucleotides between positions 290 and 309 and 1045 and 1064 of the E. coli 16 S rRNA gene. The 50.0 µL of PCR reaction mixture contained 1.0 µL of template DNA, 5.0 µL of 10 buffer, 1.0 µL of 25.0 µM $MgCl_2$, 1.0 µL of dNTPs (5 µM each of dATP, dCTP, dGTP, and dTTP), 1.0 µL of 10.0 µM forward primer, 1 µL of 10 µM reverse primer, 45 µL of sterile water, and 1 unit of Taq polymerase. The PCR was conducted as follows: 94°C predenaturing for 5 min; 30 cycles of 95°C denaturing for 30 s, 56°C annealing for 30 s,

and 72°C extension for 30 s. This process was followed by 72°C extension for 10 min. The PCR amplification products were purified using a QIAquick PCR purification Kit (Qiagen, UK). The PCR-amplified DNA products were separated by DGGE on 8% polyacrylamide gels with a linear gradient of 5–30% denaturant (100% denaturant was 40% (v/v) formamide plus 42% (w/v) urea) using the DCodeTM System (Bio-Rad, Hercules, CA, USA). After purification, the PCR products were sent to a sequencing service (Macrogen Inc, Korea). The nucleotide sequences of each 16 S rRNA gene were aligned using Clustal X (Higgins et al., 1996). Identification of the sequences was made after performing BLAST searches of the NCBI database.

12.2.3 Studied compounds

All chemicals of analytical grade were Ph, 4-CPh, 2,4-DCPh, catechol, and hydroquinone. These compounds were purchased from Sigma Chemical Co. All these chemical products had 99% purity. These compounds were prepared in different initial concentrations from 50 to 1000 mg L^{-1}.

12.2.4 Batch experiments

Erlenmeyer flasks of 250 mL capacity containing 90 mL of mineral media supplemented with different initial phenol concentrations were used for batch experiments. The flasks were inoculated with 9 mL of the preadapted microbial population (initial biomass concentration of 80.1 ± 1.42 mg L^{-1}, OD0 0.29–0.3).

The initial pH was 7.0. Reactors were shaken at 200 rpm in an orbital shaker at 25°C.

All experiments were performed in duplicates. Phenol concentrations in the aqueous solutions were periodically measured in duplicate. Serological bottles were used of 125 mL capacity having 30 mL of mineral media supplemented with a range of the phenol concentrations (50 to 1000 mg L^{-1}). The bottles were sealed with Mininert valves. The substrate consumption at each initial phenol concentration was tested individually (Fig. 12.1A).

Samples of the headspace were taken to evaluate the CO_2 production due to the phenol metabolization. The final CO_2 production was determined by using a gas chromatograph equipped with a thermal conductivity detector. The analysis conditions were the same as those reported previously (Ramírez-Sáenz et al., 2009). The CO_2 concentration in liquid was calculated using the dimensionless constant of Henry's law (H) at 25°C. Biomass concentration was also evaluated at different phenol concentrations. The entire set of experiments was performed in duplicate. Data on the substrate consumption,

the CO_2 produced, the product of the complete oxidation of the substrate, and the final biomass were used to perform the mass balance on carbon (C).

12.2.5 Trickling packed-bed reactor

The characterization of the lava rock packing material of TPBR was performed as previously described by Ramírez-Sáenz et al. (2009). *In situ* bacterial immobilization was facilitated by recirculation of the microbial culture, which was previously adapted to phenol, using a peristaltic pump at a flow of 0.11 L min^{-1}. The TPBR was made of the glass column of 0.25 m length and 2.5 cm internal diameter. The packed volume of the column was 0.250 L. Both gas and liquid streams were fed at the top of the reactor packed with lava rock. The gas stream of humidified air was fed into the reactor using a mass flow controller at the inlet flow of 0.25 L min^{-1}, and the recirculation of the liquid phase was provided with a peristaltic pump at a flow of 0.25 L min^{-1}. Sample ports were located in both the input and the output of the liquid stream.

The biodegradation of phenol was evaluated by recirculating a synthetic liquid stream with increasing concentrations of this compound. Liquid samples from the inlet and outlet of the reactor were periodically collected. The phenol concentrations were measured to determine the substrate consumption in the TPBR system (Fig. 12.1B).

12.2.6 Phenol ozonation procedure

The oxidation of the phenol solutions was realized in a semi-batch reactor (500 mL with a diameter of 5 cm and a height of 26 cm) with an ozone concentration of 28–30 mg L^{-1} and a gas flow of 0.5 L min^{-1} at pH values of 12 and 7.

12.2.7 Analytical methods

The Ph and CPh concentrations were determined using a spectrophotometer (Perkin-Elmet Lambda 2B) in both reaction systems: batch culture and TBPR. The corresponding maximum absorbances were as follows: for the Ph was 270 nm, for 4-CPh 225 and 280 nm, for 2,4-DCPh 200 and 285 nm, for catechol 275 nm, and for hydroquinone 289 nm. The Ph, CPh, and ozonation products (intermediate and final) were identified both after the ozonation and during the biodegradation tests by HPLC (Perkin-Elmer) equipped with the UV-Vis detector series 200. We used a reverse phase C-18 column (Nova Pack C-18, Waters). The mobile phase was water : acetonitrile : phosphoric acid (50:49.9:0.1) at a flow of 0.8 mL min^{-1}. Or-

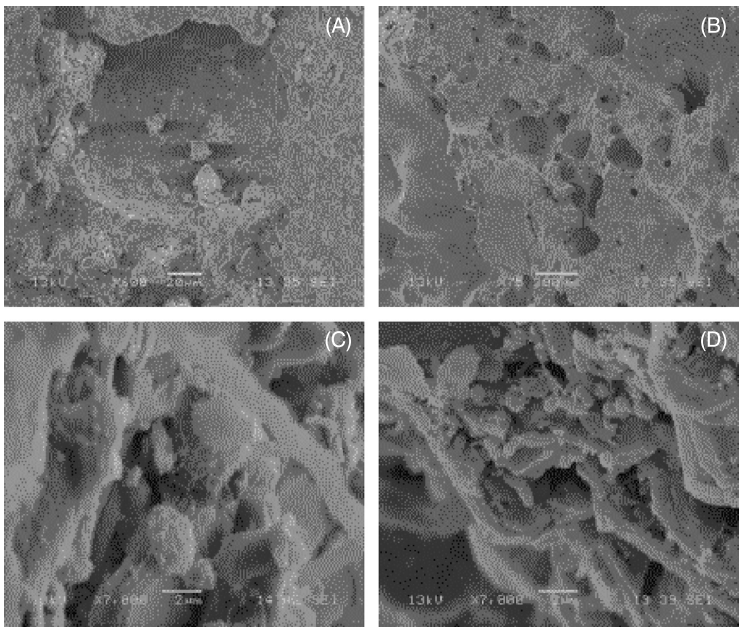

■ **FIGURE 12.2** SEM of porosity (A) and surface characteristics (B) of the support material; extra cellular polysaccharides (C) and microbial cells (D).

ganics acids were identified using the column Prevail Organic Acid, 5 μm (150 · 4.6 mm of Alltech).

Cell growth was determined spectrophotometrically by measuring the absorbance at $\lambda = 550$ nm. The calibration curves were obtained by plotting the dry weight of biomass per liter against the optical density of the suspension. Pieces of packing material having an average size of 1 cm were washed and prepared for scanning electron microcopy (SEM) observation as reported previously (Ramírez-Sáenz et al., 2009). In Figure 12.2A–D, the SEM microphotographs of supported materials and immovilized cells are shown.

12.3 RESULTS AND DISCUSSION

This section represents the results in three main parts: the first one describes the identification of the microbial population, the second one describes the pure microbial decomposition of different initial compositions including phenols and their chlorinated derivatives, and finally the third section describes the biodegradation of preozonated phenol mixtures.

12.3.1 Identification of the microbial population in preadapted cultures

The predominant bacterium, *Xanthomonas sp*, was found in both preadapted cultures (organic acids (1) and phenol (2)). The amplified 16 S rRNA sequences strongly match (99%) a 16 S rRNA sequence in GenBank for *Xanthomonas sp*. Another family of *Xanthomonas* was developed during the preadaptation to the organic acids. *Ancylobacter sp.* was also detected in both cultures, whereas *Rhodopseudomonas* was present only in the organic acids adapted culture. Some species of *Xanthonomas* have been found to degrade different pollutants. Recently, the bacterial strain *Xanthomonas sp.* ICH12, capable to biodegrade hexachlorocyclohexane (HCH), was isolated from HCH-contaminated soil (Manickam et al., 2007). *Xanthomonas autotrophicus* GJ10 was also found to be able to degrade 2-chloroethanol. Two strains of *Ancylobacter aquaticus* (AD25, AD27) were reported as able to grow and degrade 2-chloroethylvinylether (van den Wijngaard et al., 1993). *Rhodopseudomonas* is recognized as one of the most metabolically versatile bacteria; it grows both in the absence and presence of oxygen. Under aerobic conditions, it can degrade organic compounds such as succinate (Harrison and Harwood, 2005) and toxic compounds such as 3-chlorobenzoate (Kamal and Wyndham, 1990).

As one can see, when the phenol concentration is lowered, the reaction rate is almost unchanged. However, when the initial concentration increases, the reaction rate is not increased proportionally, which strongly depends on the type of microorganism.

The biomass production, obtained in this study (at different initial phenol concentrations in batch cultures), is shown in Fig. 12.3. The Haldane–Andrews model (Wolfram Mathematica 7.0) was used to fit the specific growth rate as a function of the phenol concentration.

The μ max, Ks, and Ki values were 0.2082 h^{-1}, 4.99 mg L^{-1}, and 392.76 mg L^{-1}, respectively. The data obtained in this work are in agreement with those reported in the literature (Banerjee and Ghoshal, 2010; El-Naas et al., 2010; Jiang et al., 2006; Saravanan et al., 2008; Wei et al., 2008; Yan et al., 2005). Based on these results, we can suggest that phenol causes partial inhibition of the cell growth at low concentration in the free cell culture, although microbial activity and substrate degradation continue at lower degradation rates.

The mass balance of carbon considering the total amount of CO_2 (mg of CO_2 in gas phase + mg of CO_2 in liquid phase) and biomass produced at different initial phenol concentrations are shown in Table 12.1. The initial

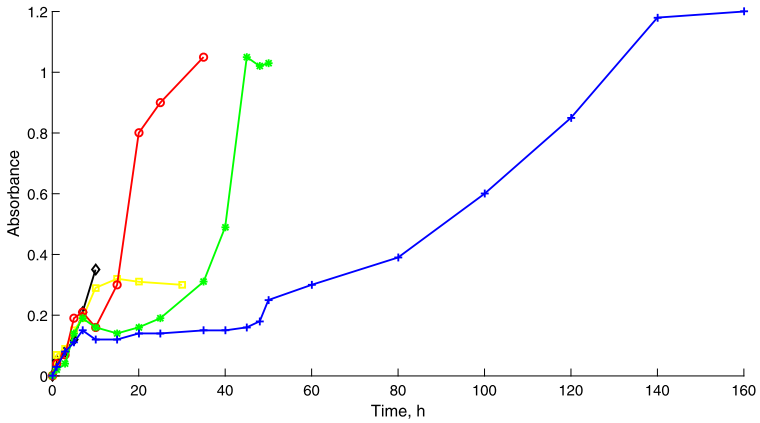

■ **FIGURE 12.3** Biomass accumulation at different phenol concentrations: 50 (black), 120 (yellow), 250 (red), 500 (green), and 800 (blue) mg L^{-1}. (Note: The color figures will appear in color in all electronic versions of this book.)

phenol concentrations of 120, 250, 500, and 1000 mg L^{-1} were partially mineralized to CO_2 yielding 45, 56, 45, and 57% conversion, respectively, at the end of the experiment. These conversions are statistically equal. Based on this result, one may conclude that the mineralization degree of phenols was independent of their initial concentrations. Taking into account the final amount of biomass measured at different concentrations of phenols (Table 12.1), 45.0, 26.0, 40.0 or 23.0% of the carbon was used for biomass production, respectively. The carbon balance in the experiments shows that approximately 80 to 90% of the consumed carbon may be recovered as CO_2 and transformed into biomass. The difference to close the C balance could imply that, under these conditions, phenol assimilation results in a transient accumulation of metabolic intermediates. Catechol, as the metabolic intermediate, was determined at the different stages of the culture. For the initial concentration of phenol of 250 mg L^{-1}, 1.6 and 2.3 mg L^{-1}, the catechol was measured in the liquid medium at 14 and 16 h of culture, respectively. After 27 h of culture, it was consumed and its final concentration of 0.27mg L^{-1} was found.

The data, mentioned above, suggest that the phenol was degraded through the catechol metabolic pathway and the transformation of this metabolic intermediate can be the limiting step of the process. In order to verify this hypothesis, the cultures were grown in the presence of hydroquinone or catechol, both at a concentration of 120 mg L^{-1}. These compounds were eliminated within 18 or 130 h, respectively. The degradation of byproducts obtained after preozonation could also be of interest, because compounds

Table 12.1 Mass balance of carbon, considering the total amount of CO_2 and biomass produced at the different initial phenol concentrations.

Substrate mg L^{-1}	Initial carbon mass in the substrate, mg	Final biomass production, mg	Carbon recovered as biomass, %
120	2.8	1.2	45
250	5.7	1.5	26
500	11.5	4.6	40
1000	23	5.4	23
Substrate concentration, mg L^{-1}	**Total CO_2 production, mg gas + mg liq**	**CO_2 production, mg**	**Carbon recovered as CO_2, %**
120	3.3	1.2	45
250	8.6	3.2	56
500	13.8	5.2	45
1000	34.9	13.1	57

such as hydroquinone and catechol are natural metabolic intermediates that could be used as a substrate for many bacterial strains.

12.3.1.1 Biodegradation of 4-chlorophenol and 2,4-dichlorophenol

The degradation of 4-CPh or 2,4-DCPh (100 or 120 mg L^{-1}, respectively) was analyzed in the batch shake flasks (Fig. 12.4). The 4-CPh was not consumed by the microbial consortium. A low initial reduction of the substrate concentration (approximately 5%) during the first hours of culture could be explained due to an absorption on the biomass, until equilibrium is reached (Zhao et al., 2009a). The initial concentration of 120 mg L^{-1} of 2,4-DCPh in the batch system was degraded 40% after 250 h of culture (Fig. 12.4).

This could be explained by the production of some metabolic intermediates that could be toxic to the microorganisms (Contreras et al., 2003). Some of the bacteria, found in the phenol preadapted culture, have been associated with a dechlorination activity. Therefore, it is reasonable to assume that this microbial community is responsible for the partial degradation of the 2,4-DCPh. The degradation of 2,4-DCPh in the TPBR was also evaluated at two different initial concentrations (100 or 200 mg L^{-1}). The degradation efficiency of 2,4-DCPh was 61 or 80%, respectively, after 45 h of culture (Fig. 12.4). In general, the CPhs were poorly removed by the microbial consortium. This result was expected because the CPhs were known to be resistant to biodegradation. The removal efficiency of 42% was determined for 10 mg L^{-1} of 2,4-DCPh by *Bacillus insolitus* (Wang et al., 2000). These

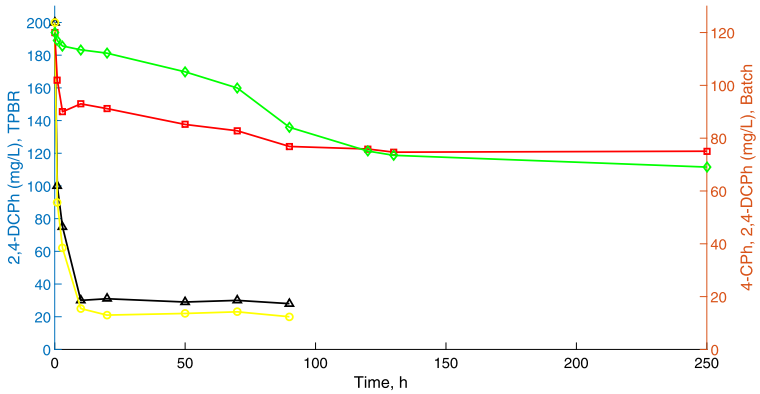

■ **FIGURE 12.4** Degradation of chlorinated phenols: 4-CPh (100 mg L^{-1}) (green) and 2,4-DCPh (120 mg L^{-1}) (blue) in batch culture. Degradation of 2,4-DCPh in the TPBR: 100 mg L^{-1} (red) and 200 mg L^{-1} (yellow).

data showed that the immobilized microbial consortium in the TBPR could be effectively used for the degradation of phenol, even at higher concentrations of 1000 mg L^{-1}. In contrast, the biodegradation was unsuccessful in the elimination of chlorophenols. Similarly, Essam et al. (2010) have reported the isolation of an *Alcaligenes* strain that was able to grow in the presence of phenol, but not chlorophenols.

12.3.2 Ozonation of phenol mixtures

12.3.2.1 Degradation of phenol using only ozonation

Phenol decomposition was also performed using only the ozonation procedure. The initial phenol concentration, similar to the one selected in the biodegradation, was used here. The complete phenol decomposition was achieved after 70 min. This time was extremely small compared to the one used to achieve the complete biological degradation of phenol; however, the chemical elimination produces a higher byproduct accumulation. This was the case even when hydroquinone and catechol were almost completely decomposed (90 and 85%, respectively).

Despite the fact that a high efficiency for phenol removal was obtained, when the ozonation was applied, the total organic matter was not completely eliminated. In consequence, the total organic carbon (TOC) content was not completely reduced, that is, pollutants cannot be decomposed to carbon dioxide and water (mineralization). The concentration of simple organic acids, obtained by the ozonation, was higher. In particular, oxalic and formic acids were accumulated (up to 50 mg L^{-1} for the formic acid), com-

pared to the biodegradation. The microorganisms, used to eliminate phenol, have proven to be efficient in decomposing these organic acids.

An alternative for decomposition of the organic acids is to combine ozonation as a pretreatment before biodegradation. Maybe, one drawback here is the final pH achieved after the phenol decomposition: it is in the range of 4 to 5. Microorganisms are not so efficient in that pH range, but this parameter can be adjusted before the biodegradation.

12.3.2.2 Degradation of chlorophenols using ozonation

Chlorophenols were also exposed to ozone using the same initial concentration as those considered in the biodegradation treatment. Ozonation was efficient in eliminating the chlorine from the chlorophenol, and its complete decomposition was achieved before 15 min.

Phenol was detected during the whole reaction period. Moreover, byproducts were accumulated for 30 min. After this period, all byproducts were almost completely degraded. Nevertheless, all organic acids were accumulated, specially the oxalic acid that reached a final concentration of 58 mg L^{-1}. Once again, ozone was not appropriate to eliminate this acid, because the larger concentration of this gas is required. All facts stated in this subsection are in agreement with results obtained by some authors in several studies published in recent years (Nam et al., 2001; Poznyak and Vivero, 2005; Poznyak et al., 2005).

12.3.3 Biodegradation of ozonated phenol mixtures

Several byproducts obtained after ozonation (such as catechol or some organic acids) may be used as a substrate by the microorganism identified within the consortium. Indeed, similar concentrations produced by the phenol ozonation were used to test the adapted microorganisms showing good growth dynamics.

12.3.3.1 Ozonation of phenol and chlorophenols

A preliminary treatment with ozone improving biodegradation at either high concentrations of phenol (1000 mg L^{-1}) or low concentrations of chlorophenols (120 mg L^{-1}) was performed.

Table 12.2 shows the required ozonation time to obtain the complete decomposition of chlorophenols, which was smaller than those reported in the literature (Benitez et al., 2003; Contreras et al., 2003).

After the ozonation, two strategies can be followed: to strip ozone from the liquid phase by injecting oxygen or to inoculate the liquid phase with the mi-

Table 12.2 Phenols' ozonation conditions.

Compound	Concentration (mg L^{-1})	pH	Time (s)
Phenol	1000	12	4380
4-Chlorophenol	120	7	1514
		12	484
2,4-Diclorophenol	120	7	1830
		12	307

croorganism in the presence of residual ozone. It is well known that residual ozone may affect the lag phase of biodegradation. The delay of the microorganism's growth phase enforced by ozone in the liquid phase does not have a significant effect on the final biomass concentration. A possible explanation of this behavior is that the final products, accumulated after ozonation, are taken by the microorganisms in advanced stages of their metabolism. As a consequence, ozonation improves the mineralization efficiency. Therefore, we may propose that this advance is due to the microorganism's metabolism only.

Despite the ozone negative effect on the biomass growth reported in different studies, all intermediates, obtained after phenol ozonation, are decomposed almost completely (between 10 and 80%). The best ozonation conditions for all phenols was at a pH of 12 because, the reaction time is reduced (307–484 s) and the ozonation time was fixed at 5 min. Additionally, the byproduct concentrations are reduced, but they are not completely eliminated. However, biodegradation succeeded to remove a big part of the remainder pollutants. Then it is straightforward to consider that microorganisms can metabolize the byproducts formed after the phenol ozonation.

12.3.3.2 Biodegradation of ozonated chlorophenols

Fig. 12.5A and B represent the UV spectrum variation of the 4-CPh and of the 2,4-DCPh (120 mg L^{-1}, which corresponds to an initial COD of 252.6 mg L^{-1}). These tests were obtained during the biodegradation after 10, 15, and 30 min of ozonation for 4-CPh and 8 min of ozonation for 2,4-DCPh.

The UV spectrum profiles of the 4-CPh are compared in Fig. 12.5A. The ozonated spectra show only the presence of organic acids (approximately 20% of the initial COD removal), found in the typical wavelength region for these compounds (210 nm).

Table 12.3 summarizes the intermediates and final products formed after ozonation at a pH of 7 or 12 after 191 h. One can note from this table that oxalic and formic acids are the main identified byproducts for all phenols.

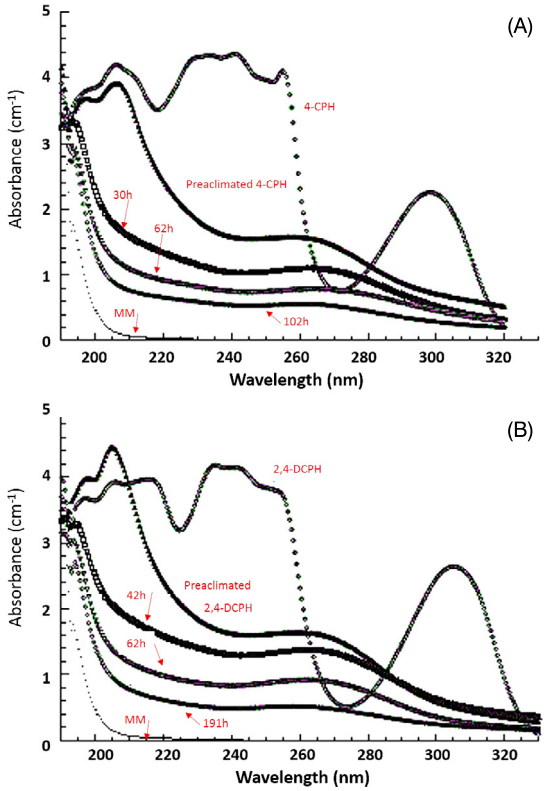

■ **FIGURE 12.5** (A) Variation in the UV spectra in batch culture. Mineral medium (MM) spectrum (dot), 4-CPh 120 mg L^{-1} (empty diamond), 4-CPh preozonated (filled triangle). Biodegradation of preozonated 4-CPh by a mixed microbial consortium at 30 h (empty square), 62 h (empty inverted triangle), 102 h (empty circle) of culture, respectively. (B) MM spectrum (dot), 2,4-DCPh 120 mg/L (empty diamond), 2,4-DCPh preozonated (filled triangle). Biodegradation of preozonated 2,4-DCPh by a mixed microbial consortium at 30 h (empty square), 72 h (empty inverted triangle), and 191 h of culture, respectively.

Also, all phenolic intermediates different from hydroquinone and cathecol were not detected, nor the organic acids that have been reported in other studies (Nam et al., 2001; Poznyak and Vivero, 2005; Poznyak et al., 2005). The variation of the intermediates in ozonation and biodegradation are not shown.

After 30 h of culture, 62.5% of the organic acids were removed and after 102 h, the 85% removal was obtained. After 10 h of culture, approximately 50% of the initial amount of oxalic acid was assimilated by the microbial consortium. Between 20 and 30 h of culture, formic acid was found in the liquid medium. After 40 h, this acid had been completely assimilated by microorganisms. These data show that formic acid was a possible

Table 12.3 Intermediates obtained in the phenols ozonation. BDL = below the detect level, ND = No identified.

Intermediate	Phenol 1000 mg L^{-1}	4-CPh 120 mg L^{-1}		2,4-DCPh 120 mg L^{-1}	
pH	12	7	12	7	12
Catechol	ND	10.0	ND	BDL	ND
Hydroquinone	BDL	10.0	BDL	BDL	BDL
Oxalic acid	50.0	32.0	31.0	63.8	27.0
Formic acid		46.9	ND	78.0	ND

metabolic intermediate during biodegradation, but this compound was completely eliminated after 40 h of culture.

Similar results for preozonated 2,4-DCPh (120 mg L^{-1}) were obtained. In this case, after 191 h of culture, 87% of the organic acids was removed. During the first 10 h of culture, oxalic and formic acids were excreted from the microbial cells. Between 15 and 30 h, both acids were simultaneously degraded and then almost completely assimilated after 40 h.

2,4-DCPh was not degraded by biodegradation. However, in the combination of the two processes, 85% of this compound was removed after 191 h. The degradation of 2,4-DCPh was enhanced from 40 to 87%.

The presence of organics acids and the remaining phenolic compounds still represent an important treatment challenge. The mixture of organics obtained after 8 min of ozonation was adequate for the microorganism growth, as shown by the significant reduction of the biodegradation time (191 h vs. 7 days).

An additional issue, considered here, is to define the best ozonation time. When different ozonation times (10, 15, and 30 min) are realized, the intermediates mixture, fed to the microorganism, is different. These times were selected observing the complete decomposition of chlorophenols (10 min) and the phenolic compounds (30 min). If the phenolic compounds are completely decomposed (30 min), the biodegradation process is not so effective, compared to the results obtained, when the chlorophenol solution is ozonated only for 10 min. This difference is explained by the mixture composition obtained after the ozonation. When the 4-CPh solution is ozonated for 10 min, cathecol is in the reactor. This compound is part of the metabolism of the main microorganisms identified in the consortium. When the initial mixture is ozonated for 30 min, only a mixture of the organic acids is obtained, that is, also a part of the microorganism's metabolism, but they are less attractive from the energetic point of view. The organic acid mixture, obtained after 30 min, is not efficiently decomposed compared with the 10-min ozonated mixture.

A similar result was obtained in the case of 2,4-DCPh with two different ozonation times (5 and 8 min) with a pH initially fixed to 7. The most remarkable aspect, which can be seen from this experiment, is that 8-min ozonated solution is better assimilated by the microorganisms because 2,4-DCPh was decomposed completely. Indeed, the biomass concentration was incremented up to 33%, when the solution was ozonated for 8 min and just up to 9%, when the ozonation was 5 min long.

The pH effect was also studied. The initial mixture was studied using two pH values (7.0 and 12.0). At basic pH, two positive conditions are obtained:

- The first one is associated with the combined reaction mechanism, appearing during ozonation.
- The second one is achieved by the final pH obtained after ozonation. When the pH is 7.0, the final pH is acid. This condition is not preferred for the identified microorganism strains. When the initial pH is 12, the final pH is close to neutral, which is the optimal condition for the microorganisms.

For 2,4-DCPh at an initial pH of 12, the biomass increment was 35%. Besides, the phenolic compounds were decomposed to 25% when the initial pH was 12, compared to the 34% at the pH of 7.0. Organic acids were decomposed with a final efficiency of 20% at both pHs. If the ozonated 4-CPh was biodegraded and the pH was 12, the biomass increment and the intermediate decomposition were similar to the pH = 7.0 case, but the ozonation time was 30 min. Therefore, a relevant decomposition improvement was obtained if the initial pH was 12 (Tables 12.4, 12.5).

Here we also define a class of criteria to connect the two processes: preliminary ozonation and biodegradation. Several papers have proposed mixed treatments, using a preliminary chemical process and the ulterior biological treatment, but no one of them (to the best of the author's knowledge) has discussed what the key aspect is to decide, when the mixture must be moved from the first to the second process. So, the ozonation time, which defines the intermediate mixture obtained, can be used as the keystone criterion to stop ozonation and start biodegradation.

12.4 REAL WASTE WATERS

The main product of the pulp and paper industry (PPI) is cellulose pulp. This product is obtained from the Kraft process applied to wood (cellulose 45%–50%, hemicelluloses 20%–25%, lignin 20%–25% and other organic extractable products 5%–25%). The remaining final components of the Kraft process consist of some other fibers and recycled material (Rowell,

Table 12.4 Summary of total concentration of organic acids, phenolic compounds, and biomass growth obtained by UV/Vis spectrum for 4-CPh.

Comp.	pH	O_3 time, min	Biodegradation, days	Biomass, absorb.	Phenols, mV	Org. acids, mV
4-CPh	7	10	0	0.507	4196	1695
			4	0.525	2126	661
			7	0.568	1278	159
		15	0	0.520	2945	1185
			4	0.527	1072	277
			7	0.574	838	221
		30	0	0.517	1508	746
			4	0.540	468	164
			7	0.551	327	110
	12	5	0	0.855	3869	1460
			4	0.902	1489	270
			7	0.957	1155	240

Table 12.5 Summary of total concentration of organic acids, phenolic compounds, and biomass growth obtained by UV/Vis spectrum.

Comp.	pH	O_3 time, min	Biodegradation, days	Biomass, absorb.	Phenols, mV	Org. acids, mV
2,4-DCPh	7	5	0	0.834	3376	1164
			4	0.858	1628	352
			7	0.900	1780	300
		8	0	0.689	2879	1289
			4	0.788	1430	313
			7	0.878	1031	283
	12	5	0	0491	2557	1023
			4	0.514	889	202
			7	0.566	784	205

2012). The cellulose goes through the chemical bleaching stage to eliminate some organic matter from the pulp. The resulting liquid stream contains organic compounds such as lignin and their derivatives: phenols, terpenes, steroids, tannins and resinic acids, dioxins, and dioxin-like compounds, which are the usual components of wood. These compounds are eliminated or transformed to chlorinated organic compounds at the bleaching stage in the Kraft process (Pokhrel and Viraraghavan, 2004). The main characteristics of the pulp and paper mills after the bleaching step are: high color

degree, large content of suspended solids, non-regulated levels of chemical oxygen demand (COD) and biological oxygen demand (BOD), abundant concentrations of chlorinated compounds and unstable pH range (Catalkaya and Kargi, 2007; Freire et al., 2001; Peng and Roberts, 2000).

These residuals, dissolved in PPI waste water, create a serious environmental problem. This is even more worrying taking into account that this industry is one of the biggest consumers of natural raw materials and one of the most significant toxic contaminants sources (solids, liquids, and gaseous effluents). In general, to produce only 1 ton of paper, 72 tons of highly contaminated liquid effluents are generated. This ratio may cause irreversible pollution of rivers, lakes, seas, and soils (Kansal et al., 2008). These residues have toxic, mutagenic, and genotoxic effects in some plants and animals (Johnsen et al., 1998; Tsang et al., 2007). Indeed, they contain lignin and its derivatives. Additionally, a complex mixture of inorganic compounds, which are highly recalcitrant and resistant to biological treatments, is regularly found in this kind of residual effluents (Karrasch et al., 2006).

Over the last two decades, a lot of different sewage treatments for these effluents were developed using physical, biological, and chemical methods or their combinations (De los Santos Ramos et al., 2009; Poznyak and Vivero, 2005; Ramalho, 1990; Rodríguez et al., 2006). All treatments are commonly controlled by BOD, COD, and TOC determinations.

Chemical treatments promote faster decomposition of many different highly concentrated toxic compounds (Amat et al., 2005b). Several authors studied discoloration of waste water samples from the Kraft process with ozone (Herath et al., 2011). Here, the reaction conditions were fixed to 240 min of reaction time and two different pH values (3 and 10). Under these conditions, a significant decrement of phenolic compounds after the treatment (70% and 52%, respectively) was attained. These methods were efficient, but expensive if the mineralization was the main goal of the treatment. The sequential application of flocculation–precipitation and ozonation (using the flocculation–precipitation like pretreatment to remove the undissolved organic and inorganic matter by decantation) yields a water clarification, as a result of the dissolved residues oxidation. This outcome also shows the increment of biodegradability (De los Santos Ramos et al., 2009; Tünay et al., 2008).

On the other hand, biological treatment is cheaper and more environmentally friendly tuned, but it requires longer reaction treatment time to eliminate pollutants and it exhibits microorganism inhibition, when bigger concentrations of contaminants and/or accumulation of toxic metabolites occur. In the textile and paper industries, different mixtures of microorgan-

isms (bacteria, fungi, and algae) were used to fulfill the biological treatments: *Pseudomonas mendocina, Pseudomonas alcaligenes, Curvulariaina equalis, Phanerochaet echrysosporium, Pleurotus sajorcaju, Pleurotus ostreatus* and many others to eliminate organic matter (Belem et al., 2008; Husain, 2010; Ruiz-Dueñas and Martínez, 2009). Researchers working with a fungal strain (*Aspergillus awamori*) were successful to biodegrade 1 g L^{-1} of some toxic organic compounds successfully (such as phenol, catechol, 2,4-dichlorophenol, and 2,6-dimethoxyphenol). Certainly, they obtained their complete decomposition in 3, 5, 7, and 8 days, respectively (Stoilova et al., 2006).

Taking into account that effluents, generated during the bleaching stage, contain suspended solids, a primary treatment is usually made using different types of filters. The secondary and tertiary treatments are usually performed by conventional methods, but the elimination of soluble organic matter is not efficient, because BOD and COD remained above the reported levels in different local and national legislations (Sridhar et al., 2011).

This inefficient result motivates the idea of ozonation, followed by biodegradation, to represent a suitable alternative for the treatment of a complex mixture of organic compounds that can be found in the residual effluents of the pulp and paper industry. This kind of treatment, formed by the sequence of ozonation and biodegradation, has been tested in some preceding studies (Ali and Sreekrishnan, 2001; Assalin et al., 2009; Poznyak and Vivero, 2005; Ratledge, 2012), (De los Santos Ramos et al., 2009; Guerra et al., 2013; Laari et al., 2000). However, in the cited work, only different model compounds (analytical degree) or actual waste water without identification of contaminants before and after treatment were considered. Moreover, the final toxicity of organics mixture has not been evaluated.

12.4.1 Materials and methods

12.4.1.1 Waste water samples preparation

Residual water samples were taken from the effluent of the bleaching stage of a typical Kraft process. These samples were taken from an anonymous private company located at Morelia, Michoacan, Mexico. In the first stage of this specific Kraft process, white liquor formed by sodium hydroxide (NaOH) and sodium sulfide (Na_2S) is used to cook wood in digesters at higher temperature and pressure. The cooked wood is moved from the digester and washed to separate the cooking chemical and dissolved organics from the fibers. These fibers are further processed according to the following sequence. One round of chlorination followed by two rounds of extraction and application of dioxine formed the waste water treatment. Then the

shorthand description of the bleaching process is CEDED, according to the standard notation on the process of pulp and mill production.

All samples were collected and stored at 4°C. These samples were sterilized in a regular autoclave at the temperature of 12°C and a pressure of 15 psi during 20 min. To avoid the characteristic foaming of real waste water, and also to simplify the analysis of the samples, the untreated residual water was diluted 1:10 with distilled water and they were used in all experiments. After dilution, the main physicochemical characteristics of the residual water were pH = 8, $SDT = 3.5$ g L^{-1}, coloration of 1400 cu measured by the Pt_Co method (Murillo, 2011), a COD of 670 mg L^{-1}, and conductivity of 1.0 mS/cm. All results were reported for the original sample. The diluted sample was prepared in order to obtain a sample that can be analyzed by standard spectroscopic and chromatographic methods. Even when all results can be reported using the reverse factor (10), these rescaled results cannot be directly ensured for the original waste water. One may notice that this is a regular method, when real waste waters are considered, because the levels of color units and the concentrations of diluted organics might be above the maximum level of detectability in the aforementioned specialized equipment.

12.4.1.2 Ozonation procedure

An ozone/oxygen mixture flow of 0.5 L min^{-1} with an initial ozone concentration of 30 mg L^{-1} is injected through a ceramic porous filter in the semi-batch glass reactor (0.25 L) with samples of 0.10 L (ii) during 30 and 60 min. The ozonation system has been already depicted in Chapter 1.

12.4.1.3 Biodegradation procedure

The operational conditions of the biological treatment were selected based on a previous investigation (García-Peña et al., 2012). The biodegradation was carried out in a batch reactor with constant magnetic agitation of 300 revolutions per minute, at a fixed pH of 7.0 at ambient temperature (Fig. 12.6). Erlenmeyer flasks of 0.25 L containing 0.1 L of mineral media (1.0 L of solution contains 3 g $(NH_4)_2SO_4$, 0.6 g KH_2PO_4, 2.4 g K_2HPO_4, 1.5 g $MgSO_4 \bullet 7H_2O$, 0.15 g $CaSO_4$, and 0.03 g $FeSO_4$) were supplemented with:

- Inoculum of the preacclimated consortium (with phenol and acids, Ph:A = 1:1) to the original sample.
- Inoculum of the preacclimated consortium (with oxalic and formic acids (OFA)) to the ozonated samples.

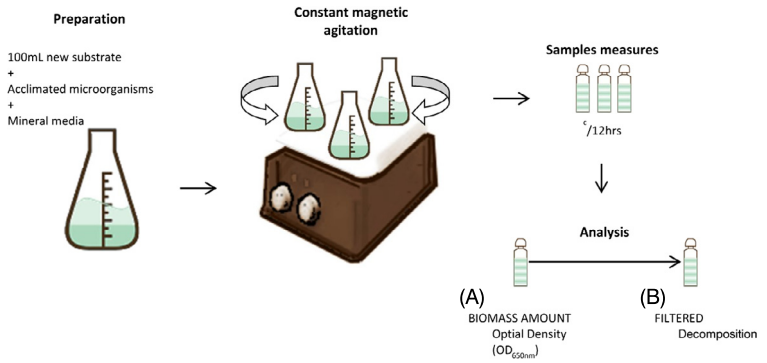

■ **FIGURE 12.6** General diagram of biodegradation.

To obtain the best consortium acclimation, the method of fill-and-draw (F&D) (Vazquez-Rodriguez et al., 2006) was used. Here, a complex microbial consortium was used to perform the biodegradation that has been previously identified (García-Peña et al., 2012) by the extraction of DNA samples using an Easy-DNATM Kit (Invitrogen, USA).

The predominant microorganisms for this consortium are the bacteria *Xanthomomnassp, Rhodopseudomonassp*, and *Ancylobactersp*, which can degrade chlorohexanes (Manickam et al., 2007), 2-chloroethanol and 2-cloroetylvynyl ether (van den Wijngaard et al., 1993), 3-chlorobenzoate (Kamal and Wyndham, 1990), etc. During all biological procedures, the bonus amount and the organic degradation were measured through time.

12.4.1.4 Analytical methods

This section describes the set of analytical methods used to characterize, identify, and quantify the effect of the proposed treatment on the samples.

UV-Vis spectroscopy (Perkin-Elmer Lambda 25) was used to obtain the preliminary information of the treatment efficiency and monitoring the organic compound decomposition in ozonation (at 210 nm and 260 nm). These absorbances are selected as characteristic for lignin and its derivatives (260 nm), as well as simple organic acids (210 nm).

Discoloration (465 nm) and biodegradation efficiency of the organic source (210 nm) of real water and microbial growth (600 nm) were also determined using the same technique. The initial composition of the mixture of organic compounds, intermediates, and final products formed in the ozonation and biodegradation stages were partially identified by a high performance liquid chromatography (HPLC, Perkin-Elmer, Series 200) with UV-detector at 210 and 260 nm under different analysis conditions.

Table 12.6 HPLC analysis conditions for the identification of intermediates and products of ozonation and biodegradation.

Ozonation				
	I	**II**	**III**	**IV**
Column	Nova Pack C-18, 250 · 4.6 mm: 10 µm			Prevail Organic Acid, 150 · 4.06 mm
Mobile phase	CH_3OH–H_2O (50:50)	C_2H_3N–H_2O (30:70)	C_2H_3N–H_2O (70:30)	H_2O–KH_2PO_4
Flow rate, mL min^{-1}		1.0		
Injection volume, µL	30	30	30	30
λ, nm		260.0	260.0	210
		210.0	210	
Biodegradation (V)				
Col V		Prevail Organic Acid, 150 · 4.06 mm		
Mobile phase		H_2O–KH_2PO_4		
Flow rate, mL min^{-1}		1.0		
Injection volume, µL		30		
λ, nm		210.0		

In Table 12.6, the HPLC analysis conditions for the identification of intermediates and final products of either ozonation and biodegradation are detailed. The five selected methods of the analysis were used to obtain a better separation of the complex mixture, contained in the samples of the residual water. Thus, the methods I and III were used to obtain the time variation for the concentration of phenolic compounds, the method II was specifically used to get the characterization of phenolic compounds and acids. Finally, the methods IV and V were specifically applied to separate and characterize the distribution of organic acids.

To determine the efficiency of the contaminant degradation, the identification of the raw material and the products of the ozonation and biodegradation was carried out by a gas chromatograph with a mass detector, the GC-MS Claurus600 Perkin-Elmer with helium as a carrier gas, 0.8 mL min^{-1} was the feed flow, the split ratio was 1:20 and the temperature of the analysis was 230°C. In Table 12.7 the GC-MS analysis conditions are presented.

12.5 RESULTS AND DISCUSSION

An initial GC-MS analysis was made to characterize the content of untreated residual waste water. The sample of residual water contained a wide vari-

Table 12.7 GC-MS condition used to determine the concentrations of the initial contaminants and their byproducts.

Column	Elite 5MS; 30 m × 0.32 mm × 0.25 mm
Mobile phase	Helium
Sample volume, µL	0.5
Split	20%
Flow rate, mL/min	0.8
Injector temperature	230
Temperature program	60°C@3 min; 60–240°C 30°C/min 240°C@10 min
Source temperature	230°C
Transfer temperature	230°C
Ionization energy, eV	70
Mass, m/z	25 to 400

ety of organic compound groups, such as aliphatic, aromatic, chlorinated, polar (acids, esters, ketones, etc.). In general, about 80 organic compounds (C_1–C_{28}) were identified (Tables 12.8–12.11). These compounds were selected from the fragment graphs considering the most abundant peaks. A more detailed characterization of compounds included in the original waste water sample was obtained with the sequential extraction of sample with chloroform, by acid hydrolysis and classification according to the Carrez II method

Three treatment methods were evaluated: ozonation, biodegradation (without preliminary ozonation), and combined treatment (sequential scheme with ozonation followed by biodegradation). The original residual water sample was chosen as a control for comparison purposes (WoPT). A set of experiments was executed to evaluate the conventional biodegradation without preliminary ozonation. Two different ozonation experiments were carried out: the first one was stopped after 30 min (M300) and the second one was stopped after 60 min (M600) of ozonation. These two specific reaction periods were chosen, because under the selected experimental conditions the byproducts, formed in ozonation, achieved their maximum concentration (measured in terms of TOC) after 30 min of ozonation, meanwhile these byproducts were almost undetectable after 60 min Results obtained in each treatment are described below.

Table 12.8 Composition of original residual water obtained by GC-MS. MW = molecular weight, RT = retention time.

Waste water					
RT	**Formula**	**MW**	**RT**	**Formula**	**MW**
1.620	CH_3OH	32	6.98, 8.22	$C_{10}H_8$	128
3.33	C_2Cl_4	164	5.317	$C_{10}H_{20}$	140
4.633	C_5H_8O	84	4.833, 6.30, 8.068	$C_{10}H_{22}$	142
4.450	$C_5H_{10}O_3$	118	5.37, 6.15, 6.20, 6.45, 6.70	$C_{10}H_{24}$	144
1.700	C_5H_{12}	72	7.65, 7.35, 7.75	$C_{11}H_{10}$	142
5.620	$C_6H_4Cl_2$	146	7.070	$C_{11}H_{16}$	148
2.100	C_6H_6	78	8.068	$C_{12}H_{10}$	154
2.075	C_6H_{10}	82	5.7, 5.8, 6.02, 6.07, 7.07	$C_{11}H_{24}$	156
1.98, 2.12	C_6H_{12}	84	8.22, 8.29, 8.3, 8.4, 8.47	$C_{12}H_{12}$	156
2.42, 3.15	$C_6H_{10}O$	98	8.59, 8.64	$C_{13}H_{12}$	168
1.75, 1.78, 1.8, 1.87, 1.97	C_6H_{14}	86	7.55, 11.29	$C_{12}H_{26}$	170
2.849	C_7H_8	92	8.69, 8.80–8.97	$C_{13}H_{14}$	170
3.62, 4.25	C_7H_{14}	98	9.60	$C_{14}H_{12}$	180
5.2	$C_7H_{14}O_3$	146	9.09, 9.23	$C_{14}H_{14}$	182
2.15, 2.22, 2.43, 3.45, 4.24, 4.97	C_7H_{16}	100	9.42	$C_{14}H_{16}$	184
11.27	$C_8H_{14}O_4$	174	10.62	$C_{14}H_{18}O_4$	250
3.660	C_8H_{16}	112	16.94	$C_{16}H_{22}O_4$	278
2.50, 2.58, 2.75, 2.8, 2.88, 3.2	C_8H_{18}	114	10.42	$C_{17}H_{34}O_2$	270
4.68, 5, 5.08, 5.17, 5.25, 5.42, 5.67	C_9H_{12}	120	9.84	$C_{18}H_{38}$	254
4.967	$C_9H_{16}O$	140	11.47	$C_{19}H_{36}O_2$	296
4.57, 4.77	$C_9H_{18}O$	142	14.52, 16.24	$C_{26}H_{54}$	366
4.38, 6.751, 6.98	C_9H_{20}	128	16.51	$C_{28}H_{34}O$	286

12.5.1 Ozonation

The sample discoloration (obtained at $\lambda_{max} = 465$ nm) was observed during the first 60 min of ozonation. Reduction of color units from 1400 to 304 cu (experimental data are not presented) was obtained (78%).

In Fig. 12.7, the time variation of lignin and its derivatives and simple organic acids in ozonation (obtained by the UV absorbance measured at 260 nm and 210 nm, respectively) are shown. Absorbance of lignin derivatives is reduced in 67%, after the first 3 min of ozonation. On the other

Table 12.9 Composition of treated water extracted with chloroform MW = molecular weight, RT = retention time.

Extract by CH_3Cl		
RT	**Formula**	**MW**
1.620	CH_3OH	32
1.72	C_5H_{12}	72
2.25, 2.37, 2.48	$C_5H_{12}O$	88
5.12	C_6H_8O	96
2.8, 2.92, 3.19, 3.68	$C_6H_{10}O$	98
4.95	C_6H_{12}	84
1.77, 1.8, 1.88, 1.99	C_6H_{14}	86
2.48	C_7H_{16}	100
3.13, 5.27	$C_7H_{14}O$	114
2.53	$C_7H_{16}O$	116
8.75, 8.84	$C_8H_{12}O_3$	156
3.62	$C_8H_{18}O$	130
6.32	$C_{11}H_{24}$	156
7.001	$C_{12}H_{26}$	170
9.85	$C_{13}H_{28}$	184
6.77	$C_{15}H_{32}$	212
9.39	$C_{15}H_{28}O_2$	240
13.28, 14.02	$C_{20}H_{42}$	282
18.67	$C_{26}H_{54}$	366

Table 12.10 Composition of treated water after acid hydrolysis. MW = molecular weight, RT = retention time.

Acid hydrolysis H+		
RT	**Formula**	**MW**
1.62	CH_3OH	32
3.29	C_2Cl_4	164
1.83	C_6H_{12}	84
2.28	C_7H_{16}	100
6.82	$C_{12}H_{16}$	160
9.49	$C_{12}H_{24}$	168
13.95	$C_{14}H_{12}O_4$	244
10.64	$C_{16}H_{22}O_4$	278
11.77	$C_{18}H_{38}$	254

Table 12.11 Composition of original residual water obtained by GC-MS (Carrez classification).

Carrez classification II		
RT	**Formula**	**MW**
1.61	CH_3OH	32
4.817	$C_5H_8O_4$	132
1.782	$C_5H_{10}O_2$	102
2.08	C_6H_{12}	84
5.08	$C_6H_{10}O_3$	130
3.066	$C_6H_{12}O$	100
6.418	$C_6H_{12}O_2$	116
4.917	$C_6H_{14}O_2$	118
1.82, 1.85, 1.87, 1.95	C_6H_{14}	86
2.28	C_6H_8	80
4.82, 4.92, 5.08	C_7H_{16}	100
4.583	$C_7H_{14}O$	114
7.085	$C_7H_{14}O_2$	130
1.948	$C_7H_{16}O$	116
7.651	$C_8H_{16}O_2$	144
1.948	$C_7H_{16}O$	116
7.651	$C_8H_{16}O_2$	144
2.933	C_9H_{20}	128
15.27	$C_{18}H_{38}$	254
12.57	$C_{11}H_{24}$	156
13.64	$C_{20}H_{42}$	282

hand, organic acids absorbance is reduced in 83%, after the first 2 min of ozonation.

The HPLC analysis of intermediates and final products proved the existence of oxalic, fumaric, maleic and formic acids, as well as of some phenolic compounds (pseudocumene; 3-methoxy-methyl-ester-propanoic acid; catechol, hydroquinone, dichlorobenzene, decanoic-acid-methyl-ester). Figs. 12.8 and 12.9 depict the behavior of some identified toxic compounds formed in ozonation. In particular, catechol and hydroquinone were almost entirely (99.0%) removed after 20 and 30 min of ozonation, because their decomposition reaction constants were $k = 3.0 \cdot 10^5$ L mol^{-1} s^{-1}. All other identified (except oxalic acid) byproducts obeyed the same dynamics and they were decomposed within the ozonation time (Fig. 12.8).

After 30 min of ozonation, the lignin and their derivatives were transformed into simple organic acids (94%). However, the organic acid concentration changed just 4% during the next 20 min of ozonation, and after this time

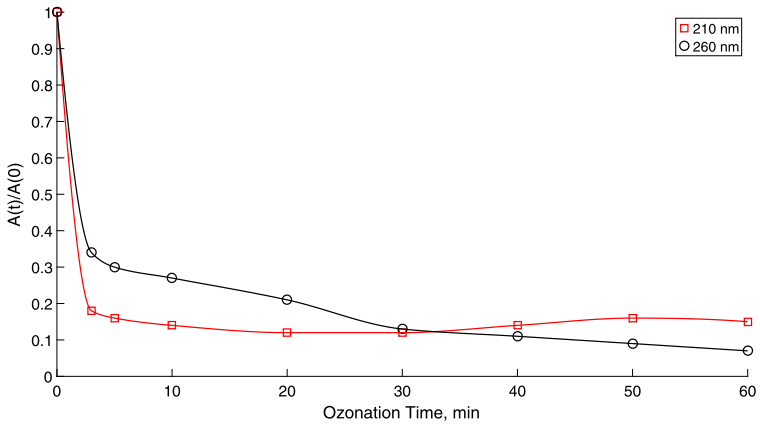

■ **FIGURE 12.7** Time variation of lignin and its derivatives (280 nm), and simple organic acids (210 nm) in ozonation.

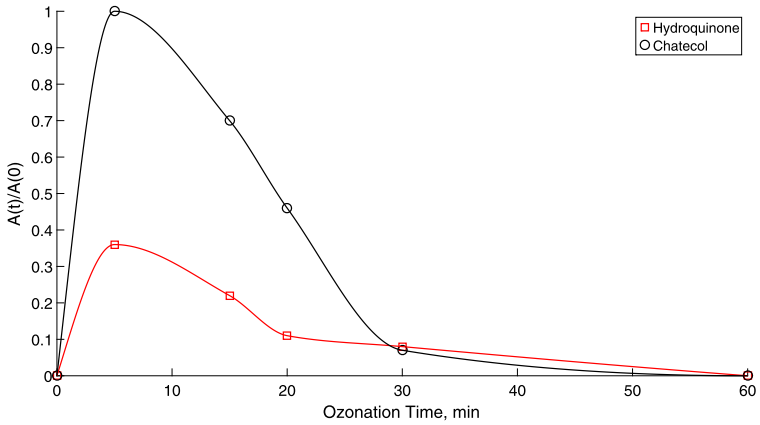

■ **FIGURE 12.8** Decomposition behavior of hydroquinone and chatecol obtained by HPLC.

the concentration did not vary at all. This behavior can be explained considering that these compounds are not reactive with ozone (Fig. 12.9). As an example, $k < 4.0 \cdot 10^{-2}$ L mol^{-1} s^{-1} was calculated for oxalic acid, which was in the same range of values found by some other authors (Hoigné and Bader, 1983b; Munter et al., 1993). Oxalic acid was recognized as the main accumulated byproduct.

Oxalic acid, as the final product of ozonation (recalcitrant product), was accumulated during the entire ozonation, and its concentration changed from 2.4 mg L^{-1}, in the initial residual water sample, to 55.0 mg L^{-1}, after

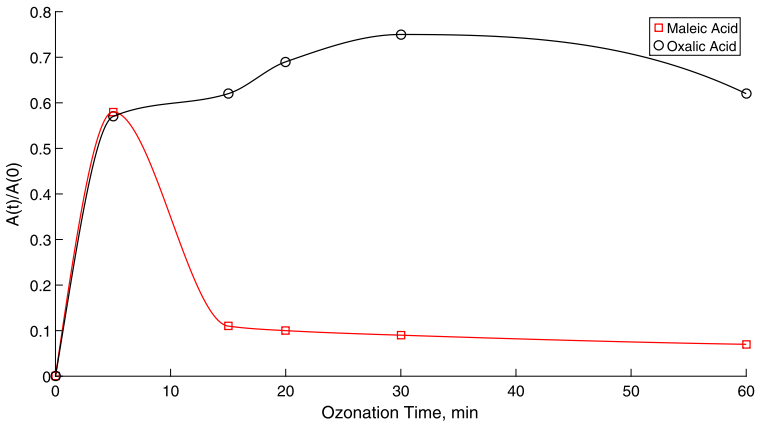

■ **FIGURE 12.9** Decomposition behavior of maleic acid and oxalic acid obtained by HPLC.

60 min of ozonation. This variation is a consequence of interaction between organic high molecular weight compounds and ozone.

12.5.2 Inoculum acclimation prior to biodegradation

Biodegradation was applied after the preliminary acclimation of microorganisms, which was important to improve the mineralization degree of the organic matter. This strategy was proposed to make a fair comparison between the results obtained in the ozonation treatment and the sequential process.

Three series of experiments were executed considering the acclimation procedure. The first series used a sample without pretreatment with ozone, and this mixture of the acclimated microorganism consortium was used for the comparison purposes (WoPT). The second set of experiments used the sample pretreated with ozone for 30 min (M300). The third one used the sample pretreated with ozone for 60 min (M60O). In the last two cases, the acclimated microorganisms consortium was referred to as organisms fold to the ambient (OFA).

This stage used a specific carbon source and a set of 10 biodegradation cycles (5 days, each one) of consortia maintenance (García-Peña et al., 2012) was implemented. In this phase, the microorganisms were forced to consume higher concentrations of the substrate. As a consequence, their proliferation, as well as the consumption of the organic source, increased.

Figs. 12.10, 12.11, and 12.12 show the growth of microorganisms during the acclimation phase in the three different experiments, described above. When the first cycle of 5 days was evaluated, the biomass growth was 12

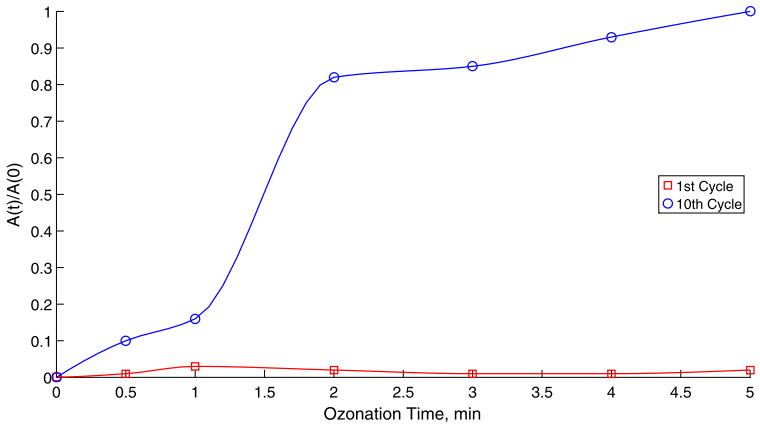

■ **FIGURE 12.10** Microorganism growth dynamics in the first and the tenth cycles of acclimation with the specific organic source in WoPT.

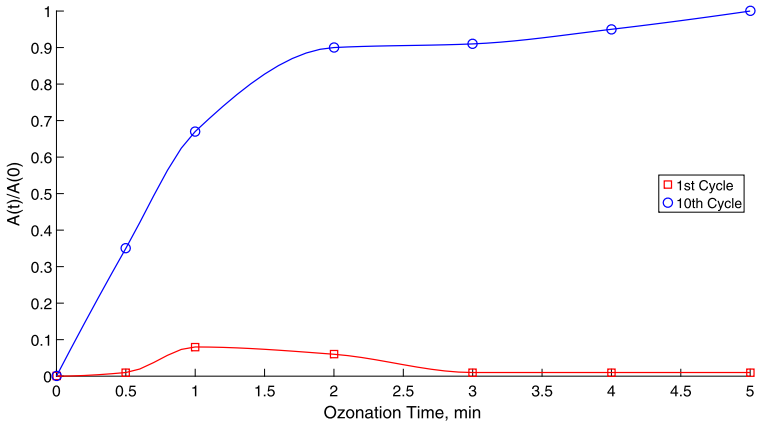

■ **FIGURE 12.11** Microorganism growth dynamics in the first and the tenth cycles of acclimation with the specific organic source: sample previously ozonated by 30 min in M300.

times smaller than the one observed when the tenth cycle of acclimation was considered. This condition was obtained with and without the preliminary ozonation and also appeared no matter what the preliminary ozonation time was.

The effect of the previous ozonation was evident on the biomass accumulation. When no previous treatment was applied to the biodegradation, biomass growth was slower than the growth observed in the experiments with previous ozonation. However, after 10 cycles of acclimation (Figs. 12.10, 12.11, and 12.12), despite the prior treatment with ozone, the

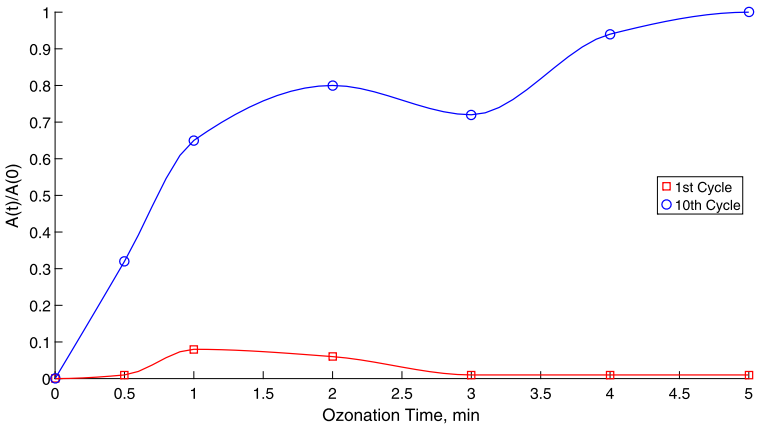

■ **FIGURE 12.12** Microorganism growth dynamics in the first and the tenth cycles of acclimation with the specific organic source: sample previously ozonated in M600.

same trend of biomass accumulation was observed for the sets of experiments, when ozonation was used as pretreatment. The acclimation procedure was efficient in improving the capability of microorganisms to use the specific byproducts mixture (mainly organic acids) as carbon source. Moreover, this strategy provided a more adequate form to compare the decomposition efficiency results for the pulp and paper industry waste water.

The short initial lag phase, observed in the microorganism growth, does not allow one to use a regular modeling strategy to characterize the effect of the acclimation on biomass growth. Moreover, the specific biomass quantification method was not implemented. Therefore, the biomass accumulation in the tenth cycle of the acclimation was modeled as pseudomonomolecular kinetics, as a useful strategy to characterize the biomass growth. The selected model was

$$A = A_{max}(1 - e^{-bt}),$$

where A is the absorbency measured at 600 nm, A_{max} is its corresponding maximum absorbency, and t is the reaction time.

For comparison purposes, the treatment without the acclimation and without prior ozonation was also investigated. In this case, the constant b was $0.48\ d^{-1}$. If the set of microorganisms was acclimated during 10 cycles, this kinetic parameter was modified to $1.13\ \mathrm{h}^{-1}$. This variation obeyed the selective growth of microorganisms that were able to degrade the compounds in the water samples. A similar increment of the same parameter was detected for the cases that the pretreatments with ozone were carried out. Similar

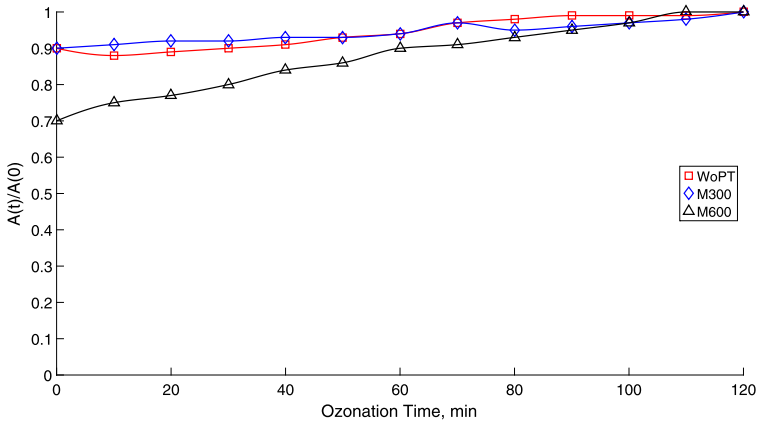

■ **FIGURE 12.13** Microbial growth for the WoPT and pretreated samples of M300 and M600 at the initial pH = 7.

variations of parameter b were observed when preozonated samples were analyzed.

12.5.3 Biological treatment without ozonation

The biodegradation with the acclimated microorganisms showed an incomplete decomposition of the organic compounds considering the complexity and heterogeneity of the waste water samples. In general, after 120 h of treatment, the increment of the optical density (OD at 600 nm) indicated only the partial decomposition of the organic compounds in 20%:10% in the first 20 min and, 10% additional after 50 min of ozonation, without variation until the end of the experiment. The lines labeled WoPT in Figs. 12.13 and 12.14 show these tendencies. These experiments also proved that despite the acclimation, the variability of waste water sample may reduce the effectiveness of the microorganism to decompose organic matter.

12.5.4 Combined treatment

Figs. 12.13 and 12.14 also show the global degradation of organics obtained as a result of the combined sequential treatment. The UV-Vis spectra at $\lambda =$ 210 nm, corresponding to the concentration of simple acids, and the OD at 600 nm in both experiments with 30 and 60 min of ozonation were used as general indicators of the biomass growth in the biodegradation treatment. After ozonation, most of the organic matter was decomposed to the oxalic acid and other acids.

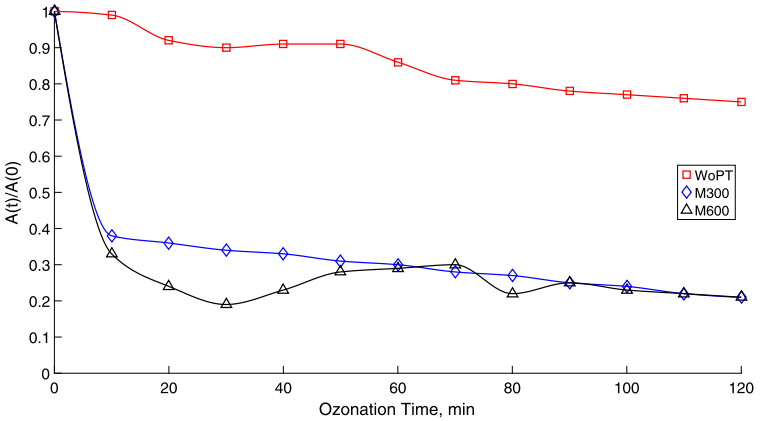

■ **FIGURE 12.14** Biodegradation of organic matter for the WoPT and pretreated samples of M300 and M600 at the initial pH = 7.

After biodegradation, all of these acids are metabolized to CO_2, H_2O, and some additional non-toxic metabolites. Notice that these results motivate the application of sequential treatment. Two treated samples significantly reduced the pollutants content after the first 12 h of the combined process in 72% for the M300 and 78% for M600. As it can be observed, the degradation of all compounds started from the first minutes of the process. If the pretreatment with ozone was executed for 60 min, the organic matter was 78% eliminated during the first 30 h. However, its concentration did not change from 30 up to 120 h. This behavior can be attributed to the formation of some specific metabolites that inhibit the growth of microorganisms.

At the end of the bioprocesses (after 120 h), the total decrement of the organic matter reached 82% for M300 and 83% for M600. The preliminary ozonation guarantees the increased biomass accumulation. This is a consequence of the effect of the substrate composition, obtained after ozonation. One may notice that lower ozonation times may have the same decomposition effectiveness after 120 h of treatment. Moreover, a similar decomposition effectiveness is achieved just after 50 h of treatment. The reduction of treatment time (120 vs. 50 h) represents the first step towards the possible optimization of the pulp and paper waste water treatment.

The characterization of the microorganism growth can be done by estimating the specific growth rate (SGR or λ_{max}). This parameter was calculated using a Monod reaction rate. Without the previous ozonation, the SGR was calculated as $\lambda_{max} = 8.33 \cdot 10^{-4}$ h^{-1}. If the preliminary ozonation was run out for 30 min, the SGR was increased up to $2.08 \cdot 10^{-3}$ h^{-1}. This impor-

tant increment of SGR was explained by the effect of ozone, which increases their biodegradability.

If the preliminary ozonation was performed for 60 min, the SGR was reduced to $6.05 \cdot 10^{-4}$ h^{-1}, which can be explained by the reduction of the microorganisms capability to eliminate the polar compounds (C_5–C_{17}), which were formed after this ozonation time. The presence of these polar compounds (organic acids) decreased the SGR to a level below the one obtained in conventional biodegradation. In this particular case, it was demonstrated that oxidized products were not attractive for microorganisms as the carbon and energy sources.

As was known from previous HPLC analysis of the treated samples, the main recalcitrant product formed during the ozonation was the oxalic acid. Therefore, its decomposition dynamics was studied using the same three sets of experimental conditions as described above. The global effect of the biodegradation was the mineralization of the oxalic acid. Oxalic acid concentration was reduced for all the three systems, with and without ozonation.

The final oxalic acid concentration decreased to 18% in the non-ozonated sample, and it was decreased similarly by 90% for both pretreated samples ($M300$ and $M600$). However, the best result was reached, when the waste water sample was ozonated during 30 min (M300), because the ozonation time was reduced by 50%. The mineralization of oxalic acid with other intermediates was confirmed by the determination of TOC that decreased down to 80% after 30 min of ozonation (from 680 up to 150 mg L^{-1} in the diluted water samples).

Furthermore, the results obtained by GC-MS, confirmed that after ozonation the water samples contained different organic compounds from those obtained at the original sample (Tables 12.12–12.13). In Table 12.14, a summary is presented of the results obtained by the GC-MS technique of the original and treated water samples. Indeed, during the bioprocesses, 23 compounds from 38 (60%) were eliminated after 30 min of ozonation. In general, the compounds eliminated were organic acids, fatty acids, esters, and ketones, among others. At the end of the experiments the accumulation of the heavy alkanes (C_{27}, C_{28}) and polar compounds was observed, which can be characterized as possible products of the bacterial metabolism. Even when there is not a detailed characterization of byproducts, formed during the sequential treatment, one may notice a relevant variation of the organics distribution after treatment. Moreover, there is a significant decrement in the average molecular weight of byproducts. This is an indirect confirmation that biomass growth consumes a high percentage of organics of high molecular weight.

Table 12.12 Composition of organic compounds after ozonation and after biodegradation (a). MW= Molecular weight, BB=Before biodegradation, AB=After biodegradation.

No	Comp.	MW	M300		M600	
			RT BB	RT AB	RT BB	RT AB
1	CH_4O	32	1.30	1.32	1.30	1.27
2	$C_5H_{10}O$	118	4.47	5.68	4.47	
3	C_6H_6	78	2.09			
4	$C_6H_{10}O$	98		3.19		
5	$C_6H_{12}O$	100		2.58		2.58
6	C_6H_{12}	84		1.98 2.13		
7	C_6H_{14}	86		1.87		
8	$C_6H_{12}O_2$	116		3.37		
9	$C_6H_{12}O_3$	132		3.98	4.67	3.98
10	C_7H_8	91	2.82			
11	C_7H_{14}	98	2.03 2.25			
12	$C_7H_{12}O_4$	160			4.78	5.23
13	$C_7H_{14}O_2$	130			2.13	
14	$C_7H_{14}O_3$	146		5.28		
15	C_7H_{16}	100	2.12 2.28 2.50			2.87
16	C_8H_{10}	106	3.97 4.07 4.33		3.97	
17	C_8H_{18}	114	2.22 2.43 2.52 2.90 3.32 6.42		4.33 2.43	3.37
18	$C_8H_{14}O$	126			2.52	

12.6 NUMERICAL SIMULATIONS OF COMBINED PROCESSES USING DNNO

The search for the optimal experimental conditions to establish the combined treatment may use a simple mathematical model of the two processes in interconnected form. This model can be eventually used to formulate the theoretical solution of the best ozonation time, which is recognized as the most important parameter that may enhance the degradation of complex contaminants mixture. The model also can be used to predict how the

Table 12.13 Composition of organic compounds after ozonation and after biodegradation (b). MW= Molecular weight, BB=Before biodegradation, AB=After biodegradation.

No	Comp.	MW	M300		M600	
			RT BB	RT AB	RT BB	RT AB
19	C_9H_{12}	120	5.01 5.08 5.27 5.45	4.68	4.40 5.00 5.08 5.42 5.45	
20	$C_9H_{18}O$	142			4.78	
21	C_9H_{20}	142	4.40		2.89	
22	$C_{10}H_{14}$	134	5.68 6.48	5.40	5.70 5.98 6.48	5.40
23	$C_{10}H_{18}O$	154			4.88	
24	$C_{10}H_{22}$	142	5.46			
25	$C_{11}H_{10}$	142	7.27		7.65	
26	$C_{11}H_{16}$	148	6.68		6.63	
27	$C_{11}H_{24}$	156	6.30		6.30	
28	$C_{12}H_{10}$	154	8.07		8.07	
29	$C_{12}H_{12}$	168	8.38		8.40	
30	$C_{13}H_{14}$	170	8.97		8.95	
31	$C_{13}H_{28}$	184	7.55		11.27	
32	$C_{14}H_{10}$	178				10.09
33	$C_{14}H_{30}$	198	6.98		6.98	
34	$C_{14}H_{18}O_4$	250			10.64	
35	$C_{17}H_{34}O_2$	270	5.80		10.42	
36	$C_{27}H_{56}$	380	9.11 9.22 10.42 11.27			9.13 10.40 14.44
37	$C_{28}H_{58}$	394		15.01 16.29 18.58		15.72 16.41 18.59

biodegradation time can be reduced by the variation of the substrate composition (which is the intermediate mixture after ozonation).

Three sequences of numerical simulations were executed to confirm how the interconnection of ozonation and biodegradation systems may help to reduce the contaminant and the byproduct concentrations. These three simulations considered the following conditions: the ozonation system was evaluated with the different simulation times of 5, 60, and 120 min. The model used to simulate the ozonation system was the one proposed in Chap-

Table 12.14 Summary of the results obtained by the GC-MS technique of the original and treated water samples. WW= Waste water, AO=After ozonation, AB=After biodegradation.

Hydrocarbons %	WW	AO M30O	AB	AO M60O	AB
Chlorinated	4.4	–	–	–	–
Alkanes	17.7 C_5–C_{12}, C_{18}–C_{26}	47.4 C_7–C_{14}, C_{28}	53.3 C_{28}	13.3 C_{27}, C_{28}	53.3 C_{27}, C_{28}
Unsaturated	33.0	50.0 C_{10}–C_{14}	–	53.4 C_{11}–C_{14}	20.0
Polar	31.1 C_5–C_{28}	–	46.7 C_5–C_6	33.3 C_5–C_{17}	26.7
Aromatic	13.5	2.6	–	–	–
Total	100.0	100.0	100.0	100.0	100.0

Table 12.15 Parameter values for the ozonation model.

$V_g = 0.2$ L	$V_{liq} = 0.7$ L
$W_g = 0.5$ L min^{-1}	$Q_{\max} = 0.5$ mol
$k_{sat} = 0.4$ s^{-1}	$k_1 = 450$ L mol^{-1} s^{-1}
$c^g_{in} = 6.25 \cdot 10^{-4}$ mol L^{-1}	$c_1(0) = 6.25 \cdot 10^{-4}$ mol L^{-1}
$c^g(0) = 1.56 \cdot 10^{-3}$ mol L^{-1}	$Q(0) = 0.0$ mol

ter 2 (2.17). The model parameters used in the simulation are shown in Table 12.15.

The model used to represent the biodegradation dynamics, satisfies the following set of ordinary differential equations:

$$\frac{d}{dt}C(t) = \begin{bmatrix} \mu(X, S(t))X(t) \\ -\rho(S)X(t) \\ \mu_{P,1}X(t) \\ \mu_{P,2}X(t) \end{bmatrix},$$

$$\rho\left(S(t)\right) = \rho_m \frac{S(t)}{S(t) + K_S},$$

$$\mu\left(S(t), N(t)\right) = \bar{\mu}\left[\left(\frac{S(t)}{K_S + S(t)}\right) + \left(\frac{N(t)}{K_N + N(t)}\right)\right].$$

The parameters used to simulate the combined model are detailed in Table 12.16.

Table 12.16 Parameter values for the combined system.

$V_g = 0.2\ \text{L}$	$V_{liq} = 0.7\ \text{L}$
$W_g = 0.5\ \text{L min}^{-1}$	$Q_{\max} = 0.5\ \text{mol}$
$k_{sat} = 0.4\ \text{s}^{-1}$	$k_1 = 450\ \text{L mol}^{-1}\ \text{s}^{-1}$
$c_{in}^g = 6.25 \cdot 10^{-4}\ \text{mol L}^{-1}$	$c_1(0) = 6.25 \cdot 10^{-4}\ \text{mol L}^{-1}$
$c^g(0) = 1.56 \cdot 10^{-3}\ \text{mol L}^{-1}$	$Q(0) = 0.0\ \text{mol}$
$\bar{\mu} = 0.16\ \text{h}^{-1}$	$\rho^m = 0.04\ \text{h}^{-1}$
$K_S = 1.40\ \text{mg L}^{-1}$	$K_N = 0.98\ \text{mg L}^{-1}$
$X(0) = 0.01 \cdot 10^{-3}\ \text{mg L}^{-1}$	$S(0) = 20.0 \cdot 10^{-3}\ \text{mg L}^{-1}$
$P_1(0) = 0.00\ \text{mg L}^{-1}$	$P_2(0) = 0.00\ \text{mg L}^{-1}$

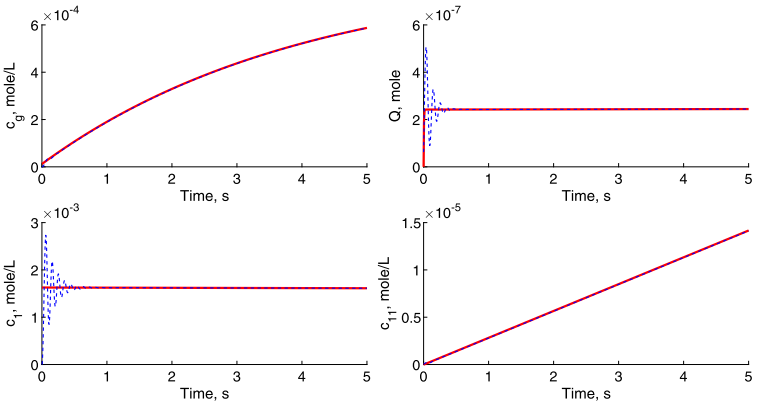

■ **FIGURE 12.15** States comparison of the ozonation model with the estimates obtained by the DNNO. The period time of ozonation was 5 min.

Fig. 12.15 shows the time evolution of the ozonation states evaluated during a period of 5 min. This simulation condition establishes the decomposition of 15% of the initial concentration of the main contaminant considered in the ozonation reaction. The DNNO using the learning laws proposed in Eq. (4.11) estimated the variables that cannot be measured online using the ozone concentration at the reactor's output as the only available information. Fig. 12.16 shows all the variables of the ozonation system and the DNNO during the first second of simulation. This figure highlights the first time instants of the DNNO weights adjustment that eventually yields the reconstruction of all the states of the ozonation system.

The mixture of the non-decomposed initial contaminant and the obtained byproduct was used as initial substrate (S_1 and S_2, respectively) in the biodegradation.

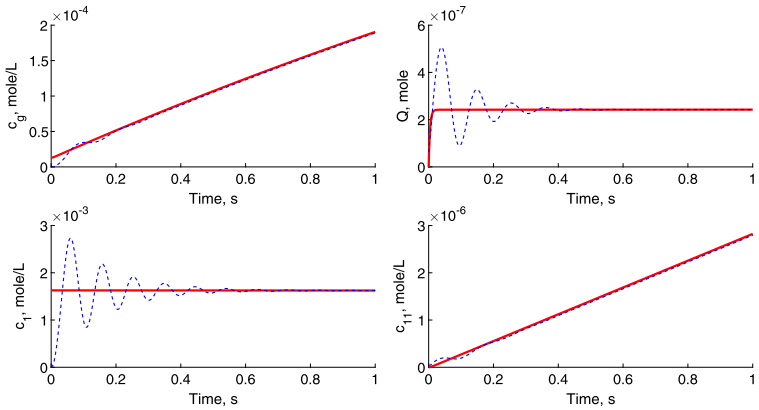

■ **FIGURE 12.16** Closer view (1 min) of comparison of the states of the ozonation model with the estimates obtained by the DNNO. The period time of ozonation was 5 min.

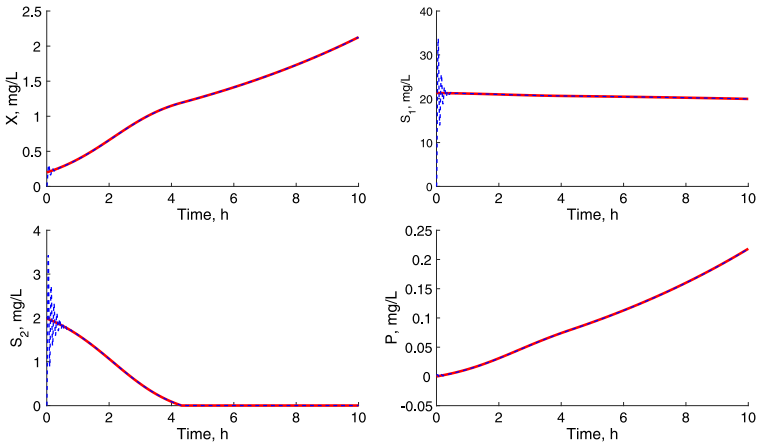

■ **FIGURE 12.17** State comparison of the biodegradation model with the estimates obtained by the DNNO. The period time of the previous ozonation was 5 min.

Two different substrate affinity constants were used to characterize the effect of the initial contaminant (which is assumed to be less biodegradable) and the byproduct which was considered as a more biodegradable compound. The affinity constants used for the initial contaminant and the byproduct were $K_{A,1} = 20.3$ mg/L and $K_{A,2} = 48.2$ mg/L.

Figs. 12.17 and 12.18 depict the simulation of the biodegradation system. The first one shows the numerical results for the reaction of 10 h of biomass X, substrate 1 S_1 (initial contaminant), substrate 2 S_2 (byproduct) and a secondary metabolite produced by the microorganism activity P.

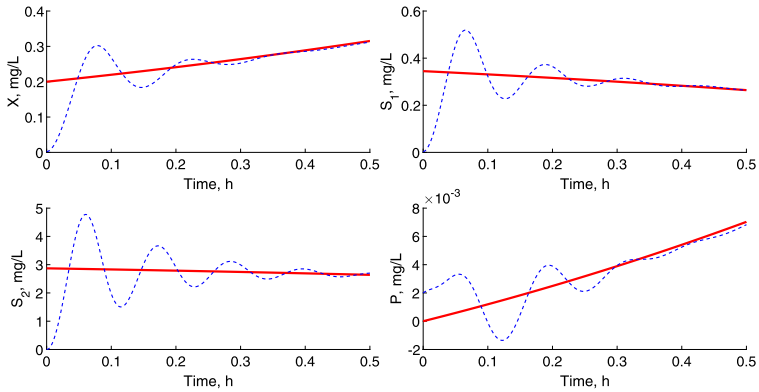

■ **FIGURE 12.18** Closer view to the states comparison of the biodegradation model with the estimates obtained by the DNNO (0.5 h). The time of the previous ozonation was 5 min.

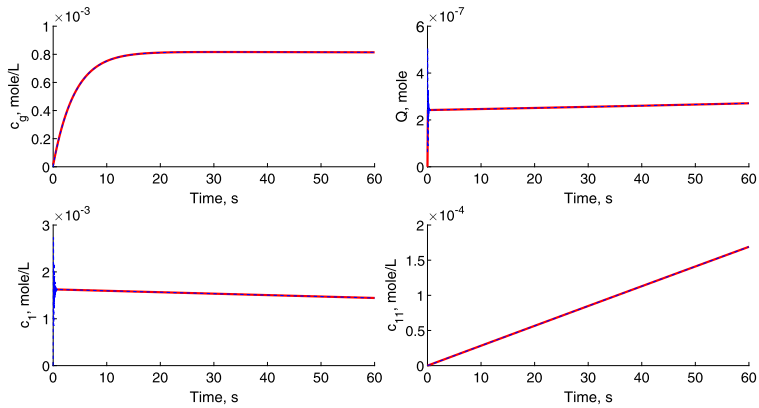

■ **FIGURE 12.19** State comparison of the ozonation model with the estimates obtained by the DNNO. The time of ozonation was 60 min.

The second figure depicts the same numerical results, but only for the first 0.5 h. This second figure exhibits the effect of the weight adjustments on the estimated states, when the product is considered as the measurable information in the biodegradation.

Fig. 12.19 demonstrates the variation of the variables in the ozonation system when the treatment period was 60 min.

The increment of the simulation time is used to evaluate the effect of degrading the contaminant more than in the case presented above. The time of 60 min was selected because at this time, the highest concentration of the byproduct was simulated. This simulation condition yields an initial

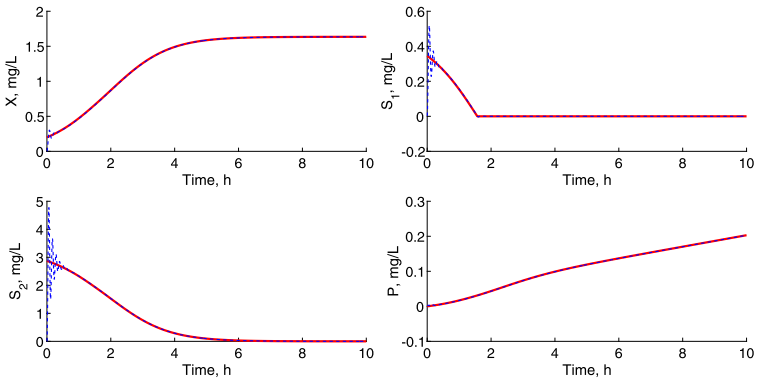

■ **FIGURE 12.20** State comparison of the biodegradation model and the estimates obtained by the DNN observers. The time of the previous ozonation was 60 min.

contaminant decomposition of 84%. The same learning laws (4.11) were applied to the DNNO structure.

The non-decomposed initial contaminant and the byproduct served as substrates (S_1 and S_2, respectively) in the biodegradation system. The above used substrate affinity constants ($K_{A,1} = 20.3$ mg/L and $K_{A,2} = 48.2$ mg/L) were kept to evaluate the effect of the increased degradation of the initial contaminant and the consequent increased byproduct concentration.

Fig. 12.20 depicts the simulated states of the biodegradation system.

This figure shows the numerical results for the biomass X, substrate 1 S_1 (initial contaminant), substrate 2 S_2 (byproduct), and a secondary metabolite evolution, evaluated for the entire period of 10 h.

Fig. 12.21 shows the variables in the ozonation system, when the treatment period was 120 min, and the corresponding states obtained by the DNNO.

The simulation time was selected because it demonstrates a common technique used, when the ozonation and biodegradation systems are interconnected: ozonation is executed to the maximum time allowed for by the technical conditions. Then the biodegradation is evaluated equally despite the byproduct distribution.

This simulation condition yields an initial contaminant decomposition of 100%. Notice that in this case, the byproduct is also decomposed almost completely.

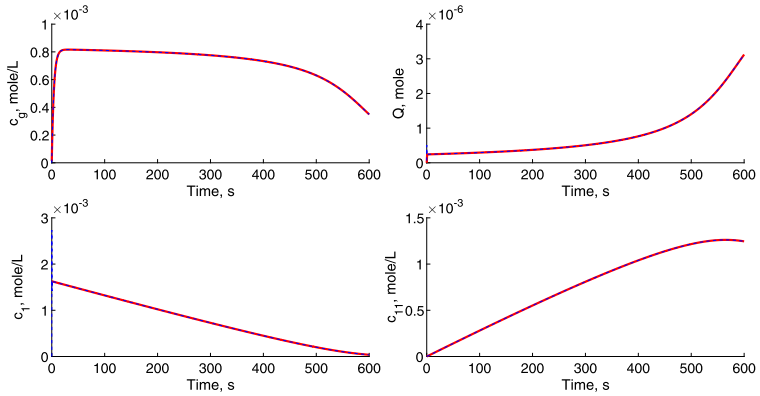

■ **FIGURE 12.21** States comparison of the ozonation model a with the estimates obtained by the DNNO. The time of ozonation was 120 min.

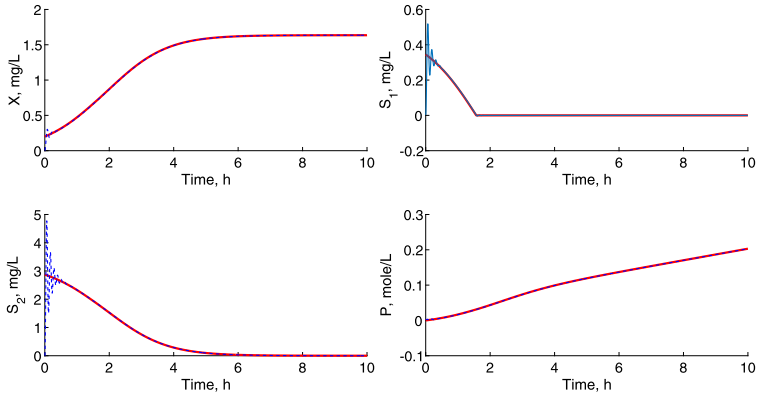

■ **FIGURE 12.22** State comparison of the biodegradation model, with the estimates obtained by the DNNO. The time of the previous ozonation was 120 min.

The almost completely decomposed initial contaminant and the byproduct barely served as substrates (S_1 and S_2, respectively) in the biodegradation, because their low concentrations were obtained after 120 min of ozonation.

Fig. 12.22 depicts the simulated states of the biodegradation system. This figure shows the numerical results for the biomass X, substrate 1 S_1 (initial contaminant), substrate 2 S_2 (byproduct), and a secondary metabolite evolution, evaluated for the entire period of 10 h.

12.7 **CONCLUSIONS**

Based on the experimental results obtained, the following conclusions may be drawn:

- The proposed sequential combination of ozonation and biodegradation of toxic compounds in the pulp and paper mill effluent after the bleaching step of the Kraft process demonstrated remarkable results. In general, after 30 min of ozonation, a significant amount of initial toxic contaminants (83%) was decreased, which then were transformed into non-toxic organic acids that were easily degraded by 85% in the biodegradation after 72 h.
- The acclimation of microorganisms was an important step in the bioprocesses treatment because it promoted the enhancement of the microorganisms growth. The corresponding pseudo-monomolecular constant b, associated with the biomass growth, was modified from 0.48 d^{-1} up to 1.13 d^{-1} after acclimation.
- Ozonation time plays a key role in the enhancement of biomass growth and the decrease of the concentration of organic matter. In general, without the previous ozonation, the specific growth rate was $\mu_{\max} = 8.33\ d^{-1}$ and it increases up to $2.08 \cdot 10^{-3}\ \mathrm{h}^{-1}$, when the sample was ozonated for 30 min. If the preliminary ozonation was carried out during 60 min, this reaction constant was reduced to $6.05 \cdot 10^{-4}\ \mathrm{h}^{-1}$.
- Under the experimental conditions, the ozonation time of 30 min could be considered as optimal, because the mineralization degree after 72 h of biodegradation is almost the same for both preozonated times (89% vs. 85%), but the ozonation time is reduced by half.
- The DNNO was applied to recover the state variation of a novel mathematical model, which aggregates the ozonation and the biodegradation. Three sequences of numerical simulations confirm the interconnection of ozonation and biodegradation.

Appendix A

Mathematical aspects

A.1 MATHEMATICAL ASPECTS OF CHAPTER 1

A.1.1 Ozone generator as a switched system

The mathematical model of the ozone generator can be interpreted as the nominal model of the corona discharge ozone generator (CDOG). It represents an idealization of the considered system. A more realistic mathematical representation of such system should consider also the presence of internal uncertainties as well as external perturbations. Such a model has the following structure:

$$\frac{d}{dt}x(t) = A_{\sigma(t)}x(t) + B_{\sigma(t)}u(t) + \zeta_{\sigma(t)}(x,t), \tag{A.1}$$

where $x_t,\ x_0 \in R^n, t \in R_+$, are the state and the initial condition vectors, respectively. The time dependent switching mechanism in (A.1) is determined by a piecewise-constant function,

$$\sigma_t \in \mathcal{I} = \{1, ..., 3\},\ t \in \mathbb{R}_+. \tag{A.2}$$

This function indicates the currently active subsystem given by the selected A_{σ_t}, B_{σ_t} on the stage where the ozone generator is working. Since the working frequency of the CDOG is finite, the Zeno behavior (infinite switching in a finite time) in (A.1) is excluded. The matrices A_i represent the formal description of the electromechanical circuit. For the same reason, the matrices B_i describe the effect of the external voltage used here for the regulation of the electronic circuit. Notice that each pair (A_i, B_i) is controllable for every $i = 1, 2, 3$. The term $\zeta_{\sigma(t)}(x,t)$ includes the uncertainties/perturbations that affect the CDOG performance. The sources of these uncertainties/perturbations are non-modeled sections of the electronic circuit, electronic perturbations due to the temperature of the tube used to produce ozone, etc.

Here the following assumptions were considered.

Assumption A.1. *The terms $\zeta_i(z,t)$ fulfill*

$$\|\zeta_i(x,t)\|^2 \leq \zeta_{0,i} + \zeta_{1,i}\|x\|^2 \quad \forall t \geq 0,$$

where $\zeta_{0,i}, \zeta_{1,i} \in \mathbb{R}_+$ are known. Clearly, the model presented for the ozone generator satisfies this assumption.

Assumption A.2. *The "matching condition" of $\zeta_i(x,t)$, that is,*

$$\zeta_i(x,t) = B_i \gamma_i(x,t),$$

is fulfilled for each subsystem i with

$$\|\gamma_i(x,t)\| \leq \gamma_i^+.$$

Assumption A.3. *The rank of B_i is 1 for each subsystem. This condition assumes that all electrical coils remain active during the whole operation period of the ozone reactor. The constant value proposed for the matrix B_i ensures the validity of this condition.*

The system given by (A.1) belongs to the class of switched system. By a switched system we mean a dynamic system that contains a set of continuous-time subsystems and a rule that determines the switching between them (see Liberzon, 2003). Most of the existing results in the automatic control literature concerning the stability of SS uses two main frameworks:

– the first one deals with conditions that guarantee the stability of the switched system under arbitrary switching rules;

– on the other hand, the second one deals with the issue of design of a switching signal that makes the equilibrium point of each subsystem stable (Liberzon, 2003), (Lin and Antsaklis, 2009), (Lunze and Lamnabhi-Lagarrigue, 2009).

The contributions, regarding the stability analysis of switched systems and using the Lyapunov stability concept, can be found in Branicky (1998), Liberzon and Morse (1999), DeCarlo et al. (2000), Lin and Antsaklis (2009), Shorten and Cairbre (2001) and Wicks et al. (1994) and the references therein.

The representation of ozone generator as a switched system brings about several issues. In particular, the control of the ozone generator as a switched system has not been addressed yet. The natural problem of this controller design is the presence of uncertainties and external perturbations. A feasible solution must consider a kind of active rejection controller but this should be solved in fixed time. Indeed, this time is predefined by the switching period. Below we discuss the solution of the ozone generator control using a class of modified *super-twisting algorithm* to compensate the matched perturbations in fixed time. Once that task is solved, a switching linear controller is

implemented to force the asymptotically stabilization of the tracking trajectory problem. The following subsection formalizes the problem formulated in this section.

A.1.2 Control challenge

The control action u must be designed such that the trajectory of the ozone generator states x tracks the reference trajectory given by

$$\frac{d}{dt}x^*(t) = A_{\sigma(t)}x^*(t) + B_{\sigma(t)}v_{\sigma(t)}(t) \tag{A.3}$$

where $x^*, x_0^* \in R^n$ are the reference state and its corresponding initial condition vector, respectively. The fixed term $v_{\sigma(t)}$ is a scalar time varying function used to force the desired reference trajectory and it satisfies

$$\left\|v_{\sigma(t)}\right\| \leq v_{0,i} + v_{1,i}\left\|x^*(t)\right\|^2 \quad \forall t \geq 0.$$

This tracking problem is equivalent to the problem of characterization if the dynamics of the trajectory tracking error

$$z = x - x^*$$

has a stable attractive zone including the origin. In other words, this problem consists in the construction of an admissible controller u such that the practical stability of the tracking trajectory error can be gotten, that is, to guarantee the property

$$\limsup_{t\longrightarrow\infty}\|z(t)\| \leq \varpi,$$

where ϖ is a positive scalar that must be proportional to the power of uncertainties or perturbations and the state obeys

$$\frac{d}{dt}z(t) = A_{\sigma_t}z(t) + B_{\sigma(t)}u(t) + \xi_{\sigma(t)}(x,t) \tag{A.4}$$

with

$$\xi_{\sigma(t)}(x,t) = \zeta_{\sigma(t)}(x,t) + v_{\sigma(t)}.$$

By the previous assumptions, this term satisfies the inequality

$$\left\|\xi_{\sigma(t)}(x,t)\right\|^2 \leq \xi_{0,\sigma(t)} + \xi_{1,\sigma(t)}\|z\|^2 \quad \forall t \geq 0.$$

A.1.3 Uniform super-twisting algorithm

The main characteristics offered by the sliding mode approach are robustness against parametric uncertainties and external perturbations. The first

order differentiator applying sliding modes is based on the second order sliding mode structure denominated supert-wisting algorithm (STA) (Levant, 2007). A complete description of second order sliding mode theory can be found in Levant (1993, 2007). The STA has been studied in several papers and it has been applied as a controller (Gonzalez et al., 2012), state estimator (Davila et al., 2005) or robust exact differentiator (RED) (Levant, 1998).

The stability analysis for finite-time convergence in second order sliding mode schemes had been done in terms of geometric proofs (majorant curves). However, this analysis technique does not admit a constructive way for tuning the algorithms. Recently, non-smooth Lyapunov functions based on the Zubov theorem have been developed to prove the STA stability (Poznyak, 2008a), (Clarke et al., 1998), (Moreno, 2011). With this kind of Lyapunov functions, the gain selection is easily obtained for ensuring finite-time convergence of the STA (Moreno and Osorio, 2012).

The emerging of these Lyapunov functions brings about new opportunities to develop several algorithms that can include observers (Moreno and Osorio, 2012) and adaptive gain versions of STA (Gonzalez et al., 2012). In particular, Lyapunov functions have been successfully used to demonstrate how the STA may be modified in order to obtain a better and an uniform convergence. Thus modification of the STA is called *uniform robust exact differentiator* (Cruz-Zavala et al., 2011c).

The uniform super-twisting algorithm (with respect to the initial conditions) used in this study fulfills the following differential equation:

$$\left.\begin{aligned} \frac{d}{dt}\upsilon_1(t) &= \upsilon_2 + k_1\phi_1\left(\upsilon_1(t),\alpha_1\right), \\ \frac{d}{dt}\upsilon_2(t) &= k_2\phi_2\left(\upsilon_1(t),\alpha_1\right). \end{aligned}\right\} \tag{A.5}$$

The nonlinear functions $\phi_1(\upsilon_1,\alpha_1)$ and $\phi_2(\upsilon_1,\alpha_1)$ were designed in agreement with the proposal given in Cruz-Zavala et al. (2011c):

$$\begin{aligned} \phi_1(\upsilon_1,\alpha_1) &= |\upsilon_1|^{1/2}\operatorname{sign}(\upsilon_1) + \alpha_1|\upsilon_1|^{3/2}\operatorname{sign}(\upsilon_1), \\ \phi_2(\upsilon_{1t},\alpha_1) &= \frac{1}{2}\operatorname{sign}(\upsilon_1) + 2\alpha_1\upsilon_1 + \frac{3}{2}\alpha_1^2|\upsilon_1|^2\operatorname{sign}(\upsilon_1). \end{aligned} \tag{A.6}$$

The parameter α_j is an extra gain to be adjusted according to the result presented in the main proposition given below. For the purposes of this study,

the *sign* function was defined as follows:

$$\operatorname{sign}(z) = \begin{cases} -1 & if \quad z < 0, \\ [-1, +1] & if \quad z = 0, \\ 1 & if \quad z > 0. \end{cases}$$

We need to recall that the solution of (A.5) is understood in the sense of Filippov (see, for example, Poznyak, 2008b and Filippov, 1998). The observer proposed in this study provides the so-called fixed-time stability for the origin of the estimation error. To clarify this concept, we introduce the following definition.

Definition A.1. *The origin* $\zeta = 0$ *of the dynamics*

$$\frac{d}{dt}\zeta(t) = \psi(\zeta, t), \quad \zeta(0) = \zeta_0 \in \mathbb{R}^n, \ \psi : \mathbb{R}^{n+1} \to \mathbb{R}^n$$

is said to be:

a) globally finite-time stable if it is globally asymptotically stable and any solution $\zeta(t, \zeta_0)$ *reaches the equilibrium point at some finite time* ($\zeta(t, \zeta_0) = 0, \forall t \geq T(\zeta_0)$)*;*

b) globally fixed-time stable if it is globally finite-time stable and the convergence time $T(\zeta_0)$ *is bounded, that is, there exists a time-moment* T_M *such that* $T(\zeta_0) \leq T_M \ \forall \zeta_0$.

Based on the previous definition, the observer convergence can be proven according to the result presented in the following section.

A.1.4 Robust control of ozone generator

The following theorem describes how to design the control action $u_{\sigma(t)}$ for each subsystem.

Proposition A.1. *If the system (A.13) is driven by the so-called uniform super-twisting controller given by*

$$\left.\begin{aligned} u_{\sigma(t)} &= \Phi(\varsigma^1(t), s_{\sigma(t)}) - k_{1,\sigma(t)}\phi_1\left(s_{\sigma(t)}\right) - \int_{\tau=0}^{t} k_{2,\sigma(\tau)}\phi_2\left(s_{\sigma(\tau)}(\tau)\right)d\tau, \\ \Phi(\varsigma^1(t), s_{\sigma(t)}) &= -\left(A_i^{21} + A_i^{22}H_{\sigma_t} - H_{\sigma_t}A_i^{11} - H_{\sigma_t}A_i^{12}H_{\sigma_t}\right)\varsigma_t^1 \\ &\quad - \left(A_i^{22} - H_{\sigma_t}A_i^{12}\right)s_{\sigma_t} - v_{\sigma_t}, \end{aligned}\right\} \tag{A.7}$$

where $\phi_1\left(s_{\sigma(t)}\right)$ *and* $\phi_2\left(s_{\sigma(\tau)}\right)$ *are defined in (A.6), then the trajectories of* s_{σ_t} *are globally fixed-time stable if the gain of the corresponding control function belongs to the following set:*

$$K_{\sigma(t)} = \left\{ \left(k_{1,\sigma(t)}, k_{2,\sigma(t)}\right) \in \mathbb{R}^2 |\, 0 < k_{1,\sigma_t} < 2\sqrt{L_{\sigma_t}},\ \ \frac{k_{1,\sigma_t}}{4} + \frac{L_{\sigma_t}^2}{k_{1,\sigma_t}^2} < k_{2,\sigma_t} \right\}$$
$$\cup \left\{ \left(k_{1,\sigma_t}, k_{2,\sigma_t}\right) \in \mathbb{R}^2 |\, 2\sqrt{L_{\sigma_t}} < k_{1,\sigma_t}, 2L_{\sigma_t} < k_{2,\sigma_t} \right\}.$$

The guaranteed convergence $T_{s,\sigma_t} \geq T_{\sigma_t}$ *is*

$$T_{s,\sigma_t} = \frac{4\lambda_{\max}^{1/2}\{P_i\}\,\eta_i^{1/2}}{\epsilon_i} + 12\,(2C_{2i})^{7/6}\,(\epsilon_i)^{-1/6},$$
$$\epsilon_i \geq C_{1i}\left(2C_{3i} + 2\sqrt{C_{3i}^2 + C_{4i}}\right),$$

with the positive constants $C_{1i}, C_{2i}\, C_{3i}, C_{4i}$ *and* η_i *satisfying the following inequalities:*

$$\left.\begin{array}{c} C_{1i}\left\|\xi_{\sigma(t)}^{\top}\right\|_{r,p}^3 \leq V_{\sigma_t}(s_{\sigma(t)}, \Delta_{\sigma(t)}) \leq 2^{1/7} C_{2i}\left\|\xi_{\sigma(t)}^{\top}\right\|_{r,p}^3, \\ r, p \ \text{positive integers}, \\ C_{3i}, C_{4i} > 0, \\ \xi_{\sigma(t)}^{\top} = \left[\begin{array}{cc} \phi_{11}\left(s_{\sigma(t)}, \alpha_1\right) & \Delta_{\sigma(t)} \end{array}\right], \\ V_{\sigma_t}(s_{\sigma(t)}, \Delta_{\sigma(t)}) = \dfrac{\delta}{2}\mu^2 k_{i2}\left|s_{\sigma_{(t)}}\right|^3 - s_{\sigma_t}\left|\Delta_{\sigma(t)}\right|^{4/3}\operatorname{sign}(\Delta_2) \\ + \dfrac{\delta}{2}\left|\Delta_{\sigma_t}\right|^2, \quad \delta, \mu > 0. \end{array}\right\}$$

The matrices P_i *are solutions of the following linear matrix inequalities with* $N_i \geq |z_{i+1}(t)|\ \forall t \geq 0$*:*

$$\left.\begin{array}{c} \left[\begin{array}{cc} P_i A_i + A_i^{\top} P_i + \epsilon_i I + 4N_i^2 C^{\top} C & P_i B \\ B^{\top} P_i & -1 \end{array}\right] \leq 0, \\ A_i = \left[\begin{array}{cc} -k_{1i} & 1 \\ -k_{2i} & 0 \end{array}\right],\ \ C^{\top} = \left[\begin{array}{c} 1 \\ 0 \end{array}\right],\ \ B = \left[\begin{array}{c} 0 \\ 1 \end{array}\right]. \end{array}\right\} \tag{A.8}$$

A.1.5 Proof of Proposition A.1

Proof. To solve the robust control design for the CDOG, a relevant definition is included here. The dynamic transitions between the given subsystems (initially enumerated by i) occur at the given switching times t_k, where

$k \in \mathbb{Z}$. The assumption of the controllability of the pair $(A_{\sigma(t)}, B_{\sigma(t)})$ for a given $\sigma(t)$ ensures the existence of a set of three linear transformations T_i operating over x such that

$$\varsigma_i = T_i z, \quad T_i = \begin{bmatrix} B_i^{\perp} \\ B_i^{+} \end{bmatrix}, \quad B_i^{+} = (B_i^{\top} B_i)^{-1} B_i^{\top}, \quad B_i^{\perp} B_i = 0, \tag{A.9}$$

where

$$\varsigma_i = \begin{bmatrix} \varsigma_i^1 \\ \varsigma_i^2 \end{bmatrix}, \varsigma_i \in \mathbb{R}^n, \varsigma_i^1 \in \mathbb{R}^{n-m}, \text{ and } \varsigma_i^m.$$

The application of the transformation T_i over the state model of the ozone generator yields the equivalent form

$$\begin{bmatrix} \frac{d}{dt}\varsigma^1(t) \\ \frac{d}{dt}\varsigma^2(t) \end{bmatrix} = \begin{bmatrix} A_i^{11} & A_i^{12} \\ A_i^{21} & A_i^{22} \end{bmatrix} \begin{bmatrix} \varsigma^1(t) \\ \varsigma^2(t) \end{bmatrix} + \begin{bmatrix} 0 \\ u_{\sigma(t)} + v_{\sigma(t)} \end{bmatrix} + \begin{bmatrix} 0 \\ \tilde{\xi}_{\sigma(t)}\left(\varsigma^1, \varsigma^2, t\right) \end{bmatrix}. \tag{A.10}$$

The nature of the transformation T_i has been rigorously studied in several references. Indeed, T_i ensures that the pair (A_i^{11}, A_i^{12}) is controllable. Using the new coordinates system presented in (A.10), the control challenge presented in the previous section can now be stated as follows: Define the following auxiliary variable (sliding mode surface for each subsystem):

$$s_{\sigma(t)} = \varsigma^2 - H_{\sigma(t)}\varsigma^1. \tag{A.11}$$

If the controller u_{σ_t} can be designed to reach the manifold defined by each sliding surface s_{σ_t}, then a set of reduced order models is obtained:

$$\frac{d}{dt}\varsigma_t^1 = \left(A_i^{11} + A_i^{12} H_{\sigma_t}\right)\varsigma_t^1.$$

To propose the main result of this study, the following assumption is required. Suppose that the terms $\tilde{\xi}_{\sigma_t}$ in (A.10) can be represented as

$$\tilde{\xi}_{\sigma(t)}\left(\varsigma^1, s_{\sigma(t)} + H_{\sigma(t)}\varsigma^1, t\right) = \tilde{\xi}_{a,\sigma_t}\left(\varsigma^1, s_{\sigma_t}, t\right) + \tilde{\xi}_{b,\sigma_t}\left(\varsigma^1, H_{\sigma_t}\varsigma^1, t\right)$$

where the function $\tilde{\xi}_{a,\sigma_t}\left(\varsigma^1, s_{\sigma_t}, t\right)$ satisfies

$$\tilde{\xi}_{a,\sigma_t}\left(\varsigma^1, s_{\sigma_t}, t\right) = 0 \text{ if } s_{\sigma_t} = 0$$

within each subsystem. Moreover, these functions satisfy the following upper estimates:

$$\left.\begin{aligned}\left\|\tilde{\xi}_{a,\sigma_t}\left(\varsigma^1, s_{\sigma_t}, t\right)\right\| &\leq \gamma^1\left(\varsigma^1, t\right)\left|\phi^1(s_{\sigma_t})\right|,\\ \left\|\frac{d}{dt}\tilde{\xi}_{b,\sigma_t}\left(\varsigma^1, H_{\sigma_t}\varsigma^1, t\right)\right\| &\leq \gamma^2\left(\varsigma^1, t\right)\left|\phi^2(s_{\sigma_t})\right|,\end{aligned}\right\} \tag{A.12}$$

where $\gamma^1\left(\varsigma^1, t\right), \gamma^2\left(\varsigma^1, t\right)$ are known continuous functions independent of the subsystem where the transformed systems is evolving. Using the linear transformation (A.9), the system presented in (A.10) can be reorganized as follows:

$$\left.\begin{aligned}\frac{d}{dt}\varsigma^1(t) &= \left(A_i^{11} + A_i^{12}H_{\sigma_t}\right)\varsigma^1(t) - A_i^{12}H_{\sigma_t}s_{\sigma_t},\\ \frac{d}{dt}s_{\sigma_t} &= \left(A_i^{21} + A_i^{22}H_{\sigma_t} - H_{\sigma_t}A_i^{11} - H_{\sigma_t}A_i^{12}H_{\sigma_t}\right)\varsigma_t^1,\\ &\quad + \left(A_i^{22} - H_{\sigma_t}A_i^{12}\right)s_{\sigma_t} + u_{\sigma_t} + \tilde{\xi}_{\sigma_t}\left(\varsigma_t^1, \varsigma_t^2, t\right).\end{aligned}\right\} \tag{A.13}$$

The solutions of the previous discontinuous differential equations and inclusions are understood in the sense of Filippov (1998). Let us take the last two variables of (A.13), that is, let us consider a new vector $\chi_{\sigma_t} = [s_{\sigma_t}\ z_{\sigma_t}]^\top$ where

$$z_{\sigma_t} = \int_{\tau=0}^{t} k_{2,\sigma(\tau)}\phi_2\left(s_{\sigma_\tau}\right)d\tau.$$

If the control action $u(t)$ is applied on the system (A.13), the dynamics of this new vector can be represented as follows:

$$\begin{aligned}\frac{d}{dt}\chi_{\sigma(t)}(t) &= \begin{bmatrix}\frac{d}{dt}s_{\sigma(t)}(t)\\ \frac{d}{dt}\Delta_{\sigma(t)}(t)\end{bmatrix} =\\ &\begin{bmatrix}\Delta_{\sigma_t} - k_{1,\sigma_t}\phi_1\left(s_{\sigma_t}\right) + \tilde{\xi}_{a,\sigma_t}\left(\varsigma_t^1, s_{\sigma_t}, t\right)\\ -k_{2,\sigma_t}\phi_2\left(s_{\sigma_t}\right) + \tilde{\xi}_{b,\sigma_t}\left(\varsigma_t^1, H_{\sigma_t}\varsigma_t^1, t\right).\end{bmatrix}\end{aligned} \tag{A.14}$$

The solution of this differential inclusion is also understood in the Filippov sense. The two functions $\tilde{\xi}_{a,\sigma(t)}\left(\varsigma^1, s_{\sigma(t)}, t\right)$ and $\tilde{\xi}_{b,\sigma(t)}\left(\varsigma^1, H_{\sigma(t)}\varsigma^1, t\right)$ can be replaced by

$$\begin{aligned}\tilde{\xi}_{a,\sigma(t)}\left(\varsigma^1, s_{\sigma_t}, t\right) &= \psi_{a,\sigma_t}\left(\varsigma^1, s_{\sigma_t}, t\right)\phi_1\left(s_{\sigma_t}, \alpha_1\right),\\ \tilde{\xi}_{b,\sigma_t}\left(\varsigma^1, H_{\sigma_t}\varsigma^1, t\right) &= \psi_{b,\sigma_t}\left(\varsigma^1, s_{\sigma_t}, t\right)\phi_2\left(s_{\sigma_t}, \alpha_1\right).\end{aligned}$$

The previous inequality holds if

$$\left\|\psi_{a,\sigma_t}\left(\varsigma^1, s_{\sigma_t}, t\right)\right\| \leq \gamma^1\left(\varsigma^1, t\right),$$
$$\left\|\psi_{b,\sigma_t}\left(\varsigma^1, s_{\sigma_t}, t\right)\right\| \leq \gamma^2\left(\varsigma^1, t\right).$$

Using these new functions, the dynamics of the vector χ_{σ_t} satisfies

$$\frac{d}{dt}\chi_{\sigma(t)}(t) = \begin{bmatrix} z_{\sigma_t} + \left(\psi_{a,\sigma_t}\left(\varsigma^1, s_{\sigma_t}, t\right) - k_{1,\sigma_t}\right)\phi_1\left(s_{\sigma_t}\right) \\ \left(\psi_{b,\sigma_t}\left(\varsigma^1, s_{\sigma_t}, t\right) - k_{2,\sigma_t}\right)\phi_2\left(s_{\sigma_t}\right) \end{bmatrix}.$$

The main part of this proof is based on the existence of a strict Lyapunov function $V_{\sigma(t)}$ defined for each subsystem. The basic form of this strict Lyapunov function was developed in Cruz-Zavala et al. (2011c). This function has the following structure:

$$V_{\sigma(t)} = V_{1,\sigma(t)}(\xi_{\sigma(t)}) + V_{2,\sigma(t)}(s_{\sigma(t)}, \Delta_{\sigma(t)}),$$
$$V_{1,\sigma(t)}(\xi_{\sigma(t)}) = \xi_{\sigma(t)}^{\top} P_1 \xi_{\sigma(t)},$$
$$V_{2,\sigma_t}(s_{\sigma(t)}, \Delta_{\sigma(t)}) = \frac{\delta}{2}\mu^2 k_{i2}\left|s_{\sigma(t)}\right|^3 - s_{\sigma(t)}\left|\Delta_{\sigma(t)}\right|^{4/3}\text{sign}(\Delta_2) + \frac{\delta}{2}\left|\Delta_{\sigma(t)}\right|^2.$$

The properties of this function are positive definite, radially unbounded, everywhere continuous and differentiable in the entire space $\mathbb{R}^2$ except on the submanifold $s_{\sigma(t)} = 0$. The uniform exact convergence of (A.5) to the trajectories of (A.13) is proven by the combination of these two Lyapunov-like functions. The meaning of these two functions was explained in Cruz-Zavala et al. (2011c). The first Lyapunov function shows the global and exact convergence of (A.5) to the trajectories of (A.9), but not the uniformity with respect to the initial conditions, that is, $V_{1,\sigma(t)}(\xi_{\sigma(t)})$ provides the finite-time stability of $\sigma(t)$, but it cannot be used to prove the fixed-time stability. The second Lyapunov-like function ensured the robust uniform convergence of the same trajectories, that is, the function $V_{2,\sigma_t}(e_{\sigma_t}, \Delta_{\sigma_t})$ is used to ensure the fixed-time stability of σ_t. The first order derivative of V_{σ_t} is

$$\frac{d}{dt}V_{\sigma(t)} = \frac{d}{dt}V_{1,\sigma(t)}(\xi_{\sigma(t)}) + \frac{d}{dt}V_{2,\sigma(t)}(s_{\sigma(t)}, \Delta_{\sigma(t)}) \tag{A.15}$$

where

$$\frac{d}{dt}V_{1,\sigma(t)}(\xi_{\sigma(t)}) = \phi_1'\left(s_{\sigma(t)}\right)\xi_{\sigma(t)}^{\top}\left(P_i A_i + A_i P_i\right)\xi_{\sigma(t)}.$$

Based on the matrix inequality proposed in the statement of the theorem of Eq. (A.8), the following relation is derived:

$$\frac{d}{dt}V_{1,\sigma(t)}(\xi_{\sigma_t}) \leq -\phi_1'\left(s_{\sigma_t}\right)\xi_{\sigma_t}^{\top} Q_i \xi_{\sigma_t}.$$

Using the structure of matrix Q_i, one can show that

$$\frac{d}{dt}V_{1,\sigma_t}(\xi_{\sigma_t}) \leq -\kappa\phi_1'\left(s_{\sigma_t}\right)\left\|\xi_{\sigma_t}\right\|^2. \tag{A.16}$$

The structure of $\phi_1\left(s_{\sigma(t)}\right)$ shows that

$$\phi_1'\left(s_{\sigma_t}\right) = \left(\frac{1}{2\left|s_{\sigma_t}\right|^{1/2}} + \frac{3\alpha_1}{2}\left|s_{\sigma_t}\right|^{1/2}\right).$$

The expression given in (A.6) is considered here to prove that

$$\left\|\xi_{\sigma(t)}\right\|^2 = \left|s_{\sigma(t)}\right| + 2\alpha_1\left|s_{\sigma(t)}\right|^2 + \alpha_1^2\left|s_{\sigma(t)}\right|^3 + \Delta_{\sigma(t)}^2.$$

Since

$$\lambda_{\min}(P_i)\left\|\xi_{\sigma_t}\right\|^2 \leq \xi_{\sigma_t}^{\top}P_i\xi_{\sigma_t} \leq \lambda_{\max}(P_i)\left\|\xi_{\sigma_t}\right\|^2$$

this equation above can be used to show that

$$|\sigma_t|^{1/2} \leq \left\|\xi_{\sigma_t}\right\| \leq \frac{V_{1,\sigma_t}^{1/2}(\xi_{\sigma_t})}{\lambda_{\min}^{1/2}(P_i)}.$$

These last results applied to (A.16) yield

$$\frac{d}{dt}V_{1,\sigma_t}(\xi_{\sigma_t}) \leq -\delta_{11}V_{1,\sigma_t}^{1/2}(\xi_{\sigma_t}) - \delta_{12}V_{1,\sigma_t}(\xi_{\sigma_t}),$$
$$\delta_{11}, \delta_{12} > 0.$$

Now let us analyze the second part of (A.15), that is, $\frac{d}{dt}V_{2,\sigma(t)}(s_{\sigma_t}, \Delta_{\sigma_t})$. Based on the results of Theorem 2 proposed in Cruz-Zavala et al. (2011c), it can be proved that

$$\frac{d}{dt}V_{2,\sigma_t}(s_{\sigma_t}, \Delta_{\sigma_t}) \leq -\frac{V_{2,\sigma_t}^{7/2}(s_{\sigma_t}, \Delta_{\sigma_t})}{2^{9/2}C_{2,\sigma_t}}, \quad \forall s_{\sigma_t} \in \Gamma$$

where

$$\Gamma = \left\{\left[s_{\sigma_t}, \Delta_{\sigma_t}\right], V_{2,\sigma_t}(s_{\sigma_t}, \Delta_{\sigma_t}) \geq \epsilon_i\right\}.$$

What is more important, any trajectory of (A.14) started on Γ enters robustly and uniformly (despite the presence of the admissible perturbations and independently of the initial condition) in its complement

$$\Gamma^c = \left\{\left[s_{\sigma_t}, \Delta_{\sigma_t}\right], V_{2,\sigma_t}(s_{\sigma_t}, \Delta_{\sigma_t}) < \epsilon_i\right\},$$

which is a compact set that contains the origin. According to the previous results and using the arguments presented in Cruz-Zavala et al. (2011c), the fixed time of convergence described in the theorem statement is gotten. The complete analysis of the control design proposed here must consider the dynamics of

$$\frac{d}{dt}\varsigma^1(t) = \left(A_i^{11} + A_i^{12}H_{\sigma(t)}\right)\varsigma^1 - A_i^{12}H_{\sigma(t)}s_{\sigma(t)}.$$

Considering that $T_{s,\sigma_t} \leq t \leq T_{\sigma_t}$ the previous differential relation becomes

$$\frac{d}{dt}\varsigma^1(t) = \left(A_i^{11} + A_i^{12}H_{\sigma(t)}\right)\varsigma^1(t). \tag{A.17}$$

So, the following theorem shows how to design the control gain $H_{\sigma(t)}$ such that ς^1 is asymptotically stable. Despite the fact that $H_{\sigma(t)}$ can be designed to enforce $A_i^{11} + A_i^{12}H_{\sigma(t)}$ to be a Hurwitz matrix, this is not enough to prove that ς^1 is asymptotically stable. Under these conditions one is required to show that (A.17) is globally asymptotically stable. Therefore,

$$T_{\sigma_t} - T_{s,\sigma(t)} \geq T^*$$

where T^* is the dwell time (the minimal time needed to define the change from one subregion to the next one). □

Proposition A.2. *If there exist a collection (sequence) of gain matrices H_{σ_t} such that the matrices*

$$\tilde{A}_i = A_i^{11} + A_i^{12}H_{\sigma_t}$$

are Hurwitz and satisfy

$$e^{\tilde{A}_i T^*}P_{i+1}e^{\tilde{A}_i T^*} - P_i < 0 \tag{A.18}$$

where the matrix P_i satisfy

$$P_i\tilde{A}_i + \tilde{A}_i^{\top}P_i = -Q_i, \quad Q_i > 0, \tag{A.19}$$

then the equilibrium point of (A.17) is globally asymptotically stable.

Proof. Using the results proposed in Geromel et al. (2008), one may conclude the proof. Because the pair $\left(A_i^{11}, A_i^{12}\right)$ is controllable with each subsystem, the condition (A.19) is straightforwardly satisfied. □

A.1.6 Design of control gains

Assuming that

$$H_{i+1} = H_i + \Delta H_i,$$

the corresponding application of (A.19) yields

$$P_{i+1}\left(A_i^{11} + A_i^{12}H_i + A_i^{12}\Delta H_i\right) + \left(A_i^{11} + A_i^{12}H_i + A_i^{12}\Delta H_i\right)^\top P_{i+1} = -Q_{i+1}.$$

A reorganization of the previous equation can be used to obtain

$$P_{i+1}\left(A_i^{11} + A_i^{12}H_i + A_i^{12}\Delta H_i\right) + \left(A_i^{11} + A_i^{12}H_i + A_i^{12}\Delta H_i\right)^\top P_{i+1} = -Q_{i+1}.$$

The corresponding adjustment of the controller gain produces a modification of the matrix $P_{i+1} = P_i + \Delta P_i$ with ΔP_i a positive definite matrix. This modification used in the previous equation produces

$$P_i\left(A_i^{12}\Delta H_i\right) + \left(A_i^{12}\Delta H_i\right)^\top P_i + \Delta P_i\left(A_i^{11} + A_i^{12}H_i + A_i^{12}\Delta H_i\right) + \left(A_i^{11} + A_i^{12}H_i + A_i^{12}\Delta H_i\right)^\top \Delta P_i = -Q_{i+1} - Q_i.$$

Because $A_i^{11} + A_i^{12}H_i$ is a Hurwitz matrix, there is a positive definite matrix $\tilde{Q}_i$ such that

$$\Delta P_i\left(A_i^{11} + A_i^{12}H_i\right) + \left(A_i^{12}\Delta H_i\right)^\top \Delta P_i = -\tilde{Q}_i.$$

By substitution of the previous equation, one gets

$$P_{i+1}\left(A_i^{12}\Delta H_i\right) + \left(A_i^{12}\Delta H_i\right)^\top P_{i+1} = -Q_{i+1} - Q_i - \tilde{Q}_i. \tag{A.20}$$

Therefore, if ΔH_i is selected in such a way that $A_i^{12}\Delta H_i$ is a Hurwitz matrix, then P_{i+1} is a positive definite matrix as required in (A.19).

A second condition on the control gains design is obtained by using the condition (A.18), which can be translated to

$$0 < \Delta P_i < e^{-\tilde{A}_i^\top T^*} P_i e^{-\tilde{A}_i T^*} - P_i. \tag{A.21}$$

Based on the previous discussion, one can use the following procedure to obtain the control gains H_i:

1. Calculate the controller gain H_i using some available techniques such as pole placement, optimal control, linear matrix inequalities, etc.
2. Determine a suitable Lyapunov matrix P_i for a given positive definite matrix Q_i.
3. Determine a new suitable Lyapunov matrix ΔP_i for a given positive definite matrix $\tilde{Q}_i$
4. Verify the condition proposed in (A.21).
5. If the previous condition is verified, fix $P_{i+1} = P_i + \Delta P_i$. If not, go to step 2 and modify the matrix Q_i.
6. Calculate ΔH_i using the matrix equation (A.20).
7. Fix the controller gains as $H_{i+1} = H_i + \Delta H_i$.

The constraints (A.20) are in a class of bilinear matrix equations. This problem can be solved using some standard and advanced computational tools (the PENBMI-MATLAB package, for example).

A.2 MATHEMATICAL ASPECTS OF CHAPTER 2

A.2.1 First estimation method

The model presented in (2.15) is composed of a set of equations formed by aggregations of rational functions depending on its states. The equivalent and simplified representation can be reorganized as a sum of two rational functions. The first one depends on the uncertain parameters included in the model and the second one does not. Therefore, each equation introduced in the model (2.15) can be generalized as follows:

$$\frac{dC_{it}}{dt} = \frac{P_{1,i}\left(C_t\right)^{\top} a_i + N_{1,i}\left(C_t\right)}{P_{2,i}\left(C_t\right)^{\top} b_i + N_{2,i}\left(C_t\right)} + P_{3,i}\left(C_t\right) \tag{A.22}$$

where $P_{1,i}$ and $P_{2,i}$ are nonlinear vectors formed with polynomials of variables involved in model (A.22). The polynomial $P_{3,i}$ represents the parameter independent terms that usually appear in chemical models. The variable C_i represents the ith state of (A.22). The vectors a_i and b_i are formed by the uncertain parameters of the systems presented in (A.22).

Based on the representation (A.22) one can get an equivalent representation such as

$$\int_0^T \frac{dC_i}{dt}(t) P_{2,i}\left(C(t)\right)^{\top} b_i dt + \int_0^T N_{2,i}\left(C_t\right) \frac{dC_{it}}{dt} dt -$$

$$\int_0^T P_{3,i}\left(C_t\right)\left[N_{2,i}\left(C_t\right)+P_{2,i}\left(C_t\right)^{\top} b_i\right]dt=$$
$$\int_0^T\left[P_{1,i}\left(C_t\right)^{\top} a_i+N_{1,i}\left(C_t\right)\right]dt.$$

A straightforward integration-by-parts of the left-hand side part of the previous equation leads to

$$P_{2,i}\left(C_T\right)^{\top} C_{iT} b_i-\int_0^T \frac{dP_{2,i}\left(C_t\right)^{\top}}{dt} C_{it}dt b_i+$$
$$N_{2,i}\left(C_T\right) C_{iT}-\int_0^T \frac{dN_{2,i}\left(C_t\right)}{dt} C_{it}dt-$$
$$\int_0^T P_{3,i}\left(C_t\right)\left[N_{2,i}\left(C_t\right)+P_{2,i}\left(C_t\right)^{\top} b_i\right]dt=$$
$$\int_0^T P_{1,i}\left(C_t\right)^{\top} dt a_i+\int_0^T N_{1,i}\left(C_t\right)dt$$

where the derivatives of $P_{2,i}$ and $N_{2,i}$ can be calculated as follows:

$$\frac{dP_{2,i}\left(C_t\right)}{dt}=P'_{2,i}\left(C\right)F(C_t),$$
$$\frac{dN_{2,i}\left(C_t\right)}{dt}=N'_{2,i}\left(C\right)F(C_t),$$
$$P'_{2,i}(C)=\frac{dP_{2,i}\left(C\right)}{dC} N'_{2,i}(C)=\frac{dN_{2,i}\left(C\right)}{dC}.$$

Certainly, the previous structure can be represented as follows:

$$Y_i(T)=\Phi_i(T)^{\top}\Theta_i \tag{A.23}$$

where

$$Y_i(T)=\int_0^T N_{1,i}\left(C_t\right)dt-N_{2,i}\left(C_t\right)C_i(T)+$$
$$\int_0^T \frac{dN_{2,i}\left(C_t\right)}{dt} C_{i,t}dt-\int_0^T P_{3,i}\left(C_t\right)N_{2,i}\left(C_t\right)dt,$$
$$\Phi_i(T)=\begin{bmatrix} -\int_0^T P_{1,i}\left(C_t\right)dt \\ P_{2,i}(C(T))\,C_i(T)-\int_0^T\left[\frac{dP_{2,i}(C_t)}{dt} C_{it}-P_{3,i}(C_t)\,P_{2,i}(C_t)\right]dt \end{bmatrix},$$
$$\Theta_i^{\top}=\begin{bmatrix} a_i^{\top} & b_i^{\top} \end{bmatrix}.$$

A.2.2 LMS step by step identification method

Based on the regular technique of the well-known least mean square method (LMS), the parametric identification problem presented in (A.23) can be solved as follows:

$$\Theta_i^* = \left[\sum_{k=0}^{N} \Phi_{i,k}(T)\Phi_{i,k}(T)^\top\right]^{-1}\left[\sum_{k=0}^{N} Y_{i,k}(T)\Phi_{i,k}(T)\right]$$

where the index k is used to represent the number of experiments considered in the study, while N is the total number of experiments.

A.2.3 Second estimation method

It is evident that each differential equation of the model presented above satisfies

$$\frac{dz_i(t)}{dt} = \frac{f^i(z(t),\alpha_1^i)}{g^i(z(t),\alpha_2^i)} + \zeta^i(z(t),t), \quad z_i \in \mathbb{R}, \tag{A.24}$$

where z_i is any variable in the model presented in (A.22). The entire set of variables z_i is lumped in the super-twisting algorithm vector $z \in \mathbb{R}^n$ and n is the number of variables. Then z represents all the variables involved in the metabolic network under study. Also, it is assumed that all the functions f^i and g^i are linearly parametrized by $\alpha_1^i \in \mathbb{R}^{P_{1,i}}$ and $\alpha_2^i \in \mathbb{R}^{P_{2,i}}$, respectively. The nonlinear functions $f^i : \mathbb{R}^{n+P_{1,i}} \longrightarrow \mathbb{R}$, $g^i : \mathbb{R}^{n+P_{2,i}} \longrightarrow \mathbb{R}$ satisfy

$$|f^i(z_1,\cdot) - f^i(z_2,\cdot)| \leq L^i\|z_1 - z_2\| \;\forall z_1, z_2 \in \mathbb{R}^n,$$
$$|g^i(z,\alpha)| \neq 0 \,\forall z \in \mathbb{R}^n \,\alpha \in \mathbb{R}^{P_{2,i}}.$$

Therefore, a couple of nonlinear functions $\psi_1^i : \mathbb{R}^n \longrightarrow \mathbb{R}^{P_{1,i}}$ and $\psi_2^i : \mathbb{R}^n \longrightarrow \mathbb{R}^{P_{2,i}}$ exist such that

$$f^i(z) = \left[\alpha_1^i\right]^\top \psi_1^i(z) + \varphi_1^i(z),$$
$$g^i(z) = \left[\alpha_2^i\right]^\top \psi_2^i(z) + \varphi_2^i(z).$$

The nonlinear functions $\varphi_1^i : \mathbb{R}^n \longrightarrow \mathbb{R}$ and $\varphi_2^i : \mathbb{R}^n \longrightarrow \mathbb{R}$ are introduced to define the so-called residual representation of f^i and g^i. In the unrealistic case when the derivative of the whole vector z can be measured, the ODE described in (A.24) can be alternatively represented as

$$y_t^i = \left[\theta^i\right]^\top x_t^i + \zeta^i(z_t,t),$$

$$\theta^i = \begin{bmatrix} \alpha_1^i \\ \alpha_2^i \end{bmatrix},\ x_t^i = \begin{bmatrix} \psi_1^i(z) \\ \left[\zeta^i(z,t) - \dfrac{dz_{it}}{dt}\right]\psi_2^i(z) \end{bmatrix},$$
$$y_t^i = \left[\frac{dz_{it}}{dt} - \zeta^i(z,t)\right]\varphi_2^i(z) - \varphi_1^i(z).$$

This form has the regular linear regression form. The solution for the parametric identification can be obtained as in Ljung (1987):

$$\bar{\theta^i}_t = \left(\int_0^t x^i(\tau)\left[x^i(\tau)\right]^\top d\tau\right)^{-1}\left(\int_0^t x^i(\tau)y^i(\tau)d\tau\right).$$

The previous equation needs the time-derivative of z_i. As it was a super-twisting algorithm, it is not usual to have this derivative online and simultaneously for all the variables involved in the metabolic network. This is the main motivation to propose a robust differentiator to approximate $\dfrac{dz_{it}}{dt}$ (robust with respect to parametric uncertainties and external perturbations). Here the super-twisting algorithm is considered as a feasible method to solve this problem. The super-twisting algorithm as differentiator has the following structure (Cruz-Zavala et al., 2011b; Moreno and Osorio, 2008):

$$\left.\begin{aligned} \frac{d\hat{z}_a^i(t)}{dt} &= \hat{z}_b^i(t) + k_1^i|e^i(t)|^{\frac{1}{2}}\operatorname{sign}(e_t^i), \\ \frac{d\hat{z}_{bt}^i}{dt} &= k_2^i\operatorname{sign}(e_t^i). \end{aligned}\right\} \tag{A.25}$$

Here, the differentiator error is represented by the variable e^i, which is defined as $e^i = z^i - \hat{z}_a^i$.

Indeed, this algorithm serves as differentiator of the uncertain signal z_t^i. This fact can be supported considering that the signal z_t^i can be represented as

$$z^i(t) = z_{at}^i,\ \frac{dz_t^i}{dt} = z_{bt}^i,$$
$$\frac{dz_{at}^i}{dt} = z_{bt}^i,$$
$$\frac{dz_{bt}^i}{dt} = \frac{d^2z_{at}^i}{dt^2},\ |\frac{d^2z_t^i}{dt^2}| < z^{+,i},\ z^{+,i} \in \mathbb{R}^+.$$

Then the differentiation error $e_1^i = z_a^i - \hat{z}_a^i$, $e_2^i = z_b^i - \hat{z}_b^i$ satisfies

$$\frac{de_{1t}^i}{dt} = e_{2t}^i - k_1^i|e_{1t}^i|^{\frac{1}{2}}\operatorname{sign}(e_{1t}^i),$$

$$\frac{de_{2t}^i}{dt} = -k_2^i \text{sign}(e_{1t}^i) + \frac{d^2 z_t^i}{dt^2}.$$

According to the result presented by Moreno and Osorio (2008), it can be proven that

$$|e_1^i| = 0, \quad |e_2^i| = 0 \ \ \forall t \geqslant T^{*,i} = \sqrt{\frac{0.5V^i(0)}{2}}.$$

The function V^i satisfies the expression $V^i(\xi^i) = \left[\xi^i\right]^\top P^i \xi^i$ with

$$\left[\xi^i\right]^\top = \left[\begin{array}{cc} |e_1^i|^{\frac{1}{2}} \text{sign}(e_1^i) & e_2^i \end{array}\right].$$

Each matrix $P^i \in \mathbb{R}^{2\times 2}$ is positive definite and symmetric. If the variables y_t^i and x_t^i are changed by $\hat{x}^i$ and $\hat{y}^i$ the parametric identification can be solved as

$$\theta_t^{*,i} = \left(\int_0^t \hat{x}^i(\tau)\left[\hat{x}^i(\tau)\right]^\top d\tau\right)^{-1} \left(\int_0^t \hat{x}^i(\tau)\hat{y}^i(\tau)d\tau\right). \tag{A.26}$$

The parameter identification method presented in (A.26) can be used for the whole ozonation reaction period.

A.3 MATHEMATICAL ASPECTS OF CHAPTER 3

This book follows the paradigm of *reinforcement learning* for the minimization of the "*penalty function*", which reflects the proximity of the current outputs of the applied DNN to a desired trajectory realizing the so-called tracking process. Such penalty functions are usually referred to as *Luapunov-like* (or "energetic") functions and have the following structure:

$$\left.\begin{array}{c} \mathcal{L}(e(t)) := e^{\intercal}(t) P e(t) + \\ \frac{k_\sigma}{2}\text{tr}\left\{\Delta W_\sigma(t)\Delta W_\sigma^{\intercal}(t)\right\} + \frac{k_\varphi}{2}\text{tr}\left\{\Delta W_\varphi(t)\Delta W_\varphi^{\intercal}(t)\right\}, \\ \Delta W_\sigma(t) := W_\sigma(t) - W_\sigma^*, \ \Delta W_\varphi(t) := W_\varphi(t) - W_\varphi^*, \ k_\sigma > 0, \ k_\varphi > 0, \end{array}\right\}$$

where $e(t) = \hat{x}(t) - x^*(t)$ is the current tracking error, which has to be minimized by the corresponding adjustment of the DNNs weights $W_\sigma(t)$ and $W_\varphi(t)$. The general DNN structure is as follows (see (3.2)):

$$\frac{d}{dt}\hat{x}(t) = A\hat{x}(t) + W_\sigma(t)\sigma\left(\hat{x}(t)\right) + W_\varphi(t)\varphi\left(\hat{x}(t)\right)u(y(t)).$$

Here $\hat{x}(t) \in \mathbb{R}^n$ is a vector of state estimates, $\sigma\left(\hat{x}(t)\right)$ and $\varphi\left(\hat{x}(t)\right) \in \mathbb{R}^{n \times k_\varphi}$ are a vector and a matrix of activating functions, $u(y(t), t)$ is an external signal (or control action) depending on the measurable system output $y(t)$. For our problem of the contaminant concentration estimation the corresponding DNN is given in (4.10) where $e(t) = \hat{c}(t) - c(t)$ has the meaning of the difference between obtained contaminant concentration $\hat{c}(t)$ and its real value in time t.

In the subsections of this appendix the direct analysis of the time-derivative $\frac{d}{dt}\mathcal{L}(e(t))$ of this Lyapunov function permits one to realize both aims:

– to find the corresponding zone z of the convergence $(\limsup_{t \to \infty} \|e(t)\| \leq z)$ for the error tracking $e(t)$,

– to derive exactly the corresponding learning (adjustment) laws (4.11) for the DNN weights in the differential form

$$\left.\begin{aligned} \dot{W}_\sigma(t) &= \Phi_\sigma\left(W_\sigma(t), \hat{x}(t), u(y(t))\right), \\ \dot{W}_\varphi(t) &= \Phi_\varphi\left(W_\varphi(t), \hat{x}(t), u(y(t))\right), \end{aligned}\right\} \tag{A.27}$$

which minimize the convergence zone z, providing a good quality of the desired tracking process.

The reinforcement learning process (A.27) consists in the realization of an adequate adjustment of the weight matrices $W_\sigma(t)$ and $W_\varphi(t)$ of the process, namely, proceeding in such a way that the current state estimates $\hat{x}(t)$ would be as closed as possible to the current real state $x(t)$ of the modeled real-life system. The RL-rules (A.27) are specific for each considered problem.

Thus, we present the mathematical details of this approach.

A.3.1 Error of state estimation and its dynamics

For the error of state estimation $e_t := \hat{x}_t - x_t$ we have

$$\dot{e}_t = (A - LC)\, e_t + W_{0t}\varphi\left(\hat{x}_t\right) + W_{1t}\psi\left(\hat{x}_t\right) u + \zeta(x_t, t) \tag{A.28}$$

with the uncertain part

$$\zeta(x_t, t) = L\eta_t - \tilde{\xi}(x_t, t), \tag{A.29}$$

which is also depends on the gain matrix L of the observer.

A.3.2 The energetic function and its evaluation

Consider the following *energetic function*:

$$\left.\begin{array}{c}\mathcal{L}(e) := e^{\mathsf{T}} P e + \dfrac{k_0}{2}\mathrm{tr}\left\{\Delta W_0 \Delta W_0^{\mathsf{T}}\right\} + \dfrac{k_1}{2}\mathrm{tr}\left\{\Delta W_1 \Delta W_1^{\mathsf{T}}\right\}, \\ \Delta W_0 := W_0 - W_0^*,\ \Delta W_1 := W_1 - W_1^*,\ k_0 > 0,\ k_1 > 0,\end{array}\right\} \quad \text{(A.30)}$$

where the matrices W_0^* and W_1^* will be defined below. Its full time-derivative on the trajectories of (A.28) is

$$\begin{array}{c}\dfrac{d}{dt}L(e_t) = 2e^{\mathsf{T}} P\dot{e} + k_0 tr\left\{\dot{W}_0 \Delta W_0^{\mathsf{T}}\right\} + k_1 tr\left\{\dot{W}_1 \Delta W_1^{\mathsf{T}}\right\} = \\ 2e^{\mathsf{T}} P(A - LC)e + 2e^{\mathsf{T}} P\left[W_0\varphi(\hat{x}) + W_1\psi(\hat{x})u(\hat{x},t)\right] + \\ 2e^{\mathsf{T}} P\left[L\eta_t - \tilde{\xi}(x,t)\right] + k_0\mathrm{tr}\left\{\dot{W}_0 \Delta W_0^{\mathsf{T}}\right\} + k_1 tr\left\{\dot{W}_1 \Delta W_1^{\mathsf{T}}\right\} = \\ 2e^{\mathsf{T}} P(A - LC)e + 2e^{\mathsf{T}} P\left[\Delta W_0\varphi(\hat{x}) + \Delta W_1\psi(\hat{x})u(\hat{x},t)\right] + \\ 2e^{\mathsf{T}} P W_0^*\varphi(\hat{x}) + 2e^{\mathsf{T}} P W_1^*\psi(\hat{x})u(\hat{x},t) + \\ 2e^{\mathsf{T}} P\left[L\eta_t - \tilde{\xi}(x,t)\right] + k_0\mathrm{tr}\left\{\dot{W}_0 \Delta W_0^{\mathsf{T}}\right\} + k_1 tr\left\{\dot{W}_1 \Delta W_1^{\mathsf{T}}\right\}.\end{array} \quad \text{(A.31)}$$

Using the Λ-inequality (see Poznyak, 2008a)

$$2x^{\mathsf{T}} y \le x^{\mathsf{T}}\Lambda x + y^{\mathsf{T}}\Lambda^{-1} y,$$

valid for any matrix $\Lambda = \Lambda^{\mathsf{T}} > 0$, we can obtain the following upper estimates:

$$\begin{array}{c}2e^{\mathsf{T}} P\Delta W_0\varphi(\hat{x}) \le e^{\mathsf{T}} P\Lambda Pe + \varphi^{\mathsf{T}}(\hat{x})\Delta W_0^{\mathsf{T}}\Lambda^{-1}\Delta W_0\varphi(\hat{x}) \\ = e^{\mathsf{T}} P\Lambda Pe + \mathrm{tr}\left\{\left[\Lambda^{-1}\Delta W_0\varphi(\hat{x})\varphi^{\mathsf{T}}(\hat{x})\right]\Delta W_0^{\mathsf{T}}\right\}\end{array}$$

and

$$\begin{array}{c}2e^{\mathsf{T}} P\left[\Delta W_1\psi(\hat{x})u(\hat{x},t)\right] \le \\ e^{\mathsf{T}} P\Lambda_1 Pe + u^{\mathsf{T}}(\hat{x},t)\psi^{\mathsf{T}}(\hat{x})\Delta W_1^{\mathsf{T}}\Lambda_1^{-1}\left[\Delta W_1\psi(\hat{x})u(\hat{x},t)\right] = \\ e^{\mathsf{T}} P\Lambda_1 Pe + \mathrm{tr}\left\{\left[\Lambda_1^{-1}\Delta W_1\psi(\hat{x})u(\hat{x},t)u^{\mathsf{T}}(\hat{x},t)\psi^{\mathsf{T}}(\hat{x})\right]\Delta W_1^{\mathsf{T}}\right\}.\end{array}$$

Using those in (A.31) we get

$$\begin{array}{c}\dfrac{d}{dt}\mathcal{L}(e_t) \le 2e^{\mathsf{T}} P(A - LC)e + e^{\mathsf{T}} P\Lambda Pe \\ + \mathrm{tr}\left\{\left[\Lambda^{-1}\Delta W_0\varphi(\hat{x})\varphi^{\mathsf{T}}(\hat{x})\right]\Delta W_0^{\mathsf{T}}\right\} + e^{\mathsf{T}} P\Lambda Pe \\ + \mathrm{tr}\left\{\left[\Lambda^{-1}\Delta W_1\psi(\hat{x})u(\hat{x},t)u^{\mathsf{T}}(\hat{x},t)\psi^{\mathsf{T}}(\hat{x})\right]\Delta W_1^{\mathsf{T}}\right\}\end{array}$$

$$
\begin{aligned}
&+2e^{\intercal}PW_0^*\varphi\left(\hat{x}\right)+2e^{\intercal}PW_1^*\psi\left(\hat{x}\right)u\left(\hat{x},t\right)+\\
&2e^{\intercal}P\left[L\eta_t-\tilde{\xi}\left(x,t\right)\right]+k_0\mathrm{tr}\left\{\dot{W}_0\Delta W_0^{\intercal}\right\}+k_1\mathrm{tr}\left\{\dot{W}_1\Delta W_1^{\intercal}\right\} \qquad \text{(A.32)}\\
&=e^{\intercal}\left[P\left(A-LC\right)+\left(A-LC\right)^{\intercal}P+P\left(\Lambda+\Lambda_1\right)P\right]e+\\
&\mathrm{tr}\left\{\left[k_0\dot{W}_0+\Lambda^{-1}\Delta W_0\varphi\left(\hat{x}\right)\varphi^{\intercal}\left(\hat{x}\right)+\alpha\frac{k_0}{2}\Delta W_0\right]\Delta W_0^{\intercal}\right\}+\\
&\mathrm{tr}\left\{\left[k_1\dot{W}_1+\Lambda^{-1}\Delta W_1\psi\left(\hat{x}\right)u\left(\hat{x},t\right)u^{\intercal}\left(\hat{x},t\right)\psi^{\intercal}\left(\hat{x}\right)+\alpha\frac{k_1}{2}\Delta W_1\right]\Delta W_1^{\intercal}\right\}\\
&-\alpha\frac{k_0}{2}\mathrm{tr}\left\{\Delta W_0\Delta W_0^{\intercal}\right\}-\alpha\frac{k_1}{2}\mathrm{tr}\left\{\Delta W_1\Delta W_1^{\intercal}\right\}+\\
&2e^{\intercal}PW_0^*\varphi\left(\hat{x}\right)+2e^{\intercal}PW_1^*\psi\left(\hat{x}\right)u\left(\hat{x},t\right)+2e^{\intercal}P\left[L\eta_t-\tilde{\xi}\left(x,t\right)\right].
\end{aligned}
$$

The RL law (3.17) implies

$$
\begin{aligned}
&\mathrm{tr}\left\{\left[k_0\dot{W}_0+\Lambda^{-1}\Delta W_0\varphi\left(\hat{x}\right)\varphi^{\intercal}\left(\hat{x}\right)+\alpha\frac{k_0}{2}\Delta W_0\right]\Delta W_0^{\intercal}\right\}=0,\\
&\mathrm{tr}\left\{\left[k_1\dot{W}_1+\Lambda^{-1}\Delta W_1\psi\left(\hat{x}\right)u\left(\hat{x},t\right)u^{\intercal}\left(\hat{x},t\right)\psi^{\intercal}\left(\hat{x}\right)\right.\right.\\
&\left.\left.+\alpha\frac{k_1}{2}\Delta W_1\right]\Delta W_1^{\intercal}\right\}=0,
\end{aligned}
$$

so that (A.32) becomes

$$
\begin{aligned}
\frac{d}{dt}\mathcal{L}\left(e_t\right)\leq\ & e^{\intercal}\left[P\left(A-LC\right)+\left(A-LC\right)^{\intercal}P+P\left(\Lambda+\Lambda_1\right)P\right]e\\
&+2e^{\intercal}PW_0^*\varphi\left(\hat{x}\right)+2e^{\intercal}PW_1^*\psi\left(\hat{x}\right)u\left(\hat{x},t\right)+\\
&2e^{\intercal}P\left[L\eta_t-\tilde{\xi}\left(x,t\right)\right]-\\
&\alpha\frac{k_0}{2}\mathrm{tr}\left\{\Delta W_0\Delta W_0^{\intercal}\right\}-\alpha\frac{k_1}{2}\mathrm{tr}\left\{\Delta W_1\Delta W_1^{\intercal}\right\}.
\end{aligned}
\qquad \text{(A.33)}
$$

A.3.3 LMI and stability property

Represent the right-hand side of (A.33) as a quadratic form of some extended vector. Introduce the extended vector

$$
z=\begin{pmatrix} e\\ \eta_t\\ \tilde{\xi}\left(x,t\right)\\ \varphi\left(\hat{x}\right)\\ \psi\left(\hat{x}\right)u \end{pmatrix}. \qquad \text{(A.34)}
$$

Then the inequality (A.33) becomes

$$\begin{gathered}\frac{d}{dt}\mathcal{L}(e_t) \le z^{\mathsf{T}}\mathsf{W}z - \alpha e^{\mathsf{T}}Pe - \alpha\frac{k_0}{2}\mathrm{tr}\left\{\Delta W_0 \Delta W_0^{\mathsf{T}}\right\} \\ -\alpha\frac{k_1}{2}\mathrm{tr}\left\{\Delta W_1 \Delta W_1^{\mathsf{T}}\right\} + \\ \varepsilon\left(\|\eta_t\|^2 + \left\|\tilde{\xi}(x,t)\right\|^2 + \left\|\varphi(\hat{x})\right\|^2 + \left\|\psi(\hat{x})u\right\|^2\right) = z^{\mathsf{T}}Wz \\ -\alpha\mathcal{L}(e_t) + \varepsilon\left(\|\eta_t\|^2 + \left\|\tilde{\xi}(x,t)\right\|^2 + \left\|\varphi(\hat{x})\right\|^2 + \left\|\psi(\hat{x})u\right\|^2\right)\end{gathered} \tag{A.35}$$

where W is defined in (3.26). Applying the upper estimates

$$\|\eta_t\|^2 \le \eta_+^2,\ \left\|\tilde{\xi}(x,t)\right\|^2 \le c_0 + c_1\|x\|^2,$$
$$\left\|\varphi(\hat{x})\right\|^2 \le \varphi_+^2,\ \left\|\psi(\hat{x})u\right\|^2 \le k^2\psi_+^2,$$

to the right-hand side of (A.35), we get

$$\begin{gathered}\frac{d}{dt}\mathcal{L}(e_t) \le z^{\mathsf{T}}\mathsf{W}z - \alpha\mathcal{L}(e_t) + \\ \varepsilon\left(\eta_+^2 + c_0 + c_1\|x\|^2 + \varphi_+^2 + k^2\psi_+^2\right).\end{gathered} \tag{A.36}$$

In view of the uniform boundedness property (3.11) we have

$$\begin{gathered}\frac{d}{dt}\mathcal{L}(e_t) \le z^{\mathsf{T}}\mathsf{W}z - \alpha\mathcal{L}(e_t) + \varepsilon\beta, \\ \beta := C_0 + k^2 C_1, \\ C_0 := \eta_+^2 + c_0 + c_1 d_0 + \varphi_+^2,\ C_1 := \psi_+^2 + c_1 d_1.\end{gathered} \tag{A.37}$$

Supposing that for given matrices A and C there exist

$$P > 0, L, W_0^*, W_1^*, \Lambda, \Lambda_1,$$

and positive constants α and ε such that

$$\mathsf{W} = \mathsf{W}\left(P, L, W_0^*, W_1^*, \Lambda, \Lambda_1 \mid \alpha, \varepsilon\right) < 0, \tag{A.38}$$

then from (A.37) it follows that

$$\frac{d}{dt}\mathcal{L}(e_t) \le -\alpha\mathcal{L}(e_t) + \varepsilon\beta. \tag{A.39}$$

As a result, we get

$$\limsup_{t\to\infty} e_t^{\mathsf{T}} P e_t \le \limsup_{t\to\infty}\mathcal{L}(e_t) \le \frac{\varepsilon}{\alpha}\beta,$$

which leads to (3.27).

A.4 MATHEMATICAL ASPECTS OF CHAPTER 4

Proposition A.3. *Consider the class of nonlinear systems given by (4.1) with the unmodeled dynamics (4.6), satisfying (4.7), and the DNN-observer, given by (4.10) with the gain matrices L_1, L_2, and L_3, satisfying (4.12), and using the updating laws for the weights W_i and V_i ($i = 1, 2$), governed by (4.11). If there exist positive definite matrices Λ_j ($j = \overline{1,7}$), Q_0, P_1, and a positive constant δ, which guarantee the existence of a positive definite solution for the following matrix Riccati equation:*

$$PA + A^{\intercal}P + PRP + Q = 0 \tag{A.40}$$

with

$$R = 2\bar{W}_1 + 2\bar{W}_2 + \sum_{k=1}^{2} \Lambda_k,$$

$$Q = \delta \sum_{k=3}^{6} \Lambda_k^{-1} + \Lambda_\sigma + \left(u^+\right)^2 \Lambda_\phi + k\delta I_{n\times n} + P_1 + C^{\intercal}\left(\Upsilon_2^{-1}\Lambda_7^{-1}\left[\Upsilon_2^{-1}\right]^{\intercal}\right)C + k\delta I_{n\times n} + Q_0,$$

then the following upper bound for the averaged estimation error holds:

$$\limsup_{T\to\infty} \|\Delta_t\|_P^2 \leq \frac{\rho_Q}{\left(k\sqrt{\alpha_P} + k^2\sqrt{\alpha_P} + \alpha_Q\rho_Q\right)} \tag{A.41}$$

with

$$\rho_Q = \eta_1 + \Upsilon_1 + \left(7 + 4k\sqrt{n}\right)\Upsilon_2 + k\theta,$$

$$\alpha_P = \lambda_{\min}\left(P^{-1/2}\left[C^{\intercal}C + \delta I_{n\times n}\right]P^{-1/2}\right) > 0,$$

$$\alpha_Q = \lambda_{\min}\left(P^{-1/2}Q_0P^{-1/2}\right) > 0.$$

Proof. Let us define the state estimation error as $\Delta_t = x_t - \hat{x}_t$ and the output error as

$$e_t = y_t - \hat{y}_t = Cx_t + \xi_{2,t} - C\hat{x}_t = C\Delta_t + \xi_{2,t}$$

for which the following identities hold:

$$C^T e_t = C^T\left[C\Delta_t + \xi_{2,t}\right] = N_\delta^{-1}\Delta_t + C^T\xi_{2,t} - \delta\Delta_t,$$

$$\Delta_t = N_\delta\left(C^T e_t - C^T\xi_{2,t} + \delta\Delta_t\right).$$

The dynamics of Δ_t is governed by the following ODE:

$$\dot{\Delta}_t = \dot{x}_t - \frac{d\hat{x}_t}{dt} = A^{(0)}\Delta_t + \tilde{W}_{1,t}\sigma\left(\hat{x}_t\right)$$

$$+ W_1^0 \tilde{\sigma}\left(x, \hat{x}_t\right) + \tilde{W}_{2,t}\varphi\left(\hat{x}\right)u_t - W_2^0 \tilde{\varphi}\left(x, \hat{x}_t\right)u + \tilde{f}_t + \xi_{1,t} - K_1\left(y_t - \hat{y}_t\right) - K_2 \frac{y_t - \hat{y}_t}{\left\| y_t - \hat{y}_t \right\|},$$

where $\tilde{\sigma}_t := \sigma\left(x_t\right) - \sigma\left(\hat{x}_t\right)$ and $\tilde{\varphi}\left(x, \hat{x}_t\right) = \varphi\left(x\right) - \varphi\left(\hat{x}_t\right)$. Define the energetic function as

$$V := V\left(\Delta, \hat{x}, \tilde{W}\right) = \bar{V}\left(x_t\right) + \|\Delta\|_P^2 + 2^{-1}k_{1,t}^{-1}\mathrm{tr}\left\{\tilde{W}_{1,t}^T \tilde{W}_{1,t}\right\} + 2^{-1}k_{2,t}^{-1}\mathrm{tr}\left\{\tilde{W}_{2,t}^T \tilde{W}_{2,t}\right\}.$$

Its time-derivative is

$$\dot{V} = \frac{d}{dt}\bar{V}\left(x_t\right) + 2\Delta_t^T P\dot{\Delta}_t - 2^{-1}k_{1,t}^{-2}\dot{k}_{1,t}\mathrm{tr}\left\{\tilde{W}_{1,t}^T \tilde{W}_{1,t}\right\} + k_{1,t}^{-1} tr\left\{\tilde{W}_{1,t}^T \dot{W}_{1,t}\right\} - 2^{-1}k_{2,t}^{-2}\dot{k}_{2,t}\mathrm{tr}\left\{\tilde{W}_{2,t}^T \tilde{W}_{2,t}\right\} + k_{2,t}^{-1}\mathrm{tr}\left\{\tilde{W}_{2,t}^T \dot{W}_{2,t}\right\} = 2\Delta_t^T P_1\dot{\Delta}_t + \mathrm{tr}\left\{k_{1,t}^{-1}\tilde{W}_{1,t}^T\left[-2^{-1}k_{1,t}^{-1}\dot{k}_{1,t}\tilde{W}_{1,t} + \dot{W}_{1,t}\right]\right\} + \mathrm{tr}\left\{k_{2,t}^{-1}\tilde{W}_{2,t}^T\left[-2^{-1}k_{2,t}^{-1}\dot{k}_{2,t}\tilde{W}_{2,t} + \dot{W}_{2,t}\right]\right\}.$$

Using the last equation and the corresponding state estimation error dynamics, the following identity could be explored:

$$\Delta_t^T P\dot{\Delta}_t = \Delta_t^T P\left[A^{(0)}\Delta_t + \tilde{W}_{1,t}\sigma\left(\hat{x}_t\right) + W_1^0\tilde{\sigma}\left(x, \hat{x}_t\right)\right] + \Delta_t^T P\left[\tilde{W}_{2,t}\varphi\left(\hat{x}\right)u_t + W_2^0\tilde{\varphi}\left(x, \hat{x}_t\right)u + \tilde{f}_t\right] + \Delta_t^T P\left[\xi_{1,t} - K_1\left(y_t - \hat{y}_t\right) - K_2\frac{y_t - \hat{y}_t}{\left\| y_t - \hat{y}_t \right\|}\right].$$

Notice that

$$\Delta_t^T P A^{(0)}\Delta_t = \frac{1}{2}\Delta_t^T\left[P A^{(0)} + \left(A^{(0)}\right)^T P\right]\Delta_t.$$

Let us estimate the rest of the terms in the last equation, by means of the matrix inequality

$$X^T Y + \left(X^T Y\right)^T \leq X^T \Lambda^{-1} X + Y^T \Lambda Y,$$
$$X, Y \in \mathbb{R}^{n\times m} < \Lambda = \Lambda^T \in \mathbb{R}^{n\times m}.$$

The following upper bound for the Lyapunov time-derivative expression is derived:

$$
\begin{gathered}
2\Delta_t^T P_1 \dot{\Delta}_t = \Delta_t^T \left[P\bar{A} + \bar{A}^T P \right] \Delta_t + \\
\Delta_t^T P \left[W_2^0 \Lambda_\varphi^{-1} \left[W_2^0 \right]^T + W_1^0 \Lambda_\sigma^{-1} \left[W_1^0 \right]^T \right] P \Delta_t + \\
\Delta_t^T P \left[\Lambda_f^{-1} + \Lambda_{\xi_1}^{-1} + \Lambda_3^{-1} \right] P \Delta_t + \Delta_t^T \left[\Lambda_1 + \Lambda_2 \right] \Delta_t + \\
\tilde{\sigma}^T \left(x, \hat{x}_t \right) \Lambda_\sigma \tilde{\sigma} \left(x, \hat{x}_t \right) + \\
\left(\tilde{\varphi} \left(x, \hat{x}_t \right) u \right)^T \Lambda_\varphi \tilde{\varphi} \left(x, \hat{x}_t \right) u + \tilde{f}_t^T \Lambda_f \tilde{f}_t + \xi_{1,t}^T \Lambda_{\xi_1} \xi_{1,t} + \\
K_1^T \Lambda_3 K_1 + 3\xi_{2,t}^T \Lambda_{\xi_2} \xi_{2,t} - \\
2\Delta_t^T P K_2 \frac{y_t - \hat{y}_t}{\left\| y_t - \hat{y}_t \right\|} + e_t^T C N_\delta P \tilde{W}_{1,t} \sigma \left(\hat{x}_t \right) + \\
e_t^T C N_\delta P \tilde{W}_{2,t} \varphi \left(\hat{x} \right) u_t + \\
\sigma^T \left(\hat{x}_t \right) \tilde{W}_{1,t}^T P N_\delta \Pi_1 N_\delta P \tilde{W}_{1,t} \sigma \left(\hat{x}_t \right) + \\
\left[\varphi \left(\hat{x} \right) u_t \right]^T \tilde{W}_{2,t}^T P N_\delta \Pi_2 N_\delta P \tilde{W}_{2,t} \varphi \left(\hat{x} \right) u_t,
\end{gathered}
$$

where

$$
\Pi_j := C^T \Lambda_{\xi_2}^{-1} C + \delta^2 \Lambda_j^{-1},\ j = 1, 2.
$$

Using the results derived in this appendix, by means of the following inequality and the K_2 selection, one can use the following inequality:

$$
\begin{aligned}
\Delta_t^T P K_2 \frac{C\Delta_t + \xi_{2,t}}{\left\| C\Delta_t + \xi_{2,t} \right\|} &= k \left(C\Delta_t \right)^T \frac{C\Delta_t + \xi_{2,t}}{\left\| C\Delta_t + \xi_{2,t} \right\|} \\
&\geq k \left(\sum_{i=1}^{n} \left| \left[C\Delta_t \right]_i \right| - 2\sqrt{n} \left\| \xi_{2,t} \right\| \right) \\
&\geq k \left(\sqrt{\alpha_P} \left\| \Delta_t \right\|_P - \sqrt{\delta \Delta_t^T \Delta_t} - 2\sqrt{n} \left\| \xi_{2,t} \right\| \right).
\end{aligned}
$$

The matrix inequality introduced earlier allows one to represent the time-derivative Lyapunov function:

$$
\begin{gathered}
2\Delta_t^T P_1 \dot{\Delta}_t = \Delta_t^T \left[P\bar{A} + \bar{A}^T P \right] \Delta_t + \\
\Delta_t^T \left[\Lambda_1 + \Lambda_2 + l_\sigma \Lambda_\sigma' + l_\varphi v_0 \Lambda_\varphi' + Q_0 \right] \Delta_t \\
+ \Delta_t^T P \left[W_2^0 \Lambda_\varphi^{-1} \left[W_2^0 \right]^T + W_1^0 \Lambda_\sigma^{-1} \left[W_1^0 \right]^T \right] P \Delta_t + \\
\Delta_t^T P \left[\Lambda_f^{-1} + \Lambda_{\xi_1}^{-1} + \Lambda_3^{-1} \right] P \Delta_t - \left\| \Delta_t \right\|_{Q_0}^2 + \tilde{f}_0 +
\end{gathered}
$$

$$\tilde{f}_1 \|x_t\|^2_{\Lambda^1_{\tilde{f}}} + \Upsilon_1 + K_1^T \Lambda_3 K_1 + 3\Upsilon_2$$
$$-2k\sqrt{\alpha_P}\,\|\Delta_t\|_P + 2k\sqrt{\delta \Delta_t^T \Delta_t} + 4\sqrt{n}k\,\|\xi_{2,t}\|$$
$$+\operatorname{tr}\left\{\tilde{W}_{1,t}^T P N_\delta C^T e_t \sigma^T\left(\hat{x}_t\right)\right\} +$$
$$\operatorname{tr}\left\{\tilde{W}_{2,t}^T P N_\delta C^T e_t \left[\varphi\left(\hat{x}\right) u_t\right]^T\right\} +$$
$$\operatorname{tr}\left\{\tilde{W}_{1,t}^T P N_\delta \Pi_1 N_\delta P \tilde{W}_{1,t} \sigma\left(\hat{x}_t\right) \sigma^T\left(\hat{x}_t\right)\right\} +$$
$$\operatorname{tr}\left\{\tilde{W}_{2,t}^T P N_\delta \Pi_2 N_\delta P \tilde{W}_{2,t} \varphi\left(\hat{x}\right) u_t \left[\varphi\left(\hat{x}\right) u_t\right]^T\right\}.$$

If the last upper bound is substituted in the expression of $\dot{V}$ and by the Raleigh inequality, $\dot{V}$ is upper bounded as follows:

$$\dot{V} \leq \left(-\lambda_1 + \lambda_2 \|\xi_{1,t}\| + \tilde{f}_1 \left\|\Lambda^1_{\tilde{f}}\right\|\right) \|x_t\|^2 +$$
$$\bar{A}^T P + P\bar{A} + PRP + Q$$
$$-\alpha_Q \|\Delta_t\|_P^2 + \tilde{f}_0 + \Upsilon_1 + K_1^T \Lambda_3 K_1 +$$
$$3\Upsilon_2 + 4\sqrt{n}k\,\|\xi_{2,t}\|$$
$$-2k\left(\sqrt{\alpha_P} - \sqrt{\delta\lambda_{\max}\left(P^{-1}\right)}\right)\|\Delta_t\|_P +$$
$$\operatorname{tr}\left\{\tilde{W}_{1,t}^T P N_\delta C^T e_t \sigma^T\left(\hat{x}_t\right) + \tilde{W}_{2,t}^T P N_\delta C^T e_t \left[\varphi\left(\hat{x}\right) u_t\right]^T\right\} +$$
$$\operatorname{tr}\left\{\tilde{W}_{1,t}^T P N_\delta \Pi_1 N_\delta P \tilde{W}_{1,t} \sigma\left(\hat{x}_t\right) \sigma^T\left(\hat{x}_t\right)\right\} +$$
$$\operatorname{tr}\left\{\tilde{W}_{2,t}^T P N_\delta \Pi_2 N_\delta P \tilde{W}_{2,t} \varphi\left(\hat{x}\right) u_t \left[\varphi\left(\hat{x}\right) u_t\right]^T\right\} +$$
$$\operatorname{tr}\left\{k_{1,t}^{-1} \tilde{W}_{1,t}^T \left[-2^{-1} k_{1,t}^{-1} \dot{k}_{1,t} \tilde{W}_{1,t} + \dot{W}_{1,t}\right]\right\} +$$
$$\operatorname{tr}\left\{k_{2,t}^{-1} \tilde{W}_{2,t}^T \left[-2^{-1} k_{2,t}^{-1} \dot{k}_{2,t} \tilde{W}_{2,t} + \dot{W}_{2,t}\right]\right\}.$$

In view of the existence of the Riccati equation solution (P), the learning laws can be applied to the neural network observer. And if

$$\lambda_1 \geq \lambda_2 \|\xi_{1,t}\| + \tilde{f}_1 \left\|\Lambda^1_{\tilde{f}}\right\|$$

then

$$\dot{V} \leq -\alpha_Q \|\Delta_t\|_P^2 -$$
$$2k\left(\sqrt{\alpha_P} - \sqrt{\delta\lambda_{\max}\left(P^{-1}\right)}\right)\|\Delta_t\|_P$$
$$+\tilde{f}_0 + \Upsilon_1 + K_1^T \Lambda_3 K_1 + 3\Upsilon_2 +$$
$$4\sqrt{n}k\,\|\xi_{2,t}\| = -\alpha_Q V_t +$$

$$\alpha_Q\left(\bar{V}\left(x_t\right)+2^{-1}k_{1,t}^{-1}\mathrm{tr}\left\{\tilde{W}_{1,t}^T\tilde{W}_{1,t}\right\}+2^{-1}k_{2,t}^{-1}\mathrm{tr}\left\{\tilde{W}_{2,t}^T\tilde{W}_{2,t}\right\}\right)$$
$$-2k\left(\sqrt{\alpha_P}-\sqrt{\delta\lambda_{\max}\left(P^{-1}\right)}\right)\left\|\Delta_t\right\|_P$$
$$-2k\left(\sqrt{\alpha_P}-\sqrt{\delta\lambda_{\max}\left(P^{-1}\right)}\right)\left[\bar{V}\left(x_t\right)+\right.$$
$$\left.2^{-1}k_{1,t}^{-1}\mathrm{tr}\left\{\tilde{W}_{1,t}^T\tilde{W}_{1,t}\right\}+2^{-1}k_{2,t}^{-1}\mathrm{tr}\left\{\tilde{W}_{2,t}^T\tilde{W}_{2,t}\right\}\right]^{1/2}+$$
$$\tilde{f}_0+\Upsilon_1+K_1^T\Lambda_3K_1+3\Upsilon_2+4\sqrt{n}k\left\|\xi_{2,t}\right\|$$
$$\leq-\alpha_QV_t+\alpha_Q\bar{V}\left(x_t\right)+$$
$$2^{-1}\alpha_Qk_{1,t}^{-1}\mathrm{tr}\left\{\tilde{W}_{1,t}^T\tilde{W}_{1,t}\right\}+2^{-1}\alpha_Qk_{2,t}^{-1}\mathrm{tr}\left\{\tilde{W}_{2,t}^T\tilde{W}_{2,t}\right\}-$$
$$-2k\left(\sqrt{\alpha_P}-\sqrt{\delta\lambda_{\max}\left(P^{-1}\right)}\right)\left(\sqrt{V_t}-\sqrt{\bar{V}\left(x_t\right)}\right)+$$
$$2k\left(\sqrt{\alpha_P}-\sqrt{\delta\lambda_{\max}\left(P^{-1}\right)}\right)\cdot$$
$$\left[\sqrt{2^{-1}k_{1,t}^{-1}}\sum_{i=1}^{n}\left|\tilde{W}_{1,t}^{(i,i)}\right|+\sqrt{2^{-1}k_{2,t}^{-1}}\sum_{i=1}^{n}\left|\tilde{W}_{2,t}^{(i,i)}\right|\right]$$
$$+\tilde{f}_0+\Upsilon_1+K_1^T\Lambda_3K_1+3\Upsilon_2+4\sqrt{n}k\left\|\xi_{2,t}\right\|$$
$$=-\alpha_QV_t+\bar{V}\left(x_t\right)+$$
$$2^{-1}\alpha_Qk_{1,t}^{-1}\mathrm{tr}\left\{\tilde{W}_{1,t}^T\tilde{W}_{1,t}\right\}+2^{-1}\alpha_Qk_{2,t}^{-1}\mathrm{tr}\left\{\tilde{W}_{2,t}^T\tilde{W}_{2,t}\right\}-$$
$$-2k\left(\sqrt{\alpha_P}-\sqrt{\delta\lambda_{\max}\left(P^{-1}\right)}\right)\cdot$$
$$\left(\sqrt{V_t}-\sqrt{\bar{V}\left(x_t\right)}\right)+2k\left(\sqrt{\alpha_P}-\sqrt{\delta\lambda_{\max}\left(P^{-1}\right)}\right)\cdot$$
$$\mathrm{tr}\left\{\sqrt{2^{-1}k_{1,t}^{-1}}\mathrm{diag}\left\{\tilde{W}_{1,t}^{(i,i)}\mathrm{sign}\left(\tilde{W}_{1,t}^{(i,i)}\right)\right\}\right\}+$$
$$\mathrm{tr}\left\{\sqrt{2^{-1}k_{2,t}^{-1}}\mathrm{diag}\left\{\tilde{W}_{2,t}^{(i,i)}\mathrm{sign}\left(\tilde{W}_{2,t}^{(i,i)}\right)\right\}\right\}$$
$$+\tilde{f}_0+\Upsilon_1+K_1^T\Lambda_3K_1+3\Upsilon_2+4\sqrt{n}k\left\|\xi_{2,t}\right\|. \qquad \square$$

A.5 MATHEMATICAL ASPECTS OF CHAPTER 5

A.5.1 Modified DNNO for nonlinear system estimation

In the present study a modification of the observer structure given in Poznyak et al. (2005) and related with the variable structure term (K_2) is introduced. The main modification on the DNNO structure is associated with the term $K_2\dfrac{y_t-\hat{y}_t}{\left\|y_t-\hat{y}_t\right\|}$, which corresponds to the so-called variable structure

element (here $\|\cdot\|$ represents the Euclidean norm). The new term is added to the DNNO scheme to improve the convergent rate from the state estimator trajectories to those provided by the nonlinear system (Luenberger, 1964). The class of systems to be treated during this work is described by the vector nonlinear differential equation

$$\begin{aligned} \dot{x}_t &= f(x_t, u_t) + \xi_{1,t}, \\ y_t &= Cx_t + \xi_{2,t}, \end{aligned} \tag{A.42}$$

where $x_t \in \Re^n$ is the system state, $y_t \in \Re^p$ is the system output ($p \leq n$), $u_t \in \Re^m$ is the bounded control action ($m \leq n$) belonging to the following admissible set:

$$U^{adm} := \left\{ u : \|u\|^2_{\Lambda_u} = u^T \Lambda_u u \leq v_0 < \infty \right\},$$
$$\Lambda_u = \Lambda_u^T > 0.$$

The output matrix $C \in \Re^{p \times n}$ is assumed to be known a priori. The nominal closed-loop dynamics is quadratically stable for a fixed control $u_t^* \in U^{adm}$, that is, there exists a Lyapunov function $\bar{V}_t$ such that:

$$\frac{\partial \bar{V}_t}{\partial x} f(x_t, u_t) \leq -\lambda_1 \|x_t\|^2 < 0,$$
$$\left\| \frac{\partial \bar{V}_t}{\partial x} \right\| \leq \lambda_2 \|x_t\|^2 < \infty \;\; \lambda_1, \lambda_2 > 0.$$

The vectors $\xi_{1,t}$ and $\xi_{2,t}$ represent the state and output deterministic bounded (unmeasurable) disturbances, i.e.,

$$\left\|\xi_{j,t}\right\|^2_{\Lambda_{\xi_j}} \leq \gamma_j, \;\; \Lambda_{\xi_j} = \Lambda_{\xi_j}^T > 0, \; j = 1, 2,$$

and they do not violate the existence of the solution to ODE (A.42). The nominal output system (without external perturbations $\xi_{2,t} = 0$) is uniformly observable, that is, the following (observability) matrix $\tilde{O}$ is not singular for any $t \geq 0$, that is,

$$\operatorname{rank} \tilde{O} := n,$$
$$\tilde{O} = \nabla_x \left[C^T, \left[L_f (Cx_t)\right]^T, \left[L_f^2 (Cx_t)\right]^T, ..., \left[L_f^{n-1} (Cx_t)\right]^T \right]^T.$$

Here $L_f(\cdot)$ is the Lie derivative operator. To ensure the uniqueness and the existence of the nonlinear dynamics, it is supposed that the class of nonlinear functions in (A.42) satisfies the Lipschitz condition on the two first arguments, that is,

$$\|f(x, u) - f(y, v)\| \leq L_1 \|x - y\| + L_2 \|u - v\|,$$

$$\|f(0,0)\|^2 \le C_1;\ x, y \in \Re^n;\ u, v \in \Re^m,$$
$$0 \le L_1, L_2 < \infty.$$

The last assumption automatically implies the following cone-property:

$$\|f(x_t, u_t)\|^2 \le C_1 + C_2 \|x_t\|^2,$$

which is valid for any x, u and t. Notice that (1) always could be represented as

$$\left.\begin{aligned} \dot{x}_t &= f_0(x_t, u_t|\Theta) + \tilde{f}_t + \xi_{1,t}, \\ \tilde{f}_t &:= f(x_t, u_t) - f_0(x, u|\Theta), \end{aligned}\right\}$$

where $f_0(x, u|\Theta)$ is treated as a possible "*nominal dynamics*" which can be selected according to designer desires and $\tilde{f}_t$ is a vector called the "*no modeled dynamics*". Here the parameters Θ are subjected to adjustment in order to obtain the complete matching between the nominal and the nonlinear dynamics. In view of (6) and the corresponding boundedness property, the following upper bound for the no modeled dynamics $\tilde{f}_t$ occurs:

$$\left\|\tilde{f}_t\right\|^2_{\Lambda_f} \le \tilde{f}_0 + \tilde{f}_1 \|x_t\|^2_{\Lambda^1_{\tilde{f}}},\ \Lambda_f, \Lambda^1_{\tilde{f}} > 0.$$

According to the DNN approach, we will define the nominal dynamics as

$$f_0(x, u, t|\Theta) = A^0 x + W_1^0 \sigma(x) + W_2^0 \varphi(x) u,$$
$$\Theta := \left[W_1^0, W_2^0\right], A^0 \in \Re^{n\times n},$$
$$W_1^0, W_2^0, \in \Re^{n\times n}, \sigma \in \Re^{l\times 1}, \varphi \in \Re^{n\times m}.$$

The activation vector-functions $\sigma_i(\cdot)$ and $\varphi(\cdot)$ are usually constructed with sigmoid function components,

$$\sigma_j(x) := a_j \left(1 + b_j \exp\left(-\sum_{j=1}^{n} c_j x_j\right)\right)^{-1},$$
$$\varphi_{kl}(x) := a_{kl} \left(1 + b_{kl} \exp\left(-\sum_{j=1}^{n} c_{kl} x_l\right)\right)^{-1},$$
$$j = \overline{1,n},\ k = \overline{1,n},\ l = \overline{1,m}.$$

It is easy to prove that each component in the activation functions satisfies the following sector conditions:

$$\left\|\sigma(x) - \sigma\left(x'\right)\right\|^2_{\Lambda_\sigma} \le l_\sigma \left\|x - x'\right\|^2_{\Lambda'_\sigma},$$

$$\left\| \left(\varphi\left(x\right) - \varphi\left(x'\right)\right) u_t \right\|_{\Lambda_\varphi}^2 \leq l_\varphi v_0 \left\| x - x' \right\|_{\Lambda'_\varphi}^2 .$$

The modified DNN state estimator is covered by the following ordinary nonlinear differential equation:

$$\begin{aligned} \frac{d}{dt}\hat{x}_t &= A\hat{x}_t + W_{1,t}\sigma\left(\hat{x}_t\right) + W_{2,t}\varphi\left(\hat{x}_t\right) u_t \\ &\quad + K_1 e_t + K_2 \frac{y_t - \hat{y}_t}{\left\| y_t - \hat{y}_t \right\|}, \\ \hat{y}_t &= C\hat{x}_t . \end{aligned} \tag{A.43}$$

Here $\hat{x}_t \in \mathbb{R}^n$ is the state vector of DNNO representing the current estimates of the phenol concentration, $u_t \in \mathbb{R}^m$ is the input vector for DNNO and the experimental system (in this case it is the concentration of the inflow), $\hat{y}_t \in \mathbb{R}^p$ is the output of DNN corresponding to the estimates of the measurable ozone concentration in the gas phase; $A \in \mathbb{R}^{n\times n}$, $K_1 \in \mathbb{R}^{n\times p}$ and $K_2 \in \mathbb{R}^{n\times p}$ are constant matrices, adjusted during DNN training, $\sigma\left(.\right) \in \Re^n$ and $\varphi\left(.\right) \in \mathbb{R}^{n\times m}$ are standard vector fields constructed (each element) by sigmoid functions, $C \in \mathbb{R}^{p\times n}$ is an output matrix, $W_i \in \mathbb{R}^{n\times n}$, $i = 1, 2$, are the weight layers (the first one corresponds to the self feedback adjustment and the second is related with the input effect on the state estimation process) tuning by a special online *learning procedure* (Poznyak et al., 2001).

The measurable data are the ozone concentration variation in the gas phase in the reactor output, that is, $y_t = x_1 \in \Re$. So, $C = (1, 0, ..., 0)$. The gain matrix K_1 corresponds to a linear correction term (Poznyak et al., 2006a), K_2 is a sliding mode-type correction term matrix (Lewis et al., 1998). The adequate learning of DNNO (A.43) provides a small enough upper bound (in an average sense) for the state estimation error $\Delta_t = \hat{x}_t - x_t$. The learning process is given by

$$\begin{aligned} \dot{W}_{j,t} &= -k_{j,t}\left[\Lambda_j P C^T e_t + \tfrac{1}{2}\Pi_j P \tilde{W}_{j,t}\chi_j + P\hat{x}_t\right]\chi_j^T, \\ \chi_1 &= \sigma\left(\hat{x}_t\right), \chi_2 = \varphi\left(\hat{x}_t\right) u_t, \\ \Pi_j = \Pi_j^T > 0,\ \Pi_j &\in \mathbb{R}^{n\times n},\ P = P^T > 0,\ P \in \mathbb{R}^{n\times n}, \\ \Lambda_j = \Lambda_j^T &> 0,\ \Lambda_j \in \mathbb{R}^{n\times n},\ j = 1, 2, \\ \tilde{W}_{j,t} &= W_{j,t} - W_{j,t}^*,\ k_j > 0,\ k_j \in \mathbb{R}, \end{aligned} \tag{A.44}$$

where the matrix P is the positive definite solution for the Riccati equation,

$$\begin{aligned} P\tilde{A}^{(0)*} + \left(\tilde{A}^{(0)*}\right)^T P + PRP + Q = 0, \\ \bar{A} := A^{(0)*} - K_1 C, \end{aligned}$$

$$Q := \Lambda_1^{-1} + \Lambda_2^{-1} + \Lambda_\sigma + v_0\Lambda_\varphi + Q_0,$$
$$R := W_1^0\Lambda_\sigma^{-1}\left[W_1^0\right]^T + W_2^0\Lambda_\varphi^{-1}\left[W_2^0\right]^T +$$
$$\Lambda_{\tilde{f}}\Lambda_{\xi_1} + K_1\Lambda_{\xi_2}K_1^T + K_2\Lambda K_2^T.$$

Here it is important to notice that the observer (A.43) does not use any information on the model structure of the real process, that is, any a priori given dynamic model of the process does not require to be in use for the suggested DNN observers. In this sense, the suggested technique may be treated as a physical model-free process. Let us consider the DNNO defined by (A.43) with the corresponding learning law governed by (A.44). It is possible to ensure the following upper bound for the estimation process:

$$\limsup_{t\to\infty}\frac{1}{t+\varepsilon}\int_{s=0}^{t}\left\|\hat{x}_s - x_s\right\|_{Q_0} ds \le \frac{\rho_Q}{\alpha_Q},$$
$$\rho_Q := \tilde{f}_0 + v_0 + \gamma_1 + 3\gamma_2 + 8\lambda\sqrt{n\gamma_2}, \tag{A.45}$$
$$\alpha_Q := \lambda_{\min}\left(P^{-1/2}Q_0P^{-1/2}\right).$$

The last inequality means that the reconstructed trajectories for the immeasurable variables, involved in the ozonation, are close to their real values as small as the disturbances values are, as expected. The details on the meaning of the upper limit for the averaged estimation error (A.45), the convergence properties of the learning algorithm (A.44), and any other special feature on the DNNO structure and its philosophy are discussed in Poznyak et al. (2001), Poznyak and Vivero (2005).

Proof of proposition. Define the estimation error as $\Delta_t = x_t - \hat{x}_t$ and the output error as

$$e_t = y_t - C\hat{x}_t = Cx_t + \xi_{2,t} - C\hat{x}_t,$$

which implies

$$C^T e_t = \left(C^TC + \delta I_{n\times n}\right)\Delta_t + C^T\xi_{2,t} - \delta\Delta_t$$

and

$$\Delta_t = N_\delta\left(C^Te_t + C^T\xi_{2,t} + \delta I_{n\times n}\Delta_t\right),$$
$$N_\delta := \left[CC^T + \delta I_{n\times n}\Delta_t\right]^{-1}.$$

Thus, we have

$$\dot{\Delta}_t = A\Delta_t + W_{1,0}\sigma\left(V_{1,0}\hat{x}_t\right) +$$

$$
\begin{gathered}
W_{2,0}\varphi\left(V_{2,0}\hat{x}_t\right)\gamma\left(u_t\right)+ \\
\Delta f\left(x_t,u_t,t\right)+\xi_{1,t}+ \\
\tilde{W}_{1,t}\sigma\left(V_{1,t}\hat{x}_t\right)+\tilde{W}_{2,t}\varphi\left(V_2\hat{x}_t\right)\gamma\left(u_t\right)- \\
K_1\left(y_t-\hat{y}_t\right)-K_2\mathrm{sign}\left(y_t-\hat{y}_t\right)- \\
\frac{K_3}{h}\left(\left(y_t-y_{t-h}\right)-\left(\hat{y}_t-\hat{y}_{t-h}\right)\right)
\end{gathered}
$$

with

$$
\begin{gathered}
\tilde{W}_{1,t}=W_{1,0}-W_{1,t},\ \tilde{W}_{2,t}=W_{2,0}-W_{2,t}, \\
\tilde{V}_{1,t}=V_{1,0}-V_{1,t},\ \tilde{V}_{2,t}=V_{2,0}-V_{2,t}.
\end{gathered}
$$

Define the Lyapunov–Krasovskii function as

$$
\begin{gathered}
V_t:=\bar{V}_t+\|\Delta_t\|_P^2+k_1^{-1}tr\left\{\tilde{W}_{1,t}\tilde{W}_{1,t}^T\right\}+ \\
k_2^{-1}tr\left\{\tilde{W}_{2,t}\tilde{W}_{2,t}^T\right\}+k_3^{-1}tr\left\{\tilde{V}_{1,t}\tilde{V}_{1,t}^T\right\}+ \\
k_4^{-1}tr\left\{\tilde{V}_{2,t}\tilde{V}_{2,t}^T\right\}+\int_{\tau=t-h}^{t}\|\Delta_\tau\|_{P_1}^2d\tau, \\
P=P^T>0,\qquad P_1=P_1^T>0.
\end{gathered}
$$

$\bar{V}_t$ is the Lyapunov function for the original unknown system (4.1). By direct differentiation, we obtain

$$
\begin{gathered}
\dot{V}_t:=\frac{d}{dt}\bar{V}_t+2\Delta_t^TP\dot{\Delta}_t+ \\
2k_1^{-1}\mathrm{tr}\left\{\dot{W}_{1,t}\tilde{W}_{1,t}^T\right\}+2k_2^{-1}\mathrm{tr}\left\{\dot{W}_{2,t}\tilde{W}_{2,t}^T\right\}+ \\
2k_3^{-1}\mathrm{tr}\left\{\dot{V}_{1,t}\tilde{V}_{1,t}^T\right\}+2k_4^{-1}\mathrm{tr}\left\{\dot{V}_{2,t}\tilde{V}_{2,t}^T\right\}+ \\
\|\Delta_t\|_{P_1}^2-\|\Delta_{t-h}\|_{P_1}^2.
\end{gathered}
\tag{A.46}
$$

Applying the matrix inequality

$$
X^TY+Y^TX\le X^T\Lambda X+Y^T\Lambda^{-1}Y,
$$

valid for any positive definite matrix Λ and any X and Y of the same size, we may derive the upper bounds for all terms in (A.46):

1)

$$
2\Delta_t^TPA\Delta_\mathrm{t}=\Delta_t^TPA\Delta_\mathrm{t}+\Delta_t^TPA\Delta_\mathrm{t}=\Delta_t^T\left(PA+A^TP\right)\Delta_\mathrm{t},
$$

2)

$$
2\Delta_t^TP\tilde{W}_{1,t}\sigma\left(V_{1,t}\hat{x}_t\right)\le 2e_t^TCN_\delta^TP\tilde{W}_{1,t}\sigma\left(V_{1,t}\hat{x}_t\right)+
$$

$$\xi_{2,t}^T \Lambda_3^{-1} \xi_{2,t} + \delta \Delta_t^T \Lambda_4^{-1} \Delta_t +$$
$$\sigma\left(V_{1,t}\hat{x}_t\right)^T \tilde{W}_{1,t}^T P N_\delta C^T \Lambda_3 C N_\delta^T P \tilde{W}_{1,t} \sigma\left(V_{1,t}\hat{x}_t\right) +$$
$$\delta\sigma\left(V_{1,t}\hat{x}_t\right)^T \tilde{W}_{1,t}^T P N_\delta \Lambda_4 N_\delta^T P \tilde{W}_{1,t} \sigma\left(V_{1,t}\hat{x}_t\right),$$

3)

$$2\Delta_t^T P \xi_{1,t} \leq \Delta_t^T P \Lambda_{10}^{-1} P \Delta_t + \xi_{1,t}^T \Lambda_{10} \xi_{1,t}$$
$$\leq \Delta_t^T P \Lambda_{10}^{-1} P \Delta_t + \Upsilon_1.$$

Using the same technique for the rest of the terms in the right-hand side of (A.46), we finally obtain

$$\begin{gathered}
\dot{V}_t \leq \left(-\lambda_1 - \lambda_2\sqrt{\Upsilon_1} + \eta_2 \|\Lambda_9\|\right) \left\|\hat{x}_t\right\|^2 + \\
\eta_1 + \Upsilon_1 + 6\Upsilon_2 + \\
\Delta_t^T \left(PA + A^T P + P_1 + \delta\Lambda_{17}^{-1} + \delta\Lambda_4^{-1}\right. \\
\left. + \delta\Lambda_6^{-1} + \delta\Lambda_{15}^{-1} + \Lambda_\sigma + \bar{u}^2\Lambda_\varphi + Q_0\right)\Delta_t + \\
\Delta_t^T P \left(2\bar{W}_1 + 2\bar{W}_2 + \Lambda_9^{-1} + \Lambda_{10}^{-1}\right) P\Delta_t \\
-\Delta_t^T Q_0 \Delta_{\mathrm{t}} - 2k\left(\sqrt{\alpha_P}\,\|\Delta_t\|_P - \sqrt{\delta\Delta_t^T\Delta_t}\right) + \\
4k\sqrt{N\Upsilon_2} + tr\left\{2k_1^{-1}\dot{W}_{1,t}\tilde{W}_{1,t}^T\right\} + \\
\mathrm{tr}\left\{2PN_\delta C^T e_t \sigma\left(V_{1,t}\hat{x}_t\right)^T \tilde{W}_{1,t}^T\right\} + \\
\mathrm{tr}\left\{PN_\delta C^T \Lambda_3 C N_\delta^T P \tilde{W}_{1,t} \sigma\left(V_{1,t}\hat{x}_t\right) \sigma\left(V_{1,t}\hat{x}_t\right)^T \tilde{W}_{1,t}^T\right\} + \\
\mathrm{tr}\left\{\delta PN_\delta \Lambda_4 N_\delta^T P \tilde{W}_{1,t} \sigma\left(V_{1,t}\hat{x}_t\right) \sigma\left(V_{1,t}\hat{x}_t\right)^T \tilde{W}_{1,t}^T\right\} + \\
\mathrm{tr}\left\{2k_2^{-1}\dot{W}_{2,t}\tilde{W}_{2,t}^T\right\} + \\
\mathrm{tr}\left\{2PN_\delta C^T e_t \gamma(u)^T \varphi\left(V_{2,t}\hat{x}_t\right)^T \tilde{W}_{2,t}^T\right\} + \\
\mathrm{tr}\left\{PN_\delta C^T \Lambda_5 C N_\delta^T P \tilde{W}_{2,t} \varphi\left(V_{2,t}\hat{x}_t\right) \gamma(u)\gamma(u)^T \varphi\left(V_{2,t}\hat{x}_t\right)^T \tilde{W}_{2,t}^T\right\} + \\
\mathrm{tr}\left\{\delta PN_\delta \Lambda_6 N_\delta^T P \tilde{W}_{2,t} \varphi\left(V_{2,t}\hat{x}_t\right) \gamma(u)\gamma(u)^T \varphi\left(V_{2,t}\hat{x}_t\right)^T \tilde{W}_{2,t}^T\right\} - \\
\mathrm{tr}\left\{2N_\delta C^T e_t \hat{x}_t^T{}_t \tilde{V}_{1,t}^T D_\sigma^T \tilde{W}_{1,t}^T\right\} - \\
\mathrm{tr}\left\{2N_\delta C^T e_t \hat{x}_t^T{}_t \tilde{V}_{2,t}^T D_\varphi^T \tilde{W}_{2,t}^T\right\} + \\
\mathrm{tr}\left\{2k_3^{-1}\dot{V}_{1,t}\tilde{V}_{1,t}^T\right\} + \mathrm{tr}\left\{2k_4^{-1}\dot{V}_{2,t}\tilde{V}_{2,t}^T\right\} +
\end{gathered} \tag{A.47}$$

$$\operatorname{tr}\left\{\delta D_\sigma^T \left(W_1^*\right)^T N_\delta \Lambda_{15} N_\delta^T W_1^* D_\sigma \tilde{V}_{1,t} \hat{x}_t \hat{x}_t^T \tilde{V}_{1,t}^T\right\} +$$
$$\operatorname{tr}\left\{l_1 \Lambda_7 \tilde{V}_{1,t} \hat{x}_t \hat{x}_t^T \tilde{V}_{1,t}^T\right\} + \operatorname{tr}\left\{2 D_\sigma^T W_{1,t}^T N_\delta C^T e_t \hat{x}_t^T \tilde{V}_{1,t}^T\right\} +$$
$$\operatorname{tr}\left\{D_\sigma^T \left(W_1^*\right)^T N_\delta C^T \Lambda_{16} C N_\delta^T W_1^* D_\sigma \tilde{V}_{1,t} \hat{x}_t \hat{x}_t^T \tilde{V}_{1,t}^T\right\} +$$
$$\operatorname{tr}\left\{\delta D_\varphi^T \left(W_2^*\right)^T N_\delta \Lambda_{17} N_\delta^T W_2^* D_\varphi \tilde{V}_{2,t} \hat{x}_t \hat{x}_t^T \tilde{V}_{2,t}^T\right\} +$$
$$\operatorname{tr}\left\{l_2 \Lambda_8 \tilde{V}_{2,t} \hat{x}_t \hat{x}_t^T \tilde{V}_{2,t}^T\right\} + tr\left\{2 D_\varphi^T W_{2,t}^T N_\delta C^T e_t \hat{x}_t^T \tilde{V}_{2,t}^T\right\} +$$
$$\operatorname{tr}\left\{D_\varphi^T \left(W_2^*\right)^T N_\delta C^T \Lambda_{18} C N_\delta^T W_2^* D_\varphi \tilde{V}_{2,t} \hat{x}_t \hat{x}_t^T \tilde{V}_{2,t}^T\right\} -$$
$$2\Delta_t^T \left[P K_1 C - P K_1 \Lambda_{18}^{-1} K_1^T P\right] \Delta_t + \Upsilon_2 +$$
$$\Delta_t^T P \left(\frac{1}{h^2} K_3 \left(\Lambda_{12}^{-1} + C \Lambda_{13}^{-1} C^T + \Lambda_{14}^{-1}\right) K_3^T P - 2\frac{K_3}{h} C\right) \Delta_t.$$

In view of the accepted learning laws (4.11), the upper bound for the time-derivative of Lyapunov function becomes

$$\dot{V}_t \leq \left(-\lambda_1 - \lambda_2 \left\|\xi_{1,t}\right\| + \eta_2 \left\|\Lambda_9\right\|\right) \left\|\hat{x}_t\right\|^2 +$$
$$\eta_1 + \Upsilon_1 + 7\Upsilon_2 +$$
$$\Delta_t^T \left(P A + A^T P + P_1 + \delta \Lambda_{17}^{-1} + \delta \Lambda_4^{-1} + \delta \Lambda_6^{-1}\right) \Delta_t +$$
$$\Delta_t^T \left(\delta \Lambda_{15}^{-1} + \Lambda_\sigma + \bar{u}^2 \Lambda_\varphi + k\delta \Xi I_{n\times n} + Q_0\right) \Delta_t +$$
$$\Delta_t^T \left(C^T \xi_{2,t}^{-1} \Lambda_{18}^{-1} \left(\xi_{2,t}^{-1}\right)^T C - C^T \Lambda_{\xi_{2,t}}^{-1} C\right) \Delta_{\mathrm{t}}$$
$$-2k\sqrt{\alpha_P} \left\|\Delta_t\right\|_P + 4k\sqrt{N} \left\|\xi_{2,t}\right\| + k\Xi +$$
$$\Delta_t^T P \left(2\bar{W}_1 + 2\bar{W}_2 + \Lambda_9^{-1} + \Lambda_{10}^{-1}\right) P \Delta_t - \Delta_t^T Q_0 \Delta_t$$
$$= \left(-\lambda_1 - \lambda_2 \sqrt{\Upsilon_1} + \eta_2 \left\|\Lambda_9\right\|\right) \left\|\hat{x}_t\right\|^2 +$$
$$\eta_1 + \Upsilon_1 + 7\Upsilon_2 + 4k\sqrt{N} \left\|\xi_{2,t}\right\| +$$
$$k\Xi - \Delta_t^T Q_0 \Delta_{\mathrm{t}} - 2k\sqrt{\alpha_P} \left\|\Delta_t\right\|_P.$$

Selecting Λ_9 such that

$$\eta_2^{-1} \left(\lambda_1 + \lambda_2 \sqrt{\Upsilon_1}\right) \leq \left\|\Lambda_9\right\|,$$

and integrating both sides in (A.47), we get

$$\int_{t=0}^{T} \dot{V}_t dt = V_T - V_0 \leq \int_{t=0}^{T} \rho_Q dt -$$
$$\alpha_Q \int_{t=0}^{T} \left\|\Delta_t\right\|_p^2 dt - 2k\sqrt{\alpha_P} \int_{t=0}^{T} \left\|\Delta_t\right\|_P dt.$$

Taking the upper limit for the last inequality one gets

$$\alpha_Q \overline{\lim_{T\to\infty}} \frac{1}{T} \int_{t=0}^{T} \|\Delta_t\|_p^2 dt +$$
$$2k\sqrt{\alpha_P}\, \overline{\lim_{T\to\infty}} \frac{1}{T} \int_{t=0}^{T} \|\Delta_t\|_P\, dt - \rho_Q \le 0.$$

Defining $\beta := \overline{\lim_{T\to\infty}} \frac{1}{T} \int_{t=0}^{T} \|\Delta_t\|_P\, dt$ and applying the Jensen inequality,

$$\overline{\lim_{T\to\infty}} \frac{1}{T} \int_{t=0}^{T} \|\Delta_t\|_p^2 dt \ge \left(\overline{\lim_{T\to\infty}} \frac{1}{T} \int_{t=0}^{T} \|\Delta_t\|_P dt \right)^2,$$

lead to (A.41). □

A.6 MATHEMATICAL ASPECTS OF CHAPTER 10

Consider the nonlinear continuous-time system with measured output which is given by the following ODE:

$$\begin{aligned} \dot{x}_t &= f(x_t, t) + g(x_t)\, u_t + \xi_t,\ x_0 \text{ is fixed,} \\ y_t &= C x_t + \eta_t, \end{aligned} \tag{A.48}$$

where $x \in \mathbb{R}^n$ is the state vector at time $t \ge 0$, $u \in \mathbb{R}^m$ is the control-vector, which describes the input affecting the system, $y \in \mathbb{R}^p$ is the corresponding output, available for a designer at any time, $C \in \mathbb{R}^{p\times n}$ is the state-output transformation (matrix), ξ and η are the noise in the state dynamics and in the output, respectively.

In many practical problems, it is known a priori that the state vector x_t belongs to a given *compact set* X (even in the presence of noise). For example, the dynamic behavior of some reagents participating in chemical reactions always keeps non-negative the concentration values of these components; they cannot be negative. The same comment seems to be true for other physical variables and their dynamics such as temperature, pressure, light intensity, and many other features.

The *state observation problem* consists in designing a vector-function $\hat{x}_t = \hat{x}_t\left(y_{\tau\in[0,t]}\right)\hat{x} \in \mathbb{R}^n$ depending only on the available data $y_{\tau\in[0,t]}$ available up to the time t in such a way that it would be, respectively, close to its real (but non-measurable) value x. The measure of that *closeness* depends on the accepted assumptions concerning the state dynamics as well as the

noise effects. The vast majority of state observers solving this problem are presented also as an ODE. Therefore, it is usual that they are ruled by the following dynamic representation:

$$\frac{d}{dt}\hat{x}_t = F\left(\hat{x}_t, t, y_{\tau\in[0,t]}\right) + g\left(\hat{x}_t\right)u_t,\ \ \hat{x}_0 \text{ is a fixed vector.} \tag{A.49}$$

The function $F\left(\hat{x}_t, t, y_{\tau\in[0,t]}\right)$ is usually presented as a copy of the nonlinear system to be estimated plus a correction term Ψ depending on the output error $e = y - \hat{y}$, that is,

$$F\left(\hat{x}_t, t, y_{\tau\in[0,t]}\right) = f\left(\hat{x}_t, t\right) + \Psi(e_t). \tag{A.50}$$

It seems to be very important to keep the generated state estimates $\hat{x}_t$ always remaining within a given compact set X, that is,

$$\hat{x}_t \in X. \tag{A.51}$$

Indeed, if the state estimates are supposed to be used in some (in fact, feedback) control construction, for example, $u_t = K\hat{x}_t$, then any changing of a sign in $\hat{x}_t$ may lead to a significant instability effect of the corresponding close-loop dynamics. One of feasible solutions (which seemed to be evident) consists in the introduction of some projection operator $\pi_S\{\cdot\}$ acting to the right-hand side of (A.49) keeping the property $\hat{x}_t \in X$, i.e.,

$$\frac{d}{dt}\hat{x}_t = \pi_S\left\{F\left(t, \hat{x}_t, y_{\tau\in[0,t]}\right) + g\left(\hat{x}_t\right)u_t\right\}. \tag{A.52}$$

But such an *evident* solution immediately provides many constructive problems since the set S, where one needs to realize the projection for the right-hand side of (A.49), should be significantly nonlinear and non-stationary, that is, we should have $S = S\left(t, \hat{x}_t, \frac{d}{dt}\hat{x}_t\right)$, since the scheme (A.52) realizes the projection of the estimates of the state derivative, but not the state vector $\hat{x}_t$. That is why the problem of designing of other observer structures, verifying (A.51), presents a real challenge for the engineering community.

A.7 BASIC ASSUMPTIONS

Suppose that the following assumptions hold:

A1) The function $f(x,t)$ is uniformly (on $t \geq 0$) A-Lipschitz continuous in $x \in X$, that is, for all $t \geq 0$ and all $x, x' \in X$ there exist a matrix $A \in \mathbb{R}^{n\times n}$ and a constant $L_f < \infty$ such that

$$\left\|f(x,t) - f\left(x',t\right) - A\left(x - x'\right)\right\| \leq L_f\left\|x - x'\right\| \tag{A.53}$$

and there exists a constant $L_\delta < \infty$ such that for all $t \geq h$

$$\|\delta_t - \delta_{t-h}\| \leq L_\delta h \tag{A.54}$$

where $\delta_t := \hat{x}_t - x_t$ is the state estimation error at time t.

A2) The input associated function g is continuous and locally bounded with a upper bound g^+, that is,

$$\|g(x)\| \leq g^+. \tag{A.55}$$

A3) The class of controls u in (A.48) belongs to the following admissible control set:

$$U_{adm} = \left\{ u : \|u\|^2 \leq u_0 + u_1 \|x\|^2 \right\}. \tag{A.56}$$

The set U_{adm} may include bounded external injections and/or state feedback control designs.

A4) $x_t \in X \subset \mathbb{R}^n$ and X is convex compact. This means that $\|x\| \leq x^+$.

A5) The pair (C, A) is observable in the Kalman sense, that is, there exists a gain matrix K of the projection observer such that

$$\tilde{A} := A - KC = -\lambda I, \ \lambda > 0. \tag{A.57}$$

A6) The noises ξ_t and η_t acting to the system (A.14) are uniformly (on t) bounded such that

$$\begin{aligned} \|\xi_t\|^2_{\Lambda_\xi} &:= \xi_t^\mathsf{T} \Lambda_\xi \xi \leq 1, \\ \|\eta_t\|^2_{\Lambda_\eta} &:= \eta_t^\mathsf{T} \Lambda_\eta \eta_t \leq 1, \end{aligned} \tag{A.58}$$

where Λ_ξ and Λ_η are known *normalizing* non-negative definite matrices which permit one to operate with vectors having components of a different physical nature.

A.8 PRACTICAL STABILITY ANALYSIS FOR THE STATE ESTIMATION ERROR

The following theorem demonstrates the practical stability of the origin in the space of the estimation error.

Proposition A.4. *Assume that conditions A1–A4 hold for any $\lambda_0 > 0$ and a sufficiently small positive h such that the following inequality is satisfied:*

$$\lambda_0 - 3h\left(L_f + \lambda_0\right)^2 > 0, \quad \lambda := 2L_f + \lambda_0,$$

in (A.57), the projectional observer (A.52) armed with the output error injection function (A.50) provides the following upper bound for the averaged estimation error:

$$\limsup_{t\to\infty}\frac{1}{t}\int_{\tau=0}^{t}\left\|\hat{x}_\tau - x_\tau\right\| d\tau \le \frac{b}{a}+\sqrt{\frac{b^2}{a^2}+\frac{c}{a}}, \tag{A.59}$$

where

$$\begin{aligned} a &= \lambda_0 - 3h\left(L_f+\lambda_0\right)^2 > 0\,,\\ b &= \varsigma + \frac{h}{2}\left[L_\delta\left(4L_f+\lambda_0\right)\right],\\ c &= 3L_\delta^2 h^3 + 3\zeta^2 h,\\ \varsigma &= \|K\|\left\|\Lambda_\eta^{-1}\right\|^{1/2} + \left\|\Lambda_\xi^{-1}\right\|^{1/2}. \end{aligned} \tag{A.60}$$

Proof. Using the functional proposed in (A.60) we have

$$\dot{V}_t = \|\delta_t\|^2 - \|\delta_{t-h}\|^2 = -\|\delta_{t-h}\|^2 + \left\|\pi_X\left\{\hat{x}_{t-h}+\int_{\tau=t-h}^{t} F\left(\tau,\hat{x}_\tau,y_{s\in[0,\tau]}\right)d\tau\right\} - x_t\right\|^2 \le \alpha_t+\beta_t.$$

Here the condition proposed in A2, that is, $x_t \in X$ was used. The functions α_t and β_t satisfy the following identities:

$$\begin{aligned} \alpha_t &= \left\|\int_{\tau=t-h}^{t}\left[\tilde{\varphi}\left(x_\tau,\hat{x}_\tau,u_\tau,\tau\right) - KC\delta_\tau + K\eta_\tau - \xi_\tau\right]d\tau\right\|^2,\\ \beta_t &= 2\left(\delta_{t-h},\int_{t-h}^{t}\left[\tilde{\varphi}\left(x_\tau,\hat{x}_\tau,u_\tau,\tau\right) - KC\delta_\tau + K\eta_\tau - \xi_\tau\right]d\tau\right), \end{aligned}$$

where $\tilde{\varphi}\left(x_\tau,\hat{x}_\tau,u_\tau,\tau\right) = \varphi\left(\hat{x}_\tau,u_\tau,\tau\right) - \varphi\left(x_\tau,u_\tau,\tau\right)$ and $\varphi\left(x_t,u_t,t\right) = f\left(x_t,t\right) + g\left(x_t\right)u_t$. The application of the Cauchy–Schwartz inequality on the term $\|\eta_\tau\|$ yields the following inequality:

$$\|\eta_\tau\| = \sqrt{\left(\Lambda_\eta^{1/2}\eta_\tau,\Lambda_\eta^{-1}\Lambda_\eta^{1/2}\eta_\tau\right)} \le \sqrt{\left\|\Lambda_\eta^{-1}\right\|\|\eta_\tau\|_{\Lambda_\eta}^2} \le \left\|\Lambda_\eta^{-1}\right\|^{1/2}. \tag{A.61}$$

The substitution of the bound found in (A.61) generates the following upper estimate for the function β_t:

$$\beta_t \leq 2\left(\delta_{t-h}, \tilde{A} \int_{\tau=t-h}^{t} \delta_\tau d\tau\right) + 2h\|\delta_{t-h}\|\varsigma + 2\left(L_f + g^+\left(u_0^{1/2} + u_1^{1/2}\left[x^+\right]^{1/2}\right)\right)\|\delta_{t-h}\| \int_{\tau=t-h}^{t} \|\delta_\tau\| d\tau.$$

By (A.54) the right-hand side in the last inequality may be estimated from above by

$$\beta_t \leq h\left[\left(2L_f - \lambda\right)\|\delta_{t-h}\|^2 + \|\delta_{t-h}\|\left(2\varsigma + h\left[L_\delta\left(\lambda + 2L_f\right)\right]\right)\right].$$

Analogously, the application of the triangle and Jensen inequalities justifies the following inequality:

$$\alpha_t \leq \int_{\tau=t-h}^{t} \left\|\tilde{\varphi}\left(x_\tau, \hat{x}_\tau, u_\tau, \tau\right) - KC\delta_\tau\right\|^2 d\tau + \int_{\tau=t-h}^{t} \|K\eta_\tau\|^2 d\tau + \int_{\tau=t-h}^{t} \|\xi_\tau\|^2 d\tau,$$

$$\alpha_t \leq \left(\left(L_f + \lambda\right) \int_{\tau=t-h}^{t} \|\delta_\tau\| d\tau + \zeta h\right)^2 \leq 3h^2\left(\left(L_f + \lambda\right)^2\|\delta_{t-h}\|^2 + L_\delta^2 h^2 + \zeta^2\right),$$

which finally implies

$$\dot{V}_t \leq h\left[-a\|\delta_{t-h}\|^2 + 2\|\delta_{t-h}\|b + c\right] = \left[\left(-a\left[\|\delta_{t-h}\| - \frac{b}{a}\right]^2 + \frac{b^2}{a}\right) + c\right]h. \tag{A.62}$$

Rearranging and integrating (A.63), by the Jensen inequality

$$\frac{1}{t}\int_{t=h}^{t}\left[\|\delta_{t-h}\| - \frac{b}{a}\right]^2 dt \geq \left(\frac{1}{t}\int_{t=h}^{t}\left[\|\delta_{t-h}\| - \frac{b}{a}\right] dt\right)^2,$$

we get

$$\frac{1}{t}\int_{t=h}^{t}\|\delta_{t-h}\| dt - \frac{b}{a}\frac{t-h}{t} \leq \left|\frac{1}{t}\int_{t=h}^{t}\left[\|\delta_{t-h}\| - \frac{b}{a}\right] dt\right|$$

$$\leq \frac{1}{t}\int_{t=h}^{t}\left[\|\delta_{t-h}\|-\frac{b}{a}\right]^2 dt \leq \sqrt{\frac{V_0}{ah\cdot t}+\frac{b^2}{a^2}+\frac{c}{a}},$$

which leads to (A.59). □

Remark A.1. *For small enough h the upper bound (A.59) is*

$$\limsup_{t\to\infty}\frac{1}{t}\int_{\tau=0}^{t}\left\|\hat{x}_\tau - x_\tau\right\| d\tau \leq h\ \text{const} + o(h)$$
$$+ 2\lambda_0^{-1}\left(\|K\|\left\|\Lambda_\eta^{-1}\right\|^{1/2} + \left\|\Lambda_\xi^{-1}\right\|^{1/2}\right).$$

Proof. Using the functional (A.60), and taking into account that $x_t \in X$ by A2, we have

$$\dot{V}_t = \|\delta_t\|^2 - \|\delta_{t-h}\|^2 = -\|\delta_{t-h}\|^2 +$$
$$\left\|\pi_X\left\{\hat{x}_{t-h} + \int_{\tau=t-h}^{t} F\left(\tau, \hat{x}_\tau, y_{s\in[0,\tau]}\right) d\tau\right\} - x_t\right\|^2 \leq$$
$$\alpha_t + \beta_t,$$

where

$$\alpha_t = \left\|\int_{\tau=t-h}^{t}\left[f\left(\hat{x}_\tau,\tau\right) - f\left(x_\tau,\tau\right) - KC\delta_\tau + K\eta_\tau - \xi_\tau\right] d\tau\right\|^2,$$
$$\beta_t = 2\left(\delta_{t-h}, \int_{t-h}^{t}\left[f\left(\hat{x}_\tau,\tau\right) - f\left(x_\tau,\tau\right) - KC\delta_\tau + K\eta_\tau - \xi_\tau\right] d\tau\right).$$

Since

$$\|\eta_\tau\| = \sqrt{\left(\Lambda_\eta^{1/2}\eta_\tau, \Lambda_\eta^{-1}\Lambda_\eta^{1/2}\eta_\tau\right)} \leq$$
$$\sqrt{\left\|\Lambda_\eta^{-1}\right\|\|\eta_\tau\|^2_{\Lambda_\eta}} \leq \left\|\Lambda_\eta^{-1}\right\|^{1/2},$$

the following upper estimate holds:

$$\beta_t \leq 2\left(\delta_{t-h}, \tilde{A}\int_{\tau=t-h}^{t}\delta_\tau d\tau\right) +$$
$$2h\|\delta_{t-h}\|\varsigma + 2L_f\|\delta_{t-h}\|\int_{\tau=t-h}^{t}\|\delta_\tau\| d\tau.$$

By (A.54) the right-hand side in the last inequality may be estimated as

$$\beta_t \le h\left[\left(2L_f-\lambda\right)\|\delta_{t-h}\|^2+\|\delta_{t-h}\|\left(2\varsigma+h\left[L_\delta\left(\lambda+2L_f\right)\right]\right)\right]$$

Analogously,

$$\alpha_t \le \left(\left(L_f+\lambda\right)\int\limits_{\tau=t-h}^{t}\|\delta_\tau\|\,d\tau+\zeta h\right)^2 \le 3h^2\left(\left(L_f+\lambda\right)^2\|\delta_{t-h}\|^2+L_\delta^2h^2+\zeta^2\right),$$

which finally implies

$$\dot V_t \le h\left[-a\|\delta_{t-h}\|^2+2\|\delta_{t-h}\|\,b+c\right]= \left[\left(-a\left[\|\delta_{t-h}\|-\frac{b}{a}\right]^2+\frac{b^2}{a}\right)+c\right]h. \tag{A.63}$$

Rearranging and integrating (A.63), by the Jensen inequality

$$\frac{1}{t}\int\limits_{t=h}^{t}\left[\|\delta_{t-h}\|-\frac{b}{a}\right]^2dt \ge \left(\frac{1}{t}\int\limits_{t=h}^{t}\left[\|\delta_{t-h}\|-\frac{b}{a}\right]dt\right)^2,$$

we get

$$\frac{1}{t}\int\limits_{t=h}^{t}\|\delta_{t-h}\|\,dt-\frac{b}{a}\frac{t-h}{t} \le \left|\frac{1}{t}\int\limits_{t=h}^{t}\left[\|\delta_{t-h}\|-\frac{b}{a}\right]dt\right| \le \frac{1}{t}\int\limits_{t=h}^{t}\left[\|\delta_{t-h}\|-\frac{b}{a}\right]^2dt \le \sqrt{\frac{V_0}{ah\cdot t}+\frac{b^2}{a^2}+\frac{c}{a}},$$

which leads to (A.59). □

Remark A.2. *For small enough h the upper bound (A.59) is*

$$\limsup_{t\to\infty}\frac{1}{t}\int\limits_{\tau=0}^{t}\left\|\hat x_\tau-x_\tau\right\|d\tau \le h\,\mathrm{const}+o\left(h\right) + 2\lambda_0^{-1}\left(\|K\|\left\|\Lambda_\eta^{-1}\right\|^{1/2}+\left\|\Lambda_\xi^{-1}\right\|^{1/2}\right). \tag{A.64}$$

Proof. Let us consider the dynamics for the weight matrix $\tilde W_{1,t}$ and the following (suggested) Lyapunov function V_1:

$$V_1 := \frac{1}{2}\mathrm{tr}\left\{\tilde W_{1,t}^{\mathsf T}\tilde W_{1,t}\right\}+\frac{c}{4}\left[k_{1,t}-k_{1,\min}\right]_+^2,$$

which immediately implies (by direct differentiation)

$$\dot{V}_1 := \mathrm{tr}\left\{\tilde{W}_{1,t}^{\intercal}\left(-k_{1,t}\,\Xi_1 - 2^{-1}k_{1,t}^{-1}\dot{k}_{1,t}\tilde{W}_{1,t}\right)\right\} +$$
$$2^{-1}c\dot{k}_{1,t}\left[k_{1,t} - k_{1,\min}\right]_+ \leq k_{1,t}\left|\mathrm{tr}\left\{\tilde{W}_{1,t}^{\intercal}\,\Xi_1\right\}\right| +$$
$$2^{-1}\dot{k}_{1,t}\left(\frac{1}{k_{1,t}}\mathrm{tr}\left\{\tilde{W}_{1,t}^{\intercal}\tilde{W}_{1,t}\right\} + c\left(k_{1,t} - k_{1,\min}\right)\right).$$

If $\dot{V}_1$ is desired to be nonpositive, the free parameter $\dot{k}_{1,t}$ could be adjusted to obtain the asymptotic behavior for the DNN weights dynamics in the following manner:

$$\dot{k}_{1,t} \leq -\frac{2k_{1,t}^2\left|\mathrm{tr}\left\{\tilde{W}_{1,t}^{\intercal}\,\Xi_1\right\}\right|}{tr\left\{\tilde{W}_{1,t}^{\intercal}\tilde{W}_{1,t}\right\} + ck_{1,t}\left(k_{1,t} - k_{1,\min}\right)}.$$

We show below a simple example of the adaptive learning law where the following definition is applied:

$$s\left(\tilde{W}_{j,t}^{\intercal}, e_t\right) := \frac{2k_{j,t}^2\left|\mathrm{tr}\left\{\tilde{W}_{j,t}^{\intercal}\,\Xi_j\right\}\right|}{tr\left\{\tilde{W}_{j,t}^{\intercal}\tilde{W}_{j,t}\right\} + ck_{j,t}\left(k_{j,t} - k_{\min\,.j}\right)}.$$

The example uses the sigmoidal representation,

$$k_{j,t} := \frac{k_{0,j}}{1 + a\left(\tilde{W}_{j,t}^{\intercal}, e_t\right)\exp\left(b_j t\right)} + k_{\min,j}, \quad k_{\min,j} > 0.$$

The corresponding time history $\dot{k}_{j,t}$ could easily be derived:

$$\dot{k}_{j,t} := -k_{j,t}\frac{a\left(\tilde{W}_{j,t}^{\intercal}, e_t\right)b_j\exp\left(b_j t\right)}{1 + a\left(\tilde{W}_{j,t}^{\intercal}, e_t\right)\exp\left(b_j t\right)} < -s\left(\tilde{W}_{j,t}^{\intercal}, e_t\right),$$

which itself satisfies

$$a\left(\tilde{W}_{j,t}^{\intercal}, e_t\right)\exp\left(b_j t\right)\left(k_{j,t}b_j - s\left(\tilde{W}_{j,t}^{\intercal}, e_t\right)\right) > s\left(\tilde{W}_{j,t}^{\intercal}, e_t\right).$$

The last inequality is fulfilled if and only if the weight dependent parameter $a\left(\tilde{W}_{j,t}^{\intercal}, e_t\right)$ is selected in such a way that

$$a\left(\tilde{W}_{j,t}^{\intercal}, e_t\right) > s\left(\tilde{W}_{j,t}^{\intercal}, e_t\right)\exp\left(-b_j t\right)\Psi_j^{-1}$$
$$\Psi_j := k_{j,t}b_j - s\left(\tilde{W}_{j,t}^{\intercal}, e_t\right).$$

□

Bibliography

Abdel-Daiem, M.M., Rivera-Utrilla, J., Ocampo-Pérez, R., Méndez-Díaz, J.D., Rivera-Utrilla, J.M., 2012. Environmental impact of phthalic acid esters and their removal from water and sediments by different technologies – a review. Journal of Environmental Management (ISSN 0301-4797) 109, 164–178. https://doi.org/10.1016/j.jenvman.2012.05.014. http://www.sciencedirect.com/science/article/pii/S0301479712002721.

Abraham, A., 2005. Artificial neural networks. In: Handbook of Measuring System Design.

Abrishamifar, A., Ale Ahmad, A., Mohamadian, M., 2012. Fixed switching frequency sliding mode control for single-phase unipolar inverters. IEEE Transactions on Power Electronics 27 (5), 2507–2514.

Abuhamed, T., Bayraktar, E., Mehmetoğlu, T., Mehmetoğlu, Ü., 2004. Kinetics model for growth of pseudomonas putida f1 during benzene, toluene and phenol biodegradation. Process Biochemistry 39 (8), 983–988.

Adams, C.D., Cozzens, R.A., Kim, B.J., 1997. Effects of ozonation on the biodegradability of substituted phenols. Water Research 31 (10), 2655–2663.

Adav, S.S., Chen, M.-Y., Lee, D.-J., Ren, N.-Q., 2007. Degradation of phenol by acinetobacter strain isolated from aerobic granules. Chemosphere 67 (8), 1566–1572.

Aguilar, C.M., Rodríguez, J.L., Chairez, I., Tiznado, H., Poznyak, T., 2016. Naphthalene degradation by catalytic ozonation based on nickel oxide: study of the ethanol as cosolvent. Environmental Science and Pollution Research, 1–11.

Aguilar Melo, C.M., 2018. Acoplamiento de un proceso de ozonización catalítica basado en películas de óxido de níquel y un sistema de biodegradación aerobio para la eliminación de naftaleno y naproxeno. PhD thesis. UPIBI, IPN.

Ahmed, S., Rasul, M., Brown, R., Hashib, M., 2011. Influence of parameters on the heterogeneous photocatalytic degradation of pesticides and phenolic contaminants in wastewater: a short review. Journal of Environmental Management 92 (3), 311–330.

Akita, K., Yoshida, F., 1974. Bubble size, interfacial area, and liquid-phase mass transfer coefficient in bubble columns. Industrial & Engineering Chemistry Process Design and Development 13 (1), 84–91.

Alfaro, M., Arguelles, A., Chairez, I., 2016. Pattern recognition for electroencephalographic signals based on continuous neural networks. Neural Networks.

Ali, M., Sreekrishnan, T., 2001. Aquatic toxicity from pulp and paper mill effluents: a review. Advances in Environmental Research 5 (2), 175–196.

Alonso, J., Valdes, M., Calleja, A., Ribas, J., Losada, J., 2003. High frequency testing and modeling of silent discharge ozone generators. Ozone: Science & Engineering 25 (5), 363–376.

Alotaiby, T., Alshebeili, S., Alshawi, I., El-Samie, F., 2014. EEG seizure detection and prediction algorithms: a survey. EURASIP Journal on Advances in Signal Processing, 1–21.

Alvarez, P.M., García-Araya, J.F., Beltrán, F.J., Giráldez, I., Jaramillo, J., Gómez Serrano, V., 2006. The influence of various factors on aqueous ozone decomposition by granular activated carbons and the development of a mechanistic approach. Carbon 44 (14), 3102–3112.

Álvarez, P.M., Masa, F.J., Jaramillo, J., Beltran, F.J., Gomez-Serrano , V., 2008. Kinetics of ozone decomposition by granular activated carbon. Industrial & Engineering Chemistry Research 47 (8), 2545–2553.

Am. Water Works Res. F., Langlais, B., Reckhow, D.A., Brink, D.R., 1991. Ozone in Water Treatment: Application and Engineering. American Water Works Research Foundation. CRC Press.

Amat, A., Arques, A., López, F., Miranda, M., 2005a. Solar photo-catalysis to remove paper mill wastewater pollutants. Solar Energy 79 (4), 393–401.

Amat, A., Arques, A., Miranda, M., Lopez, F., 2005b. Use of ozone and/or uv in the treatment of effluents from board paper industry. Chemosphere 60 (8), 1111–1117.

Ambrożek, B., 2008. Removal and recovery of volatile organic compounds (VOCs) from waste air streams in thermal swing adsorption (TSA) system with closed-loop regeneration of adsorbent. Environment Protection Engineering 34 (4), 18–27.

Amokrane, A., Comel, C., Veron, J., 1997. Landfill leachates pretreatment by coagulation–flocculation. Water Research 31 (11), 2775–2782.

Andelman, J.B., Suess, M.J., 1970. Polynuclear aromatic hydrocarbons in the water environment. Bulletin of the World Health Organization 43 (3), 479.

Anderson, J.A., 2006. McCulloch–Pitts neurons. In: Encyclopedia of Cognitive Science.

Andreozzi, R., Caprio, V., Insola, A., Marotta, R., 1999. Advanced oxidation processes (AOP) for water purification and recovery. Catalysis Today 53 (1), 51–59.

Aparicio, M., Eiroa, M., Kennes, C., Veiga, M.C., 2007. Combined post-ozonation and biological treatment of recalcitrant wastewater from a resin-producing factory. Journal of Hazardous Materials 143 (1), 285–290.

Aranda-Bricaire, E., Moog, C., Pomet, J., 1995. A linear algebraic framework for dynamic feedback linearization. IEEE Transactions on Automatic Control 40 (1), 127–132.

Arany, E., Szabó, R.K., Apáti, L., Alapi, T., Ilisz, I., Mazellier, P., Dombi, A., Gajda-Schrantz, K., 2013. Degradation of naproxen by uv, vuv photolysis and their combination. Journal of Hazardous Materials 262, 151–157.

Assalin, M.R., d, E., Almeida, S., Durán, N., 2009. Combined system of activated sludge and ozonation for the treatment of kraft e1 effluent. International Journal of Environmental Research and Public Health 6 (3), 1145–1154.

Atlas, R.M., 1984. Petroleum Microbiology.

Avramescu, S.M., Bradu, C., Udrea, I., Mihalache, N., Ruta, F., 2008. Degradation of oxalic acid from aqueous solutions by ozonation in presence of Ni/Al2O3 catalysts. Catalysis Communications 9 (14), 2386–2391.

Bader, H., Hoigné, J., 1981. Determination of ozone in water by the indigo method. Water Research 15 (4), 449–456.

Baez, A., Cho, K.M., Liao, J.C., 2011. High-flux isobutanol production using engineered escherichia coli: a bioreactor study with in situ product removal. Applied Microbiology and Biotechnology 90 (5), 1681–1690.

Bagchi, D., Bagchi, M., Balmoori, J., Vuchetich, P., Stohs, S., 1998. Induction of oxidative stress and DNA damage by chronic administration of naphthalene to rats. Research Communications in Molecular Pathology and Pharmacology 101 (3), 249–257.

Bahnemann, D.W., Robertson, P.K., 2015. Environmental Photochemistry. Part III. Springer.

Baig, S., Coulomb, I., Courant, P., Liechti, P., 1999. Treatment of landfill leachates: Lapeyrouse and satrod case studies. Ozone: Science & Engineering.

Bailey, P.S., 1958. The reactions of ozone with organic compounds. Chemical Reviews 58 (5), 925–1010.

Bajaj, M., Gallert, C., Winter, J., 2009. Phenol degradation kinetics of an aerobic mixed culture. Biochemical Engineering Journal 46 (2), 205–209.

Balcıoğlu, I.A., Tarlan, E., Kıvılcımdan, C., Saçan, M.T., 2007. Merits of ozonation and catalytic ozonation pre-treatment in the algal treatment of pulp and paper mill effluents. Journal of Environmental Management 85 (4), 918–926.

Balestrino, A., Innocenti, M., 1990. The hyperstability approach to VSCS design. Deterministic Control of Uncertain Systems 40, 170.

Banerjee, A., Ghoshal, A.K., 2010. Isolation and characterization of hyper phenol tolerant bacillus sp. from oil refinery and exploration sites. Journal of Hazardous Materials 176 (1), 85–91.

Barsanti, L., Gualtieri, P., 2006. Algae. Anatomy, Biochemistry, and Biotechnology. CRC Press.

Beaman, M., Lambert, S., Graham, N., Anderson, R., 1998. Role of ozone and recirculation in the stabilization of landfills and leachates. Ozone: Science & Engineering.

Belem, A., Panteleitchouk, A., Duarte, A., Rocha-Santos, T., Freitas, A., 2008. Treatment of the effluent from a kraft bleach plant with white rot fungi pleurotus sajor caju and pleurotus ostreatus. Global NEST Journal 10 (3), 426–431.

Beltrán, F., García-Araya, J., Rivas, F., Alvarez, P., Rodríguez, E., 2000. Kinetics of competitive ozonation of some phenolic compounds present in wastewater from food processing industries. Ozone: Science & Engineering 22 (2), 167–183.

Beltran, F.J., 2003. Ozone-uv radiation-hydrogen peroxide oxidation technologies. Environmental Science and Pollution Control Series, 1–76.

Beltran, F.J., Ovejero, G., Garcia-Araya, J.F., Rivas, J., 1995. Oxidation of polynuclear aromatic hydrocarbons in water. 2. uv radiation and ozonation in the presence of uv radiation. Industrial & Engineering Chemistry Research 34 (5), 1607–1615.

Beltrán, F.J., Encinar, J., González, J.F., 1997. Industrial wastewater advanced oxidation. Part 2. Ozone combined with hydrogen peroxide or uv radiation. Water Research 31 (10), 2415–2428.

Beltrán, F.J., González, M., Ribas, F.J., Alvarez, P., 1998. Fenton reagent advanced oxidation of polynuclear aromatic hydrocarbons in water. Water, Air, & Soil Pollution 105 (3–4), 685–700.

Beltrán, F.J., García-Araya, J.F., Álvarez, P.M., 1999a. Wine distillery wastewater degradation. 1. Oxidative treatment using ozone and its effect on the wastewater biodegradability. Journal of Agricultural and Food Chemistry 47 (9), 3911–3918.

Beltrán, F.J., García-Araya, J.F., Álvarez, P.M., 1999b. Wine distillery wastewater degradation. 2. Improvement of aerobic biodegradation by means of an integrated chemical (ozone) – biological treatment. Journal of Agricultural and Food Chemistry 47 (9), 3919–3924.

Beltrán, F.J., Rivas, J., Álvarez, P.M., Alonso, M.A., Acedo, B., 1999c. A kinetic model for advanced oxidation processes of aromatic hydrocarbons in water: application to phenanthrene and nitrobenzene. Industrial & Engineering Chemistry Research 38 (11), 4189–4199.

Beltran, F.J., García-Araya, J.F., Alvarez, P.M., 2000. Continuous flow integrated chemical (ozone)-activated sludge system treating combined agroindustrial-domestic wastewater. Environmental Progress 19 (1), 28–35.

Beltrán, F.J., García-Araya, J.F., Navarrete, V., Rivas, F.J., 2002a. An attempt to model the kinetics of the ozonation of simazine in water. Industrial & Engineering Chemistry Research 41 (7), 1723–1732.

Beltrán, F.J., Rivas, F.J., Fernández, L.A., Álvarez, P.M., Montero-de Espinosa, R., 2002b. Kinetics of catalytic ozonation of oxalic acid in water with activated carbon. Industrial & Engineering Chemistry Research 41 (25), 6510–6517.

Beltrán, F.J., Rivas, J., Alvarez, P., Montero-de Espinosa, R., 2002c. Kinetics of heterogeneous catalytic ozone decomposition in water on an activated carbon. Ozone: Science & Engineering 24 (4), 227–237.

Beltrán, F.J., Pocostales, P., Alvarez, P., Oropesa, A., 2009. Diclofenac removal from water with ozone and activated carbon. Journal of Hazardous Materials 163 (2), 768–776.

Beltran-Heredia, J., Torregrosa, J., Dominguez, J.R., Garcia, J., 2000. Aerobic biological treatment of black table olive washing wastewaters: effect of an ozonation stage. Process Biochemistry 35 (10), 1183–1190.

Benitez, F., Beltran-Heredia, J., Real, F., Acero, J., 2000. Wine vinasses treatments by ozone and an activated sludge system in continuous reactors. Bioprocess Engineering 23 (2), 149–154.

Benitez, F.J., Real, F.J., Acero, J.L., Garcia, J., Sanchez, M., 2003. Kinetics of the ozonation and aerobic biodegradation of wine vinasses in discontinuous and continuous processes. Journal of Hazardous Materials 101 (2), 203–218.

Bérces, T., Dombi, J., 1980. Evaluation of the rate coefficients and arrhenius parameters of hydrogen atom transfer reactions. ii. Application of the method. International Journal of Chemical Kinetics 12 (3), 183–214.

Bernard, O., Queinnec, I., 2008. Dynamic Models of Biochemical Processes: Properties of the Models. Hermes Science, Paris.

Biel, D., Fossas, E., Guinjoan, F., Alarcón, E., Poveda, A., 2001. Application of sliding-mode control to the design of a buck-based sinusoidal generator. IEEE Transactions on Industrial Electronics 48 (3), 563–571.

Bila, D.M., Montalvao, A.F., Silva, A.C., Dezotti, M., 2005. Ozonation of a landfill leachate: evaluation of toxicity removal and biodegradability improvement. Journal of Hazardous Materials 117 (2), 235–242.

Bin, A., Roustan, M., 2000. Mass transfer in ozone reactors. In: Proceedings, pp. 99–131.

Bingemer, H.G., Crutzen, P.J., 1987. The production of methane from solid wastes. Journal of Geophysical Research: Atmospheres 92 (D2), 2181–2187.

Birk, J., Zeitz, M., 1988. Extended Luenberger observer for non-linear multivariable systems. International Journal of Control 47 (6), 1823–1836.

Blakey, N.C., 1992. 2.1 Model prediction of landfill leachate production. In: Landfilling of Waste: Leachate, vol. 1, p. 17.

Blatchley, E.R., Weng, S., Afifi, M.Z., Chiu, H.-H., Reichlin, D.B., Jousset, S., Erhardt, R.S., 2012. Ozone and uv254 radiation for municipal wastewater disinfection. Water Environment Research 84 (11), 2017–2029.

Boari, G., Brunetti, A., Passino, R., Rozzi, A., 1984. Anaerobic digestion of olive oil mill wastewaters. Agricultural Wastes 10 (3), 161–175.

Boe, K., Angelidaki, I., 2009. Serial CSTR digester configuration for improving biogas production from manure. Water Research 43 (1), 166–172.

Boizot, N., Busvelle, E., Gauthier, J.-P., 2010. An adaptive high-gain observer for nonlinear systems. Automatica 46 (9), 1483–1488.

Boltyanski, V., Poznyak, A., 2012. Robust Maximum Principle: Theory and Applications. Birkhauser, Boston.

Borowitzka, M., Moheimani, N. (Eds.), 2013. Algae for Biofuels and Energy. Springer.

Bose, S., Vahabzadeh, S., Bandyopadhyay, A., 2013. Bone tissue engineering using 3D printing. Materials Today 16 (12), 494–504.

Branicky, M.S., 1998. Multiple Lyapunov functions and other analysis tools for switched and hybrid systems. IEEE Transactions on Automatic Control 43, 475–482.

Brennan, L., Owende, P., 2010. Biofuels from microalgae – a review of technologies for production, processing, and extractions of biofuels and co-products. Renewable and Sustainable Energy Reviews 14, 557–577.

Budzianowski, W., Koziol, A., 2005. Stripping of ammonia from aqueous solutions in the presence of carbon dioxide: effect of negative enhancement of mass transfer. Chemical Engineering Research and Design 83 (2), 196–204.

Budzianowski, W.M., Miller, R., 2008. Auto-thermal combustion of lean gaseous fuels utilizing a recuperative annular double-layer catalytic converter. The Canadian Journal of Chemical Engineering 86 (4), 778–790.

Buffle, M.-O., von Gunten, U., 2006. Phenols and amine induced ho* generation during the initial phase of natural water ozonation. Environmental Science & Technology 40 (9), 3057–3063.

Bustos, Y.A., Vaca, M., López, R., Torres, L.G., 2010. Disinfection of a wastewater flow treated by advanced primary treatment using o3, uv and o3/uv combinations. Journal of Environmental Science and Health, Part A 45 (13), 1715–1719.

Cachada, A., Pato, P., Rocha-Santos, T., da Silva, E.F., Duarte, A., 2012. Levels, sources and potential human health risks of organic pollutants in urban soils. Science of the Total Environment 430, 184–192.

Cai, Z., Kim, D., Sorial, G.A., 2007. A comparative study in treating two VOC mixtures in trickle bed air biofilters. Chemosphere 68 (6), 1090–1097.

Calvo, L., Gilarranz, M., Casas, J., Mohedano, A., Rodríguez, J., 2007. Detoxification of kraft pulp ECF bleaching effluents by catalytic hydrotreatment. Water Research 41 (4), 915–923.

Calvosa, L., Monteverdi, A., Rindone, B., Riva, G., 1991. Ozone oxidation of compounds resistant to biological degradation. Water Research 25 (8), 985–993.

Camel, V., Bermond, A., 1998. The use of ozone and associated oxidation processes in drinking water treatment. Water Research 32 (11), 3208–3222.

Carpinteyro-Urban, S., Vaca, M., Torres, L., 2012. Can vegetal biopolymers work as coagulant–flocculant aids in the treatment of high-load cosmetic industrial wastewaters? Water, Air, & Soil Pollution 223 (8), 4925–4936.

Catalkaya, E.C., Kargi, F., 2007. Color, toc and aox removals from pulp mill effluent by advanced oxidation processes: a comparative study. Journal of Hazardous Materials 139 (2), 244–253.

Çeçen, F., 1999. Investigation of substrate degradation and nonbiodegradable portion in several pulp bleaching wastes. Water Science and Technology 40 (11–12), 305–312.

Cerniglia, C.E., 1992. Biodegradation of polycyclic aromatic hydrocarbons. In: Microorganisms to Combat Pollution. Springer, pp. 227–244.

Cerniglia, C.E., 1993. Biodegradation of polycyclic aromatic hydrocarbons. Current Opinion in Biotechnology 4 (3), 331–338.

Chaichanawong, J., Yamamoto, T., Ohmori, T., 2010. Enhancement effect of carbon adsorbent on ozonation of aqueous phenol. Journal of Hazardous Materials 175 (1), 673–679.

Chairez, I., 2009. Wavelet differential neural network observer. IEEE Transactions on Neural Networks 20 (9), 1439–1449.

Chairez, I., 2013. Differential neuro-fuzzy controller for uncertain nonlinear systems. IEEE Transactions on Fuzzy Systems 21 (2), 369–384.

Chairez, I., 2014. Finite time convergent learning law for continuous neural networks. Neural Networks 50.

Chairez, I., Poznyak, A., Poznyak, T., 2006. New sliding-mode learning law for dynamic neural network observer. IEEE Transactions on Circuits and Systems II 53, 1338–1342.

Chairez, I., Poznyak, A., Poznyak, T., 2008. High order dynamic neuro observer: application for ozone generator. In: International Workshop on Variable Structure Systems (VSS '08).

Chairez, I., Fuentes, R., Poznyak, T., Franco, M., Poznyak, A., 2010. Numerical modeling of the benzene reaction with ozone in gas phase using differential neural networks. Catalysis Today 151 (1–2), 159–165.

Chamarro, E., Marco, A., Esplugas, S., 2001. Use of Fenton reagent to improve organic chemical biodegradability. Water Research 35 (4), 1047–1051.

Chen, M., Xu, P., Zeng, G., Yang, C., Huang, D., Zhang, J., 2015. Bioremediation of soils contaminated with polycyclic aromatic hydrocarbons, petroleum, pesticides, chlorophenols and heavy metals by composting: applications, microbes and future research needs. Biotechnology Advances 33 (6), 745–755.

Chen, J., Ni, C., 1999. The ozonation of 2, 4-dichlorophenol: mechanism and by-products. In: Proceedings of the 14th Ozone World Congress, pp. 163–177.

Chen, K.-C., Lin, Y.-H., Chen, W.-H., Liu, Y.-C., 2002. Degradation of phenol by PAA-immobilized candida tropicalis. Enzyme and Microbial Technology 31 (4), 490–497.

Cheng, S.-p., Zhang, X.-x., et al., 2006. PTA wastewater molecular toxicity detected with gene chip. Journal of Environmental Sciences 18 (3), 514–518.

Chiang, P.-C., Chang, E., Liang, C., 2002. NOM characteristics and treatabilities of ozonation processes. Chemosphere 46 (6), 929–936.

Chiang, P.-C., Chang, E.-E., Chang, P.-C., Huang, C.-P., 2009. Effects of pre-ozonation on the removal of THM precursors by coagulation. Science of the Total Environment 407 (21), 5735–5742.

Chisti, Y., 2007. Biodiesel from microalgae. Biotechnologies Advances 25, 294–306.

Choi, H., Kim, Y.-Y., Lim, H., Cho, J., Kang, J.-W., Kim, K.-S., 2001. Oxidation of polycyclic aromatic hydrocarbons by ozone in the presence of sand. Water Science and Technology 43 (5), 349–356.

Choi, H., Lim, H.-N., Kim, J., Hwang, T.-M., Kang, J.-W., 2002. Transport characteristics of gas phase ozone in unsaturated porous media for in-situ chemical oxidation. Journal of Contaminant Hydrology 57 (1), 81–98.

Chong, M.N., Jin, B., Chow, C.W., Saint, C., 2010. Recent developments in photocatalytic water treatment technology: a review. Water Research 44 (10), 2997–3027.

Christensen, J.B., Jensen, D.L., Grøn, C., Filip, Z., Christensen, T.H., 1998. Characterization of the dissolved organic carbon in landfill leachate-polluted groundwater. Water Research 32 (1), 125–135.

Christenson, L., Sims, R., 2011. Production and haversting of microalgae for wastewater treatment, biofuels, and bioproducts. Biotechnologies Advances 25, 686–702.

Ciccarella, G., Dalla Mora, M., Germani, A., 1993. A Luenberger-like observer for nonlinear systems. International Journal of Control 57 (3), 537–556.

Clarke, F.H., Ledyaev, Y., Stern, R., Wolensky, P.R., 1998. Nonsmooth Analysis in Control Theory. Springer, New York.

Contreras, S., Rodrıguez, M., Al Momani, F., Sans, C., Esplugas, S., 2003. Contribution of the ozonation pre-treatment to the biodegradation of aqueous solutions of 2,4-dichlorophenol. Water Research 37 (13), 3164–3171.

Correa, J.M., Poznyak, A., et al., 2001. Switching structure robust state and parameter estimator for MIMO non-linear systems. International Journal of Control 74 (2), 175–189.

Cresser, M., Hargitt, R., 1976. The determination of chromium (iii) and chromim (vi) by total anion exchange and atomic absorption spectrometry. Analytica Chimica Acta 81 (1), 196–198.

Cruz-Zavala, E., Moreno, J.A., Fridman, L., 2011a. Uniform robust exact differentiator. IEEE Transactions on Automatic Control 56 (11), 2727–2733.

Cruz-Zavala, E., Moreno, J.A., Fridman, L., 2011b. Second-order uniform exact sliding mode control with uniform sliding surface. In: 50th IEEE Conference on Decision and Control and European Control Conference (CDC-ECC), vol. 50, pp. 12–15.

Cruz-Zavala, E., Moreno, J.A., Fridman, L.M., 2011c. Adaptive gains super-twisting algorithm for systems with growing perturbations. IFAC Proceedings Volumes 44 (1), 3039–3044.

Cullen, P., Tiwari, B., O'Donnell, C., Muthukumarappan, K., 2009. Modelling approaches to ozone processing of liquid foods. Trends in Food Science & Technology 20 (3), 125–136.

Dabroom, A., Khalil, H.K., 1997. Numerical differentiation using high-gain observers. In: Proceedings of the 36th IEEE Conference on Decision and Control, vol. 5. IEEE, pp. 4790–4795.

Danckwerts, P.V., Lannus, A., 1970. Gas-liquid reactions. Journal of the Electrochemical Society 117 (10), 369C–370C.

Davila, J., Fridman, L., Levant, A., 2005. Second-order sliding-mode observer for mechanical systems. IEEE Transactions on Automatic Control 50 (11), 1785–1789.

Davis, A.P., Huang, C., 1990. The removal of substituted phenols by a photocatalytic oxidation process with cadmium sulfide. Water Research 24 (5), 543–550.

de Bruyn, W.J., Clark, C.D., Ottelle, K., Aiona, P., 2012. Photochemical degradation of phenanthrene as a function of natural water variables modeling freshwater to marine environments. Marine Pollution Bulletin 64 (3), 532–538.

De los Santos Ramos, W., Poznyak, T., Chairez, I., et al., 2009. Remediation of lignin and its derivatives from pulp and paper industry wastewater by the combination of chemical precipitation and ozonation. Journal of Hazardous Materials 169 (1), 428–434.

De Morais, J.L., Zamora, P.P., 2005. Use of advanced oxidation processes to improve the biodegradability of mature landfill leachates. Journal of Hazardous Materials 123 (1), 181–186.

de Oliveira, T.F., Chedeville, O., Fauduet, H., Cagnon, B., 2011. Use of ozone/activated carbon coupling to remove diethyl phthalate from water: influence of activated carbon textural and chemical properties. Desalination 276 (1–3), 359–365.

DeCarlo, R., Branicky, M., Petterson, S., Lennartson, S., 2000. Perspectives and results on the stability and stabilizability of hybrid systems. In: Proceedings IEEE: Special Issue Hybrid Systems, vol. 88, pp. 1069–1082.

Deckwer, W.-D., Schumpe, A., 1993. Improved tools for bubble column reactor design and scale-up. Chemical Engineering Science 48 (5), 889–911.

Dehouli, H., Chedeville, O., Cagnon, B., Caqueret, V., Porte, C., 2010. Influences of pH, temperature and activated carbon properties on the interaction ozone/activated carbon for a wastewater treatment process. Desalination 254 (1–3), 12–16.

Delgado, A., Kambhampati, C., Warwick, K., 1995. Dynamic neural network for system identification and control. IEE Proceedings Control Theory and Applications 142 (4), 307–314.

Derudi, M., Venturini, G., Lombardi, G., Nano, G., Rota, R., 2007. Biodegradation combined with ozone for the remediation of contaminated soils. European Journal of Soil Biology 43 (5), 297–303.

Deshusses, M.A., Johnson, C.T., 2000. Development and validation of a simple protocol to rapidly determine the performance of biofilters for VOC treatment. Environmental Science & Technology 34 (3), 461–467.

Devinny, J.S., Deshusses, M.A., Webster, T.S., 1998. Biofiltration for Air Pollution Control. CRC Press.

Dissanayake, M., Phan-Thien, N., 1994. Neural-network-based approximations for solving partial differential equations. International Journal for Numerical Methods in Biomedical Engineering 10 (3), 195–201.

Dong, W., Wang, W., Li, J., 2008a. A multiscale mass transfer model for gas–solid riser flows. Part 1–sub-grid model and simple tests. Chemical Engineering Science 63 (10), 2798–2810.

Dong, W., Wang, W., Li, J., 2008b. A multiscale mass transfer model for gas–solid riser flows. Part ii–sub-grid simulation of ozone decomposition. Chemical Engineering Science 63 (10), 2811–2823.

Dong, Y., Yang, H., He, K., Wu, X., Zhang, A., 2008c. Catalytic activity and stability of y zeolite for phenol degradation in the presence of ozone. Applied Catalysis B: Environmental 82 (3), 163–168.

Drakunov, S.V., 1992. Sliding-mode observers based on equivalent control method. In: Proceedings of the 31st IEEE Conference on Decision and Control.

Droop, M., 1968. Vitamin B12 and marine ecology iv: the kinetics of uptake growth and inhibition in monochrisis lutheri. Journal of the Marine Biological Association 48 (3), 689–733.

Edalatmanesh, M., Mehrvar, M., Dhib, R., 2008. Optimization of phenol degradation in a combined photochemical–biological wastewater treatment system. Chemical Engineering Research and Design 86 (11), 1243–1252.

Edwards, C., Spurgeon, S., 1998. Sliding Mode Control: Theory and Applications. CRC Press.

El-Din, A.G., Smith, D.W., 2002. A neural network model to predict the wastewater inflow incorporating rainfall events. Water Research 36 (5), 1115–1126.

El-Din, M.G., Smith, D.W., 2001. Maximizing the enhanced ozone oxidation of kraft pulp mill effluents in an impinging-jet bubble column. Ozone: Science & Engineering 23 (6), 479–493.

El Mansi, E.M.T., Holms, W.H., 1989. Control of carbon flux to acetate excretion during growth of escherichia coli in batch and continuous cultures. Journal of General Microbiology 135 (11), 2875–2883.

El-Naas, M.H., Al-Zuhair, S., Makhlouf, S., 2010. Batch degradation of phenol in a spouted bed bioreactor system. Journal of Industrial and Engineering Chemistry 16 (2), 267–272.

Elman, J.L., 1993. Learning and development in neural networks: the importance of starting small. Cognition 48 (1), 71–99.

Elmolla, E.S., Chaudhuri, M., 2010. Degradation of amoxicillin, ampicillin and cloxacillin antibiotics in aqueous solution by the UV/ZnO photocatalytic process. Journal of Hazardous Materials 173 (1), 445–449.

Emberton, J., Parker, A., 1987. The problems associated with building on landfill sites. Waste Management & Research 5 (4), 473–482.

Epa, U., 2004. Air Quality Criteria for Particulate Matter. US Environmental Protection Agency, Research Triangle Park.

Ericson, G., Larsson, A., 2000. DNA adducts in perch (perca fluviatilis) living in coastal water polluted with bleached pulp mill effluents. Ecotoxicology and Environmental Safety 46, 167–173.

Esmaeil, A.-S., Drobiova, H., Obuekwe, C., 2009. Predominant culturable crude oil-degrading bacteria in the coast of Kuwait. International Biodeterioration & Biodegradation 63 (4), 400–406.

Espejo, A., Aguinaco, A., García-Araya, J., Beltrán, F.J., 2014. Sequential ozone advanced oxidation and biological oxidation processes to remove selected pharmaceutical contaminants from an urban wastewater. Journal of Environmental Science and Health, Part A 49 (9), 1015–1022.

Essam, T., Amin, M.A., El Tayeb, O., Mattiasson, B., Guieysse, B., 2010. Kinetics and metabolic versatility of highly tolerant phenol degrading alcaligenes strain TW1. Journal of Hazardous Materials 173 (1), 783–788.

Evelyn, Z.-P., Neftalí, R.-V., Isaac, C., Luis Gilberto, T., 2013. Coliforms and helminth eggs removals by coagulation–flocculation treatment based on natural polymers. Journal of Water Resource and Protection, 2013.

Eykhoff, P. Parks, P.C., 1990. Identification and system parameter estimation; where do we stand now?

Falkowski, P.G., Raven, J.A., 2007. Aquatic Photosynthesis. PaperBack.

Faria, P., Órfão, J., Pereira, M., 2008a. Activated carbon catalytic ozonation of oxamic and oxalic acids. Applied Catalysis B: Environmental 79 (3), 237–243.

Faria, P., Órfão, J., Pereira, M., 2008b. Catalytic ozonation of sulfonated aromatic compounds in the presence of activated carbon. Applied Catalysis B: Environmental 83 (1), 150–159.

Faria, P.C., Órfão, J.J., Pereira, M.F.R., 2006. Ozone decomposition in water catalyzed by activated carbon: influence of chemical and textural properties. Industrial & Engineering Chemistry Research 45 (8), 2715–2721.

Farines, V., Baig, S., Albet, J., Molinier, J., Legay, C., 2003. Ozone transfer from gas to water in a co-current upflow packed bed reactor containing silica gel. Chemical Engineering Journal 91 (1), 67–73.

Farmer, P.B., Singh, R., Kaur, B., Sram, R.J., Binkova, B., Kalina, I., Popov, T.A., Garte, S., Taioli, E., Gabelova, A., et al., 2003. Molecular epidemiology studies of carcinogenic environmental pollutants: effects of polycyclic aromatic hydrocarbons (PAHs) in environmental pollution on exogenous and oxidative DNA damage. Mutation Research/Reviews in Mutation Research 544 (2), 397–402.

Fatta-Kassinos, D., Vasquez, M., Kümmerer, K., 2011. Transformation products of pharmaceuticals in surface waters and wastewater formed during photolysis and advanced oxidation processes–degradation, elucidation of byproducts and assessment of their biological potency. Chemosphere 85 (5), 693–709.

Faugeras, B., Bernard, O., Sciandra, A., Levy, M., 2004. A mechanistic modelling and data assimilation approach to estimate the carbon/chlorophyll and carbon/nitrogen ratios in a coupled hydrodynamical–biological model. Nonlinear Processes in Geophysics 11, 515–533.

Faungnawakij, K., Sano, N., Charinpanitkul, T., Tanthapanichakoon, W., 2006. Modeling of experimental treatment of acetaldehyde-laden air and phenol-containing water using corona discharge technique. Environmental Science & Technology 40 (5), 1622–1628.

Fernández Linares, L.C., Linares, L.C.F., 2006. Manual de técnicas de análisis de suelos aplicadas a la remediación de sitios contaminados. Technical report. Mexican Institute of Oil.

Ferral-Pérez, H., Torres Bustillos, L., Méndez, H., Rodríguez-Santillan, J., Chairez, I., 2016. Sequential treatment of tequila industry vinasses by biopolymer-based coagulation/flocculation and catalytic ozonation. Ozone: Science & Engineering 38 (4), 279–290.

Fettig, J., Stapel, H., Steinert, C., Geiger, M., 1996. Treatment of landfill leachate by preozonation and adsorption in activated carbon columns. Water Science and Technology 34 (9), 33–40.

Filippov, A., 1998. Differential Equations with Discontinuous Right-Hand Side. Kluwer, Dordrecht, The Netherlands.

Fontanier, V., Farines, V., Albet, J., Baig, S., Molinier, J., 2006. Study of catalyzed ozonation for advanced treatment of pulp and paper mill effluents. Water Research 40 (2), 303–310.

Fortescue, G., Pearson, J., 1967. On gas absorption into a turbulent liquid. Chemical Engineering Science 22 (9), 1163–1176.

Fouillet, B., Chambon, P., Chambon, R., Castegnaro, M., Weill, N., 1991. Effects of ozonation on mutagenic activity of polycyclic aromatic hydrocarbons. Bulletin of Environmental Contamination and Toxicology 47 (1), 1–7.

Freire, R., Kubota, L., Duran, N., 2001. Remediation and toxicity removal from kraft e1 paper mill effluent by ozonization. Environmental Technology 22 (8), 897–904.

Fridman, L., Levant, A., 1996. Higher order sliding modes as a natural phenomenon in control theory. In: Robust Control via Variable Structure and Lyapunov Techniques. Springer, pp. 107–133.

Fuentes, I., Rodríguez, J.L., Poznyak, T., Chairez, I., 2014. Photocatalytic ozonation of terephthalic acid: a by-product-oriented decomposition study. Environmental Science and Pollution Research 21 (21), 12241–12248.

Fuentes, R., Poznyak, A., Chairez, I., Poznyak, T., 2009. Neural numerical modeling for uncertain distributed parameter systems. In: International Joint Conference on Neural Networks, 2009. IJCNN 2009. IEEE, pp. 909–916.

Fulekar, M.H., Singh, A., Bhaduri, A.M., 2009. Genetic engineering strategies for enhancing phytoremediation of heavy metals. African Journal of Biotechnology 8 (4).

Gandhi, V., Mishra, M., Rao, M., Kumar, A., Joshi, P., Shah, D., 2011. Comparative study on nano-crystalline titanium dioxide catalyzed photocatalytic degradation of aromatic carboxylic acids in aqueous medium. Journal of Industrial and Engineering Chemistry 17 (2), 331–339.

Gao, Y., Xiong, W., Ling, W., Xu, J., 2006. Sorption of phenanthrene by soils contaminated with heavy metals. Chemosphere 65 (8), 1355–1361.

Gao, Z., 2006. Active disturbance rejection control: a paradigm shift in feedback control system design. In: Proceedings of the 2006 American Control Conference.

Garcia, R.A., D'Atellis, C.E., 1995. Trajectory tracking in nonlinear systems via nonlinear reduced-order observers. International Journal of Control 62, 685–715.

García-Peña, E.I., Zarate-Segura, P., Guerra-Blanco, P., Poznyak, T., Chairez, I., 2012. Enhanced phenol and chlorinated phenols removal by combining ozonation and biodegradation. Water, Air, & Soil Pollution 223 (7), 4047–4064.

Gauthier, J., Bornard, G., 1981. Observability for any u (t) of a class of nonlinear systems. IEEE Transactions on Automatic Control 26 (4), 922–926.

Gauthier, J.P., Hammouri, H., Kupka, I., 1991. Observers for nonlinear systems. In: Proceedings of the IEEE Conference on Conference: Decision and Control, vol. 31, pp. 875–880.

Gauthier, J.P., Hammouri, H., Othman, S., 1992. A simple observer for nonlinear systems applications to bioreactors. IEEE Transactions on Automatic Control 37 (6), 875–880.

Gehr, R., Wagner, M., Veerasubramanian, P., Payment, P., 2003. Disinfection efficiency of peracetic acid, uv and ozone after enhanced primary treatment of municipal wastewater. Water Research 37 (19), 4573–4586.

Geider, R.J., MacIntyre, H.L., Kana, T.M., 1998. A dynamic regulatory model of phytoplanktonic acclimation to light, nutrients, and temperature. Limnology and Oceanography 43 (4), 679–694.

Genovese, M., Crisafi, F., Denaro, R., Cappello, S., Russo, D., Calogero, R., Santisi, S., Catalfamo, M., Modica, A., Smedile, F., Genovese, L., Golyshin, P.N., Giuliano, L., Yakimov, M.M., 2014. Effective bioremediation strategy for rapid in situ cleanup of anoxic marine sediments in mesocosm oil spill simulation. Frontiers in Microbiology 5, 162.

Geromel, J.C., Colaneri, P., Bolzern, P., 2008. Dynamic output feedback control of switched linear systems. IEEE Transactions on Automatic Control 53 (3), 720–733.

Gershenson, C., 2003. Artificial neural networks for beginners. arXiv preprint arXiv:cs/0308031 [cs.NE].

Ghauch, A., Tuqan, A.M., Kibbi, N., 2015. Naproxen abatement by thermally activated persulfate in aqueous systems. Chemical Engineering Journal 279, 861–873.

Gibon-Fargeot, A.M., Celle-Couenne, F., Hammouri, H., 2000. Cascade estimation design for CSTR models. Computers and Chemical Engineering 24 (11), 2355–2566.

Godjevargova, T., Ivanova, D., Aleksieva, Z., Burdelova, G., 2006. Biodegradation of phenol by immobilized trichosporon cutaneum r57 on modified polymer membranes. Process Biochemistry 41 (11), 2342–2346.

Goi, A., Trapido, M., 2004. Degradation of polycyclic aromatic hydrocarbons in soil: the Fenton reagent versus ozonation. Environmental Technology 25 (2), 155–164.

Gómez-Alvarez, M., Poznyak, T., Ríos-Leal, E., Silva-Sánchez, C., 2012. Anthracene decomposition in soils by conventional ozonation. Journal of Environmental Management 113, 545–551.

Gonzalez, T., Moreno, J.A., Fridman, L., 2012. Variable gain super-twisting sliding mode control. IEEE Transactions on Automatic Control 57 (8), 2100–2105.

Gould, J.P., Weber Jr., W.J., 1976. Oxidation of phenols by ozone. Journal (Water Pollution Control Federation), 47–60.

Gourdon, R., Comel, C., Vermande, P., Veron, J., 1989. Fractionation of the organic matter of a landfill leachate before and after aerobic or anaerobic biological treatment. Water Research 23 (2), 167–173.

Grau, P., 1991. Textile industry wastewaters treatment. Water Science and Technology 24 (1), 97–103.

Griesbeck, A.G., Oelgemöller, M., Ghetti, F., 2012. CRC Handbook of Organic Photochemistry and Photobiology, vol. 1. CRC Press.

Griffini, O., Bao, M.L., Barbieri, K., Burrini, D., Santianni, D., Pantani, F., 1999. Formation and removal of biodegradable ozonation by-products during ozonation–biofiltration treatment: pilot-scale evaluation. Ozone: Science & Engineering.

Grymonpre, D.R., Finney, W.C., Locke, B.R., 1999. Aqueous-phase pulsed streamer corona reactor using suspended activated carbon particles for phenol oxidation: model-data comparison. Chemical Engineering Science 54 (15), 3095–3105.

Guerra, P., Amacosta, J., Poznyak, T., Siles, S., García, A., Chairez, I., 2013. Aerobic biodegradation coupled to preliminary ozonation for the treatment of model and real residual water. In: Biodegradation-Engineering and Technology. InTech.

Guiza, M., Ouederni, A., Ratel, A., 2004. Decomposition of dissolved ozone in the presence of activated carbon: an experimental study. Ozone: Science & Engineering 26 (3), 299–307.

Gurol, M.D., Nekouinaini, S., 1984. Kinetic behavior of ozone in aqueous solutions of substituted phenols. Industrial & Engineering Chemistry Fundamentals 23 (1), 54–60.

Guzel-Seydim, Z.B., Greene, A.K., Seydim, A., 2004. Use of ozone in the food industry. LWT-Food Science and Technology 37 (4), 453–460.

Haapea, P., Tuhkanen, T., 2006. Integrated treatment of PAH contaminated soil by soil washing, ozonation and biological treatment. Journal of Hazardous Materials 136 (2), 244–250.

Haapea, P., Korhonen, S., Tuhkanen, T., 2002. Treatment of industrial landfill leachates by chemical and biological methods: ozonation, ozonation + hydrogen peroxide, hydrogen peroxide and biological post-treatment for ozonated water. Ozone: Science & Engineering 24 (5), 369–378.

Hadj-Sadok, M.Z., Gouzé, J.L., 2011. Estimation of uncertain models of activated sludge processes with interval observers. Journal of Process Control 11 (3), 299–310.

Hamdi, M., 1992. Toxicity and biodegradability of olive mill wastewaters in batch anaerobic digestion. Applied Biochemistry and Biotechnology 37 (2), 155–163.

Hansen, L.D., Nestler, C., Ringelberg, D., Bajpai, R., 2004. Extended bioremediation of PAH/PCP contaminated soils from the POPILE wood treatment facility. Chemosphere 54 (10), 1481–1493.

Hanst, P.L., Stephens, E.R., Scott, W.E., Doerr, R.C., 1958. Atmospheric Ozone–Olefin Reactions. Franklin Institute, Philadelphia, PA.

Haritash, A., Kaushik, C., 2009. Biodegradation aspects of polycyclic aromatic hydrocarbons (PAHs): a review. Journal of Hazardous Materials 169 (1), 1–15.

Harmsen, J., 1983. Identification of organic compounds in leachate from a waste tip. Water Research 17 (6), 699–705.

Harrison, F.H., Harwood, C.S., 2005. The pimFABCDE operon from rhodopseudomonas palustris mediates dicarboxylic acid degradation and participates in anaerobic benzoate degradation. Microbiology 151 (3), 727–736.

Hautaniemi, M., Kallas, J., Munter, R., Trapido, M., 1998a. Modelling of chlorophenol treatment in aqueous solutions. 1. Ozonation and ozonation combined with uv radiation under acidic conditions. Ozone: Science & Engineering.

Hautaniemi, M., Kallas, J., Munter, R., Trapido, M., Laari, A., 1998b. Modelling of chlorophenol treatment in aqueous solutions. 2. Ozonation under basic conditions. Ozone: Science & Engineering.

Haykin, S., 1994. Neural Networks. A Comprehensive Foundation. IEEE Press, New York.

He, S., Reif, K., Unbehauen, R., 2000. Multilayer neural networks for solving a class of partial differential equations. Neural Networks 13 (3), 385–396.

Head, I.M., Jones, D.M., Röling, W.F., 2006. Marine microorganisms make a meal of oil. Nature Reviews Microbiology 4 (3), 173.

Helble, A., Schlayer, W., Liechti, P.-A., Jenny, R., Möbiust, C.H., 1999. Advanced effluent treatment in the pulp and paper industry with a combined process of ozonation and fixed bed biofilm reactors. Water Science and Technology 40 (11–12), 343–350.

Herath, N.K., Ohtani, Y., Ichiura, H., 2011. Color and phenolic compounds reduction of kraft pulp mill effluent by ozonation with some pretreatments. American Journal of Scientific and Industrial Research 2 (5), 798–806.

Hermosilla, D., Merayo, N., Gascó, A., Blanco, Á., 2015. The application of advanced oxidation technologies to the treatment of effluents from the pulp and paper industry: a review. Environmental Science and Pollution Research 22 (1), 168–191.

Higgins, D.G., Thompson, J.D., Gibson, T.J., 1996. Using CLUSTAL for multiple sequence alignments. Methods in Enzymology 266, 383–402.

Hikita, H., Asai, S., Tanigawa, K., Segawa, K., Kitao, M., 1981. The volumetric liquid-phase mass transfer coefficient in bubble columns. Chemical Engineering Journal 22 (1), 61–69.

Hoigné, J., Bader, H., 1983a. Rate constants of reactions of ozone with organic and inorganic compounds in water I: non-dissociating organic compounds. Water Research 17, 173–183.

Hoigné, J., Bader, H., 1983b. Rate constants of reactions of ozone with organic and inorganic compounds in water II: dissociating organic compounds. Water Research 17 (2), 185–194.

Hong, P.A., Zeng, Y., 2002. Degradation of pentachlorophenol by ozonation and biodegradability of intermediates. Water Research 36 (17), 4243–4254.

Hong, S., Elimelech, M., 1997. Chemical and physical aspects of natural organic matter (nom) fouling of nanofiltration membranes. Journal of Membrane Science 132 (2), 159–181.

Hopfield, J.J., 1982. Neural networks and physical systems with emergent collective computational abilities. Proceedings of the National Academy of Sciences 79 (8), 2554–2558.

Husain, Q., 2010. Peroxidase mediated decolorization and remediation of wastewater containing industrial dyes: a review. Reviews in Environmental Science and Bio/Technology 9 (2), 117–140.

Ikeda, M., Arai, K., Masai, H., 1996. Ctbp1/rbp1, a saccharomyces cerevisiae protein which binds to t-rich single-stranded DNA containing the 11-bp core sequence of autonomously replicating sequence, is a poly(deoxypyrimidine)-binding protein. European Journal of Biochemistry 238 (1), 38–47.

Ikhlaq, A., Brown, D.R., Kasprzyk-Hordern, B., 2015. Catalytic ozonation for the removal of organic contaminants in water on alumina. Applied Catalysis B: Environmental 165, 408–418.

Imai, D., Dabwan, A.H., Kaneco, S., Katsumata, H., Suzuki, T., Kato, T., Ohta, K., 2009. Degradation of marine humic acids by ozone-initiated radical reactions. Chemical Engineering Journal 148 (2), 336–341.

Íñiguez-Covarrubias, G., Peraza-Luna, F., 2007. Reduction of solids and organic load concentrations in tequila vinasses using a polyacrylamide (PAM) polymer flocculant. Revista Internacional de Contaminación Ambiental 23 (1).

Intergubernamental, S.T., 1990. Programa integral contra la contaminación atmosférica de la zona metropolitana de la ciudad de México (PICCA, 1990). México, STI.

Iranpour, R., Cox, H.H., Deshusses, M.A., Schroeder, E.D., 2005. Literature review of air pollution control biofilters and biotrickling filters for odor and volatile organic compound removal. Environmental Progress & Sustainable Energy 24 (3), 254–267.

Isidori, A., 1995. Nonlinear Control Systems. Communications and Control Engineering Series, vol. 1. Springer-Verlag.

Jallouli, N., Elghniji, K., Hentati, O., Ribeiro, A.R., Silva, A.M., Ksibi, M., 2016. Uv and solar photo-degradation of naproxen: TiO2 catalyst effect, reaction kinetics, products identification and toxicity assessment. Journal of Hazardous Materials 304, 329–336.

Jans, U., Hoigné, J., 1998. Activated carbon and carbon black catalyzed transformation of aqueous ozone into oh-radicals. Ozone: Science & Engineering.

Jia, C., Batterman, S., Godwin, C., 2008a. VOCs in industrial, urban and suburban neighborhoods, part 1: indoor and outdoor concentrations, variation, and risk drivers. Atmospheric Environment 42 (9), 2083–2100.

Jia, C., Batterman, S., Godwin, C., 2008b. VOCs in industrial, urban and suburban neighborhoods–part 2: factors affecting indoor and outdoor concentrations. Atmospheric Environment 42 (9), 2101–2116.

Jiang, Y., Wen, J., Caiyin, Q., Lin, L., Hu, Z., 2006. Mutant AFM 2 of alcaligenes faecalis for phenol biodegradation using He–Ne laser irradiation. Chemosphere 65 (7), 1236–1241.

Jimenez-Cisneros, B., Maya-Rendon, C., 2007. Helminths and sanitation. Communicating Current Research and Educational Topics and Trends in Applied Microbiology 1, 60–71.

Joglekar, H., Samant, S., Joshi, J., 1991. Kinetics of wet air oxidation of phenol and substituted phenols. Water Research 25 (2), 135–145.

Johnsen, K., Tana, J., Lehtinen, K.-J., Stuthridge, T., Mattsson, K., Hemming, J., Carlberg, G.E., 1998. Experimental field exposure of brown trout to river water receiving effluent from an integrated newsprint mill. Ecotoxicology and Environmental Safety 40 (3), 184–193.

Jordan, M.I., 1996. Computational aspects of motor control and motor learning. Handbook of Perception and Action 2, 71–120.

Kamal, V.S., Wyndham, R.C., 1990. Anaerobic phototrophic metabolism of 3-chlorobenzoate by rhodopseudomonas palustris WS17. Applied and Environmental Microbiology 56 (12), 3871–3873.

Kanakaraju, D., Motti, C.A., Glass, B.D., Oelgemöller, M., 2015. TiO2 photocatalysis of naproxen: effect of the water matrix, anions and diclofenac on degradation rates. Chemosphere 139, 579–588.

Kang, K.-H., Shin, H.S., Park, H., 2002. Characterization of humic substances present in landfill leachates with different landfill ages and its implications. Water Research 36 (16), 4023–4032.

Kansal, S., Singh, M., Sud, D., 2008. Effluent quality at kraft/soda agro-based paper mills and its treatment using a heterogeneous photocatalytic system. Desalination 228 (1–3), 183–190.

Kargi, F., Eker, S., 2005. Removal of 2,4-dichlorophenol and toxicity from synthetic wastewater in a rotating perforated tube biofilm reactor. Process Biochemistry 40 (6), 2105–2111.

Karrasch, B., Parra, O., Cid, H., Mehrens, M., Pacheco, P., Urrutia, R., Valdovinos, C., Zaror, C., 2006. Effects of pulp and paper mill effluents on the microplankton and microbial self-purification capabilities of the Biobio river, Chile. Science of the Total Environment 359 (1–3), 194–208.

Karunakaran, C., Dhanalakshmi, R., 2008. Photocatalytic performance of particulate semiconductors under natural sunshine–oxidation of carboxylic acids. Solar Energy Materials and Solar Cells 92 (5), 588–593.

Kasprzyk-Hordern, B., Andrzejewski, P., Nawrocki, J., 2005. Catalytic ozonation of gasoline compounds in model and natural water in the presence of perfluorinated alumina bonded phases. Ozone: Science & Engineering 27 (4), 301–310.

Kelmans, G.K., Chernitser, A.V., Poznyak, A., 1981. Adaptive locally optimal control. International Journal of Systems Sciences 12 (2), 235–254.

Kelmans, G.K., Poznyak, A., Chernitser, 1982. Locally optimal control of plants with unknown parameters. Automation and Remote Control 43 (10), 1293–1303.

Kemeny, T.E., Banerjee, S., 1997. Relationships among effluent constituents in bleached kraft pulp mills. Water Research 31 (7), 1589–1594.

Kerc, A., Bekbolet, M., Saatci, A.M., 2003. Sequential oxidation of humic acids by ozonation and photocatalysis. Ozone: Science & Engineering 25 (6), 497–504.

Khaksar Toroghi, M., Goffaux, G., Perrier, M., 2013. Output feedback passivity-based controller for microalgae cultivation. In: Preprints of the 12th IFAC Symposium on Computer Applications in Biotechnology, the International Federation of Automatic Control. Mumbai, India.

Khalil, H.K., 2002. Nonlinear Systems, 3rd. edition. Prentice-Hall, Upper Saddle River, New Jersey.

Khokhawala, I.M., Gogate, P.R., 2010. Degradation of phenol using a combination of ultrasonic and uv irradiations at pilot scale operation. Ultrasonics Sonochemistry 17 (5), 833–838.

Kim, J., Choi, H., 2002. Modeling in situ ozonation for the remediation of nonvolatile PAH-contaminated unsaturated soils. Journal of Contaminant Hydrology 55 (3), 261–285.

Kim, J.-H., Han, S.-J., Kim, S.-S., Yang, J.-W., 2006. Effect of soil chemical properties on the remediation of phenanthrene-contaminated soil by electrokinetic-Fenton process. Chemosphere 63 (10), 1667–1676.

King, C., 1966. Turbulent liquid phase mass transfer at free gas–liquid interface. Industrial & Engineering Chemistry Fundamentals 5 (1), 1–8.

Kitis, M., Adams, C.D., Kuzhikannil, J., Daigger, G.T., 2000. Effects of ozone/hydrogen peroxide pretreatment on aerobic biodegradability of nonionic surfactants and polypropylene glycol. Environmental Science & Technology 34 (11), 2305–2310.

Kleerebezem, R., Pol, L.W.H., Lettinga, G., 1999. Anaerobic biodegradability of phthalic acid isomers and related compounds. Biodegradation 10 (1), 63–73.

Knobloch, H.W., Isidori, A., Flocherzi, D., 1993. Topics in Control Theory. Birkhauser Verlag, Basel, Boston, Berlin.

Korhonen, S., Tuhkanen, T., 2000. Effects of ozone on resin acids in thermomechanical pulp and paper mill circulation waters. Ozone: Science & Engineering 22 (6), 575–584.

Kornmüller, A., Wiesmann, U., 1999. Continuous ozonation of polycyclic aromatic hydrocarbons in oil/water-emulsions and biodegradation of oxidation products. Water Science and Technology 40 (4–5), 107–114.

Kosjek, T., Heath, E., Krbavčič, A., 2005. Determination of non-steroidal anti-inflammatory drug (NSAIDs) residues in water samples. Environment International 31 (5), 679–685.

Koyuncu, I., Yalcin, F., Ozturk, I., 1999. Color removal of high strength paper and fermentation industry effluents with membrane technology. Water Science and Technology 40 (11–12), 241–248.

Krener, A.J., Isidori, A., 1980. Nonlinear zero distributions. In: IEEE Conference on Decision and Control, vol. 3, pp. 665–668.

Krener, A.J., Isidori, A., 1983. Linearization by output injection and nonlinear observers. Systems & Control Letters 3 (1), 47–52.

Krener, A.J., Respondek, W., 1985. Nonlinear observers with linearizable error dynamics. SIAM Journal on Control and Optimization 23 (2), 197–216.

Krstic, M., Kanellakopoulos, I., Kokotovic, P.V., 1995. Nonlinear and Adaptive Control Design. Wiley.

Kulik, N., Goi, A., Trapido, M., Tuhkanen, T., 2006. Degradation of polycyclic aromatic hydrocarbons by combined chemical pre-oxidation and bioremediation in creosote contaminated soil. Journal of Environmental Management 78 (4), 382–391.

Kumar, A., Kumar, S., Kumar, S., 2005. Biodegradation kinetics of phenol and catechol using pseudomonas putida MTCC 1194. Biochemical Engineering Journal 22 (2), 151–159.

Kuo, C., 1982. Mass transfer in ozone absorption. An approximate analytical equation is derived for predicting the enhancement of mass transfer by decomposition and ozanation reactions. Environmental Progress & Sustainable Energy 1 (3), 189–195.

Kuo, C., Huang, C.H., 1995. Aqueous phase ozonation of chlorophenols. Journal of Hazardous Materials 41 (1), 31–45.

Kuo, C., Huang, C.H., 1998. Kinetics of ozonation of pentachlorophenol in aqueous solutions. Ozone: Science & Engineering.

Kuraica, M.M., Obradović, B.M., Manojlović, D., Ostojić, D.R., Purić, J., 2004. Ozonized water generator based on coaxial dielectric-barrier-discharge in air. Vacuum 73 (3), 705–708.

Kurniawan, T.A., Lo, W.-H., Chan, G.Y., 2006. Degradation of recalcitrant compounds from stabilized landfill leachate using a combination of ozone-GAC adsorption treatment. Journal of Hazardous Materials 137 (1), 443–455.

Kwamena, N.-O.A., Earp, M.E., Young, C.J., Abbatt, J.P., 2006. Kinetic and product yield study of the heterogeneous gas–surface reaction of anthracene and ozone. The Journal of Physical Chemistry A 110 (10), 3638–3646.

Laari, A., Korhonen, S., Tuhkanen, T., Verenich, S., Kallas, I., 1999. Ozonation and wet oxidation in the treatment of thermomechanical pulp (TMP) circulation waters. Water Science and Technology 40 (11–12), 51–58.

Laari, A., Korhonen, S., Kallas, J., Tuhkanen, T., 2000. Selective removal of lipophilic wood extractives from paper mill water circulations by ozonation. Ozone: Science & Engineering 22 (6), 585–605.

Laari, A., Nissen, M., Kallas, J., et al., 2001. Combination of coagulation and catalytic wet oxidation for the treatment of pulp and paper mill effluents. Water Science and Technology: A Journal of the International Association on Water Pollution Research 44 (5), 145–152.

Lafont, F., Busvelle, E., Gauthier, J.P., 2011. An adaptive high-gain observer for wastewater treatment systems. Journal of Process Control 21 (6), 893–900.

Lamont, J.C., Scott, D., 1970. An eddy cell model of mass transfer into the surface of a turbulent liquid. American Institute of Chemical Engineers Journal 16 (4), 513–519.

Larisch, B.C., Duff, S.J., 1997. Effect of h 2 o 2 on characteristics and biological treatment of TCF bleached pulp mill effluent. Water Research 31 (7), 1694–1700.

Larsson, C., Nilsson, A., Blomberg, A., Gustafsson, L., 1997. Glycolytic flux is conditionally correlated with ATP concentration in saccharomyces cerevisiae: a chemostat study under carbon- or nitrogen-limiting conditions. Journal of Bacteriology 179 (23), 7243–7250.

Leahy, J.G., Colwell, R.R., 1990. Microbial degradation of hydrocarbons in the environment. Microbiological Reviews 54 (3), 305–315.

Ledakowicz, S., Michniewicz, M., Jagiella, A., Stufka-Olczyk, J., Martynelis, M., 2006. Elimination of resin acids by advanced oxidation processes and their impact on subsequent biodegradation. Water Research 40 (18), 3439–3446.

Lee, B.-T., Kim, K.-W., 2002. Ozonation of diesel fuel in unsaturated porous media. Applied Geochemistry 17 (8), 1165–1170.

Lee, Y., von Gunten, U., 2010. Oxidative transformation of micropollutants during municipal wastewater treatment: comparison of kinetic aspects of selective (chlorine, chlorine dioxide, ferratevi, and ozone) and non-selective oxidants (hydroxyl radical). Water Research 44 (2), 555–566.

Levant, A., 1993. Sliding order and sliding accuracy in sliding mode control. International Journal of Control 58 (6), 1247–1263.

Levant, A., 1998. Robust exact differentiation via sliding mode technique. Automatica 34 (3), 379–384.

Levant, A., 2002. Sliding mode control in engineering. In: High Order Sliding Modes. Marcel Dekker, Inc., pp. 53–101.

Levant, A., 2007. Principles of 2-sliding mode design. Automatica 43 (4), 576–586.
Levin, A.U., Narendra, K.S., 1995. Identification using feedforward networks. Neural Computation 7 (2), 349–369.
Lewis, F., Jagannathan, S., Yesildirak, A., 1998. Neural Network Control of Robot Manipulators and Non-linear Systems. CRC Press.
Li, D., Haneda, H., Ohashi, N., Saito, N., Hishita, S., 2005. Morphological reform of ZnO particles induced by coupling with mo x (m = v, w, ce) and the effects on photocatalytic activity. Thin Solid Films 486 (1), 20–23.
Li, H.-s., Zhou, S.-q., Sun, Y.-b., Feng, P., et al., 2009. Advanced treatment of landfill leachate by a new combination process in a full-scale plant. Journal of Hazardous Materials 172 (1), 408–415.
Li, J., Wang, H.O., Niemann, D., Tanaka, K., 2000. Dynamic parallel distributed compensation for Takagi–Sugeno fuzzy systems: an LMI approach. Information Sciences 123 (3–4), 201–221.
Li, N., Descorme, C., Besson, M., 2007. Catalytic wet air oxidation of aqueous solution of 2-chlorophenol over Ru/zirconia catalysts. Applied Catalysis B: Environmental 71 (3), 262–270.
Liberzon, D., 2003. Switching in Systems and Control, Foundations & Applications. Systems & Control. Birkhauser, Boston, MA.
Liberzon, D., Morse, A.S., 1999. Basic problems in stability and design of switched systems. IEEE Control Systems Magazine 19, 59–70.
Lim, H.-N., Choi, H., Hwang, T.-M., Kang, J.-W., 2002. Characterization of ozone decomposition in a soil slurry: kinetics and mechanism. Water Research 36 (1), 219–229.
Lin, H., Antsaklis, P., 2009. Stability and stabilizability of switched linear systems: a survey of recent results. IEEE Transactions on Automatic Control 54 (2), 308–322.
Lin, T.C., Lee, C.S., 1991. Neural network based fuzzy logic control and decision system. IEEE Transactions on Computers 40 (12), 1320–1336.
Liu, D., Gibaru, O., Perruquetti, W., 2014. Synthesis on a class of algebraic differentiators and application to nonlinear observation. In: Proceedings of the 33rd Chinese Control Conference.
Liu, Z.-Q., Ma, J., Cui, Y.-H., Zhang, B.-P., 2009. Effect of ozonation pretreatment on the surface properties and catalytic activity of multi-walled carbon nanotube. Applied Catalysis B: Environmental 92 (3), 301–306.
Ljung, L., 1979. Asymptotic behavior of the extended Kalman filter as a parameter estimator for linear systems. IEEE Transactions on Automatic Control 24 (1), 36–50.
Ljung, L., 1987. System Identification: Theory for the User. Prentice Hall, Englewood Cliff, New Jersey.
López-López, A., Davila-Vazquez, G., León-Becerril, E., Villegas-García, E., Gallardo-Valdez, J., 2010. Tequila vinasses: generation and full scale treatment processes. Reviews in Environmental Science and Bio/Technology 9 (2), 109–116.
Lucas, M.S., Peres, J.A., Lan, B.Y., Puma, G.L., 2009. Ozonation kinetics of winery wastewater in a pilot-scale bubble column reactor. Water Research 43 (6), 1523–1532.
Lucas, M.S., Peres, J.A., Puma, G.L., 2010. Treatment of winery wastewater by ozone-based advanced oxidation processes (o3, o3/uv and o3/uv/h2o2) in a pilot-scale bubble column reactor and process economics. Separation and Purification Technology 72 (3), 235–241.
Luenberger, D.G., 1964. Observing the state of a linear system. IEEE Transactions on Military Electronics 8 (2), 74–80.
Luenberger, D.G., 1979. Introduction to Dynamic Systems: Theory, Models, and Applications. John Wiley & Sons, New York.
Lundstedt, S., 2003. Analysis of PAHs and Their Transformations Products in Contaminated Soil and Remedial Processes. PhD thesis. Kemi.

Lunze, J., Lamnabhi-Lagarrigue, F., 2009. Handbook of Hybrid Systems Control: Theory, Tools and Applications. Cambridge University Press, New York, NY, USA.

Luster-Teasley, S., Ubaka-Blackmoore, N., Masten, S., 2009. Evaluation of soil pH and moisture content on in-situ ozonation of pyrene in soils. Journal of Hazardous Materials 167 (1), 701–706.

Luthy, R.G., Dzombak, D.A., Peters, C.A., Roy, S.B., Ramaswami, A., Nakles, D.V., Nott, B.R., 1994. Remediating tar-contaminated soils at manufactured gas plant sites. Environmental Science & Technology 28 (6), 266A–276A.

Luviano-Juárez, A., Chairez, I., 2013. Active disturbance rejection control based on a simultaneous adaptive observer and a time varying parameter identifier. In: European Control Conference.

Magallanes, D., Rodríguez, J.L., Poznyak, T., Valenzuela, M.A., Lartundo, L., Chairez, I., 2015. Efficient mineralization of benzoic and phthalic acids in water by catalytic ozonation using a nickel oxide catalyst. New Journal of Chemistry 39 (10), 7839–7848.

Makris, S.P., Banerjee, S., 2002. Fate of resin acids in pulp mill secondary treatment systems. Water Research 36 (11), 2878–2882.

Malato, S., Oller, I., Fernández-Ibánez, P., Fuerhacker, M., 2010. Technologies for advanced wastewater treatment in the Mediterranean region. In: Waste Water Treatment and Reuse in the Mediterranean Region. Springer, pp. 1–28.

Manickam, N., Misra, R., Mayilraj, S., 2007. A novel pathway for the biodegradation of γ-hexachlorocyclohexane by a xanthomonas sp. strain ich12. Journal of Applied Microbiology 102 (6), 1468–1478.

Manning, D., Bewsher, A., 1997. Determination of anions in landfill leachates by ion chromatography. Journal of Chromatography A 770 (1–2), 203–210.

Martinez-Guerra, R., Poznyak, A., Gortcheva, E., de Leon, V.D., 2000. Robot angular link velocity estimation in the presence of high-level mixed uncertainties. IEE Proceedings Control Theory and Applications 147 (5), 515–522.

Marttinen, S., Kettunen, R., Sormunen, K., Soimasuo, R., Rintala, J., 2002. Screening of physical–chemical methods for removal of organic material, nitrogen and toxicity from low strength landfill leachates. Chemosphere 46 (6), 851–858.

Martínez-Fonseca, N., Chairez, I., Poznyak, A., 2014. Uniform step by step observer for aerobic bioreactor based on super-twisting algorithm. Bioprocess and Biosystems Engineering.

Mascolo, G., Ciannarella, R., Balest, L., Lopez, A., 2008. Effectiveness of uv-based advanced oxidation processes for the remediation of hydrocarbon pollution in the groundwater: a laboratory investigation. Journal of Hazardous Materials 152 (3), 1138–1145.

Mata, T., Martins, A., Caetano, N., 2010. Microalgae for biodiesel production and other applications: a review. Renewable and Sustainable Energy Reviews 14, 217–232.

Mehrjouei, M., Müller, S., Möller, D., 2011. Degradation of oxalic acid in a photocatalytic ozonation system by means of Pilkington Active^{TM} glass. Journal of Photochemistry and Photobiology A: Chemistry 217 (2), 417–424.

Mejbri, R., Matejka, G., Lafrance, P., Mazet, M., 1995. Fractionnement et caractérisation de la matière organique des lixiviats de décharges d'ordures ménagères. Revue des Sciences de l'eau/Journal of Water Science 8 (2), 217–236.

Méndez-Acosta, H.O., Snell-Castro, R., Alcaraz-González, V., González-Álvarez, V., Pelayo-Ortiz, C., 2010. Anaerobic treatment of tequila vinasses in a CSTR-type digester. Biodegradation 21 (3), 357–363.

Méndez-Arriaga, F., Esplugas, S., Giménez, J., 2008a. Photocatalytic degradation of non-steroidal anti-inflammatory drugs with TiO2 and simulated solar irradiation. Water Research 42 (3), 585–594.

Méndez-Arriaga, F., Gimenez, J., Esplugas, S., 2008b. Photolysis and TiO2 photocatalytic treatment of naproxen: degradation, mineralization, intermediates and toxicity. Journal of Advanced Oxidation Technologies 11 (3), 435–444.

Mexicana, N.O., 1994. Nom-127-ssa1-1994, salud ambiental. Agua para uso y consumo humano. Límites permisibles de calidad y tratamientos a que debe someterse el agua para su potabilización, México, Secretaría de Salud.

Mexicanos, P., 2001. Informe 2000: seguridad, salud y medio ambiente. PEMEX.

Meza, P., Briones, M., Ilangovan, K., 2004. Floculación-coagulación como postratamiento del efluente de un reactor anaerobio que trata vinazas tequileras meza pérez. coordinación de bioprocesos ambientales.

Mezzanotte, V., Antonelli, M., Citterio, S., Nurizzo, C., 2007. Wastewater disinfection alternatives: chlorine, ozone, peracetic acid, and uv light. Water Environment Research 79 (12), 2373–2379.

Michel, A.N., Ling, H., Liu, D., 2007. Stability of Dynamical Systems. Birkhauser, New York, NY, USA.

Mihoub, M., Nouri, A.S., Abdennour, R.B., 2011. A second order discrete sliding mode observer for the variable structure control of a semi-batch reactor. Control Engineering Practice 19, 1216–1222.

Mills, A., Le Hunte, S., 1997. An overview of semiconductor photocatalysis. Journal of Photochemistry and Photobiology A: Chemistry 108 (1), 1–35.

Minero, C., Mariella, G., Maurino, V., Pelizzetti, E., 2000. Photocatalytic transformation of organic compounds in the presence of inorganic anions. 1. Hydroxyl-mediated and direct electron-transfer reactions of phenol on a titanium dioxide–fluoride system. Langmuir 16 (6), 2632–2641.

Monje, I., 2004. Ozonación de lixiviados estabilizados de rellenos sanitarios para transformar materia orgánica recalcitrante soluble. PhD thesis. UNAM.

Monje-Ramirez, I., De Velasquez, M.O., 2004. Removal and transformation of recalcitrant organic matter from stabilized saline landfill leachates by coagulation–ozonation coupling processes. Water Research 38 (9), 2359–2367.

Moraes, P.B., Bertazzoli, R., 2005. Electrodegradation of landfill leachate in a flow electrochemical reactor. Chemosphere 58 (1), 41–46.

Moreno, J.A., 2011. Lyapunov approach for analysis and design of second order sliding mode algorithms. In: Sliding Modes After the First Decade of the 21st Century, vol. 1(1), pp. 113–149.

Moreno, J.A., Osorio, M., 2008. A Lyapunov approach to second order sliding mode controllers and observers. In: IEEE Conference on Decision and Control, vol. 47, pp. 2856–2861.

Moreno, J.A., Osorio, M., 2012. Strict Lyapunov functions for the super-twisting algorithm. IEEE Transactions on Automatic Control 57 (4), 1035–1040.

Mottier, P., Parisod, V., Turesky, R.J., 2000. Quantitative determination of polycyclic aromatic hydrocarbons in barbecued meat sausages by gas chromatography coupled to mass spectrometry. Journal of Agricultural and Food Chemistry 48 (4), 1160–1166.

Mukherjee, A.K., Das, K., 2005. Correlation between diverse cyclic lipopeptides production and regulation of growth and substrate utilization by bacillus subtilis strains in a particular habitat. FEMS Microbiology Ecology 54 (3), 479–489.

Mulder, H., Breure, A., Rulkens, W., 2001. Prediction of complete bioremediation periods for PAH soil pollutants in different physical states by mechanistic models. Chemosphere 43 (8), 1085–1094.

Munter, R., Preis, S., Kamenev, S., Siirde, E., 1993. Methodology of ozone introduction into water and wastewater treatment. Ozone: Science & Engineering.

Murata, T., Okita, T., Noguchi, M., Takase, I., 2004. Basic parameters of coplanar discharge ozone generator. Ozone: Science & Engineering 26 (5), 429–442.

Murillo, D., 2011. Análisis de la influencia de dos materias primas coagulantes en el aluminio residual del agua tratada. Trabajo de grado Química Industrial.

Muruganandham, M., Wu, J., 2008. Synthesis, characterization and catalytic activity of easily recyclable zinc oxide nanobundles. Applied Catalysis B: Environmental 80 (1–2), 32–41.

Na, P.S., Kim, H., So, H.-M., Kong, K.-J., Chang, H., Ryu, B.H., Choi, Y., Lee, J.-O., Kim, B.-K., Kim, J.-J., et al., 2005. Investigation of the humidity effect on the electrical properties of single-walled carbon nanotube transistors. Applied Physics Letters 87 (9), 093101.

Nacheva, P.M., Bustillos, L.T., Camperos, E.R., Armenta, S.L., Vigueros, L.C., 1996. Characterization and coagulation–flocculation treatability of Mexico City wastewater applying ferric chloride and polymers. Water Science and Technology 34 (3–4), 235–247.

Nair, I.C., Jayachandran, K., Shashidhar, S., 2007. Treatment of paper factory effluent using a phenol degrading alcaligenes sp. under free and immobilized conditions. Bioresource Technology 98 (3), 714–716.

Nam, K., Kukor, J.J., 2000. Combined ozonation and biodegradation for remediation of mixtures of polycyclic aromatic hydrocarbons in soil. Biodegradation 11 (1), 1–9.

Nam, K., Rodriguez, W., Kukor, J.J., 2001. Enhanced degradation of polycyclic aromatic hydrocarbons by biodegradation combined with a modified Fenton reaction. Chemosphere 45 (1), 11–20.

Nanny, M.A., Ratasuk, N., 2002. Characterization and comparison of hydrophobic neutral and hydrophobic acid dissolved organic carbon isolated from three municipal landfill leachates. Water Research 36 (6), 1572–1584.

Nataraj, S., Sridhar, S., Shaikha, I., Reddy, D., Aminabhavi, T., 2007. Membrane-based microfiltration/electrodialysis hybrid process for the treatment of paper industry wastewater. Separation and Purification Technology 57 (1), 185–192.

Nemerow, N.L., Dasgupta, A., 1991. Industrial and Hazardous Waste Treatment. New York, NY (United States).

Neta, P., Huie, R.E., Ross, A.B., 1988. Rate constants for reactions of inorganic radicals in aqueous solution. Journal of Physical and Chemical Reference Data 17 (3), 1027–1284.

Nicosia, S., Tornambe, A., 1989. High gain observer in the state and parameter estimations of robots having elastic joins. Systems & Control Letters 13, 331–337.

Niessen, J., Harnisch, F., Rosenbaum, M., Schroder, U., Scholz, F., 2006. Heat treated soil as convenient and versatile source of bacterial communities for microbial electricity generation. Electrochemistry Communications 8, 869–873.

Nozhevnikova, A., Lebedev, V., Lifshitz, A., 1992. Microbiological processes occurring in landfills. In: Proceedings of the International Symposium on Anaerobic Digestion of Solid Waste. Venice, Italy, pp. 303–312.

Ntampou, X., Zouboulis, A., Samaras, P., 2006. Appropriate combination of physicochemical methods (coagulation/flocculation and ozonation) for the efficient treatment of landfill leachates. Chemosphere 62 (5), 722–730.

U. D. of Health, H. Services, et al., 1995. Toxicological Profile for Polycyclic Aromatic Hydrocarbons (PAHs). Agency for Toxic Substances and Disease Registry, Atlanta.

C. S. of Soil Science, 1978. In: McKeague, J., et al. (Eds.), Manual on Soil Sampling and Methods of Analysis. Canadian Society of Soil Science.

Oller, I., Malato, S., Sánchez-Pérez, J., 2011. Combination of advanced oxidation processes and biological treatments for wastewater decontamination–a review. Science of the Total Environment 409 (20), 4141–4166.

Öman, C., Hynning, P.-Å., 1993. Identification of organic compounds in municipal landfill leachates. Environmental Pollution 80 (3), 265–271.

Oppenländer, T., 2003. Photochemical Purification of Water and Air: Advanced Oxidation Processes (AOPs)-Principles, Reaction Mechanisms, Reactor Concepts. John Wiley & Sons.

W. H. Organization, 2004. Guidelines for Drinking-Water Quality: Recommendations, vol. 1. World Health Organization.

Orta de Velásquez, M., Corro, J.A., Ramirez, I.M., Brito, O.M., 1998. Improvement of wastewater coagulation using ozone. Ozone: Science & Engineering.

Orta de Velasquez, M.T., Rojas-Valencia, M.N., Ayala, A., 2008. Wastewater disinfection using ozone to remove free-living, highly pathogenic bacteria and amoebae. Ozone: Science & Engineering 30 (5), 367–375.

O'Mahony, M.M., Dobson, A.D., Barnes, J.D., Singleton, I., 2006. The use of ozone in the remediation of polycyclic aromatic hydrocarbon contaminated soil. Chemosphere 63 (2), 307–314.

O'melia, C., Becker, W., Au, K.-K., 1999. Removal of humic substances by coagulation. Water Science and Technology 40 (9), 47–54.

Pahlow, M., Dietze, H., Oschlies, A., 2013. Optimality-based model of phytoplankton growth and diazotrophy. Marine Ecology Progress Series 489, 1–16.

Paraskeva, P., Graham, N.J., 2002. Ozonation of municipal wastewater effluents. Water Environment Research 74 (6), 569–581.

Pariente, M.I., Martinez, F., Melero, J.A., Botas, J.A., Velegraki, T., Xekoukoulotakis, N.P., Mantzavinos, D., 2008. Heterogeneous photo-Fenton oxidation of benzoic acid in water: effect of operating conditions, reaction by-products and coupling with biological treatment. Applied Catalysis B: Environmental 85 (1–2), 24–32.

Park, H., Park, Y., Kim, W., Choi, W., 2013. Surface modification of TiO2 photocatalyst for environmental applications. Journal of Photochemistry and Photobiology C: Photochemistry Reviews 15, 1–20.

Park, J.-H., Kim, T.-H., Sugie, T., 2011. Output feedback model predictive control for LVP systems based on quasi-min max algorithm. Automatica 47, 2052–2058.

Payne, B., Biesinger, M., McIntyre, N., 2009. The study of polycrystalline nickel metal oxidation by water vapour. Journal of Electron Spectroscopy and Related Phenomena 175 (1), 55–65.

Peng, G., Roberts, J.C., 2000. Solubility and toxicity of resin acids. Water Research 34 (10), 2779–2785.

Perraudin, E., Budzinski, H., Villenave, E., 2007. Identification and quantification of ozonation products of anthracene and phenanthrene adsorbed on silica particles. Atmospheric Environment 41 (28), 6005–6017.

Piehler, M., Swistak, J., Pinckney, J., Paerl, H., 1999. Stimulation of diesel fuel biodegradation by indigenous nitrogen fixing bacterial consortia. Microbial Ecology 38 (1), 69–78.

Pierpoint, A.C., Hapeman, C.J., Torrents, A., 2003. Ozone treatment of soil contaminated with aniline and trifluralin. Chemosphere 50 (8), 1025–1034.

Pokhrel, D., Viraraghavan, T., 2004. Treatment of pulp and paper mill wastewater–a review. Science of the Total Environment 333 (1), 37–58.

Poznyak, A., 2004a. Variable structure systems: from principles to implementation. Chapter 3. In: IEE Control Series, vol. 66. The IET, London, UK, pp. 45–78.

Poznyak, A., 2004b. Deterministic output noise effects in sliding mode observation. Variable Structure Systems: From Principles to Implementation, 45–80.

Poznyak, A., 2008a. Advanced Mathematical Tools for Automatic Control Engineers. Vol. 1: Deterministic Systems. Elsevier Science.

Poznyak, A., Yu, W., Sánchez, E., Pérez, J., 1998. Stability analysis of dynamic neural networks. Expert Systems and Applications 14 (1), 227–236.

Poznyak, A., Sanchez, E., Yu, W., 2001. Differential Neural Networks for Robust Nonlinear Control (Identification, State Estimation and Trajectory Tracking). World Scientific.

Poznyak, A., Chairez, I., Poznyak, T., 2006a. Sliding mode neurocontrol with applications. In: International Workshop on Variable Structure Systems, 2006. VSS'06. IEEE, pp. 5–10.

Poznyak, A., Poznyak, T., Chairez, I., 2006b. Dynamic neuro-observers and their application for identification and purification of water by ozone. Automation and Remote Control 67 (6), 887–899.

Poznyak, A., Polyakov, A., Azhmyakov, V., 2014. Attractive Ellipsoids in Robust Control. Springer.

Poznyak, A.S., Azhmyakov, V., Mera, M., 2011. Practical output feedback stabilisation for a class of continuous-time dynamic systems under sample-data outputs. International Journal of Control, 1408–1416.

Poznyak, A.S., 2008b. Advanced Mathematical Tools for Automatic Control Engineers. Vol. 1: Deterministic Techniques. Elsevier.

Poznyak, A.S., Cordero, A.O., 1994. Suboptimal robust filtering of states of finite dimensional linear systems with time-varying parameters under nonrandom disturbances. In: Proceedings of the 33rd IEEE Conference on Decision and Control, 1994, vol. 4. IEEE, pp. 3931–3936.

Poznyak, A.S., Wen, Y., Poznyak, T.I., Najim, K., 2004. Simultaneous states and parameters estimation of an ozonation reactor based on dynamic neural network. J. Theory, Application & Computer Simulations, Special Issue: Differential Equations and Dynamical Systems 12 (1–2), 195–221.

Poznyak, T., 2000. Estimation of unsaturated hydrocarbon pollutants in air based on selective gas chromatography with ozone. Fresenius' Journal of Analytical Chemistry 367 (3), 275–278.

Poznyak, T., Araiza G., B., 2005. Ozonation of non-biodegradable mixtures of phenol and naphthalene derivatives in tanning wastewaters. Ozone: Science & Engineering 27 (5), 351–357.

Poznyak, T., Chairez, I., 2011. Kinetic study of toxic pollutants decomposition by ozone in landfill leachate using a numerical adaptive method. International Journal of Environmental Engineering. Special Issue in Progress in Landfill Management and Landfill Emission Reduction 3 (3–4), 221–239.

Poznyak, T., Vivero, J., 2005. Degradation of aqueous phenol and chlorinated phenols by ozone. Ozone: Science & Engineering 27 (6), 447–458.

Poznyak, T., Chairez, I., Poznyak, A., 2005. Application of a neural observer to phenols ozonation in water: simulation and kinetic parameters identification. Water Research 39 (12), 2611–2620.

Poznyak, T., García, A., Chairez, I., Gómez, M., Poznyak, A., 2007. Application of the differential neural network observer to the kinetic parameters identification of the anthracene degradation in contaminated model soil. Journal of Hazardous Materials 146 (3), 661–667.

Poznyak, T., Bautista, G.L., Chaírez, I., Córdova, R.I., Ríos, L.E., 2008. Decomposition of toxic pollutants in landfill leachate by ozone after coagulation treatment. Journal of Hazardous Materials 152 (3), 1108–1114.

Poznyak, T.I., 2003. Use of ozone for the polymer microstructure characterization. analytical aspect of the ozone application. Ozone: Science & Engineering 25 (2), 145–153.

Poznyak, T.I., Lisitsyn, D.M., Novikov, D.D., 1977. Selective detector for unsaturated substances in liquid chromatography, mathematical design of reaction cell. Journal of Analytical Chemistry 32 (11), 2218–2226.

Poznyak, T.I., Manzo, A., Mayorga, J.L., 2003. Elimination of chlorinated unsaturated hydrocarbons from water by ozonation: simulation and experimental data comparison. Revista de la Sociedad Química de México 47 (1), 58–65.

Prieto, M.B., Hidalgo, A., Serra, J.L., Llama, M.J., 2002. Degradation of phenol by rhodococcus erythropolis upv-1 immobilized on biolite® in a packed-bed reactor. Journal of Biotechnology 97 (1), 1–11.

Qiu, R., Zhang, D., Mo, Y., Song, L., Brewer, E., Huang, X., Xiong, Y., 2008. Photocatalytic activity of polymer-modified ZnO under visible light irradiation. Journal of Hazardous Materials 156 (1), 80–85.

Quintana, J.B., Weiss, S., Reemtsma, T., 2005. Pathways and metabolites of microbial degradation of selected acidic pharmaceutical and their occurrence in municipal wastewater treated by a membrane bioreactor. Water Research 39 (12), 2654–2664.

Quinzaños, S., Dahl, C., Strube, R., Mujeriego, R., 2008. Helminth eggs removal by microscreening for water reclamation and reuse. Water Science and Technology 57 (5), 715–720.

Rajeshwari, K., Balakrishnan, M., Kansal, A., Lata, K., Kishore, V., 2000. State-of-the-art of anaerobic digestion technology for industrial wastewater treatment. Renewable and Sustainable Energy Reviews 4 (2), 135–156.

Ralph, J., Lundquist, K., Brunow, G., Lu, F., Kim, H., Schatz, P.F., Marita, J.M., Hatfield, R.D., Ralph, S.A., Christensen, J.H., et al., 2004. Lignins: natural polymers from oxidative coupling of 4-hydroxyphenyl-propanoids. Phytochemistry Reviews 3 (1–2), 29–60.

Ramalho, R.S., 1990. Tratamiento de aguas residuales. Reverté.

Ramaroson, J., Dirion, J.-L., Nzihou, A., Depelsenaire, G., 2009. Characterization and kinetics of surface area reduction during the calcination of dredged sediments. Powder Technology 190 (1), 59–64.

Ramírez-Sáenz, D., Zarate-Segura, P.B., Guerrero-Barajas, C., Garcia-Peña, E.I., 2009. H 2 s and volatile fatty acids elimination by biofiltration: clean-up process for biogas potential use. Journal of Hazardous Materials 163 (2), 1272–1281.

Ratledge, C., 2012. Biochemistry of Microbial Degradation. Springer Science & Business Media.

Razumovskii, S., Zaikov, G.E., et al., 1984. Ozone and Its Reactions with Organic Compounds. Elsevier.

Rehman, S., Ullah, R., Butt, A., Gohar, N., 2009. Strategies of making TiO2 and ZnO visible light active. Journal of Hazardous Materials 170 (2), 560–569.

Reitzer, L., 2003. Nitrogen assimilation and global regulation in escherichia coli. Annual Reviews of Microbiology 57, 155–176.

Rivas, F.J., 2006. Polycyclic aromatic hydrocarbons sorbed on soils: a short review of chemical oxidation based treatments. Journal of Hazardous Materials 138 (2), 234–251.

Rivas, F.J., Beltrán, F., Carvalho, F., Acedo, B., Gimeno, O., 2004. Stabilized leachates: sequential coagulation–flocculation + chemical oxidation process. Journal of Hazardous Materials 116 (1), 95–102.

Rivas, F.J., Beltrán, F.J., Carvalho, F., Alvarez, P.M., 2005. Oxone-promoted wet air oxidation of landfill leachates. Industrial & Engineering Chemistry Research 44 (4), 749–758.

Rivas, J., Gimeno, O., Ruth, G., Beltrán, F.J., 2009. Ozone treatment of PAH contaminated soils: operating variables effect. Journal of Hazardous Materials 169 (1), 509–515.

Rivera-Utrilla, J., Méndez-Díaz, J., Sánchez-Polo, M., Ferro-García, M., Bautista-Toledo, I., 2006. Removal of the surfactant sodium dodecylbenzenesulphonate from water by simultaneous use of ozone and powdered activated carbon: comparison with systems based on o 3 and o 3/h 2 o 2. Water Research 40 (8), 1717–1725.

Rodríguez, A., Letón, P., Rosal, R., Dorado, M., Villar, S., Sanz, J., 2006. Tratamientos avanzados de aguas residuales industriales. Informe de vigilancia tecnológica de la Universidad de Alcalá del Círculo de Innovación en Tecnologías Medioambientales y Energía (CITME), España.

Rodrıguez, J., Castrillon, L., Maranon, E., Sastre, H., Fernandez, E., 2004. Removal of non-biodegradable organic matter from landfill leachates by adsorption. Water Research 38 (14), 3297–3303.

Rodriguez, J., García, A., Poznyak, T., Chairez, I., 2017. Phenanthrene degradation in soil by ozonation: effect of morphological and physicochemical properties. Chemosphere 169, 53–61.

Rodríguez, J.L., Valenzuela, M.A., Pola, F., Tiznado, H., Poznyak, T., 2012. Photodeposition of Ni nanoparticles on TiO2 and their application in the catalytic ozonation of 2, 4-dichlorophenoxyacetic acid. Journal of Molecular Catalysis A: Chemical 353, 29–36.

Rodríguez, J.L., Poznyak, T., Valenzuela, M.A., Tiznado, H., Chairez, I., 2013a. Surface interactions and mechanistic studies of 2, 4-dichlorophenoxyacetic acid degradation by catalytic ozonation in presence of Ni/TiO2. Chemical Engineering Journal 222, 426–434.

Rodríguez, J.L., Valenzuela, M.A., Poznyak, T., Lartundo, L., Chairez, I., 2013b. Reactivity of NiO for 2, 4-d degradation with ozone: XPS studies. Journal of Hazardous Materials 262, 472–481.

Rojas-Valencia, M., 2011. Research on ozone application as disinfectant and action mechanisms on wastewater microorganisms. Virus 3, 4.

Rosal, R., Rodríguez, A., Gonzalo, M., García-Calvo, E., 2008. Catalytic ozonation of naproxen and carbamazepine on titanium dioxide. Applied Catalysis B: Environmental 84 (1), 48–57.

Ross, O.N., Geider, R.J., 2009. New cell-based model of photosynthesis and photoacclimation: accumulation and mobilisation of energy reserves in phytoplankton. Marine Ecology Progress Series 383, 53–71.

Roth, J.A., Sullivan, D.E., 1981. Solubility of ozone in water. Industrial & Engineering Chemistry Fundamentals 20 (2), 137–140.

Rowell, R.M., 2012. Handbook of Wood Chemistry and Wood Composites. CRC Press.

Roy-Arcand, L., Archibald, F., 1996. Selective removal of resin and fatty acids from mechanical pulp effluents by ozone. Water Research 30 (5), 1269–1279.

Ruiz-Dueñas, F.J., Martínez, Á.T., 2009. Microbial degradation of lignin: how a bulky recalcitrant polymer is efficiently recycled in nature and how we can take advantage of this. Microbial Biotechnology 2 (2), 164–177.

Rusu, C., 2002. Sliding mode fuzzy control for the step motors. Journal of Control Engineering and Applied Informatics 4 (3), 13–18.

Salgado, I., Chairez, I., 2009. Discrete time recurrent neural network observer. In: 2009 International Joint Conference on Neural Networks, pp. 909–916.

Salgado, I., Chairez, I., 2014. Discrete time recurrent neural network observer. Neurocomputing.

Sanches, S., Leitão, C., Penetra, A., Cardoso, V., Ferreira, E., Benoliel, M., Crespo, M.B., Pereira, V., 2011. Direct photolysis of polycyclic aromatic hydrocarbons in drinking water sources. Journal of Hazardous Materials 192 (3), 1458–1465.

Sanchez, N., Alanis, Y., Loukianov, A., 2008. Discrete-Time, High Order Neural Control: Trained with Kalman Filtering. Springer Verlag, London.

Sánchez-Polo, M., Leyva-Ramos, R., Rivera-Utrilla, J., 2005. Kinetics of 1,3,6-naphthalenetrisulphonic acid ozonation in presence of activated carbon. Carbon 43 (5), 962–969.

Sangave, P.C., Gogate, P.R., Pandit, A.B., 2007. Ultrasound and ozone assisted biological degradation of thermally pretreated and anaerobically pretreated distillery wastewater. Chemosphere 68 (1), 42–50.

Santillan, J.L.R., Pola, F., Valenzuela-Zapata, M.A., 2010. Photocatalytic deposition of nickel nanoparticles on titanium dioxide. In: 19th International Materials Research Congress 2010.

Santos, A., Yustos, P., Quintanilla, A., Garcia-Ochoa, F., Casas, J., Rodriguez, J., 2004. Evolution of toxicity upon wet catalytic oxidation of phenol. Environmental Science & Technology 38 (1), 133–138.

Sarafraz-Yazdi, A., Amiri, A.H., Es'Haghi, Z., 2009. Separation and determination of benzene, toluene, ethylbenzene and o-xylene compounds in water using directly suspended droplet microextraction coupled with gas chromatography-flame ionization detector. Talanta 78 (3), 936–941.

Saravanan, P., Pakshirajan, K., Saha, P., 2008. Growth kinetics of an indigenous mixed microbial consortium during phenol degradation in a batch reactor. Bioresource Technology 99 (1), 205–209.

Saravanan, V., Rajamohan, N., 2009. Treatment of xylene polluted air using press mud-based biofilter. Journal of Hazardous Materials 162 (2), 981–988.

Savant, D., Abdul-Rahman, R., Ranade, D., 2006. Anaerobic degradation of adsorbable organic halides (aox) from pulp and paper industry wastewater. Bioresource Technology 97 (9), 1092–1104.

Sayigh, A., 2013. Sustainability, Energy and Architecture: Case Studies in Realizing Green Buildings. Academic Press.

Sayler, G.S., Ripp, S., 2000. Field application of genetically engineered microorganisms for bioremediation processes. Current Opinion in Biotechnology 11, 286–289.

Sayre, I.M., 1988. International standards for drinking water. Journal-American Water Works Association 80 (1), 53–60.

Schnell, A., Steel, P., Melcer, H., Hodson, P., Carey, J., 2000. Enhanced biological treatment of bleached kraft mill effluents–i. Removal of chlorinated organic compounds and toxicity. Water Research 34 (2), 493–500.

Schultz, B., Kjeldsen, P., 1986. Screening of organic matter in leachates from sanitary landfills using gas chromatography combined with mass spectrometry. Water Research 20 (8), 965–970.

Seabra, M., Salvado, I.M., Labrincha, J., 2011. Pure and (zinc or iron) doped titania powders prepared by sol–gel and used as photocatalyst. Ceramics International 37 (8), 3317–3322.

Sefriti, S., Boumhidi, J., Naoual, R., Boumhidi, I., 2014. Adaptive neural network sliding mode control for electrically-driven robot manipulators. Journal of Control Engineering and Applied Informatics 14 (4), 27–32.

Sehested, K., Corfitzen, H., Holcman, J., Fischer, C.H., Hart, E.J., 1991. The primary reaction in the decomposition of ozone in acidic aqueous solutions. Environmental Science & Technology 25 (9), 1589–1596.

Selcuk, H., 2005. Decolorization and detoxification of textile wastewater by ozonation and coagulation processes. Dyes and Pigments 64 (3), 217–222.

Senior, E., 1995. Microbiology of Landfill Sites. CRC Press.

Shah, F., Hadim, H., Korfiatis, G., 1995. Laboratory studies of air stripping of VOC-contaminated soils. Soil and Sediment Contamination 4 (1), 93–109.

Sharma, V., Rai, S., Dev, A., 2012. A comprehensive study of artificial neural networks. International Journal of Advanced Research in Computer Science and Software Engineering 2 (10).

Shemer, H., Linden, K.G., 2007. Photolysis, oxidation and subsequent toxicity of a mixture of polycyclic aromatic hydrocarbons in natural waters. Journal of Photochemistry and Photobiology A: Chemistry 187 (2), 186–195.

Shih, Y.-h., Li, M.-s., 2008. Adsorption of selected volatile organic vapors on multiwall carbon nanotubes. Journal of Hazardous Materials 154 (1), 21–28.

Shin, W.-T., Garanzuay, X., Yiacoumi, S., Tsouris, C., Gu, B., Mahinthakumar, G.K., 2004. Kinetics of soil ozonation: an experimental and numerical investigation. Journal of Contaminant Hydrology 72 (1), 227–243.

Shing-Lee, Y., Primavera, J.H., Dahdouh-Guebas, F., McKee, K., Bosire, J., Cannicci, S., Diele, K., Fromard, F., Koedam, N., Marchand, C., 2014. Global Ecology and Biogeography 23 (7), 726–743.

Shorten, R., Cairbre, F.O., 2001. A proof of global attractivity for a class of switching systems using non-quadratic Lyapunov approach. IMA Journal of Mathematical Control and Information 18 (3), 341–353.

Sigman, M.E., Schuler, P.F., Ghosh, M.M., Dabestani, R., 1998. Mechanism of pyrene photochemical oxidation in aqueous and surfactant solutions. Environmental Science & Technology 32 (24), 3980–3985.

Siles, J., García-García, I., Martín, A., Martín, M., 2011. Integrated ozonation and biomethanization treatments of vinasse derived from ethanol manufacturing. Journal of Hazardous Materials 188 (1–3), 247–253.

Sira-Ramirez, H., Nunez, C., Visairo, N., 2010. Robust sigma–delta generalised proportional integral observer based control of a "buck" converter with uncertain loads. International Journal of Control 83 (8), 1631–1640.

Slotine, J.J.E., 1984. Sliding controller design for nonlinear systems. International Journal of Control 40, 421–434.

Spong, M., Vidyasagar, M., 1989. Robot Dynamic and Control. John Wiley and Sons, Inc., New York, USA.

Sridhar, R., Sivakumar, V., Immanuel, V.P., Maran, J.P., 2011. Treatment of pulp and paper industry bleaching effluent by electrocoagulant process. Journal of Hazardous Materials 186 (2–3), 1495–1502.

Stehr, J., Müller, T., Svensson, K., Kamnerdpetch, C., Scheper, T., 2001. Basic examinations on chemical pre-oxidation by ozone for enhancing bioremediation of phenanthrene contaminated soils. Applied Microbiology and Biotechnology 57 (5–6), 803–809.

Stingley, R.L., Khan, A.A., Cerniglia, C.E., 2004. Molecular characterization of a phenanthrene degradation pathway in mycobacterium vanbaalenii pyr-1. Biochemical and Biophysical Research Communications 322 (1), 133–146.

Stohs, S.J., Ohia, S., Bagchi, D., 2002. Naphthalene toxicity and antioxidant nutrients. Toxicology 180 (1), 97–105.

Stoilova, I., Krastanov, A., Stanchev, V., Daniel, D., Gerginova, M., Alexieva, Z., 2006. Biodegradation of high amounts of phenol, catechol, 2,4-dichlorophenol and 2,6-dimethoxyphenol by aspergillus awamori cells. Enzyme and Microbial Technology 39 (5), 1036–1041.

Stowell, J., Jensen, J., Weber, A., 1992. Sequential chemical/biological oxidation of 2-chlorophenol. Water Science and Technology 26 (9–11), 2085–2087.

Sturrock, M.G., Cline, E.L., Robinson, K.R., 1963. The ozonation of phenanthrene with water as participating solvent. The Journal of Organic Chemistry 28 (9), 2340–2343.

Tatsi, A., Zouboulis, A., Matis, K., Samaras, P., 2003. Coagulation–flocculation pretreatment of sanitary landfill leachates. Chemosphere 53 (7), 737–744.

Taylor, E., Cook, B., Tarr, M., 1999. Dissolved organic matter inhibition of sonochemical degradation of aqueous polycyclic aromatic hydrocarbons. Ultrasonics Sonochemistry 6 (4), 175–183.

Thakuria, D., Talukdar, N., Goswami, C., Hazarika, S., Boro, R., Khan, M., 2004. Characterization and screening of bacteria from rhizosphere of rice grown in acidic soils of Assam. Current Science, 978–985.

Thamsiriroj, T., Murphy, J.D., 2011. Modelling mono-digestion of grass silage in a 2-stage CSTR anaerobic digester using ADM1. Bioresource Technology 102 (2), 948–959.

Theilliol, D., Ponsart, J.C., Harmand, J., Join, C., Gras, P., 2003. On-line estimation of unmeasured inputs for anaerobic wastewater treatment processes. Control Engineering Practice 11 (9), 1007–1019.

Theofanous, T., Houze, R., Brumfield, L., 1976. Turbulent mass transfer at free, gas–liquid interfaces, with applications to open-channel, bubble and jet flows. International Journal of Heat and Mass Transfer 19 (6), 613–624.

Timilsina, G., Sherestha, A., 2011. How much hope should we have for biofuels? Energy 36, 2055–2069.

Tizaoui, C., Bickley, R., Slater, M., Wang, W., Ward, D., Al-Jaberi, A., 2008. A comparison of novel ozone-based systems and photocatalysis for the removal of water pollutants. Desalination 227 (1–3), 57–71.

Tomiyasu, H., Fukutomi, H., Gordon, G., 1985. Kinetics and mechanism of ozone decomposition in basic aqueous solution. Inorganic Chemistry 24 (19), 2962–2966.

Tong, S.-P., Yu, S., Gao, Y., Ma, C.-A., 2013. Effect of inorganic ions on the oxidative efficiency of ti (iv)-catalyzed h2o2/o3 process in the pH range of 1.0 to 6.0. Ozone: Science & Engineering 35 (5), 359–365.

Torlapati, J., Boufadel, M.C., 2014. Evaluation of the biodegradation of Alaska North Slope oil in microcosms using the biodegradation model BIOB. Frontiers in Microbiology 5, 212–216.

Tornambè, A., 1989. Use of asymptotic observers having-high-gains in the state and parameter estimation. In: Proceedings of the 28th IEEE Conference on Decision and Control, 1989. IEEE, pp. 1791–1794.

Torres, L.G., Carpinteyro-Urban, S.L., Vaca, M., 2012. Use of prosopis laevigata seed gum and opuntia ficus-indica mucilage for the treatment of municipal wastewaters by coagulation–flocculation. Natural Resources 3 (2), 75–96.

Traczewska, T., 2000. Changes of toxicological properties of biodegradation products of anthracene and phenanthrene. Water Science and Technology 41 (12), 31–38.

Trapido, M., Veressinina, J., Munter, R., 1994. Ozonation and AOP treatment of phenanthrene in aqueous solutions. Ozone: Science & Engineering 16 (6), 475–485.

Trapido, M., Veressinina, Y., Munter, R., 1995. Ozonation and advanced oxidation processes of polycyclic aromatic hydrocarbons in aqueous solutions-a kinetic study. Environmental Technology 16 (8), 729–740.

Trapido, M., Hirvonen, A., Veressinina, Y., Hentunen, J., Munter, R., 1997. Ozonation, ozone/uv and uv/h2o2 degradation of chlorophenols. Ozone: Science & Engineering.

Trebouet, D., Schlumpf, J., Jaouen, P., Quemeneur, F., 2001. Stabilized landfill leachate treatment by combined physicochemical-nanofiltration processes. Water Research 35 (12), 2935–2942.

Tsang, Y., Hua, F., Chua, H., Sin, S., Wang, Y., 2007. Optimization of biological treatment of paper mill effluent in a sequencing batch reactor. Biochemical Engineering Journal 34 (3), 193–199.

Tukaj, Z., Aksmann, A., 2007. Toxic effects of anthraquinone and phenanthrenequinone upon scenedesmus strains (green algae) at low and elevated concentration of co 2. Chemosphere 66 (3), 480–487.

Tünay, O., Erdeml, E., Kabdaşli, I., Ölmez, T., 2008. Advanced treatment by chemical oxidation of pulp and paper effluent from a plant manufacturing hardboard from waste paper. Environmental Technology 29 (10), 1045–1051.

Ugwu, C., Aoyagi, H., Uchiyama, H., 2008. Photobioreactors for mass cultivation of algae. Biore 99, 4021–4028.

Ünlü, S., Alpar, B., 2006. Distribution and sources of hydrocarbons in surface sediments of Gemlik bay (Marmara sea, Turkey). Chemosphere 64 (5), 764–777.

USEPA, 2014. Cercla. URL www.atsdr.cdc.gov.

Utkin, V., 1992. Sliding Modes in Control Optimization. Springer Verlag, Berlin.

Utkin, V., 1993. Sliding mode control design principles and applications to electric drives. IEEE Transactions on Industrial Electronics 40 (1), 23–26.

Utkin, V., Guldner, J., Shi, J., 1999. Sliding Modes in Electromechanical Systems. Taylor & Francis, London.

Valsania, M.C., Fasano, F., Richardson, S.D., Vincenti, M., 2012. Investigation of the degradation of cresols in the treatments with ozone. Water Research 46 (8), 2795–2804.

van den Wijngaard, A.J., Prins, J., Smal, A.J., Janssen, D.B., 1993. Degradation of 2-chloroethylvinylether by ancylobacter aquaticus ad25 and ad27. Applied and Environmental Microbiology 59 (9), 2777–2783.

van Heeswijk, W.C., Westerhoff, H., Boogerd, F.C., 2013. Nitrogen assimilation in escherichia coli: putting molecular data into a systems perspective. Microbiology and Molecular Biology Reviews 77 (4), 628–695.

Vazquez-Rodriguez, G., Youssef, C.B., Waissman-Vilanova, J., 2006. Two-step modeling of the biodegradation of phenol by an acclimated activated sludge. Chemical Engineering Journal 117 (3), 245–252.

Vega, S., Ortiz, R., Gutiérrez, R., Gibson, R., Schettino, B., 2012. Presence of polycyclic aromatic hydrocarbons (PAHs) in semi-rural environment in Mexico City. In: Fossil Fuel and the Environment. InTech.

Velegraki, T., Nouli, E., Katsoni, A., Yentekakis, I.V., Mantzavinos, D., 2011. Wet oxidation of benzoic acid catalyzed by cupric ions: key parameters affecting induction period and conversion. Applied Catalysis B: Environmental (ISSN 0926-3373) 101 (3), 479–485. https://doi.org/10.1016/j.apcatb.2010.10.019. http://www.sciencedirect.com/science/article/pii/S0926337310004662.

Venosa, A.D., Lee, K., Suidan, M.T., Garcia-Blanco, S., Cobanli, S., Moteleb, M., Haines, J.R., Tremblay, G., Hazelwood, M., 2002. Bioremediation and biorestoration of a crube oil-contaminated freshwater wetland on the St. Lawrence River. Bioremediation Journal 6 (3), 261–281.

Verenich, S., Kallas, J., 2001. Coagulation as a post-treatment process for wet oxidation of pulp and paper mill circulation waters. Chemical Engineering & Technology 24 (11), 1183–1188.

Verma, A.K., Dash, R.R., Bhunia, P., 2012. A review on chemical coagulation/flocculation technologies for removal of colour from textile wastewaters. Journal of Environmental Management 93 (1), 154–168.

Vinodgopal, K., Kamat, P.V., 1995. Enhanced rates of photocatalytic degradation of an azo dye using SnO2/TiO2 coupled semiconductor thin films. Environmental Science & Technology 29 (3), 841–845.

Vinu, R., Madras, G., 2012. Environmental remediation by photocatalysis. Journal of the Indian Institute of Science 90 (2), 189–230.

Vrbaski, T., Cvetanović, R., 1960. Relative rates of reaction of ozone with olefins in the vapor phase. Canadian Journal of Chemistry 38 (7), 1053–1062.

Walcott, B., 1990. State observation of nonlinear control systems via the method of Lyapunov. In: Deterministic Control of Uncertain Systems, vol. 40, p. 333.

Walcott, B., Zak, S., 1987. State observation of nonlinear uncertain dynamical systems. IEEE Transactions on Automatic Control 32 (2), 166–170.

Walcott, B., Corless, M., Żak, S., 1987. Comparative study of non-linear state-observation techniques. International Journal of Control 45 (6), 2109–2132.

Walcott, B.L., Zak, S.H., 1988. Combined observer-controller synthesis for uncertain dynamical systems with applications. IEEE Transactions on Systems, Man, and Cybernetics 18 (1), 88–104.

Wang, B., Gu, L., Ma, H., 2007. Electrochemical oxidation of pulp and paper making wastewater assisted by transition metal modified kaolin. Journal of Hazardous Materials 143 (1), 198–205.

Wang, C.C., Lee, C.M., Kuan, C.H., 2000. Removal of 2,4-dichlorophenol by suspended and immobilized bacillus insolitus. Chemosphere 41 (3), 447–452.

Wang, F., El-Din, M.G., Smith, D., 2004. Oxidation of aged raw landfill leachate with o3 only and o3/h2o2: treatment efficiency and molecular size distribution analysis. Ozone: Science & Engineering 26 (3), 287–298.

Wang, J., Zhang, X., Li, G., 2012. Effects of ozonation on soil organic matter of contaminated soil containing residual oil. Journal of Soils and Sediments 12 (2), 117–127.

Wang, L.X., Mendel, J.L., 1992. Fuzzy basic functions, universal approximation and orthogonal least squares. IEEE Transactions on Neural Networks 3, 807–814.

Wang, P., Huang, B., Zhang, Q., Zhang, X., Qin, X., Dai, Y., Zhan, J., Yu, J., Liu, H., Lou, Z., 2010. Highly efficient visible light plasmonic photocatalyst ag@ ag (br, i). Chemistry-A European Journal 16 (33), 10042–10047.

Wang, S., Shiraishi, F., Nakano, K., 2002a. A synergistic effect of photocatalysis and ozonation on decomposition of formic acid in an aqueous solution. Chemical Engineering Journal 87 (2), 261–271.

Wang, Y., Zhao, H., Chai, S., Wang, Y., Zhao, G., Li, D., 2013. Electrosorption enhanced electro-Fenton process for efficient mineralization of imidacloprid based on mixed-valence iron oxide composite cathode at neutral pH. Chemical Engineering Journal 223, 524–535.

Wang, Z.-p., Zhang, Z., Lin, Y.-j., Deng, N.-s., Tao, T., Zhuo, K., 2002b. Landfill leachate treatment by a coagulation–photooxidation process. Journal of Hazardous Materials 95 (1), 153–159.

Wei, G., Yu, J., Zhu, Y., Chen, W., Wang, L., 2008. Characterization of phenol degradation by rhizobium sp. ccnwtb 701 isolated from astragalus chrysopteru in mining tailing region. Journal of Hazardous Materials 151 (1), 111–117.

Welander, U., Henrysson, T., 1998. Physical and chemical treatment of a nitrified leachate from a municipal landfill. Environmental Technology 19 (6), 591–599.

Wen, G., Ma, J., Liu, Z.-Q., Zhao, L., 2011. Ozonation kinetics for the degradation of phthalate esters in water and the reduction of toxicity in the process of o3/h2o2. Journal of Hazardous Materials 195, 371–377.

Werker, A., Hall, E.R., 1999. Limitations for biological removal of resin acids from pulp mill effluent. Water Science and Technology 40 (11–12), 281–288.

Westerhoff, P., Aiken, G., Amy, G., Debroux, J., 1999. Relationships between the structure of natural organic matter and its reactivity towards molecular ozone and hydroxyl radicals. Water Research 33 (10), 2265–2276.

Wicks, M.A., Peleties, P., DeCarlo, R.A., 1994. Construction of piecewise Lyapunov functions for stabilizing switched systems. In: Proceedings of the 33rd Conference on Decision and Control. Lake Buena Vista, FL, USA, pp. 3492–3497.

Wilcke, W., 2007. Global patterns of polycyclic aromatic hydrocarbons (PAHs) in soil. Geoderma 141 (3), 157–166.

Williamson, D., 1977. Observation of bilinear systems with application to biological control. Automatica 13 (3), 243–254.

Wright, P.C., Meeyoo, V., Soh, W.K., 1998. A study of ozone mass transfer in a cocurrent downflow jet pump contactor. Ozone: Science & Engineering.

Wu, J., Xiao, Y.-Z., Yu, H.-Q., 2005. Degradation of lignin in pulp mill wastewaters by white-rot fungi on biofilm. Bioresource Technology 96 (12), 1357–1363.

Xia, X.-H., Gao, W.-B., 1989. Nonlinear observer design by observer error linearization. SIAM Journal on Control and Optimization 27 (1), 199–216.

Xiao, J., Xie, Y., Cao, H., 2015. Organic pollutants removal in wastewater by heterogeneous photocatalytic ozonation. Chemosphere 121, 1–17.

Xing, S., Hu, C., Qu, J., He, H., Yang, M., 2007. Characterization and reactivity of mno x supported on mesoporous zirconia for herbicide 2, 4-d mineralization with ozone. Environmental Science & Technology 42 (9), 3363–3368.

Xu, P., Janex, M.-L., Savoye, P., Cockx, A., Lazarova, V., 2002. Wastewater disinfection by ozone: main parameters for process design. Water Research 36 (4), 1043–1055.

Yan, J., Jianping, W., Hongmei, L., Suliang, Y., Zongding, H., 2005. The biodegradation of phenol at high initial concentration by the yeast candida tropicalis. Biochemical Engineering Journal 24 (3), 243–247.

Yan, M., Wang, D., Shi, B., Wang, M., Yan, Y., 2007a. Effect of pre-ozonation on optimized coagulation of a typical north-china source water. Chemosphere 69 (11), 1695–1702.

Yan, W., Utkin, V., Xu, L., 2007b. Sliding mode pulse modulation. In: Proceedings of the 2007 American Control Conference. New York, USA.

Yang, L., Hu, C., Nie, Y., Qu, J., 2010. Surface acidity and reactivity of β-feooh/Al2O3 for pharmaceuticals degradation with ozone: in situ ATR-FTIR studies. Applied Catalysis B: Environmental 97 (3–4), 340–346.

Yaz, E., Azemi, A., 1994. Robust/adaptive observers for systems having uncertain functions with unknown bounds. In: American Control Conference, 1994, vol. 1. IEEE, pp. 73–74.

Yeber, M., Rodríguez, J., Freer, J., Baeza, J., Durán, N., Mansilla, H.D., 1999. Advanced oxidation of a pulp mill bleaching wastewater. Chemosphere 39 (10), 1679–1688.

Yershov, B., Morozov, P., Gordeev, A., Seliverstov, A., 2009. Kinetic regularities of ozone decomposition in water. Journal of Water Chemistry and Technology 31 (6), 381–388.

Yordanov, R., Melvin, M., Law, S., Littlejohn, J., Lamb, A., 1999. Effect of ozone pretreatment of colored upland water on some biological parameters of sand filters. Ozone: Science & Engineering 21 (6), 615–628.

Yu, D., Shields, D.N., 1996. A bilinear fault detection observer. Automatica 32 (11), 1597–1602.

Zamudio-Pérez, E., Torres, L.G., Chairez, I., 2014. Two-stage optimization of coliforms, helminth eggs, and organic matter removals from municipal wastewater by ozonation based on the response surface method. Ozone: Science & Engineering 36 (6), 570–581.

Zayas, T., Rómero, V., Salgado, L., Meraz, M., Morales, U., 2007. Applicability of coagulation/flocculation and electrochemical processes to the purification of biologically treated vinasse effluent. Separation and Purification Technology 57 (2), 270–276.

Zeitz, M., 1987. The extended Luenberger observer for nonlinear systems. Systems & Control Letters 9 (2), 149–156.

Zeng, Y., Hong, P.A., 2002. Slurry-phase ozonation for remediation of sediments contaminated by polycyclic aromatic hydrocarbons. Journal of the Air & Waste Management Association 52 (1), 58–68.

Zhang, H., Ji, L., Wu, F., Tan, J., 2005. In situ ozonation of anthracene in unsaturated porous media. Journal of Hazardous Materials 120 (1), 143–148.

Zhang, H., Zhang, D., Zhou, J., 2006. Removal of cod from landfill leachate by electro-Fenton method. Journal of Hazardous Materials 135 (1), 106–111.

Zhang, L., He, M., Liu, J., 2014. The enhancement mechanism of hydrogen photoproduction in chlorella protothecoides under nitrogen limitation and sulfur deprivation. International Journal of Hydrogen Energy 39 (17), 8969–8976.

Zhang, T., Guay, M., 2002. Adaptive nonlinear observers of microbial growth processes. Journal of Process Control 12 (5), 633–643.

Zhang, T., Li, W., Croué, J.-P., 2012. A non-acid-assisted and non-hydroxyl-radical-related catalytic ozonation with ceria supported copper oxide in efficient oxalate degradation in water. Applied Catalysis B: Environmental 121, 88–94.

Zhang, Z., Hong, H., Zhou, J., Yu, G., 2004. Phase association of polycyclic aromatic hydrocarbons in the Minjiang River Estuary, China. Science of the Total Environment 323 (1), 71–86.

Zhao, G., Zhou, L., Li, Y., Liu, X., Ren, X., Liu, X., 2009a. Enhancement of phenol degradation using immobilized microorganisms and organic modified montmorillonite in a two-phase partitioning bioreactor. Journal of Hazardous Materials 169 (1), 402–410.

Zhao, L., Sun, Z., Ma, J., 2009b. Novel relationship between hydroxyl radical initiation and surface group of ceramic honeycomb supported metals for the catalytic ozonation of nitrobenzene in aqueous solution. Environmental Science & Technology 43 (11), 4157–4163.

Zhou, H., Smith, D.W., Stanley, S., 1994. Modeling of dissolved ozone concentration profiles in bubble columns. Journal of Environmental Engineering 120 (4), 821–840.

Zhu, R., Chai, T., Shao, C., 1997. Robust nonlinear adaptive observer design using dynamic recurrent neural networks. In: Proceedings of the American Control Conference, 1997, vol. 2. IEEE, pp. 1096–1100.

Zienkiewicz, O.C., Taylor, R.L., Zienkiewicz, O.C., Taylor, R.L., 1977. The Finite Element Method, vol. 3. McGraw-Hill, London.

Zou, L., Zhu, B., 2008. The synergistic effect of ozonation and photocatalysis on color removal from reused water. Journal of Photochemistry and Photobiology A: Chemistry 196 (1), 24–32.

Index

P

Q

R

S

T

U

V

W

Ozonation and Biodegradation in Environmental Engineering

Dynamic Neural Network Approach

Ozonation and Biodegradation in Engineering deals with the description of ozonation as a major method for organic contaminant degradation in three different phases: liquid, solid, and gaseous. The book presents in detail both the chemical basis and the mathematical modeling of ozonation. The concept of Dynamic Neural Networks (DNNs) is introduced, which can help the reader to understand how unmeasurable contaminant dynamics may be reconstructed online using information on the ozone concentration in the reactor output only. Ozonation, as a principal treatment method for organic contaminant elimination in water, is considered in detail, including catalytic and photocatalytic ozonation to remove recalcitrant and complex organics. The combination of physical-chemical methods with ozonation is profoundly discussed. In addition, the book presents the automatic control aspects for the optimization of ozonation in liquid phase as well as the kinetics studies of this process, using the DNN approach. The subsequent parts of the book discuss the remediation of contaminated soil and air, including a detailed mathematical model description. The rest of the book deals with the main principles of biodegradation and the advantages of its combination with ozonation to increase the efficiency of each process for the optimization of a joint treatment. All mathematical aspects of modeling and DNN-optimization are in the appendix. A comprehensive list of references concludes the book.

Key features:

- Oriented to researchers in chemical engineering, particularly, environmental engineering, and to those interested in the application of modern results from computer science and automatic control
- Provides a wide list of references for researchers and engineers, helping them to find the information required for their current scientific work
- Effective as a textbook for advanced undergraduate or graduate level courses in environmental engineering and in applied theory of control engineering, computer science, and related areas
- Beneficial to students and working engineers to learn and implement DNN, using inexpensive commercial PC-based software tools

Authors:

Tatyana I. Poznyak, Professor of Environmental Chemical Engineering at SEPI-ESIQIE-IPN, Mexico City, Mexico.

Isaac Chairez Oria, Professor of Bioengineering at SEPI-UPIBI-IPN, Mexico City, Mexico.

Alexander S.Poznyak, Professor of Automatic Control at CINVESTAV-IPN, Mexico City, Mexico.

Technology and Engineering
Chemical and Biochemical

ISBN 978-0-12-812847-3

9 780128 128473

ELSEVIER

elsevier.com/books-and-journals